Aerodynamic interactions of space debris during atmospheric re-entry : experimental study in rarefied flow regime

Vincente Cardona

UNIVERSITÉ D'ORLÉANS

ÉCOLE DOCTORALE
ENERGIE, MATERIAUX, SCIENCES DE LA TERRE ET DE L'UNIVERS

INSTITUT DE COMBUSTION AÉROTHERMIQUE
RÉACTIVITÉ ET ENVIRONNEMENT

THÈSE présentée par :

Vincente CARDONA

soutenue le : **21 Avril 2023**

pour obtenir le grade de : **Docteur de l'Université d'Orléans**

Discipline/ Spécialité : Physique

Aerodynamic interactions of space debris during atmospheric re-entry: experimental study in rarefied flow regime

Interactions aérodynamiques de débris spatiaux lors de la rentrée atmosphérique : étude expérimentale en régime raréfié

THÈSE dirigée par :

Mrs. LAGO Viviana	HDR, CNRS, ICARE, France

RAPPORTEURS :

Mr. LAURENCE Stuart J	Associate Professor, University of Maryland, USA
Mr. MAGIN Thierry	Professor, Von Karman Institute for Fluid Dynamics, Belgique

---

JURY :

Mr. DUDOK DE WIT Thierry	Président du Jury, HDR, Pr. Université d'Orléans, CNRS, France
Mr. CONSTANT Eddy	PhD, RTECH, France
Mr. GALERA Stéphane	PhD, CNES, France
Mr. KOURTA Azeddine	HDR, Pr. Université d'Orléans, PRISME, France
Mrs. VARENNE Marielle	PhD, CEA, CESTA, France

Acknowledgments

First of all, I would like to aknowledge the researches who have kindely accepted to read and evaluate this manuscript, Dr. Stuart J. Laurence and Pr. Thierry Magin. I also am gratefull for the implication of the President of jury, Pr. Thierry Dudok De Wit, and all the jury members, Dr. Eddy Constant, Dr. Stéphane Galera, Pr. Azzedine Kourta and Dr. Marielle Varenne.

These three years of thesis, and the years before, were supported by an important number of advisors, friends and family members. I will express them my gratitude in our shared language.

Cette thèse, cet apprentissage à la recherche, n'aurait rien été sans ma directrice de thèse, Viviana Lago. Je te remercie sincèrement pour m'avoir tant appris, et fait confiance sur ce projet. La "Patronne" de l'équipe FAST est toujours d'attaque pour la réflexion scientifique, et pour les petits tracas du quotidien, et tout cela, bien sûr avec la joie de vivre. Encore merci pour tout ce que tu m'as apporté, j'espère pouvoir un jour te rendre la pareille.

Je souhaite également remercier mes anciens tuteurs, en particulier Dr. Yannick Bury et Dr. Jean-Michel Desse, qui ont révélé, à travers leurs propres passions, mon goût pour la recherche et m'ont encouragée à poursuivre dans cette voie.

Une très grande pensée pour les doctorants de la team FAST, Hugo (Remhy ou Hugon), Léo, et Nico, sans qui l'ambiance de travail n'aurait pas été aussi joviale et les manips pas aussi efficaces. Je remercie aussi Juan Esteban Morales-Martinez et Quentin Stremsdoerfer qui ont contribué activement à mon travail de thèse sur la partie numérique via leur projets étudiants. Merci également à Pascal Lasgorceix, voisin de bureau blagueur, qui, à de nombreuses reprises, a assisté l'équipe sur des difficultés d'ordre électrique.

Une thèse c'est du travail, mais c'est aussi un moment de vie durant lequel on fait des rencontres. J'ai eu la chance de partager ces trois années avec des personnes drôles et attachantes. Je remercie bien évidemment les doctorants et étudiants avec qui j'ai passé la majorité de mon temps : la team FAST bien sûr, et les autres inconditionnels amis du midi : Antoine, Camille, Hugoch, Hugok, Fanny, Giorgia, Maxence, Nell, Nesrine, Samuel, Falentin, Victor. Je ne pourrais pas résumer tous nos fous-rires, nos mots doux, nos désaccords redondants sur les couleurs, nos conversations folles sur les planètes donut... Mais tous ces moments, autour d'un verre, d'une raclette ou d'un jeu de cartes ont été superbes, comme vous ! Vous êtes une vraie petite famille, ma famille Orléanaise.

Maxence, nous avons partagé bien plus que ces agréables moments, et je te remercie du fond du coeur d'être à mes côtés depuis le début de cette aventure. Tu m'as apporté le calme nécessaire à compléter mon grain de folie, et offert un cocon chaleureux. Tu m'as supportée, même pendant mes périodes de stress, et pour cela tu mérites une médaille d'Or !

Enfin, j'ai une grande pensée pour mes parents, mon frère et Valérian, qui m'ont toujours encouragée à

poursuivre mes envies. Vous m'avez soutenue de manière inconditionnelle, sans douter de mes choix, et je n'aurais jamais les mots suffisants pour vous remercier.

Chacun à votre manière, vous avez contribué à l'aboutissement de ce travail, et je vous en suis très reconnaissante.

Contents

List of Figures

List of Tables

Nomenclature

Latin letters

$\vec{a}$	Acceleration vector (m.s^{-2})
C_1 to C_6	Sphere couples
Cd	Drag coefficient
Cd_f	Drag coefficient due to friction contribution
Cd_p	Drag coefficient due to pressure contribution
Cl	Lift coefficient
Cl_f	Lift coefficient due to friction contribution
Cl_p	Lift coefficient due to pressure contribution
d	Distance to the surface of a sphere
$\vec{D_F}$	Displacement vector (N)
$\vec{F}$	Resultant force (N)
Fp_x	Pressure force on the sphere surface in the $\vec{x}$-direction (mN)
Fp_z	Pressure force on the sphere surface in the $\vec{z}$-direction (mN)
$\vec{F_x}$	Drag force (N)
$\vec{F_z}$	Lift force (N)
g	Acceleration due to gravity 9.81m.s^{-2}
I	Luminous intensity
Kn	Knudsen number
L	Characteristic length (m)
m	Mass (g)
Ma	Mach number
M_m	Molar mass (kg.mol^{-1})
N1, N2, N3	Nozzles
p	Pressure (Pa)
p_{02}	Pressure after shock (Pa)
P	Spatial point
R	Radius (m)
r	Radius (m)
Re	Reynolds number

Re_2	Reynolds number after shock
R_m	Specific gas constant ($m^2.s^{-2}.K^{-1}$)
R_s	Altitude of the middle of shock for a given longitudinal distance (m)
S	Sphere
S	Reference area (m^2)
$\vec{T}$	Tension force (N)
Te	Temperature (K)
U	Electric signal (mV/V)
V	Flow speed ($m.s^{-1}$)
X	Longitudinal distance (m)
Z	Vertical distance (m)
$\vec{W}$	Weight vector (N)

Greek letters

α	Angle of the wire in the swinging sphere technique
β	Angle of incident shock (°)
Δ	Stand-off distance
γ	Adiabatic coefficient
λ	Mean free path
μ	Dynamic viscosity (Pa.s)
$\emptyset$	Sphere diameter
ρ	Density ($kg.m^{-3}$)
σ	Similarity number
Θ_i	Angle formed between P_i and the centre of a sphere towards the horizontal (°)
Θ_{ml}	Angle formed between P_{ml} and the centre of a sphere towards the horizontal (°)
Θ_{wp}	Measurement angle of the wall pressure at the surface of the sphere (°)
ω	Viscosity-temperature index

Subscripts

∞	Free-stream parameter
0	Nose of a sphere
1	First sphere
2	Second sphere
i	Intersection point between the middle of incident shock waves and the middle of the bow shock
loc	Local parameter
ml	Most luminous point
ref	Reference case
w	Wall measurement

Acronyms

ADR	Active Debris Removal
ASI	*Agenzia Spaziale Italiana*
AUPC	Area Under the Curve of wall Pressure distribution
BGK	Bhatnagar-Gross-Krook
BL	Boundary Layer
CLL	Cercignani-Lampis-Lord
CNES	*Centre National des Etudes Spatiales*
CNRS	*Centre National de la Recherche Scientifique*
CNSA	China National Space Administration
CSA	Canadian Space Agency
DLR	*Deutsches Zentrum für Luft- und Raumfahrt*
DSMC	Direct Simulation Monte Carlo
ESA	European Space Agency
FRIPON	Fireball Recovery and InterPlanetary Observation Network
FS	Foot of Shock
FSD	Fourier Self-Deconvolution
GEO	Geostationary Earth Orbit
GRAVES	*Grand Réseau Adapté à la VEille Spatiale*
IADC	Inter-Agency Space Debris Coordination Committee
ICARE	*Institut de Combustion, Aérothermique, Réactivité et Environnement*
IR	InfraRed
ISRO	Indian Space Research Organisation
ISS	International Space Station
JAXA	Japan Aerospace Exploration Agency
KARI	Korea Aerospace Research Institute
LCSR	*Laboratoire de Combustion et des Systèmes Réactifs*
LEO	Low Earth Orbit
MARHy	*Mach Adaptable Raréfié Hypersonique*
MS	Middle of shock
MSISE	Mass Spectrometer - Incoherent Scatter
NASA	National Aeronautics and Space Administration
PIV	Particle Image Velocimetry
POM	PolyOxyMethylene
ROSCOSMOS	Russian Space State Corporation
RSSS	Russian Space Surveillance System
SPARTA	Stochastic PArallel Rarefied-gas Time-accurate Analyzer
SSAU	State Space Agency of Ukraine

SSI	shock/shock interferences
SSN	Space Surveillance Network
SSON	Sapienza Space debris Observatory Network
UKSA	United Kingdom Space Agency
USA	United States of America
USSR	Union of Soviet Socialist Republics
UV	Ultra Violet

Summary

English

During the atmospheric re-entry, space debris can fragment and generate a cloud of smaller debris. In the debris cloud, the fragments evolving in close proximity to each other can have different behaviours: either they do not interact and thus they evolve independently, or they interact and their aerodynamics are modified. In the case of a fragment evolving behind a parent piece of debris, the interactions between debris can result in the modification of the aero-thermodynamic conditions perceived by the following fragment. Among the many relative positions that can take the two debris, the fragment can suffer from harsher conditions or benefit less severe conditions depending on if it is located on the shock-wave of its parent or into its wake. In both cases, the aerodynamics of the fragment is different from its behaviour in free-stream and thus its trajectory is modified.
Since the first studies on the atmospheric re-entry, the aerodynamic interactions between fragments are known to play an important role in debris survival and in their change of trajectory. The fragmentation of space debris generally occurs between 90 and 65 km, where the environment properties are different from Earth's ground. At these altitudes, the density of air molecules and the pressure are so low that the physics of fluids is different. This rarefied regime (slip and transition) has such a repercussion on the flow, that at this time, there is still a certain lack of knowledge.
Due to the fragmentation, to the increasing number of fragments and to aerodynamic interactions and to the physics of rarefied flows, there is a large dispersion of fragments, still not well predictable. Their impact area and time are not accurately determined, which constitutes a major security issues whether for the population, the environment or built structures. To better predict the ground risks induced by the atmospheric re-entry of space debris, it is necessary to qualitatively estimate the effects of aerodynamic interactions between the debris.

The main objective of the work presented is to estimate the effect of aerodynamic interactions between fragments of debris just after its fragmentation, *i.e.* at high altitude. This thesis presents experimental results concerning the effect of interactions between two spheres on the aerodynamics of secondary debris. The experiments were conducted with spheres of various sizes, in different rarefied flows, characterised by the Knudsen number. The MARHy wind tunnel, a low-density facility can generate flows of different Mach numbers and densities. The aerodynamic interactions were studied in three flow conditions: Mach 4 - 2.67 Pa, Mach 4 - 8 Pa, Mach 20 - 0.07 Pa.
Results were obtained with several diagnostics, each one giving different information to build a complete database. The flow visualisation with the glow discharge technique, along with a shock-wave detection method adapted for rarefied flows, allowed to identify different types of shock/shock interferences and to obtain a first idea of their physics. The use of an aerodynamic balance enabled to measure the drag and lift forces experienced by the following sphere. A pendulum method was developed and validated to measure more quickly the drag force of the following sphere, allowing mapping it on a large set of relative positions. Previous results were also correlated with the measurement of wall pressures and heat flux. The develop-

ment of an electron beam gun finally allowed to measure local density in the near area of the following sphere.

With these diagnostics and methods, the aerodynamic interactions were studied for different Mach numbers and Knudsen numbers. Three main analyses were conducted, demonstrating the impact of the global rarefaction level, of the local rarefaction level, and of the free-stream velocity on the aerodynamic interactions between two spheres.

This work has been conducted as part of the project IPROF fully funded by the Agence National de la Recherche: ANR-19-CE39-0003-01.

Experimental hours

The number of hours corresponding to experimental work, i.e. working hours of the MARHy wind tunnel, is presented in Figure 1. The total number of hours is of 540 hours, which does not take into account the conception of the models and the setting-up of the experiments.

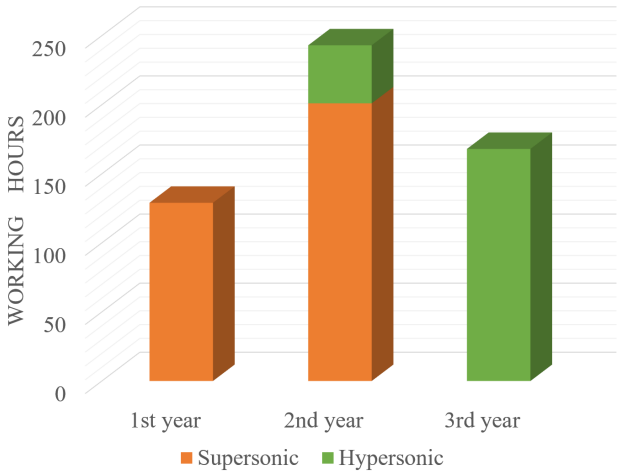

Figure 1: Working hours of the MARHy wind tunnel.

Publications

V Cardona, R Joussot and V Lago. "Shock/shock interferences in a supersonic rarefied flow: experimental investigation". In: *Experiments in Fluids* 62.6 (2021), pp. 1–14. doi:https://doi.org/10.1007/s00348-021-03225-4.

V Cardona and V Lago. "Aerodynamic forces of interacting spheres representative of space debris re-entry: Experiments in a supersonic rarefied wind-tunnel". In: *Acta Astronautica* 191 (2022), pp. 148–159. doi:https://doi.org/10.1016/j.actaastro.2021.10.036.

Conferences

V Cardona and V Lago. "Interaction aérodynamique entre deux sphères représentatives de la rentrée atmosphérique: étude expérimentale en régime supersonique raréfié". *Hypersonique des Ecoulements Raréfiés workshop (HERA)*, Fauga-Mauzac, France, Octobre 2021.

V Cardona and V Lago. “The effect of rarefaction level on shock/shock interferences applied to atmospheric re-entry: Experimental study in a supersonic rarefied flow”. In: *2nd International Conference on Flight Vehicles, Aerothermodynamics and Re-entry Missions Engineering (FAR)*, Heilbronn, Germany, June 2022.

V Cardona and V Lago. “Experimental Study of Shock/Shock Interferences in a Hypersonic Mach 20.2 Rarefied Flow”. In: *2nd International Conference on High-Speed Vehicle Science and Technology (HiSST)*, Bruges, Belgium, September 2022.

Science popularization

As a young woman from the countryside, I know how much it is important to give a testimony of our professions to encourage teenagers, girls or boys, to consider scientific carrier. In this idea, I strongly think that science popularization, which is meant for everyone, everywhere, can open doors. During this three years doctoral period, I contributed to different events:

- Regional finalist of the French-speaking competition MT180 (180 seconds to described a doctoral subject): https://www.youtube.com/live/60NQHDCpRGo?feature=share&t=4917,

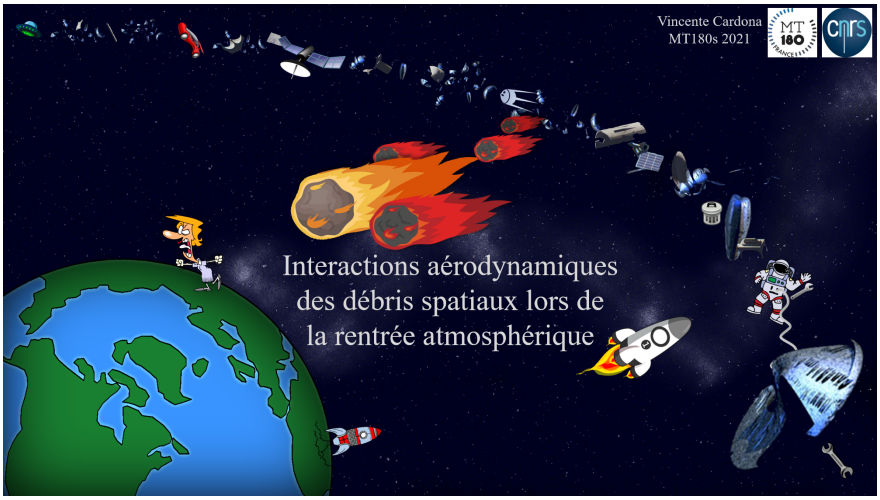

Figure 2: MT180.

- Intervention in teenage school classes with the association "Les cordées de la réussite",
- Member of the association "Agence Vertiges" whose purpose is to build an artistic teaching of science, with the reflection of a large panel of professions.

Français

Lors de la rentrée atmosphérique, les débris spatiaux peuvent se fragmenter et créer un nuage de débris plus petits. Dans ce nuage, les fragments évoluant à proximité les uns des autres peuvent avoir différents comportements: soit ils n’intragissent pas, ainsi chacun évolue indépendamment, soit ils interagissent, et alors leurs aérodynamiques est modifiée. Dans le cas où un fragment (ou débris secondaire) évolue derrière un débris parent (ou débris primaire), les interactions entre débris peuvent se traduire par une modification des conditions aérothermodynamiques perçues par le débris secondaires. Parmi les différentes positions

relatives que peuvent prendre les deux débris, le débris secondaire peut souffrir de conditions plus sévères ou bénéficier de conditions plus souples selon s'il est positionné sur l'onde de choc du débris primaire ou s'il est localisé dans son sillage. Dans les deux cas, l'aérodynamique du débris secondaire est différente de son comportement en écoulement libre et donc sa trajectoire s'en voit modifiée.
Depuis les toutes premières études sur la rentrée atmosphérique, les interactions aérodynamiques entre débris sont connues pour jouer un rôle important dans la survie des débris et dans leur changement de trajectoire. La fragmentation des débris spatiaux se produit généralement entre 90 et 65 km, où les propriétés de l'environnement sont différentes de celles observées au niveau de la mer. A ces altitudes, la densité des molécules d'air et la pression sont si faibles que la physique des fluides est différente. Ce régime raréfié (glissement et transition) a une telle répercussion sur l'écoulement, qu'à l'heure actuelle, il existe encore un certain manque de connaissances.
En raison de la fragmentation, du nombre croissant de fragments, des interactions aérodynamiques et de la physique des écoulements raréfiés, il existe une grande dispersion des fragments, encore peu prévisible. La zone et le moment de leur impact ne sont pas déterminés avec précision, ce qui constitue un problème de sécurité majeur, que ce soit pour la population, l'environnement ou les infrastructures de la planète. Afin de mieux prédire les risques au sol induits par la rentrée atmosphérique des débris spatiaux, il est nécessaire d'estimer qualitativement les effets des interactions aérodynamiques entre les débris.

L'objectif principal du travail exposé est d'estimer l'effet des interactions aérodynamiques entre les fragments d'un débris juste après sa fragmentation, c'est-à-dire à haute altitude. Cette thèse de doctorat expose des résultats expérimentaux concernant l'effet des interactions entre deux sphères sur l'aérodynamique du débris secondaire. Les expériences ont été menées avec des sphères de tailles variables, dans différents écoulements raréfiés, caractérisés par le nombre de Knudsen. La soufflerie MARHy, une installation à faible densité, peut générer des écoulements de différents nombres de Mach et densités. Les interactions aérodynamiques ont été étudiées dans quatre conditions d'écoulement : Mach 4 - 2,67 Pa, Mach 4 - 8 Pa, Mach 20,2 - 0,07 Pa.
Les résultats ont été obtenus avec plusieurs diagnostics, chacun donnant des informations différentes pour construire une base de données complète. La visualisation de l'écoulement avec la technique de décharge luminescente, ainsi qu'une méthode de détection des ondes de choc adaptée aux écoulements raréfiés, ont permis d'identifier différents types d'interférences choc/choc et d'obtenir une première idée de leur comportement physique. L'utilisation d'une balance aérodynamique a permis de mesurer les forces de traînée et de portance subies par la sphère secondaire. Une méthode de pendule a été développée et validée pour mesurer plus rapidement la force de traînée de la sphère secondaire, permettant de la cartographier sur un large ensemble de positions relatives. Les résultats précédents ont également été corrélés avec la mesure des pressions pariétales et du flux thermique. Le développement d'un canon à électrons a enfin permis de mesurer la densité locale dans la zone proche de la sphère suivante.

Grâce à ces diagnostics et méthodes, les interactions aérodynamiques ont été étudiées pour différents nombres de Mach et de Knudsen. Trois analyses principales ont été menées, démontrant l'impact du niveau de raréfaction global, du niveau de raréfaction local et de la vitesse du flux libre sur les interactions aérodynamiques entre deux sphères.

Ces travaux ont été réalisés dans le cadre du projet IPROF entièrement financé par l'Agence National de la Recherche: ANR-19-CE39-0003-01.

Part I

Motivation of the Study

Partie I
Résumé en Français

Cette partie s'intéresse aux motivations du sujet de la thèse. Elle est composée de trois chapitres qui exposent le contexte de l'étude, l'état de l'art en matière de rentrées atmosphériques, et enfin l'apport scientifique de ce travail de thèse.

Chapitre 1

Les rapports scientifiques sont clairs, l'activité spatiale montre une croissance exponentielle. Le nombre de charges utiles envoyées dans l'espace chaque année ne fait qu'augmenter. Ceci est principalement dû aux nouvelles activités commerciales, notamment à la mise en orbite de constellations de satellites. Depuis le début de la course à l'espace, les vaisseaux spatiaux s'accumulent. Malheureusement, envoyer des objets dans l'espace est une activité qui génère des débris. Lors du lancement, la fusée se décompose petit à petit, se délestant de différents étages, de sa coiffe… Puis vient la fin de vie de la charge utile, devenant elle aussi un débris spatial. Malheureusement, ces objets ne sont plus contrôlables, et encombrent les orbites terrestres. De nombreux réseaux de surveillance sont mis en place aux moyens de télescopes visuels et radios. Aujourd'hui, sur le nombre total d'objets en orbite, on compte seulement une trentaine de pourcent des satellites actifs. Ceci pose un réel problème en orbite. Les débris peuvent rentrer en collision avec d'autres débris, ou même satellites, ce qui ne fait qu'accroître leur nombre. Les agences spatiales, conscientes du problème, ont mis en place un grand nombre de recommandations pour réduire la génération de nouveaux débris, imposant aux compagnies de modifier la conception et la gestion des nouvelles missions spatiales. De plus, de nombreuses équipes scientifiques se penchent sur diverses solutions qui pourrait améliorer la situation en orbite, telles que la collecte active des débris, des manœuvres d'évitement des débris, ou encore la réduction de la durée de vie moyenne en orbite, notamment par le biais de la rentrée atmosphérique, solution privilégiée. Malheureusement la rentrée atmosphérique engendre un risque terrestre important, que ce soit au niveau humain, rural ou environnemental. Pour limiter ce risque, il est nécessaire de connaître, avec précision, la zone et l'heure d'impact. De multiples études tentent d'améliorer les prévisions, mais dû à différents paramètres, l'exercice s'avère plus difficile qu'un simple calcul de trajectoire. En effet, la majorité des études considèrent que les débris rentrent dans l'atmosphère à des altitudes de l'ordre de 90 km. A ces altitudes, l'air est dit raréfié, ce qui lui confère des propriétés aérothermodynamiques ne répondant plus à la mécanique des fluides classique décrite par les équations de Navier-Stokes. De plus, les fortes contraintes thermiques, ainsi que la densification de l'air, provoquent la fragmentation des débris pénétrant l'atmosphère à des vitesses supersoniques. Les fragments naissants vont alors interagir entre eux, et probablement s'influencer les uns, les autres, modifiant leurs trajectoires. Ainsi les propriétés de l'air et la configuration des nuages de débris augmentent les difficultés de prévisions d'impact.

Chapitre 2

Ce chapitre approfondie la physique derrière les rentrées atmosphériques, par le biais d'une étude bibliographique approfondie. Deux parties seront présentées : l'une concerne l'étude des écoulements raréfiés, alors que l'autre se penche sur l'étude de corps en interactions. Dans la première partie, la théorie des écoulements raréfiés est brièvement abordée, montrant qu'aujourd'hui encore, les connaissances de ce milieu ne sont pas suffisantes. Cela se répercute sur les résultats obtenus avec les divers codes de calculs développés spécifiquement pour les écoulements raréfiés. Des données expérimentales pourraient permettre de répondre à un certain nombre de questions, même si les souffleries ne permettent pas de reproduire l'intégralité de la physique des rentrées atmosphériques. Dans la deuxième partie, l'étude bibliographique est orientée sur les interactions entre objets, que ce soit en milieu continu ou raréfié. Cette étude révèle en particulier l'importance des interactions choc / choc dans la modification des trajectoires. Des effets de surf sur les ondes de choc ou de sillage sont également responsable de la modification de l'aérodynamique des divers objets. Grâce à une meilleure connaissance des contraintes physiques, nous pourront mieux aborder les difficultés liées à l'interaction de deux corps en milieu raréfié.

Chapitre 3

Avec l'aide de l'étude bibliographique réalisée, la problématique de l'interaction aérodynamique des débris spatiaux lors de leur rentrée atmosphérique est mieux perçue. Ce chapitre aborde les intentions de ce travail de thèse vis-à-vis du sujet. Une explication claire des objectifs à atteindre est donnée, permettant d'élaborer le plan de ce manuscrit.

Chapter 1

Context of the study

Contents

The space race began in the mid-1950s between the United States of America and Russia (USSR at the time) during the Cold War. This space conquest had for the purpose to show the opponent how technologically superior they were and so demonstrate the power of their country. This important challenge was built on the most impossible task at that time: to place a satellite into the Earth's orbit. On October 4, 1957, the Russians were the first to reach their goal with the success mission of Sputnik 1. This day also marked the first space debris that re-entered Earth's atmosphere. Since then, the space race continues, initially in the context of military development, next for scientific exploration, telecommunication, and now also for the space tourism. Every year the quantity of space launch is constantly increasing, as is the amount of space debris.

1.1 The growing problem of space debris

1.1.1 The space debris population

According to the IADC [50], "space debris are all man-made objects including fragments and elements thereof, in Earth orbit or re-entering the atmosphere, that are non-functional". Space debris can be the result of three main causes in the course of the lifetime of a spacecraft: mission-related operations, intentional creation or accidents. Concerning the mission-related operations, we can think of the rocket launch, during which, different parts, such as boosters, stages and payload fairing's separate from the main body, thus becoming uncontrolled objects. In the same idea, at the end-of-life of a satellite, it becomes itself a space debris. Some intentional creation of space debris were reported. In the past, satellite weapons were designed to explode near their target, destroying it with the fragments of shrapnel. The last to use this method was China in 2007, destroying one of its own satellites in space, Fengyun-1C [97]. More recently, we heard about the management of the International Space Station trash, which is dropped in space in a cargo ship in order to be burned while re-entering the atmosphere [90]. In orbit, the formation of debris can also be accidental. For example, when an astronaut works outside the International Space Station, he can lose control of a tool, how it was the case in 2007, when US astronaut Heidemarie Stefanyshyn Piper watched her toolkit floats off into space [54]. However, this kind of accident remains low in comparison with the formation of space debris due to collisions. These collisions occur between two debris, or between a piece of debris and a functional satellite. In any case, the collision leads to their fragmentation into a greater number of smaller debris. In 2009, the first accidental in-orbit collision was reported between Iridium-33 and the inactive Cosmos-2251 satellites, leading to their destruction generating 1850 fragments greater than 10 cm, and potentially more

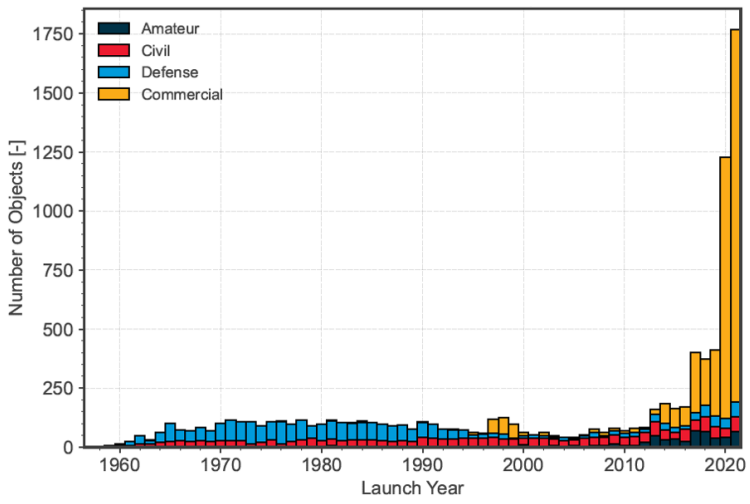

Figure 1.1: Evolution in time of the payload launch traffic in LEO [67].

than 100,000 fragments greater than 1 cm [205].

These last few years, the number of launched payloads in orbit around Earth is considerably increasing (see Figure 1.1), passing from 200 to 1750 per year, in 5 years. From the 2022 annual report of ESA [67], this increase is mostly observed in low Earth orbit (LEO) with a maximal concentration between 500 and 1000 km, and is almost exclusively due to commercial activities. Most of them concern the mega-constellations of satellites from companies such as SpaceX, OneWeb, Telesat or Amazon [154]. Unfortunately, this number will keep increasing, which accentuates the risk of space debris collision. From a 2021 NASA report [150], the graph in Figure 1.2 shows the monthly increase in objects orbiting around Earth.

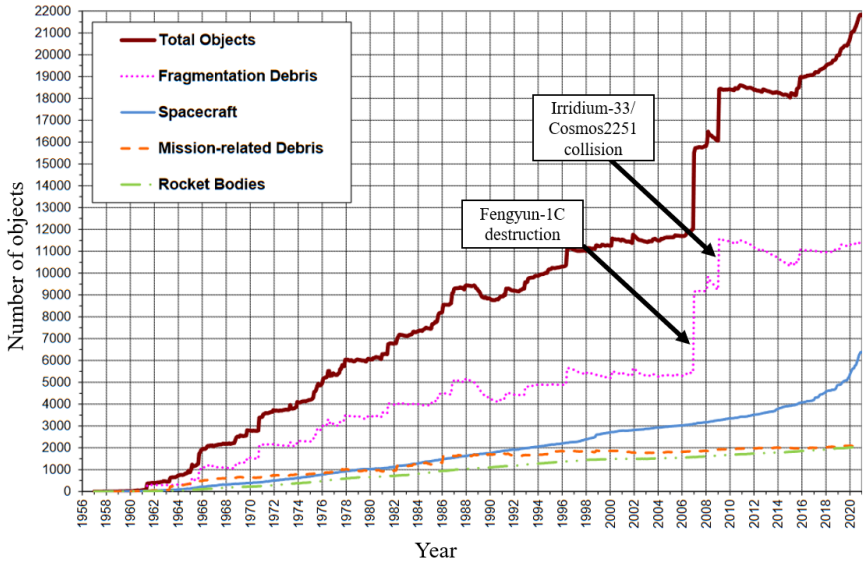

Figure 1.2: Monthly number of objects in Earth Orbit by object type [150].

What is really interesting is to observe that the number of effective spacecraft is representative of about 33% of the object in orbits. As can be seen, the two most important collision/destruction events observed in 2007 and 2009 are clearly marked by a strong increase in the number of detected fragmentation debris. Unfortunately, the massive amount of space debris can lead to the Kessler's syndrome [100]: with a strong density of space debris, the collisions between objects could cause a cascade in which each collision generates space debris that increase, furthermore, their number and thus the number of collisions.

1.1.2 The space debris surveillance

The debris population is actively watched by space surveillance systems since the total object's mass increase shows no sign of a slowing down [126]. Most of the information comes from the US Space Surveillance Network (SSN) which allows to detect, track, catalogue and identify the artificial object orbiting around Earth. In particular, it can obtain information for object larger than 10 cm in geostationary Earth orbit (GEO), and a few millimetres for the LEO. However the accurate locations given in NASA's reports only concern the object larger than 1 m in GEO and 10 cm in LEO. Outside the USA, country groups create networks to track objects, meteoroids or space debris, that enters the Earth's atmosphere. As an example, France is invested in FRIPON (Fireball Recovery and InterPlanetary Observation Network) since 2016 thanks to its large GRAVES system which counts around 100 observation stations. This network concentrates the data collected by 21 countries located in Africa, South America, Canada, western Europe, and Oceania, which allow covering a large sky area [49]. Some independent countries have created their own network such as Russia, with the RSSS; or in collaboration with others, such as Italy with the Sapienza Space debris Observatory Network (SSON) [89].

All these observations are realised by means of optical or radio telescopes in order to have the knowledge of the debris behaviour. Indeed, it is important to track their location to predict possible debris risks: impact or re-entry.

1.1.3 Debris risk assessment

Due to the evolution of the space debris number, the risk of collision in orbit is increased, and so is the risk of a ground impact in case of an atmospheric re-entry.
In orbit, the major risk is the collision of debris with active satellites. Damages can be minor, as it was the case for Copernicus Sentinel-1A satellite which solar panel was hit by a 1 cm particle in 2016. A more recent event of this type happened in May 2021 on the Canadarm2 of the ISS [19]. A debris, so small that it could not have been tracked, damaged the thermal blanket and the boom underneath, as shown in Figure 1.3. Fortunately, these events did not cause major failure. But in some cases, the debris impact can lead to

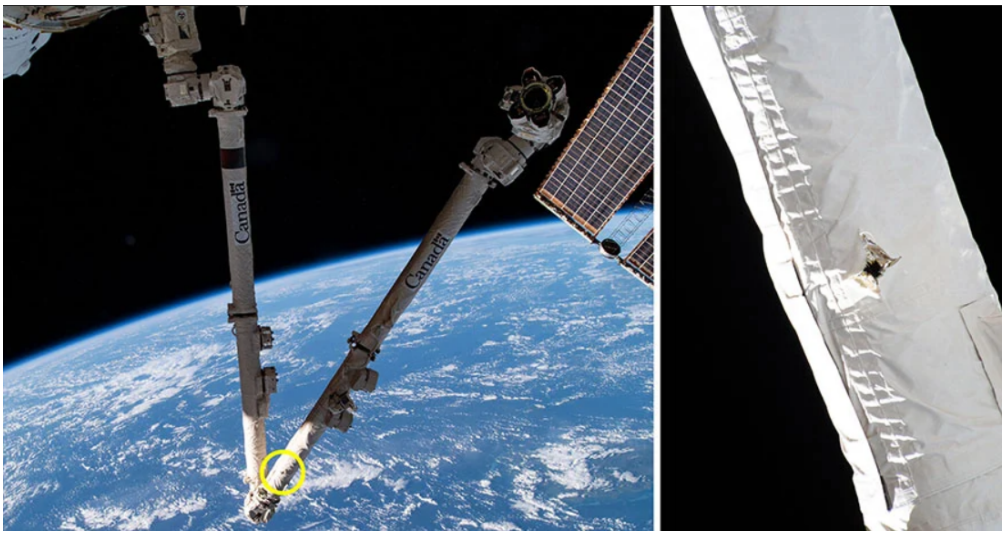

Figure 1.3: Canadarm2 damaged by space debris [Source: NASA/CSA].

the full fragmentation of both the debris and the satellite, as observed in 2009 between Cosmos-2251 and Iridium-33. This event led to the release of more than 2300 fragments [14], which increase, furthermore, the risk of debris collision. This type of catastrophic accident represents only 5% of all collisions of which 30% are due to small impactors (<10 cm) [114]. However, if considering such a terrible event occurring on a manned mission, the loss would be inestimable.
More than polluting the spatial environment, and causing expensive damage, space debris can re-enter the atmosphere and reach the Earth. For controlled atmospheric re-entry, the spacecraft is reaching a targeted safe location [204], generally placed in a remote ocean region, to avoid any human damage [165]. This is one of the reasons why at the Nemo Point, the furthest point from any land on Earth, at least 260 spacecraft were thrown there between 1971 and 2016 [156]. More than the global degradation of the spacecraft structures, some of them were carrying toxic or radioactive materials [68, 192], which increase the marine pollution already present with ground activities. For uncontrolled space debris, the problem is not that easy. According to Ailor *et al.* [3], 10 to 40% of the biggest debris' mass reach Earth. Most of them finish their flight in the 70% of Earth composed with water, contributing a little more to the ocean pollution. But a non-negligible part of them reach the ground, and sometimes in a populated area. According to ESA [176], which collected information about space debris recovered on Earth through different types of sources, 166 debris were recovered over 50 years in a total of about 80 impacted areas (see Figure 1.4). Among this list, which is possibly not complete, most of the debris are spherical (42%) or cylindrical (23%) in shape. In the recent years, some major uncontrolled re-entries questioned human safety. The 8-ton Tiangong-1 satellite,

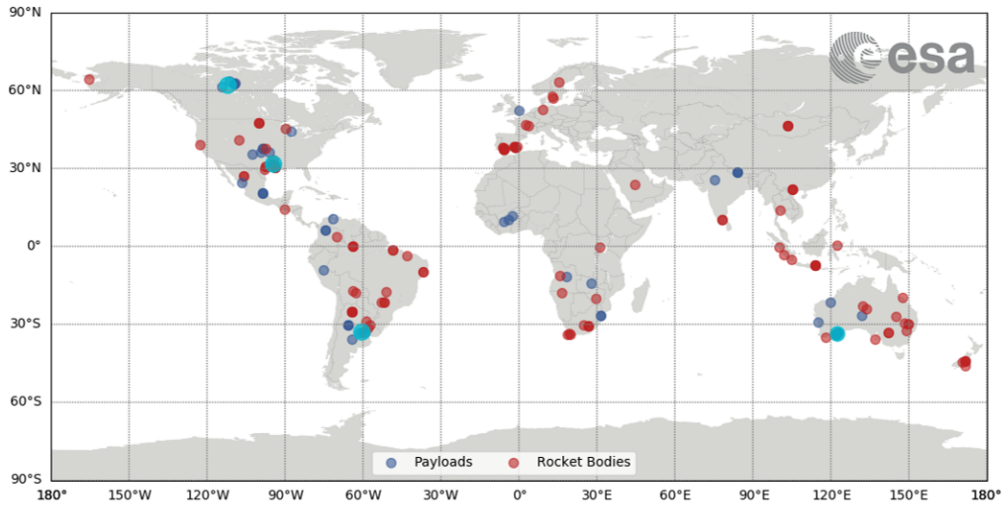

Figure 1.4: Recovered debris location [176].

which size was compared to that of a bus, re-entered the atmosphere in 2018. The debris fell down in the Southern Pacific Ocean in an area of the order of thousands of kilometres (2,632 km x 2,698 km) [2], which is about the size of Australia. Most recently, in October 2022, Long March 5B rocket, a 23-ton piece of debris re-entered the atmosphere, uncontrolled and without any shared calculated trajectory. It is unnecessary to develop the potential risk to the population, if such a spacecraft fall down on the ground. Beyond human risk, debris can cause structural damage of housing, or environmental pollution. For now, nobody can be held responsible for these damages, and still, almost every day, a debris enters the atmosphere.

1.2 Actions taken against space debris

1.2.1 The necessity for legal actions

In 2020, Kaineg [95] called for all the actors present in space to cooperate despite the business opportunity that represents a new orbiting satellite, and recall the importance of creating international laws to protect "the Common Heritage of Mankind".
Today, the scientific space community is fully aware of the space debris problem, and most of the actors are invested in reducing these risks. Outer space law was developed within the United Nations in 1957 with the launch of Sputnik-1. A first Committee for Peaceful Uses of Outer Space (COPUOS) was created to establish the foundation stones of the law. Along with the United Nations Register of Objects Launches into Outer Space (UNOOSA), some normative guidelines were established for space exploration. At some points, discussions rose between space agencies highlighted the importance of space debris management, in order to limit the important risks they generate. These discussions gave birth in 1993 to the Inter-Agency Space Debris Coordination Committee (IADC). Today, this committee is composed of 13 actors: Italy (ASI), France (CNES), Chine (CNSA), Canada (CSA), Germany (DLR), Europe (ESA), India (ISRO), Japan (JAXA), Korea (KARI), USA (NASA), Russia (ROSCOSMOS), Ukraine (SSAU) and UK (UKSA). All together they managed to think a certain amount of rules to regulate the creation of new space debris, which would make it impossible for a new mission to occupy the terrestrial orbits.
Since 2002, the IADC established a "Space Debris Mitigation Guidelines" [51], which is regularly revised. This document focuses on four main improvement axes, described as follows:

- **Limitation of debris released during normal operations**
  Spacecraft and orbital stages should be designed not to release debris during normal operations. If not

possible, the released debris have to be minimised in number, area, and orbital lifetime. In that case, a study must report an acceptably low effect on the orbital environment.

- **Minimise the potential for on-orbit break-ups**
  After each completion of mission operations, the spacecrafts and orbital stages must be passivated. It consists in depleting all on-board sources of stored energy. If it is not possible, these sources have to be secured when they are no longer needed for the mission or post-mission disposal. Moreover, each project has to demonstrate that no failure mode can lead to an accidental explosion. If it is not possible, the probability has to be inferior to 10^{-3}. A periodic surveillance of the spacecraft has to be realised during the mission. Any malfunction that could lead to a break-up has to be corrected, or the passivation should be conducted. Of course, any intentional destruction should be avoided.

- **Post Mission Disposal**
  To limit the number of objects in LEO, the spacecraft in orbits should be deorbited, with a preference for direct atmospheric re-entry. Limiting the residual orbital lifetime to 25 years, or less, is necessary not to increase, furthermore, the amount of debris. In case of a re-entry, the debris that may survive and touch the ground must not be too risky for the population or the environment.

- **Prevention of on-orbit collisions**
  The on-orbit collisions are a threat for orbital environment because of the large increase in space debris number that they can cause. Thus, each program has to estimate and limit the probability of an accidental collision. In case there are sufficient reliable data, avoidance manoeuvres should be considered for spacecraft in the operational phase. After the end of all operational phases, the previous point must be applied to minimise the probability for accidental collision.

1.2.2 Scientific actions against space debris collision

In a collective desire to improve the orbital environment, and to be able to continue planning future space missions, a large number of research teams throw themselves into finding improved or new solutions that would limit the number of space debris, and space debris collisions. Four main axes are explored to respond to IADC Guidelines:

- **Reduction of orbital lifetime**
  Reducing the orbital lifetime of a spacecraft has proven to reduce the risk of on-orbit collisions. For the upper stage of Ariane 5, Renard et al. [181] described an "End Of Life Manoeuvre",*i.e.* the passivation, that is implemented at the end of the payloads separation. It consists in stopping the boost after the perigee, simultaneously ejecting the unnecessary gases in the appropriate direction to produce a thrust that reduces the altitude of Ariane 5, reducing its orbital lifetime.

- **Collision avoidance**
  In case of a known foreseen collision, active satellite can be manoeuvred to avoid the debris. This type of operation is called "Pre Determined Debris Avoidance Manoeuvre". For example, the ISS realised this operation two to three times a year, by firing its thrusters for a calculated among of time, increasing its altitude to get away from the debris path, with a sufficient margin of error.

- **Active debris removal**
  The on-orbit servicing refers to the maintenance of systems in orbit. By means of a robotic approach it would allow many actions as the refuel, repair, upgrade, transport, or the rescue of spacecrafts [72]. It would even be possible to clean space from space debris. Some space vehicles are specifically designed to realise active debris removal, such as a chaser satellite equipped with a morphing robotic arm [142], or PERSEPHONE [141], which aim to catch debris and impulsively manoeuvrer them for controlled

atmospheric re-entries. This work is a preliminary study but full of innovative ideas. More generally, the ADR allows to catch the biggest debris by means of robotic arms, nets, tethered space robots or harpoon, to transport them out of the orbit thanks to divers transportation methods [118]. Other methods consist in moving space objects without physical contact, by means of an electromagnetic field, laser or ion beam [195].

- **Optimisation of the conception for atmospheric re-entry**
  This last option is useful for space debris re-entry. The idea is to conceive a spacecraft that will completely burn during its atmospheric re-entry so that they never reach the ground. This last point requires to have a good knowledge of the different process occurring during the re-entry.

1.3 Atmospheric re-entry

De-orbiting the space debris is the preferred solution to remove them from active orbits. Generally, the altitude of space debris is decreased so that they re-enter the atmosphere. This solution is mostly used because of the capacity of the atmosphere to burn the debris, preventing a large part of them to reach the ground. Unfortunately, we previously exposed the impact on the ground, and it is not negligible.
In order to limit ground damages, it is necessary to know with accuracy the impact time and area. This would allow protecting the potential populated area, or to better collect space debris for environmental reasons. A lot of studies are dedicated to this aim.

1.3.1 Re-entry prediction

Nowadays, research centres and space agencies develop predictive codes for the atmospheric re-entry trajectory and survivability. The available codes can be classified into two main categories: object-oriented codes and spacecraft-oriented codes [128]. The object-oriented method is based on simplifying the complicated geometry of objects into simple shapes such as sphere, cylinder, box, etc. Tools using this method are DAS, ORSAT and DRAPS. In particular ORSAT, developed by NASA, also includes thermal/ablation models to determine the debris survivability assessment [153]. ESA with SCARAB has opted for the spacecraft-oriented method to simulate the re-entry of spacecraft as real as possible. Nevertheless, due to a much more complex analysis strategy, this method requires great modelling efforts and computing resources [112, 129]. PAMPERO developed by the CNES agency since 2013 is also another predictive code based on spacecraft-oriented tools [13]. The determination of destructive re-entries and the prediction of the potential for ground risk due to the arrival of fragmented objects on the ground are the main purposes of these numerical codes. As an example, these types of code can be developed by industries [69] to assess the re-entry of their space equipment, and know if their project respond to IADC [51] recommendations.
Some research teams develop their own predictive methods, and use past events to validate them, as did Kim *et al.* [106] with the Tiangong-1 uncontrolled re-entry [196]. Trajectory reconstructions are realised for the atmospheric re-entry of space debris [3], but also for the re-entry of meteoroids [188], which have very similar problematic.
Unfortunately, all these predictive computations still give large impact areas [2], and the real time of impact is in the range of hours. Moreover, the more accurate predictions of impact are only known a few hours prior (Figure 1.5), which limits the time to prevent the on-ground risk.

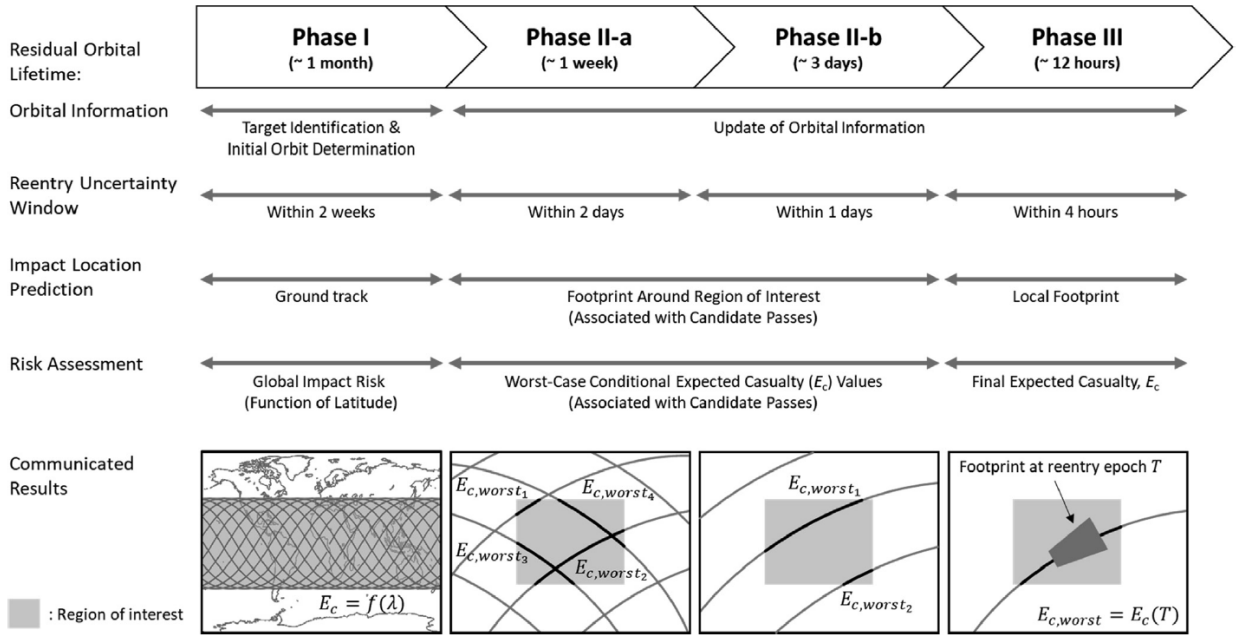

Figure 1.5: Three-phase procedure for managing the reentry risk of space objects [106].

1.3.2 Uncertainty factors

It is to be noted that the atmospheric re-entry is a complex problem that involves many factors of uncertainty. Mainly, these uncertainties come from the nature of the flow during atmospheric re-entry, and the material properties and shape of space debris. These two parameters are important in the fragmentation phenomenon which makes trajectory calculations even more complex.

1.3.2.1 Atmospheric environment

The atmospheric re-entry is considered to occur at the Von Kármán line set at 100 km in altitude, but this "limit" is often discussed [139]. The classical range of altitudes considered for atmospheric re-entry is between 75 and 120 km.
The altitude governs the variations of temperature, and static pressure, which results in variations of density. As a consequence, all the deducted properties vary according to the altitude. In particular, we observe a variation in the sound speed, viscosity, and mean free-path, the distance between two collisions of molecules [187].
As a consequence of air densification as the altitude decreases [94, 143], the space debris will evolve through four different flow regimes during the atmospheric re-entry:

- initially, the debris is in orbit, where the regime is free-molecular;
- then, as its altitude decreases, the air gets slightly thicker, this concerns the slip and transitional regimes, also called the rarefied regime;
- and finally, the density of air gets close enough to that of our human surrounding environment, this is the continuum regime.

The free-molecular and rarefied regimes are characterised by important viscous effects. The aerodynamics encounter for these regimes are different from the classic fluid mechanics described by the Navier-Stokes

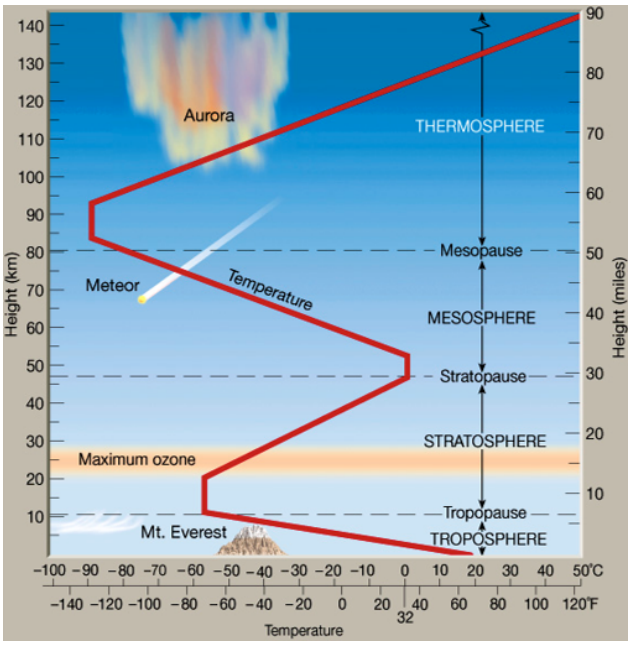

Figure 1.6: Temperature evolution according the altitude [134].

equations. More in-depth explanations will be given in chapter 2.
In addition to the specifics of rarefied flows, space debris enters the atmosphere with hypervelocities close to 7800 m.s^{-1} [160, 173]. At such velocities the aerodynamic forces are coupled with non-equilibrium heat transfer [26]. As a consequence, the flying objects are constraints to many complex forces, which can lead to their fragmentation.

1.3.2.2 Fragmentation

Due to the rapid increase in dynamic pressure and heat flux, most debris are considered to fragment at altitudes between 91 and 65 km [98, 163, 173]. The fragmentation altitude depends on many variables: mechanical composition of the debris, the size, mass density and materials of the different components [127], their initial flight conditions and more specifically their mean velocity, and spinning momentum [145]. Since these parameters are usually not known, the fragmentation altitude is generally observed and not predicted, which add uncertainty for the calculation of the debris trajectory. In any case, this process produces multiple fragments of debris in the rarefied regime, which still needs to be better described.
In their first moment of existence, the fragments will interact, even for a short period of time. Depending on the scenario, the interaction may induce the fragments preservation, when small debris remain in the wake of a larger piece; or the fragment ablation, when the object cannot withstand thermal loads. In any case, the interactions between debris lead to a change in their trajectory, which increases the difficulty of predicting ground impacts.

In the end, the trajectory of space debris depends on their fragmentation and on the physical properties of the atmosphere. In particular, the fragmentation leads to interaction effects between the different objects. According to many studies, even in the continuum regime, the aerodynamic interactions, such as the shock/shock interferences, wake effects and shock-wave surfing have a great impact of the aerodynamic of multiple bodies [119, 161, 209, 208]. Thus, the separation behaviour of fragments and their trajectories are impacted by the interactions. The majority of studies related to this topic uses spheres, cylinders, or cubes for models. Indeed, most of the debris recovered on Earth are tanks or pressure vessels, and their shape is usually cylindrical (23%) or spherical (42%) [176]. More over, these canonical geometries allow to better

understand the aerodynamic interactions on a theoretical point of view.

1.4 The various applications of interactions in the rarefied regime

At high altitudes, the aerodynamic interactions occur for the re-entry of space debris, but also the entry of meteoroids. The differences will concern the entry velocity, which can be about ten times that of a space debris [169], the size of the entering object, and their material. In all cases, meteoroids fragment, as can be observed with Figure 1.7. Most of the final break-up of meteoroids seems to concern low altitudes, in the

Figure 1.7: Meteoroid fragmentation [76, 199].

range of 25 to 60 km [40, 92, 140, 194]. But the Jicamarca Radio Observatory observed some high-altitude meteors with fragmentation occurring between 180 and 70 km [75]. In any case, as for space debris, the atmospheric entry of meteors represents an impact risk for the population. As an example, Jenniskens et al. [92] presents the results of the entry of the 2008 TC_3 asteroid. Sixty-seven pieces of mass ranging between 4 g and 378.7 g were recovered. The total mass of 39 kg was spread in a 30 km-long strewn field in the Nubian desert between Egypt and Sudan. Considering impact speed in the order of 13 $km.s^{-1}$ [40], damages in populated area would be terrible. As an example, a fragment of the 2023CX1 asteroid was recovered near a populated area in France.

Figure 1.8: Recovered fragment of the 2023CX1 [Source: FRIPON/Vigie-Ciel].

For these reasons, the same interaction problems are discussed [21, 210] for the meteoroids than for the space debris.

In another domain, the problem of aerodynamic interactions was discussed concerning the success of space mission. Two configurations are mainly identified: during the launch of a Two-Stage-To-Orbit (TSTO), at the stage separation, or due to the geometry of the space vehicle. The X-15 (Figure 1.9) and X-37B (Figure 1.10) vehicles were likely to suffer both configurations. Many studies focus on the interaction that can occur during stage separation. Indeed, according to the size of the different stage, one can influence the other, or both can be affected by their proximity [157]. This influence in the first moment after the separation could lead to a trajectory disturbance of the orbiter, or of the booster of a TSTO [34, 83, 93, 206]. In the case of

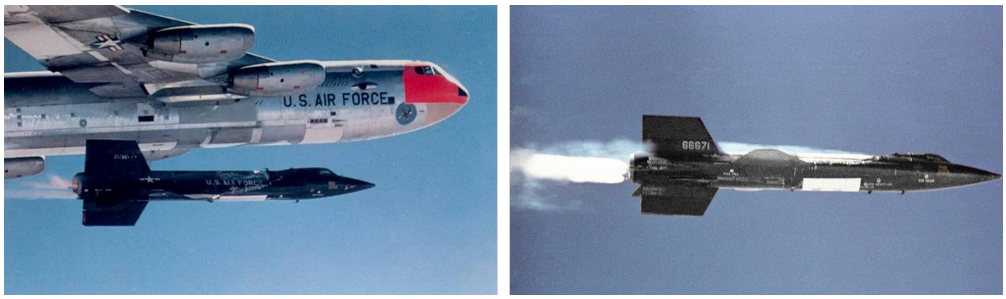

Figure 1.9: X-15 separation from B-52 (left), and in flight (right) [Source: NASA Gallery].

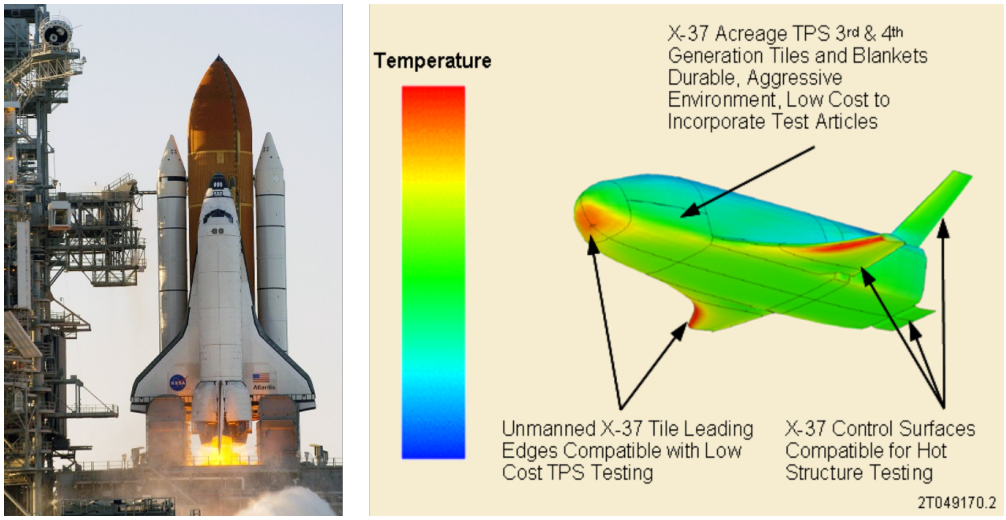

Figure 1.10: Space shuttle X-37B (left) [Source: NASA Gallery], and simulation of the surface temperature (right) [80].

shock/shock interaction due to the geometry [133], the X-15A-2 suffered airframe damages leading to its rear body destruction. Another terrible example it that of the space shuttle, which destruction during the re-entry was caused to many factors. A study of the surface heating (right image of Figure 1.10) demonstrates that it is very likely that shock/shock interferences caused structural damages [80].
For all these reasons, the shock/shock interferences and more generally aerodynamic interactions have to be studied in the rarefied regime as explained with Figure 1.11 [1]. This would help improve the geometry of spacecraft [15, 46, 107, 218] and the managing of stage separation.

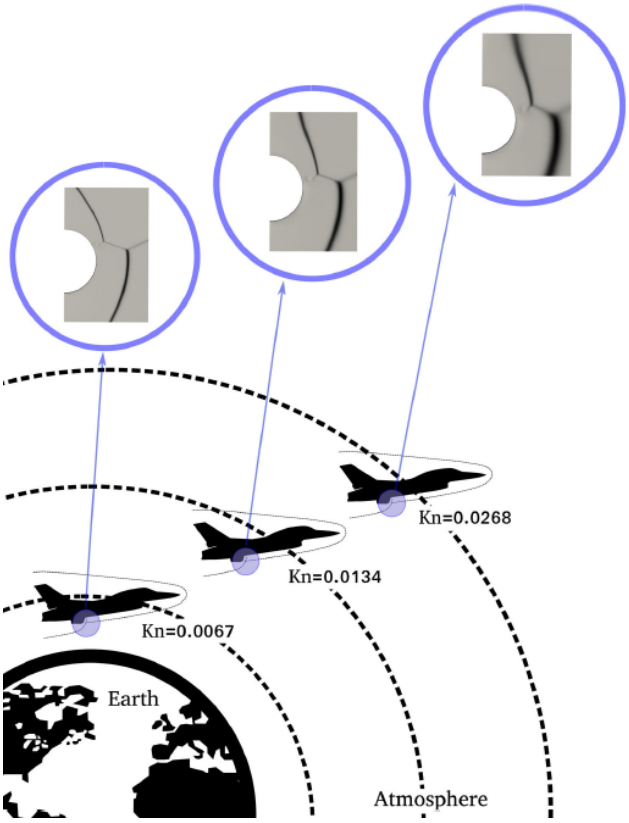

Figure 1.11: Schematics of Edney patterns for different rarefaction level [1].

Chapter 2

Aerodynamic interactions in rarefied regime

Contents

From the above context, we understand the importance of bringing some light on the aerodynamic interactions occurring in the rarefied regime, for supersonic and hypersonic conditions. First, this chapter presents the state of the art concerning the flow conditions, and in particular the aerodynamic properties of the slip-rarefied regime. A second part is dedicated to the aerodynamic interactions generated by proximal bodies. More specifically, a description is given of major events observed: the shock/shock interferences, the shock-wave surfing, and the wake effects.

2.1 The rarefied regime

2.1.1 Atmospheric re-entry conditions

In any study of fluid mechanics, in addition to knowing the speed of the object of study, it is important to also define the environmental conditions in which it evolves such as pressure, density and temperature. Indeed the physical properties of the environment will have a definite influence on the physical equations that will be used to describe the motion of this object.

2.1.1.1 The space environment

For high altitudes, some model exists to describe the different parameters according to the altitude. In this work, we used the model NRLMSIS 2.0 [152] fully described by Emmert *et al.* [66]. This model gives, inter alia, the values of temperature and mass density as a function of altitude, as seen in Figure 2.1. In

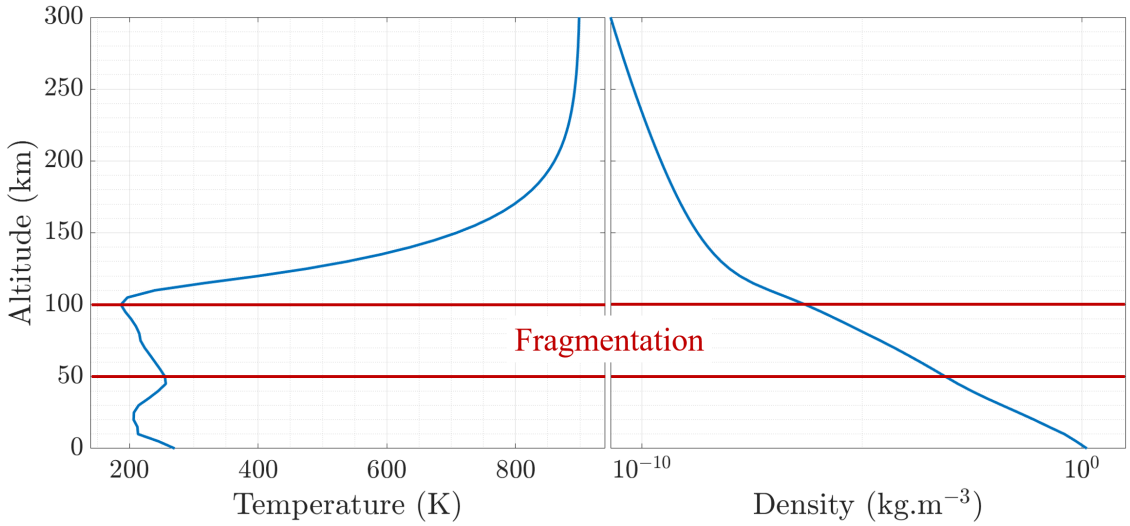

Figure 2.1: Temperature and mass density profiles in Earth atmosphere from NRLMSIS 2.0 [152].

the range of altitudes where occur fragmentation, temperatures are comprised between 200 and 300 K, and the density between 5.10^{-7} and 8.10^{-4} kg.m^{-3}.Under these conditions, the air density is very low and no longer behaves as a continuous medium. The air molecules are so far from each other that they have to be observed on a microscopic point of view. In such a medium, the fluid dynamics need to be described from a molecular aspect, which involves the collisions between particles. Commonly, the mean free-path (λ) is used to characterise the rarefied flows. This parameter is representative of the distance a molecule travel between two collisions and is calculated with Equation 2.1 ([29]), where Rm is the specific gas constant.

$$\lambda_\infty = \frac{2(7-2\omega_\infty)(5-2\omega_\infty)}{15\sqrt{\pi}} \frac{\mu_\infty}{\rho_\infty \sqrt{2R_m T e_\infty}} \tag{2.1}$$

The mean free-path depends on the free-stream viscosity μ_∞, viscosity temperature index ω_∞, and temperature Te. The viscosity is calculated with the power law of Sutherland given by Equation 2.2.

$$\begin{cases} \text{if } Te < B, & \mu = \frac{A.Te}{2.B^{1/2}} \\ \text{if } Te \geq B, & \mu = \frac{A.Te^{1+\frac{1}{2}}}{B+Te} \end{cases} \tag{2.2}$$

For air, $A = 1.458 \times 10^{-6}$ Pa.s and $B = 110.4$ K
For N_2, $A = 1.374 \times 10^{-6}$ Pa.s and $B = 100$ K

The viscosity temperature index depends on the viscosity and temperature of the stagnation conditions (subscript $_0$) and free-stream conditions (subscript $_\infty$) of the flow. It can be calculated with Equation 2.3.

$$\omega_\infty = \frac{log\left(\frac{\mu_\infty}{\mu_0}\right)}{log\left(\frac{Te_\infty}{Te_0}\right)} \tag{2.3}$$

To quantify the rarefaction level, it is necessary to confront the environment to the flying object. In 1934,

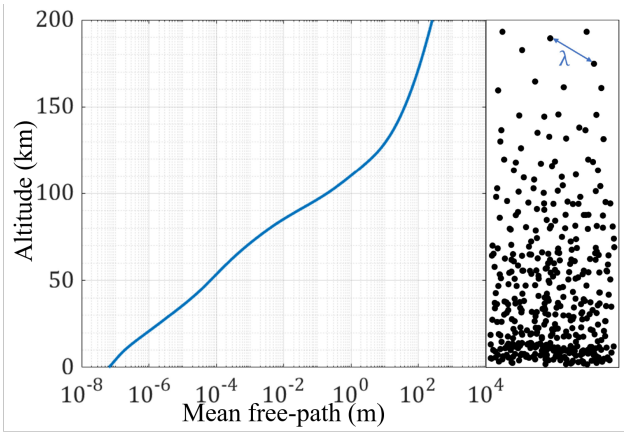

Figure 2.2: Mean free-path profiles in Earth atmosphere [179].

Knudsen [109] proposed a dimensionless number, which relates the mean free-path to the characteristic length of the object L. The Knudsen number, Kn is calculated with Equation 2.4.

$$Kn = \frac{\lambda}{L} \tag{2.4}$$

Four flow regimes were determined based on the Knudsen number, as described in Table 2.1. Contrarily

Table 2.1: Flow regimes.

Kn < 0.01	Continuum regime
0.01 < Kn < 0.1	Slip regime
0.1 < Kn < 10	Transitional regime
10 < Kn	Free-molecular regime

to the low altitudes, in the higher atmosphere, where the mean free-path is high, the number of collisions is low. Thus, the highest Knudsen number characterising the free-molecular regime needs to be defined from a molecular point of view. However, the Navier-Stokes equations, usually used to solve fluid dynamic problem, are describing a macroscopic behaviour. To study the microscopic behaviour, it is necessary to

use a probabilistic method for the calculation of molecules collisions. This method is well described by the Boltzmann equation. This equation is also valid in the continuum regime, however, since the number of collisions depends on the number of molecules, the computation time also depends on it, and becomes prohibitive. It is to be noted that, even if the limit of the continuum regime is set for value inferior to 0.01, experimental results showed that rarefaction effects are still occurring. Rembaut [179] observed differences with the literature in terms of shock stand-off distances until around 0.001, and in drag coefficient for even lower Knudsen. This can be due to the fact that the Knudsen number does not take into account the dynamic behaviour of the flying object, which needs to be investigated.

2.1.1.2 Dynamic behaviour of an atmospheric re-entry

Considering a 1 m diameter entering the atmosphere, Prévereaud *et al.* [173] calculated the decrease in velocity V according to altitudes between 76 and 5 km. Before the atmospheric re-entry, the speed of space debris is of about 7800m.s^{-1}. Thus, we extrapolated Prévereaud values, as shown in Figure 2.3.

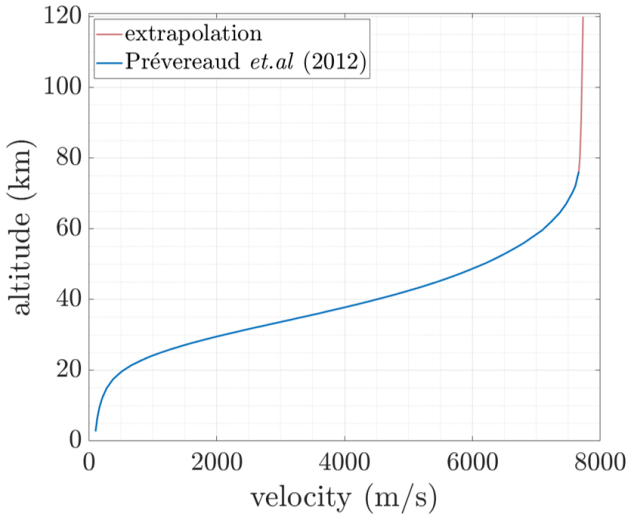

Figure 2.3: Velocity of a 1 m diameter debris fragment.

Generally, a flow is not described by its velocity, but by its Mach number which describes the flow in terms of velocity according to the ambient medium. Ma, as described with Equation 2.5, where c is the speed of sound which depends on the ambient temperature Te.

$$Ma = \frac{V}{c} = \frac{V}{\sqrt{\gamma R_m Te}} \tag{2.5}$$

Four different speed regimes are defined: subsonic ($Ma < 0.8$), transonic ($0.8 < Ma < 1.2$), supersonic ($1.2 < Ma < 5$) and hypersonic ($1.2 < Ma < 5$). The last regime involves viscous effects that are not found for the supersonic regime, while the structure of the shock-waves are similar.

Finally, a last dimensionless number allows characterising the flow in terms of dynamic behaviour: the Reynolds number, as described by Equation 2.6.

$$Re = \frac{\rho V L}{\mu} \tag{2.6}$$

The Reynolds number is also partitioned into four aerodynamic regimes: Stokes regime ($Re \ll 1$), laminar ($Re < 2000$), transitional ($2000 < Re < 10000$) and turbulent ($10000 < Re$).
Taking back our example of the re-entry of a 1 m diameter debris, with the velocities given in Figure 2.3, we

can now estimate approximately its flight conditions. Note that, at a certain point, the object may fragment, changing slightly its dynamic behaviour. In Figure 2.4 is plotted the correspondence altitude-Knudsen number for the different sizes considered. Most studied consider the fragmentation altitude between 91

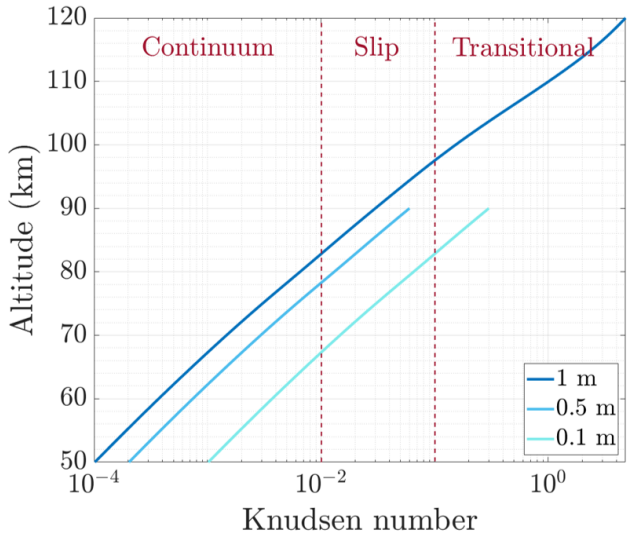

Figure 2.4: Knudsen number of a 1 m diameter object, and its potential fragments (50 cm and 10 cm).

and 50 km [163, 173, 98]. For our object and its potential fragments, the Knudsen number predicts that they pass through flows in sliding and continuous regimes. Again, Knudsen number does not consider the dynamics of the objects. This is why it should be useful to also estimate nondimensional parameters related to dynamic behaviour such as Mach and Reynolds number, presented respectively in the left and right graphs of Figure 2.5. The velocity was estimated for a 1 m-diameter sphere and give a hypersonic regime.

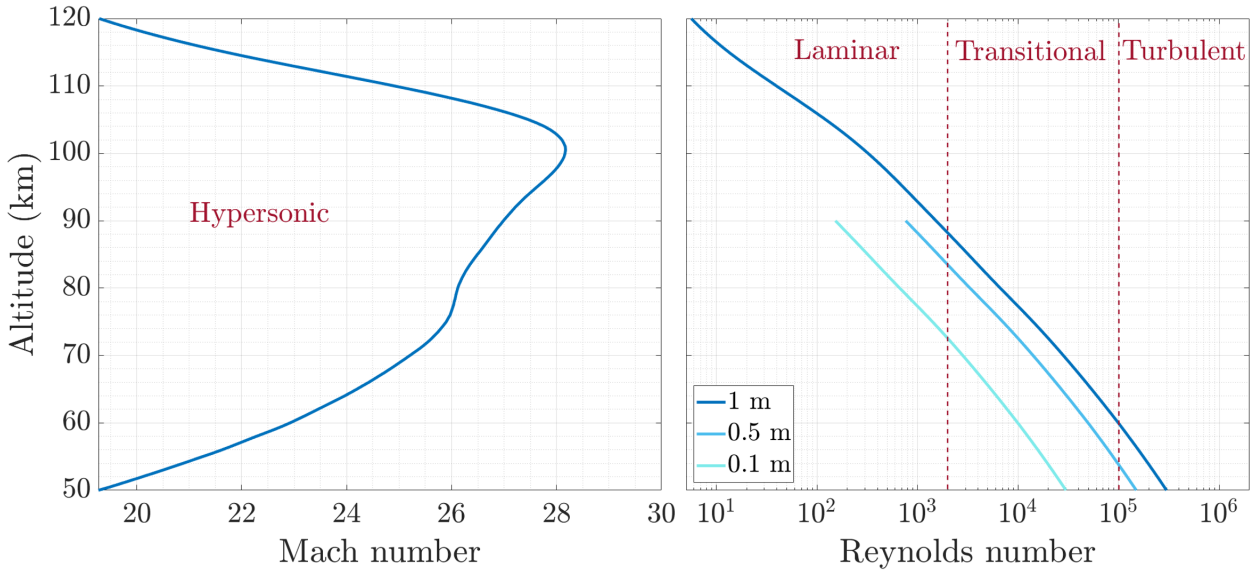

Figure 2.5: Mach and Reynolds number of a 1 m diameter object, and its potential fragments (50 cm and 10 cm).

Even if decreasing the size of the considered object, given the value shown in the graph, the fragment will be in hypersonic regime. The Reynolds number, for its part, depends on the size of the fragment. For the fragmentation altitudes, the debris begins the re-entry in a laminar regime and then mainly cross the transitional regime.
As previously said, the limit between the different regime can be discussed. In particular, the Knudsen number, largely used in the literature, is a static parameter, which only describes the rarefaction level of the

medium. However, other dimensionless numbers exist and take into consideration the dynamic behaviour of the flying object. Macrossan [135] described in particular a dimensionless number: the Tsien's parameter, also found as the "similarity parameter". This parameter is described in Equation 2.7, and is proportional to $\frac{\lambda}{\delta}$, where δ is the boundary layer thickness of the object. Thus, σ takes into account both the dynamic and viscous effects.

$$\sigma = \frac{Ma}{\sqrt{Re}} \tag{2.7}$$

This is the reason why the similarity parameter is sometimes used to determine the flow regime, as shown in Figure 2.6. Moreover, to our knowledge, there is no ground-based-facility able to reproduce all the re-entry condition in only one experiment. The similarity parameter will be used as a scale parameter to estimate the experimentally simulated altitude.

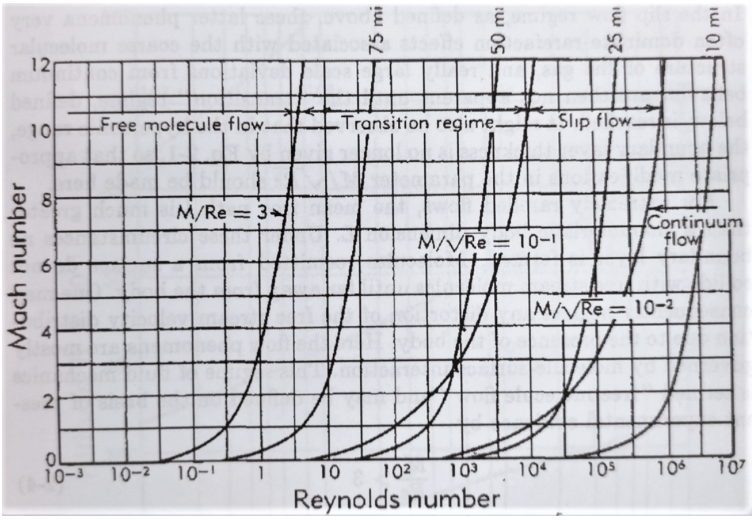

Figure 2.6: The regimes of gas dynamics [44].

2.1.2 The rarefied flow-fields

This section focuses on the effect of the rarefaction level on the aerodynamics of a sphere, the canonical geometry that will be used all along this work. In the first instance, we will briefly give the reasons for choosing this geometry. Then we will describe the main differences in a sphere flow-field, observed between the continuum and the rarefied regimes. This point will help understand the necessity of studying rarefied flows for single flying objects, which motivate the study of proximal bodies.

2.1.2.1 Choice of the geometry

During the atmospheric re-entry, debris fragment, and a lot of work is devoted to the understanding of the fragment interactions. The simulation of their trajectory and the prediction of their survivability still remains a challenge, as the numerous ongoing studies demonstrate. Many tools are being developed by several agencies and laboratories, some of them based on an object-oriented approach. This method considers an object to be the assembly of simple individual shapes. One can cite DEBRISK [12], which includes five simple 3D topologies: spheres, straight edge cylinders, hemispherical cylinders, boxes and flat plates; and six new topologies: open cylinders, open truncated cones, spherical caps as well as the angular sectors of these three shapes. DRAPS [221] has a little more extended possibility with 15 different topologies but in most cases they represent simple shapes (see Figure 2.7). For more fundamental studies on interactions,

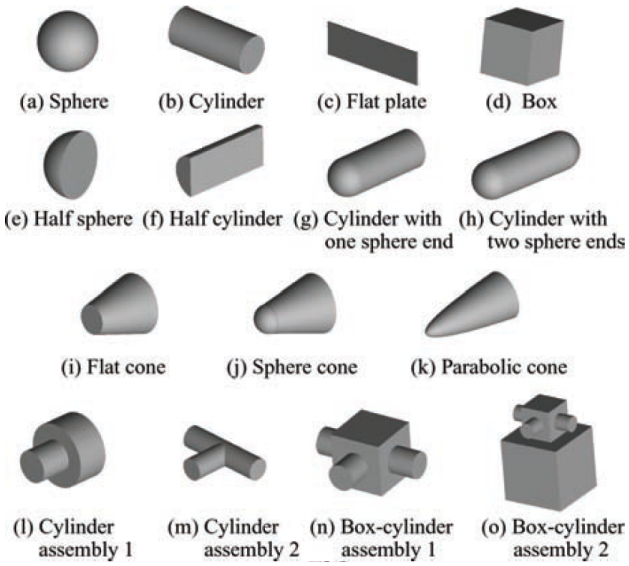

Figure 2.7: Object shape types in DRAPS [221].

the geometries used to understand this phenomenon are also canonical. Most of them are based on the interaction between:

- an oblique shock and a cylinder [36, 57, 81, 144, 170, 182, 211];
- an oblique shock and a hemisphere or a sphere [65, 87, 103, 105, 115];
- two spheres [20, 71, 116, 121, 137];
- and more rarely, two cubes [79] or multiple cylinders [119, 203];

Some flow-fields of the geometries interactions are presented in Figure 2.8. It should be noted that most

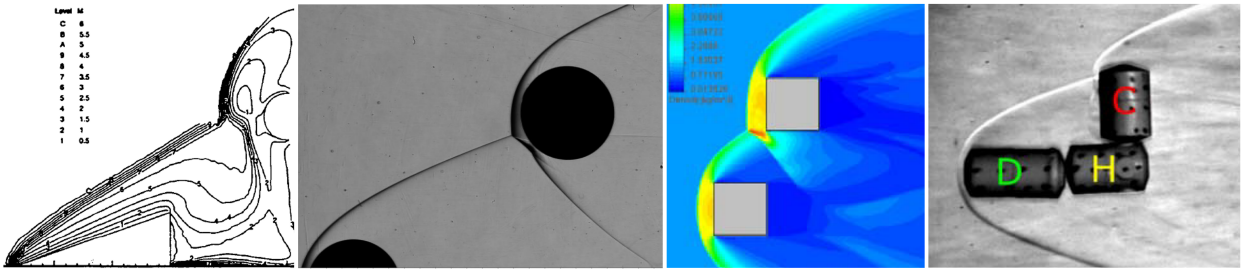

Figure 2.8: Interacting geometries. From left to right: wedge-cylinder [182], sphere-sphere [71], cube-cube [79], cylinders [119].

of these geometric shapes will form bow shock-waves, the combination of which in case of interference could lead to quite complex patterns, as observed by Passey and Melosh [164] and later, by Artem'eva and Shuvalov. Thus, to investigate the bow shock interactions of two nearby fragments, we chose two spheres to simplify the study.
Firstly, from an experimental point of view, the obstruction generated by two spheres in the test section is less important than with a wedge or cylinder. As a consequence, these geometries allow us to explore a wider range of relative positions between the two spheres, experimenting with a greater latitude in terms of interactions. Moreover, the symmetry of the spheres makes it possible to avoid problems of the orientation of one sphere regarding the other, and the shock-waves, which significantly simplifies the experimental

measurements. The choice of spheres also allows us to compare the results obtained in this work with some other results from the literature. It will enable to assess the viscous effects of the slip regime on the interferences of two objects compared to the continuum regime.

2.1.2.2 Aerodynamics of a sphere in the rarefied regime

Generally, investigations related to the flow past a body focus on two major aspects: the structure of the flow and the forces endured by the flying object.
In the super and hypersonic continuum regimes, the flow-field of a sphere is described as schematically shown in Figure 2.9. A bow shock-wave is present upstream of the sphere, with a detachment distance

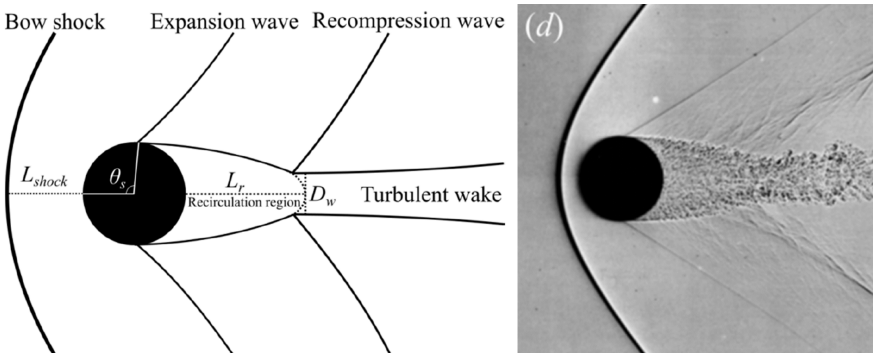

Figure 2.9: Schematic of the flow structure past a sphere [148].

L_{shock}, also called shock stand-off distance. According to the dynamic regime, *i.e.* the Reynolds number, different structures can be present in the flow-field of the sphere. As is observed, a recirculation area can be present behind the sphere, giving rise to an expansion wave and a recompression wave.
In the rarefied regime, we observe some differences in the flow structure. First, the bow shock is not as delimited as in the continuum regime. Indeed, an increase in the rarefaction level leads to a more diffuse shock-wave. Rembaut [179] visualised Mach 4 flow-fields for different levels of rarefaction. Figure 2.10

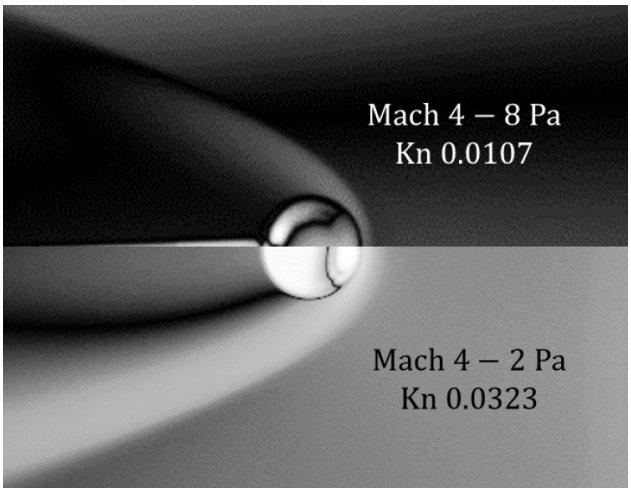

Figure 2.10: Flow-field of a sphere in Mach 4 rarefied flows. [179].

shows that the bow shock does not appear as a clear discontinuity. Furthermore, the stand-off distance is increased with the increase in Knudsen number. Numerically, Dogra *et al.* [63] simulated the hypersonic flow around a sphere for different Knudsen numbers. Figure 2.11 give the Mach number contour for the extreme cases. As can be observed, the Mach lines are well extended and detached from the sphere in the most rarefied flow.

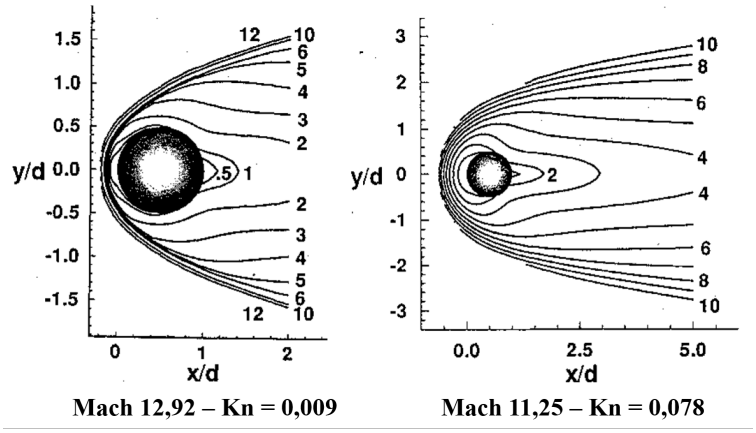

Figure 2.11: Mach contour around a sphere in hypersonic rarefied flows. [63].

More than the modification of the bow shock of the sphere, the level of rarefaction acts on the downstream structure of the flow. Whether in hydrodynamics, or in aerodynamics, it has been shown that the recirculation behind the sphere is well described by the Reynolds number, which is low in the rarefied regime. Taneda [197], Nakamura [149], and Nagata *et al.* [148] dedicated a lot of work on the evolution of the recirculation area. Specifically, Nagata *et al.* showed that, for a Mach 2 flow, a decrease in the Reynolds number led to a diminishing of the separation length (corresponding to L_r in Figure 2.9). Also, they observed an increase in Θ_s, which defines the separation point at the rear of the sphere. For a Reynolds 50, they obtained $\Theta_s = 180°$ and $L_s = 0$ mm which means that there is no more a recirculation area. It is to be noted that, this vanishing appears for higher Reynolds number when increasing the Mach number. Thus, for higher Mach number, it is easier to obtain a sphere flow without a recirculation area.
Besides the non-presence of the recirculation zone, the expansion and recompression waves no longer occur. As an example, Rembaut [179] made Pitot pressure measurements in the wake of a sphere placed in a Mach 4 flow, with $Re = 3984$. The corresponding results obtained for a Knudsen number of 0.0012 (limit slip/continuum regime) are presented in Figure 2.12. Between the centreline of the flow and the shock,

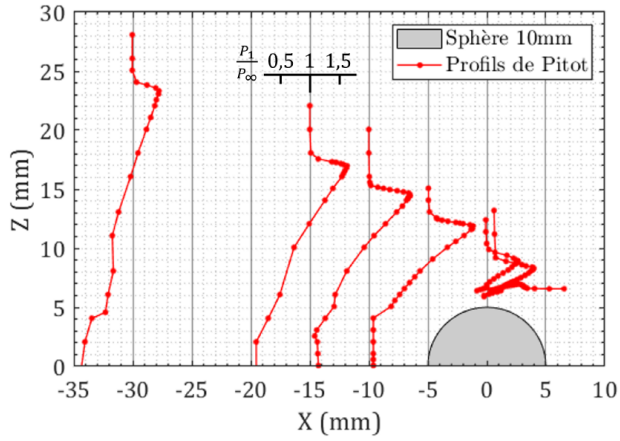

Figure 2.12: Normalized Pitot pressure profiles in a sphere flow-field for Mach 4, $Re \approx 4000$ [179].

besides from the increase created by the shock-wave, we do not observe any increase in stagnation pressure. This means that there is no re-compressed area, and thus suggests that the flow-field does not have expansion nor re-compression waves.

The modification of the flow-field is accompanied with variations of the aerodynamic parameters of the sphere. In particular, a large number of studies has been devoted to the determination of the drag coefficient

of a sphere for continuum, rarefied, and free-molecular regimes.
Experimentally, in the continuum regime, studies of drag forces were focusing on the Mach effect. Hodges [86] measured the drag coefficient of a sphere for Mach numbers between 2 and 10. He showed that, for Mach number higher than 4, the drag coefficient remains constant and its value is of 0.359. Charters and Thomas [45] measured the drag coefficient for Mach number ranging between 0 and 4. From Mach 4 to 1.5, they observed a slight increase of Cd which reaches 0.4. Then for lower Mach number, the Cd strongly decreases.
Then, other researches were willing to determine the impact of the Reynolds number on the drag coefficient. Aroesty [16], Bailey and Hiatt [17, 18], or Koppenwallner and Legge [111], to name but a few, all contributed to the creation of an immense experimental database of drag coefficients over a wide range of Mach and Reynolds numbers. These results, partly presented in Figure 2.13 highlighted the variation of the drag coefficient in terms of Reynolds and Knudsen numbers. This variation of the drag coefficient is

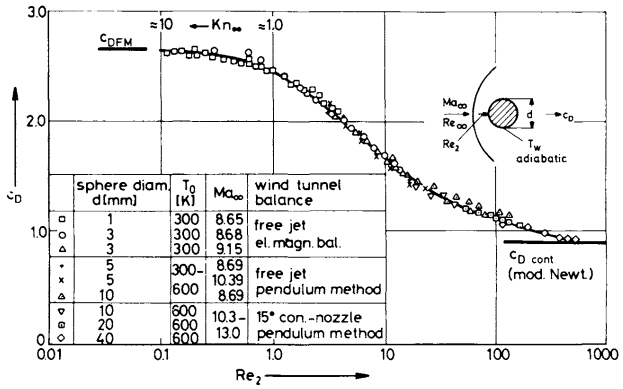

Figure 2.13: Drag coefficient of a sphere for variable Reynolds number [111].

mostly explained by the viscous effects that rise when the level of rarefaction increases. Dogra *et al.* [63] numerically investigated the drag coefficient of a sphere and the drag contribution in terms of pressure and friction. The two cases presented in Figure 2.11 were obtained for approximately the same Mach number ($Ma \approx 12$), but with an increase in the rarefaction level. The maximal local pressure coefficient showed an increase in Cd of 14%, while the maximal local friction coefficient is increased by 150%. For $Ma = 2$, Dogra simulated six levels of rarefaction; for the extreme cases, $\sigma = 0.282$ and $\sigma = 0.115$. The level of rarefaction is increased by 2.5, which results in a drag coefficient increased by 70%. This increase is due to an increase in pressure drag coefficient by 14% and in viscous drag coefficient by 200%. These two studies well agree on the fact that viscous effects have a predominant impact on the total drag coefficient.

As the viscous effects strongly modify the aerodynamic of single objects, it motivates the interest of studying their effects on the problem of proximal bodies.

2.1.3 Numerical simulations

To address the problematic of rarefied flows, many numerical codes were, and are still, under development. Their physical model is based on molecular gas dynamics.
The Direct Simulation Monte Carlo (DSMC) was mostly developed by Bird [74] who created 2D (DS2V) and 3D (DS3V) codes that are in open access. Many others followed, such as the DSMC code MONACO devised in the mid 1990s by Dietrich and Boyd [60]. A most recent code, SPARTA, is largely used today, but discussions on the collision frequency reproduction are still relevant [168].
Other types of collisional model, such as BGK (Bhatnagar-Gross-Krook) or ES-BGK (Ellipsoidal-Statistical-BGK) are used to develop in-house codes [58].
In any case, one of the major issues is the determination of the accommodation coefficient, theoretically used for the bridging function of drag and lift coefficient [110, 214, 198]. But in practice, they depend on many

factors: "gas composition, impact energy of the impinging molecules, temperature, material and roughness of the surface, angle of incidence" [223]. This is partly why research teams are in demand for data. Some recent results for numerical studies [200, 186] were compared with the experimental data obtained in the MARHy wind tunnel, even with the Mach 20 conditions explored later in this work [10].
If the need of experimental data is important for the study of a single object flow-field, the demand is even greater for interacting models, which drastically increase the numerical inaccuracies.

2.2 Studies of proximal bodies

Different scenarios can occur leading to a longer preservation of the following debris, or to their accelerated destruction. In any case, the interactions between debris lead to a change in their trajectory, which increases the difficulty of predicting ground impacts [2]. These difficulties are mainly due to viscous effects that have to be considered when analysing and describing the aerodynamic interactions occurring in hypersonic rarefied flows. Many studies have been realised on the proximal bodies' behaviour whether experimentally or numerically. These studies can be regrouped in three main categories: the separation behaviour of two objects, the study of the Edney shock/shock interferences, and the wake effects.

2.2.1 Shock/shock interferences

Many studies concerning the interaction of objects focused on the study of the shock/shock interferences first described by Edney [65]. He experimentally investigated the shock/shock interferences (SSI) between an oblique shock (from a wedge) and the shock of a hemisphere (see Figure 2.14), a flat face, and a cone. The experiment consisted in visualising the flow-field, measuring the heat transfer rate and the wall pressure

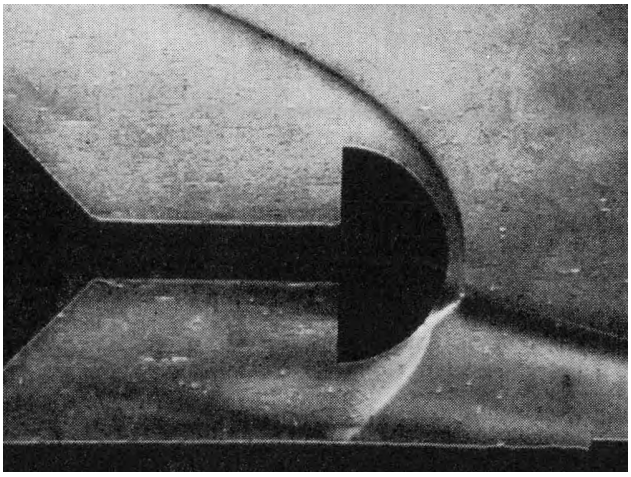

Figure 2.14: Edney type III shock/shock interferences [65].

distribution. The results allowed him to identify six types of interferences, whatever the geometry of the interacting model.
Thereafter, the shock/shock interferences have been extensively studied to improve their description. A common schematisation was proposed by many searching teams and is presented in Figure 2.15. In the continuum regime, numerous experimental and theoretical studies investigated the interferences between an oblique shock, generated by a wedge, and a bow shock, most often produced by a cylinder [101, 88]. As done by Edney, most of them present visualisations, wall pressure measurements and heat flux measurements. The SSI demonstrated a major role in the aerothermodynamics, with high local heating rates at supersonic and hypersonic speeds.

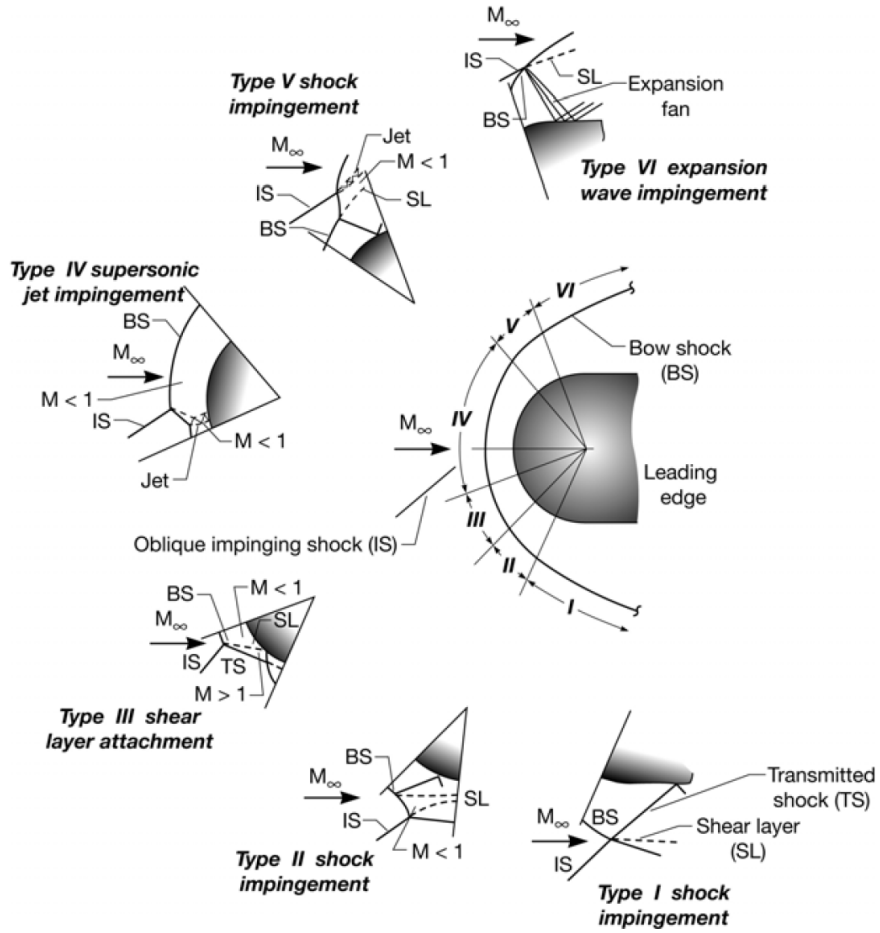

Figure 2.15: Schematics of the shock/shock interferences [6].

Many studies have focused on the type IV SSI as it appears to be the most critical shock-impact interaction. The supersonic jet that emanates from the interaction impinges on the body, creating strong aerothermal loads at the wall.[35, 33, 87]. The type III and V SSI also arouse curiosity with important aerothermal load [133, 103]. As these types also delimit the end of the type IV SSI, some work was dedicated to the transition between them [37, 215].

Most of these results were obtained in the continuum regime, from experiments in shock tubes or numerically with a CFD approach [124, 158, 103, 184, 215]. Only a few authors have shown interest in studying the influence of viscous effects the SSI [43, 78, 133, 144, 182, 170, 81]. However, they seem to observe a vanishing of the SSI specificities as the level of rarefaction increase. In particular, the shock-wave becomes thicker and more diffuse which lead to a decrease in heat and pressure loads [1, 211]. To our knowledge, only two experimental works have been carried out in the slip and transitional regimes. Pot *et al.* [170] experimented an oblique shock interacting with a cylinder in a Mach 10 flow. Their investigations focused on the wall pressure and temperature measurements for the types III and IV SSI. The experimental results were then used as a reference case for some numerical simulations [1, 57, 78, 144]. Riabov [182] also investigated the SSI for an oblique shock impacting a cylinder, but for an even greater level of rarefaction. With the results he obtained for the six types of SSI, Riabov stated that the type IV SSI does not take place for such a rarefied flow. To go further, White and Kontis [211], and more recently Agir *et al.* [1] numerically investigated the effect of the global rarefaction level on the SSI. They also observed the evolution of the SSI with the variation of Knudsen number. These results demonstrate the interest of experimentally investigating the effects of rarefaction on the SSI.

2.2.2 Aerodynamic behaviour

Proximal bodies were not only studied in the context of shock/shock interferences, which mostly inform on the aerothermal load, interesting to study for the structural aspect of a spacecraft or a material. Indeed, one other important interest in studying proximal bodies is to observe the aero-dynamic behaviour of interacting models.
To this aim, a certain number of experimental and numerical studies were carried out in the continuum regime. Generally, the configuration used are of two types: interaction of an incident oblique wave with a cylinder, and interferences occurring between two spheres, and sometimes two cylinders for 2D numerical simulations. These configurations are shown in Figure 2.16. Whether in one configuration or in the others,

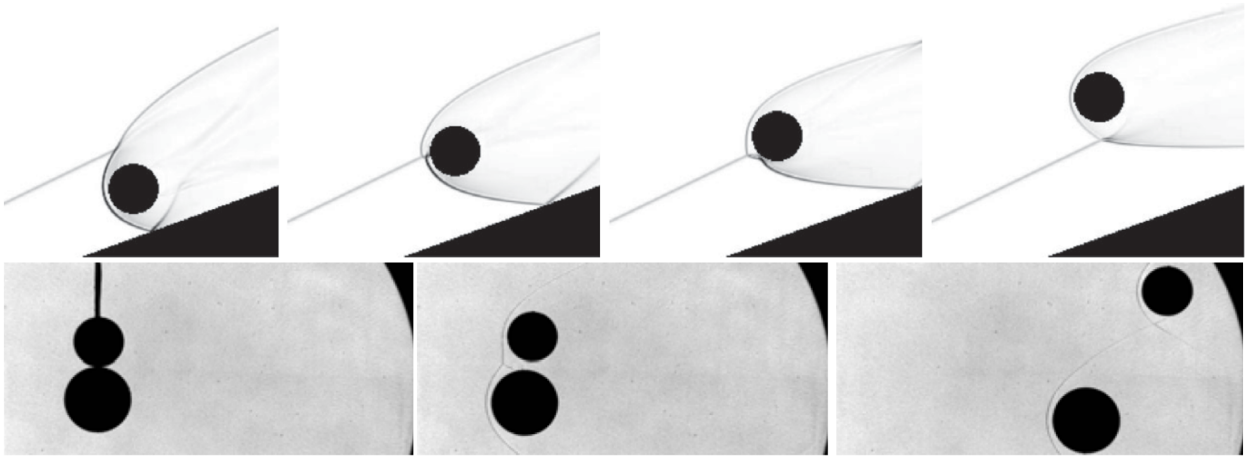

Figure 2.16: General interaction configuration for the aerodynamic studies [115, 117].

three main types of results are used to describe the aerodynamic behaviour of the models: the drag and lift coefficients [219, 71], and the pressure and friction coefficients [120], the separation velocity.
Laurence *et al.* [116] investigated the drag and lift coefficient of a sphere placed in the flow-field of another one, and specifically below the incident shock. They observed, specifically, that the increase in the secondary sphere size leads to an increasingly negative lift. Barri [21] observed a strong deceleration of the following sphere, when in the wake of the parent sphere, which is not the case for a location where the following sphere interacts with the incident shock. She also described the detachment of peripheral spheres. This phenomenon was also studied by Laurence *et al.* [117] and Park and Park [161] who estimated the separation velocities of the following sphere, which gives important information on its trajectory. They observed that a small sphere is more likely to be entrained in the wake of the first object. Register *et al.* [178] agree with these results, and demonstrate a strong dependence of the initial conditions. In particular the size of the second sphere, and its location will lead to a different final region, as it is explained in Figure 2.17. "For example, the fragment F2 depicted in the figure has diameter D2= 0.25D1 and is initially located at an angle

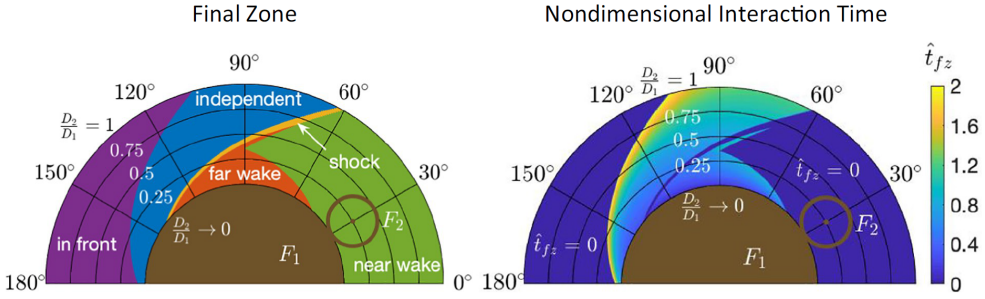

Figure 2.17: Final zone and interaction time according the size and initial location of the second sphere [178].

of 30°. Its final position is in the near wake behind fragment F1, and the interaction time is zero". Different scenarios and in the end the phenomenon of shock-wave surfing are discussed. This described the fact that, in certain conditions, the following sphere moves in such a way as to follow the incident shock-wave. Thanks to the drag and lift coefficients, and with the knowledge of the separation velocities, Laurence [115] and Marwege *et al.* [137] described, and gave the necessary conditions to this rare phenomenon.
To our knowledge, only one numerical work has been carried out in a hypersonic rarefied flow. Vashchenkov [203] simulated the interaction of two interacting cylinders, and created a mapping of drag and lift coefficients for different sizes of secondary object. This result is of great interest, but comes from a numeric study, and no experiments can be compared. Thus, it would be very interesting to bring some experimental data to validate the described behaviour.

2.2.3 Wake effects

From the literature, we have seen that the following sphere is strongly impacted by the flow-field of the parent one. However, very few work is dedicated to the impact that the following sphere can have on the primary one. Nevertheless, some hydrodynamic experiments have highlighted a very weak impact of the following sphere location. [220] aligned two spheres in the direction of the flow, and made their inter-distance vary. A very slight variation of the drag force of the primary sphere is observed as the inter-sphere distance is reduced. The force variation of a leading sphere was also observed numerically by Li et al. [120], and Golubev [79]. For a Mach number of 4, Golubev observed a variation of the force for inter-sphere distance of less than 3

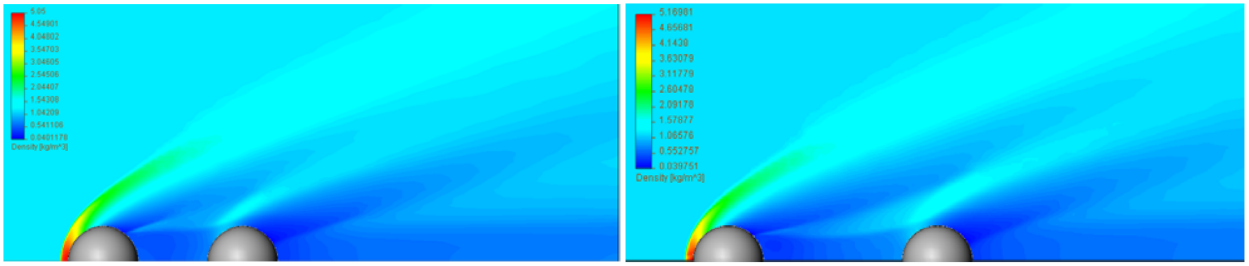

Figure 2.18: Numerical flow-fields of two aligned spheres [79].

diameters, with less than 10% difference. These effects are weak, but at the scale of an atmospheric re-entry, it may induce a variation of the leading debris trajectory.

In Appendix A, a non-exhaustive list of authors and their articles is given. These works correspond to the main results found on the topic of aerodynamic interactions. All along this work, certain results of the literature will be more detailed, and some comparison will be made with our results.

Chapter 3

Overview of the thesis

Contents

3.1 Aim of the thesis

This doctoral work is a fundamental work that aims to bring some light on the problematic of aerodynamic interactions occurring between space debris' fragment during the atmospheric re-entry. The studies of proximal bodies and shock/shock interferences conducted in the continuum regime did show strong interactions' impact on the fragments' behaviour. Some numerical studies were focusing on the viscous effect induced by the rarefaction level at high altitudes. However, the very few number of experimental works on the topic does not allow to confront the numerical results. In this context, we propose to create a strong experimental database based on shock/shock interferences. The experimental results are obtained in supersonic and hypersonic rarefied flow, representative of space debris fragmentation altitudes.

3.2 Main objectives of this doctoral research

At the outset of this research, some objectives were established and had to be fulfilled:

- characterise the flow-field and aerodynamics of a single sphere to have reference knowledge;
- identify different types of shock/shock interferences (SSI) with respect to Edney's types;
- numerically simulated the flow-field of a single sphere with a Direct Simulation Monte Carlo;
- measure the drag and lift forces of the following sphere;
- measure the pressure at the wall of the following sphere;
- characterise the effect of the SSI on the aerodynamic behaviour of the following sphere, in particular with the quantification of pressure and friction contributions;
- characterise the effect of global and local rarefaction level on the SSI;
- estimate the overall impact of the rarefaction level and Mach number on the SSI, and on the following sphere behaviour.

3.3 Thesis overview

To respond to these objectives, different aspects of the work have to be explored.

In Part II, we will discuss the experimental conditions of the study. A brief description of the work environment is given, followed by the description of the facility without which none of the results would have been obtained, MARHy. The choice of the model and of the experimental conditions are explained and allow to obtain the simulated re-entry altitude. All the diagnostics used to acquire the results are then fully described. In the last chapter of this part, we will characterise the flow-field and aerodynamic behaviour of a single sphere in the three chosen free stream (Ma 4 - 2.67 Pa, Ma 4 - 8 Pa, Ma 20.2 - 0.07 Pa).

Part III is dedicated to the analysis of experimental and numerical results. This part is composed of four chapters. In Chapter 7, we discussed the identification of the different types of shock/shock interferences in supersonic conditions. Chapter 8 is dedicated to the full study of a couple of spheres, equal in size, in the Ma 4 - 2.67 Pa flow. The results describe the aerodynamic behaviour of the following sphere as a function of shock/shock interferences, but also concerns the in-wake locations. A brief analysis demonstrates

the impact of the following sphere on the parent one. Chapter 9 is devoted to the impact of the rarefaction level on SSI and the consequences on the following sphere aerodynamic. Two key areas of discussion are given: the variation of the global rarefaction level, by changing the free stream flow (Ma 4 - 2.67 Pa vs. Ma 4 - 8 Pa); the variation of the local rarefaction level, by changing the size of the following sphere for a same free stream flow. Finally, Chapter 10 is focused on the hypersonic rarefied results. In this chapter, a discussion over the vanishing of the types of SSI is set, and aero-dynamic results are analysed.

Finally, Part IV will close this work. First a complete technical conclusion is given, that allows resuming the entire results and have a global visualisation of the contribution of this work. Then, a brief summary of the thesis will be given, followed by the envisaged perspectives.

Part II

Experimental Conditions

Partie II
Résumé en Français

Cette partie décrit les conditions dans lesquelles ont été réalisé les expériences d'interactions aérodynamiques en régime raréfié. Elle est composée de trois chapitres qui permettront de mieux appréhender le travail réalisé durant ces trois années de thèse.

Chapitre 4

Ce chapitre décrit l'environnement de travail et en particulier la soufflerie MARHy grâce à laquelle l'ensemble des résultats ont été obtenus. Son principe de fonctionnement est entièrement expliqué et ses performances sont présentées. Il est montré en quels points les différentes tuyères de la soufflerie sont représentative de la rentrée atmosphérique, ce qui a permis de choisir trois tuyères. Le choix des maquettes est également expliqué, ce qui permet d'expliciter les différentes conditions de rentrée atmosphérique simulées.

Chapitre 5

Après avoir décrit la configuration générale de la mise en place expérimentale, les divers diagnostiques permettant l'obtention des résultats sont décrits. Les diagnostiques sont les suivants :

- visualisation des écoulements par le biais de la méthode de décharge électro-luminescente ;
- mesures de pressions Pitot pour la caractérisation de l'écoulement d'une sphère seule ;
- mesures de pressions pariétales ;
- mesures de forces aérodynamiques par le bais d'une balance aérodynamique (trainée et portance) ainsi qu'avec une technique de pendule (trainée).

Les différents capteurs et méthodes d'analyses sont explicitées tout au long du chapitre.

Chapitre 6

Ce travail de thèse s'intéresse plus précisément à l'aérodynamique d'une sphère (S_2) se trouvant dans l'écoulement d'une première sphère (S_1). Deux éléments sont à connaître pour évaluer l'effet des interactions choc/choc sur S_2 : l'écoulement dans lequel elle est immergée, et son aérodynamique quand elle est seule dans l'écoulement, c'est-à-dire, sans interaction avec S_1. Pour cela, ce chapitre décrit l'écoulement de toutes les sphères utilisées, lorsqu'elles sont seules dans les trois écoulements libres expérimentés. Grâce aux visualisations, l'onde de choc d'une sphère, et notamment la distance de détachement du choc sont discutées. Une nouvelle loi est proposée pour calculer la distance de détachement du choc d'une sphère quels que soient ses nombres et Mach et de Reynolds. Les mesures de forces de trainée des différentes sphères permettent de valider les méthodes de mesures, et de calculer leur coefficient de trainée. Les pressions pariétales, quant à elles, permettent d'évaluer la contribution des efforts de pression, et donc de friction, sur le coefficient de

trainée. Des simulations numériques ont été réalisées avec la simulation directe Monte Carlo (DSMC), permettant le calcul d'écoulement raréfié. Les deux codes utilisés sont DS2V et DS3V, codes libres d'accès permettant d'effectuer des calculs respectivement en deux et trois dimensions. La difficulté du milieu raréfié réside notamment dans la détermination de coefficients d'accommodations qui caractérise les conditions de glissement à la paroi. C'est aujourd'hui le point faible de ces codes de calculs. Grâce aux résultats expérimentaux obtenus pour les différentes sphères seules, il a été possible d'itérer ces coefficients d'accommodations jusqu'à trouver ceux donnant la meilleure solution, c'est-à-dire, pour lesquels les résultats numériques sont les plus proches des résultats expérimentaux. Ainsi, les résultats numériques dans l'écoulement d'une sphère seule pourront être utilisé pour l'interprétation des résultats obtenus sur la deuxième sphère.

Chapter 4

The experimental conditions

Contents

4.1 ICARE Research Laboratory

The full content of this doctoral work was realised at ICARE, the Institute of Combustion, Aerothermic, Reactivity and Environment. ICARE is a laboratory of the CNRS (Orléans, France) which exists since 2007 from the merger between two laboratories: the *Laboratoire d'Aérothermique* (Meudon, France) and the LCSR. This merging is the result of a common purpose: to strengthen the French research on aerospace technologies and to increase its European and international visibility.
This laboratory, mainly experimental, provides results in three major axes:

- analysis of combustion phenomena and reactive systems;
- study of chemical processes in the atmosphere and its application to the environment;
- analysis of high velocity flow and development of new technologies for space propulsion.

The present study is inscribed in the last thematic which is composed of three main platforms:

- FAST: Facilities for Aerothermodynamics and Supersonic Technologies;
- NExET: New Experiment on Electric Thrusters;
- PIVOINE 2G: new experiments on stationary plasma thrusters.

The experiments presented in this thesis were realised in the FAST platform whose test facilities were inherited from the *Laboratoire d'Aérothermique*. This platform is dedicated to the study of different flow regimes with supersonic and hypersonic velocities. Three complementary wind tunnels enable to study the peculiarities of the rarefied flows occurring at different stages of an atmospheric re-entry (Figure 4.1).

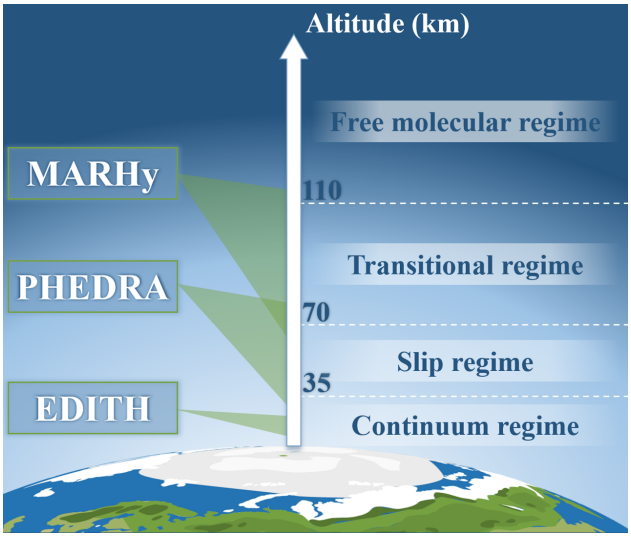

Figure 4.1: Rarefied regimes crossed during an atmospheric re-entry and the associated wind tunnels.

- MARHy (**M**ach **A**daptable **R**arefied **Hy**personic) is a continuous low-density supersonic or hypersonic wind tunnel that simulates high flight altitude.

- PHEDRA (non-equilibrium plasma of atmospheric entries) is a continuous high-enthalpy supersonic wind tunnel that simulates medium flight altitudes, where the friction of air molecules gets strong.
- EDITH (study of the interactions and transfers in hypersonic) is a jet wind tunnel dedicated to the study of shock-waves, principally for the characterisation of supersonic nozzles.

All the experiments performed for this doctoral work were carried out in the MARHy wind tunnel. It is the most appropriate to simulate flight conditions corresponding to the early stage of space debris re-entry, and more specifically to the fragmentation altitudes.

4.2 The MARHy wind tunnel

4.2.1 The test facility

The MARHy wind tunnel, formerly known as SR3, was built in 1963 after the CNES decided to build a facility for the study of aerodynamic and aerothermal effects, at flight altitudes from 80 to 100 km. The facility was designed to simulate hypersonic velocities in a low-density flow, characteristic of the high atmosphere.
SR3 was progressively improved and its pumping unit entirely renovated in 2000, when it was moved from the *Laboratoire d'Aérothermique* in Meudon to ICARE in Orléans. There, it became the MARHy wind tunnel. Today, thanks to a set of interchangeable nozzles, this wind tunnel can simulate subsonic to hypersonic flows at representative altitudes between 50 and 90 km.
Figure 4.2 presents pictures of the MARHy wind tunnel (a) and its pumping unit (b). As described in the schematic view (c), the wind tunnel is composed of three main parts: the settling chamber; the test chamber separated from the previous one by the nozzle; and the diffuser that connects the test chamber to the pumping unit.

The settling chamber
The settling chamber is cylindrical with 1.2 m in diameter and 2.6 m long. It is used to stabilise the gas with a suitable stagnation pressure and temperature before it goes through the nozzle. This chamber is only used for subsonic and supersonic nozzles, for which the gas used is the ambient air of the experimental hall, where the temperature is regulated at 20 °C. The air enters the settling chamber through a micrometric valve that allows to regulate the pressure accurately. At the gas inlet, a flow breaking cone allows avoiding flow turbulence in the settling chamber, leading to stable stagnation conditions.
For hypersonic flows, the settling chamber is not used as a gas reservoir, but to receive the nozzle. The gas used, dinitrogen, is stocked at 200 bars in a rack of eight gas cylinders. The settling pressure is regulated in the pressure line and is directly injected at the entrance of the pressure line of the nozzle.

The nozzle
The nozzle of the wind tunnel can be changed, each nozzle of them having a specific design that corresponds to one flow condition. The free-stream Mach number and density depend on the stagnation pressure and temperature, which are regulated upstream of the nozzle; and on the free-stream pressure in the test chamber. Two kinds of geometry are found among the 19 nozzles that can equip the MARHy wind tunnel: curved or conical as shown in Figure 4.3.
The curved nozzles correspond to subsonic and supersonic flows. For this kind of nozzle, the stagnation

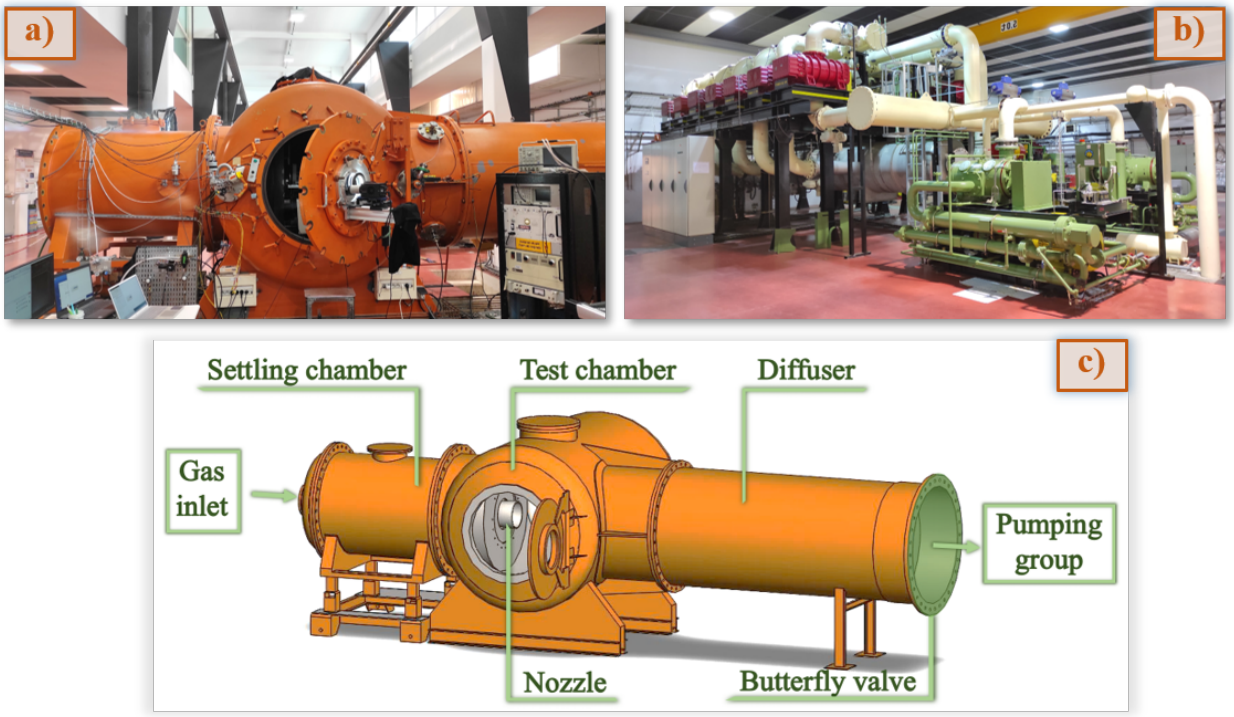

Figure 4.2: Images of the MARHy wind tunnel (a) and its pumping group (b). Schematics of the MARHy wind tunnel (c).

conditions of the settling chamber (at ambient temperature) are sufficient to produce homogeneous and isentropic flows. But it is not the case for conical nozzles, used for hypersonic flows, operating with dinitrogen. As previously explained, the inlet pressure is obtained by regulating it directly from the line of the gas bottles. To obtain a maximal expansion without condensation and freezing, the gas also needs to be heated. This stage is realised by conduction when the gas passes through a helical resistance in graphite, itself heated by a high electric intensity (about 600 A). Once the stagnation conditions before the nozzle throat correspond to the operating conditions, the generated flows is steady and the free-stream conditions are described by Christou [48]. Concerning the hypersonic nozzles, a detailed presentation of the nozzle composition and operation was given by Allegre and Raffin in 1972 [9] at the time of the SR3 wind tunnel, and then by Coumar [52] updated the functioning adapted to the MARHy wind tunnel in her doctoral work.

The test chamber

Passing through the divergent section of the nozzle, the gas expands into the test chamber, where experiments are performed. This chamber is cylindrical with a diameter of 2.3 m and a length of 5 m. On one side, a 1.2 m diameter door enables to access the inside of the chamber. Two optical windows (one on the door, the other on the roof of the chamber) allow to capture images of the flow-field. Two types of window material can be used: quartz for the recording of images, and selenium-zinc for the measurement of temperature with an infrared camera. In the test chamber is placed a triaxial motorised displacement system.
As previously said, the free stream flow, in which are realised the experiments, is obtained by regulating the stagnation and free-stream pressures. The stagnation pressure is regulated upstream of the nozzle throat, and the free-stream pressure is regulated by means of the pumping rate of the rest of the flow line.

The diffuser

In the test chamber, the flow expands toward the pumping group via the diffuser. The diffuser ensures the good evacuation of the gas, maintains the level of rarefaction and so the desired free-stream pressure. It is

Figure 4.3: Pictures of some nozzles of the MARHy wind tunnel.

a pipe of 1.4 m in diameter and 7 m long. Without the diffuser, a good priming of the nozzle would need a vacuum capacity equivalent to the inlet flow rate. To do so, the pumping group should be much more powerful, increasing the cost and equivalent expenses.

The butterfly valve

The pressure in the experiment chamber is the results of a pressure balance between the inlet and the outlet. The latter depends, of course, on the pumping power involved, but it can also be adjusted by means of a valve that allows the diameter of the pumping line to be adjusted. This valve is a motorised butterfly valve of 1.4 m in diameter. It is placed on the diffuser line.

The pumping group

The pumping group is composed of three vacuum lines mounted in series. The first line to be started is the one that generates the primary vacuum of the entire line; it is composed of two rotary vacuum pumps absorbing 4600 $m^3.h^{-1}$. Once this primary vacuum is obtained, the second line can be activated by starting the two secondary Roots blowers, pumping each 29200 $m^3.h^{-1}$. Then, a more advanced vacuum level can be reached thanks to twelve secondary Roots blowers able to generate an airflow of 15250 $m^3.h^{-1}$ each.
According to the nozzle used, the free-stream pressure needed in the test chamber is different. This pressure is regulated by selecting the right number of Roots blowers to power up. Then, a thinner regulation of this pressure is obtained with the opening of the butterfly. The regulation of free-stream pressure, depending on the pumping group and the butterfly valve, is made via a human-machine interface controlling the ignition, shut down and functioning.

Once the stagnation and free-stream conditions correspond to the operating conditions, the free-stream conditions in the core of the flow are perfectly known stable and continuous due to the stability of the pumping station.

Table 4.1: Flow conditions of the different nozzles of the MARHy wind tunnel.

		Stagnation conditions		Free-stream conditions			
	Gas	p_o (Pa)	Te_o (K)	Ma_∞	p_∞ (Pa)	Te_∞ (K)	Re_∞ (m^{-1})
Subsonic	Air	41.32	293	0.8	27.11	260	$5.7e^3$
Supersonic	Air	20.86	293	2	2.67	163	$2.6e^3$
	Air	62.58	293	2	8	163	$7.9e^3$
	Air	47988	293	2	6133	163	$6e^6$
	Air	404.8	293	4	2.67	69.8	$1.8e^4$
	Air	809.6	293	4	5.33	69.8	$3.7e^4$
	Air	1214	293	4	8	69.8	$5.5e^4$
	Air	10800	293	4	71.11	69.8	$4.9e^5$
Hypersonic	N_2	$1.73e^4$	1000	6.8	5	97.6	$3.5e^4$
	N_2	$2e^5$	800	12	1.38	16.8	$1.2e^5$
	N_2	$2e^6$	1000	14.9	3.17	22	$4.6e^5$
	N_2	$5e^5$	1000	15.1	0.72	21.4	$1.1e^5$
	N_2	$2e^5$	1000	15.3	0.26	20.9	$4.2e^4$
	N_2	$6e^5$	1000	16	0.58	19.2	$1.1e^5$
	N_2	$4e^6$	1100	16.5	3.15	19.8	$5.9e^5$
	N_2	$8e^6$	1200	18.4	2.97	17.5	$7.5e^5$
	N_2	$1e^6$	1100	20	0.21	13.6	$8.3e^4$
	N_2	$3.5e^5$	1100	20.2	0.07	13.3	$2.8e^4$
	N_2	$1.2e^7$	1300	21.1	1.73	14.4	$6.7e^5$

4.2.2 Performances

Table 4.1 presents the entire set of nozzles that can be mounted in the MARHy wind tunnel. The underlined rows concern the nozzles used for this experimental work. Here are presented the stagnation (subscript $_o$) and free stream (subscript $_\infty$) pressures and temperatures, along with the gas used. The Mach number only depends on the stagnation and free-stream pressures. The corresponding values are calculated with Equation 4.1.

$$Ma_\infty = \sqrt{\frac{2}{\gamma - 1}\left[\left(\frac{p_o}{p_\infty}\right)^{\frac{\gamma-1}{\gamma}} - 1\right]} \tag{4.1}$$

The viscosity value involved for the estimation of the Reynolds number is calculated with the Sutherland's power law (Equation 2.2). The NRLMSIS Atmosphere Model 2.0 [66, 152] gives parameters of the atmosphere at high altitude, in particular the total mass density ρ and the neutral temperature Te. The pressure can be calculated with Equation 4.2.

$$P = \rho.R.Te/M_m \tag{4.2}$$

Figure 4.4 presents the graph of atmospheric pressure calculated with NRLMSIS data according to the altitude. The orange points correspond to the free-stream pressure of each nozzle, so their altitude can be found by reporting it on the NRLMSIS data. As seen, the static conditions of the entire set of nozzles correspond to altitudes ranging between 20 and 95 km. For a more realistic approach, it is therefore preferable to refer to a dynamic dimensionless parameter.
Figure 4.5 presents the similarity parameter according the altitude (Equation 2.7). The black line gives the calculated similarity parameter for a spherical object of 1 m in diameter re-entering Earth's atmosphere. It

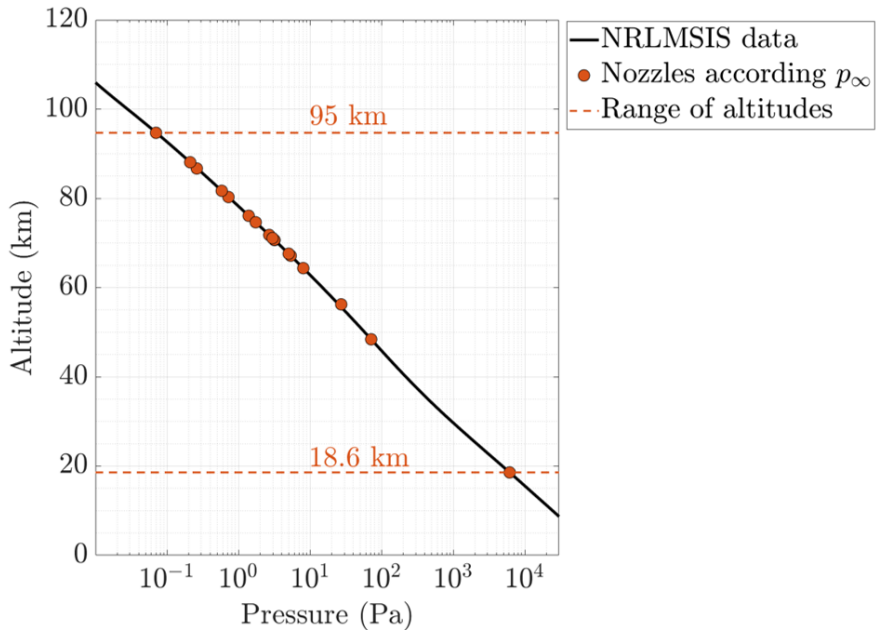

Figure 4.4: Pressure by altitude and nozzles altitude correspondence.

is calculated with the velocities given by Prévereaud *et al.* [173] (beyond 78 km values are extrapolated) (Figure 2.3), and the atmospheric data given by the NRLMSIS model. The viscosity is calculated according to the Sutherland's law (see Equation 2.2)
In the MARHy wind tunnel, the size of the model has to be limited due to the diameter of the isentropic core which is between 7 and 13 cm. The horizontal coloured lines, at the bottom of the graph, correspond to the similarity parameter calculated for some nozzles of the MARHy wind tunnel for objects raging between 5 and 50 mm in diameter. By plotting these similarity parameter values on the black curve, it is possible to give the range of altitude representative of a 1 m spherical object re-entering the atmosphere. An example of value transfer is given by the green case which gives the altitude range of the nozzle Ma 20.2 - 0.07 Pa. These ranges are represented by the vertical coloured lines at the left of the graph and show that a wide range of altitudes can be covered by the wind tunnel.
2 vertical dashed black lines are plotted. They correspond to the limit values given by Chambre and Schaaf [44]:

- $\frac{Ma}{\sqrt{Re}} < 10^{-2}$: continuum regime
- $10^{-2} < \frac{Ma}{\sqrt{Re}} < 10^{-1}$: slip regime
- $10^{-1} < \frac{Ma}{\sqrt{Re}} < 10$: transitional regime

Thus, as can be seen with Figure 4.5, the MARHy wind tunnel is representative of the slip and transitional regimes.

4.2.3 Experimental facilities for atmospheric re-entry

There is not a single experimental facility able to reproduce the full flight phenomena occuring during atmospheric re-entry. Indeed, atmospheric re-entries combine complex flight conditions such as hyper-velocities, low densities and high temperatures. Thus, to understand the physics, many classes of ground test facilities are necessary to form a solid experimental database [55, 136].

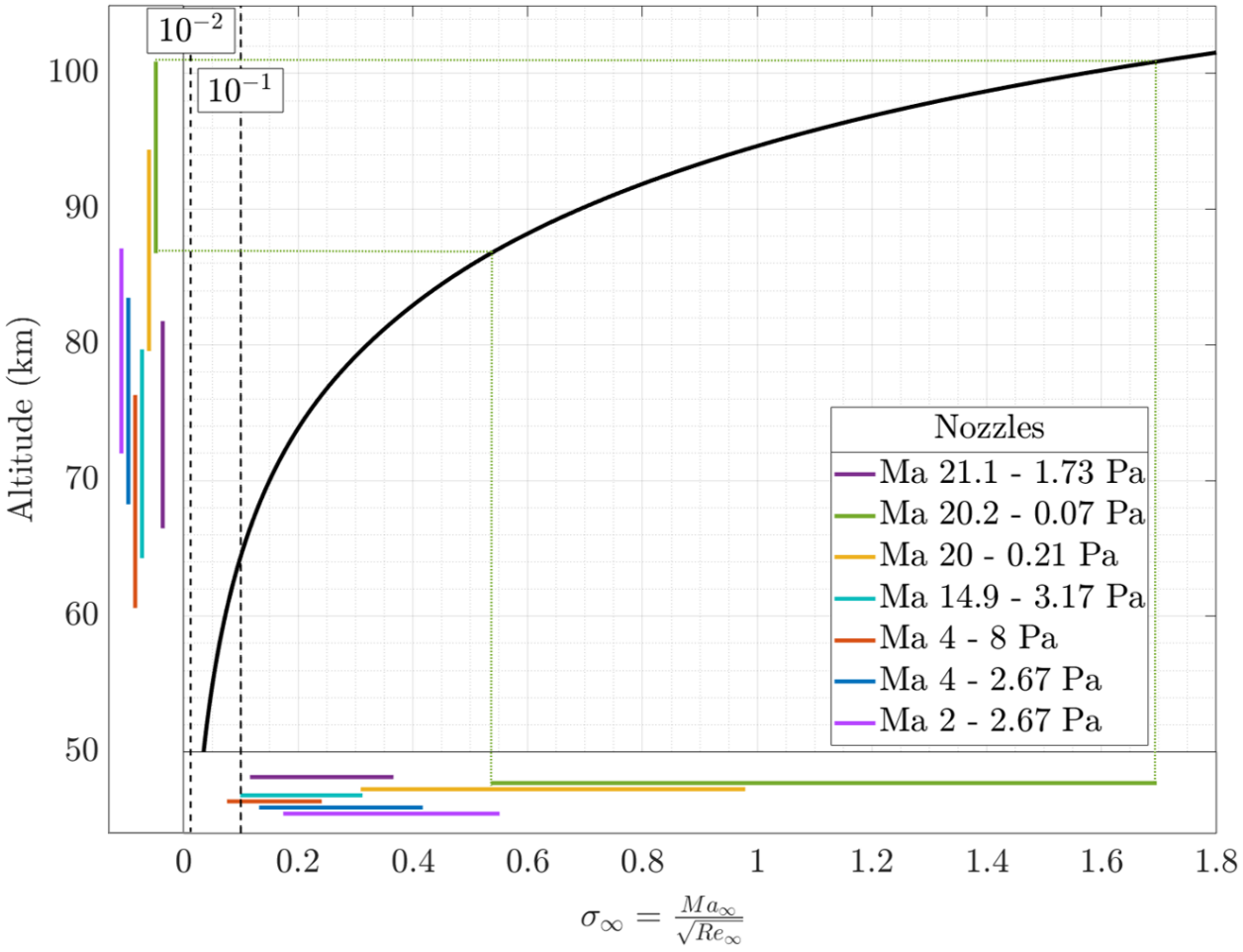

Figure 4.5: Black curve: Similarity parameter calculated for a 1 m spherical object during its atmospheric re-entry. Coloured lines: Similarity parameter calculated for some of the nozzles of the MARHy wind tunnel with models between 5 mm and 50 mm, and their corresponding range of altitudes.

This work is focused on the experimental simulation of hypersonic aerodynamic phenomena occurring at high altitude. Numerous ground test facilities were constructed in the 1960s and 1970s to experimentally study the aerodynamic properties of supersonic and hypersonic flows in transition and slip regimes. However, the scarcity of publications in this field reflects a low level of activity in the hypersonic and rarefied field over the last two decades. The Countries involved in this period were the USA with the N-3 wind tunnel at the Princeton University [201]; Germany with three test sections V1G, V2G and V3G at the German Aerospace Centre (DLR-Göttingen) [217]; United Kingdom with the Imperial College Graphite Heated Hypersonic Wind Tunnel at the Imperial College London [84], and the Low Density Wind Tunnel HS3 (LDWT) at the University of Oxford [175]; Russia with the T-327 at the Institute of Theoretical and Applied Mechanics (ITAM) in Novosibirsk [64]; and France with the rarefied wind tunnel SR3 at the Centre national de la recherche scientifique (CNRS) in Meudon, now renamed the MARHy wind tunnel. A longer non-exhaustive list of the hypersonic facilities is given in Appendix B with their capabilities in terms of velocity, temperature, pressure and running time.

4.3 Simulated re-entry conditions

Table 4.2: Operating conditions of the nozzles used.

Stagnation conditions				Free-stream conditions			
	N1	N2	N3		N1	N2	N3
gas	air	air	N_2	gas	air	air	N_2
p_o (Pa)	404.8	1214	$3.5e^5$	p_∞ (Pa)	2.67	8	0.07
Te_o (K)	293	293	1100	Te_∞ (K)	69.8	69.8	13.3
ρ_o (kg.m^{-3})	$4.80e^{-3}$	$1.44e^{-2}$	1.07	ρ_∞ (kg.m^{-3})	$1.33e^{-4}$	$3.99e^{-4}$	$1.73e^{-5}$
				μ_∞ (Pa.s)	$4.84e^{-6}$	$4.84e^{-6}$	$9.15e^{-7}$
				V_∞ (m.s^{-1})	669.92	669.92	1502.57
				Ma_∞	4	4	20.2
				λ_∞ (mm)	0.223	0.074	0.771
				ω_∞	0.92	0.92	0.866

4.3.1 The nozzles used

In this study, three flow conditions were studied thanks to the three nozzles named N1 (Ma 4 - 2.67 Pa), N2 (Ma 4 - 8 Pa), and N3 (Ma 20.2 - 0.07 Pa), and respectively detailed in Table 4.2.
The choice of these nozzles is based on multiple reasons. First, if looking at Figure 4.5, it can be seen that this selection enables to reproduce the atmospheric re-entry of a 1 m-diameter spherical piece of debris between 60 and 100 km which covers the fragmentation altitudes. Other reasons concern the free stream flow. Initially a fourth nozzle was to be experimented (N4: Ma 20.2 - 0.21 Pa), giving a full understanding of Mach effect, and of pressure effect. Unfortunately, due to experimental issues, it has not been possible to achieve these last flow conditions. From Table 4.2, it can be observed that N1 and N2 have the same Mach number; and the difference in Mach number between N3 and N4 was weak. So these nozzles give two iso-Mach conditions: one at Mach 4, and the other at Mach $\approx$ 20. The free-stream pressure being different for each nozzle, it enables to study the effect of a pressure variation at iso-Mach.
Moreover, concerning the mean-free-path of the free stream flows, there is a factor of 3 between N1 and N2, and it was also the case between N3 and N4, with $\lambda_\infty(N1) \approx \lambda_\infty(N3)$. Consequently, with a coherent size of models, an iso-Knudsen number could have been reached, enabling to study the effect of Mach number with a same level of rarefaction.

4.3.2 The models

The supersonic nozzles N1 and N2 were the first to be experimented. The diameter of their isentropic core are respectively of 7.5 and 8 cm. The experiments consist in studying the aerodynamic interactions between two spheres in different relative positions. In order for the spheres to always be located in the isentropic nozzles, and not to obstruct the flow, their diameter must not be too large.
For this work, the study of different diameter ratios between the two spheres was wished to experiment with a variation of the local rarefaction in a same free stream flow. For this reason, the diameter of the biggest diameter must not be too small.
With these needs, for N1 and N2, four diameters were studied: 16 mm, 12 mm, 10.3 mm and 8 mm.
As explained earlier, the mean free-path of N1 being close to that of N4, it was decided to choose sphere diameters that correspond to a close Knudsen number. To this end, two diameters were chosen with N3 and N4: 18 mm and 12 mm, N4 being not experimented in the end.
Depending on the nozzle used, two materials have been used. For N1 and N2, the spheres are made of polyoxymethylene, or more commonly called POM. According to the study of Allegre *et al.* [7] on the heat

transfer over a blunt body, the temperature of the models is expected to increase for N3. Thus POM, which is a plastic material, can no longer be used. Because of the use of ionising method, it was decided to exclude any metal material not to create an electrical field, in the flow around the models, which could modify their aerodynamics. Consequently, for N3, the spheres are made of boron nitride, a ceramic material which is an excellent electrical insulator and can resist to high temperatures (<1200 °C) without being dilated or melted.

4.3.3 The simulated conditions

The simulated conditions are directly linked to the size of the models. Table 4.3 gives an overview of the models tested for each nozzle. The scaling parameters Re_∞, Kn_∞, and σ_∞ are given so that conditions can be compared in terms of viscosity, static rarefaction level, and dynamic rarefaction level. The present work aims to understand the impact of aerodynamic interactions between two spheres. To this end, it is first necessary to know the original aerodynamics of a single sphere in a free stream flow. For this reason, every line presented in Table 4.3 were experimented in the MARHy wind tunnel. Thanks to the similarity parameter σ_∞, Table 4.6 enables to estimate the simulated altitudes for the different nozzles and models described in each line of Table 4.4.

	∅ (mm)	Re_∞	Re_2	Kn_∞	σ_∞
N1	16	294 .4	81.6	$1.39e^{-2}$	0.233
	12	220.8	61.2	$1.86e^{-2}$	0.269
	10.3	189.5	52.53	$2.16e^{-2}$	0.290
	8	147.2	40.8	$2.79e^{-2}$	0.330
N2	16	883.2	243.2	$4.65e^{-3}$	0.135
	12	662.4	182.4	$6.19e^{-3}$	0.155
	10.3	568.6	156.56	$7.20e^{-3}$	0.167
	8	441.6	121.6	$9.29e^{-3}$	0.190
N3	18	511.2	10.8	$4.29e^{-2}$	0.894
	12	340.8	7.2	$6.43e^{-2}$	1.095

Table 4.3: Characteristic numbers of the free-stream flows experimented.

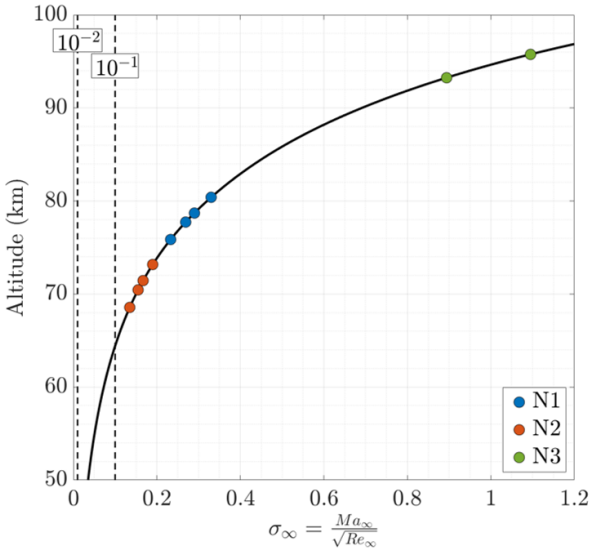

Figure 4.6: Black curve: Similarity parameter calculated for a 1 m diameter spherical debris during its atmospheric re-entry. Coloured points: experimented conditions.

As for Figure 4.5, the altitudes are calculated for a 1 m spherical object re-entering Earth's atmosphere with the velocities given by Prévereaud *et al.* [173] and the atmospheric density and temperature from NRLMSIS 2.0 model. Table 4.6 gives the experimentally simulated altitudes of the different sphere as summarised in Table 4.3.

Once single objects are studied, the couples of spheres summarised in Table 4.4 can be experimented. The comparison with the reference cases will help understand the effect of the aerodynamic interactions between two spheres. For each couple, it is considered that the global rarefaction level is that of the first object. For example, for C_2, the experimented couple is one sphere of 16 mm and the other of 8 mm. For N1, the global rarefaction level corresponds to the first line of Table 4.3.

Table 4.4: Couples of spheres tested per nozzle.

Denomination	$\emptyset_1$ (mm) - $\emptyset_2$ (mm)	$\emptyset_2/\emptyset_1$	Nozzles
C_1	16 - 16	1	N1 and N2
C_2	16 - 12	0.75	
C_3	16 - 10.3	0.64	
C_4	16 - 8	0.5	
C_5	18 - 18	1	N3
C_6	18 - 12	0.67	

Chapter 5

Diagnostic tools and methodology

Contents

5.1 General configuration

The experiments consist in studying the interactions between two spheres placed in a free stream flow. The first sphere, S_1, is representative of a parent piece of debris and is followed by a fragment represented by the second sphere, S_2. To understand the aerodynamic of debris when interacting, it is necessary to experiment with different relative positions between S_1 and S_2. As the useful core of the flow being is limited in diameter, it is important to ensure that the two spheres stay contained in it. In consequence, S_1 has to be placed with a particular caution depending on the nozzle to use, to ensure enough clearance for the displacement of S_2. Figure 5.1 and Figure 5.2 are schemes of the placement of the sphere depending on the nozzle used. The coordinate system $(\vec{i}, \vec{j}, \vec{k})$ defines the spatial referential of the nozzle core, and takes its origin at the centre of the nozzle exit C. As seen in Figure 5.1, for N1 and N2, S_1 is placed under the plane $(C, \vec{i}, \vec{j})$ in the isotropic core, while for N3 (Figure 5.2), S_1 is placed at the exact middle of the core. Two reasons determined these choices: the diameter of the useful core and the nature of the flow.
First, the diameters of the N1 and N2 useful flow-field is smaller (respectively 7.5 and 8 cm) than that of

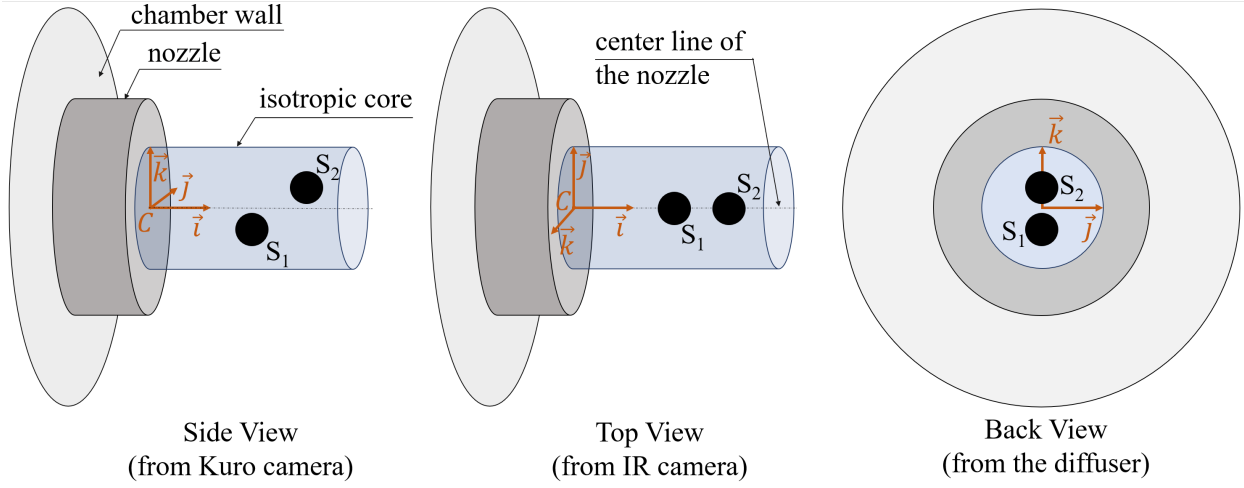

Figure 5.1: Schematics of the spheres positioning for N1 and N2.

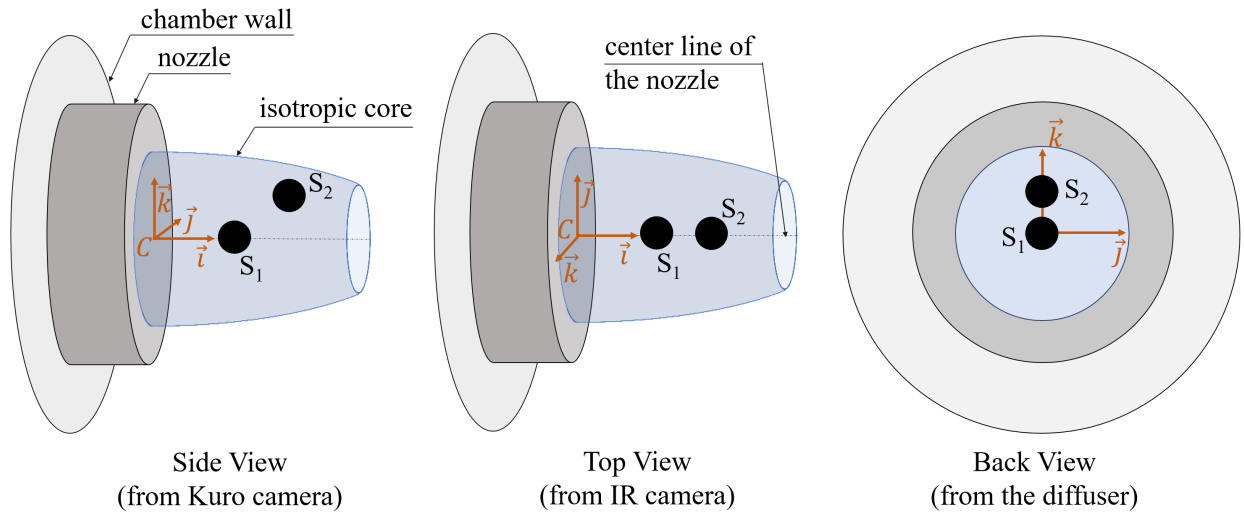

Figure 5.2: Schematics of the spheres positioning for N3.

N3, which is of 12 cm each. S_2 is moved in the $\vec{z}$-direction so that the flow-field is observed from the side

window by the Kuro camera. Thus, to have a sufficiently large area to displace S_2 without getting out of the core of the nozzle, it is necessary to lower the position of S_1 toward the centre of the core in case of the use of N1 or N2. More specifically, the centre of S_1 is placed at 30 mm above the plane $(\vec{i}, \vec{j})$. As will be discussed in section 6.1.1, the position of S_1 does not affect significantly the shock-wave.
This position of S_1 is not adopted for N3. Indeed the diameter of the flow is large enough to move up S_2. The other reason depends on the nature of the core. For N1 and N2, at the exit of the nozzle the flow is isotropic in a cylindrical core, which means that the physical parameter describing the free-stream flow remains the same whatever the direction (Appendix C, Figure C.1 and Figure C.1). This is not true for N3 because the nozzle is conical, so the flow-field properties vary according to the radial distance from the centre of the core (Appendix C, Figure C.3). As a consequence, the flow is perfectly axisymmetric in the exact middle of the core, where it is chosen to place S_1.
In any case, the stagnation point of S_1 and S_2 are included in the plane $(\vec{i}, \vec{k})$. The study of the aerodynamic interactions will be possible by moving S_2 in the $\vec{i}$ and $\vec{k}$ directions, thanks to a triaxial displacement robot, and additional translation systems with higher precision. As shown in Figure 5.3, S_2 location is given at its stagnation point O_2 by its coordinates (X_2, Y_2, Z_2) in the system $(O_1, \vec{x}, \vec{y}, \vec{z})$ taking its origin at the stagnation point of S_1.
Sometimes, for experimental reasons, some tools used need S_2 to be moved in the $\vec{j}$-direction. In this case, for N1 and N2, S_1 has to be placed in the plane $(C, \vec{i}, \vec{j})$, at -30 mm from the centre in the $\vec{j}$-direction. For N3, the location of S_1 does not change. Since all the free stream flows are axisymmetric, S_2 moving in a different radial direction does not change the flow-field it sees.

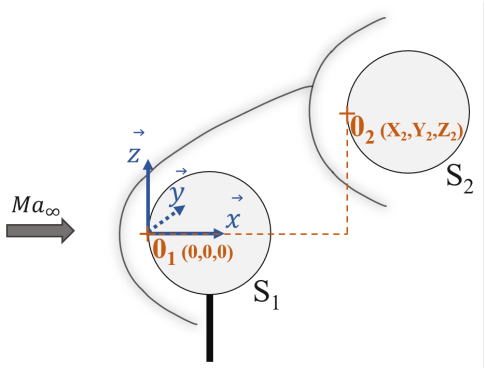

Figure 5.3: Coordinates system for S_2 positioning.

5.2 Flow-field visualisation

5.2.1 Description of the set-up

The set-up for the visualisation of the flow-field around the models is presented in Figure 5.4. S_1 is held from the bottom by a2 mm-diameter threaded rod mounted on a support profiled to reduce its obstruction of the flow. The support is held vertically in a pneumatic rotary actuator so that S_1 can be removed from the flow with a 90° rotation around the axis $\vec{i}$. S_2 is maintained by a profiled threaded holder from the rear to avoid intrusive disruption of the flow in the interference area. The holder is fixed in a profiled support, mounted on a translation system itself fixed on a triaxial displacement robot. To observe different types of interferences, S_1 is in a fixed position, and S_2 can be moved thanks to the motorised displacement tools. Both spheres can be completely removed from the flow.
As will be described in the following section, the visualisation method used to observe rarefied flow needs ionisation of molecules which is realised via a cathode. This cathode is whether made of copper or mix

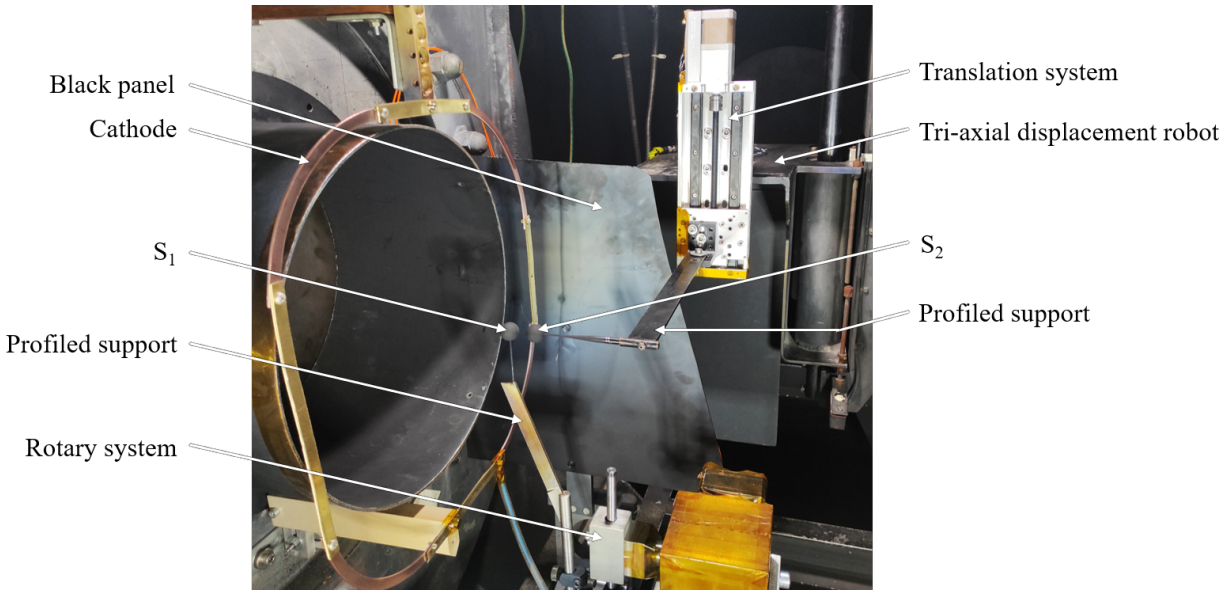

Figure 5.4: Experimental set-up for flow-field visualisations.

copper/brass. It is placed upstream of the models, around the exit of the nozzle. Behind the flow seen by the camera, a black panel is placed to homogenise the intensity level of the flow-field.

5.2.2 Glow-discharge visualisation technique

The characteristic of rarefied flows is to be low in density. In the compression areas, the number of molecules increases but remains low, and the refractive index of the gas does not present strong gradients. As a consequence, all the classical optical techniques based on the variation of optical index, such as Particle Image Velocimetry (PIV), shadowgraphy, strioscopy, do not provide the visualisation of shock-waves. On the contrary, techniques based on the ionisation of particles are efficient only in a limited range of density [213]. In the MARHy wind tunnel, the adopted visualisation method is the glow discharge. The method is based on the collision of electrons with the molecules of the flow. By applying a negative voltage on a cathode (between -1 kV and -2 kV depending on the case), a low polarisation is generated, pulling electrons from the cathode, without modifying the nature of the flow [53]. As the cathode is located near the flow, electrons will eventually collide with the molecules in the flow which leads to their excitation. To return to their initial state, they de-excite producing the illumination of emitted photons in the flow-field. Due to the low pressure, this phenomenon occurs in the near ultraviolet range with the emission of N_2^+ at 391.4 nm and N_2 at 337 nm. The shape and placement of the cathode in the test chamber are chosen so that the lighting of the flow is radially homogeneous in the core, and the luminous gradient is in the $\vec{i}$-direction, the direction of the flow. Other cathode placements were experimented but the one described here showed better results [180].
This method gives a visual as shown in Figure 5.5, allowing observing the flow-field. In a shock-wave, there is a compression of molecules so the local density is increased. Thus, locally there are more molecules and so, more collisions with electrons leading to a higher level of emitted light [96]. With a Langmuir probe, Coumar [52] measured the electronic density and showed that the luminous intensity recorded with a KURO camera equipped with a UV-visible objective is proportional to it. This means that the luminous intensity reflects the local density.
Nevertheless, the glow discharge visualisation technique produces a volumetric enlightenment, consequently the resulting intensity level on images is the result of integration along the line of sight of the camera. Thus, if the intensity level of images enable to detect shock-waves, it prevents to obtain the value of the local density. This result can be obtained with an electron gun that allows only a thin beam of molecules to be

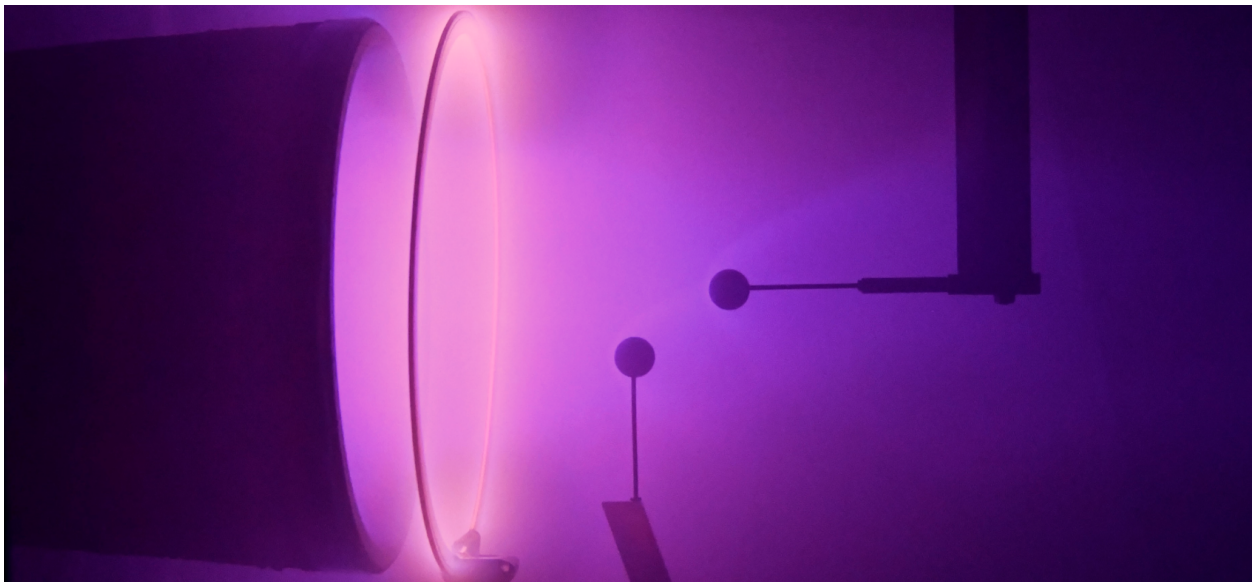

Figure 5.5: Photography of the flow-field visualised with the glow discharge technique.

excited. By calibrating the luminous intensity in a known free stream flow, a scaling law enables to calculate the local density in the flow. During my doctoral work, an electron beam has been conceived based on the work of Diop [61]. Some tests were conducted in a vacuum chamber, allowing to obtain a thin electron beam of 0.85 mm, as can be observed in Figure 5.6. Those results are encouraging on the functioning of the device. Unfortunately, tests on the MARHy wind tunnel have not yet been conducted.

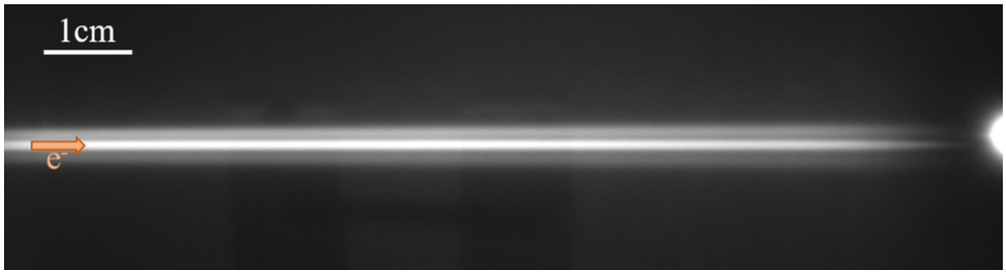

Figure 5.6: Photography of the electron beam obtained in a vacuum chamber.

5.2.3 Recordings and image post-processing

Images were recorded thanks to a Kuro CMOS camera (2048 × 2048-pixel array) with back-illuminated technologies. Due to the emission wavelength, the camera has an objective lens adapted to the ultraviolet-visible. Indeed, to minimise the loss of information, the optical equipment and the window have to agree with the bandwidth of the spectral emission. The mean resolution of the equipped camera is of 154 μm.px^{-1}. For each desired position of the models in the free stream, two sets of images are recorded. A first set of raw images is recorded with the models in the flow, at fixed positions; a second set is recorded without any models in the flow. Each set (with and without models) is composed of the same number of raw images and all the images are recorded with the same exposure time. These parameters depend on the experimental conditions and are presented in Table 5.1.
Indeed, for N1 and N2, since the free-stream density is higher than for N3, the global level of emitted luminosity is higher. Thus the exposure time has to be adapted in consequence so that the camera is not saturated. The number of images allows reducing their noise by averaging each set of images. For N3, since the exposure time is high, only a few images are necessary.

Table 5.1: Recording parameters of images.

Nozzle	Number of images per set	Exposure time (ms)
N1	200	60
N2	200	50
N3	20	400

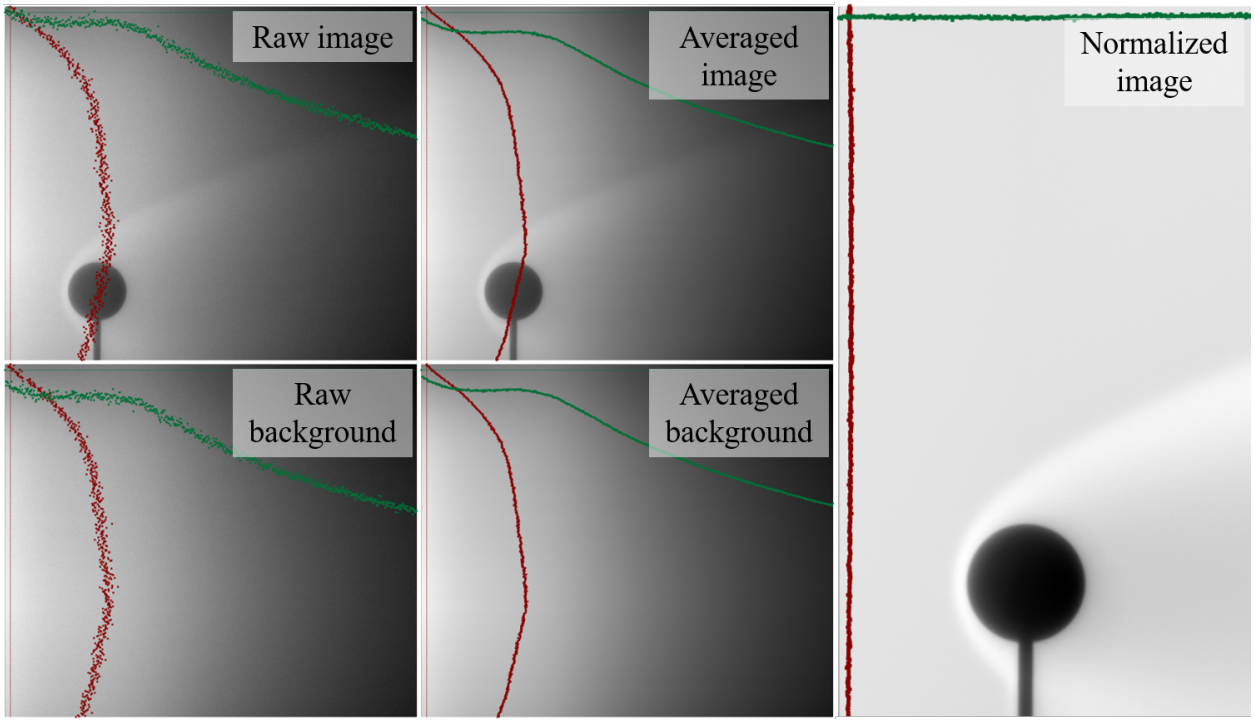

Figure 5.7: Image post-processing with vertical and horizontal free-stream intensity profiles.

Figure 5.7 presents the post-processing realised for each set of images. On the left images are presented the raw images with and without (background) the sphere. They correspond to one single image extracted from their respective set. On each image, two profiles of intensity are plotted. The green and red profiles correspond to the value of the corresponding dashed line (green for the horizontal and red for the vertical). As can be seen, on the raw images, the profiles are noisy. To weaken this phenomenon and obtain clear data, each set of images are averaged. The sets without models record the free stream flow: they are used as background images. The averaging is made possible by the steadiness of the flow during each recorded set. Averaged images are presented in the middle of Figure 5.7, where the luminous profiles are improved in terms of noise. The last step intends to cut intensity gradient due to the location of the ionisation source. By diving the averaged image by the averaged background, the image obtained is normalised (see the right image), and intensity profiles are constant and have very low noise.

5.2.4 Shock-wave detection

Whether in continuum or rarefied regimes, the detection of shock-waves is a real challenge. Difficulties come from the choice of the parameter to be analysed ([56, 216]), and to the technique to adopt for shock-wave detection [39, 73, 130, 155, 222].
In 1966, Robben and Talbot [183] experimented with the electron beam fluorescence method in rarefied flows. Based on their measures of local density, they showed that an increase in the level of rarefaction induces an increase of shock-wave thickness. Since then, and still now [180, 5], many other studies intend to

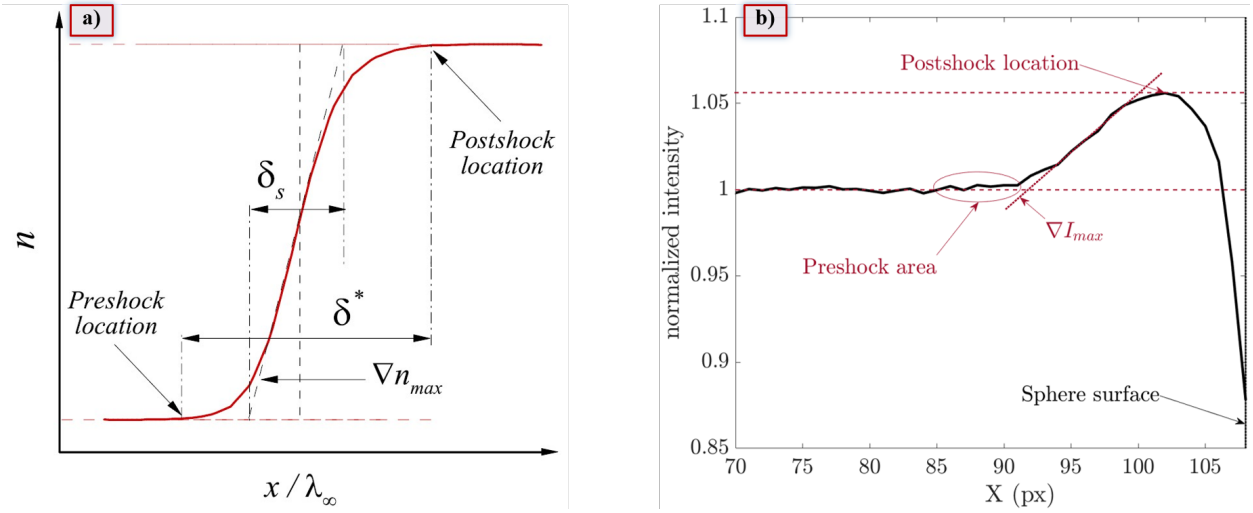

Figure 5.8: Distribution, within a thick shock-wave, of a): the number density [4], and b): the normalized intensity (present study).

better predict this thickening, which adds further difficulties on the detection of shock-waves. In rarefied flow, the shock-waves being thick and diffused, they do not induce a brutal gradient of density as in a continuum regime. In consequence, a rarefied shock-wave is not described by a single compressed line, but by a compressed area. Akhlaghi *et al.* [4] described this compressed area by three regions defined according to the density flow-field distribution. In Figure 5.8 a), these three regions correspond to the pre-shock, the shock centre, and the post-shock. The pre-shock corresponds to the point where the density begins to increase, while the post-shock corresponds to the point where it stops increasing. And between, corresponding to the location of the highest density gradient, ∇n_{max}, is the shock centre. δ_s and δ^* are the shock's width and to the shock-wave thickness.

In our case, the density being represented by the luminous intensity, an equivalent analysis can be realised on the normalised intensity, as presented in Figure 5.8 b). As can be observed, the post-shock corresponds to the maximum intensity, but the pre-shock can be hardly located due to the diffusivity of the shock-wave. So this method needs to be improved so that the shock-wave can accurately be found.

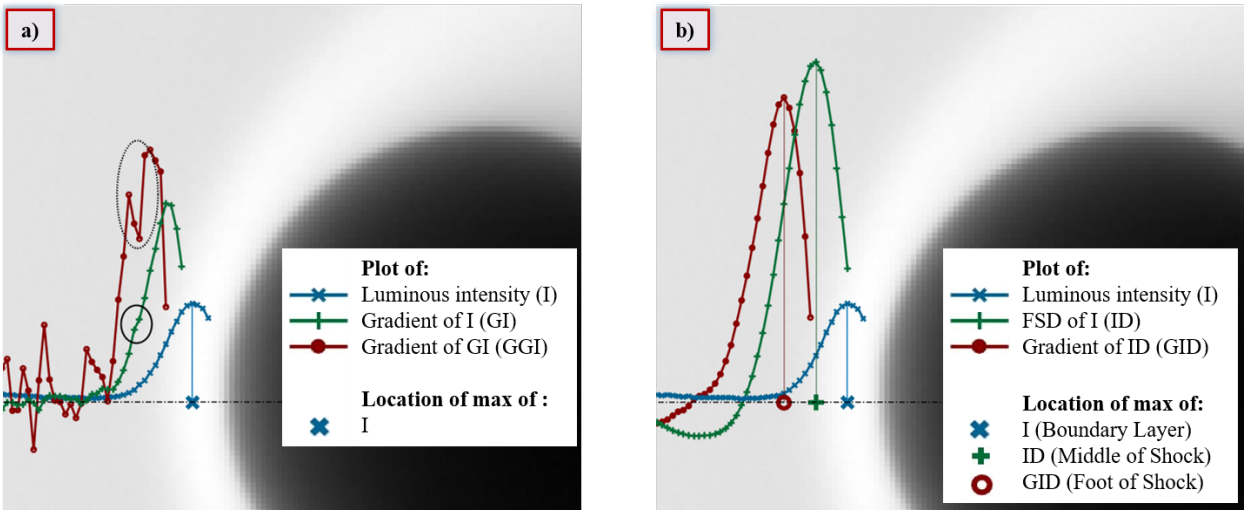

Figure 5.9: Shock-wave detection with a) the gradient method and b) the Fourier self-deconvolution method.

By observing the points of interest described earlier, the post-shock corresponds to the maximum of intensity, the middle of shock to the maximum of luminosity first derivative, and the pre-shock to the maximum of luminosity second derivative. This gradient method was adopted on each horizontal line of pixels of a

normalised image, as described in Figure 5.9 a). As can be seen, even with a clear luminosity profile, the gradient of intensity shows imperfections (black circle on the green curve). Unfortunately, this kind of perturbation can modify the location of the maximum, and has a direct repercussion on the calculation of the second derivative of intensity (red slope), which is completely deformed and prevents the detection of a proper maximum.
To overcome this problem, Kovacs *et al.* [113] proposed the Fourier self-deconvolution (FSD) method applied to the luminous intensity. His work has been realised in the same experimental conditions than the present study, so the FSD method will be the method used for the detection of shock-waves. This method magnifies the peaks in the intensity profiles but not the surrounding noise, unlike the gradient method. The result of the FSD method applied to a line of pixels in a normalised image is shown in Figure 5.9 b). As can be seen, the method consists in calculating the FSD of the intensity profile to find the middle of shock (MS), and its gradient gives the pre-shock, also called the foot of shock (FS). As for the gradient method, the maximum of intensity corresponds to the post-shock. The maximum of intensity also is the denser region. Close to the stagnation point, in the area defined by ± 1 radius of the sphere from its stagnation point, this region corresponds to the boundary layer (BL). Outside this area, the boundary layer designation is inappropriate. However, for the consistency, the maximum of luminosity region will be called the boundary layer whatever the location of the maximum.
Figure 5.10 shows the final result of the shock-wave detection by the FSD method applied on each horizontal line of pixels. From upstream to the surface of the sphere are plotted: the foot of shock, the middle of shock, and the boundary layer. This detection method has been validated experimentally by Kovacs *et al.* [113] by making a comparison with Pitot pressure profiles through the shock-wave. Results showed that the shock-wave detected with the Pitot pressure profile and with the FSD method are in good agreement: both are included in within 2 pixels, which is an acceptable error considering the resolution of the camera (154 μm.px^{-1}). Due to the automatic detection of the sphere, an error of ± 1 px is assumed. Another inaccuracy comes from the filtering of the luminous intensity which can lead to a maximal uncertainty of ± 1 px.

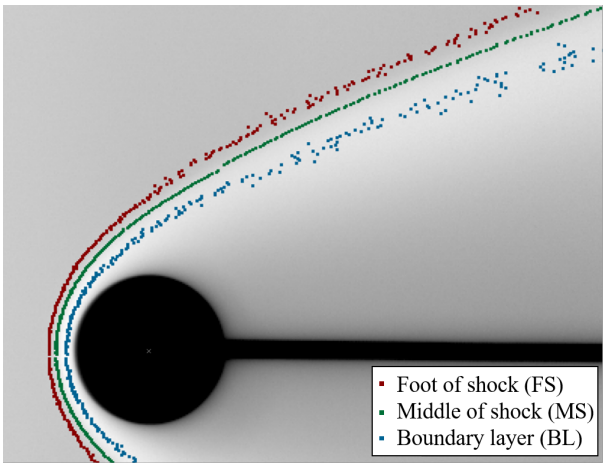

Figure 5.10: Result of the shock-wave detection with the FSD method.

5.2.5 Detection of the points of interest

In order to go farther in the study of SSI, remarkable points will be studied. These points are shown in Figure 5.11. From their location, or their level of luminous intensity, these points will give important information.
$P_{0_{BL}}$, $P_{0_{MS}}$ and $P_{0_{FS}}$ correspond respectively to the points where are detected: the boundary layer, the middle of the shock and the foot of shock on the horizontal line. These points correspond to the stand-off

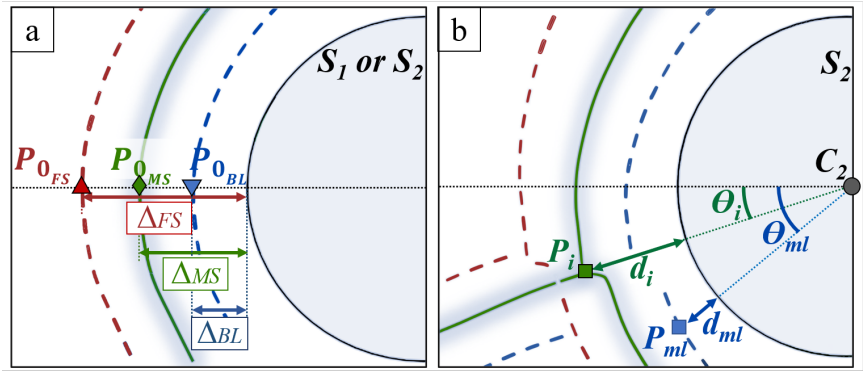

Figure 5.11: Remarkable points on the horizontal line of S_1 and S_2 (a) and in the interference area (b).

distances Δ_{BL}, Δ_{MS} and Δ_{FS}. As explained with the shock-wave detection method, the boundary layer is detected with the values of maximal intensity on each line of pixels. Thus, it is interesting to observe the behaviour of intensity values as S_2 is displaced at different positions. It was decided to record the intensity values I_0 at $P_{0_{BL}}$. All the values corresponding to the scheme a can be obtained for S_1 or S_2, the denomination will comport the corresponding index to make the distinction.
In the scheme b, the presented points are near S_2, in the interference area. P_i corresponds to the points of intersection between the middle of shock of S_1 and that of S_2. P_{ml} indicates the location of the point of maximum luminosity in the interference area. Both points are characterised by their angle and distance. Θ_i is the angle that makes the segment $[P_iC_2]$ with the horizontal, where C_2 is the centre of S_2. Θ_{ml} is found in the same way, but with the segment $[P_{ml}C_2]$. The angles are positive if the interaction occurs on the upper part of S_2, and inversely, negative if the interaction occurs on the lower part of S_2. On the segment $[P_iC_2]$, d_i is the distance between P_i and the surface of S_2. P_i is manually detected by pointing the two extreme points of the middle shock interaction. This way we can estimate d_i and Θ_i by making an average of the two points and calculating the differences between them. The uncertainty from the sphere location being smaller than that of the detection, it is not taken into account. As for Θ_{ml}, d_{ml} is found in the same manner as d_i, replacing P_i by P_{ml}. P_{ml} is numerically detected with the pixel of maximal luminosity, thus their is no inaccuracies from the detection, but only an inaccuracy from the sphere detection which is of ± 1 px.
For $P_{0_{BL1}}$, $P_{0_{BL2}}$ and P_{ml}, the values of luminous intensity are recorded and respectively noted I_{01}, I_{02} and I_{ml}. These intensities will serve as a quantitative parameter that represents the level of local density.
Note that, for the analyse of the experimental results, once the description of SSI is established, Θ_i will be used as the reference parameter that reflects the relative position of the spheres, and thus the type of SSI.

5.3 Pressure measurements

5.3.1 Pressure sensors

In this work, different pressure sensors were used to record Pitot pressure profiles and to measure wall pressures. Two kinds of sensors were used: absolute-capacitive sensors and differential sensors. A list of the sensors used is given in Table 5.2.

5.3.1.1 Absolute pressure sensors

The absolute sensors are based on the capacitance manometer technology and temperature are controlled to 45 °C. They are placed outside the wind tunnel and connected to the measuring point by an isolated pressure

Table 5.2: List of pressure sensors.

Sensor	Type	Pressure range	Precision
MKS 0.1 Torr	MKS Baratron absolute 627D.1TDD1B	0.1 Torr	0.15% of reading
MKS 1 Torr	MKS Baratron absolute 626AX01TBE	1 Torr	0.12% of reading
MKS 10 Torr	MKS Baratron absolute 627D11TDC1B	10 Torr	0.12% of reading
MKS 100 Torr	MKS Baratron absolute 627F12TDC1B	100 Torr	0.12% of reading
Validyne 0.0125 psi	Validyne differential DP103-10-N-1-S-4-D	0.0125 psi	0.5% of full range
Validyne 0.02 psi	Validyne differential DP103-12-N-1-S-4-D	0.02 psi	0.5% of full range

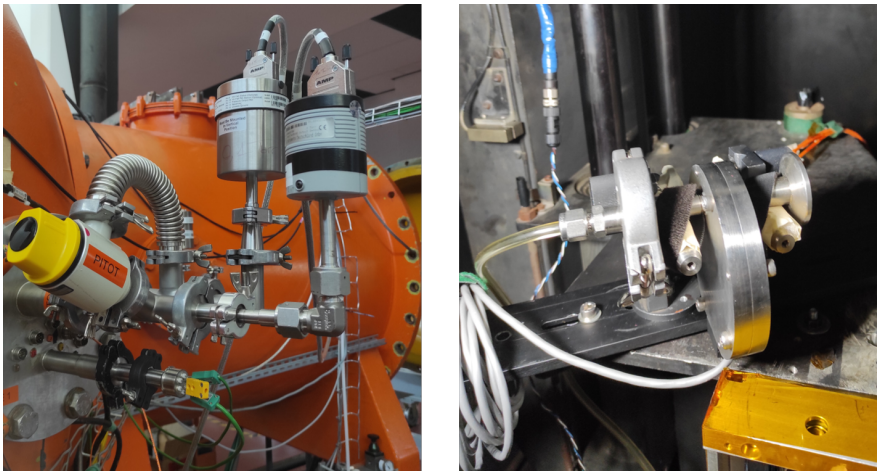

Figure 5.12: Positioning of the absolute (left picture) and differential (right picture) pressure sensors.

line (see the left picture of Figure 5.12). These sensors need to be regularly recalibrated so that the zero is correctly set. The MKS Baratron pressure sensors are monitored by an MKS digital read-out type PDR-C-2C or PR 4000B-F.

5.3.1.2 Differential pressure sensors

The differential pressure sensors are placed inside the wind tunnel, but outside the free stream flow and are monitored with a Validyne USB2251 data acquisition system. This type of sensor consists in measuring the deformation of a diaphragm placed between two cavities with different pressures. The diaphragm being sensitive to small variations of pressure, it is necessary to isolate the sensor from vibrations and gravity. To prevent noisy deformations of the diaphragm, the sensor is held on a support that absorbs vibrations and oriented so that the diaphragm is vertical, as seen in the right picture of Figure 5.12. The deformation of the diaphragms of the Validyne pressure sensors is linear, and even goes over-range as demonstrated by the calibration graphs in Figure 5.13.
The given electrical signal corresponds to the difference of pressure between the two cavities. Before realising any pressure measurement, it is important to know if there is a natural deformation of the diaphragm. To observe this phenomenon, the pressure in the two cavities must be equal. If there is a natural deformation, the corresponding signal is not null. This signal is called the offset value (U_{OF} in mV/V) and corresponds to a measurement of 0 Pa in pressure difference. To obtain this value, since our experimental conditions require very low pressures, the necessary time of vacuum conditions to equalise pressures in both cavities is of about 48 hours before any experiment can be realised. During experiments, the pressures in the two cavities are different and the given signal ($U_{measured}$ in mV/V) corresponds to the difference between the pressures. In our case, this difference is measured between the unknown pressure that is wished p (in Pa),

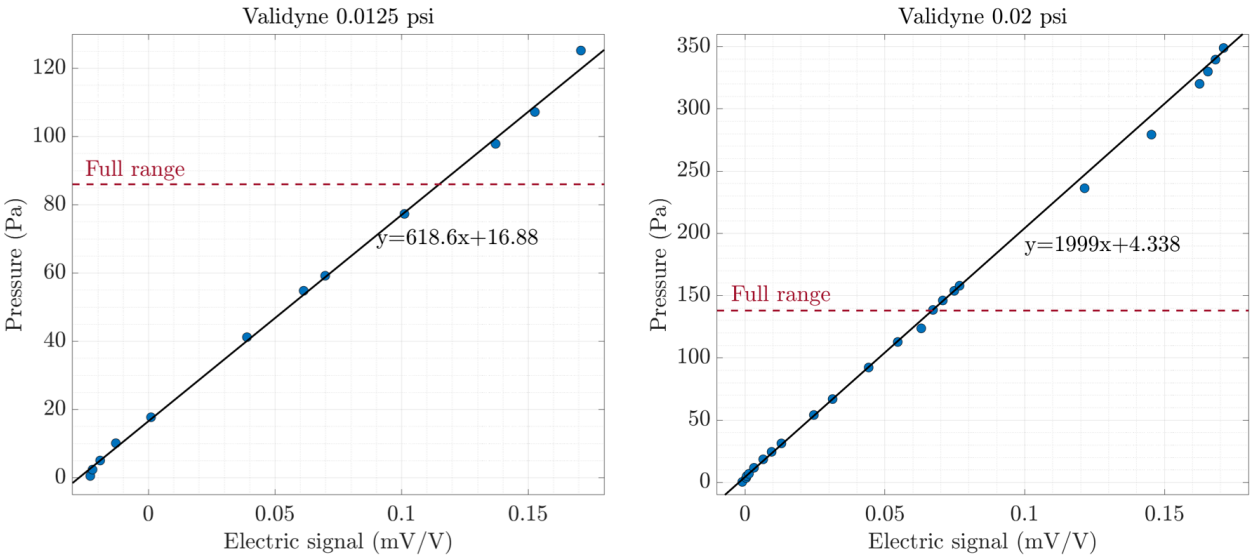

Figure 5.13: Calibration of the differential pressure sensors.

and the test chamber pressure p_1 (in Pa), known by means of an absolute pressure sensor. Due to the linear deformation of the diaphragm, the slope of the line gives the scale factor (SF) which translates the electrical signal (in mV/V) into pressure values (in Pa). In consequence, the measured pressure is calculated with the expression given in Equation 5.1.

$$p[Pa] = (U_{measured} - U_{OF})[mV/V] \times SF[mV/V \rightarrow Pa] + p_1[Pa] \tag{5.1}$$

5.3.2 Pitot pressure profiles

In order to characterize the flow-field around a single sphere, some pressure measurements in the flow were made by means of a Pitot tube.

5.3.2.1 Set-up

The tube, made of stainless steel, is 2.3 mm in outside diameter and 1.2 mm in inside diameter. The set-up for the measurement of pressure profiles around a single sphere in a free stream is shown in Figure 5.14.

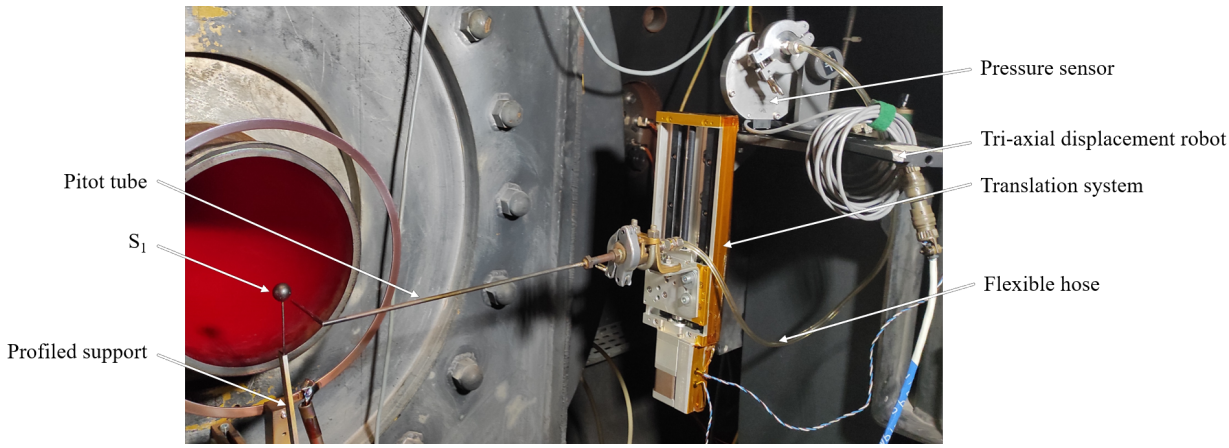

Figure 5.14: Experimental set-up for Pitot pressure measurements.

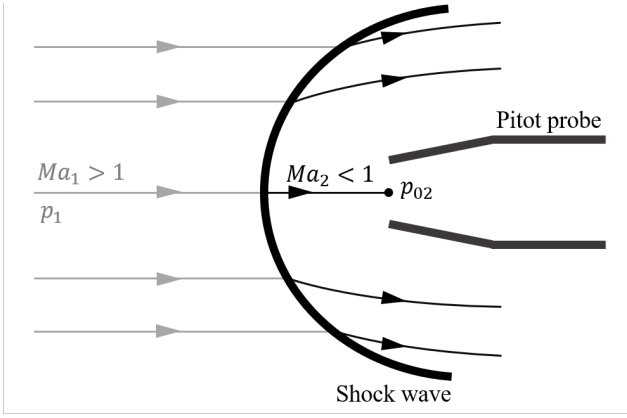

Figure 5.15: Schematics of the flow near the Pitot probe.

S_1 is held by a vertical profiled support, as for the flow-field visualisation, which allows the measurement of the pressure behind the sphere. S_1 is positioned in the centre of the nozzle to ensure the axi-symmetry of the flow. The Pitot tube is placed so that its entrance faces the flow. It is connected to a pressure sensor and monitored by the corresponding reading system (presented in Table 5.2). For N1, two pressure sensors were used (MKS 0.1 Torr and Validyne 0.0125 psi), and for N2 only the MKS 0.1 Torr was used. For each experiment, the pressure line is tested to ensure that there is no gas leak.
As described in Figure 5.15, the value recorded with the Pitot probe, p_{02}, corresponds to stagnation pressure behind the shock-wave it generates.

5.3.2.2 Numerical comparison

For comparison of the experimental values with the simulation, the numerical results need to be recalculated. Indeed, numerically, the given static pressure, p_1, corresponds to the free-stream conditions, while the experimental values are measured after the shock-wave of the Pitot probe. The Rankine-Hugoniot relation (Equation 5.2) allows converting the numerical values as if a Pitot probe was inserted in the numerical flow. With knowing the static pressure p_1, the Mach number before the shock Ma_1, and the heat capacity ratio γ, the stagnation pressure p_{02} is obtained. Thus, the experimental and numerical methods can be compared. Note that this conversion cannot be realised with the experimental values since the local parameters before the shock-wave are not known.

$$\frac{p_{02}}{p_1} = \left[\frac{(\gamma+1)^2 Ma_1^2}{4\gamma Ma_1^2 - 2(\gamma-1)}\right]^{\frac{\gamma}{\gamma-1}} \left[\frac{1-\gamma+2\gamma Ma_1^2}{\gamma+1}\right] \tag{5.2}$$

5.3.3 Wall pressure measurements

In order to obtain some information on the conditions at the wall of a model, alone or interacting with an incident shock-wave, pressure measurements were realised at the surface of a sphere.

5.3.3.1 Set-up

The general set-up used for the measurement of the wall pressure p_w is presented through Figure 5.16. This experiment allows obtaining the pressure distribution at the wall of a sphere, with and without interaction. Values are acquired in the vertical meridian plane of the sphere for different angles of measurement Θ_{wp}, as

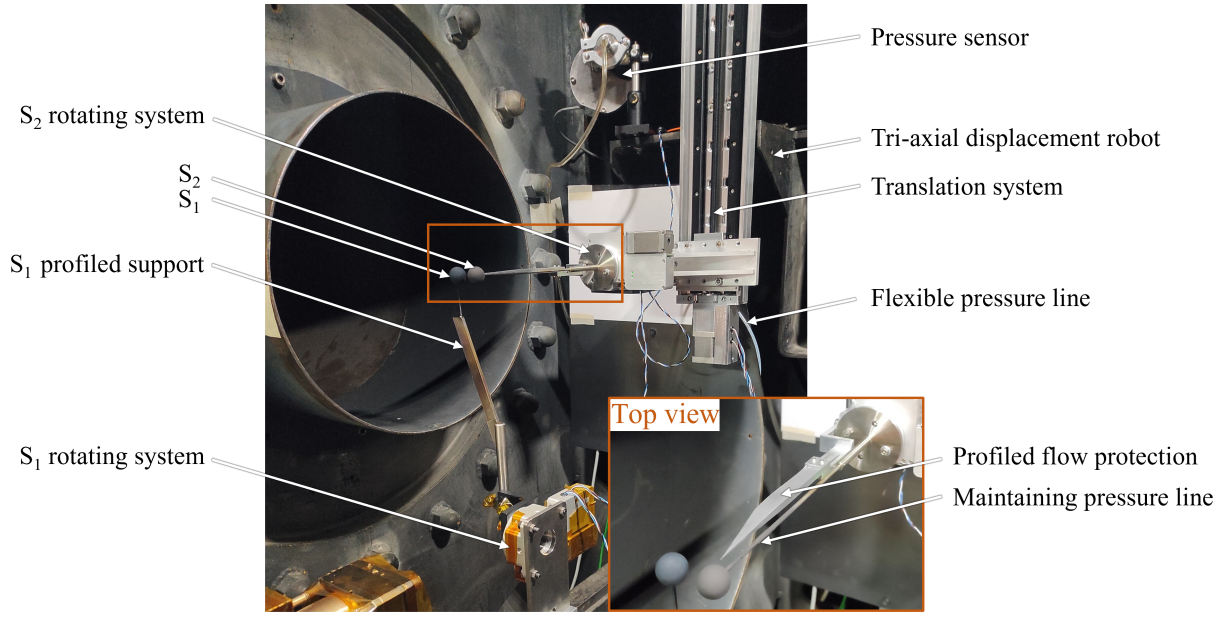

Figure 5.16: Experimental set-up for wall pressure measurements.

described by the side view of Figure 5.17.

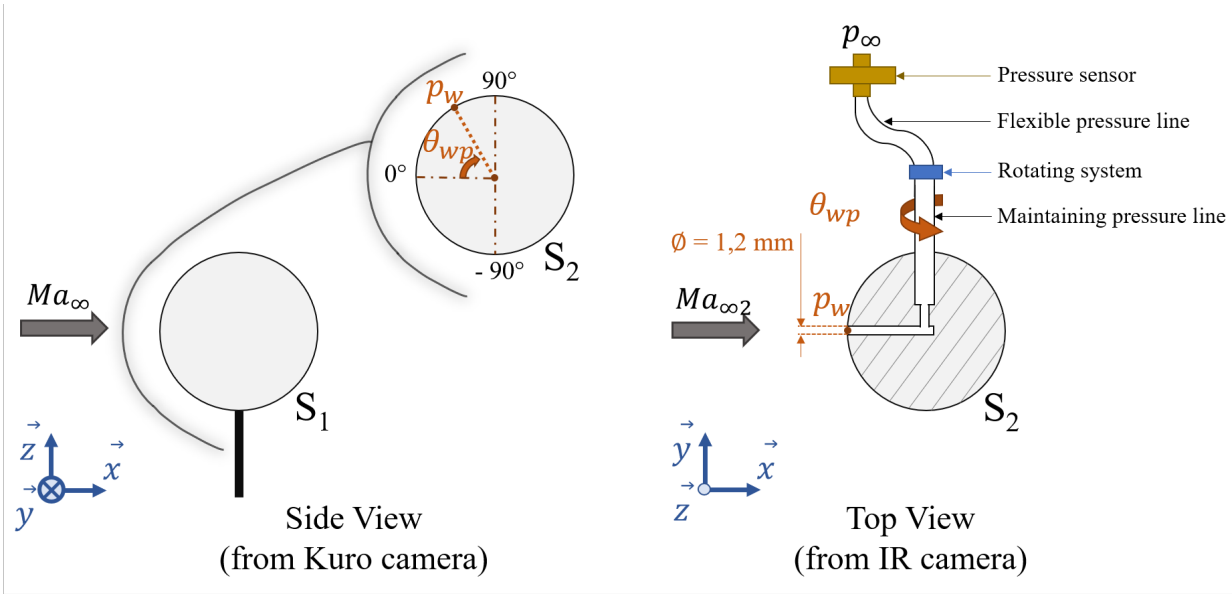

Figure 5.17: Schemes of the rotating system for wall pressure measurements.

S_1 is placed as for the previous set-ups: it is maintained by a vertical profiled support, the latter being mounted on a rotating system that enables S_1 to be getting out of the free stream flow. The models for pressure measurement are drilled as shown on the top view of Figure 5.17. Two perpendicular holes are drilled to the centre of the sphere. A first hole of 1.2 mm in diameter serves as the measurement point. This diameter is chosen according to two criteria: the desired accuracy in localisation of the measurement point, and the duration of measurement. Indeed, to integrate as little as possible the pressure on a surface, the hole has to be small to ensure a highly localised measurement. At the same time, due to the very low pressure of the experimental conditions, the hole has to be large enough to reach an equilibrium in the pressure line in a reasonable duration. The other hole serves to maintain the sphere while transmitting the pressure to the rest of the pressure line. Indeed, S_2 is maintained by a rigid tube of stainless steel that also serves as pressure lines. This tube is held in a rotating system (Zaber X-RSW60A-SV2), accurate at 0.14°. The assembly

sphere/tube/rotating system is mounted on a vertical translational system fixed to a triaxial displacement robot. This way, different positions of S_2 can be adopted during the same experiment. After the rigid tube, the pressure line is continued with a flexible hose that goes to one of the cavities of a differential pressure sensor, described earlier. The pressure sensor is chosen according to the experimental conditions (Validyne 0.0125 for N1 and N3), and Validyne 0.02 psi for N2). Differential pressure sensors were selected for their higher accuracy compared to absolute ones. Moreover, since they are placed in the wind tunnel, a shorter pressure line is possible, reducing the time of each measurement.
As shown on the top view presented in Figure 5.16, a profiled flow protection is fixed in front of the maintaining pressure line. The protection has specially been realised so, the tube is not shocked by the free-stream flow, and thus an increase in temperature of the pressure line is avoided. Also, as it is profiled, the protection also helps to reduce the blockage of the flow.

5.3.3.2 Acquisition protocol

As previously mentioned, before measuring pressures with a differential sensor, the pressure line needs to be balanced with the ambient pressure to obtain the same pressure in both cavities of the sensor. For this purpose, for wall pressure measurement, each time the wind tunnel needs to be open, then an extra 48 hours of vacuuming is needed. Thus, before the beginning of any new experiment, careful verification of the set-up is required. Once this equilibrium is reached, the flow can be set and the experiment realised.
The wall pressures of the sphere are measured over angles ranging between 90° and -90°, as described in the top view of Figure 5.17. For each angle, it is necessary to wait as long as needed so that the electrical signal sent by the sensor stabilises. For the lower pressure values, it takes about 15 minutes to record one value, while only 3 minutes are necessary for higher ones. Once all the angles are measured, the sphere is rotated back to the initial angle, and a new measurement is realised. This ensures that, for the entire duration of the experiment (about 4 hours per position), there is no deviation of the offset value.
For each flow condition, the pressure distribution is recorded for a single sphere as a reference case, and for six positions that correspond to different types of interferences.

5.3.4 Orifice effects

In rarefied flows, the pressure measurements can suffer from a bias due to experimental set-ups. Many studies [8, 193] showed that, due to viscous effect, the measured stagnation pressure of a model or of a Pitot probe is slightly different from the inviscid theory. In 1926, Hemke [85] observed that the corrective factor was dependent on the ratio of the orifice diameter to the curvature radius of the body. He also demonstrated that results were sensitive to the shape of the orifice by experimenting with sharp and rounded edges. Potter and Bailey [171] observed that the shape of the body nose itself whether it was spherical or flat, affects the measured stagnation pressure. They highlighted the importance of the orifice radius and length, and of the cavity temperature. This last influential parameter was also observed by Christou [48], who showed that the temperature of the pressure orifice or even of the pressure line impact the correction to be made.
For pressure distribution at the wall of a sphere, Potter and Bailey [172] also demonstrated that, depending on the angle of measurement, a supplementary correction was to be made, that is mostly understandable with the evolution of slip conditions around a flying body.
In conclusion, there is many parameters that impact the corrective factor, and in particular the upstream free stream. In our case, whether for the measurement of Pitot pressure profiles in the flow-field of S_1, or for the measurement of wall pressure of S_2, the local up-stream flow is unknown, so no correction can locally be made. But it was decided to correct values with the stagnation pressure of the free flow in the inviscid theory $p_{02_{th}}$, as defined in Figure 5.15 and calculated with Equation 5.2.

For the use of the Pitot probe, for each condition, a stagnation pressure measurement p_{02_m} was recorded in the free flow. For each flow conditions, by knowing the theoretical value and the measurement value, a coefficient of correction is calculated with Equation 5.3. This correction will be applied to all the Pitot measurements of the considered flow conditions.

$$C_{orifice} = \frac{p_{02_m}}{p_{02_{th}}} \tag{5.3}$$

In the case of wall pressure measurement, p_{02_m} corresponds to the stagnation pressure of a single sphere in the free-stream flow. The corrective coefficient is also calculated with Equation 5.3. The correction is applied to all the pressure measurements of S_2, the interacting sphere, whatever its position or the measurement angle.
These corrections are not the most accurate since they do not consider the local parameters, but due to the lack of information in the flow of S_1, no better solution was found. Moreover for wall pressure measurement, since the correction made is the same as the reference cases, it allows to estimate the effect of the SSI types on the pressure distribution.

5.4 Aerodynamic force measurements

Focusing on the trajectory of space debris, aerodynamic forces are of great importance. In order to better understand the effect of shock/shock interferences in rarefied flows, two measurement techniques were adopted: an aerodynamic balance and a swinging sphere technique.

5.4.1 Aerodynamic balance

The aerodynamic balance has been developed and experimented by Noubel and Lago [151]. It was specially conceived to measure small forces induced by low-density flow conditions, as generated in the MARHy wind tunnel.

5.4.1.1 Device

The balance is a sting type and is composed of two modules that measure the drag and lift forces. Each module is made of thin slats positioned perpendicularly to the force's direction to be measured (drag or lift). The applied forces produce a proportional deformation of the slats which are equipped with strain gauges that give an electrical signal. These output electrical signals (one channel for the drag and one for the lift) are given in millivolts output per volt input. To establish an equivalence between the electrical signal and the forces in Newton, a calibration is performed with a digital millinewton meter placed on a motorised micrometric displacement which applies a force of known value on each of the modules. Thus, the calibration of each module is performed independently for the drag force (the force is applied perpendicularly to the slats of the drag module) and for the lift force (the force is applied perpendicularly to the slats of the lift module). The measurements of the drag and of the lift modules are independent of each other.
It is important to note that the drag module is dependent on the position of the centre of gravity of the balance. To avoid measurement error due to the mass of the model, a counterweight is placed at the rear of the balance and its positioning and weight are calculated to keep the centre of gravity of the balance at the location of the strain gauges. Moreover, the balance is placed horizontally so that the slats are oriented perpendicularly to the gravity force, and are not deformed by it.
The design of the aerodynamic balance also includes a protective cover to prevent the flow from interfering

directly with the strain gauges by adding additional forces. Since the slats are thin, they deform easily, so any flow skimming them can generate errors since the measured forces are tiny. Another cause of inaccuracy can be due to the size of the model. If the model is too small, the shock formed in front of the model may interfere with the sting of the lift module and produce a small additional force.
This aerodynamic balance has been validated through the drag force measurements of a set of spheres with different sizes and experimental conditions [151]. Drag force values were compared with the results collected by Aroesty [16] and showed good agreement. Since the lift module is equivalent to the drag module but with a different orientation, it was validated by analogy.

5.4.1.2 Set-up

The necessary set-up for the measurement of the drag and lift forces with the aerodynamic balance is described in Figure 5.18.
The first sphere is placed as for the previous set-ups, allowing it to be removed from the flow for the measurement of the drag force of a single sphere.
The second sphere is screwed on the sting of the balance until its centre of gravity. The counterweight, placed at the rear of the balance, is placed according to the weight of the model. The balance is fixed to the triaxial displacement robot in a horizontal position. Thus, the drag force is measured according to the $\vec{x}$-direction and the lift force according to the $\vec{y}$-direction. In consequence, for the use of the aerodynamic

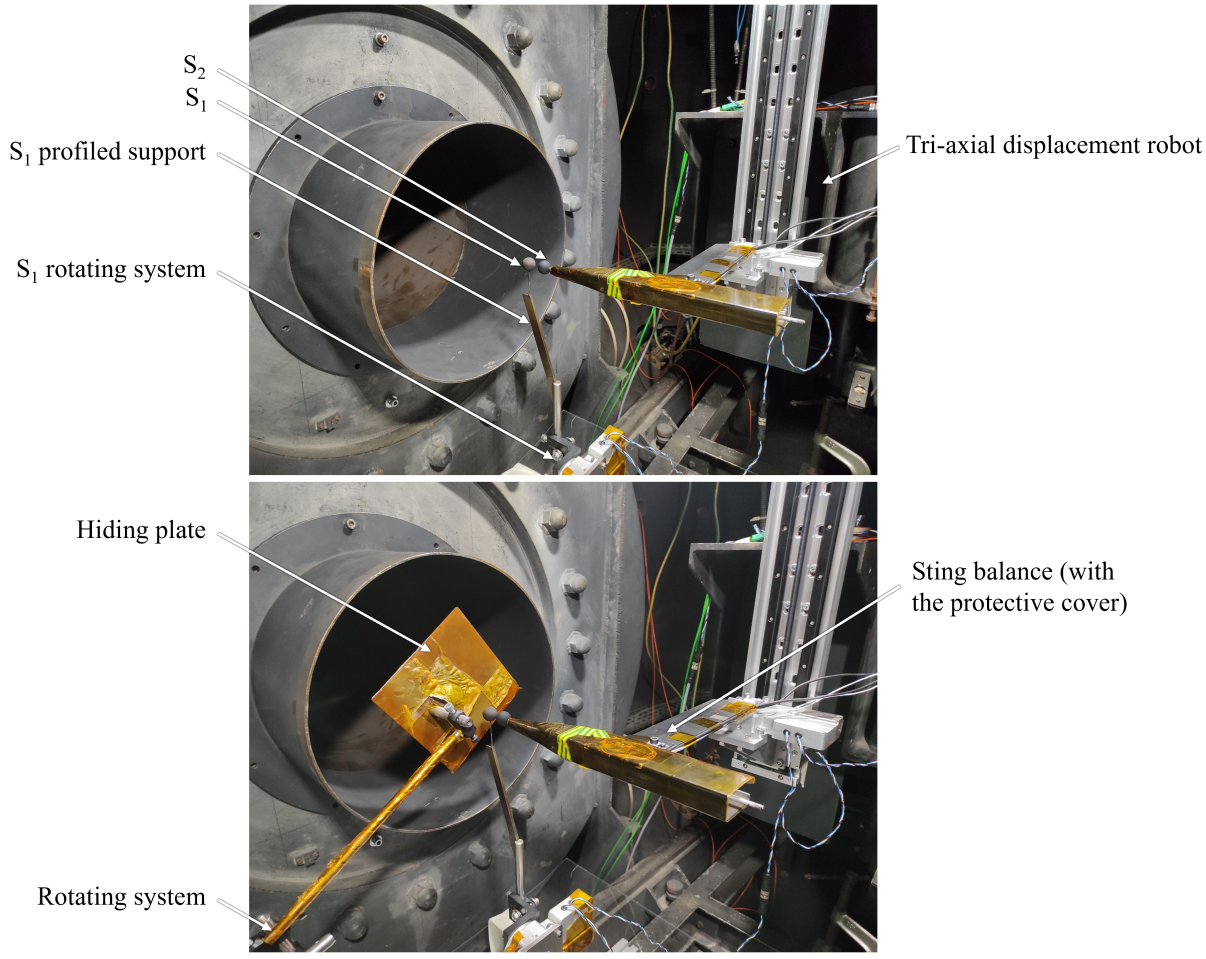

Figure 5.18: Experimental set-up for force measurements with the aerodynamic balance. Top: measurement of the total forces; bottom: measurement of residual forces.

balance, S_2 has to be displaced in the $\vec{y}$-direction and not in the $\vec{z}$-direction as for the other devices. As the flow in the core are axisymmetric whatever the nozzle used, the change in direction does not modify the free-stream flow seen by S_2, as long as the relative distances between spheres are respected. The positioning of the spheres is controlled with a Canon camera placed on the top of the test chamber. The distance between the camera and the models allows a resolution of 0.115mm/px, which is even more accurate than the KURO camera.
A hiding plate is placed on a pneumatic rotary system that allows to place it outside (top image of Figure 5.18) or inside the flow (bottom). The purpose of this system will be explained in the next paragraph.

5.4.1.3 Force measurement protocol

Once the flow is established, the spheres are placed in the flow as desired. The measurement of the forces can be started following a protocol.
As shown in Figure 5.18, two configurations can be adopted: with the model in the flow (top image), or with a plate hiding the model from the flow. In the first configuration, the recorded electrical signal corresponds to the measurement of the total drag and lift forces. These total forces are composed with the aerodynamic forces perceived by the sphere, but also with residual forces induced by the suction or the vibration of the pumping group. To evaluate these residual forces, the second configuration is adopted. By placing the plate in the flow, the spheres are protected from it, and thus the balance only records the residual signal.
For each position, the measurement of the total forces and of the residual forces are realised. Each measurement consists in acquiring the signal during 10 s with a frequency of 1000 kHz. In the supersonic flows (N1 and N2), the two measures are repeated 5 times. For the hypersonic nozzle (N3), due to experimental bias, only two repetitions are realised. Indeed, by placing the plate in the flow, the general pressure in the test chamber is slightly modified, and beyond 2 repetitions the operating conditions are no longer satisfied. Thus the flow has to be stopped and restarted later to repeat the measurements. This operation is time-consuming since about 1 hour is needed to set or start the flow. Many tests were realised by Hugo Noubel [151] which confirmed the repeatability of the measures in hypersonic conditions. Thus, it was decided to only realise two measures per positions.
For each module, drag and lift, and for each repetition, values of the total forces and of the residual forces are averaged. The mean residual force is subtracted from the mean total force to obtain the real drag and lift forces in mV/V. Then, the scaling factors found with the calibration are applied to the electrical signal to obtain the drag and lift forces in N. The different repetitions are averaged and a standard deviation is calculated to determine the uncertainties.

5.4.2 Swinging sphere technique

The swinging sphere technique consists in suspending a sphere with a wire system so it can move freely in the $\vec{x}$-direction, according to the drag force it endures. This force is calculated thanks to the angle of the wires as will be explained in this section.

5.4.2.1 Set-up

The swinging sphere technique is a non-intrusive way to measure drag forces. In consequence, it can be applied to S_2 and to S_1 with the presence of S_2 in its wake. The two configurations are shown in Figure 5.19. In both cases, the suspended sphere is drilled from side to side, passing by its centre. A thin non-elastic wire serves as the suspension maintain. For N1 and N2, the wire is 0.07 mm in diameter. For N3, the flow is cold, but the model surface is heated at around 450K, which burns the wire used for N1 and N2. Thus, for N3, a

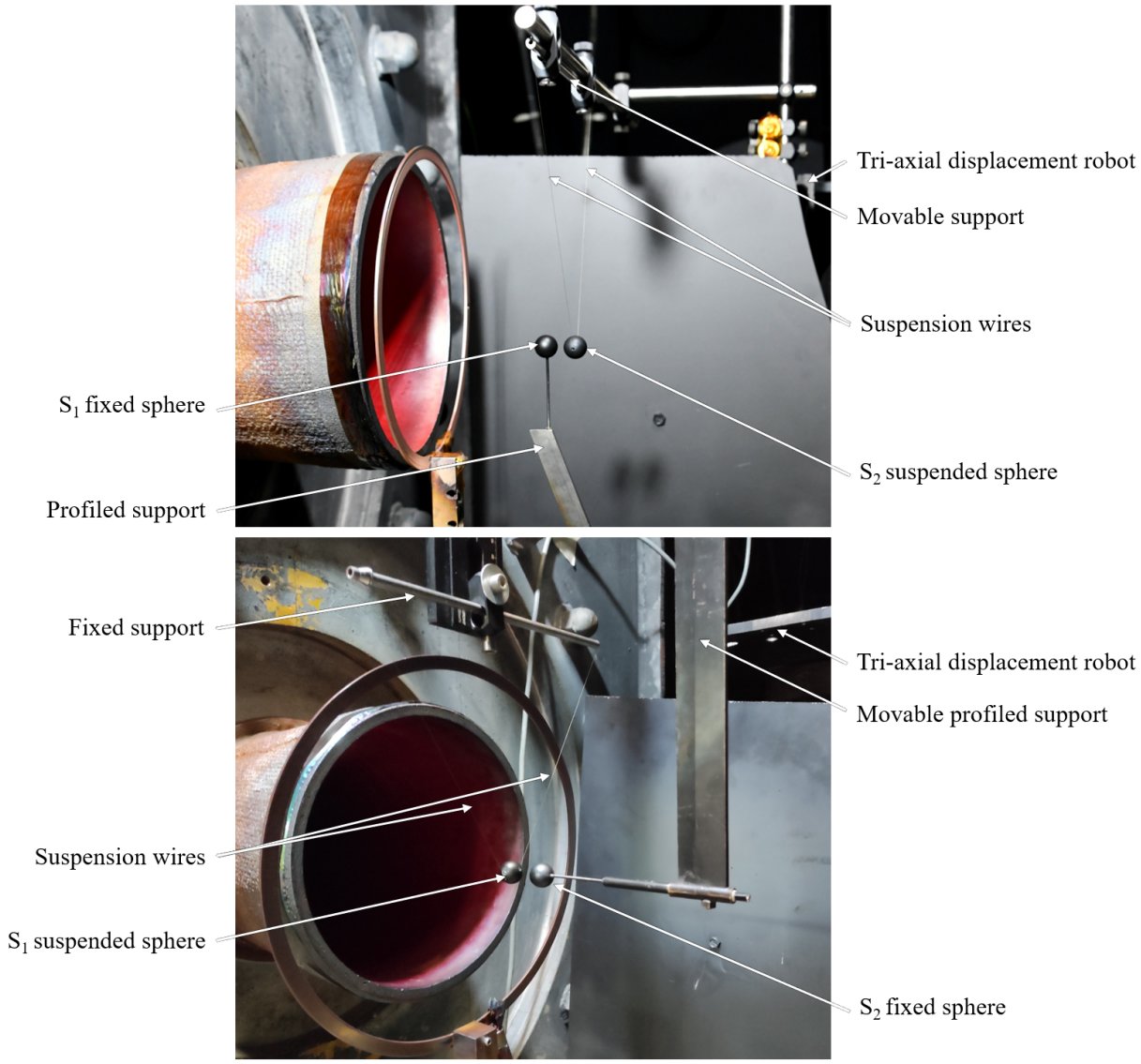

Figure 5.19: Experimental set-up for force measurement with the swinging sphere technique. Top: measurement of S_2 drag force; bottom: S_1 drag force.

wire of 0.1 mm-diameter made of enamelled Teflon was used due to a better resistance to the heat. The wire passes through the sphere and through the hollow of a tube that serves as maintaining support. The tube is positioned so that its longitudinal axis is parallel to the $\vec{y}$-direction. The tube needs to be placed above the top of the nozzle exit, not to disturb the free-stream flow. In consequence, the wire length depends on the nozzle used. In order to obtain accurate measurements, the swinging sphere has to move only in the $\vec{x}$ and $\vec{z}$ directions, which are included in the plane of the camera sight. For this purpose, the sphere is glued on the wire and the wire is glued to the tube so that the length L of both wire sides are equal, as described on the back view of Figure 5.20. Thus, both spheres are located in the plane $Y = 0$ mm.

For the drag force measurement of S_2 (top image of Figure 5.19), S_1 is placed as previously mentioned for the other devices. S_2 holding tube is maintained on the triaxial displacement robot so that it can be moved in $\vec{x}$ or in $\vec{z}$ directions. When the swinging sphere technique is applied to S_1 (bottom image of Figure 5.19), its holding tube is fixedly maintained to the wall of the test chamber. S_2 is held by a profiled support fixed on the triaxial displacement robot, as for flow-field visualisation.

In the two configurations, S_2 is displaced in the wake of S_1. Measurements can be realised statically, *i.e.* S_2 is positioned at desired coordinates and a series of images is recorded, or dynamically. For these dynamic recordings, S_2 is initially placed at the desired coordinates, then its support is moved vertically, or

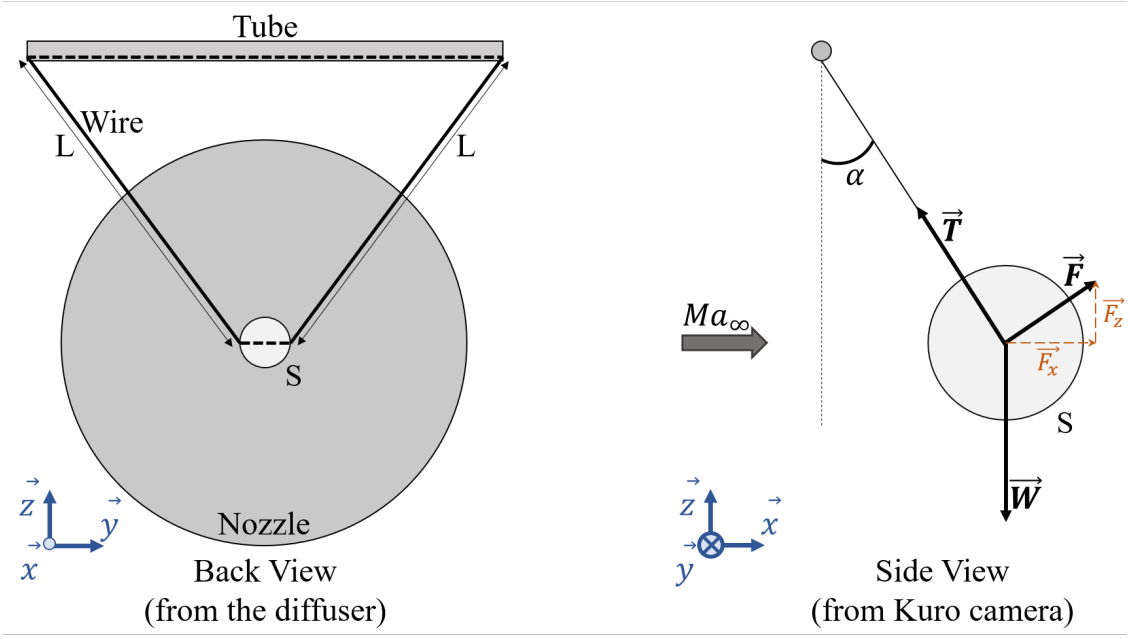

Figure 5.20: Schematics of the swinging sphere force measurement.

horizontally, with a constant velocity of 0.8 mm.s^{-1}.
Despite the high stability of the flow, a slight pendulum movement of low amplitude is observed whether for static or dynamic measurements. These oscillations are mainly due to two factors: the vibration of the pumping group transmitted by the metallic structure of the wind tunnel; and the very low density of the flow that makes it hard to stabilise the initial movement induced by the placement of the sphere in the flow. This second factor can be diminished by reducing the mass of the swinging sphere, or by waiting a long time for stabilisation. To reduce the mass of the spheres, some of them have specially been conceived to be hollow. The second option won't be adopted to limit the duration of the experiments. For N1, two spheres were tested: the 16 mm-diameter with a mass of 2.88 g, and the 8 mm-diameter with a mass of 2.2 g. For N3, only the 18 mm diameter sphere with a mass of 6.93 g was used.
Recordings are realised with the KURO camera used for flow-field visualisation. Due to the oscillations of the swinging sphere, the acquisition time has to be small enough to obtain clear visualisation of the thin wire. At the same time, due to the weight of each image, it is wished to limit the number of images recorded during one sequence to maximum 3000. A good compromise was to set the acquisition time to 20 ms per image.

5.4.2.2 Force calculation

The forces applied on the sphere are schematised on the side view of Figure 5.20. $\vec{F}$ represents the forces exercised by the flow on the swinging sphere, $\vec{W}$ the weight of the sphere, and $\vec{T}$ the tension of the wire. Since no mass variation was measured between the weighing of the sphere without or with the wire, the weight of the wire is null. Whether for N1 or N3, the nozzles experienced with the swinging experiment, the mean free-path is at least three times greater than the diameter of the wire. The mean free-path being the distance between the collision of two particles, it is unlikely that they collide with the wire. Thus, the forces exercised by the flow on the wire are supposed null. Later in this work, an estimation of the drag force of the wire will confirm this statement.

The forces of this system can be described with Equation 5.4.

$$\begin{cases} \vec{W} = -m.g.\vec{z} \\ \vec{T} = -T.sin(\alpha).\vec{x} + T.cos(\alpha).\vec{z} \\ \vec{F} = F_x.\vec{x} + F_z.\vec{z} \end{cases} \tag{5.4}$$

Each taken image allows obtaining such a system. By assuming that S_2 is in an equilibrium state at each recorded image, the second law of motion gives Equation 5.5.

$$\sum \vec{Forces} = m.\vec{a} = \vec{0} \Longrightarrow \vec{W} + \vec{T} + \vec{F} = \vec{0} \Longrightarrow \begin{cases} F_x = T.sin(\alpha) \\ F_z = m.g - T.cos(\alpha) \end{cases} \tag{5.5}$$

Without external forces ($\vec{F} = \vec{0}$), $\vec{T} = -\vec{W}$ and $\alpha = 0$, thus $T = m.g$. We assumed that the tension of the wires was constant, which gives the Equation 5.6, where F_x represents the axial force and F_z the transversal one.

$$\begin{cases} F_x = m.g.\sin\alpha \\ F_z = m.g.(1 - cos(\alpha)) \end{cases} \tag{5.6}$$

With the swinging sphere experiment, we can only calculate the axial force F_x which depends on the mass of the sphere and on the angle that makes the wire with the vertical (α). The mass is known, and the angle of the wire is determined from images. As the wire passes twice in front of the camera, it is decided to detect the angle on the front wire. To ensure the measurement is always made on the same wire, a point of varnish has been added at the top of the front wire, outside the flow. On each image, the circle function of Matlab allows finding the middle of the swinging sphere with the accuracy of ± 1 px = ± 0.163 mm. The detection of the wire is much more difficult due to its diameter (inferior to a pixel size).

5.4.2.3 Determination of the angle of the wire

An automatic detection has been tried, but, due to the short acquisition time, the noise of images made it impossible to process. The adopted solution is a manual detection that consists in pointing a pixel along the wire, as far as possible from the centre of the sphere in order to reduce inaccuracies. Knowing the centre of the sphere, and another wire location, with a simple Pythagorean calculation, the measured angle $\alpha_{measured}$ can be obtained.
Unfortunately, due to the lens of the camera, the measured angle is not the real angle α, as can be observed in Figure 5.21. It is seen that, with no flow on, the angle of the wire is not 0° as it should be, but slightly vary

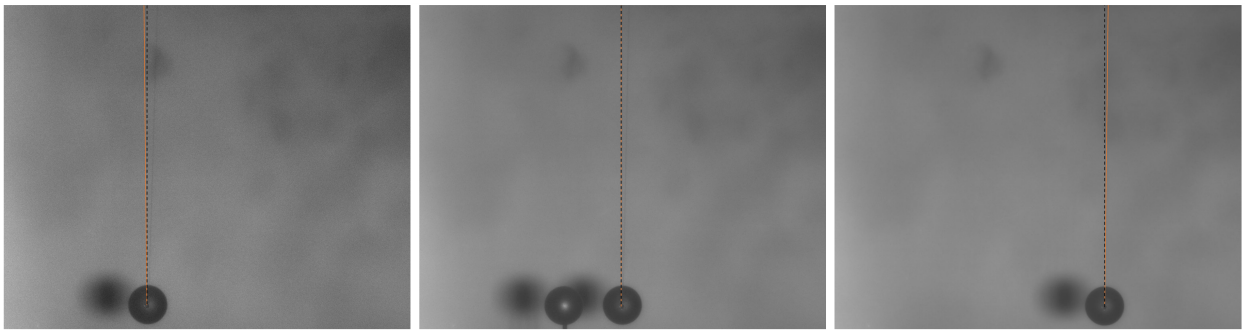

X = 875 pixel	X = 1024 pixel	X = 1191 pixel
$\alpha_{mesuread}$ = 0.5°	$\alpha_{mesuread}$ = 0°	$\alpha_{mesuread}$ = -0.55°

Figure 5.21: Camera deviation angle with no flow on (dashed black line: vertical, orange line: front wire).

according to its position towards the camera centre. As a linear deviation of the angle is observed along the horizontal axis of the camera, the measured angle can be corrected with Equation 5.7, the equation of the deviation angle, where X is the position of the sphere in pixels, on a full-size image.

$$\alpha_X = \alpha_{measured,X} - (X - (1024 - 875)) * (\alpha_{measured,1024} - \alpha_{measured,875}) \tag{5.7}$$

Of course, this equation can slightly vary from one experiment to another since the camera may have been moved and the set-up changed. Thus, the verification the deviation angle has to be realised for each experiment.
For each image, this method allows to determine the real angle of the wire. But, due to the manual detection, we assumed a pointing error of ±1px. In addition, ±1px are estimated with the numeric detection of the sphere. The maximal uncertainty of angle measurement has been calculated in the worst case scenario of each experiment, *i.e.* when the second sphere is high in the flow and thus the visible length of the wire is short. For each image, we consider this maximal error to be the inaccuracy.

Chapter 6

Reference cases

Contents

The present doctoral work intends to study the shock/shock interferences (SSI) produced when two spheres interact. In our case, a parent sphere (S_1) placed in the core flow will be surrounded by a shock-wave modifying the initial flow-field. A second "child" sphere (S_2) will be moved behind S_1 in the modified flow-field. Thus, it is first required to characterise the flow-field in which S_2 is placed. It is also necessary to analyse the physics of S_2 alone in the free-stream flow to have a reference case for comparison with the SSI cases. This chapter is dedicated to the characterisation of the flow induced by the single spheres experimented for the different operating conditions, as summarised in Table 4.3.
This chapter will also detail and validate the devices set-up and post-processing used in the entire work. Besides, the obtained results will be used to simulate numerically the flow-field of the primary sphere, allowing completing our experimental results.

6.1 Flow-field visualisation

6.1.1 Preliminary studies

The analysis of the flow-field, and in particular the detection of the shock-wave and the stand-off was carried out using the glow discharge visualisation. However, apart from the technique itself, it is important to consider how certain parameters inherent in the measurements, such as the type of support used to hold the spheres and the temperature of the spheres, can affect the shock.

6.1.1.1 Influence of the support and position of the sphere

To study the interaction between two spheres, the interacting object (S_2) was displaced all around the primary one (S_1). This imposes mechanical constraints in relation to the type of support for each of the spheres, and space constraints in relation to the useful volume of the flow. Indeed, for N1 and N2, due to the size of the nozzle core, S_1 has to be placed below the centre of the core, as shown in Figure 5.1.
In wind tunnel experiments, it is important to minimise the interaction between the models and the sting of support, and thus to minimise their influence on the aerodynamic measurements. Some works were carried out in the past to investigate the influence of the diameter and length of the sting support [99, 132, 91]. Measurements were done to determine the critical sting diameter (d) and length (l) for unchanged wake which depends on the model diameter (D) and flow conditions, specifically the Reynolds number. Sieling [189] showed that, for a Mach number of 3.88 and fully turbulent flow with Reynold number of $15.6.10^6$, the critical diameter ratio (d/D) is of 0.15, and the critical sting length of $1.3.D$. Kavanau [99] explored cone-cylinders and sphere-cylinders in flow configurations over a range of Mach number and Reynolds Number (Re_L based on the model length): $159 < Re_L < 800$ for $Ma_\infty \approx 2$ and $920 < Re_L < 7400$ for $Ma_\infty \approx 4$. Results showed that the base pressure decreased with decreasing the Reynolds number and increasing the Mach number due to the completely laminar character of the boundary-layer and critical wake region. The base pressure for Mach numbers up to 4 has been found to be unaffected for d/D up to about 0.25. The combination of both results shows that for Mach 4 flows, the increase in Reynolds number allows increasing the sting diameter without modifying the wake flow. Miller [91] worked with Mach 20 flows and Reynolds number ranging between 9.10^4 and $13.9.10^4$. Wake flow modifications were based on base pressure measurements and results presented no significant variation for $l/D > 3$ and for d/D ranging between 0.250 and 0.625.
The present work was carried out with flows at Mach numbers 4 and 20 and with Reynolds numbers of about 147 to 884. The d/D ratios for the sphere supports used are between 0.11 and 0.416. These values are comparable to or lower than those studied in previous works and, moreover, with lower Reynolds numbers. This supports the fact that the supports used in this study do not modify the wake flows of the spheres.

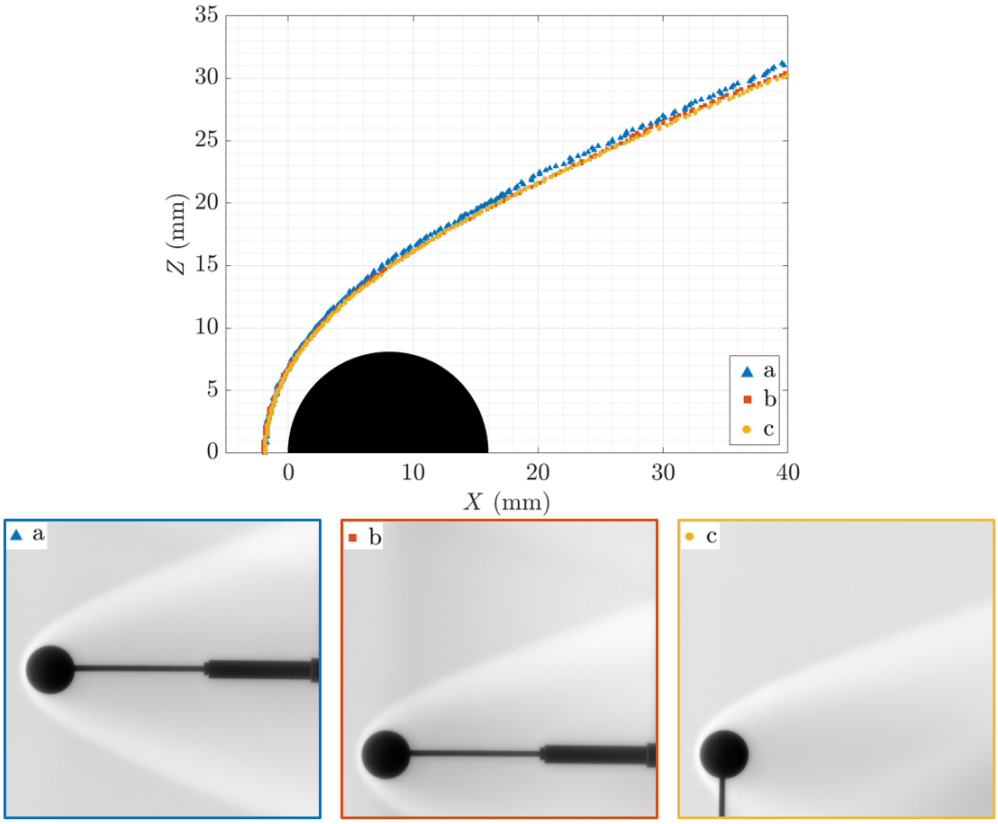

Figure 6.1: Influence of the support and position of the sphere on the shock-wave shape.

To experimentally estimate both the impact of the vertical support and of the sphere position with respect to the centre of the nozzle, three sets of images were recorded and analysed as shown in Figure 6.1. For case a, the sphere is placed at the centre of the nozzle with a rear support. This case represents the best-case scenario since no support interferes with the free stream; the sphere position ensures the best free-stream conditions. For case b, the sphere is displaced down (see Figure 5.1), still with a rear support; while for case c, the support is fixed vertically and holds the sphere by its lower half. The graph shows the superposition of the middle shock-wave obtained for each case.

Between the cases a and b, a slight variation of the rear shock altitude is observed. This can be due to a variation of static pressure as the shock-wave is closer to the top of the nozzle core for case a than b. However, between case b and c, the change of support does not seem to affect the shock-wave shape.

Since the present study focuses on the interaction between two spheres, as long as the comparisons are made

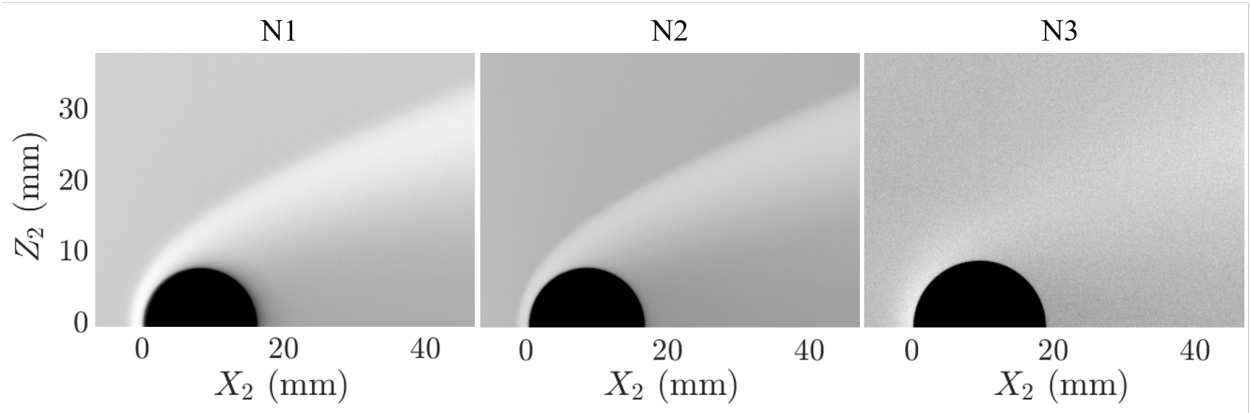

Figure 6.2: Images of a single sphere.

for the same experimental conditions, the minor difference observed by changing the position of S_1 can be overlooked.
Thus, for the study of SSI, the support used will be the one of case c. Figure 6.2 shows the images of the first sphere of the couples used for N1, N2 and N3.

6.1.1.2 Influence of the temperature of the model

At hypersonic flow conditions (N3), thermal infrared preliminary measurements showed an increase in the model surface temperature with the duration of the experiment. As shown with Figure 6.3, after 20 minutes, the temperature tends to about 165°C. It is important to note that the ionisation has no impact on the increase in temperature, which is a major point since no flow-field image can be recorded without ionisation.

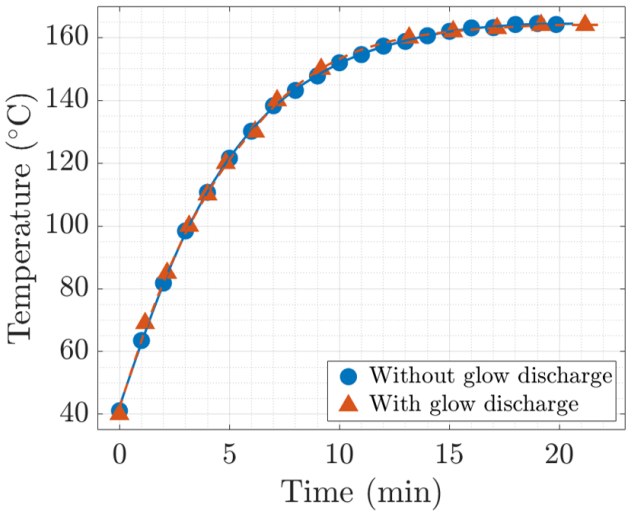

Figure 6.3: Evolution of the sphere temperature in N3 free-stream flow conditions.

To study the impact of the temperature, different series of images were recorded at different time intervals. All along the duration of the experiment, the sphere was monitored by the IR camera to measure the temperature of the model for each series of images.
Figure 6.4 shows the superposition of the middle shock-wave of the sphere at three temperatures. Although the detection of the shock-wave is noisy, the range of temperature experienced by the model does not seem

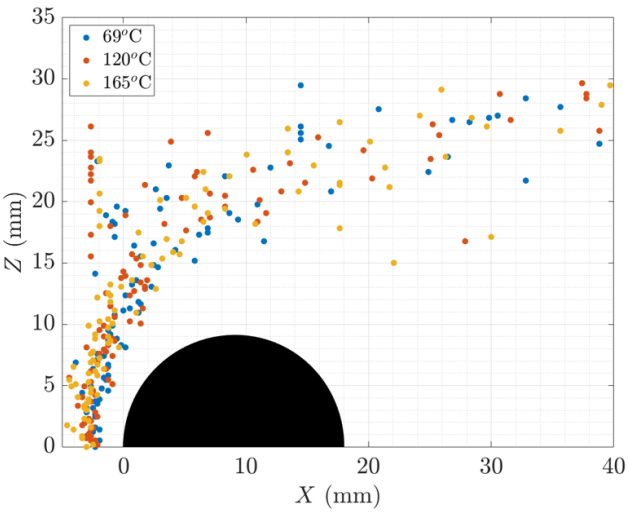

Figure 6.4: Superposition of the sphere shock-wave for different temperatures.

to affect its flow-field.
Consequently, it won't be necessary to wait for the stabilisation of the models' temperature to realise the various types of measurements foreseen in this investigation.

6.1.2 Shock-wave shapes

The analysis allows detecting the shock-waves and its structure. As demonstrated by Nicolas Rembaut [180], the stand-off distance and the shock thickness depend on the rarefaction degree that can be described by the Knudsen number and the Reynolds number. Shock shapes and stand-off distance have been mathematically described by Billig [28] as a function of the Mach number but in continuum regime, that means without any effect of the flow density.
In the present section, we propose a modification of this mathematical description to include viscous effects due to the rarefaction. For this purpose, single sphere shock-wave shapes from configuration case a shown in Figure 6.1 was used.
Figure 6.5, presents the comparison of the middle shock-wave shape determined for each sphere diameter D

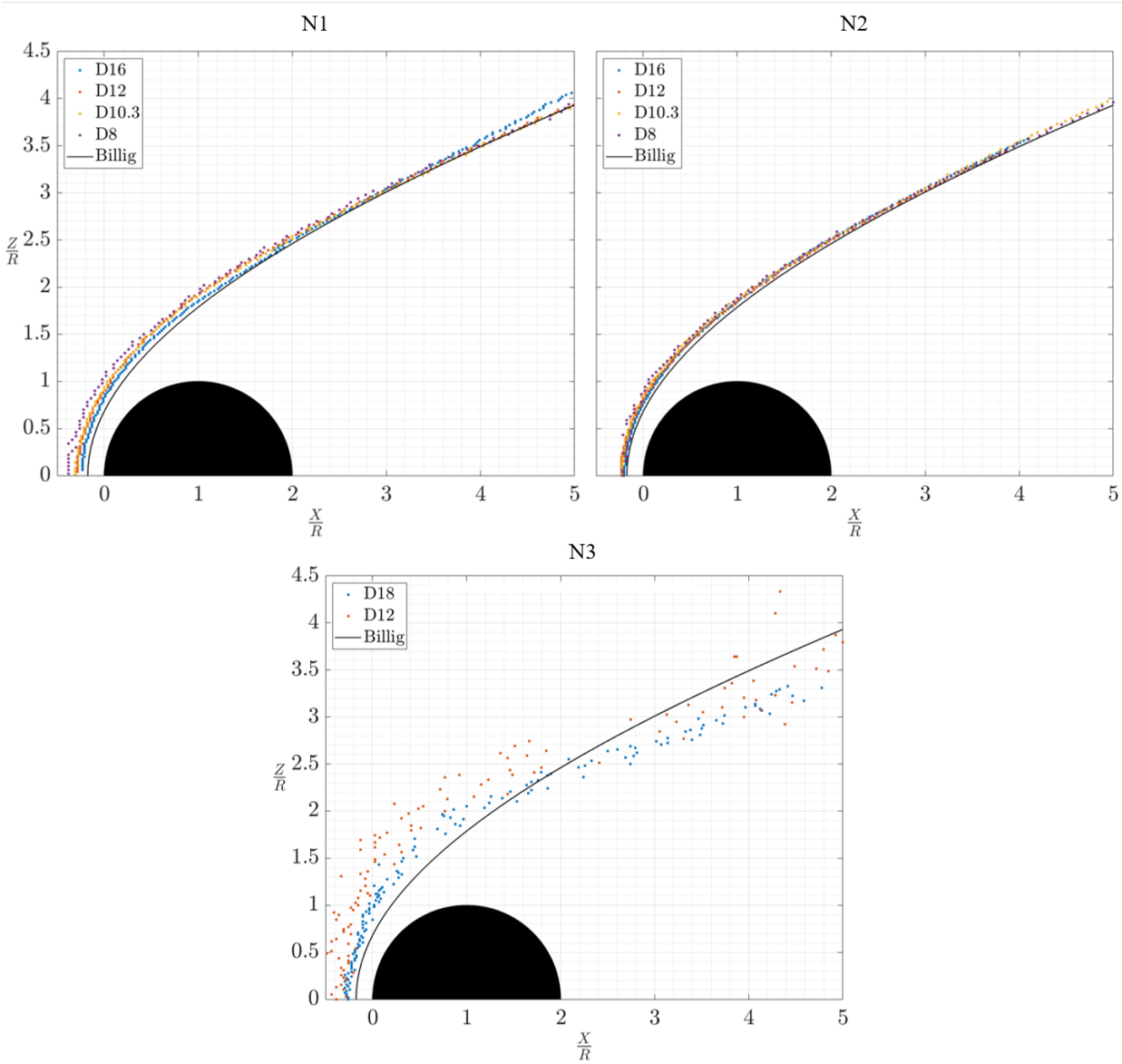

Figure 6.5: Superposition of single sphere shock-waves.

and each flow condition (N1, N2 and N3). For each flow condition, the black line represents the shock-wave shape determined with Billig's equation (Equation 6.1) [28]. It is representative of the shock-wave of a sphere in a flow of same speed (Mach 4 for N1 and N2, and Mach 20.2 for N3), but in the continuum regime.

$$X = R + \Delta - Rc.cotan^2(\beta).\left[\left(1 + \frac{Z^2.tan^2(\beta)}{R_c^2}\right)^{1/2} - 1\right] \tag{6.1}$$

Equation 6.1 depends on the stand-off distance Δ (Equation 6.2), on the curvature radius R_c (Equation 6.3) and on the Mach number since $\beta = asin\left(\frac{1}{Ma_\infty}\right)$.

$$\frac{\Delta}{R} = 0.143.exp\left(\frac{3.24}{Ma_\infty^2}\right) \tag{6.2}$$

$$\frac{R_c}{R} = 1.143.exp\left(\frac{0.54}{(Ma_\infty - 1)^{1.2}}\right) \tag{6.3}$$

As can be observed, the rear part of the shock shape seems to tend to Billig's prediction. However, major differences are observed in the front section of the shock-wave. In particular there is an increase in the stand-off distance on the stagnation line with respect to Billig's predicted values. This phenomenon is even more significant when increasing the rarefaction level and consequently, the viscous effects.
According to Ambrosio and Wortman [11], in the continuum regime, the stand-off distance, given in Equation 6.2, only depends on the Mach number and on the radius of the sphere. In Figure 6.6, the normalised stand-off distance is plotted according to the Reynolds number. As this number decreases, an increase of the stand-off distance in clearly observable.

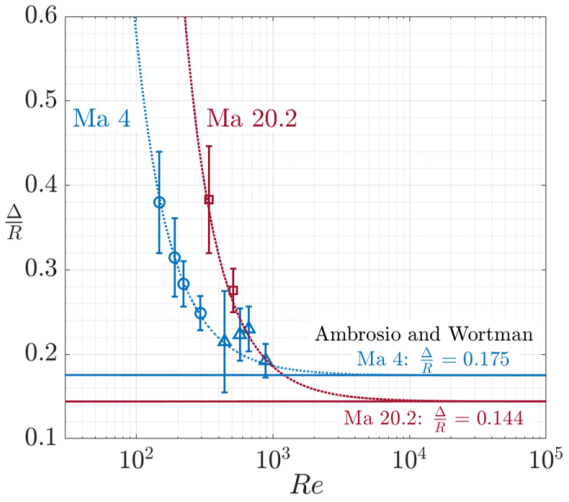

Figure 6.6: Stand-off distance of single spheres according the Reynolds number.

Based on the stand-off distance values given by (Equation 6.2), we intend to establish a generalised stand-off distance equation with dependence in viscosity. A new fitting equation is proposed, including an exponential term depending on the Mach number, the viscosity parameter ω and the Reynolds number Re. From our experimental results (table of values is given in Appendix D, Figure D.1), Equation 6.4 is proposed.

$$\frac{\Delta}{R} = \left[0.143 + exp\left(\frac{83.8.Ma_\infty.\omega^2}{Re^{3/2}}\right) - 1\right].exp\left(\frac{3.24}{Ma_\infty^2}\right) \tag{6.4}$$

By introducing Equation 6.4 in Billig's equation instead of Equation 6.2, we plotted the new shock shape on our most rarefied cases. Figure 6.7 demonstrates that the stand-off distance is not the only parameter that

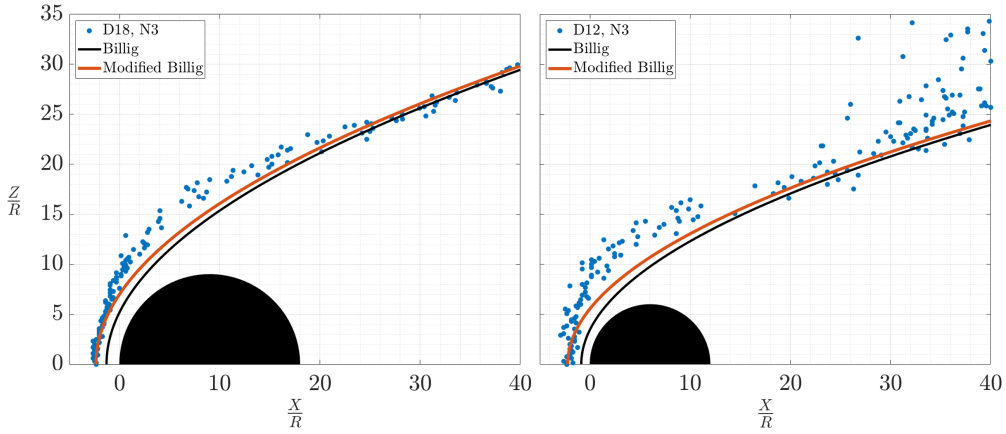

Figure 6.7: Shock-wave shape with modified Billig's equation.

needs to be modified. As can be seen, the curvature radius also seems to be modified with increasing the level of rarefaction. Unfortunately, for now, no modified R_c equation was found. In the near future, it is hoped to work on a generalised form of the Billig's equation that would be applicable whatever the regime of the free-stream flow.

For a further investigation of the results obtained for the Mach 4 flows, the stand-off distances of single spheres in N1 and N2 flow-fields have been investigated in terms of Knudsen numbers. It seems that the stand-off distances normalised with the radius of the sphere are a function of the Knudsen number, as described with Equation 6.5, Equation 6.6 and Equation 6.7 which respectively give the normalised stand-off distances of the FS, the MS and the BL.

$$\frac{\Delta_{FS}}{R} = 0.236exp(29.1Kn) \tag{6.5}$$

$$\frac{\Delta_{MS}}{R} = 0.177exp(26.8Kn) \tag{6.6}$$

$$\frac{\Delta_{BL}}{R} = 0.09exp(22.3Kn) \tag{6.7}$$

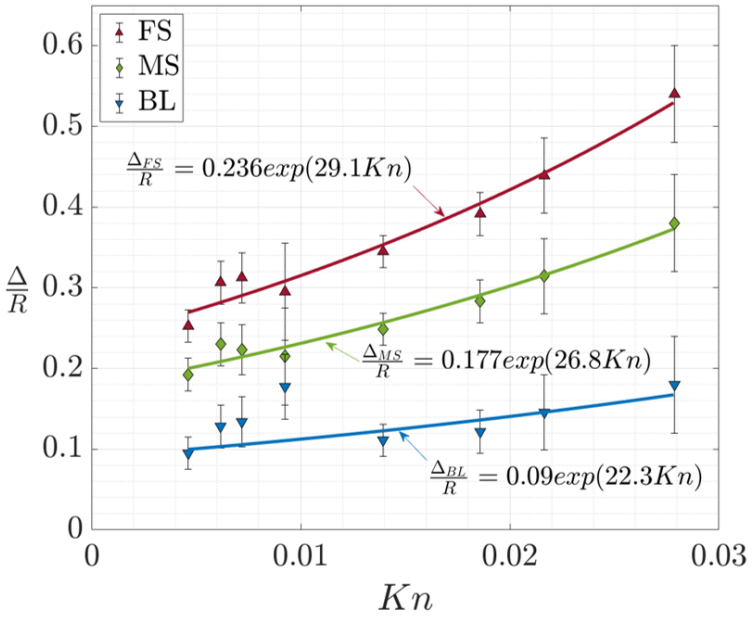

Figure 6.8: Stand-off distance of single spheres according the Knudsen number (for N1 and N2).

6.2 Drag force measurements

The measurement of the drag force of a single sphere was first realised with the aerodynamic balance. The swinging sphere technique was then used, and the calculation method discussed in the light of previous studies.

6.2.1 Aerodynamic balance

Results obtained with the aerodynamic balance are shown in Figure 6.9. The drag force values, summarised in Appendix D (Figure D.1), are shown in the left graph, while the drag coefficient values, calculated with Equation 6.8, are compared with the literature [16, 17, 207] in the right graph.

$$Cd = \frac{F_x}{\frac{1}{2}.\rho_\infty.U_\infty^2.S} = \frac{F_x}{\frac{1}{2}.\gamma.p_\infty.M_\infty^2.S} \tag{6.8}$$

Two points (one from N1 and one from N2) are clearly included in the range of expected drag coefficient. They correspond to the 16 mm diameter sphere. As the size of the sphere decreases, it seems that an inaccuracy rises. This error comes from the fact that, the slight opening between the sting balance and its cover is less and less protected from the flow. Some air passes in the balance, skimming its slats and thus, increasing slightly the perceived forces. Unfortunately, due to the magnitude of the drag forces, it is hardly complicated to remove this measurement bias.
Concerning N3, as the Mach number is different from the other two, no comparison can be made. But, due to the size of the model (18 mm diameter), and with the above observation, the measured drag force must be the real value.
Another point must be noted. For our new measurements, the flow in the nozzle core is perfectly known and stable. Thus, errors that could come from the size of the small spheres are present and identified. Nevertheless, in the previous studies, besides the number of experimental data, no error bar is given. The uncertainties from the free-stream pressure, Mach number and temperature are not known, which could lead to a certain number of errors. Moreover, the calculation of the drag coefficient from the drag force with Equation 6.8 increase the differences in terms of values. As an example, with the drag coefficients from the literature, we decided to calculate the corresponding drag forces based on the flow conditions of N1. The resulting graph, in Figure 6.10, shows a difference of maximum 0.5 mN, which is low enough to acceptable.

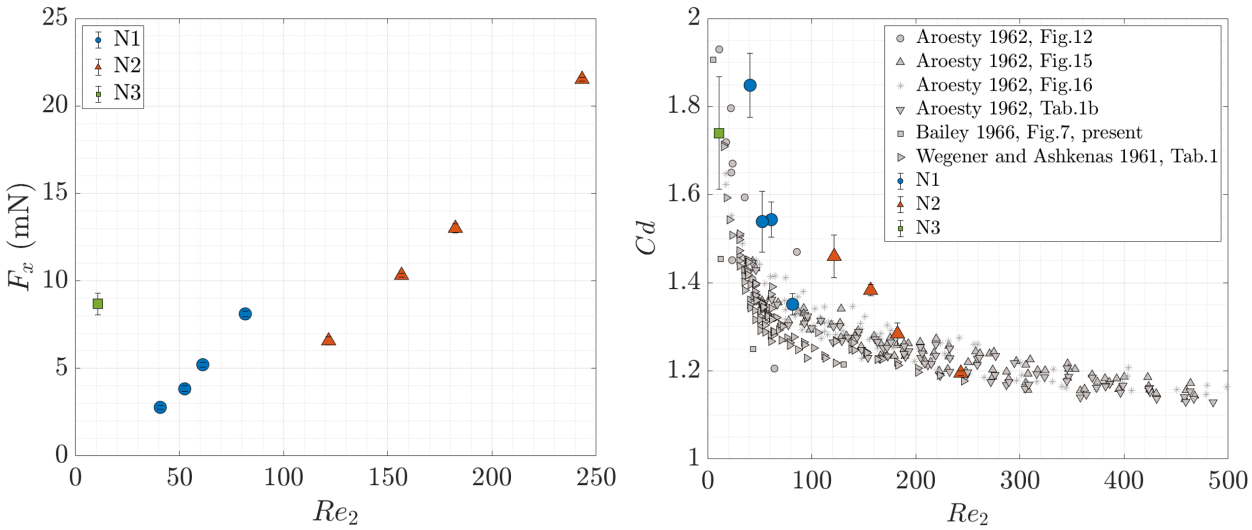

Figure 6.9: Drag forces (left graph) and coefficients (right graph) of single spheres.

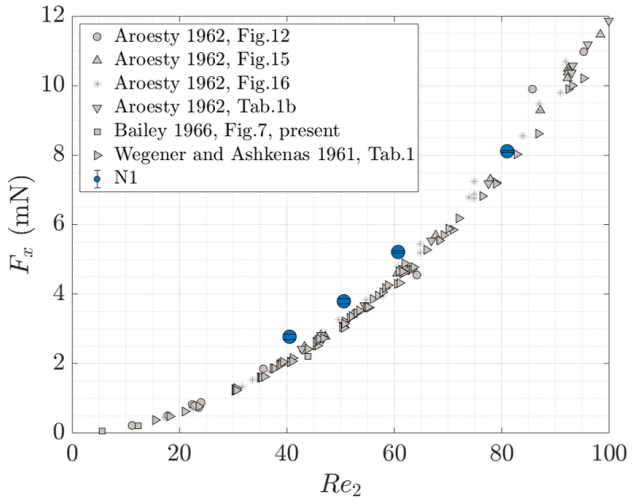

Figure 6.10: Drag forces calculated from the literature for N1 flow conditions.

We now know that an experimental bias exists on the measurement of the spheres of smaller diameters. But, in the case of SSI, errors will be equivalent than in the case of a single sphere. Thus comparing the results of SSI with the corresponding reference is coherent and will enable an understanding of the aerodynamic phenomenon occurring when two spheres interact.

6.2.2 Swinging sphere method: validation for a single sphere

Section 5.4.2 presents the swinging sphere method and the relation based on the Newton's first law to determine the force which is applied to the sphere suspended in the flow (Equation 5.6).
In the case of a single sphere, the model only suffers drag forces. But, if it is positioned in the wake of a primary one, transversal forces exists, mainly due to the interaction with the incident shock-wave which generates a non-axisymmetric flow around the swinging sphere. Thus S_2 will be submitted to drag and lift forces, as it was demonstrated by many previous studies in the continuum regime [21, 117, 137]. In the case of a rarefied flow, there is no reason for being different.
Unfortunately, the pendulum technique prevents from dissociating the drag from lift forces acting on the sphere. However, due to the low pressure of the flow, it is reasonable to assume that lift forces will be very low, and might be undetectable in terms of the wire's angle. Nevertheless, two hypotheses were considered for the calculation of forces:

a. the swinging sphere is only subjected to axial force:

$$\vec{F} = F_x.\vec{x} \tag{6.9}$$

b. the swinging sphere is subjected to axial and transversal forces:

$$\vec{F} = F_x.\vec{x} + F_z.\vec{z} \tag{6.10}$$

Considering the second law of motion, the following systems are obtained, where α is the real angle, as explained in section 5.4:

a.

$$\begin{cases} F_x = m.g.\tan\alpha \\ F_z = 0 \end{cases} \tag{6.11}$$

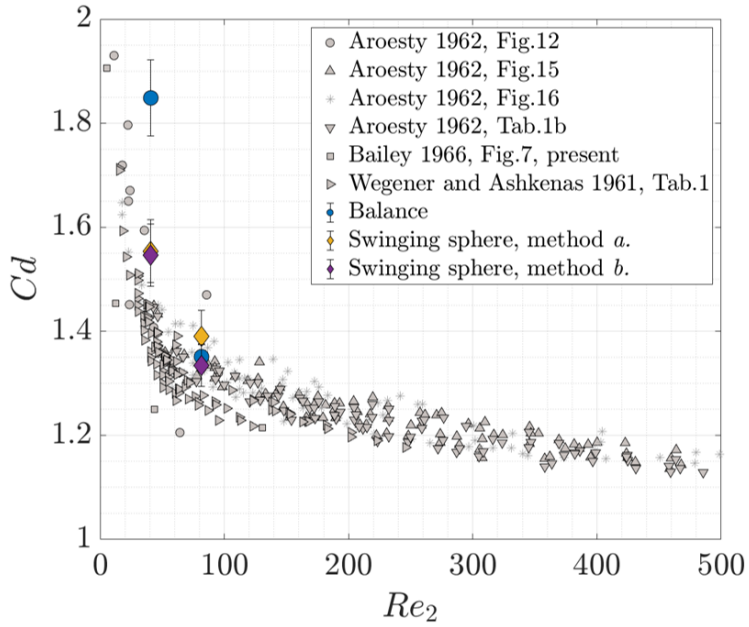

Figure 6.11: Drag coefficients of single swinging spheres.

b.

$$\begin{cases} F_x = m.g.\sin\alpha \\ F_z = m.g.(1 - cos(\alpha)) \end{cases} \tag{5.6}$$

To determine which method, *a* or *b*, is the most appropriate, two single spheres with different diameters were tested with N1: an 8 mm diameter sphere made of brass (m = 2.2 g), and a 16 mm diameter one made of POM (m = 2.88 g). The values of drag forces and coefficients are presented in Table 6.1. A comparison

Table 6.1: Drag forces and coefficients of single swinging spheres.

∅ (mm)	Method *a*		Method *b*	
	F_x (mN)	Cd	F_x (mN)	Cd
8	2.331 ± 0.09	1.554 ± 0.06	2.319 ± 0.08	1.546 ± 0.06
16	8.344 ± 0.27	1.390 ± 0.05	8.002 ± 0.24	1.334 ± 0.04

between the drag coefficients obtained with the swinging sphere technique, the aerodynamic balance and results from the literature are plotted on Figure 6.11.

The results of both methods look in agreement with the previous results. Method *a* was the calculation method used by Wegener and Ashkenas [207] who also used the swinging technique for drag force measurement. In their set-up, they only measured forces in the $\vec{x}$-direction since they placed their model in a free stream. Moreover, they used a floating stabiliser to avoid the oscillations of the sphere which may compensate the movement in the $\vec{z}$-direction.

But, in our configuration, the sphere can be submitted to forces in both the $\vec{x}$ and the $\vec{z}$ directions, so the Z component must be considered, as do method *b*, which, moreover, seems in better agreement with the literature for the 16 mm diameter sphere (Re_2 = 81.2). For the 8 mm diameter one, the results of the two methods are slightly higher than those of the literature. As a reminder, for the swinging technique, it was assumed that the drag force of the wire is negligible toward the one of the sphere. But, due to the decrease in the model's size, the surface area on which the pressure is exerted is also smaller, and so is the drag force. Thus, the forces acting on the wire are less and less negligible, and may induce a slight increase of the expected drag force. Nonetheless, it can be observed for the 8 mm diameter sphere that the swinging

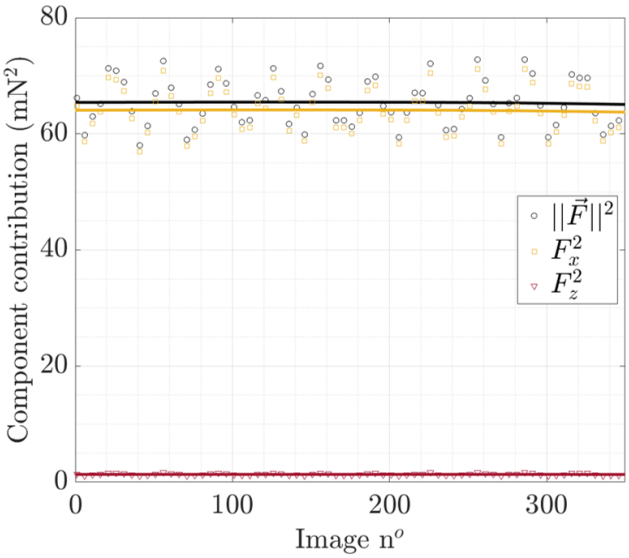

Figure 6.12: Force decomposition of a single swinging sphere.

technique gives much better results than the aerodynamic balance. It is to be noted that, even if the drag coefficient is very impacted, the difference in terms of forces is of 0.455 mN, which is about the drag force of a honeybee [147].
Thus, the swinging sphere technique gives coherent results whatever the method used, but the method *b* seems to give better results. To estimate the importance of the X and Z components in that case, the axial and transversal forces measured for the 16 mm diameter sphere are plotted in Figure 6.12.
This figure plots the contribution of the X and Z component of the total force, calculated with $||\vec{F}|| = \sqrt{F_x^2 + F_z^2}$, where F_x is the mean force in the $\vec{x}$-direction, F_z in the $\vec{z}$-direction (Equation 5.6). Beware, these two forces cannot be related to the drag and lift forces. The force's components are calculated with Equation 5.6 by measuring the angle of the wire over a range of 350 images (represented by the points on the graph). The percentage of F_z over $||\vec{F}||$ is of only of 2%, which means that the X component is largely dominant and can be considered as the drag force of a sphere.

6.3 Pressure measurements

6.3.1 Pitot pressure profiles

In the context of this investigation, interferences are studied when the child sphere S_2 is placed in the flow-field produced by the parent sphere S_1. For this purpose, a deeper characterisation of the S_1 flow-field could be helpful. Local pressure measurements using a Pitot probe have been realised but only for the 16 mm diameter sphere in N1 and N2 free-stream flow conditionss because, due to the low density, in particular in the wake flow, this kind of measurement is very time consuming.
Figure 6.13 presents the flow-field intensity for the D16 sphere obtained in N1 and N2 operating conditions where the shock shapes are identified. For several X-positions, vertical pressure distributions were measured and the resulting values, normalised to the free-stream pressure, are plotted over the intensity flow-field. For the same X-positions, the intensity profiles are plotted and compared to the pressure profiles.

As can be observed, for a same vertical axis, the pressure and intensity profiles have a similar tendency. Moreover, they enable to identify different regions of the shock-wave. The luminous intensity, representative of the density, is maximal in the BL region; while the MS corresponds to the inflection point of the pressure

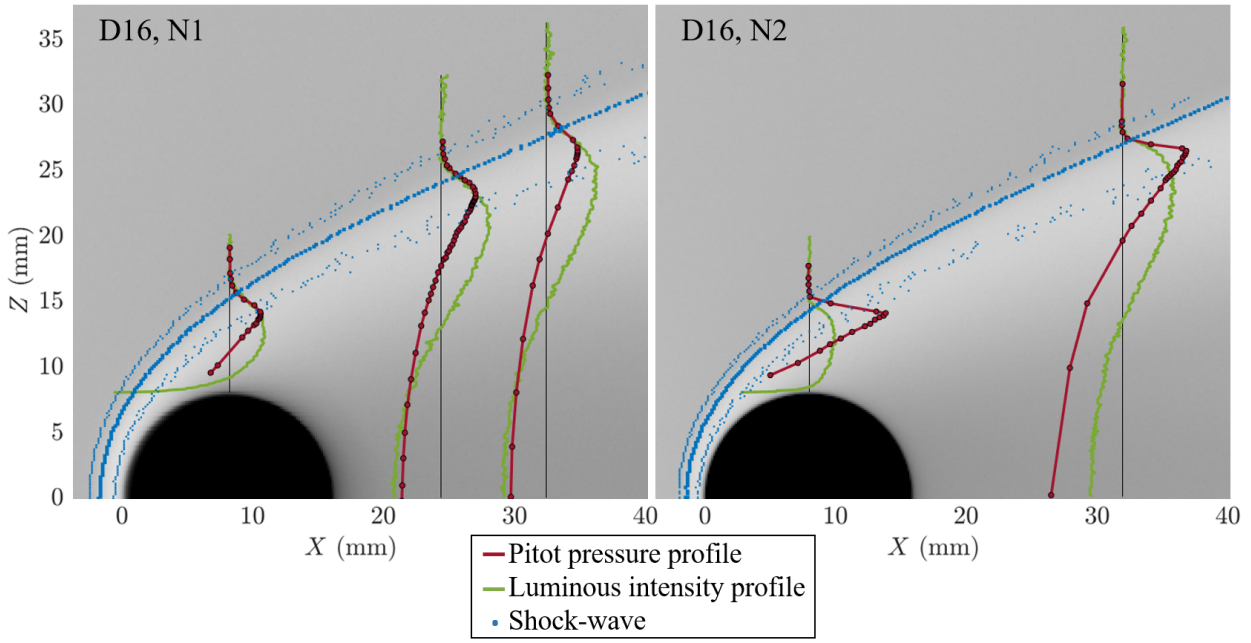

Figure 6.13: Pitot pressure and luminous intensity profiles in the wake of a single sphere.

profile, between the maximal and the free-stream values. Both profiles tend to the reference value from the FS and beyond.
Between N1 and N2 conditions, a variation of the pressure slopes is observed. Due to a higher level of rarefaction for N1, the viscous effects are higher, increasing the thickness of the shock-wave. As a consequence, the slope of the pressure profiles gets smoother as the level of rarefaction increases.
The Pitot pressure profiles were not realised for N3. Indeed, due to the very low level of pressure in the free stream, even lower in the wake of the sphere, the time of stabilisation of the pressure in the line is very long. As the intensity profiles are representative of the local density, they will be used as a comparison criterion for the numerical simulations.

6.3.2 Wall pressure distribution

In the case of SSI, wall pressure was only measured for the biggest spheres. Thus, the only needed reference cases concern the 16 mm diameter sphere for N1 and N2, and the 18 mm diameter one for N3. Wall pressure measurements were realised for angles ranging between -90° and 90° as shown in Figure 5.17. Results of wall pressure distribution are given in Appendix D, Figure D.2. Figure 6.14 shows their values (left graph) and normalised pressure (right graph), where p_0 is the stagnation pressure.
What is interesting to notice in the right graph is that, whatever the Mach number, or the level of rarefaction, the distribution of pressure is identical. Only the magnitude of pressure is modified, as shown in the left graph.
The drag force results from the friction and the pressure contribution. In viscous flows, the friction contribution can contribute for a large part. This can be deduced from the difference of the total drag and the pressure drag. As follows, the total drag coefficient (Cd), is composed of pressure and friction contributions, respectively noted Cd_p and Cd_f in Equation 6.12.

$$Cd = Cd_p + Cd_f \tag{6.12}$$

The drag coefficient due to the pressure is then given with Equation 6.13, where ρ_∞ and U_∞ are the free-stream

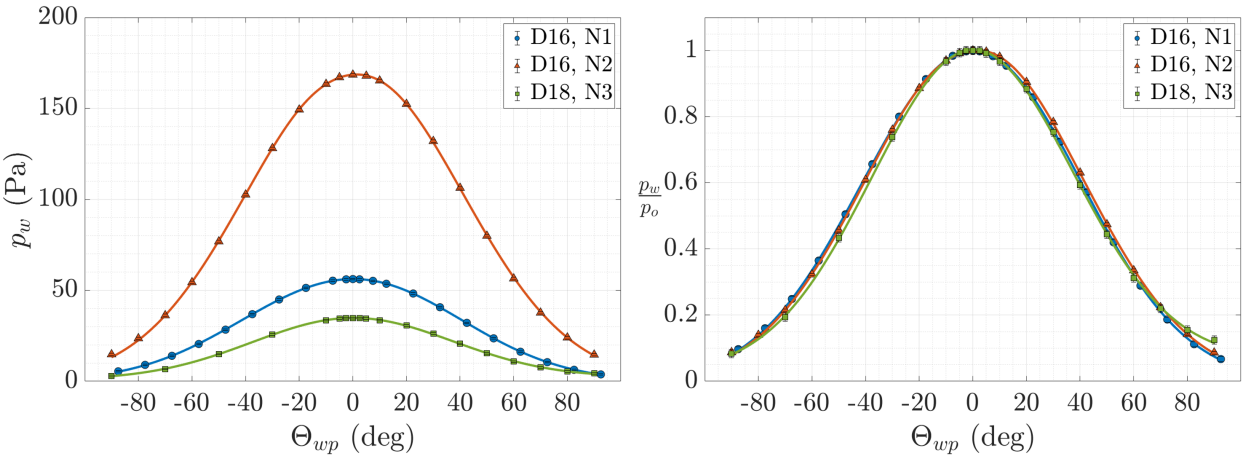

Figure 6.14: Wall pressure distribution on a single sphere.

density and velocity and S is the cross-sectional surface of the sphere $S = \pi.R^2$.

$$Cd_p = \frac{Fp_x}{\frac{1}{2}.\rho_\infty.U_\infty^2.S} \tag{6.13}$$

Fp_x represents the pressure force applied axially on the surface of the sphere. In order to facilitate the understanding of the calculation, schemes presenting the local pressures and axial forces calculated with the wall pressure distribution are shown in Figure 6.15. $\vec{n}$ is the vector which is normal to the wall, and dS is a small element of the surface.

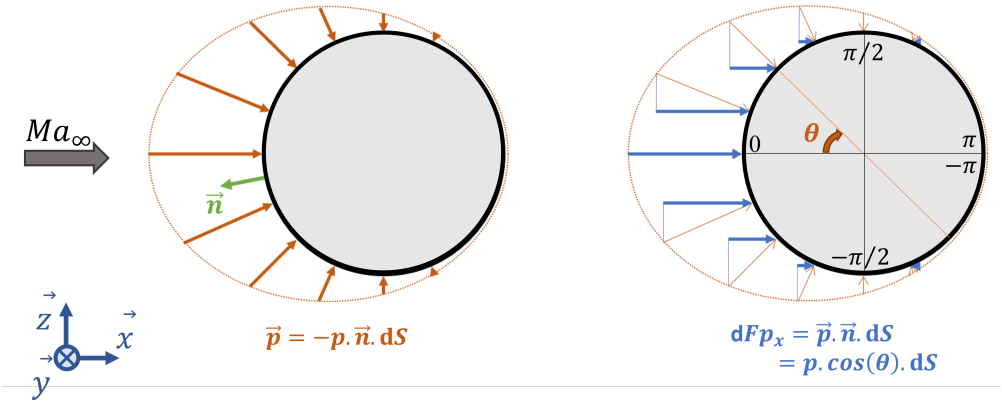

Figure 6.15: Schematics of the pressure distribution (left) for the calculation of the axial pressure force (right).

To calculate Fp_x, it is necessary to integrate dFp_x on the entire surface of the sphere. Since measurement was only realised for angles between -90° and 90°, we miss the values of the back of the spheres. Based on the numerical simulation realised for single spheres as will be described in section 6.5, it can be assumed that the wall pressure at -180° or 180° is of 0 Pa. Thus the experimental results are completed with the points at -180° and at 180°. Thus results can be extrapolated and fitted with a Gaussian function as shown in Figure 6.16. The expression of Fp_x is given in Equation 6.14, with integration over dS (Equation 6.15).

$$Fp_x = \int_S (p(\Theta) - p_\infty).cos(\Theta)\,\mathrm{d}S \tag{6.14}$$

$$\mathrm{d}S = R\mathrm{d}\Theta R sin(\Theta)\mathrm{d}\phi \tag{6.15}$$

Generally Fp_x is calculated for $0 < \Theta < \pi$, and $0 < \phi < 2\pi$. In the case of a single sphere in the free

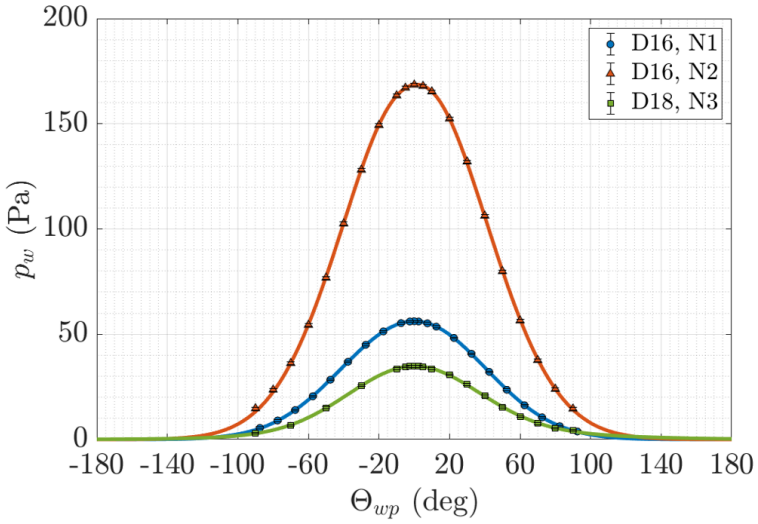

Figure 6.16: Extrapolated wall pressure distribution on a single sphere.

stream, it is feasible since the flow over the sphere is axisymmetric. Unfortunately, it is not the case in the configuration of SSI, in which the interacting sphere will see a flow which is only symmetric according the plane $Y = 0$. Indeed, both spheres are aligned longitudinally and to the flow is laminar, thus the side $Y < 0$ of the following sphere will endure the same forces than the side $Y > 0$. The sphere is thus divided in two semi-spheres: upper (Fp_x^+ on $0 < \Theta < \pi$ and $0 < \phi < \pi$) and lower (Fp_x^- on $-\pi < \Theta < 0$ and $-\pi < \phi < 0$). This way, the pressure forces are calculated on the two semi-spheres with $\mathrm{d}S_{1/2} = \pi.R^2.sin(\Theta)\mathrm{d}\Theta$. Due to the negative angles of the lower part, $Fp_x^+ = -Fp_x^-$, thus, $Fp_x^+ + Fp_x^- = 0$, which implies that $Fp_x = Fp_x^+ - Fp_x^-$, and the full expression of Fp_x is given in Equation 6.18.

$$Fp_x = \int_0^{\pi} (p(\Theta) - p_\infty) .cos(\Theta)\, \mathrm{d}S_{1/2} - \int_{-\pi}^{0} (p(\Theta) - p_\infty) .cos(\Theta)\, \mathrm{d}S_{1/2} \tag{6.16}$$

$$Fp_x = \pi.R^2 \int_0^{\pi} (p(\Theta) - p_\infty) .cos(\Theta).sin(\Theta)\, \mathrm{d}\Theta - \pi.R^2 \int_{-\pi}^{0} (p(\Theta) - p_\infty) .cos(\Theta).sin(\Theta)\, \mathrm{d}\Theta \tag{6.17}$$

$$Fp_x = \frac{1}{2}\pi.R^2 \left[\int_0^{\pi} (p(\Theta) - p_\infty) .sin(2.\Theta)\, \mathrm{d}\Theta - \int_{-\pi}^{0} (p(\Theta) - p_\infty) .sin(2.\Theta)\, \mathrm{d}\Theta \right] \tag{6.18}$$

Cd_p can be calculated, and results are presented in Table 6.2.

Table 6.2: Drag coefficients due to pressure for single spheres.

	D16, N1	D16, N2	D18, N3
Cd_p	1.01	1.02	0.9

Now, the drag coefficients (total and due to the pressure) are known for D16 (for N1 and N2) and for D18 (for N3). Thus, for these spheres we can estimate the percentage of drag that is due to the pressure and to the friction. Figure 6.17 shows the evolution of the pressure and of the friction contributions. The percentage of pressure contribution $Cd_{p_{100}}$ seems to follow a power law depending on the Reynolds number after shock (Re_2) as described by Equation 6.19.

$$Cd_{p_{100}} = -113.Re_2^{-0.35} + 100 \tag{6.19}$$

The contribution in friction being the other contribution, its percentage is equal to $100\% - Cd_{p_{100}}$.
Unfortunately, with only three verification points in such a short range of Reynolds, it is strongly possible that this tendency is inaccurate. However, it enables to observe that the friction and pressure contribution are equivalent for $Re_2 \approx 10$.

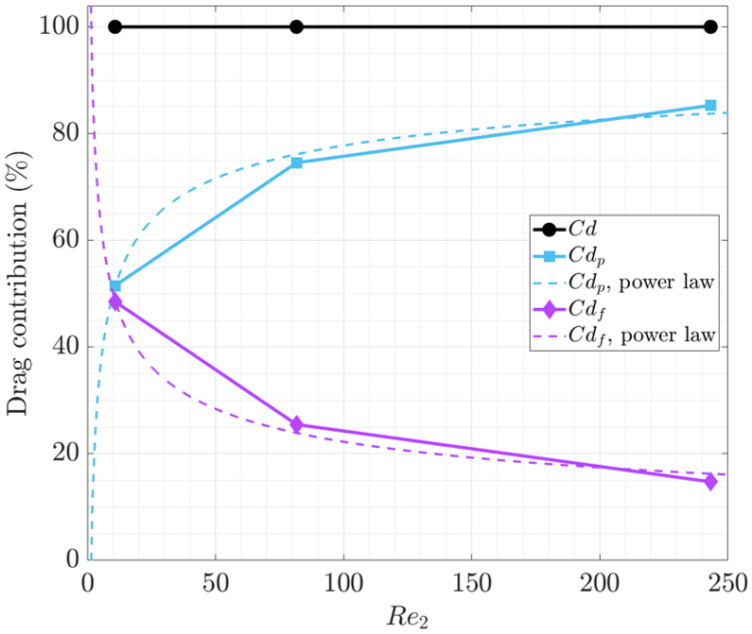

Figure 6.17: Drag coefficients of single spheres: contribution of pressure and friction.

6.4 Influence of the ionisation on the free stream

An analysis of the impact of the ionisation over the aerodynamic properties of the flow has been realised during the different types of diagnostic acquisitions applied to a single sphere with the N1 operating condition. Since the glow discharge technique is based on the operating condition enlightenment of molecules through their electronic excitation/de-excitation, one might think that this method could impact the characteristics of the flow-field.

Figure 6.18 compares two images obtained with -5 W and -32 W glow discharge. The two sets of images are recorded in the same conditions: *i.e.* same acquisition time, same number of images. At first sight, an increase of ionisation increases the contrast, and decrease the noise of the image. Indeed, the luminous intensity increases with the level of ionisation, which improves the quality of images and the detection of shock-waves. In return, if the flow-field is modified by the ionisation, images do not reflect the physical parameter measured without ionisation.

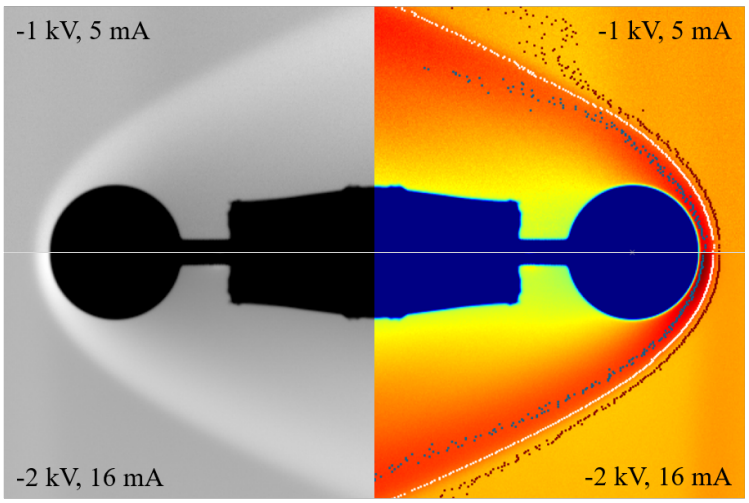

Figure 6.18: Experimental images with different levels of ionisation.

To evaluate the influence of the flow ionisation, measurements of wall pressure distribution and aerodynamic forces were realised with several discharge voltage applied to the cathode. Results are presented in Figure 6.19, where the left graph shows the wall pressure distribution, and the right graph presents the drag force measured with the balance and with the swinging sphere technique, along with the stagnation pressure.
Observing the wall pressure and the drag force measurement from the swinging experiment, only a slight increase in the values is observed, but it could be due to inaccuracies. On the contrary, a strong variation of the drag measured with the aerodynamic balance is apparent. Since the drag is not modified with the swinging technique, the variation observed for the balance is certainly due to electronic perturbations that impact its gauges.
To conclude, in the tested range of electric power, no variation in the flow-field is observed. However, the ionisation can act on the temperature of the flow, so it is necessary not to input too much power. In our cases, for each condition, we decided to use the lowest electric power that allows a good visualisation.

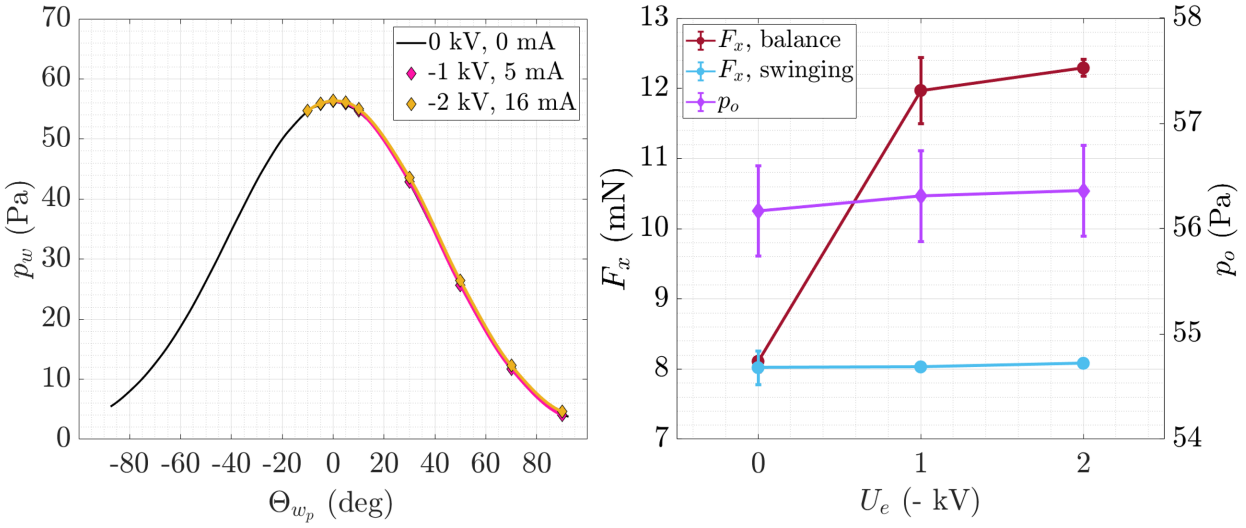

Figure 6.19: Impact of the ionisation on the wall pressure, and drag force of a single sphere.

6.5 Direct Simulation Monte-Carlo (DSMC)

To complete this study on single spheres, in particular concerning the flow-field around the primary sphere of each investigated couple (16 mm diameter for N1 and N2, 18 mm diameter for N3), numerical simulations have been carried out to obtain some parameter values that cannot be measured experimentally. The results of the simulations could, thus, be used to qualitatively characterise the flow-field seen by the next sphere (S_2), whatever its position with respect to S_1.
Simulations were realised with the DSMC code of Bird [29, 31], which is open source. Two applications are available allowing realising simulations in two dimensions (DS2V), or in three dimensions (DS3V). Both applications were used, the 2D allows simulating axisymmetric configurations such as the first sphere alone, or followed by the second one with longitudinal alignment; whereas 3D simulations allows simulating non-axisymmetric configurations such as the several interaction cases, enabling the results obtain for SSI to be compared.

Operating conditions of the present investigation correspond mainly to the slip-transitional regime, principally driven by viscous effects. This results in slipping conditions at the wall of the models. These conditions are driven by the accommodation coefficients, which determination is still not well understood. In our case, since we have experimental data characterising the flow-field of single spheres, such as the local pressure

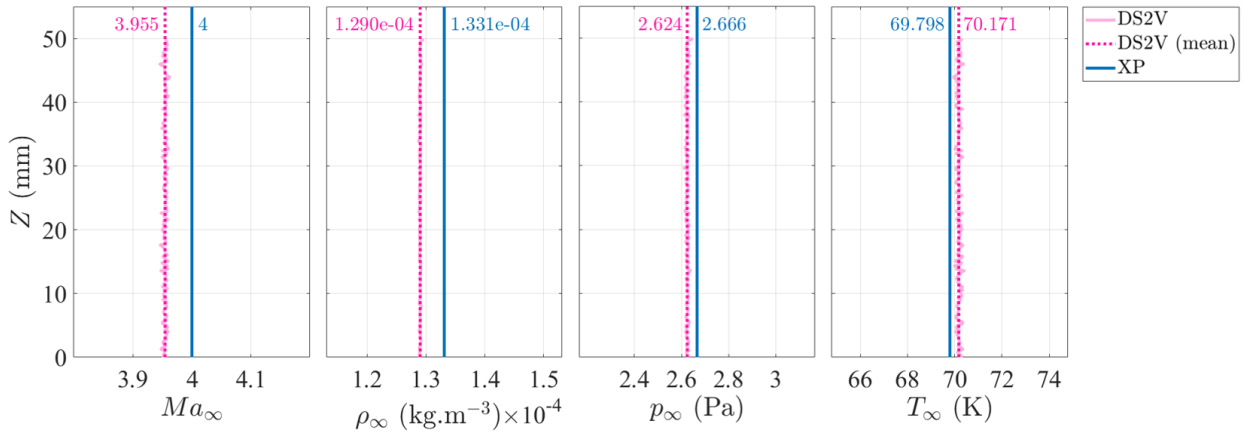

Figure 6.20: Upstream conditions of the DS2V simulation for D16, N1.

distribution, the accommodation coefficients were chosen so that the corresponding numerical parameters are as close as possible to the experimental ones. This is a crucial and important step on which the validity of the numerical simulations depends. Once the coefficients for a single sphere in the flow are found, the exact same calculations can be realised with different spheres configurations.
Here, an example is presented regarding the simulation of the 16 mm diameter sphere in the free-stream flow of N1 using the axisymmetric two-dimensional numerical simulation. Based on the comparison with the experimental results, multiple couples of accommodation coefficients were tested whether with the CLL model or with the diffuse reflection model. In this case, it was found that the best fitting was achieved with the CLL model with the following normal energy/tangential momentum accommodation coefficients: 0.6/0.4.

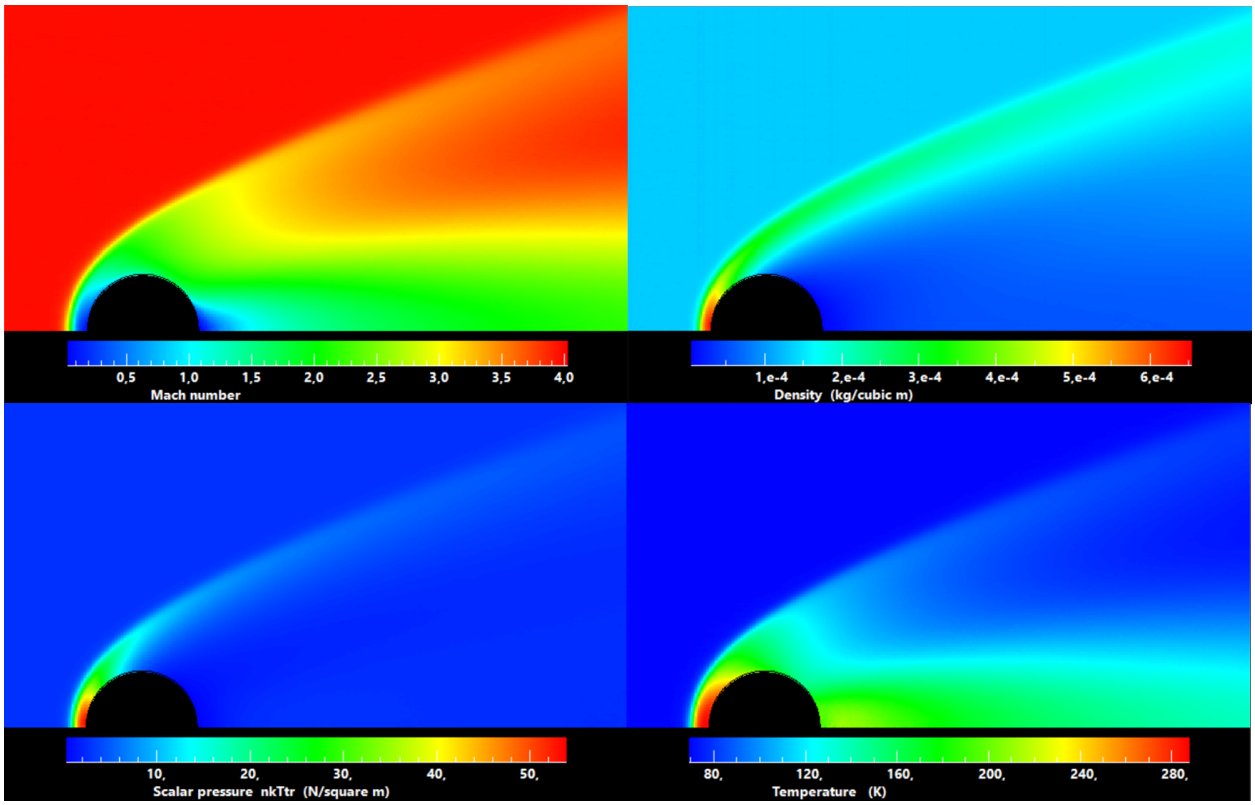

Figure 6.21: Flow-fields calculated with DS2V for D16, N1.

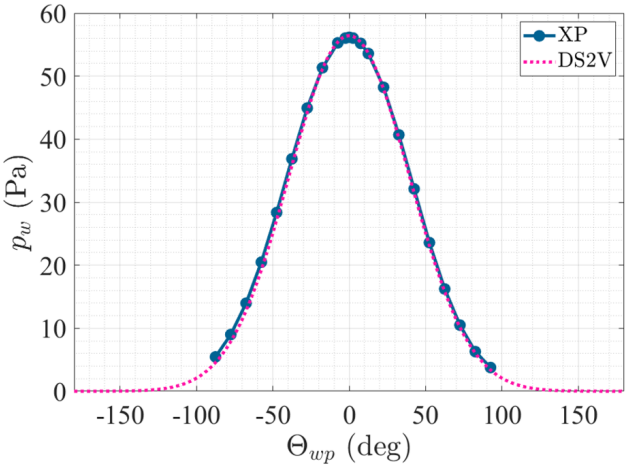

Figure 6.22: Wall pressure of the DS2V simulation for D16, N1.

First of all, for each simulation, it is necessary to ensure that the calculated free-stream flow corresponds to the experimental one. To this aim, the profiles in the upstream flow of some parameters are recorded. In Figure 6.20, the simulated profiles of Mach number, density, pressure and temperature are plotted along for an upstream vertical axis. By calculating the average value of these parameters, it can be observed that the deviation from the theoretical experimental conditions is of less than 4%, which is acceptable.
With these upstream conditions validated, the flow-field around the single sphere is the one presented with the Mach number and pressure field in Figure 6.21.

To assess the validity of the simulations DSMC, comparisons have been realised from pressure measurements. Figure 6.22 plots the wall pressure distribution on the equatorial line of the sphere. The simulation looks in total agreement with the experimental measurements. Thus, the slipping conditions must match the experiment, which confirms the choice of the accommodation coefficients.

In order to definitely validate the calculation, the flow induced by the sphere is analysed. The pressure flow-field is compared to the experimental thanks to the Pitot pressure profiles. As shown in Figure 6.23, profiles are similar. The altitudes of maximal pressure present less than 0.2 mm difference which is in the experimental accuracy of Pitot positioning. Concerning the pressure magnitude, for the $X = 8$ mm profile, DS2V pressure is higher than the experimental one with 6% of difference in the shock-wave. On the contrary, as we look farther behind the sphere, the DS2V pressures are slightly lower than experimental ones, both in the wake and in the shock-wave. The maximal difference is of 3.5%.

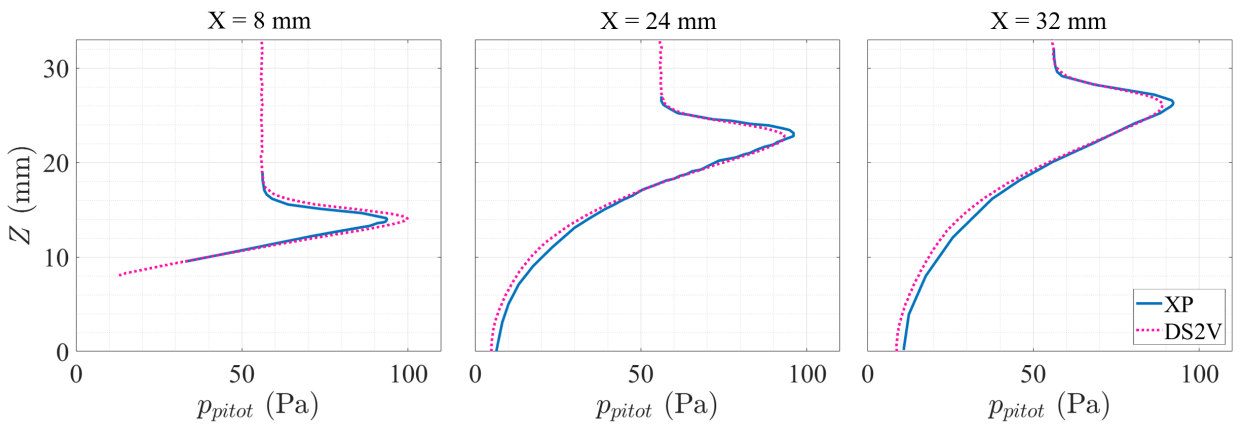

Figure 6.23: Pitot pressure profiles of the DS2V simulation for D16, N1.

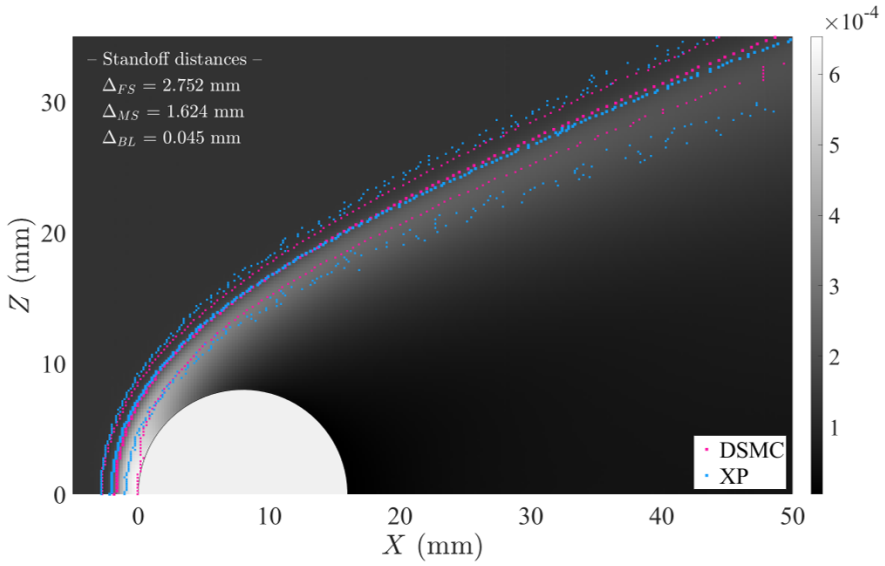

Figure 6.24: Density flow-field of the DS2V simulation for D16, N1.

Focusing on the density flow-field, a comparison with the experiment can be made by detecting the shock-wave of the numerically simulated sphere with the FSD method. Indeed, as previously said, the luminous intensity of the experimental images are representative of the density. Thus, with the experimental data, the detection of shock-waves is realised based on density variation. In Figure 6.24, the numerical density flow-field is shown with the corresponding detection of shock-waves. As observed, the three detected regions (FS, MS, and BL) are in good agreement with the experimental ones. However, the numerical BL gets closer to the sphere near the stagnation point and the thickness of the shock-wave is lower in the rear region. These differences demonstrate that the viscous effects are not perfectly matching the experimented physics.
The numerical drag force is of 6.84 mN against 8 mN for the experiment. Since the wall pressure seems to match the experiment, this difference in drag force might confirm a different friction contribution than actually experimented. Indeed, numerically $Cd = 1.15$, and the contribution of pressure is of 86.1% ($Cd_p = 0.99$) while experimentally, it was of 74.6%, showing a higher friction contribution.
Nevertheless, numerical simulation are very close to the experimental results, which will help complete the study of SSI thanks to the knowledge of additional quantitative results.

Another axisymmetric two-dimensional simulation was realised for the 16 mm diameter sphere with N2 conditions. The three-dimensional simulations were realised for N1 and N3 by master students, for one and two spheres. The accommodation coefficients are summarised in Table 6.3, and the comparison with experimental values are found in Appendix E for the validation of these coefficients.

Table 6.3: DSMC accommodation coefficients.

Simulated case	CLL method		Diffuse reflection method	
	normal energy	tangential momentum	specular reflection	adsorbed
D16, N1 (DS2V)	0.6	0.4		
D16, N1 (DS3V)			0.676	0.324
D16, N2 (DS2V)	0.75	0.25		
D18, N3 (DS3V)	1	0		

Part III

Results

Partie III
Résumé en Français

Cette partie est dédié à la présentation et à l'interprétation des résultats expérimentaux. Quatre chapitres la composent.

Chapitre 7

Basé sur les interactions choc/choc obtenues par Edney en milieu continu, le premier chapitre décrit les différents types d'interactions obtenus en écoulement raréfié pour des vitesses supersoniques. Cette première étude est réalisée à partir des visualisations d'écoulements de deux sphères en interactions. Comme en milieu raréfié, six types d'interactions sont obtenus. Cependant, les résultats font constat d'une atténuation des spécificités de chaque type lorsque le niveau de raréfaction augmente.

Chapitre 8

Maintenant que les différents types d'interactions sont connus pour nos conditions expérimentales, ceux-ci sont étudiés en détails pour un écoulement supersonique.

Selon la position de S_2 par rapport à S_1, les forces aérodynamiques et les pressions pariétales évoluent, faisant apparaître des différences de comportement selon les différents types d'interactions. L'interaction de type IV est obtenue lorsque le choc incident interagit avec le choc de S_2 à son point d'arrêt. Dans le milieu continu, elle est connue pour être la plus impactante, et les résultats révèlent également un fort impact dans le milieu raréfié. En effet, c'est pour ce type que S_2 subit la plus grande force de trainée, sa position correspondant à la pression Pitot maximale dans l'écoulement de S_1. C'est également pour cette raison que l'on observe le pic de pression pariétale le plus élevé à cet emplacement. La force de portance est maximale lorsque S_2 est portée par le choc incident. Ceci est observé pour l'interaction de transition entre les types II et III, et se vérifie avec les pressions pariétales, majoritairement réparties sur la partie inférieure de la sphère. L'analyse approfondie des résultats semble montrer que la puissance de la force résultante dépend de la force de trainée, alors que la direction de la force résultante dépend de la portance. Ainsi, malgré les faibles variations de portance observées, la trajectoire de S_2, elle, varie fortement. Pour l'interaction de type V, un emplacement spécifique a montré que les forces aérodynamiques, ainsi que les forces de pressions sont égales aux valeurs de référence. Un calcul nous a permis de montrer que cette position correspond à un point de surf. Malheureusement, toutes les conditions ne sont pas réunies pour une stabilité du phénomène. Deux méthodes de calcul des coefficients aérodynamiques sont proposées. La première considère les conditions de l'écoulement libre et permet une comparaison avec des résultats de la littérature. Ces variations ne dépendent donc que de la force, et non de l'écoulement. La deuxième est calculée avec les conditions localement subies par S2 et obtenues grâce aux simulations numériques. Ce coefficient est plus réaliste en termes d'aérodynamique puisqu'il tient compte de la force mais aussi de

l'écoulement. En considérant cette méthode locale, les coefficients de trainée et de portance montrent une valeur maximale pour l'interaction de transition entre II et II, où la contribution en pression est également maximale. Le coefficient de trainée, dont la contribution en pression est majoritaire quel que soit le type, montre également un minimum pour le type IV, alors que la force de trainée est maximale. Ceci indique que l'écoulement local, qui correspond au maximal de pression Pitot, prédomine sur la force subie. Le coefficient de portance, quant à lui, montre une contribution majoritaire des effets de pression lorsque S_2 est au-dessus du choc indicent. A l'inverse, les effets visqueux prédominent lorsque S_2 est en-dessous du choc incident. Ceci lui permet de conserver une portance positive malgré un des forces de pressions pariétales majoritairement localisées sur la partie supérieure de S_2. Ces résultats sont confrontés à ceux obtenus avec les simulations numériques. Ces derniers sont assez similaires, mais les calculs semblent montrer une plus faible contribution des effets de friction, caractéristique des écoulements raréfiés.

Dans un second temps, la technique du pendule est appliquée à S_2 positionné dans l'écoulement de S_1. Tout d'abord, la technique est validée à l'aide de mesure de balance sur une trajectoire. Puis, la technique est appliquée sur diverses trajectoires, permettant d'obtenir un mapping bi-dimensionnel des forces de trainées dans l'écoulement de S_1. Grâce à la simulation 2D-axisymmétrique de S1 dans l'écoulement libre, il nous a été possible de réaliser le mapping correspond en termes de coefficient de trainée local. Ces résultats montrent que la distance longitudinale à peu d'influence sur la valeur des forces obtenues, ce qui permet de conclure que le sillage de S_1 s'étend sur largement plus de 3.5 diamètres de S_1.

Un dernier axe d'étude est dédié aux effets de sillages. La technique du pendule a été appliqué à S_1, en déplaçant S_2 derrière, d'abord verticalement puis longitudinalement. Avec les résultats du déplacement vertical, les interactions choc/choc ne semble pas affecter l'aérodynamique de S_1. Certes la force de trainée de S_1 diminue, mais elle diminue de la manière que pour le déplacement longitudinal. Dans les deux cas, les résultats montrent une très légère variation (3%) de la force de trainée de S_1, lorsque S_2 vient se placer juste derrière elle.

Chapitre 9

Ce chapitre est dédié à l'étude des effets de raréfactions. Une première partie s'intéresse aux effets de raréfaction globale : pour le même couple de sphère que celui étudié au chapitre 8, une deuxième condition d'écoulement est expérimentée à iso-Mach mais avec une variation de la pression infini amont. Dans le deuxième cas, on s'intéresse aux effets de raréfaction locale : pour une même condition d'écoulement, on expérimente des sphères S_2 avec différents diamètres. Plus généralement, le niveau de raréfaction globale reflète la densité de l'écoulement infini amont, alors que le niveau de raréfaction locale traduit en plus les effets de taille de sphère. Dans les deux cas, les études sont basées sur l'analyse des images, des forces aérodynamiques, ainsi que des pressions pariétales (1^{er} cas seulement).

Dans le cadre de l'étude des effets de raréfaction globale, L'analyse des images montre que les couches limites sont superposées, ce qui n'est pas le cas des autres régions du choc. Le milieu de choc et le pied de choc se détachent de la sphère avec le niveau de raréfaction. Cependant, les amplitudes de variations sont bien plus importantes pour la condition la moins raréfiée, pour laquelle les efforts de pression sont plus importants. Pour autant, le taux de

compression du choc de S2 n'en est pas plus grand. De même, la variation des forces aérodynamiques est plus faible alors que le taux de raréfaction diminue. Que ce soit pour la force de trainée où pour la force de portance, les maximums évoluent vers des altitudes plus hautes. De plus, la portance devient négative alors que S_2 passe sous le choc incident, et donc sous le pic de pression Pitot. Il est donc fort probable que les effets visqueux, moins présent, n'aident plus suffisamment S_2 à être poussée vers le haut une fois dans le sillage de S_1. Les calculs de déplacement de S_2 par rapport à S_1 montrent des changements de directions sont plus brutaux pour l'écoulement le moins raréfié, ce qui traduit des effets de pressions plus importants. De même que pour les forces, les coefficients de trainée et portance locaux sont maximums pour des altitudes plus hautes pour le plus faible niveau de raréfaction. Cependant, le coefficient de trainée est minimum pour la même position quel que soit l'écoulement, là où la pression Pitot est maximale dans l'écoulement de S_1. Les mesures de pressions pariétales donnent des distributions assez similaires dans les deux écoulements. Les spécificités des interactions de type III et IV semblent exacerbées avec la décroissance du niveau de raréfaction global. Par ailleurs, les pics de pressions de chaque type sont globalement plus élevés pour le niveau de raréfaction le plus faible. Malgré cela, les forces de pression sont légèrement plus faibles, ce qui montre que la distribution des pressions pariétales, plus étendue dans le cas le plus raréfié, contre-balance les plus faibles pics de pressions pariétales. Le calcul du coefficient de trainée dû à la pression donne des résultats équivalent dans les deux conditions, ainsi, ceux sont les effets visqueux qui font augmenter le coefficient de trainée total. Une brève comparaison avec le milieu continu est effectuée pour le coefficient de trainée et la distribution des pressions pariétales. Les résultats semblent en adéquation avec la discussion présentée précédemment.

Pour l'étude de la variation du niveau de raréfaction locale, la taille de S_2 est variable. Les visualisations permettent de constater que la décroissance du diamètre induit des gradients d'intensité lumineuse plus faibles, rendant difficile la détection des ondes de chocs. L'évolution des distances de détachement est similaire quel que soit le diamètre de la sphère. Cependant, si l'on s'intéresse au maximum du détachement, obtenu pour l'interaction de type III, un calcul de nombre de Knudsen local nous permet de conclure que le choc de S_2 est plus affecté pour l'écoulement localement moins raréfié. L'étude des intensités lumineuses au nez de S2 montre que l'évolution de la densité locale des interactions de type I à IV ne dépend pas de la taille de la sphère, contrairement aux types V et VI pour lesquelles S_2 est majoritairement dans le sillage de S_1. Ceci implique que les variations de densité ne dépendent pas seulement de la taille de S_2, mais sont aussi impactées par le niveau de raréfaction locale. Pour un même écoulement, les forces aérodynamiques de trainée ou de portance de S_2 augmente avec le niveau local de raréfaction, et ce, quel que soit le type d'interaction regardé. La variation des forces de portance décroit avec la taille de S_2. Pour les cas les plus localement raréfiés, on n'observe même plus de portance négative lorsque S_2 subit une interaction de type V ou VI, alors que la pression induite par le choc incident se localise sur sa partie supérieure. Ceci a pour conséquence de modifier drastiquement le déplacement de S2 par rapport à S1, notamment lorsque S_2 se situe dans le sillage de S_1.

Ce chapitre aura montré que les effets de raréfaction globale et locale ont des effets distincts. Pour un même nombre de Knudsen local, il est important de connaître le nombre de Knudsen infini amont, puisque d'après nos résultats, et dans le cas de l'étude des interactions de chocs, les deux se complètent.

Chapitre 10

Ce dernier chapitre présente les résultats obtenus pour un écoulement hypersonique raréfié. Avec l'analyse des images, on ne peut plus parler d'interactions choc/choc au sens où Edney les avait définies dans le continu, et que l'on a pu observer avec les résultats supersoniques. Dans le cas hypersonique, nous observons une évolution floue de l'épaisse onde de choc de S_2, mais il est impossible de les rattacher aux types d'interférence présenté dans le Chapitre 7. Par ailleurs, la détection des ondes de choc, très difficile due à la grande diffusion des chocs, ne nous a pas permis de voir d'évolution en termes de distances de choc. Seule une légère distanciation de la couche limite a été observable dans la zone d'interaction pour un angle d'interaction autour de -20°. Aussi, que ce soit au nez de S_2, ou dans la zone d'interaction, le niveau d'intensité lumineuse, reflet des variations de densité locale, suit la même tendance qu'en supersonique. Ainsi, malgré les difficultés à visualiser les interactions choc/choc, nous savons qu'il existe tout de même une variation de l'aérodynamique de S_2 en fonction de sa position dans l'écoulement de S_1. Grâce aux mesures réalisées avec la balance aérodynamique, nous observons des évolutions de forces de trainée et de portance similaire aux cas Mach 4. Cependant, les amplitudes de variation semblent être bien inférieures à celle observées en supersonique, avec même des valeurs de forces de portance qui sortent difficilement de l'écart type standard de la référence. Les forces et coefficients aérodynamiques sont comparées avec celles obtenues en simulations numériques DS3V dans notre cas, mais aussi avec celles du milieu continu. En comparant avec le milieu continu, on s'aperçoit que la zone de modification du coefficient de trainée de S_2 est plus large dans notre cas, ce qui laisse suggérer que l'épaississement des ondes de choc, due à la raréfaction globale du milieu. Par contre, le coefficient de portance montre approximativement la même tendance que le milieu continu, ce qui laisse à penser qu'il ne dépend pas de la raréfaction globale du milieu, mais plutôt de la taille de S_2, et donc du paramètre de raréfaction globale.

Une dernière partie des résultats à permis, grâce à la méthode du pendule, de recréer la cartographie bi-dimensionnelle des forces de trainée de S_2 lorsque celle-ci se situe autour de S_1. La répartition de la force de trainée de S2 dans l'écoulement de S1 est similaire à celle obtenue en écoulement supersonique. Cependant, les gradients de forces dans la zone d'interactions semblent moins importants avec l'augmentation du nombre de Knudsen global, probablement due à une diminution des effets de pressions, elles-mêmes plus largement distribuées autour de S_2. Cette cartographie est ensuite comparée avec des résultats de la littérature, obtenus numériquement pour un écoulement semblable à celui subit par notre couple de sphères.

Chapter 7

Identification of the shock/shock interferences

Contents

This doctoral work is dedicated to the understanding of aerodynamic interactions in rarefied flow conditions. In this chapter, we will focus on the shock/shock interactions (SSI) identification, also called interferences, in supersonic rarefied conditions. Here, an investigation is carried out to visually identify different types of SSI, as done in the continuum regime by many studies, and in particular by Edney [65] who is the pioneer in this domain.
A first study was realised for the couple C_1 in the flow-field generated by N1. In these conditions, S_2 was placed in a large set of positions around S_1 to apprehend the experimental results. By means of the flow-field visualisation technique, six different behaviours seemed to stand out. Due to the variation of S_2 positions in both directions, and particularly in the $\vec{x}$-direction, a slight variation of incident shock angle is observed. A first study is carried out to evaluate the behaviour of the interaction of the shocks of the two spheres for a huge number of positions of S_2 with respect to the S_1. From the observations obtained, an inter-sphere distance was chosen. In a second step, for the chosen X_2 coordinates, S_2 was moved vertically, the analysis of which allowed identifying different types of interference.
To this aim, the last experiment was also realised in the flow-field generated by N2, the couple of sphere staying C_1. The level of rarefaction being lower, more specificities seems to occur, allowing describing and identify the SSI with more accuracy.

It should be noted that no SSI were previously studied in our experimental flow conditions, thus, it was uncertain what to expect. During the flow-field visualisation experiment, the direct view in the test chamber appears as shown in Figure 5.5. No clear observation of the phenomenon can be made. Thus, it was impossible to determine, directly during the experiment, the placement of the following sphere (S_2) that would allow observing the SSI. To discern the flow characteristics of the different relative positions, it was necessary to record different sets of images, and to post-process them. Thus, a first study was carried out by moving S_2 into the flow generated by N1 to understand the physics of the SSI in a rarefied flow.

7.1 Full mapping, C_1 in N1 flow-field

Both spheres of the couple C_1 were placed in the N1 flow-field, and a certain number of locations were adopted by S_2 according to a mesh grid with a path equal to the radius of S_1. For each position shown in Figure 7.1, a set of images was recorded and post-processed as described in section 5.2. Here, as we focus on SSI, the concerned images have been sorted and regrouped according to the position S_2, as shown in Appendix F, Figure F.1 and Figure F.2.

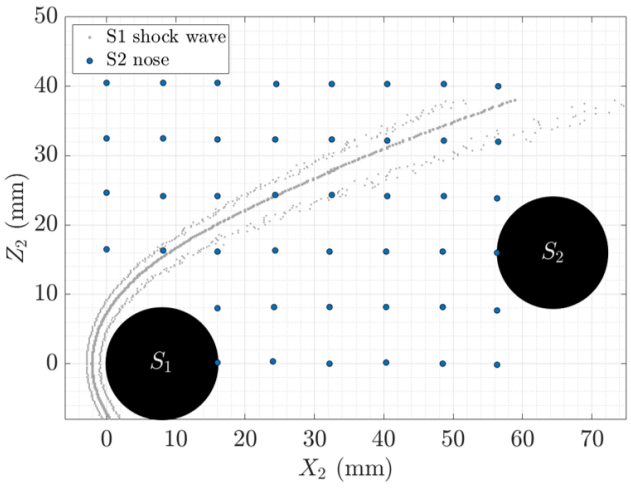

Figure 7.1: S_2 nose location.

For X_2 = 0 and 8 mm, SSI are observed, but as the spheres are very close to each other, the detection of shock-waves is made difficult. Moreover, there must exist some shock-wave/boundary-layer interactions that we do not want to confound with shock/shock interferences. Thus these cases will not be considered for the study of shock/shock interferences.
Concerning the other studied positions six groups of images were made, characterised by the shape and distribution of the denser region, and the shape of the upper part of S_2 shock-wave. These groups, noted from a to f, are described with a selection of images presented in Figure 7.2. The left column shows experimental images with enhanced contrast, obtained by cutting the lower values of intensity. Indeed the colour map, initially grey, makes it hard to observe a variation of intensity, thus, a jet colour map has been applied. It is to be remembered that the variation of intensity values corresponds to the variation of local density in the flow: the highest intensity corresponding to the densest region. In the middle column, contours are drawn with white lines over the images. One contour locates the densest (reddest) region, while the other follows the shock-waves in the interaction area. For each group, we noted the coordinates of S_2 that corresponds to the same type of SSI.
The different images were regrouped as follows:

- **Group a:** the densest region is located at the bottom of S_2. The area begins at the interaction point, then spreads itself following the lower part of S_2 shock-wave. The densest region seems particularly large, compared to the one of groups b to e.
- **Group b:** as for group a, the densest region is located on the lower half of the sphere. The region seems less extended but the wideness, even if lower than that of group a, is still important. The region mostly spreads below the point of intersection between the shock-waves. But an increase in the density level is also observed slightly above the intersection point.
- **Group c:** as it is slightly observed for group b, the densest area consistently extends toward the higher half of the sphere. This time, the densest region is observed all along the front half-sphere, the lower part being less extended but wider than the top part. At the intersection point, a sort of angled shape seems to appear. Moreover, the lower part of the densest region shows a tendency to flatten before recovering a curved shape.
- **Group d:** here, the densest region is mainly on the top half of the sphere. It appears as thin and extended as the highest region of group c, but unlike it, there is no marked density level, nor angled shape below the intersection point. It appears that, amongst all the groups, the region is the thinnest for group d.
- **Group e:** the densest region strongly resembles as the one of group d. However, the region is slightly thicker. But the main difference comes from the shape of the upper part of S_2 shock-wave. For the previous group, this part of the shock-wave looked curvy, as for a classical bow shock. Here, there is no defined curve, a sort of flattening is observed.
- **Group f:** as for group e, the upper part of S_2 shock-wave is flattened. The difference is observed on the densest region that is as thick and diffuse as for group a, but this time, the region spreads along the upper part of S_2 shock-wave.

With this classification, a study of the shock-waves shape was realised, along with a study of the normalised intensity level. This study was published in a scientific paper [41].
In Figure 7.3, the images presented on the top correspond to the images shown in Figure 7.1. Here, images are in their initial colour map, and no enhancement was made, as it is the case for the application of the shock-wave detection method. For each image, the detected shock-waves are plotted, corresponding from left to right, to the foot of shock, the middle of shock, and the boundary layer. From the shock-waves observation on all the images of each group, a first schematisation of the SSI is proposed at the bottom of Figure 7.3.

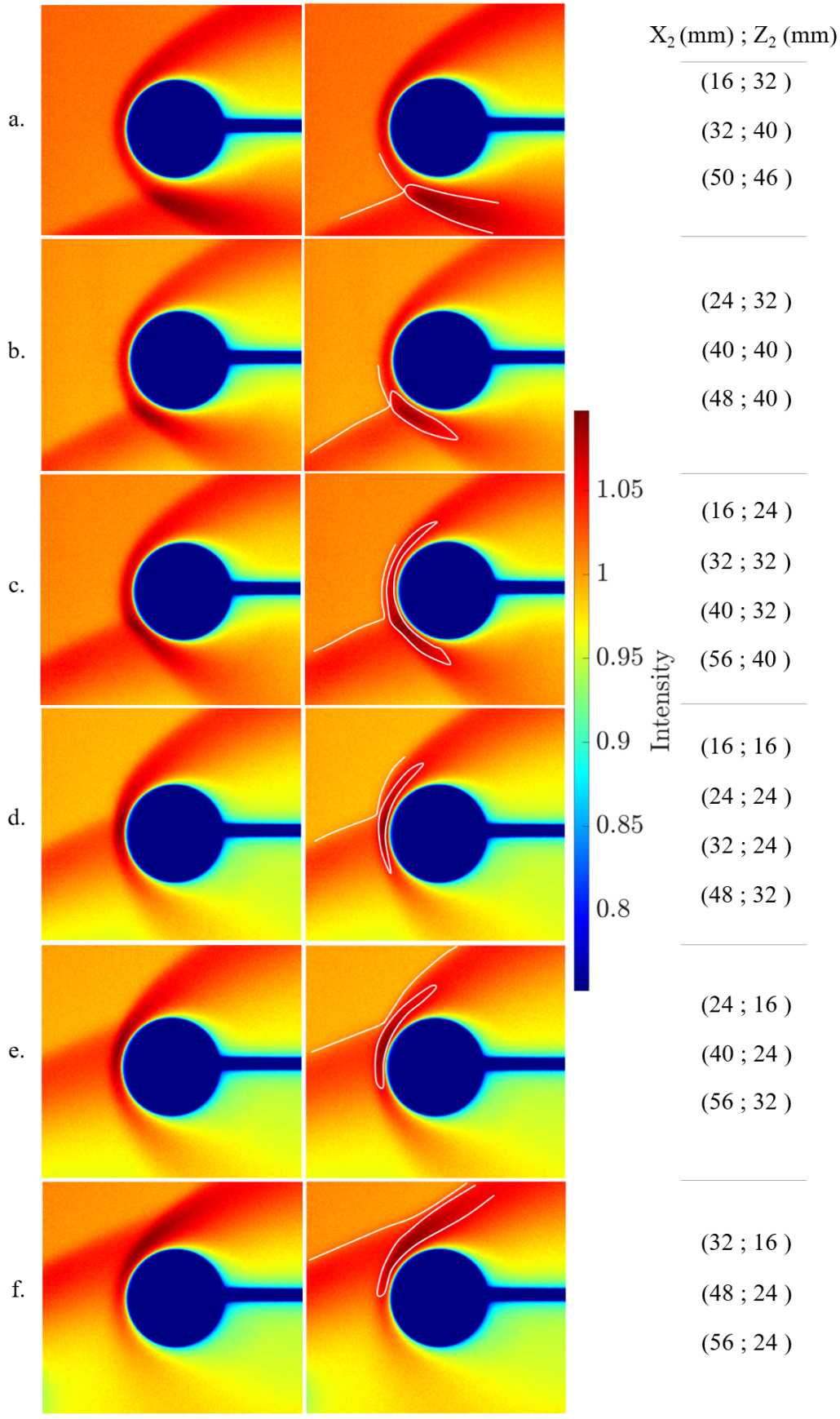

Figure 7.2: First identification of different SSI types.

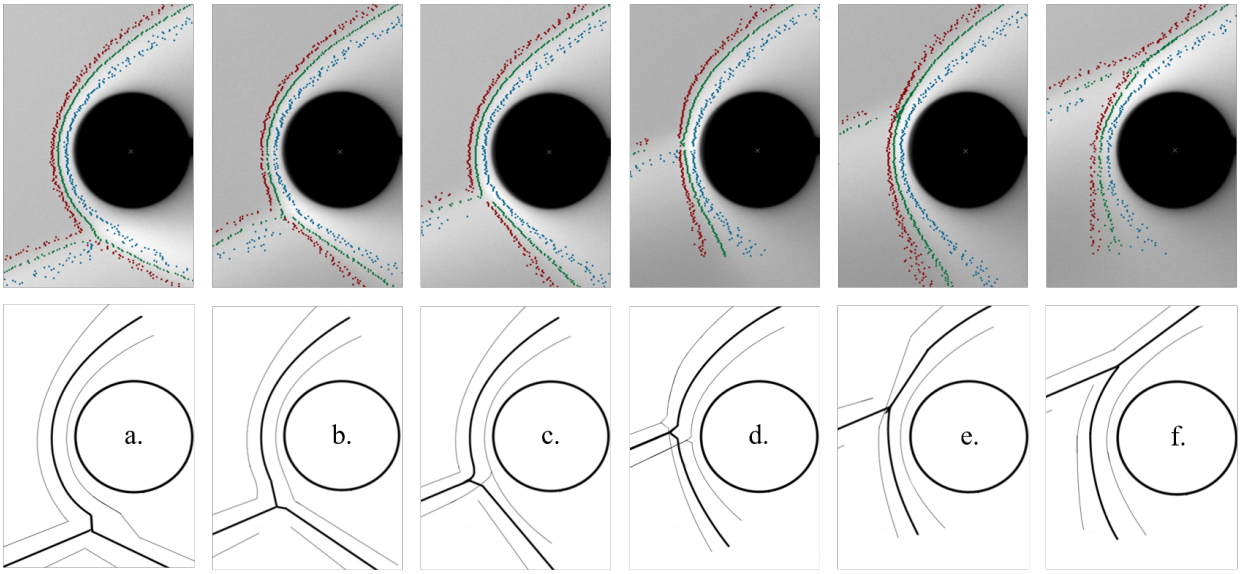

Figure 7.3: Images of the different identified groups of SSI with shock-wave detection (top); Schematics of the different SSI groups (bottom).

In the scheme of each group, the specificities have been slightly accentuated to highlight the differences observed.
Observing the proposed schemes, different general features can be observed, and some of them are shared between the different groups:

- First of all, a flattening of the shock-wave is observed. For groups a to c, the lower part of S_2 shock-wave (below the intersection point) flattens; while for group d, e and f, the flattening seems to appear on the superior part (above the intersection point). Note that for group d, the flattening is not clearly marked, but the detection of the foot of shock seems to suggest it.
- Looking at the bottom part of S_2 shock-wave, it can be seen that its orientation varies. From a to f, the inferior part of the shock-wave turns from east/south-east to south/south-east. As S_2 enters deeper in the wake of S_1, the inferior part of its shock-wave gradually opens.
- For groups a to d, a setback of the intersection point is observed which does not seem to be the case for group e and f.

Globally, it seems that the described groups have similarities. The schemes suggest that groups can be classified into two families: groups a, b and c show an interaction between two shock-waves of different directions; groups e and f show an interaction between two shock-waves of same direction. Group d marks a transition between these two families, with characteristics that can be associated with the first family (setback area), or to the second one (slight flattening of the superior part of the shock). When observing in detail, each group has its own specificities but we will not yet enter into details.
As shown with images from Figure F.1 and Figure F.2 and their post-processing, the group associated to each image depends on the angle of interaction between the incident middle shock from S_1, and the middle shock of S_2. This angle, noted Θ_i, was previously described in Figure 5.11.

In order to deepen the interpretation of the behaviour of the SSI based on the analysis of the images, a complementary analysis was carried out based on the different points of interest described in Figure 5.11. To this effect only the points located around S_2 are considered. S_2 location will be described with Θ_i, a negative angle corresponding to the positions of S_2 where it is located mainly above the incident shock; inversely, a

positive angle corresponding to the positions where S_2 is mainly below the incident shock and thus enters the wake of S_1.
The stand-off distances of S_2, Δ_2, are plotted as a function of Θ_i in Figure 7.4. These distances represents the distance between the foot (FS), the middle (MS) and the boundary layer (BL) of the shock-wave of S_2 with its surface. For these three regions, Δ_2 values show a similar evolution. For the lowest values of Θ_i, when S_2 is predominantly out of the flow of S_1, *i.e.* mainly in the free stream of N1, the stand-off distances are in the range of the reference values ($\Delta_{FS1} = 2.76 \pm 0.16$ mm, $\Delta_{MS1} = 1.99 \pm 0.16$ mm, $\Delta_{BL1} = 0.89 \pm 0.16$ mm). As S_2 goes down (Θ_i increases), Δ_2 increases and reach a maximum for group c. Then, it decreases to reach a minimum for group e. Finally, as S_2 penetrates deeper in the wake of S_1, its shock-wave moves away from its surface. In section 6.3, a correlation between the stand-off distance and the Reynolds number was found (Equation 6.4). Thus, since the front shock of S_2 does not seem to be impacted by the incident shock for the higher Θ_i, the increase in Δ_2 must indicate an increase in the rarefaction level upstream S_2.

In Figure 7.5, the distances d_i and d_{ml} are plotted versus the angle Θ_i. They describe the evolution of the distance of the interacting point P_i, and of the most luminous point P_{ml}, according to the SSI observed associated to Θ_i. The left graph shows that P_i gets closer to the surface of S_2 when the interaction occurs in an angle ranging between -5 and 20°, corresponding to group d and half of e. The right graph presents the distance of the most luminous point, which does not follow the same trend as the distance of the interaction point. For Θ_i ranging between -20 and 40° that includes groups c, d and e, the denser area remains close to the surface of the sphere and unchanged despite the distancing of the interaction area.

As previously mentioned (5.2), Coumar [52] showed that the luminous intensity reflects the local density. Thus, it was decided to look further at the most luminous point on the horizontal line of S_2 ($P_{0_{BL2}}$), and at the most luminous point in the interference area (P_{ml}), giving another quantitative parameter to be studied. The values of the luminous intensity in these two regions were recorded and plotted in Figure 7.6. In both graphs, the intensities are normalised with I_{01}, the maximal intensity on the horizontal line of S_1 (located at $P_{0_{BL1}}$), so that a comparison between images can be made. A tendency seems to appear: whether at $P_{0_{BL2}}$ or at P_{ml}, a maximum is reached for Θ_i corresponding to groups d and e. As can be observed with previous results from Figure 7.5, the maximal intensity level showed in Figure 7.6 corresponds to the interaction angles where the shock is the closest from the surface of S_2.
A decrease in d_i or in d_{ml}, along with an increase in I_{02} or in I_{ml} indicates that the maximal local density gets closer to the surface of the sphere. This suggests that wall pressure peak and heat transfer may be max-

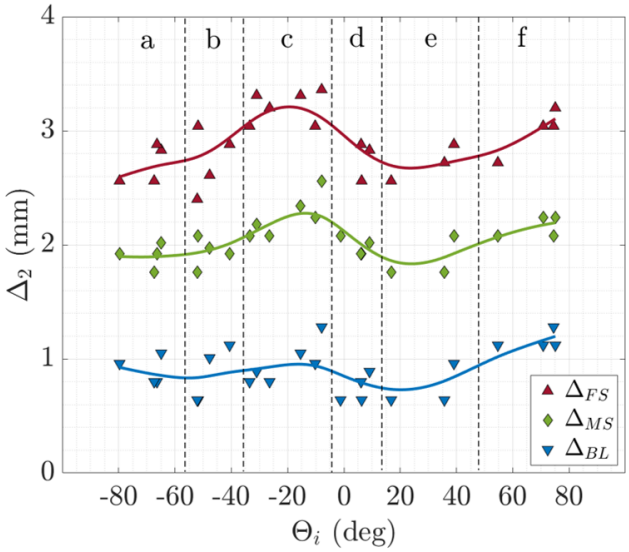

Figure 7.4: Stand-off distances of S_2 on the full mapping.

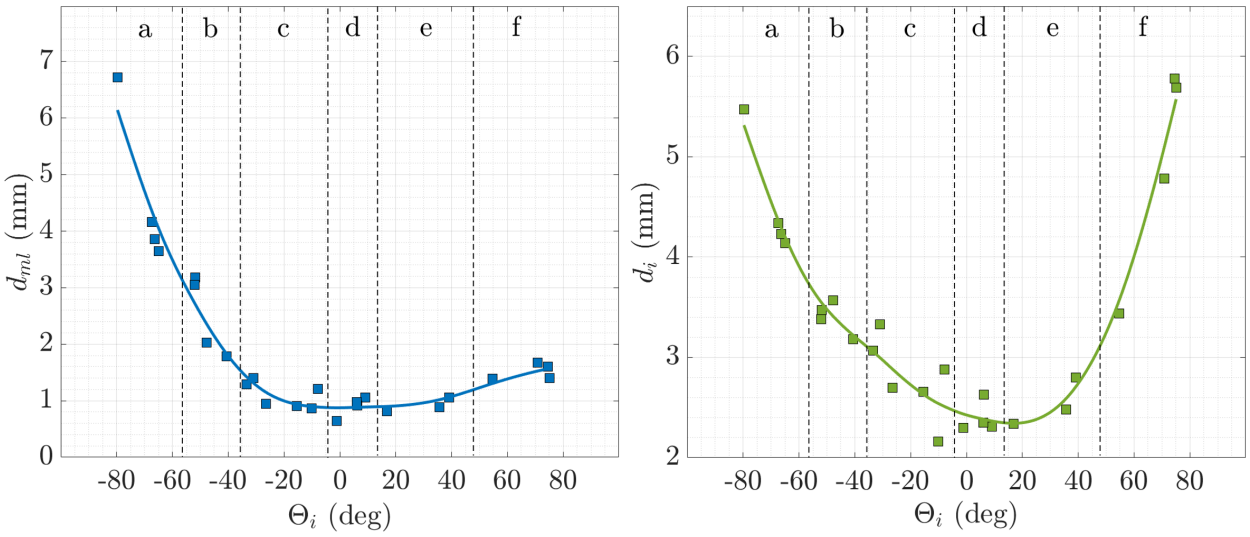

Figure 7.5: Distances of P_i (left graph) and P_{ml} (right graph) from the surface of S_2 on the full mapping.

imised for angles ranging between -5 and 20° since both points are closer to S_2 wall, and that the intensity values are the higher. According to the graph in Figure 7.4, it seems that the shock-wave of S_2 deforms depending on the SSI endured by S_2. From the graphs presented in Figure 7.5, the interaction point P_i and the most luminous point P_{ml} seem to distance themselves from the surface of the sphere depending on the SSI.

For d_i, a greater dispersion of the points is present for group c and d. As can be observed in both graphs of Figure 7.6, there is a large dispersion of the points concerning the intensity. We remind the reader that S_2 is moved both in the $\vec{x}$ and the $\vec{z}$ directions. In Figure 7.7, the profiles of luminous intensity are plotted for vertical and horizontal axis corresponding to the coordinates of S_2 nose (Figure 7.1). The different intensity profiles show a thickening of S_1 shock-wave as X_2 increases. Thus, the incident shock that interacts with S_2 will not be identical if $X_2 = 16$ mm or if $X_2 = 50$ mm, even if its positioning in the $\vec{z}$ direction allows an identical Θ_i. This means that, for the same group, and the same interaction angle, some variations can be observed on the resulting SSI, which must explain the dispersion on the previous graphs.

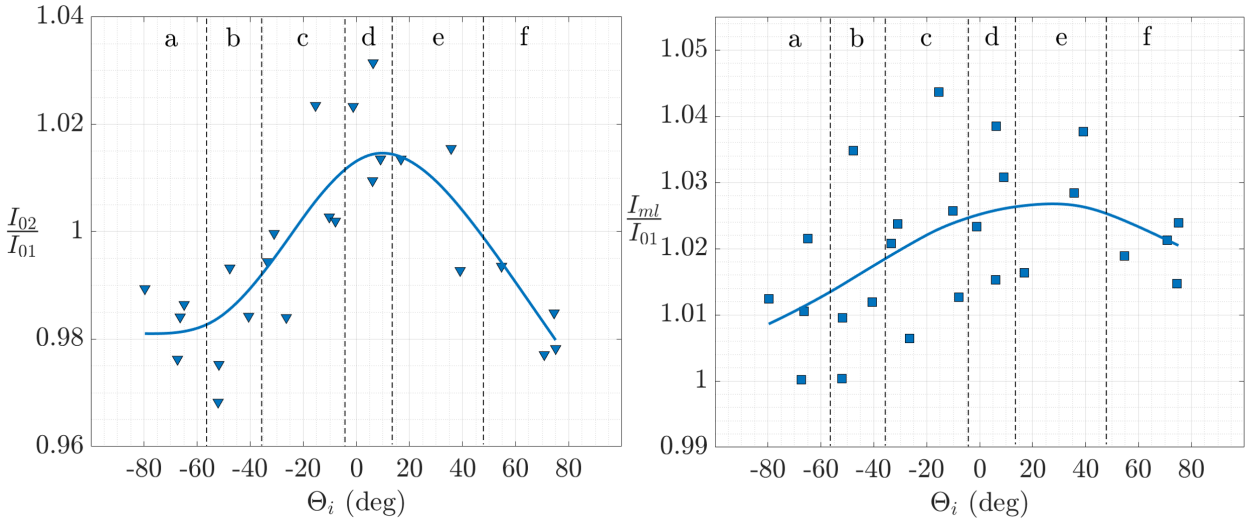

Figure 7.6: Normalized luminous intensities of $P_{0_{BL2}}$ (left graph) and P_{ml} (right graph) for S_2 located on the full mapping.

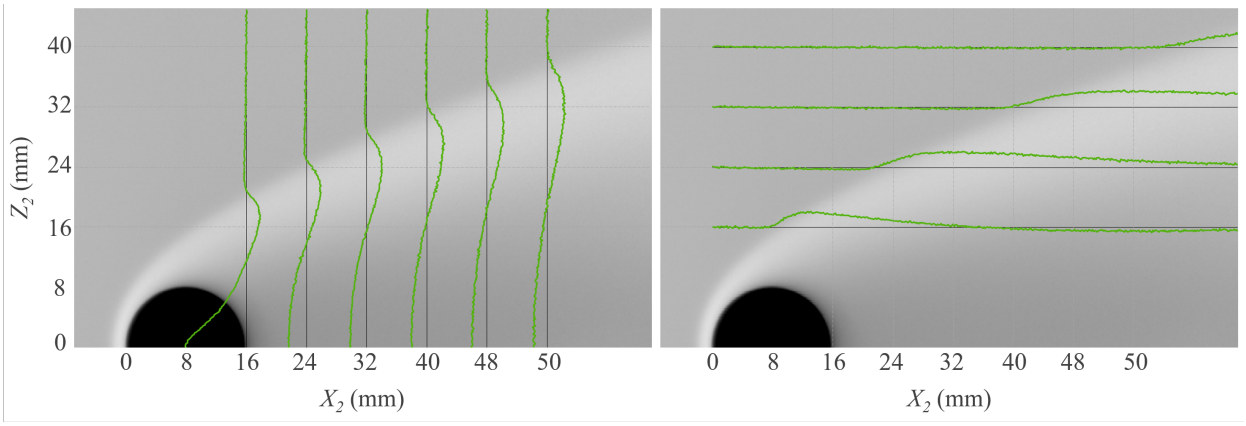

Figure 7.7: Vertical (left) and horizontal (right) profiles of luminous intensity in the flow-field of S_1.

7.2 Case C_1, N1, axis $X_2 = 24$ mm

In order to avoid differences that could arise from a variation of the flow-field seen by S_2, another experiment was realised for a fixed longitudinal distance at $X_2 = 24$ mm. Different reasons explain this choice.
For $X_2 \leq 8$ mm, images from Appendix F (Figure F.3) show that S_2 cannot be sufficiently moved down to observe the different types of SSI. Moreover, when the two spheres are really close to each other ($X_2 \leq 16$ mm), some effects coming from shock-wave/boundary layer interferences might occur. Indeed, in some cases, the proximity of two spheres makes them behave as one object (for positions (0,16) and (8,16)). In some other positions ((0,24), (8,24), (16,16)), the lower part of S_2 shock-wave does not seem to develop properly, which might modify the physics in the interaction area. Thus, to decorrelate these effects from the ones of the shock/shock interferences, and to avoid confusion, it was chosen to place S_2 not too close from S_1.
But, due to the diameter of the nozzle core, S_2 has to be contained in a certain range of altitude. Thus, to study all the types of interference, S_2 has to be close enough from S_1.
A good compromise was found with $X_2 = 24$ mm that corresponds to $3/2.D_1$. This vertical axis will mainly be the one used for the investigation of the SSI.

On this vertical axis, S_2 was placed at different altitudes, resulting in different interaction angles Θ_i. For each altitude, the image is post-processed and analysed as previously realised for the full mapping.
Amongst the numerous images, one of each group were selected for shock comparison with the reference case. Figure 7.8 reveals additional features on the deformation of S_2 shock-wave in the case of SSI. From the previous images, we already observed that with SSI, S_2 shock-wave was not symmetrical, unlike S_1, which is clearly visible by superposing both shocks. As previously noticed, the bottom part of S_2 shock-wave opens as S_2 goes down in the wake of S_1, but, with Figure 7.8 a specificity is observed for group a and b, below the intersection point, where the shock seems pushed by the incident shock. Concerning the upper part of S_2 shock-wave, for groups d to f, in addition to the flattening area the shock shows deviates upwards, probably due to the merging of the two shock-waves above S_2. These behaviours qualitatively analysed will now be quantified as previously did for the full mapping.
For this experiment, the post-processing of images was a few times realised to add the uncertainties due to the thickness and diffusion of the flow-field, but also to the sphere and shock-wave detection. The resulting graphs are presented in Figure 7.9, Figure 7.10 and Figure 7.11. From the observation of these six graphs, it can be seen that restraining the displacement to a vertical axis reduces consequently the dispersion of the points. With these new results, clear tendencies are shown and can be analysed.
In Figure 7.9, the stand-off distances of the FS, MS and BL of S_2 are plotted, along with their reference values, *i.e.* the stand-off distances of S_1. As previously observed, the stand-off distances increase for group c for SSI reasons, and for group f due to an increase of the local rarefaction level. This statement is mostly

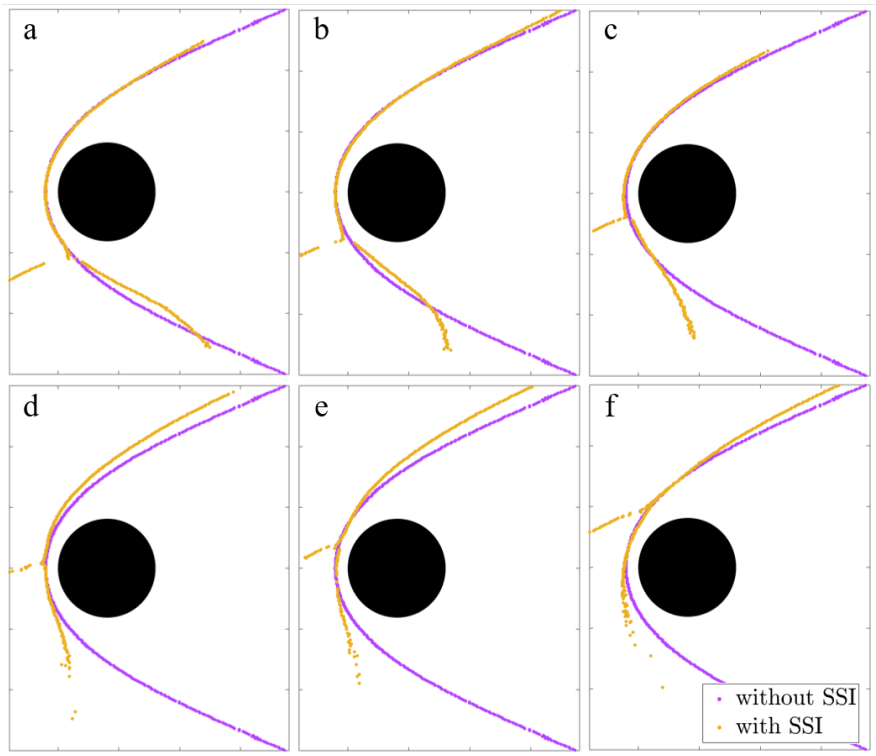

Figure 7.8: Superposition of S_2 middle of shock with and without interaction.

true for the FS and the MS. For the BL, a same tendency seems to appear, but due to the uncertainties, it is impossible to confirm that there is a deformation of the BL at the nose of S_2. The stand-off distances of S_2 are always greater or equal to the reference values. Thus, when the shock deforms, it is always to move away from the surface of S_2.

The distances of P_i and P_{ml} towards the surface of S_2 are plotted in Figure 7.10. Since P_i is the point of interaction between the middle shock regions of each sphere, for each angle, d_i is compared to the distance between the MS and the surface of S_2. On the same way, the detection of P_{ml} corresponds to the

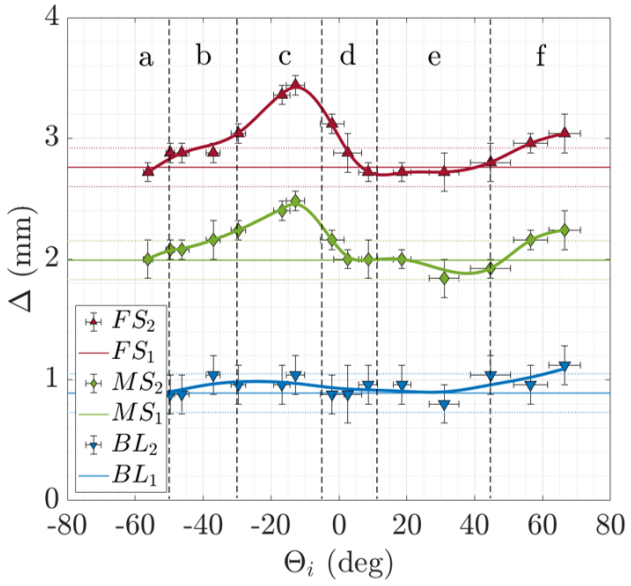

Figure 7.9: Stand-off distances of S_2 for X_2 = 24 mm.

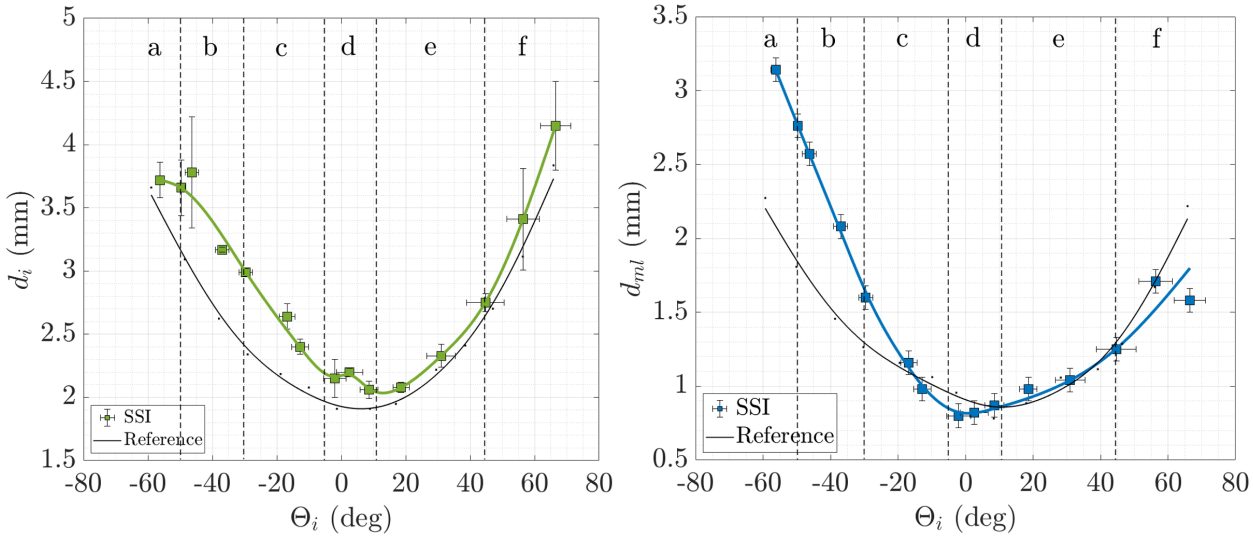

Figure 7.10: Distances of P_i (left graph) and P_{ml} (right graph) from the surface of S_2 for X_2 = 24 mm.

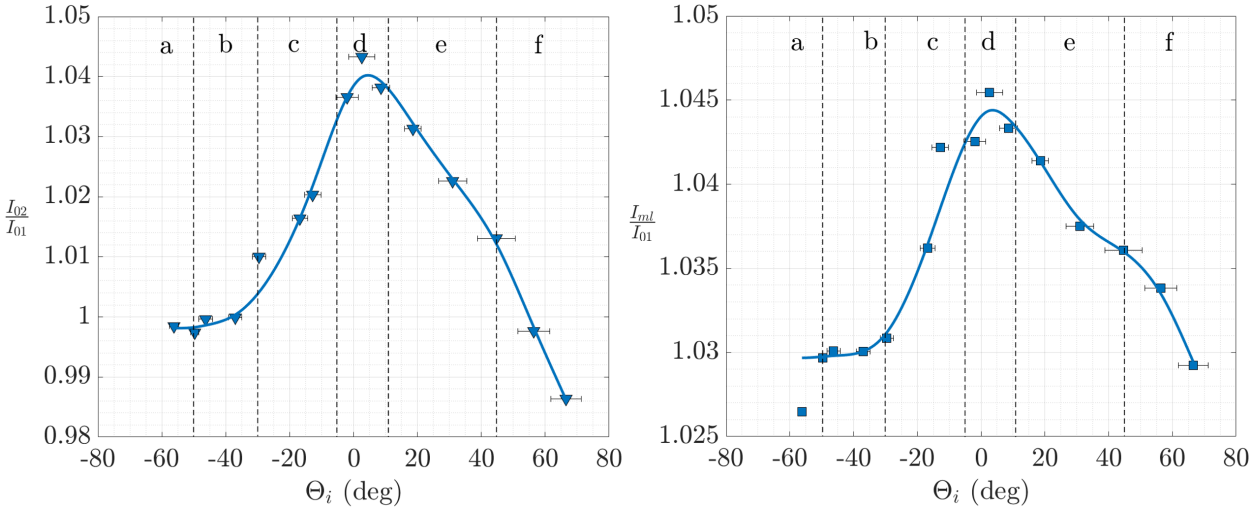

Figure 7.11: Normalized luminous intensities of $P_{0_{BL2}}$ (left graph) and P_{ml} (right graph) for X_2 = 24 mm.

maximum luminosity around S_2, which corresponds to the detection of the boundary layer. Thus, d_ml is compared to the distance between the BL and the surface of S_2.
The evolution of d_i shows that for groups a to d, the interaction point clearly moves away from the surface of S_2, compared to its reference position. This agrees with the observation of the setback area visualised on the images. For the group d, a "∧"-shape is observed, also seen on the images. Since the group d seems to be a transition area, it is possible that a very slight displacement of S_2, around the altitude corresponding to $\Theta_i = 0°$, causes a strong variation of the phenomenon observed in the interference area. For groups e and f, the intersection point has globally the same distance from S_2 than the reference shock has.
From the observation of d_{ml}, it can be stated that for groups a and b, the BL region, in the interference area, gets away from S_2 surface. Group c marks a transition where the densest region gets closer than the reference to the surface of S_2. Group d is also concerned by a BL which is closer to S_2. Then, for groups e and f, as for d_i, in the interference area d_{ml} corresponds to the reference BL.

Regarding the intensities at the nose of S_2 or at the most luminous point in the interference area, both graphs of Figure 7.11 show similarities, and in particular, a peak for group d.
The intensity at the nose of S_2 for group a, where S_2 is mainly in the free stream, is that of the reference. Then, as S_2 is displaced down (Θ_i increases), the intensity increases until around 0°, then decreases. For

group f, intensity values are lower than the reference because the surrounding density flow-field of S_2 is very low.
Concerning the maximal intensity in the interference area, the same tendency as I_{02} is observed, but values are always higher than the reference, which corresponds to the maximal intensity in S_1 boundary layer.

From the graphs of Figure 7.9, Figure 7.10 and Figure 7.11, the groups have been delimited following the same approach as for the full mapping. It can be seen that the limits have slightly changed compared to the previous experiment which is mostly due to an improvement of the post-processing image analysis. All plotted points of the graphs have been obtained by analysing the images presented in Appendix F, Figure F.3. Due to the thickness, and diffusion of the shock-waves of the rarefied flow, and to their evolution in the interference area, the change in SSI type is unclearly visible. Amongst the images presented in Figure F.3, we selected the six images (contoured in dark) that seem to best represent their own group. Some images between are hard to classify, this is why it is necessary to stay cautious about the limit angles given in the graphics.

7.3 Comparison with denser flows

As for N1, images were recorded for N2 free-stream flow with the couple of spheres C_1. The same methodology was used to determine different behaviours according to the relative positions of the sphere. In Appendix F, Figure F.4 are presented by the post-processed images. We observe groups of SSI that are equivalent to those of N1. As for N1, six images were selected, each representative of the SSI type of a group.
With the selection of images in both N1 and N2 flow conditions, we will visually compare our rarefied SSI to the continuous ones. This will allow defining the SSI types of our conditions according to the ones first described by Edney [65] in a continuum regime. Moreover we will have a first idea of the evolution of the SSI when adding viscous effects caused by a decrease in free-stream density of the flow.
In Figure 7.12 the six types of shock/shock interferences are presented for different natures of incident shock, and for different levels of rarefaction. The Schlieren images on the top are from Edney's report [65]. The SSI observed are the result of the interference between an oblique shock (generated by a wedge) and the bow shock of a hemisphere. The studied Mach number is 4.6 and the regime is continuum ($4.79.10^{-6} < Kn < 5.61.10^{-5}$). Below, we can observe the Schlieren images from the work of Fisher [71] who studied the SSI between two interacting spheres of the same size. Models are placed in a Mach 5 flow, also in the continuum regime ($1.04.10^{-5} < Kn < 5.8.10^{-5}$). The last two lines are the set of images from our experiments. They show the results of two interacting spheres in a Mach 4 flow with two different levels of rarefaction for N2 ($Kn = 4.64.10^{-3}$) and N1 ($Kn = 1.39.10^{-2}$).
These four experiments are interesting to compare since they all take an interest in describing SSI at Mach numbers in the same range, but for different rarefaction levels.
Endey and Fisher presented the six types of SSI they obtained for almost the same flow conditions. What changes between the two is the nature of the incident shock: Edney's is an oblique shock, while Fisher's is a bow shock. Although the visualisation method has been improved between these two experiments, it seems that the same patterns occur whatever the type of SSI. This means that the nature of the incident shock does not impact the physical phenomenon in the interference region. However, this analysis is based on images and not on the measurement of wall pressure, heat transfer or aerodynamic forces. Thus, we stay cautious here, only speaking in terms of patterns, and not in terms of SSI impact on the spheres' aerodynamics.
From our results for N1 flow conditions, it was uneasy to compare the SSI obtained with the one from the continuum regime. This is why we did not associate the groups presented earlier, directly to a type of SSI with regards to Edney's definition. However, the results obtained for the flow conditions of N2 make a good transition between the continuum regime and the rarefied conditions of N1. Indeed, N2 rarefaction

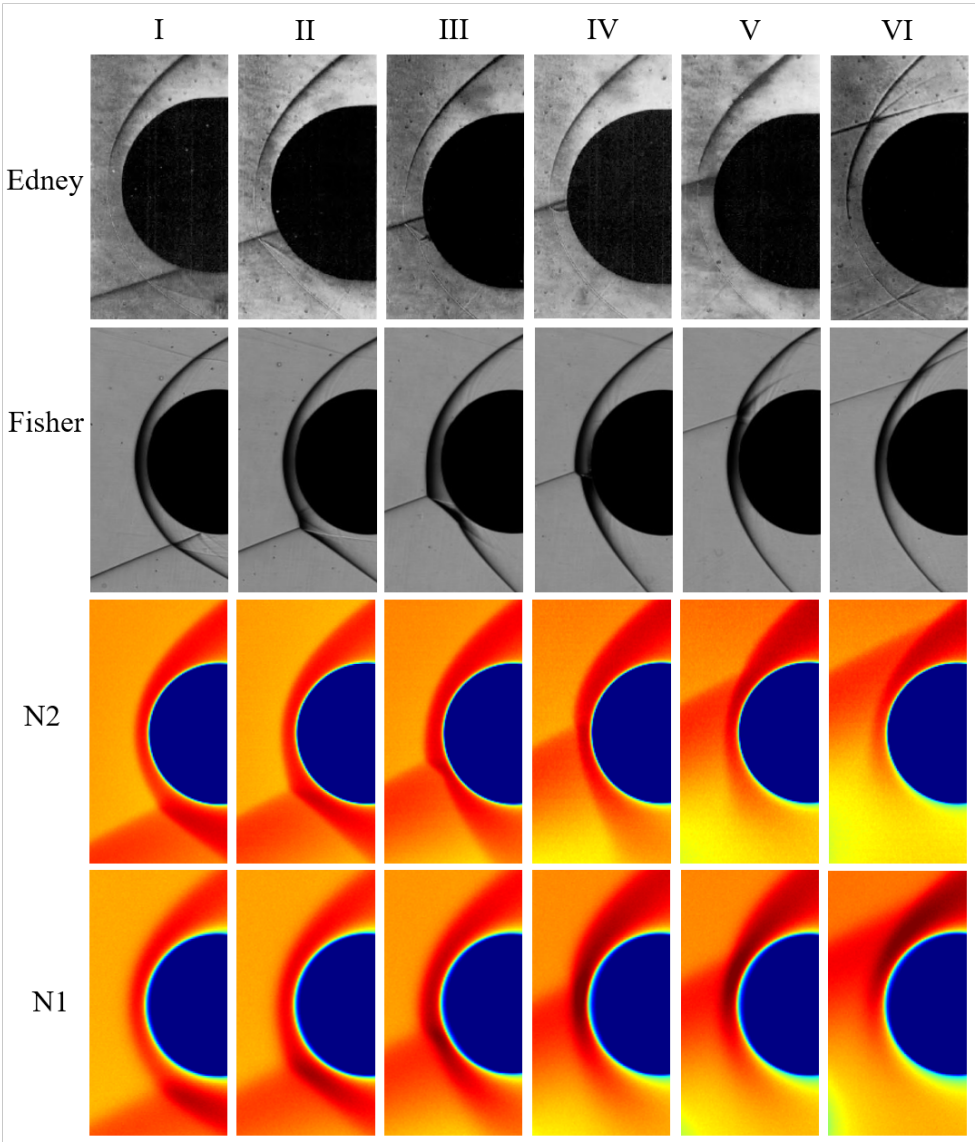

Figure 7.12: Images of the six SSI types for different levels of rarefaction.

level is three times less than that of N1, which results in less diffuse shock-waves and thus, in less blurred SSI, as can be observed with the images presented in Figure 7.12. Even if no supersonic jet, shear layer or expansion wave are clearly visible, images of N2 flow conditions show the external deformation of S_2 bow shock, and the variation of intensity allows observing an increase in the local density corresponding to the reddest area. A detailed analysis and comparison with the descriptive definition of the different types of interaction reported first by Edney, then by different authors such Simon Sanderson [184]. To ease the reading Figure 2.15 can be taken as an illustration of the SSI interferences.

They state that the SSI type I take place when the secondary shock meets the principal shock far below the sonic line. The shear layer that takes birth at the impinging point doest not meet the surface of the model, meaning that no significant local heat increase should occur. This leads to identify the group a as the type I. As the impingement point moves upward and the secondary shock meets the bow shock just below the sonic line, it corresponds to the interference type II as occurs with group b. The transition towards the type III occurs when the secondary shock intersects the bow shock within the subsonic region ahead of the model. Both the radius of curvature and the stand-off distance of the upper part of the bow shock with respect to the incident shock increase. The shear layer created at the impinging point tends to deflect and attach to the surface of the body as can be observed on group c. This behaviour can lead to an increase of the heat rate over the body surface. The type IV is generally characterised by the apparition of a supersonic jet that leads

to strong heat loads. In the present conditions with viscous flows, no supersonic jets could be identified. Nevertheless the pattern of the shock interference of type IV can be compared to group d. The shear layer becomes denser and tends to attach to the body, resulting in a decrease in the stand-off distance. Also, the shock becomes increasingly curved as the impact point moves up the model. The type V appears when the impingement point moves just up the sonic line as it occurs for group e. A weak wave tends to appear that hits the body but tends to diffuse quickly, reducing the influence of the heat transfer. This is all the more true as the interfering area becomes very rarefied. At last, the type VI occurs when the secondary shock interacts well above the sonic line as for group f. As observed on the patterns, it differs from others because it presents an expansion of the shock from the impact point. This effect is increased in our experimental conditions due to the viscous effect.

Analysing carefully the equivalent SSI obtained in N1 flow conditions, it seems that the patterns vanish but are still in accordance with what is observed in N2 flow conditions. Types III, IV, and V are the easiest to differentiate for N2, but for N1, only the type III is clearly visible without any shock-wave detection.
Finally, with this experimental image study, we could identify the six types of shock/shock interferences, and classified them according to their angle of interaction Θ_i. Figure 7.13 summarizes their distribution. We remind the reader that the limit angles between the types of SSI are given as regions and not as clear-cut limits.

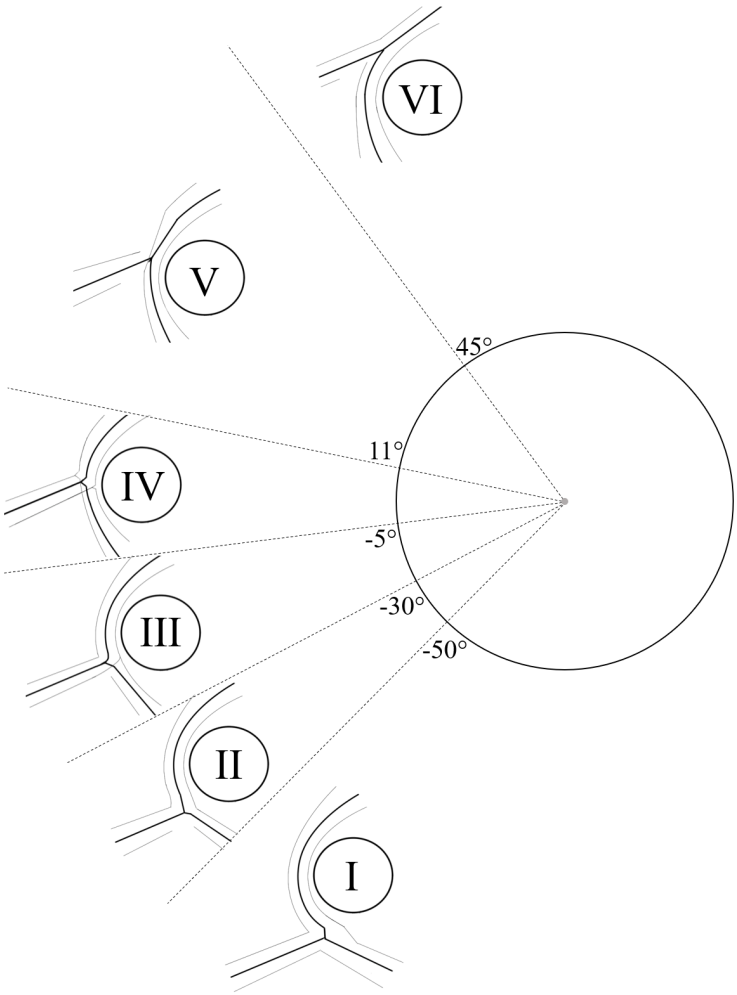

Figure 7.13: Distribution of the SSI types with the associated range of interaction angles.

Chapter 8

Complete study of the sphere couple C_1 in N1 flow-field

Contents

All the results of this chapter have been realised with the experimental conditions of the N1 nozzle which will be taken as the reference case. In this chapter, we present the results obtained for the fully studied couple of spheres, C_1, which is composed of two spheres of 16 mm diameter. In the previous chapter, different positions of S_2 towards S_1 were adopted, allowing to visually identify six types of interferences, as in the continuum regime. Each type of interference was identified along a vertical axis for a position of S_2 selected on the $X_2 = 24$ mm axis, corresponding to the contoured images of Figure F.3. For these six locations, pressure and force measurements were realised to deepen the understanding of the effect of shock/shock interferences (SSI) on the aerodynamics of S_2 in the specific Mach 4 rarefied flow generated by N1 (see Table 4.2).
By means of the swinging sphere method, complementary results allowed to obtain the drag force mapping of S_2 on a large range of positions towards S_1. Moreover, this method enabled observing not only the impact of S_1 on S_2, but also the modification of S_1 aerodynamic behaviour when S_2 is located in its vicinity.
All along this chapter, since the numerical simulation from DS2V was in good agreement with experimental results, complementary numerical results will be used in order to obtain information relative to the flow seen by S_2. Then, the experimental results on S_2 will be confronted to the DS3V simulation.

8.1 Case X2 = 24 mm: Effect of shock/shock interferences

As explained in chapter 7, in order to increase the accuracy of results and to avoid a variation of the incident flow-field generated by S_1 and seen by S_2, SSI have to be studied on a same vertical axis. With the different sets of images recorded during the full-mapping experiment (Figure F.1 and Figure F.1), it was decided to set $X_2 = 24$ mm. This section focuses on the aerodynamic behaviour of S_2 as a function of the type of interference it experiences. The analyse of SSI will be based on the flow-field visualisation presented in chapter 7, the drag and lift forces endured by S_2, and its wall pressure distribution.

8.1.1 Aerodynamic forces of S_2

This section presents the force measurements realised with the aerodynamic balance described in section 5.4.1.

8.1.1.1 Force measurements and analysis

Figure 8.1 presents the values of drag (left graph) and lift forces (right graph) of S_2 as a function of the interference angle, which is characteristic of the interference type. Black lines correspond to the reference values, *i.e.* the aerodynamic force values of S_1 when it is in the free-stream flow with no interaction with another sphere.
Concerning the drag forces, when S_2 is almost completely in the free-stream flow, for type I, F_{x_2} value is very close to the reference value. The SSI type I has a very little impact on S_2 drag force, which slightly increases its value. As the altitude of S_2 is decreased, it enters the incident shock-wave. Thus, since a shock-wave is due to the compression of molecules, the upstream flow seen by S_2 is much denser. This leads to an increase in F_{x_2}, which reaches a maximum for $\Theta_i \approx 0°$, corresponding to the SSI type IV. As S_2 penetrates deeper into the wake of S_1, it slowly gets out of the influence of the incident shock, and enters a more rarefied flow. Consequently, for SSI types V and VI, F_{x_2} decreases rapidly, reaching values that are even lower than the reference case.
The lift forces presented in the right graph of Figure 8.1 are corrected values. Indeed, for a single sphere, we measured a lift force of -0.51 ± 0.11 mN. As a sphere is an axisymmetric geometry, its theoretical lift force

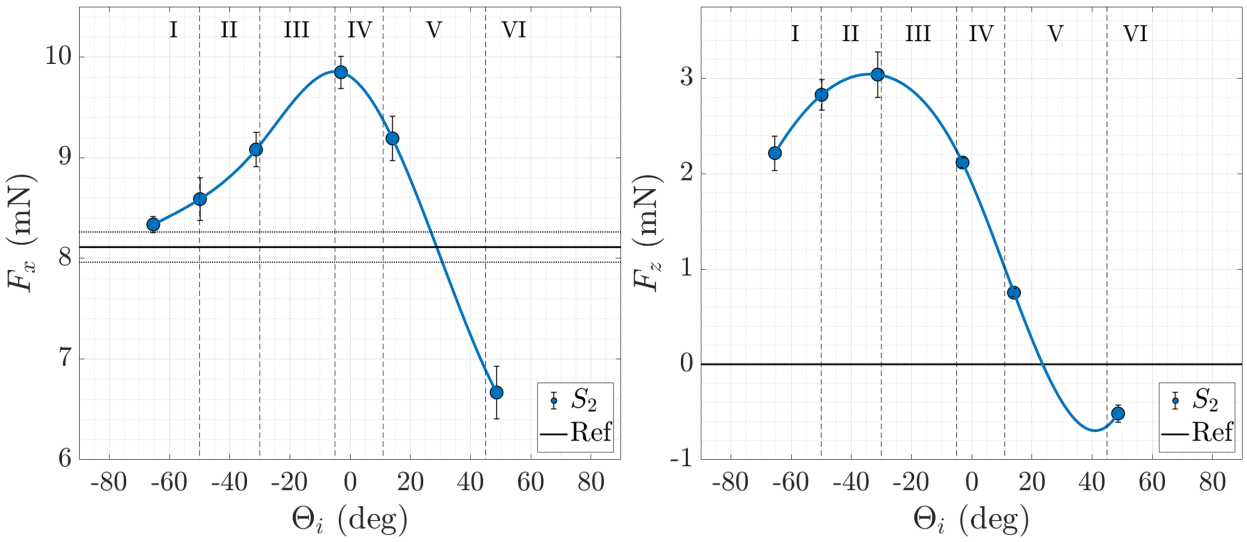

Figure 8.1: Drag and lift forces of S_2, C_1 in N1 flow-field.

is null. Thus, the measured value is the consequence of a slight angle of the aerodynamic balance relatively to the direction of the flow. Since the set-up has not been modified during the measurement of the different types of SSI, we know that this value is an offset that will be present on every measurement. For this reason, the lift values have been shifted of 0.51 mN to cancel the positioning error of the balance, which is of less than 1°.

It is interesting to note that the lift force is not negligible for the type I SSI, while the drag force has a value close to the reference value. The drag force of the SSI type I is close to the reference value. This shows that this type of interference has an impact on the lift of the S_2 sphere, while the drag force suggests the opposite. When S_2 is mainly located in the free-stream flow, but under the influence of S_1, *i.e.* for types I to III SSI, it can be seen that the lift force slowly increases. Then, as S_2 keeps getting down behind S_1, it is mainly located under the incident shock. However, for types III to V, the lift decreases but stay positive. This means that the incident shock does not create a discontinuity. In the continuum regime, if S_2 is located right above or right below the incident shock, it is strongly repulsed respectively up or down, as if ricocheting on S_1 shock-wave. This does not seem to be the case in our flow conditions. This difference might be explained by the viscous effects that are present in rarefied flows. These effects will be discussed later in this work. At some point ($\Theta_i \approx 25°$), the lift changes sign. But, since S_2 is already in the wake of S_1, it is hard to say if this change is due to the SSI or to the protection created by S_1 that could act as a shield.

Figure 8.2 shows the Pitot pressure profiles in the wake of S_1, for $X_2 = 24$ mm. On this figure are also plotted the profiles of drag and lift forces. Each profile is plotted relatively to its reference values so that their tendency can be compared. As can be observed, the variation in drag force is linked to the variation in pressure: F_{x_2} increases with the Pitot pressure. Nevertheless, the drag force shows a gentler slope than that of the pressure, which is due to the size of the sphere. As an example, we see that the pressure recovers the free-stream value around $Z_2 = 27$ mm, which corresponds to the altitude of the foot of shock. At this altitude, S_2, whose coordinates localise the nose, is still influenced by the incident shock-wave, since its upper half is in the free-stream flow, but its lower part is fully immersed in the shock. It means that the sphere has to be completely above the middle of the shock to recover its reference value.

Nevertheless, by observing the lift profile, for SSI type I, it can be seen that at $Z_2 = 27 + 8$ mm (where S_2 is schematised) the lift is not equal to the reference value. Moreover, the lift does not evolve with the pressure since F_{z_2} is maximal when S_2 is located on the FS, where the Pitot pressure retrieves its reference value. Thus, as previously discussed, the variation in S_2 aerodynamics, and in particular in lift forces, not only depends on the pressure, but might also depend on the viscous effects. Indeed, it was shown, with the study of single spheres drag coefficient (Figure 6.17), that the contribution of the friction increases with the Reynolds number after shock (Re_2). Since Re_2 decreases when increasing the level of rarefaction, we know

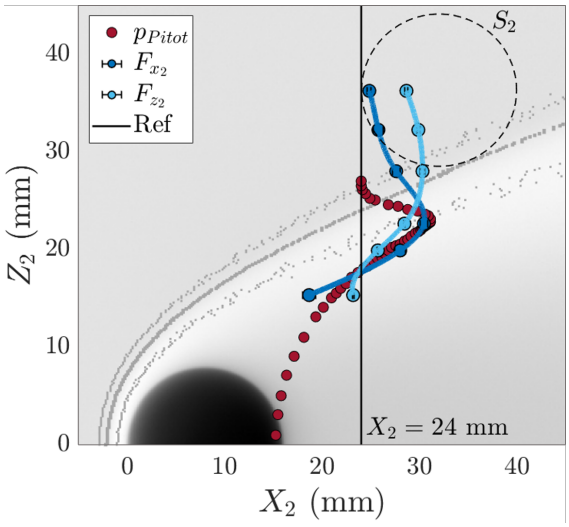

Figure 8.2: Pitot pressure profile in the wake of S_1 superposed with the drag and lift forces of S_2, C_1 in N1 flow-field.

that the friction effects increase when increasing the level of rarefaction. An equivalent study that the one made in section 6.2.2 will later be realised with the different positions that give the six types of interferences. It is interesting to observe that, below the incident shock, the three profiles all crosses their reference value at the same location. This point will be further investigated in the rest of the chapter.

With the values of drag and lift force, it is possible to calculate the resultant force $\vec{F} = \vec{F_x} + \vec{F_z}$. This resultant is defined by its norm and angle as explained in the scheme presented in Figure 8.3. These two parameters are respectively calculated with Equation 8.1 and Equation 8.2.

$$||\vec{F}|| = \sqrt{\vec{F_x}^2 + \vec{F_z}^2} \tag{8.1}$$

$$\Theta_F = atan\left(\frac{F_z}{F_x}\right) \tag{8.2}$$

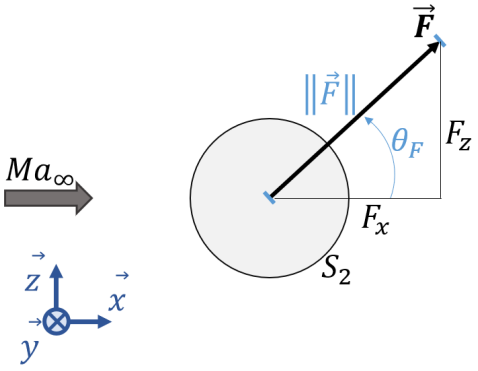

Figure 8.3: Scheme of S_2 total force, decomposition in norm and angle.

The norm and angle of the resultant force are respectively plotted in the left and right graphs of Figure 8.4. On the graphs, we superposed F_x to $||\vec{F}||$ and F_z to Θ_F. As can be seen, the trends of the curves of each graph are very similar. This might mean that the magnitude of the force is mainly due to the drag force, while the direction of the force is mostly dependent on the lift force. Moreover, results from Figure 8.2, let to think that the drag is mainly the result of pressure effects and the lift of the viscous effects. Both results should mean that the pressure is the main factor of the force magnitude and that the viscous effects are the

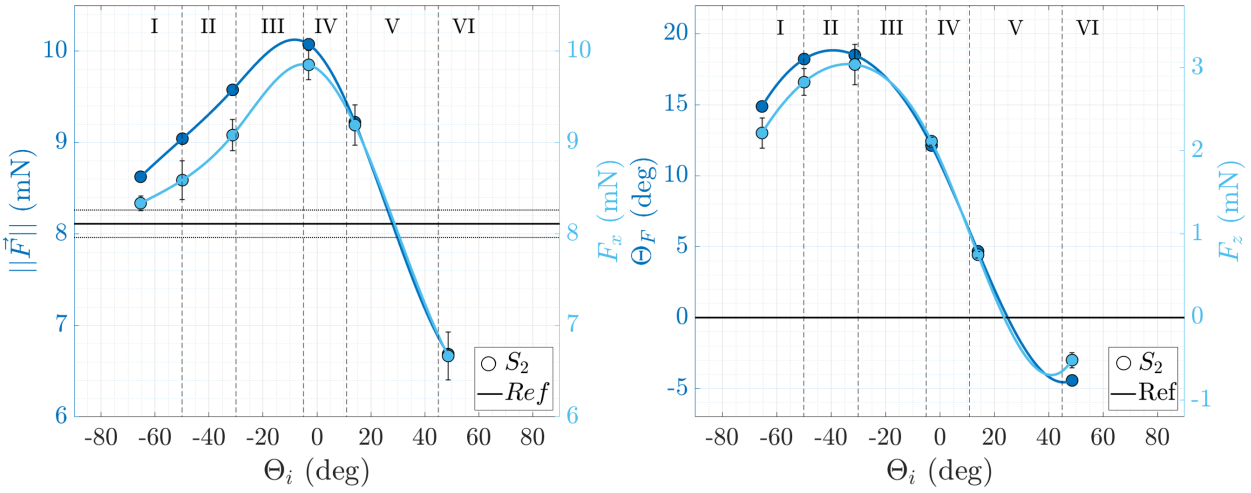

Figure 8.4: Value and angle of S_2 resultant aerodynamic force, C_1 in N1 flow-field.

leading factor for the change in direction. These remarks show the importance of considering the viscous effects characterising the rarefied flows. Thus, depending on the flight altitude, for a same initial position, it can be imagined that the trajectory of a following piece of debris would be subsequently different. This point will be further discussed chapter 9.
For now, the analysis will focus on the flow conditions of N1. According to the forces undergone by S_2 and S_1 (the reference value), the displacement of S_2 towards S_1 can be locally deduced as follows:

- if $F_{x_2} < F_{x_{ref}}$, S_2 approaches S_1 in the $\vec{x}$-direction ($\Leftarrow$)
- if $F_{x_2} > F_{x_{ref}}$, S_2 moves away from S_1 in the $\vec{x}$-direction ($\Rightarrow$)
- if $F_{z_2} < F_{z_{ref}}$, S_2 approaches S_1 in the $\vec{z}$-direction ($\Uparrow$)
- if $F_{z_2} > F_{z_{ref}}$, S_2 moves away from S_1 in the $\vec{z}$-direction ($\Downarrow$)

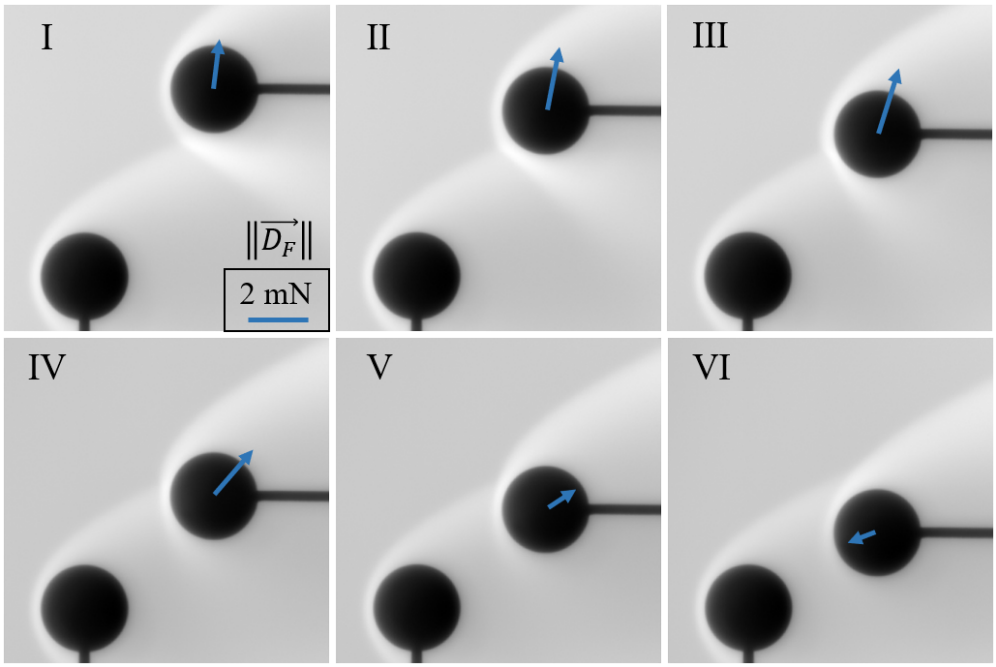

Figure 8.5: Displacement of S_2 towards S_1, C_1 in N1 flow-field.

The displacement $\vec{D_F}$ can be estimated as described in Equation 8.3. This vector is represented by the blue arrows in Figure 8.5 that shows the displacement of S_2 towards S_1.

$$\vec{D_F} = (\vec{F_{x_2}} - \vec{F_{x_{ref}}}) + (\vec{F_{z_2}} - \vec{F_{z_{ref}}}) \tag{8.3}$$

8.1.1.2 shock-wave surfing

In their publication, Marwege *et al.* [137] numerically studied the aerodynamics of two interacting spheres, and gave the necessary conditions for shock-wave surfing. These conditions are given in Equation 8.4 and Equation 8.5, where a_x and a_z are the relative acceleration of S_2 towards S_1 respectively in the $\vec{x}$ and in the $\vec{z}$ directions, and β is the angle of the incident shock.

$$\frac{\Delta a_z}{\Delta a_x} = tan(\beta), \text{ with } \Delta a_x > 0 \tag{8.4}$$

$$\frac{\partial(\Delta a_z/\Delta a_x)}{\partial Z_2} < 0 \tag{8.5}$$

The rare phenomenon of shock-wave surfing imposes these equations that can be described with the following criterion:

- the $\vec{x}$ component of the acceleration has to be positive: the $\vec{x}$ component of S_2 movement is positive;
- the total acceleration has to be tangential to the incident shock-wave: S_2 displaces according to the direction given by the incident shock-wave;
- a decrease in Z_2 must lead to an increase in $\Delta a_z/\Delta a_x$, which means that the repulsion angle, given earlier by Θ_F, has to increase.

These conditions are necessary but not sufficient. For a stable shock-wave surfing, it is necessary for the velocity vector of S_2 to be tangential to the incident shock-wave, as for the acceleration.
In our case, we consider the following flight conditions that both spheres are only submitted to their weight and to the aerodynamic forces (F_x and F_z). Thus for S_1 and S_2, we obtained the acceleration given in Equation 8.6.

$$\begin{cases} m.\vec{a_1} = m.\vec{g} + F_{x_1}.\vec{x} + F_{z_1}.\vec{z} \\ m.\vec{a_2} = m.\vec{g} + F_{x_2}.\vec{x} + F_{z_2}.\vec{z} \end{cases} \tag{8.6}$$

This leads to the relative acceleration $\vec{a}$ described in Equation 8.7.

$$\Delta\vec{a} = \vec{a_2} - \vec{a_1} = \frac{F_{x_2} - F_{x_1}}{m}.\vec{x} + \frac{F_{z_2} - F_{z_1}}{m}.\vec{z} \tag{8.7}$$

Thus, we obtain Δa_x and Δa_z the respective components of $\Delta\vec{a}$ in the $\vec{x}$ and $\vec{z}$ directions (Equation 8.8).

$$\begin{cases} \Delta a_x = \frac{F_{x_2} - F_{x_1}}{m} \\ \Delta a_z = \frac{F_{z_2}}{m} \end{cases} \tag{8.8}$$

Following the analysis of Marwege *et al.* [137] (left graph of Figure 8.6), the graph in the right summarises the results of Equation 8.4 and Equation 8.5, obtained with our results. In our case (right graph), for $\Delta a_x > 0$, the slope $\Delta a_z/\Delta a_x$ crosses $tan(\beta)$ once for $Z_2 \approx 19$ mm. Unfortunately, the slope is ascending which creates an unstable point of shock-wave surfing. But when plotting the interaction angle according to the altitude of S_2 (see Figure 8.7), we observe that $Z_2 \approx 19$ mm, corresponds to $\Theta_i \approx 22°$, which is approximately the angle where the drag, lift, and total forces and the total force angle cross their reference values. This agrees with the assumption that this point is a non-stable shock-wave surfing.

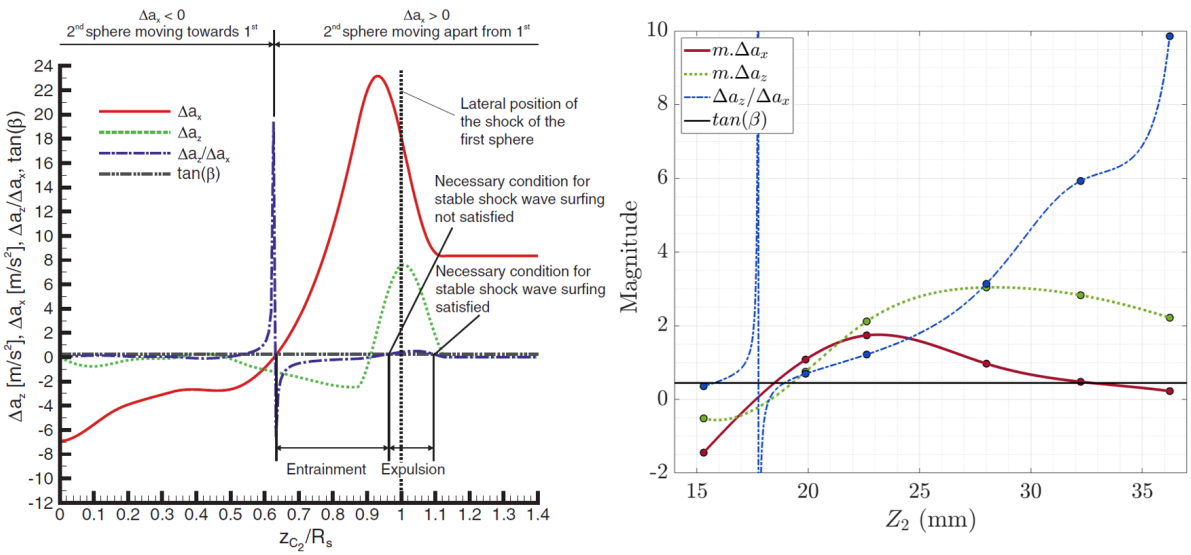

Figure 8.6: Shock-wave surfing detection method. On the left: Marwege *et al.* [137], on the right: C_1 in N1 flow-field.

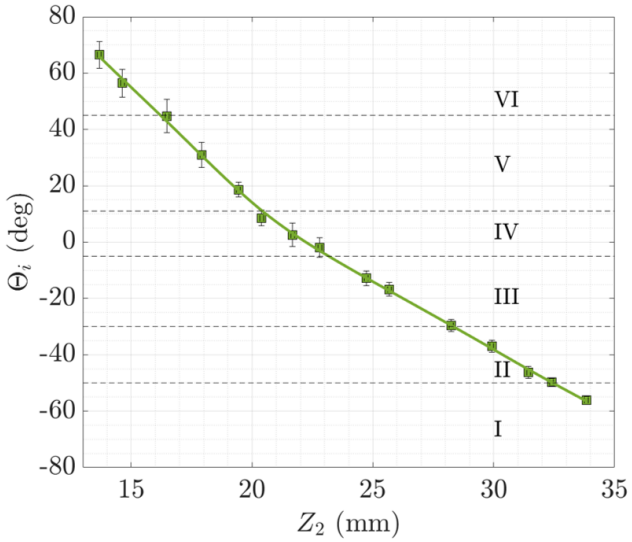

Figure 8.7: Interaction angle according the altitude of S_2.

8.1.1.3 Drag and lift coefficients

Generally, the parameters used to characterise the aerodynamics of an object are the drag and lift coefficients, which are scaled numbers that take into account the corresponding force, the surface of the object, and the free-stream flow conditions. The drag coefficient Cd was given with Equation 6.8. In the same way, the lift coefficient Cl can be calculated with Equation 8.9.

$$Cl = \frac{F_z}{\frac{1}{2}.\rho_\infty.U_\infty^2.S} = \frac{F_z}{\frac{1}{2}.\gamma.p_\infty.M_\infty^2.S} \tag{8.9}$$

In the case of an object flying in the free-stream flow, the upstream conditions (subscript ∞) are usually well known, as it was the case for single spheres (section 6.1). Unfortunately, in our conditions, S_2 is immersed in the flow-field of S_1. For experimental reasons, it is impossible to access all the parameters that could describe this flow-field. Thus, the upstream flow of S_2 is not known. Moreover, as S_2 is in interaction with S_1 shock-wave, the flow around its surface is not axisymmetric, which complicates once more the knowledge

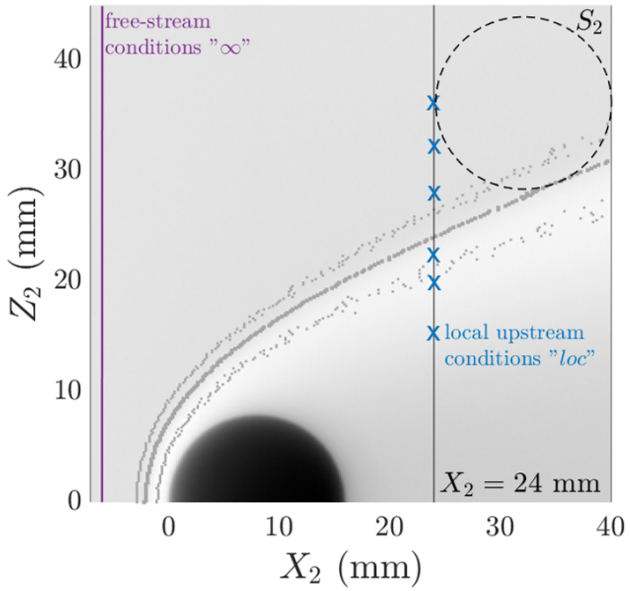

Figure 8.8: Location of the upstream conditions for the calculation of the global and local aerodynamic coefficients, C_1 in N1 flow-field.

of the surrounding flow. Thus, two methods will be used for the calculation of the drag and lift coefficients: the global and the local. Figure 8.8 will be used to ease the understanding of the reader.

From the literature, most works consider the values of the free-stream flow as the upstream values (purple conditions "∞" in Figure 8.8). To be more precise, it means that the coefficients are calculated with the free-stream conditions presented in Table 4.2. We will note these measurements as Cd_∞ and Cl_∞. However, this method does not take into account the local flow seen by S_2 which moves in the flow generated by S_1. Thus, it is questionable if this way to calculate the coefficients is effectively representative of the aerodynamics of S_2. Nevertheless, to compare with results from the literature, it will be the method used.

The second method used, allows calculating more local drag and lift coefficients (noted Cd_{loc} and Cl_{loc}). Since the results of the numerical simulations made with DS2V were in great agreement with the experimental ones, numerical results will be considered to describe the flow-field of S_1. Consequently, the local conditions seen by S_2, whatever its position towards S_1, are known. For the calculation of Cd_{loc} and Cl_{loc}, the upstream conditions used will be the one of DS2V simulation taken at the coordinates (X_2,Z_2) where were recorded the force measurements of S_2 (blue conditions "loc" in Figure 8.8). The density and flow speed flow-fields from DS2V are given in Figure 8.9. Obviously, due to the non-axisymmetry of the flow-fields seen by S_2,

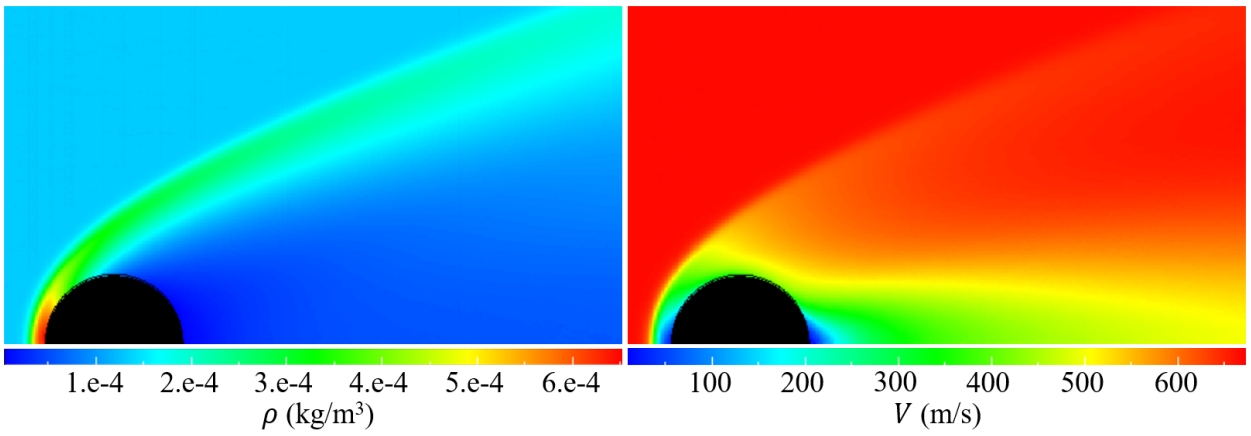

Figure 8.9: Density (left graph) and flow speed (right graph) flow-fields from DS2V for D16 in N1 flow-field.

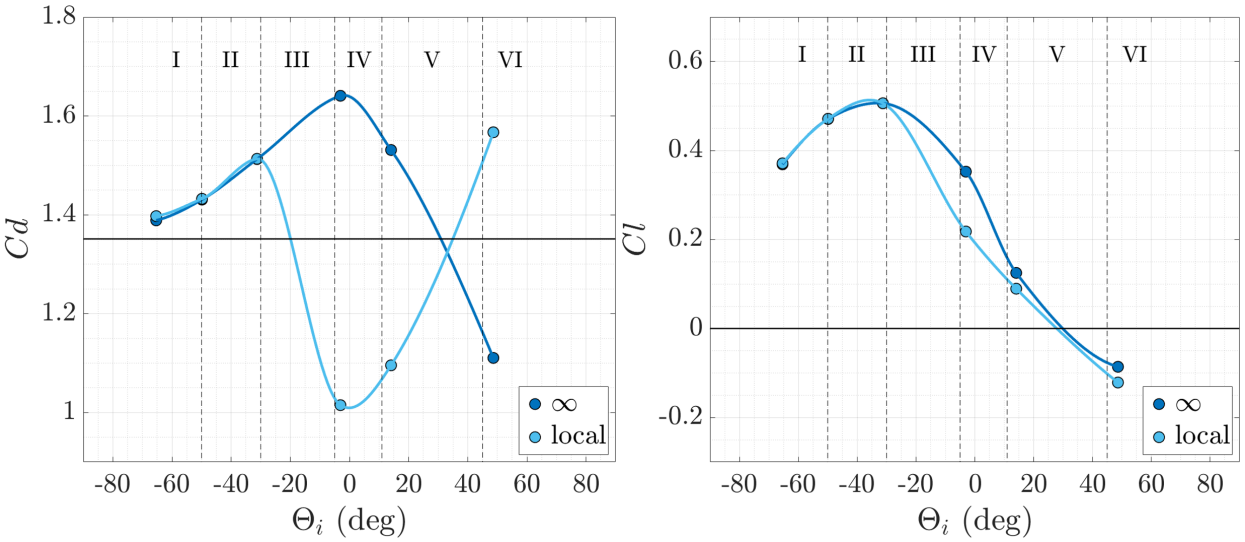

Figure 8.10: Drag (left graph) and lift (right graph) coefficients of S_2, C_1 in N1 flow-field.

this way of calculation is an approximation. However, it seems to be the only possible solution that takes into account the local flow variation, and thus gives consistent drag and lift coefficients.
The results of both the methods are given in Figure 8.10. For SSI types I and II, the aerodynamic coefficients for drag and lift remain unchanged whatever the flow parameters taken into account. Indeed, S_2 is located above the S_1 wake flow-field, so the flow parameters are those of the free stream. Then, for the other SSI types, the evolutions of the drag coefficients show opposite trends. When using the free-stream flow conditions, the drag coefficient varies with the measured drag force, since for any SSI, the flow-field parameter remains the same. But if accounting the local flow-field around S_1, flow parameters varies with the type of interaction. Density increases and reaches a maximum in the incident shock-wave, leading to the minimum value of local drag coefficient for the type IV SSI. Then for types V and VI, S_2 enters deeper in the wake of S_1, where the local density and flow speed decrease, yielding to the increase in the drag coefficient which is representative of the increase in viscous effects. As regards to the lift coefficient, the maximum value is reached for types II to III when S_2 is just over the S_1 shock where the pressure under the sphere push it up. The lift does not seem very impacted by the upstream flow taken into account, but no explanation can be given yet.

8.1.2 Wall pressure of S_2

In order to better understand the total aerodynamic forces, pressure measurements were realised at the wall of S_2. Indeed, the repartition of the wall pressure will help understand the contribution of the pressure on the behaviour of the following sphere.

8.1.2.1 Wall pressure distribution and analysis

The wall pressures were recorded along the vertical meridian plane of S_2, for angles between -90° and 90°, the step between two angles depending on the evolution of the pressure distribution. The measurements were realised for the six types of interferences. As the SSI types III, IV, and V are obtained for close altitudes, additional positions were investigated to better describe the transition between these three interferences. For each type of interference, results are presented on the graphs of Figure 8.11. The wall pressure values (p_w) are given according to the angle of the measurement point Θ_{wp} at the surface of the sphere, as described in Figure 5.17. The different shades of blue are representative of the results of SSI which are compared to the reference case in black, *i.e.* the wall pressure distribution of a single sphere in the free-stream flow.

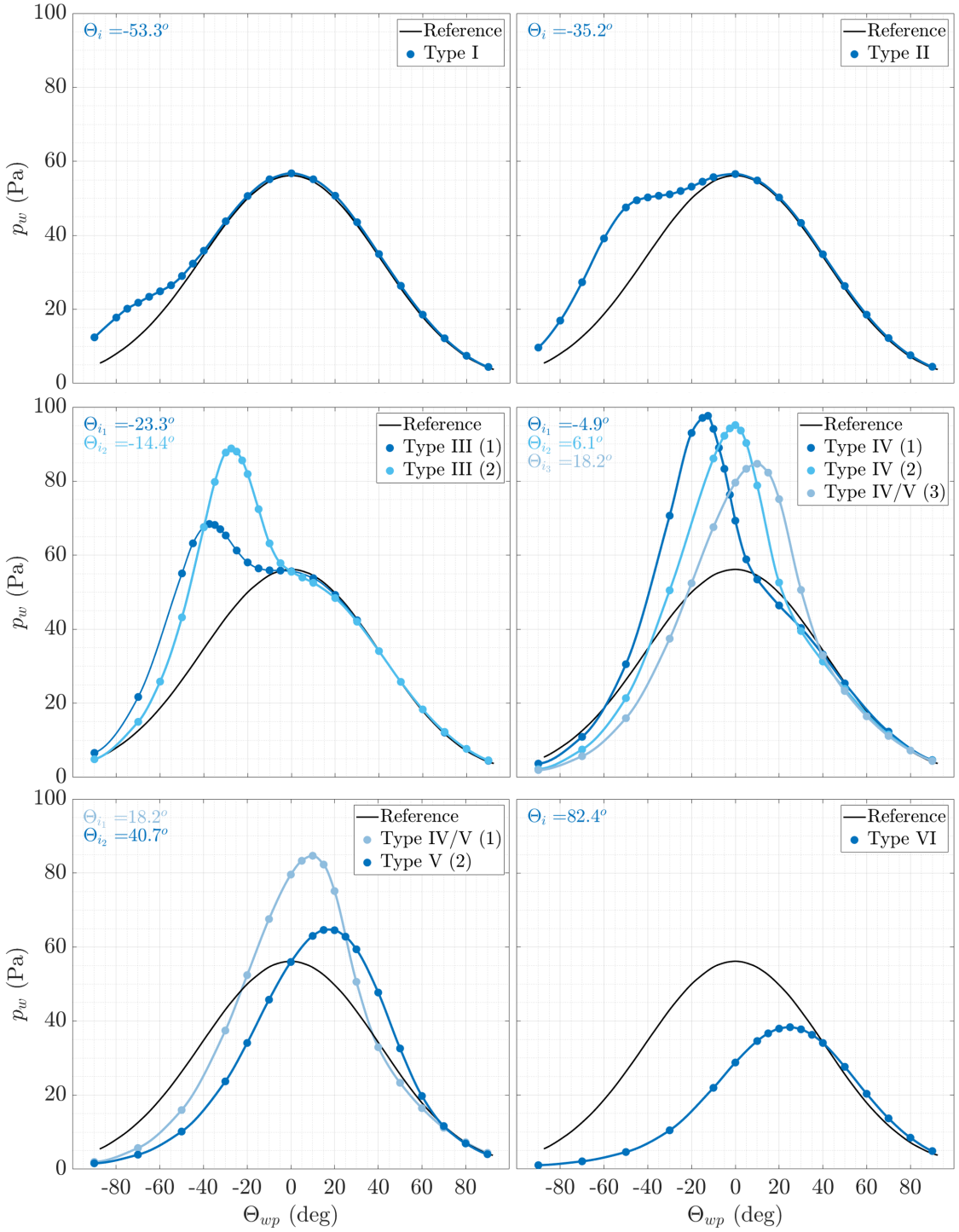

Figure 8.11: Wall pressure distribution on S_2, C_1 in N1 flow-field.

Observing the six graphs, the distribution of pressure reveals two different behaviours according to the types of SSI. For types I, II, and III, the wall pressure is only modified on the lower part of S_2 ($\Theta_{wp} < 0°$), while for SSI types IV, V and VI, the modification of the distribution is more global. Indeed, as shown for the first three SSI, the wall pressure increases with respect to the reference value, in the interference region. Above this modified region, the pressure distribution retrieves its original behaviour, which can be explained by the fact that the upper part of the sphere is globally in the free-stream flow. Thus, the wall pressure distribution is a Gaussian function with the maximum value corresponding to the stagnation point, and modified in the interaction area with another pressure peak due to the contribution of the S_1 shock. For type IV interference, when the interference coincides with the nose of the sphere, the distribution

function presents a single narrower peak, where is reached the maximum value. For SSI types V and VI, this single peak moves to the higher half of the sphere. Below the interference area, pressure values are lower than the reference case due to a less dense environment under the incident shock-wave. At the transition between type V and VI, the value of the pressure distribution peak decreases below the reference value. This behaviour is to be compared with that of the lift coefficient which passes under a value equal to 0 mN between these two types of interference. For type VI, the wall pressure is evidently lower than the reference case, which is explained by the lower density endured by S_2, when locate below the incident shock-wave.

To deepen the analysis of the wall pressure distribution, we focused on the evolution of the pressure peaks. For types III to VI, maximum wall pressure is evident, but for types I and II, a method had to be used since the peaks in the interference area are not real local maximum as presented on Figure 8.12. Mathematically, a local maximum is present when the derivative of a function is null. As observed, in the right graph, type II presents a local maximum for $\Theta_{wp} = -36.2°$. But on the left graph, for type I, the derivative never reaches 0 in the interference area, so no local maximum is found. Nevertheless, observing the minimum of the derivative in the interference area (for $\Theta_{wp} = -64.3°$), the localisation of the peak does not look incoherent.

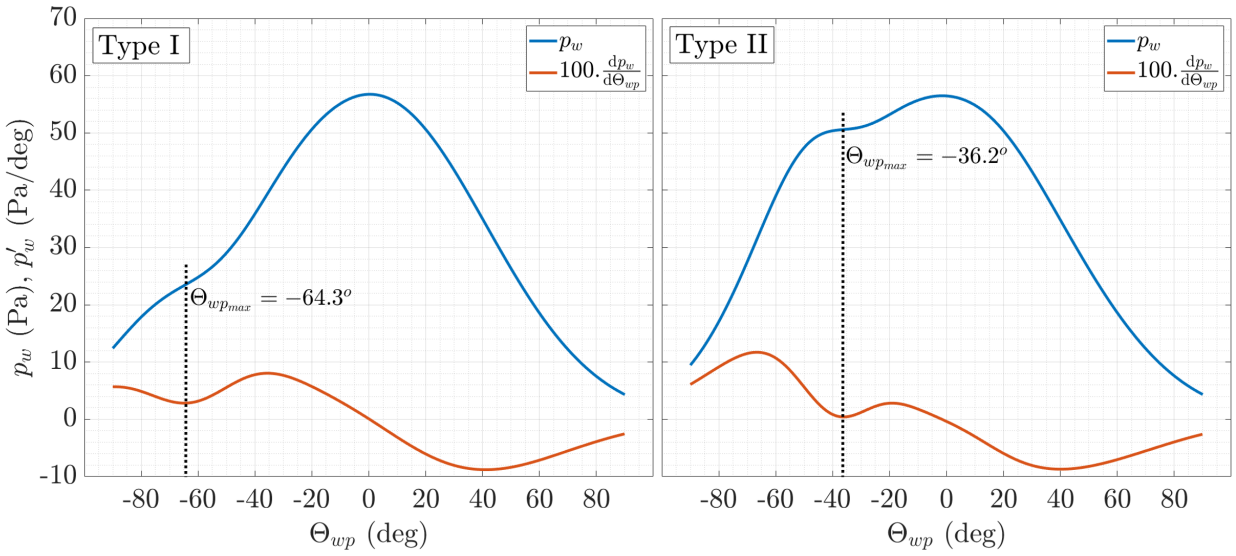

Figure 8.12: Determination of the local maximum wall pressure in the interference area ($\Theta_{wp_{max}}$ and $p_{w_{max}}$).

Thus, this method was applied to determine the values peak for the six types of interferences. The value and angle of maximal pressure in the interference area, $p_{w_{max}}$ and $\Theta_{wp_{max}}$, are plotted according to the angle of interaction Θ_i, respectively in the left and right graphs of Figure 8.13. The reference pressure peak is of 56.17 Pa at the stagnation point of S_1. As we look at the evolution of the pressure peak values, we observe a maximum of about 100 Pa for the type IV SSI. Thus the maximal increase in pressure peak is of about 80%. Moreover, this value is reached between SSI types II and III which coincides with the maximum lift value. The maximum pressure peak is reached for SSI type III/IV. It is to be reminded that, due to the thickness of the shock-waves, the angles given as a frontier are not clear delimitations, thus it is hard to exactly give the concerned type. Nevertheless, due to the shape of the pressure distribution of case IV (1) in Figure 8.11, we may think that the corresponding maximum which is located at the boundary III/IV ($\Theta_i = -4.9°$) in the left graph of Figure 8.13, corresponds to a type IV SSI. For lower S_2 locations, the value of the pressure peak decreases and passes again through the reference value between types V and VI for $\Theta_i \approx 40°$, which seems to coincide with the minimum value of the lift force plotted in Figure 8.4. However, since we did not measure forces for higher interaction angle, we need to be careful with this statement.
The right graph of Figure 8.13 indicates the localisation of the pressure peaks at the surface of S_2. As observed, between types I and II, $\Theta_{wp_{max}}$ increases almost with Θ_i. This means that the localisation of the

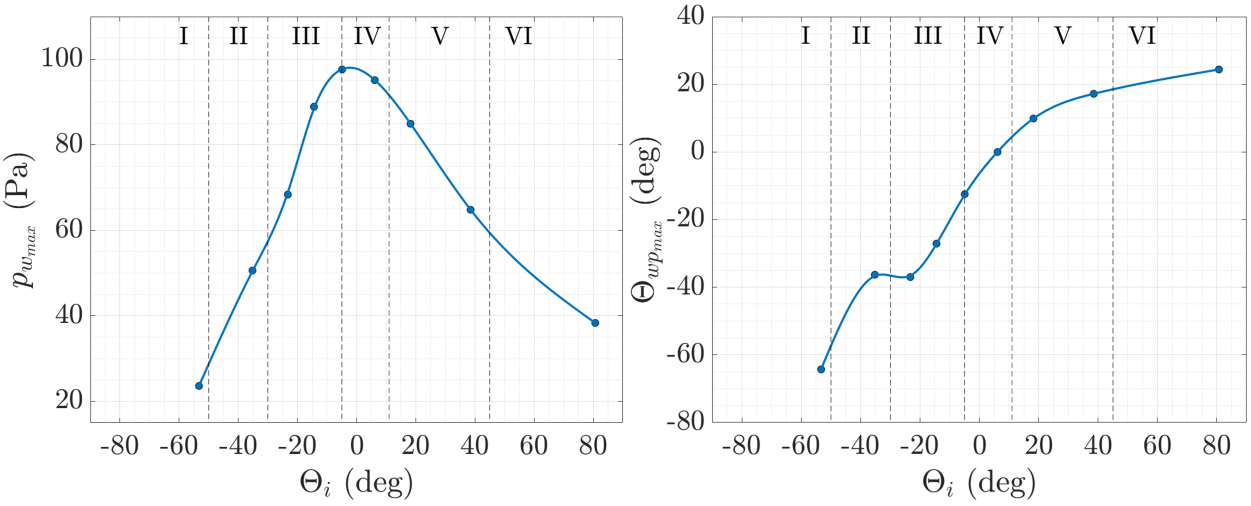

Figure 8.13: Value (left) and angle (right) of the maximal wall pressure peak on S_2 for C_1 in N1 flow-field.

point of maximum pressure corresponds approximately to the point of interaction between the two middles of shock in terms of angles. Then, between SSI types II and III, a plateau is observed. For these two types, the patterns described by Edney [65], but also obtained by Fisher [71], or in the present work (see Figure 7.12), showed that a shear layer coming from the intersection point (P_i) attaches the surface of S_2 below this point P_i, by going down. For the two considered points ($\Theta_i \approx -35°$ and $-23°$), we find similarities of behaviour with the continuum regime thanks to the determination of the angle of maximal pressure, even if, in the rarefied case, the pressure layer is less noticeable because less dense. Similarly, for type IV SSI, the supersonic jet, described by Edney, impinges slightly under the intersection point, but tends to equalise with it around 0°. Also, for SSI types V and VI, the increase in Θ_i is way larger than that in $\Theta_{wp_{max}}$. This might mean that the impact of the SSI is smoothed by the large viscosity observed in rarefied shocks.
The presence of high-pressure peaks indicates the strength of the SSI impact, while results of wall pressure reflect the distribution of the force of pressure. If pressure forces are mostly located under the nose of the sphere, it will indicate that the forces act for the sphere to be pushed up; inversely, if they are mostly located above $\Theta_{wp} = 0°$, the sphere will be pushed down. This effect can be studied from the area under pressure curve ($AUPC$) for each one presented in Figure 8.11. An example is given in the left graph of Figure 8.14

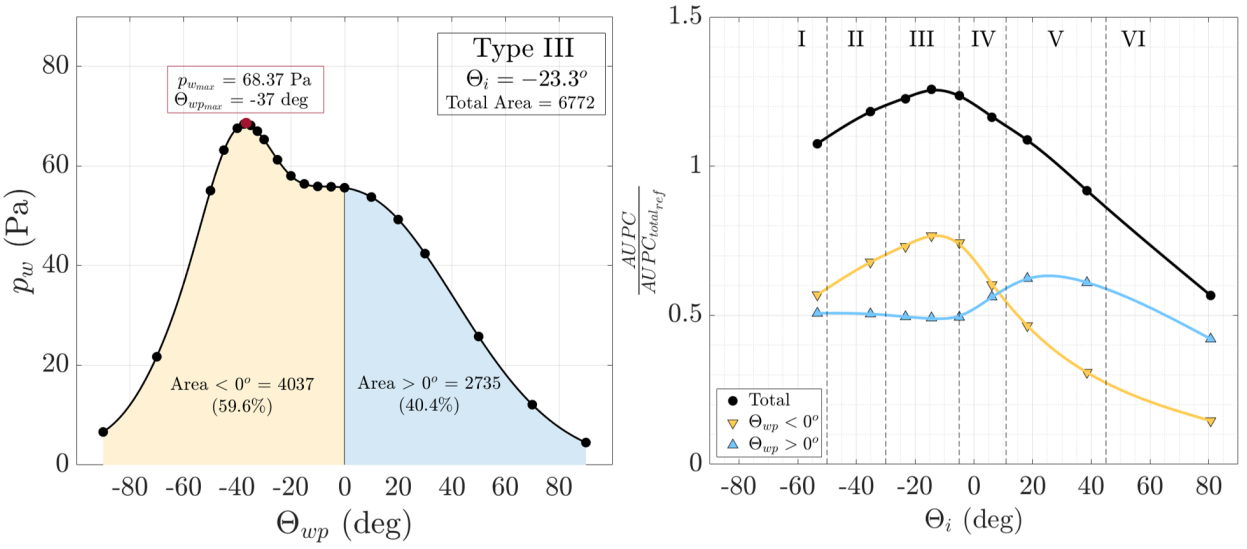

Figure 8.14: Area under wall pressure distribution curves: determination (left); Normalized AUPC for C_1 in N1 flow-field.

with one of the type III curves. The total area is the sum of the areas under ($\Theta_{wp} < 0°$) and above ($\Theta_{wp} > 0°$) the nose of the sphere. The right graph presents the results of the total area, decomposed with negative and positive angles. The three curves are normalised with the total area of the reference case ($AUPC_{total_{ref}}$).
First of all, the total area increases from type I to III, where it reaches a maximum. This means that the pressure contribution will be maximal for the type III SSI. Then, it decreases almost linearly, crossing the reference value for $\Theta_i \approx 30°$, corresponding approximately to the non-stable shock-wave surfing point, discussed earlier with the results of the aerodynamic forces acquired with the balance. From SSI type I to almost V, it can be seen that it is the inferior part of the sphere that suffers most of the wall pressure. This means that, for the corresponding angles, the pressure forces push the sphere up. Then for type V and VI, the sphere is pushed down, but, as the values are lower than for type II to IV, it can be imagined that the pressure forces are less impacting when the sphere is mostly located under the incident shock-wave. Indeed, for SSI types V and VI, both the incident shock and the bow shock of S_2 follow a close direction. Thus the interaction between the two shock-waves do not create a strong impact. Moreover, as the shock-waves are thick due to the rarefaction level of the medium, the viscosity of the flow might further reduce the pressure effects on the lift of the sphere.

8.1.2.2 Pressure contribution on drag and lift coefficients

To better understand the impact of the pressure in the aerodynamic behaviour, as for a single sphere, Cd_p, the drag coefficient due to the pressure, can be calculated as described in section 6.2.2. The drag coefficient being composed with pressure and friction contributions, these last is the calculated as the complementary of Cd_p (see Equation 6.12). The calculations have been made for the free-stream conditions (subscript ∞) and the upstream conditions directly at the coordinates of S_2 (subscript loc), as explained in section 8.1.1. The results are exposed in the graphs of Figure 8.15.
As can be observed, for both methods, the pressure contribution is preponderant over the friction, and reaches a maximum for the type III SSI as previously observed with the $AUPC$ (Figure 8.14). The type III SSI also corresponds to the minimal friction contribution.
For the calculation with free-stream conditions (left graph), the total drag is maximal for the type IV SSI, while the pressure contribution already starts to decrease. Indeed, between types III and IV, the contribution of friction suddenly increases, which compensates for the lack of pressure contributions. We remind that, for the type IV SSI, S_2 is fully immersed in the thick incident shock-wave. Thus, even if the pressure reaches higher peaks for the type IV SSI, the viscosity of the flow must reduce the impact of the pressure in the SSI

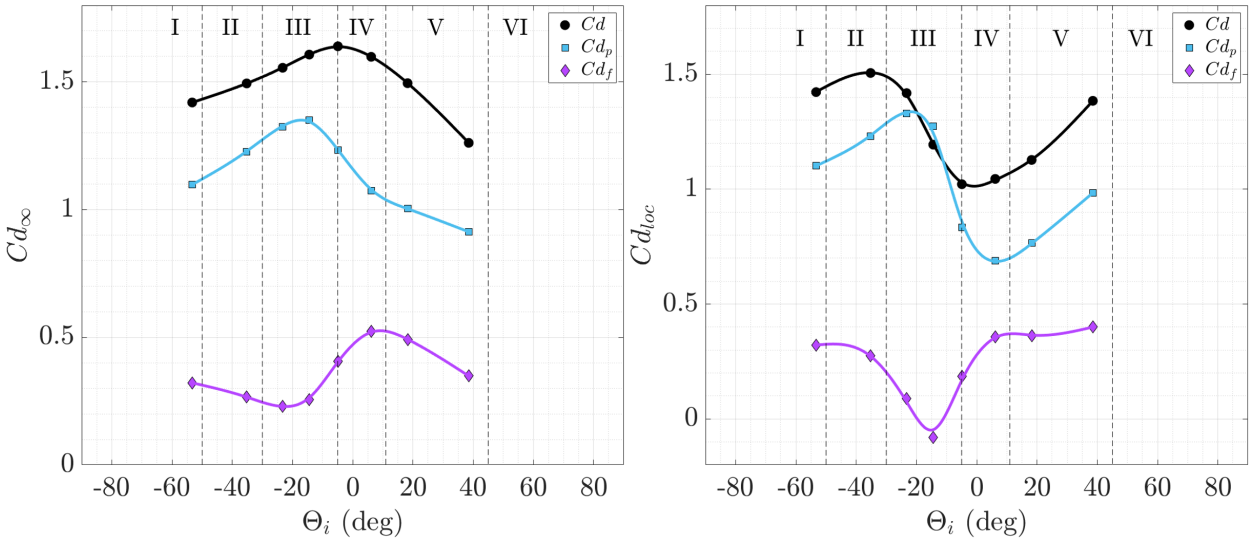

Figure 8.15: Contribution of the pressure and friction effects in the total drag coefficient, C_1 in N1 flow-field.

phenomenon.
If observing the right graph, it can be seen that Cd_f only decreases around the type III SSI, otherwise, it stays on a same level of contribution. For the type III at $\Theta_i = -14.4$, we observe that the pressure contribution is higher than the drag, leading to a negative contribution of friction. This difference possibly comes from the fact that we use the DS2V numerical results in the flow-field of S_1 to calculate the drags. Indeed, it does not seem coherent to find a negative drag force due to the viscosity in these specific conditions. If we consider a null friction drag at this position, the error is of about 7%, which does not call the rest of the results into question.

On the same manner as realised for the calculation of the pressure force according to the $\vec{x}$-direction (section 6.2.2), the pressure force can be calculated according to the $\vec{z}$-direction so that the pressure and friction contributions can be evaluated on the lift coefficient. The pressure force in the $\vec{z}$-direction is given by Equation 8.10, and developed in Equation 8.11.

$$Fp_z = \int_S (p(\Theta) - p_\infty) \, .sin(\Theta) \, \mathrm{d}S \tag{8.10}$$

$$Fp_z = \pi . R^2 \left[- \int_0^{\pi} (p(\Theta) - p_\infty) \, .sin^2(\Theta) \, \mathrm{d}\Theta + \int_{-\pi}^{0} (p(\Theta) - p_\infty) \, .sin^2(\Theta) \, \mathrm{d}\Theta \right] \tag{8.11}$$

The lift coefficient due to pressure can be calculated with Equation 8.9, replacing F_z by Fp_z. As for the drag coefficient, the lift one is calculated for both the free-stream conditions and the local conditions. The contribution of friction on the lift is the complementary of the pressure. Results are shown in Figure 8.16. For the two s to calculate the lift coefficients, the tendencies are the same. The pressure contribution is preponderant over the friction for SSI types I to III, *i.e.* when S_2 is in the higher position, and globally above the incident shock-wave. Then, as S_2 goes lower behind S_1, passing the incident shock and entering the wake of S_1, the viscous effects increase. As can be seen, $Cl_p = 0$ for $\Theta_i = 0$, where the pressure on the top of S_2 equals that of its bottom. At this position, the lift force is still positive, and this is due to the high viscosity of the rarefied shock-waves. For Θ_i up to 30°, the lift value remains positive, only thanks to the contribution of friction, as it was presupposed earlier in this work. Figure 8.16 is of great interest, since it highlights the importance of the viscous effects on the total lift force of a secondary sphere. From this result, we can imagine that, in the continuum regime, the behaviour of the lift force will follow that of the pressure force, thus increasing the negative lift area. Barri [21] showed lift coefficients that were of higher amplitude in the negative values that in the positive ones, which could be true in our conditions if the friction contribution

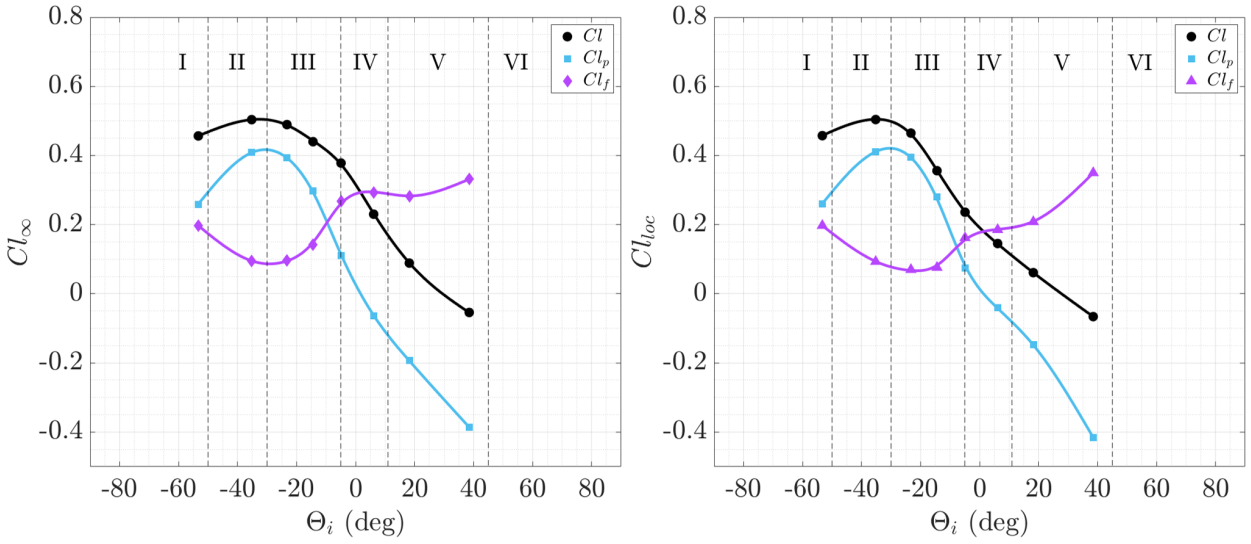

Figure 8.16: Contribution of the pressure and friction effects in the total lift coefficient, C_1 in N1 flow-field.

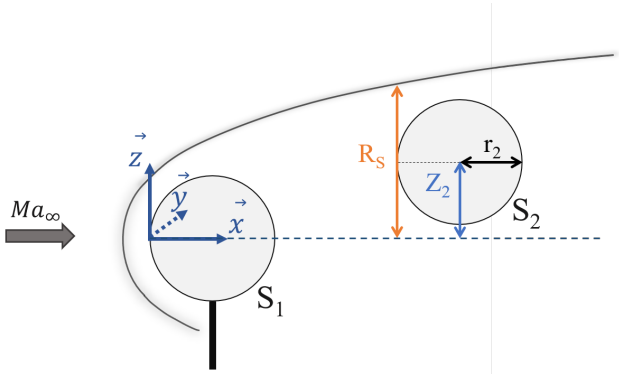

Figure 8.17: Definition of the shock radius R_s.

was null. For sphere size of $1/2.\emptyset_1$, and higher Mach numbers (10 and 50), Laurence *et al.* [116], with their three-dimensional calculation (Figure 10, a) showed that the lift of S_2 was negative when $Z_2/Rs < 0.87$, with R_s defined in Figure 8.17 as the altitude of the shock-wave, or middle shock-wave for rarefied flows. In our case, where $\emptyset_1 = \emptyset_2$, the lift force becomes negative for $Z_2/Rs < 0.78$, *i.e.* for lower position of S_2 than in the case of Laurence *et al.* This difference could be due to the size of the sphere, but in a continuum flows it seems that a decrease in $\emptyset_2$ leads to a decrease in Z_2/Rs, which does not match with our finding. The other possibility is the great difference in terms of velocities compared to the present work. Nonetheless, their results for Mach 10 and 50 show close values. The last option that could explain the difference is the level of rarefaction. On this point, we now know that the viscous effects play a role on the lift of S_2 in rarefied flows. The results of Laurence *et al.* being in the continuum regime, the observation made between the two results presented above could be explained by an increase of the viscous effects in our case. It is thus important to stay careful about this statement due to the large number of parameters that diverge.

8.1.3 Comparison with the numerical results

Since numerical simulations were realised with DS3V for each type of SSI, it was interesting to compare the numerical results with our experimental ones. We will limit the comparison to the quantitative values. In Figure 8.18 are presented the wall pressure distribution of the six types of SSI. As observed with the pink "o", the simulations give a great dispersion of the results. For the types I and II, no specificity is truly observed in the interaction area, but it might be due to the great dispersion of the results. Nevertheless, the Gaussian fitting allows observing a semblance of tendencies for the type III SSI, the most extreme wall pressure distribution in terms of shape. For types IV to VI, the pressure peak values and locations are comparable with the experiments.

In terms of aerodynamics, the drag and lift forces are directly calculated by DS3V. The coefficients are calculated with the free-stream values, and are plotted according to the altitude of S_2 in Figure 8.19. Between the experiments and the simulations, the total drag coefficients Cd show a same tendency, with a maximum when the nose of S_2 crosses the middle shock of S_1. However, the numerical results give values that are lower than the experimental ones for $Z_2 > 22$ mm, *i.e.* for SSI types I to IV. The main difference between numerical and experimental results concerns the pressure and friction contributions. The simulation gives a pressure drag Cd_p which varies with the Cd, but the friction drag Cd_f remains almost constant whatever the SSI; while, as S_2 moves down in the incident shock-wave, for $27 > Z_2 > 22$ mm, the experimental results show an increase in the friction contribution, reducing the pressure contribution. This comparison lets to think that the numerical simulations do not properly take into consideration the viscosity at the surface of the sphere.

Concerning the lift coefficients, results of the total lift force show a similar behaviour than for the drag, but with measured values up to twice the numerical ones. The simulation results shows that the friction

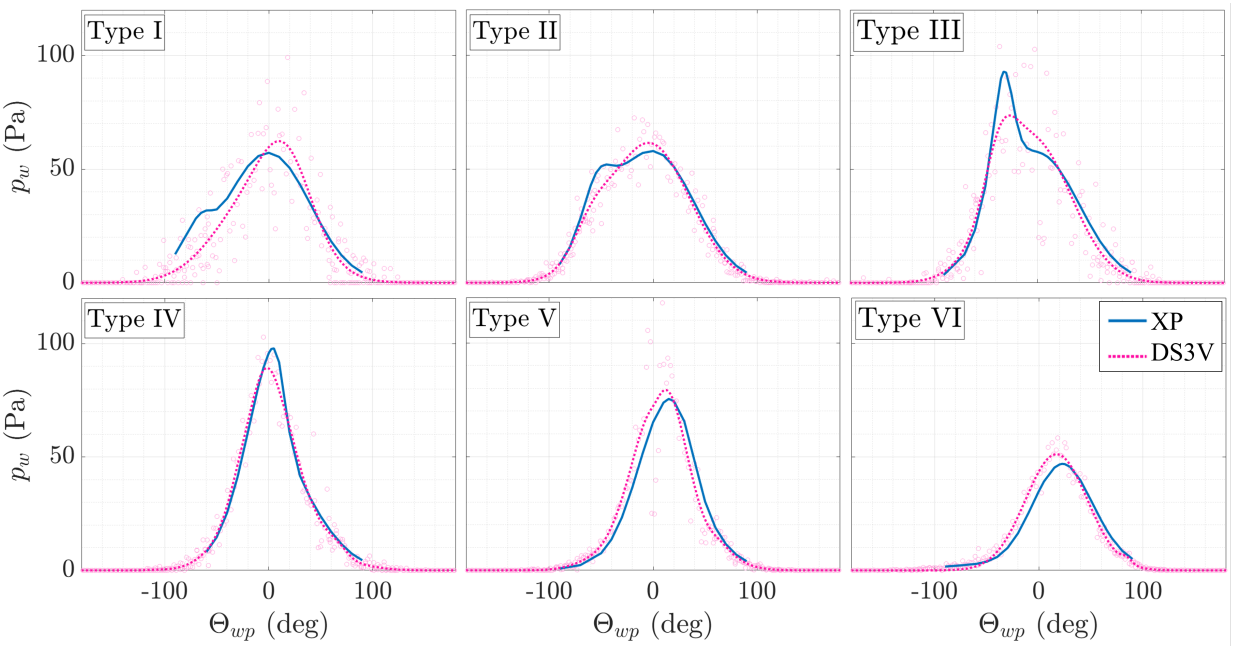

Figure 8.18: Wall pressure distribution from experiments and DS3V simulations.

contribution is almost inexistent. Nevertheless, the previous analysis of the experimental lift coefficients showed that the viscous effects are the key to a positive lift on a wider area, even when S_2 is mostly located below the incident shock-wave.

Numerical results are not completely different from the experiments. But it seems that the viscosity is not well described by the simulations. This is certainly due to the accommodation coefficients that might not be as good as desired, even though the flow-fields, experimental and numerical, of S_1 seem in great agreement. Indeed these coefficients describe the slip conditions in the boundary layer of the sphere; thus their definition is of great importance in the numerical simulations.

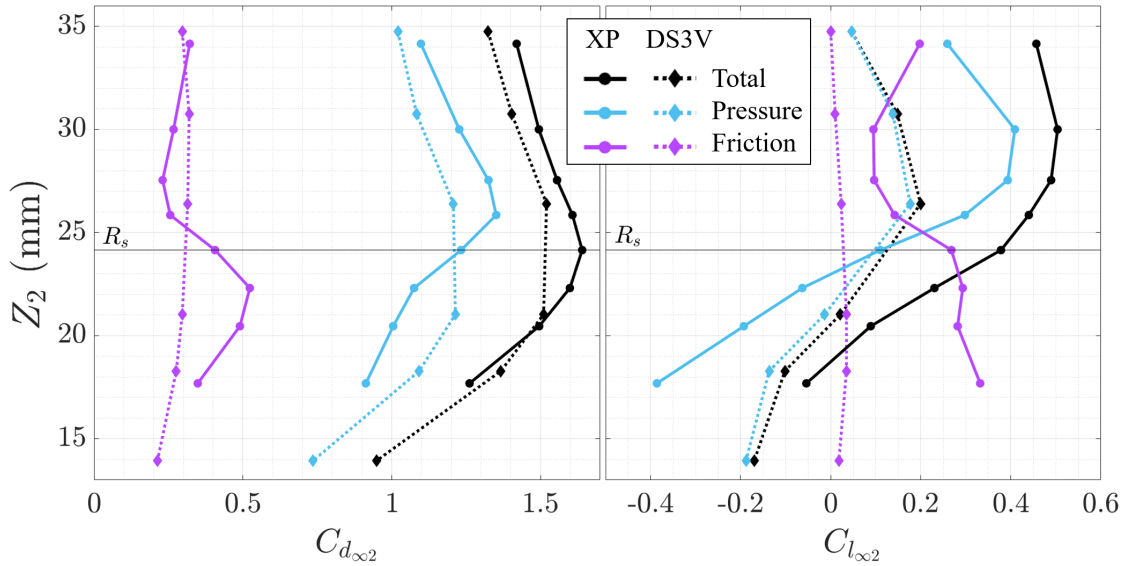

Figure 8.19: Drag (left) and lift (right) coefficients from experimental data and DS3V simulations.

8.2 Complete mapping of drag forces with the swinging experiment

The swinging sphere experiment will enable to complete the drag force results by obtaining the values on a complete mapping. The aerodynamic balance allows obtaining the drag and lift forces, but only for one position at a time. The strength of the swinging method is that S_2 can be moved continuously in the wake of S_2. By that time, an entire mapping of the drag force can be obtained. This mapping is realised step by step, by displacing the support of S_2 either up in the $\vec{z}$-direction, or longitudinally in the $\vec{x}$-direction.
First, as we did for a single sphere, the swinging sphere experiment has to be validated for S_2, *i.e.* when the upstream flow seen by S_2 is not the free stream, but a variable flow-field. This step will be realised on one vertical movement of S_2 support, allowing in the same time to analyse the behaviour of the sphere trajectory. Once the technique is validated, the entire set of results will allow us to build a two-dimensional mapping of the drag force suffered by S_2 on a large range of positions.

8.2.1 Vertical movement of S_2 support

8.2.1.1 Swinging sphere behaviour

One trajectory was chosen to be studied in detail in order to validate the method. S_2 was initially positioned right behind S_1, with the coordinates ($X_2 = 16$ mm; $Z_2 = 0$ mm), corresponding to image n°1. As the support of S_2 is moved up in the $\vec{z}$-direction, S_2 is angularly displaced in response to the incident flow in which it is located. This trajectory is called the swinging experiment "$X_2 = 16$ mm". For each image, S_2 coordinates are determined, and the corresponding coordinates are plotted in Figure 8.20. To ease the plotting of forces, as this is a 2D problem, we will refer to the image n°, 1 corresponding to the initial position and 3000 to its final position (the highest).
Figure 8.21 shows the two spheres at their initial position, and the trajectory described by the sphere S_2 is indicated by the blue points. The black line is representative of the mean trajectory. As can be observed, the movement of S_2 can be decomposed in three main behaviours:
① S_2 nose is located below the incident shock-wave. As Z_2 increases, S_2 is pushed away from S_1, reaching a maximal longitudinal distance for image n°1761, when S_2 nose is just under the middle of incident shock.
② From image n°1761 to 2341, X_2 decreases as S_2 nose crosses the middle shock, and slowly gets out from the incident shock. Its surface is less and less in contact with the thick incident shock and eventually, S_2

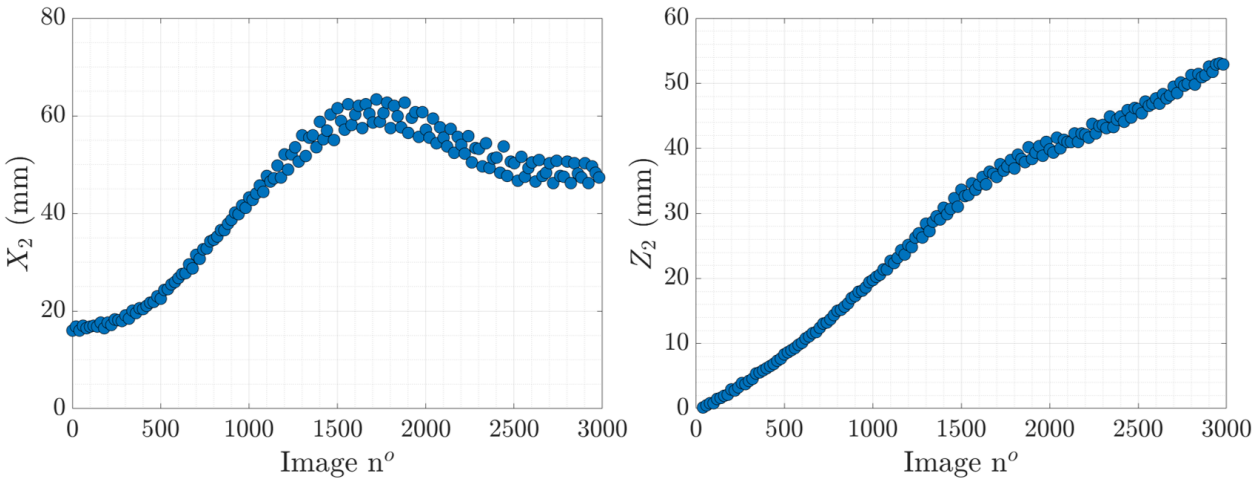

Figure 8.20: Coordinates described by S_2 during the swinging experiment "$X_2 = 16$ mm", for C_1 in N1 flow-field.

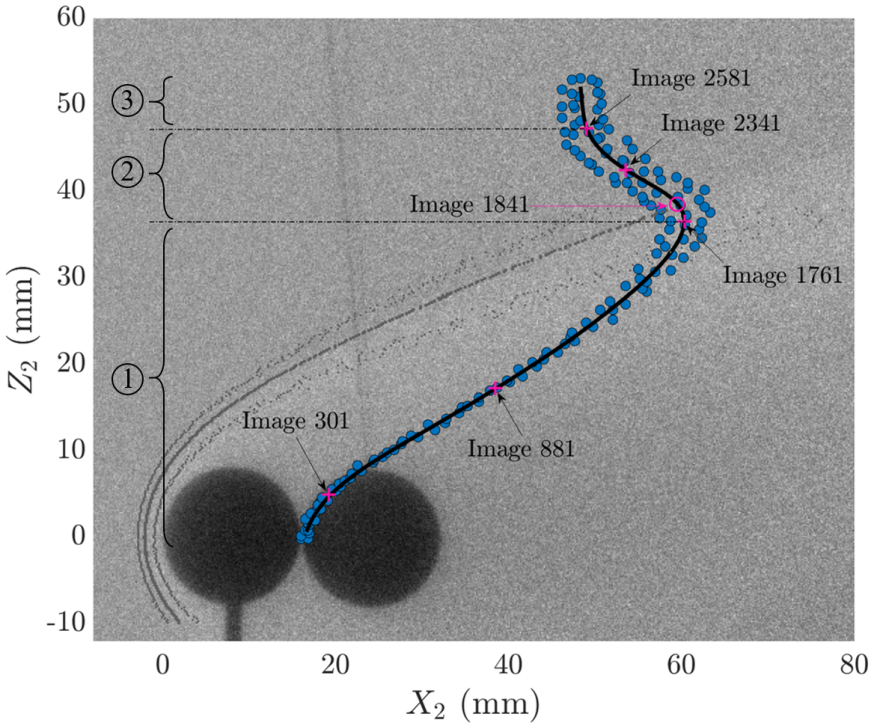

Figure 8.21: Trajectory described by S_2 during the swinging experiment "X_2 = 16 mm", for C_1 in N1 flow-field.

stops being pushed away.
③ Above image n°2341, S_2 does not seem to be much impacted by S_1 shock-wave, since its longitudinal distance stops varying. There, S_2 is located in the free-stream flow.
The pink crosses noted correspond to inflection points of the mean trajectory. One additional point has been added, corresponding to the intersection with S_1 middle shock. These positions will be adopted to record additional, images with the flow-field visualisation technique, in order to analyse the evolution of the forces, later in this section.
Just by analysing the trajectory, it was desired to look for a hysteresis phenomenon that was confirmed by

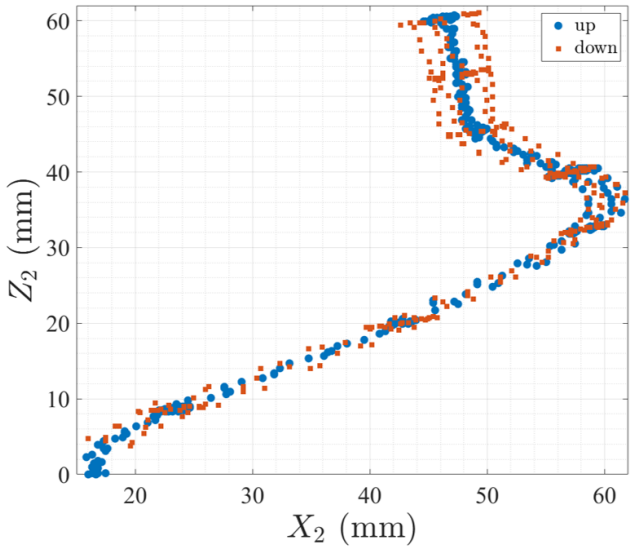

Figure 8.22: Trajectory described by S_2 during the swinging experiment "X_2 = 16 mm" for robot displacement up and down, for C_1 in N1 flow-field.

experimental studies from the literature [24, 47]. Indeed, the study of SSI has shown a different evolution of the interaction phenomenon if the secondary object goes up or down in the flow-field of primary one. In this work, with the flow-field visualisation, we did not observe any variation of the SSI if S_2 goes up or down behind S_1, but we assumed it could be due to the visualisation that is not as accurate as the methods employed in the continuum regime. It came to us that, if a hysteresis effect were present, the displacement of the swinging sphere would be different if its support is moved up or down. For the trajectory presented in Figure 8.21, the two directions were tested. The trajectories of the way up and of the way down are plotted in Figure 8.22. As can be seen, the mean trajectories are superposed. The only difference concerns the amplitude of S_2 oscillations: the way down shows a greater deviation in the higher locations. This variation of amplitude is probably due to the fact that S_2 is constraint by the wires, and at the same time it is going down on the incident shock-wave that pushes it away. It can be thought that the movement up is physically more natural. Anyway, we cannot attribute it to a hysteresis phenomenon due to a different interference pattern. Obviously, with this observation, every analysed movement will be made in the positive vertical direction.

8.2.1.2 Validation of the swinging method on S_2

The swinging method was first validated in section 6.3.2 with the measurement of a single sphere, suspended in the free-stream flow. The results were compared to the literature, and well agreed. However, this method has not yet been validated for the measurement of the forces experienced by S_2. Indeed, since S_2 is immersed in S_1 flow-field, multiple parameter can intervene. First, S_2 is confronted to drag, but also to lift forces. The wire being non-elastic, it behaves as a rigid stem, so no movement in the $\vec{z}$-direction should occur, but in doubt, an analysis will be realised. Firstly, the wire could suffer a less rarefied flow and, since the initial hypothesis neglect this force, it could introduce an error in the calculation of F_x. Finally, the variation in S_2 location slightly changes the free-stream flow conditions, which will modify S_1 flow-field and thus the forces acting on S_2.
To remove any doubt on the calculation method concerning the lift forces, an equivalent study on the total force $||\vec{F}||$ (defined in Equation 8.1) is proposed. F_x and F_z components, obtained with Equation 5.6, are squared and compared to $||\vec{F}||^2$. Figure 8.23 plots the Fz component and shows that the maximum value is

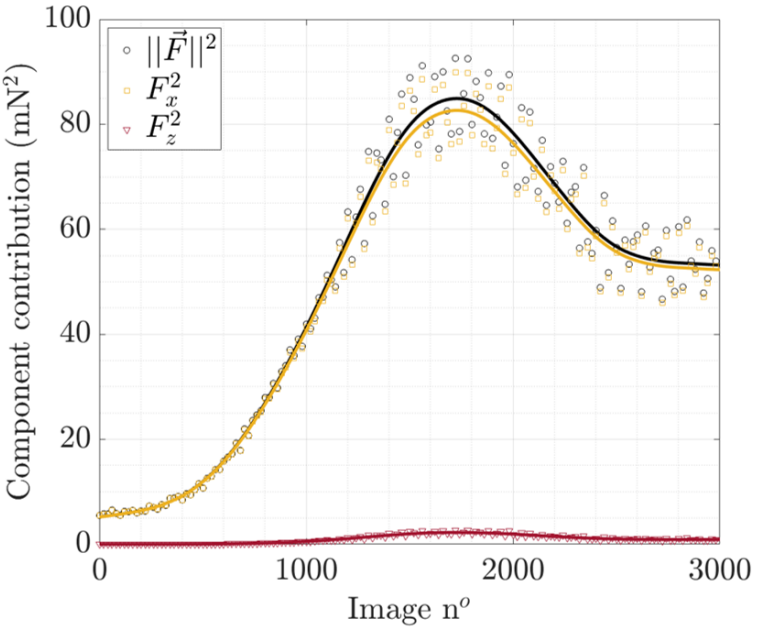

Figure 8.23: S_2 total force decomposition for the swinging measurement.

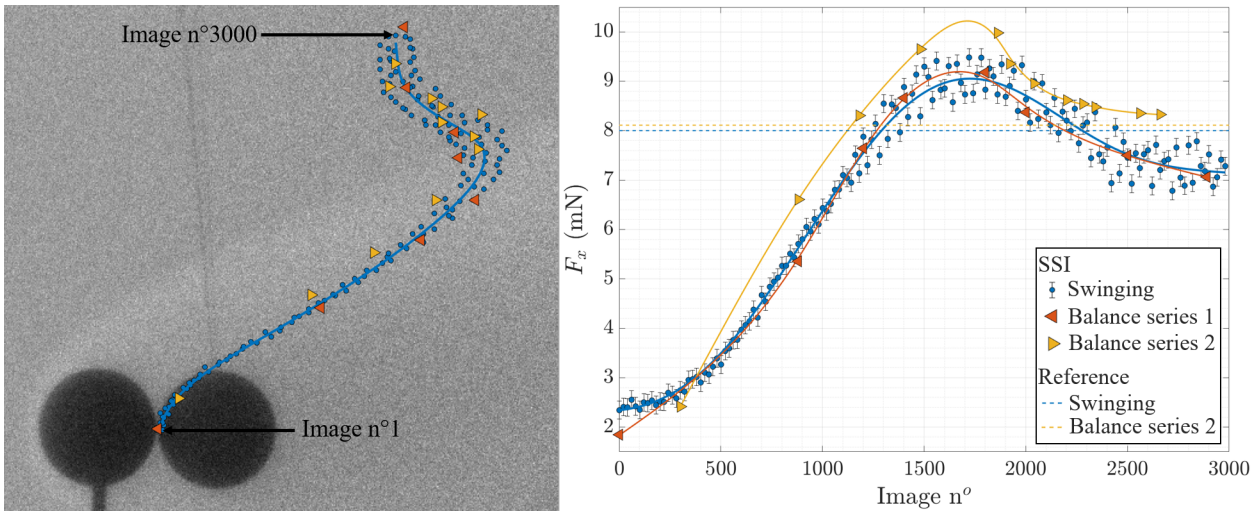

Figure 8.24: Left: swinging trajectory of S_2 and point of drag measurement with the balance. Right: Drag force according S_2 position for C_1 in N1 flow-field.

reached for image n°1731. This means that the maximum contribution for Fz is of 2.65%. As for the single sphere, the X component is largely dominant and thus F_x will be taken as the drag force of the swinging sphere.

With this statement, a comparison of the drag forces obtained with the swinging method and the aerodynamic balance is made on the trajectory presented in Figure 8.21. This comparison will enable to verify that the drag of the wires can still be neglected, even when it crosses S_1 shock-wave. It will also show the importance of the free-stream conditions.

To validate the measurement of the drag forces obtained with the swinging method, additional measurements were realised with the aerodynamic balance. The adopted positions are shown in the left image of Figure 8.24 with the orange and yellow points. The two colours correspond to two different protocols.

Before detailing the protocols, however, it is first necessary to explain how, experimentally, the flow conditions can be affected by the presence of objects in the flow core. As already mentioned, the free-stream flow in the isotropic core depends on the stagnation pressure p_0 and on the free-stream pressure p_∞. The pressure p_0 is adjusted at the beginning of the experiment and remains constant without being affected by the presence of objects in the flow. The pressure p_∞ of the free jet, on the other hand, depends on the obstruction of the core of the flow and can be adjusted with the butterfly valve that separates the test chamber and the pumping unit. Consequently, for a system with two objects, when one is moved in the flow, the free-stream pressure may vary slightly because the obstruction of the core flow is modified. For this particular swinging sphere experiment, images were acquired while the sphere S_2 was in motion, which implies that the pressure p_∞ changed slightly between the starting position, S_2 behind the sphere S_1, and the final position, "Image n°3000". In the case presented here, the free flow pressure was regulated with both spheres in the initial position, as shown in the left image of Figure 8.24. This can produce a small uncertainty in the measurement of the force with this method.

To evaluate the influence of the pressure p_∞ on the measurement of aerodynamic forces, it was decided to adopt two protocols for the measurement of drag forces with the aerodynamic balance. They differ in the way the free flow pressure was set: for measurements of Series 1, the free flow pressure p_∞ was adjusted at the beginning of the experiment when the two spheres are in their initial position ("Image n°1), then p_∞ evolved freely according to the position of S_2. The experimental conditions of this first series are equivalent to those of the swinging method. A second series of measurements was made but, this time, for each position of the sphere S_2, p_∞ was adjusted and set at the nominal value (see Table 4.2).

The three sets of drag forces measured, on the one hand, with the swinging method, and, on the other hand, with the aerodynamic balance for Series 1 and 2, are plotted on the graph on the right of Figure 8.24.

As can be seen, the trend of the three curves is the same. Series 2 shows greater values than the other

two, which are in good agreement with each other. Both protocols show the importance of the variation in free-stream pressure. An interesting point to note is at the end of the trajectory of the sphere S_2, for image numbers above 2500. In this graph, the two dashed lines give the value of the drag force of a single sphere measured with the swinging sphere experiment (blue) and with the aerodynamic balance (yellow). From image n°2500 and beyond, S_2 is not in direct interaction with the shock-wave of S_1: the two shock-waves still interact but the incident shock does not impact the surface of S_2. Thus, the aerodynamics of S_2 is almost that of a single sphere in the free-stream flow. Besides, regarding Series 2, it can be observed that the curve tends to reach an asymptote with the value of a single sphere, which is not the case for the other measurements, where values are lower.

In order to deepen the analysis of the impact of free-stream parameters on the measurement of drag forces, stagnation pressure (p_0), free-stream pressure (p_∞), and free-stream Mach number (Ma_∞) are plotted for the two aerodynamic balance Series measurements in Figure 8.25. The free-stream Mach number is calculated

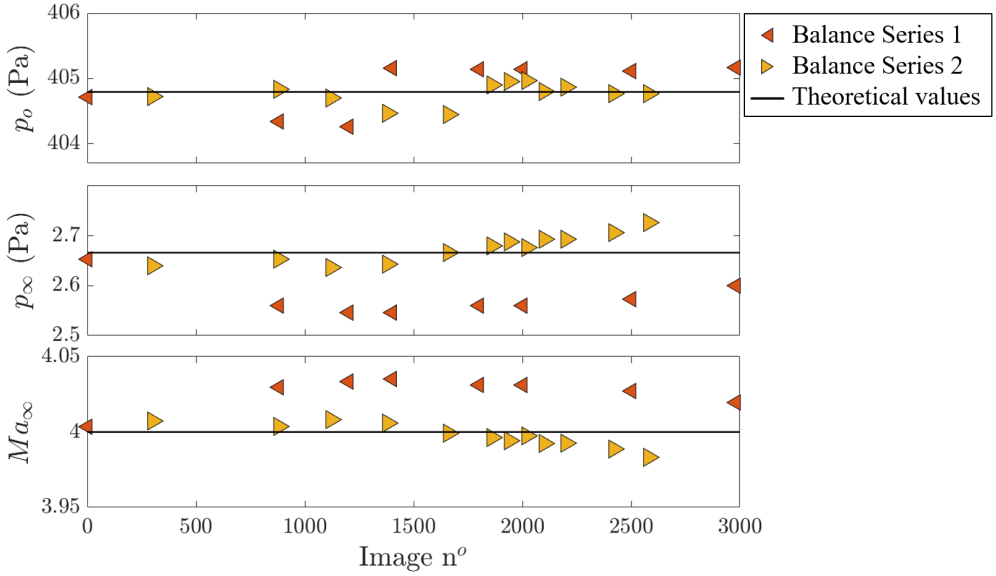

Figure 8.25: Evolution of the stagnation pressure p_0, free-stream pressure p_∞ and Mach number Ma_∞ according S_2 position for C_1 in N1 flow-field.

with both pressures as defined in Equation 8.12.

$$Ma_\infty = \sqrt{\frac{2}{\gamma - 1}\left[\left(\frac{p_\infty}{p_0}\right)^{\frac{\gamma-1}{\gamma}} - 1\right]} \tag{8.12}$$

As can be seen, the pressures and thus the Mach number of Series 2 are close to the theoretical values, as desired for this experiment (see Table 4.2). The last two points, around image number 2500 are the farthest from the theoretical values. At this position, the drag forces of S_2, which is located in the free-stream flow described in Table 4.2, should have the same value as for a single sphere. The small difference (0.2 mN) observed in Figure 8.24 might be due to this tiny deviation in free-stream pressure, or to the fact that S_2 is still under a slight influence of the shock-wave of S_1. However, the results of Series 2 are in good agreement with what was expected, contrarily to those of the swinging sphere experiment and the balance Series 1 which present 1 mN difference with the expected drag value. While it is unsurprising to observe smaller values when the free-stream pressure is lower than expected (see p_∞ in Figure 8.25), it is important to note that the pressure variations are small.

Table 8.1, presents the average value of flow pressures (p_0 and p_∞) and Mach number of Series 1 and 2. This table also includes the differences ($\neq$) calculated with respect to the theoretical values. It can be seen that the free-stream pressure of Series 1 is 3.41% smaller than the nominal values, which is ten times the

		Theoretical (th.)	Series 1		Series 2	
			Value	≠ with th. (%)	Value	≠ with th. (%)
p_0	Mean (Pa)	404.792	404.878	0.02	404.765	0.01
	Std (Pa)		± 0.388		± 0.167	
	Std (%)		± 0.10		± 0.04	
p_∞	Mean (Pa)	2.67	2.575	3.41	2.675	0.34
	Std (Pa)		± 0.036		± 0.028	
	Std (%)		± 1.40		± 1.05	
Ma_∞	Mean (Pa)	4	4.026	0.65	3.997	0.08
	Std (Pa)		± 0.010		± 0.008	
	Std (%)		± 0.26		± 0.20	

Table 8.1: Mean pressures and Mach number compared to theoretical values.

difference calculated for the measurements of Series 2. This 3.41% decrease in free flow pressure, which could be considered acceptable, results in a 12.5% decrease in the drag force measurement, which is a fairly significant error. Moreover, the Mach number increases by only 0.65%, which is very little compared to the accuracy of experiments reported in the literature. Nevertheless, it seems that, in these flow conditions, even variations considered negligible have, in fact, a great impact on measurements.
It is known that when S_2 is out of the shock-wave of S_1, its drag force is equal to the drag force of a single sphere in the free-stream flow. Thus, the measured forces of Series 1 were corrected by rescaling values with respect to the value of a single sphere. In this way, the graph in Figure 8.26 is obtained, showing three superposed curves. This means that, with one known value, the swinging method can give exploitable drag forces. The results obtained with the swinging method will be given considering a maximal error of 0.49 mN.

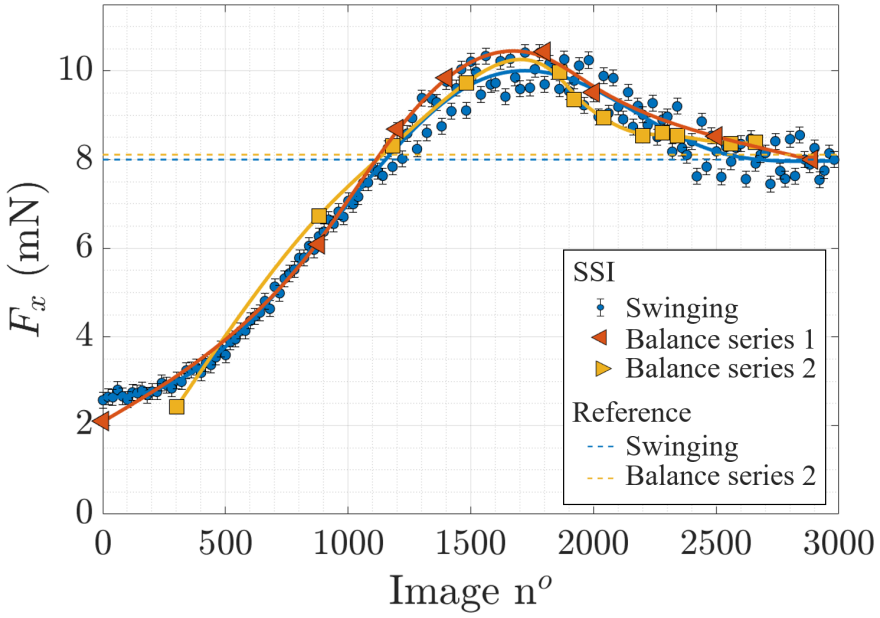

Figure 8.26: Corrected drag force according S_2 position for C_1 in N1 flow-field.

8.2.1.3 Analyse of a vertical displacement of the support

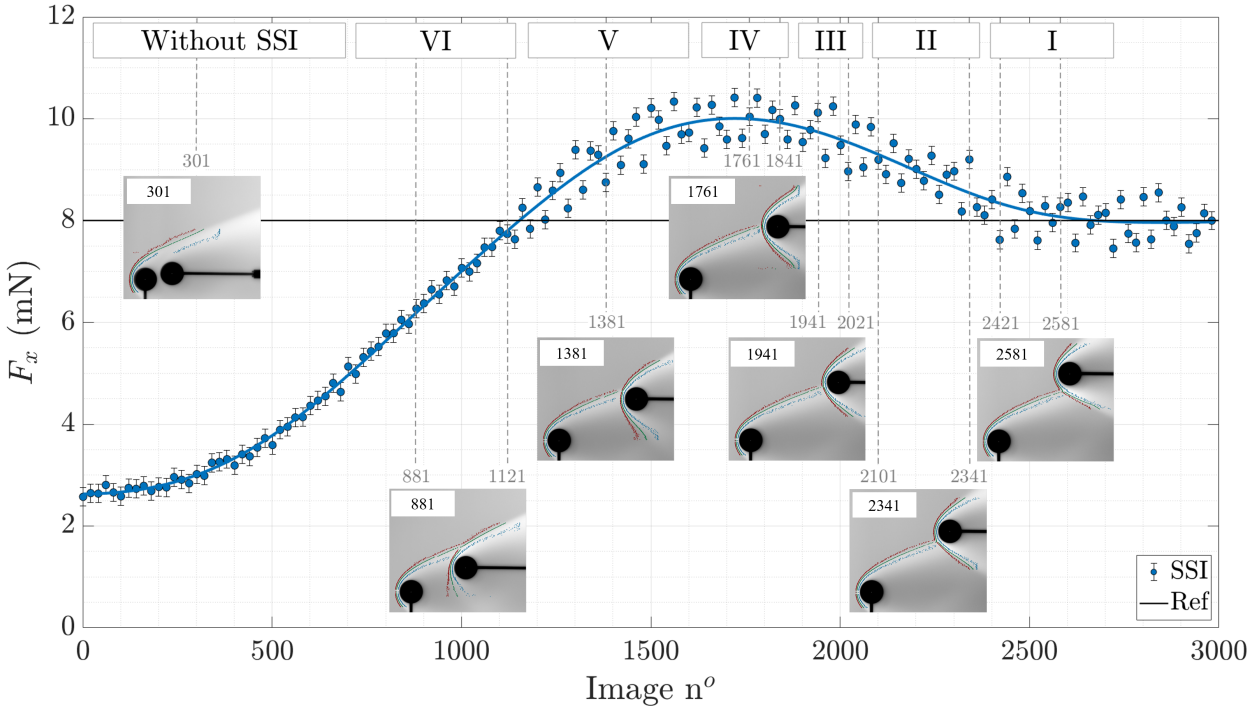

Figure 8.27: Corrected drag force according S_2 position with SSI types for C_1 in N1 flow-field.

Now we confirmed the quality of the swinging experiment results, we can plot the corrected drag force according to the image number. Figure 8.27 shows the results along with flow-field images that were recorded for the positions previously spotted in Figure 8.21 along the trajectory "X_2 = 16 mm". From the images analysis made and partly exposed in Figure 8.28, we have been able to identify the type of SSI according to the image number. It is first interesting to observe that, even when S_2 is directly behind S_1, the force endured

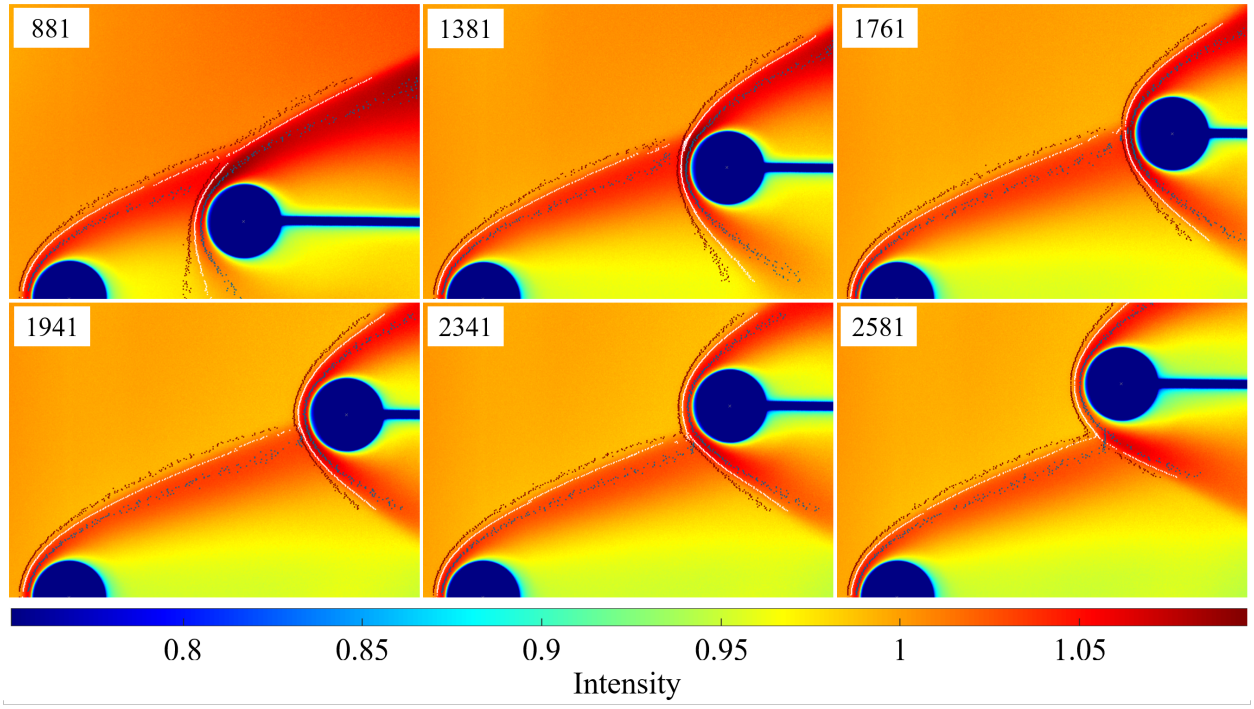

Figure 8.28: Images associated with the swinging trajectory for C_1 in N1 flow-field.

by S_2 is around 2 mN, which means that it is not completely protected by S_1. This force being positive, probably there is no recirculation behind S_1. If there is a recirculation area, it must be tiny and concentrated very closely to S_1, so that an object of the size of S_2 is not impacted. This hypothesis is confirmed by previous studies of the literature with numerical and experimental results. The studies were carried out to deepen the knowledge of the wake structure of a sphere under hypersonic rarefied flow conditions with Reynolds numbers between 194 and 2129. Experimentally the wake of a sphere was analysed with Pitot pressure measurements and hot wire velocities [146]. The numerical works were carried out with the DSMC method, some test cases of which were validated by the experimental results [63, 177]. All the results showed that the wake shows neither separation nor recirculation in the range of Reynolds numbers studied by the different authors. The same conclusions can be applied to our experimental conditions presenting a Reynolds number of 294.5.
As S_2 goes up, the drag force increases. Images n°881, which corresponds to the inflection point of ① in Figure 8.21 seems to mark the begin of the incident shock influence, with an early type VI SSI. With the increase in S_2 altitude, the force keeps increasing until image n°1761, which corresponds to the point of maximal X_2 on the considered trajectory. It is to be noted that the maximal drag force is a type IV SSI, as it was the case in section 8.1.1. Whether with the trajectory of S_2 or with the drag force, no slop variation is observed between the deep wake and the incident shock. Thus, it seems that there is no recompression area in the wake of S_1. Above the point of maximal pressure, the drag decreases until it reaches the reference drag force. Then, it is noticeable that S_2 still looks under the influence of S_1, but it seems that the incident shock has no more influence on the drag force.
Since, for some positions on this trajectory, measurements were realised with the aerodynamic balance, we also have at our disposal the value of the drag but also of the lift forces.

Out of curiosity, we decided to compare the aerodynamics of S_2 with a variation in X_2. Indeed (Figure 8.1) presented the aerodynamic forces for a vertical displacement of S_2 along for $X_2 = 24$ mm. With the balance, the series 2 allowed to access not only the drag, but also the lift on the trajectory described during the swinging experiment. Thus we have a set of result for $X_2 = 24$ mm, and another for X_2 that varies. For the swinging trajectory, it is reminded that their location is also shown in the left image of Figure 8.24. All the yellow points are located with $X_2 > 37$ mm except the lowest point for which $X_2 = 19$ mm. Figure 8.29 presents the drag and lift forces obtained for both experiments. The results are plotted according to $\frac{Z_2-R_s}{r_2}$ which represents the normalised vertical distance between the nose of S_2 and the middle shock. In blue, the results concern the study made in section 8.1.1, while in yellow, they come from the "$X_2 = 16$ mm".
It is really interesting to observe that for the drag or for the lift, results are really similar. Below the incident

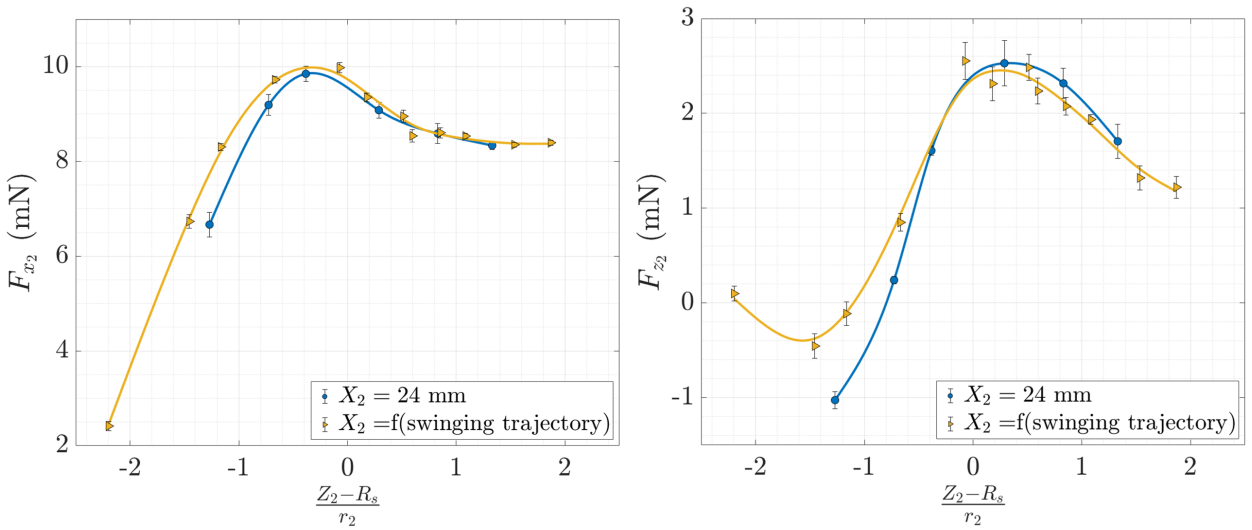

Figure 8.29: Drag and lift forces for different longitudinal distances, balance results for C_1 in N1 flow-field.

shock, values are a slightly higher for the variable X_2 than for $X_2 = 24$ mm. Indeed, as we look downstream in the wake of S_1, the Pitot pressure profile (Figure 6.17) described the diffusion of S_1 shock-wave. Moreover, between $X_2 = 8$ mm and 32 mm, the value of the pressure peak is almost unchanged, which gives a high pressure in a wider area under the shock. Consequently, S_2 is slightly more impacted by the pressure when far from S_1, increasing its drag force. Earlier, in section 8.1, we stated that the viscous effects could lead to a larger area for which S_2 would have a positive lift. Here, we saw that looking far from S_1, its shock-wave diffuses a certain increase in the viscosity of the flow, which could explain the increase in F_{z_2} for $\frac{Z_2 - R_s}{r_2} < -0.5$.
S_2 drag force does not seem to be impacted by its longitudinal distance towards S_1. Its lift, however, slightly decreases when increasing X_2. It is possible that the very little decrease in static pressure observed with the Pitot measurement lead to the decrease in F_{z_2}. Indeed, Figure 8.16 showed that the pressure is preponderant for positive lift, and when S_2 is located above S_1 shock-wave. Thus, we can easily imagine that a decrease in static pressure would lead to a decrease in S_2 wall pressure, resulting in a decrease in lift.
The variation observed on the aerodynamic forces do not exceed 0.8 mN, and this maximal are only obtained locally. Thus the longitudinal distance does not affect much the behaviour of S_2, which means that the following sphere will be affected by S_1, even far in its wake. With this statement, for the rest of the study of the swinging trajectory "$X_2 = 16$ mm", we will assume that the wall pressure distribution is similar to the results obtained for $X_2 = 24$ mm

The above aerodynamic forces, obtained with the balance, for the swinging trajectory "$X_2 = 16$ mm", enable to calculate the displacement of S_2 towards S_1 for the adopted locations. Results are shown in Figure 8.30, where the local displacements of S_2 towards S_1 are represented with the yellow arrows.
From $Z_2 = 0$ mm to approximately the transition between type VI and V, the second sphere displaces towards S_1. As it was shown from wall pressure distribution results in the case $X_2 = 24$ mm (Figure 8.11), for type VI and as can be expected for lower positions of S_2, the maximal pressure value is lower than the reference peak, which indicates a higher rarefaction level, and probably lower velocities. Thus S_2 is less constraint than S_1 in the $\vec{x}$ direction, and can approach it. Moreover the pressure distribution is mostly located on the upper part of S_2 which is pushed down. At the transition between types VI and V, the direction of S_2 is reversing. By referring to the data from $X_2 = 24$ mm, for $\Theta_i = 30°$, close to the transition between types VI

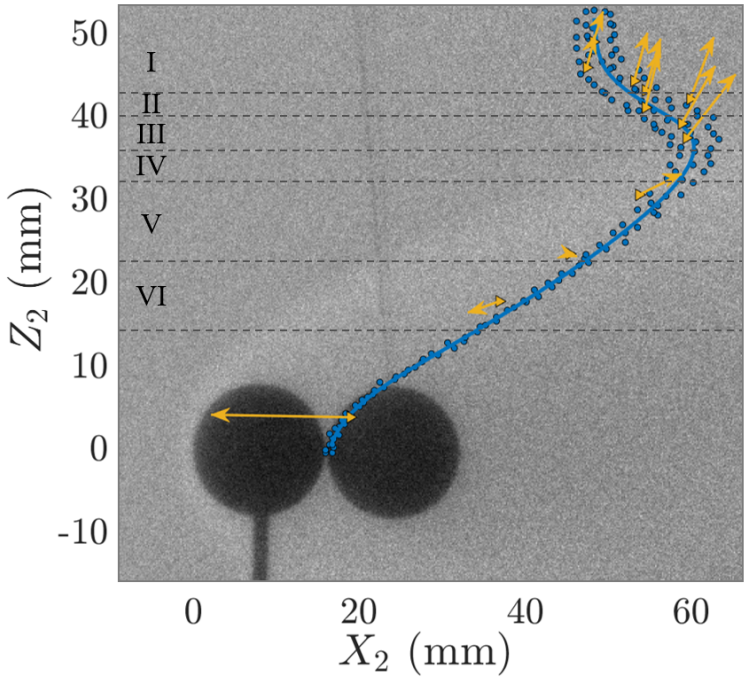

Figure 8.30: Displacement of S_2 towards S_1 on the swinging trajectory, C_1 in N1 flow-field.

and V, we discussed a possible point of unstable shock-wave surfing. The point presented here could also be concerned by that phenomenon, where for a brief instant, S_1 and S_2 would flight together without moving apart. Above this position, for type V and IV, the lift force becomes positive, while S_2 is still mainly located under the shock-wave of S_1 and the wall pressure is mostly located on the upper part of its surface. This shows once again the impact of the viscous effect on the lift forces. Then, from type III to I, S_2 is pushed away in the $\vec{z}$ direction, as was already discussed with the distribution of the wall pressure results which were mostly located on the bottom of S_2. The displacement in the $\vec{x}$ direction is strong for the type III, and, as the sphere goes up in the free stream, it will be less and less impacted by the incident shock. The X-component will decrease until it reaches the reference value, where S_2 won't move any more from S_1 in the $\vec{x}$-direction.

8.2.2 Experimental drag mapping

The swinging sphere experiments showed good agreement with the results of the balance and allowed to complete the understanding of the aerodynamic of S_2 flying in the flow-field generated by S_1 thanks to the analysis of a first trajectory "X_2 = 16 mm". To fully complete the mapping of drag forces, the swinging technique was realised for nine other trajectories, moving the support vertically or horizontally with different initial positions. In the left image of Figure 8.31 are represented the mean trajectories of S_2 for the ten different displacements realised. The colour of the slopes corresponds to the mean drag force of S_2 for each mean location. Drag forces are given with a maximal inaccuracy of ±0.5 mN. The mapping of forces applied on S_2, on the right of Figure 8.31, is obtained by interpolating these results. As it can be observed, the interpolation is not really well defined, which is due to too little number of measurements. Nonetheless, this mapping, determined from experimental data, allows obtaining a first knowledge of the drag forces of S_2 whatever its position towards S_1. Concerning the evolution of the force values, the same reasoning as previously exposed for X_2 = 24 mm, or for the swinging trajectory X_2 = 16 mm, can be applied here. The drag force is maximal along the shock-wave of S_1 with values around 8-9 mN. The wake behind S_1 is well defined, its diameter is almost that of S_1 and extends over at least 3.5 times S_1 diameter. In this area the drag force values are homogeneous with a low value of about 2.5 mN. Between this area and the area with high drag force values around the shock, a straight band that follows the shape of the shock-wave has a value similar to that of the reference drag force.
In Figure 8.32, the drag coefficients have been calculated following the two methods adopted earlier. On the left, the Cd_∞ is given, calculated with the free-stream flow-field seen by S_1; while, on the right, the Cd_{loc} is calculated with the local flow-field seen by S_2, which is given by the two-dimensional simulation of S_1 flow-field. Cd_∞ is not representative of the drag coefficient of S_2, it is only a common way to normalise the drag force according to the free stream seen by S_1. It is mostly used to compare results with the literature

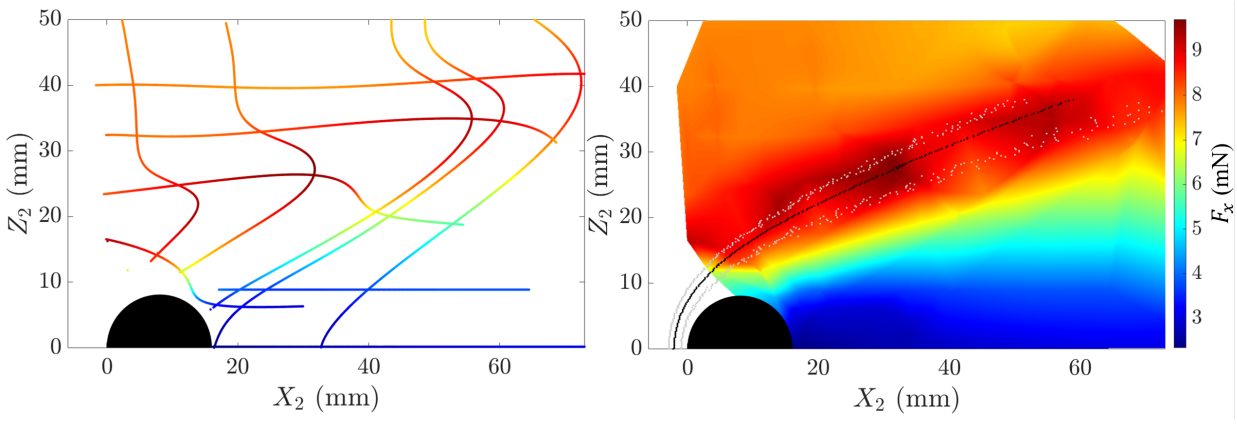

Figure 8.31: Left: S_2 mean drag forces on the different swinging trajectories. Right: Interpolated mapping of the mean drag forces, C_1 in N1 flow-field.

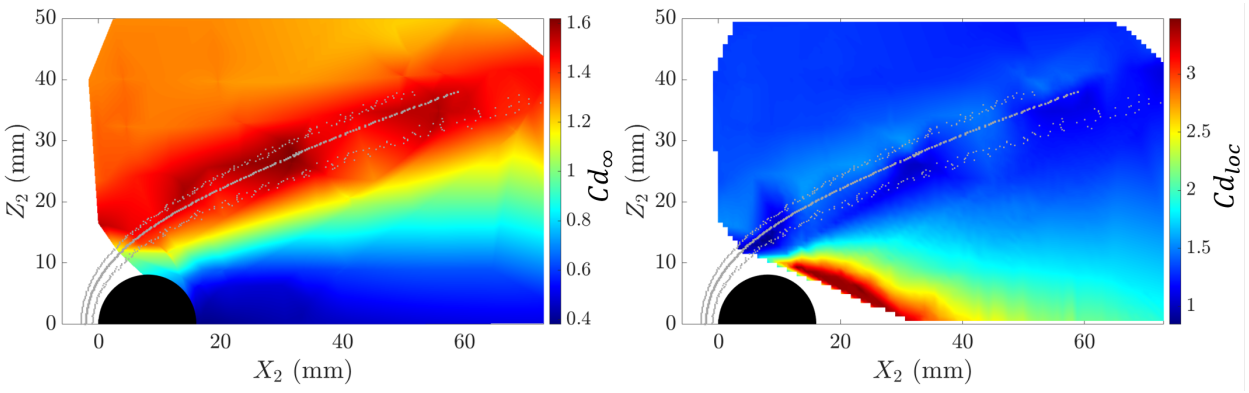

Figure 8.32: Interpolated mapping of the mean drag coefficients (left: Cd_∞, right: Cd_{loc}), C_1 in N1 flow-field.

since this is the way it is done in most publications.
The real aerodynamic coefficient is Cd_{loc}, which allows to understand the local behaviour of S_2 in the flow it faces: a small Cd_{loc} means that S_2 penetrates more easily in the flow. In our case, we calculated that the Cd_{loc} is maximum when S_2 is located in the near wake of S_1, right behind it, with values up to 6000 which has not physical sense. In order to keep a visible mapping, values over 3.5 are not plotted on the mapping. This could be counter-intuitive since the drag forces are very small in this region. From the numerical simulation of DS2V, the maximal mean free-path in S_1 flow-field is of 2.7 mm, giving $Kn_{max} = 0.17$. It means that in this region the level of rarefaction is about 12 times that of the free-stream flow. Thus, the local drag coefficient does not increase due to the force of S_2, but due to its flying environment, which is highly viscous: there, the Reynolds number is of 0.16. On the contrary, the Cd_{loc} is minimum with a value of 0.83, when S_2 is located between the BL and MS regions of the incident shock, where the drag force is the highest. There, the drag force is maximal with 9.74 mN, which is not a great increase compared to the reference value of 8 mN. And, at the same location, the rarefaction level does not decrease much with $Kn_{min} = 0.01$ compared to the $Kn_\infty = 0.0139$, but still increases sufficiently to improve the drag coefficient. In consequence, the aerodynamics of S_2 is not much due to strong force's effects, but seems highly related to the level of rarefaction of the medium, since a viscous environment will strongly increase the drag coefficient.

8.3 Effect of S_2 on the drag force of S_1

It is well known that when an object flight in the flow-field generated by a primary one, its aerodynamics is modified. With the study of spheres interaction presented earlier, and in particular of the shock/shock interferences, we, indeed, confirmed the strong impact of S_1 on S_2. But a much less studied subject is the impact of S_2 on S_1 aerodynamics.
This topic has been numerically studied in the continuum regime by Golubev [79] for different Mach numbers from 2 to 6. He observed a variation of the drag of the leading sphere, according to the position of S_2, when aligned horizontally or vertically with S_1, or when in the configuration of SSI. A similar study was conducted by Zhu *et al.* [220] in hydrodynamics, with a viscous fluid and thus low Reynolds numbers. He also showed that the drag force of S_1 can be modified following the inter-distance between S_1 and S_2.
With a first observation made numerically, indicating a very slight variation in F_{x_1}, we decided to try equivalent experiments in our rarefied flow. These tests were realised by means of the swinging sphere technique which is very advantageous since it is a non-intrusive way to quantify the drag force of S_1.

8.3.1 Case $X_2 = 24$ mm

In this section, we propose to investigate the effect of S_2 on S_1 for the six types of SSI by means of the swinging sphere technique applied to S_1, as described in section 5.4.2. For this experiment, S_1 is suspended in the free-stream flow, and S_2 is moved behind it on the vertical axis $X_2 = 24$ mm. S_2 is first placed high in the flow so that the drag force of S_1 corresponds to the reference case, as if there were only one sphere in the flow. Then, S_2 altitude is decreased until it reaches $Z_2 = 0$ mm. Earlier, with the validation of the swinging sphere applied to S_2, we noticed that the forces are strongly dependent on the free-stream flow conditions. For this experiment, to avoid any error coming from slightly changed conditions when moving S_2, it was decided to move S_2 step by step. Thus, for different fixed position of S_2, a set of 100 images were recorded and analysed. For each position, the mean results are presented in Figure 8.33 according to the altitude of S_2 towards S_1 in blue, and in pink are given the results from DS3V numerical simulations.

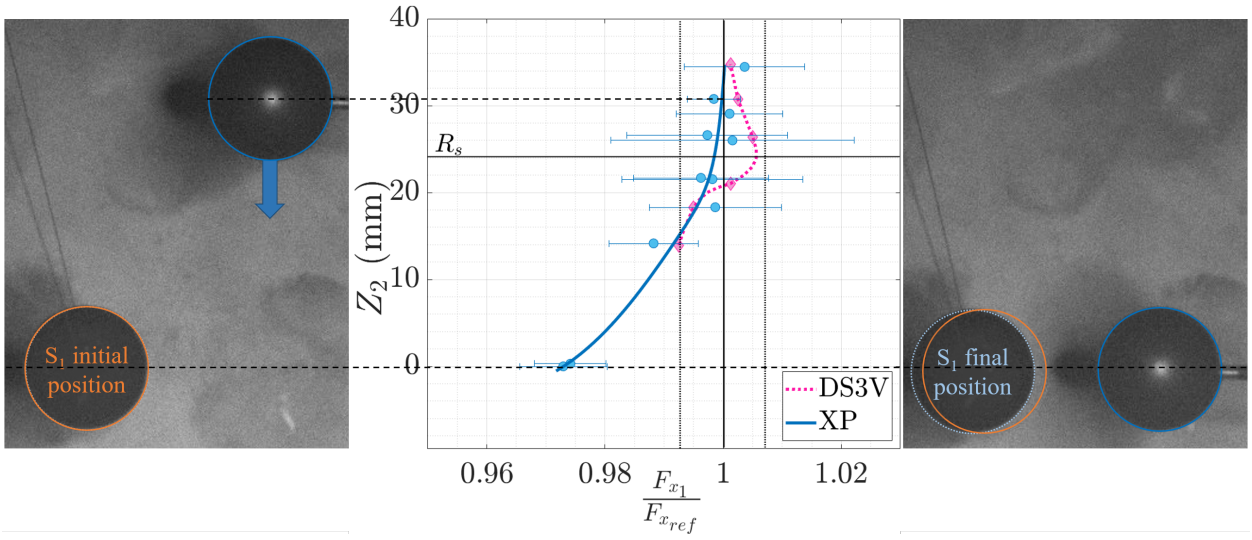

Figure 8.33: Drag force of S_1 for different altitude of S_2, with $X_2 = 24$ mm, C_1 in N1 flow-field.

Concerning the experimental results, when S_2 decreases in altitude, S_1 moves in the direction of $-\vec{x}$. The drag force associated to this displacement also decreases of about 3%. This is not a very significant change in terms of value, but it is still interesting to observe.
In Figure 8.34 are presented the normalised enhanced images (top) of some of the locations presented in the

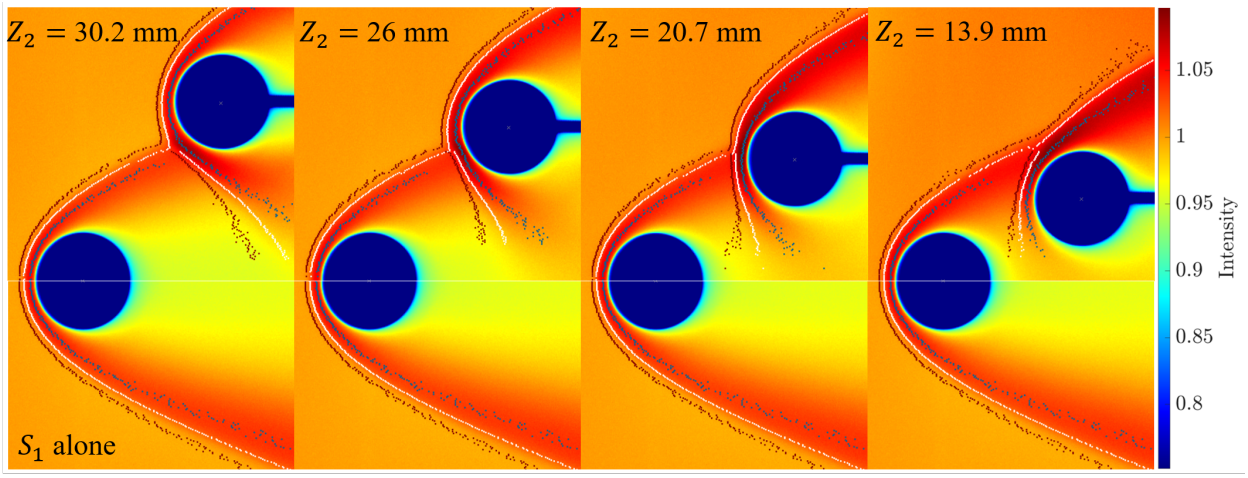

Figure 8.34: Enhanced images with shock-waves for different altitude of S_2, with $X_2 = 24$ mm, C_1 in N1 flow-field. Top images: SSI, bottom images: single sphere.

graph of Figure 8.33. The bottom images show the reference case. The comparison of the flow-fields of the wake just behind S_1 shows a slight difference when S_2 is close to S_1. As S_2 altitude decreases, it can be seen that the luminosity right behind S_1 intensifies. This means that the near wake of S_1 slowly gets denser, thus producing a lesser density gradient between the nose and the rear of S_1. As a consequence, the differential of flow being less constraining, S_1 is slightly less impacted by the free stream.
DS3V results presented in Figure 8.33 show that when S_2 crosses the incident shock-wave, F_{x_1} is locally higher than the reference, which was not observed with the experimental results. In absolute values, the difference between the reference and the maximal F_{x_1} is of 0.04 mN, which is very low, and could be due to a slight difference in the meshing of the problem. But, as the increase is specifically observed when S_2 passes the incident shock, a physical phenomenon could be responsible. In this case, since F_{x_1} increases compared to the reference, it would mean that a slight depression is created between S_1 and S_2 by the SSI, which would lead S_1 to be attracted backwards. This specificity was not experimentally observed in our conditions nor with the numerical results of Golubev [79], who observed an equivalent behaviour than our experimental results (see Appendix H).
To complete the understanding of the aerodynamics of S_1, the longitudinal and transversal velocities of the numerical results are shown in Figure 8.35. As S_2 altitude decreases, the simulation shows a decrease in V_x at the stagnation point of S_2, and also at its rear. It seems that a very small region behind S_1 is subjected to negative V_x. With the current lines, this area is not even visible, which demonstrates as small as this region must be. Contrarily to the velocity in the $\vec{x}$-direction, the velocity according to the $\vec{z}$-direction shows a global increase as S_2 gets down behind S_1. Moreover, the repartition of V_z around S_2, shows the dispersion of the bottom area of S_2 shock-wave. This area appears wider and shorter than the upper part of the S_2 shock-wave,

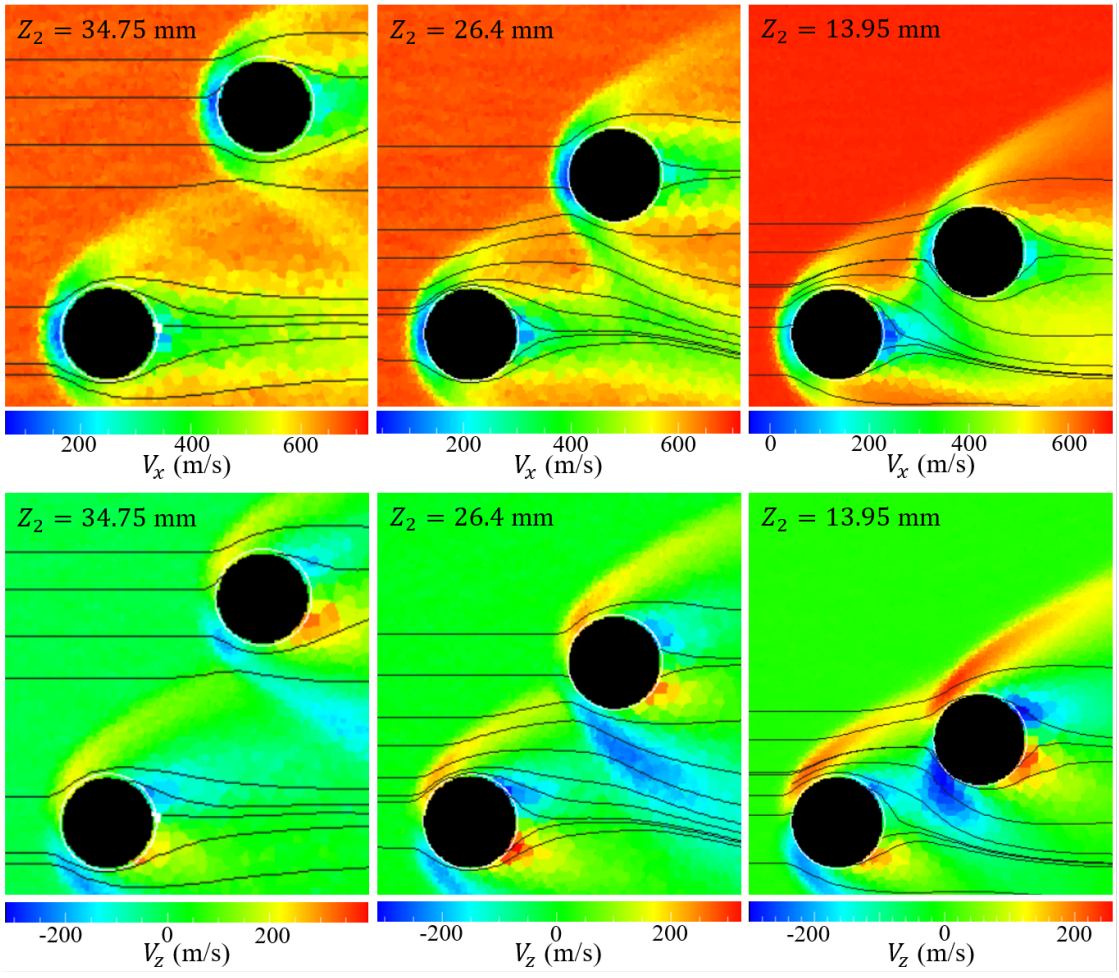

Figure 8.35: DS3V X (top) and Z (bottom) components of the velocity for X_2 = 24 mm, C_1 in N1 flow-field.

with velocities that seem to be a little higher, which may explain the increase in density observed with the experimental images of Figure 8.34.

8.3.2 Case $Z_2 = 0$ mm

The study of the drag force of S_1 was realised for S_2 moving vertically on the axis $X_2 = 24$ mm. Results showed that S_1 aerodynamics is slightly impacted, especially when S_2 is aligned horizontally with S_1. As for the previous experiment (section 8.3.1), S_2 was moved behind S_1, the suspended sphere, but this time on the horizontal axis $Z_2 = 0$ mm. This way, we will be able to determine the distance of influence of S_2 on S_1. S_2 is first placed far in the wake of S_1, so that S_1 drag force corresponds to the reference case. Then, S_2 will be progressively moved towards S_1. Figure 8.36 shows the results of this experiment. As for the case

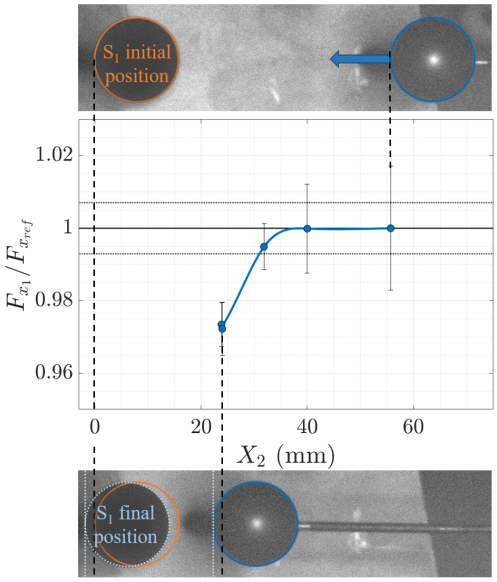

Figure 8.36: Drag force of S_1 for different longitudinal distance of S_2, with $Z_2 = 0$ mm, C_1 in N1 flow-field.

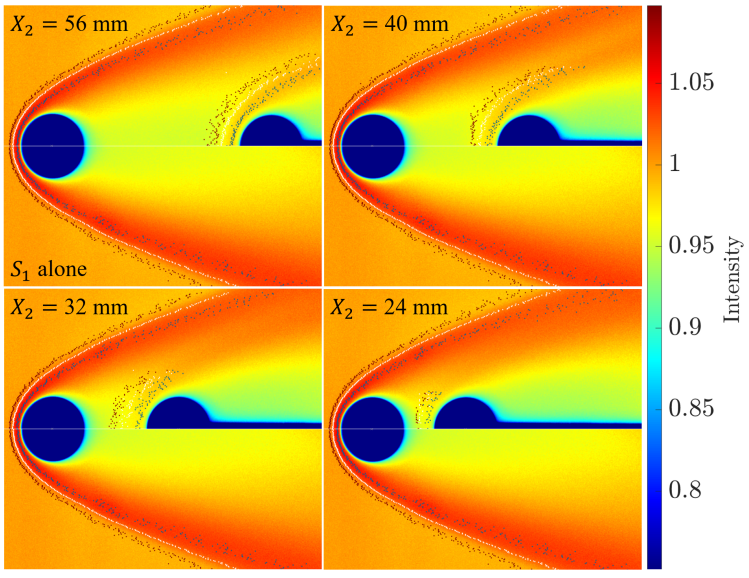

Figure 8.37: Enhanced images with shock-waves for different longitudinal distance of S_2, with $Z_2 = 0$ mm, C_1 in N1 flow-field. Top images: SSI, bottom images: single sphere.

Table 8.2: Stand-off distance of S_2 for $Z_2 = 0$ mm, C_1 in N1 flow-field.

X_2 (mm)	56	40	32	24
Ma_{DS2V}	1.84	1.65	1.46	1.07
Re_{DS2V}	39.47	34.33	37.32	15.48
ω_{DS2V}	0.852	0.844	0.839	0.834
$\Delta 2_{measured}$	4.8	5.8	6.7	3.36
$\Delta 2_{measured}/r_2$	0.6	0.73	0.84	0.42
$\Delta 2_{calc}/r_2$	1.86	2.55	4.44	32.66

$X_2 = 24$ mm, each point corresponds to a location of S_2 for which a series of 100 images were recorded and analysed. As S_2 gets close to S_1, and from a certain point, F_{x_1} begins to decrease. S_1 is affected by S_2 when $X_2 < 27$ mm$= 2.3\emptyset_1$.
From the observation of the experimental images in Figure 8.37, some interesting points can be noticed. S_2 compression wave is visible for the two furthest locations but shows the sign of highly rarefied flow with a great thickness. As S_2 gets closer to S_1, its compression wave slowly vanishes, and it is no more noticeable for $X_2 = 24$ mm. Note that the shock-wave detection technique still works in front of S_2 for this last position. However, for this last case, it is strongly possible that the detection only highlights the compression area but not a real shock. If the detection only shows the maximum compression area, thus, the given distance is not representative of the stand-off. The rarefaction of the flow is reflected in the high measured stand-off distances of the middle shock given in Table 8.2. Except for $X_2 = 24$ mm, $\Delta 2_{measured}$ increases when S_2 approaches S_1, which confirms that the level of rarefaction increases in the near wake of S_1. This means that, as S_2 gets closer, the few molecules that constitute the compression might create a predominant viscous layer that pushes S_1 upfront.
In Table 8.2 we also compared our measurements to the Equation 6.4, proposed for the determination of the stand-off distances, whatever the Reynolds number of the upstream flow. As presented in Table 8.2, $\Delta 2/r_2$ values determined by different ways are quite different. For each S_2 location, we determined $\Delta 2/r_2$ using the local Mach number and calculated the Reynolds number, at the same position in the simulation of S_1. In the wake, the Mach number is close to 1 and the Reynolds number is really low. Either the shock-wave of S_2 is not well developed due to the flow conditions, and in that case, we cannot use the generalised Ambrosio equation for the determination of stand-off distances; or this equation does not work for low Mach numbers, or for low Reynolds numbers. It would be interesting to compare results with additional experimental results to possibly improve our understanding. Due to this lack of data, the numerical simulations are used, in particular the Mach number and density flow-fields which are respectively shown in Figure 8.38 and Figure 8.39.

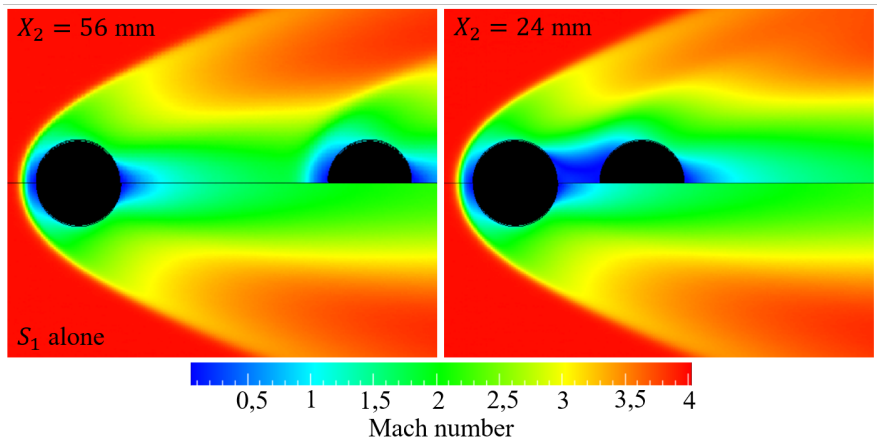

Figure 8.38: DS2V Mach number flow-fields for $Z_2 = 0$ mm, C_1 in N1 flow-field.

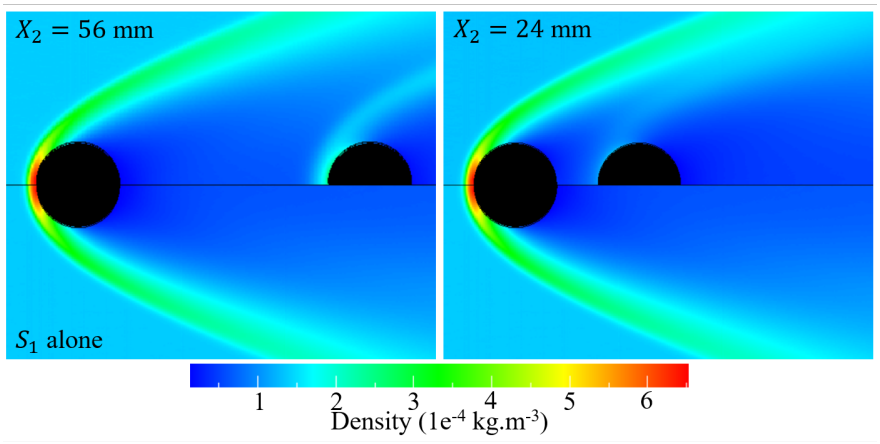

Figure 8.39: DS2V density flow-fields for Z_2 = 0 mm, C_1 in N1 flow-field.

As can be seen, for X_2 = 24 mm, the Mach flow-field is completely different from the reference case behind S_1. Thus, the Mach and Reynolds numbers and ω_{DS2V} given in Table 8.2 do not correspond to what actually endured by S_2. For this same position of S_2, no shock-wave can be observed since the upstream conditions of S_2 give a Mach number inferior to 1. However, the density flow-field shows a light compression wave, as observed with the experimental images of Figure 8.37. For X_2 = 56 mm, the near wake of S_1, does not seem modified by S_2, which is coherent with the drag force results concerning S_1.
V_x and V_z, the velocity components in the $\vec{x}$ and $\vec{z}$ directions, presented in Figure 8.40, add supplementary information. In particular, for the location X_2 = 24 mm, the streamline allows observing some recirculation in between the two spheres, which could explain that S_1 is pushed ahead. Unfortunately when S_2 is located in the near wake of S_1, the swinging technique did not show any sign of recirculation. For the swinging technique applied to S_1 or S_2, it would have been reflected in a stronger oscillatory movement of the swinging

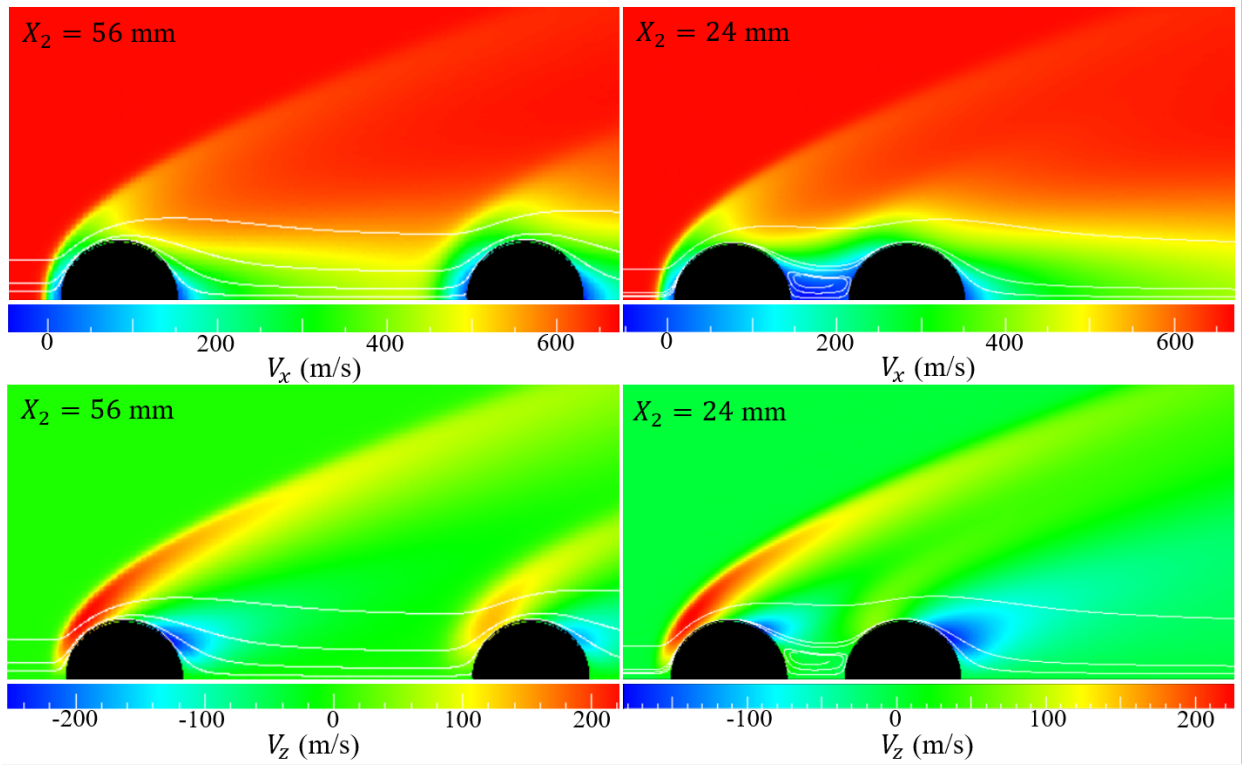

Figure 8.40: DS2V X (top) and Z (bottom) components of the velocity for Z_2 = 0 mm, C_1 in N1 flow-field.

sphere; and in the case of the swinging sphere applied to S_2, we probably would have observed a negative angle of the suspension wires. A recirculation area is not impossible in the near wake, but with a mean free-path ranging between 1.23 and 1.39 mm, the number of molecules is very low, and the velocities are relatively slow, so it is strongly probable that this recirculation area is too weak to impact the spheres.
Based on our experimental and numerical results, it was interesting to make a comparison with the continuum regime simulated by Golubev [79] for a Mach 4 flow. The comparison is shown in Figure 8.41. Our results are equivalent, even if a slight difference of l/D_1 is shown. In the continuum regime, however, this difference is of 1 diameter, which shows that S_1 is impacted by S_2 for a higher inter-distance. Moreover, in the case where the inter-distance is almost null, we observe a decrease in Cd_1 of 7%, while our conditions show about 5% of decrease compared to the reference value. Whether the higher distance of influence or the strong impact of S_2 on F_{x_1} could be due to pressure effect since the density level is higher in Golubev's conditions.

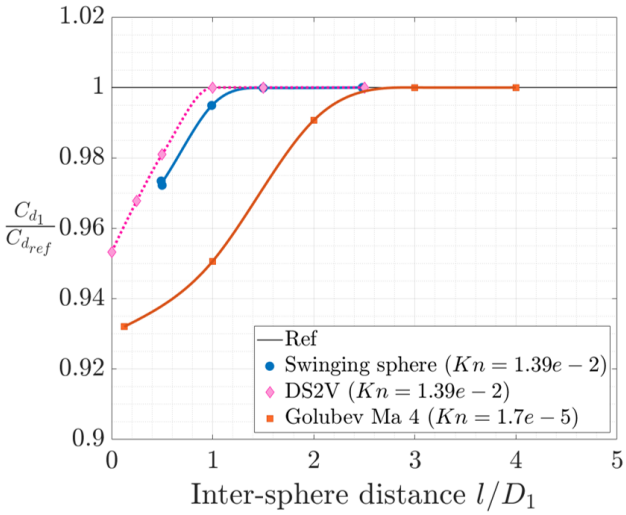

Figure 8.41: Drag coefficient of S_1 for different longitudinal distances of S_2, with $Z_2 = 0$ mm, C_1 in N1 flow-field.

Even-though the variations in F_{x_1} are almost insignificant, it is interesting to observe that S_2 also has an impact on S_1. In the case of space debris re-entry, where conditions are more extreme in particular in terms of velocities and temperature, this phenomenon is not to be ignored. Indeed, in most cases, the primary object is not followed by one simple object, but by a system of fragments. Thus the aerodynamics of the primary could be much more impacted by the presence of its fragment. In consequence, the trajectories of the fragments are modified.

Chapter 9

Rarefaction effects on the shock/shock interferences

Contents

In the previous chapter, shock/shock interferences were studied for a single couple of spheres with equal size C_1. Whether by means of flow-field visualisation or forces and wall pressure measurements, each type of SSI demonstrated a different behaviour. The present chapter investigates the evolution of the SSI impact on S_2 when changing the level of rarefaction of the flow-field. The level of rarefaction depends on the mean free-path of the flow-field, but also on the characteristic length of the model (Equation 2.1). Thus, two iso-Mach flow-fields were investigated, N1 and N2 described in Table 4.2, for four different couples of spheres, C_1, C_2, C_3 and C_4 as presented in Table 4.4. In any cases, results were acquired for a same longitudinal sphere inter-distance, *i.e.* by displacing S_2 on the vertical axis $X_2 = 24$ mm. The couple C_1 allowed to experiment with the different diagnosis as shown in section 8.1, while the other couples were analysed only with flow-field visualisation and aerodynamic forces results. First, the results of N1 and N2 will be compared for each couple of spheres. Indeed, the level of density of N2 is three times lower than that of N1, which will give information on the impact of the global rarefaction level. The local rarefaction level will then be investigated by comparing the four couples of spheres for each flow-field.

9.1 Global rarefaction effects (N1 vs. N2)

In this section, the global rarefaction level is investigated by comparing the results of N1 with N2. As a reminder N1 shows a mean free-path which is three times greater than that of N2, which means that for the comparison of one couple, the Knudsen number will be three times grater for N1 than for N2. To evaluate the impact of this global rarefaction level, both the conditions were compared for each couple of spheres. Since the couple C_1 was fully investigated for N1 and N2, as it was presented in 8.1, the comparison will be based on this couple whether than for the other three. However, to expand the impact of the global rarefaction effect of the SSI, N1 and N2 were also compared for C_2 and C_3. Results won't be discussed in this section since they show strong similarity with the couple C_1. However, all the graphs that allow the analysis are presented in Appendix I. Due to the 8 mm diameter of S_2 for the couple C_4, the visualisation did not allow to obtain enough results, and aerodynamic force measurements were not successful for the N2 flow conditions; thus, C_4 won't be used for this analysis.

9.1.1 Image analysis

In section 7.3, we had a first sight at the flow-field images obtained for N2. As previously explained, a wide set of positions was explored for $X_2 = 24$ mm as shown in Figure F.4. These images were analysed and classified according to the six different types of SSI, as for N1. In the first instance, we will focus our comparison between the two flow-fields with image analysis. For each condition, one image of each type was selected and compared, as presented in Figure 9.1. This figure shows the enhanced images coloured with a jet colour map to ease the visualisation. At first sight, the SSI of N1 and N2 looks similar. However, we can notice some differences, known to be the consequence of rarefaction effects. In particular, the thickness of the shock-waves is lower for N2 than for N1, which agrees with the observation made in section 6.1.2 and in the literature ([180, 4]). As a consequence, it seems to decrease the size of the interference area, but to accentuate the deformation of S_2 shock-wave. This phenomenon was also observed by White and Kontis [211], who numerically studied the interaction of an incident oblique shock with the bow shock of a cylinder for three Knudsen numbers ($Kn_\infty = 0.0067, 0.0133, 0.0267$), two of which being approximately the rarefaction conditions of N2 ($Kn_\infty = 0.0046$) and N1 ($Kn_\infty = 0.0139$). Another observation concerns the density gradient in the wake of S_1. It was previously mentioned that the intensity level of the recorded images is representative of the local density of the flow-field. Here, in the wake of S_1, the normalised intensity is slightly lower for N1 than for N2, while they are similar in the flow-field. This leads to a higher density gradient in S_1 flow-field for N1.

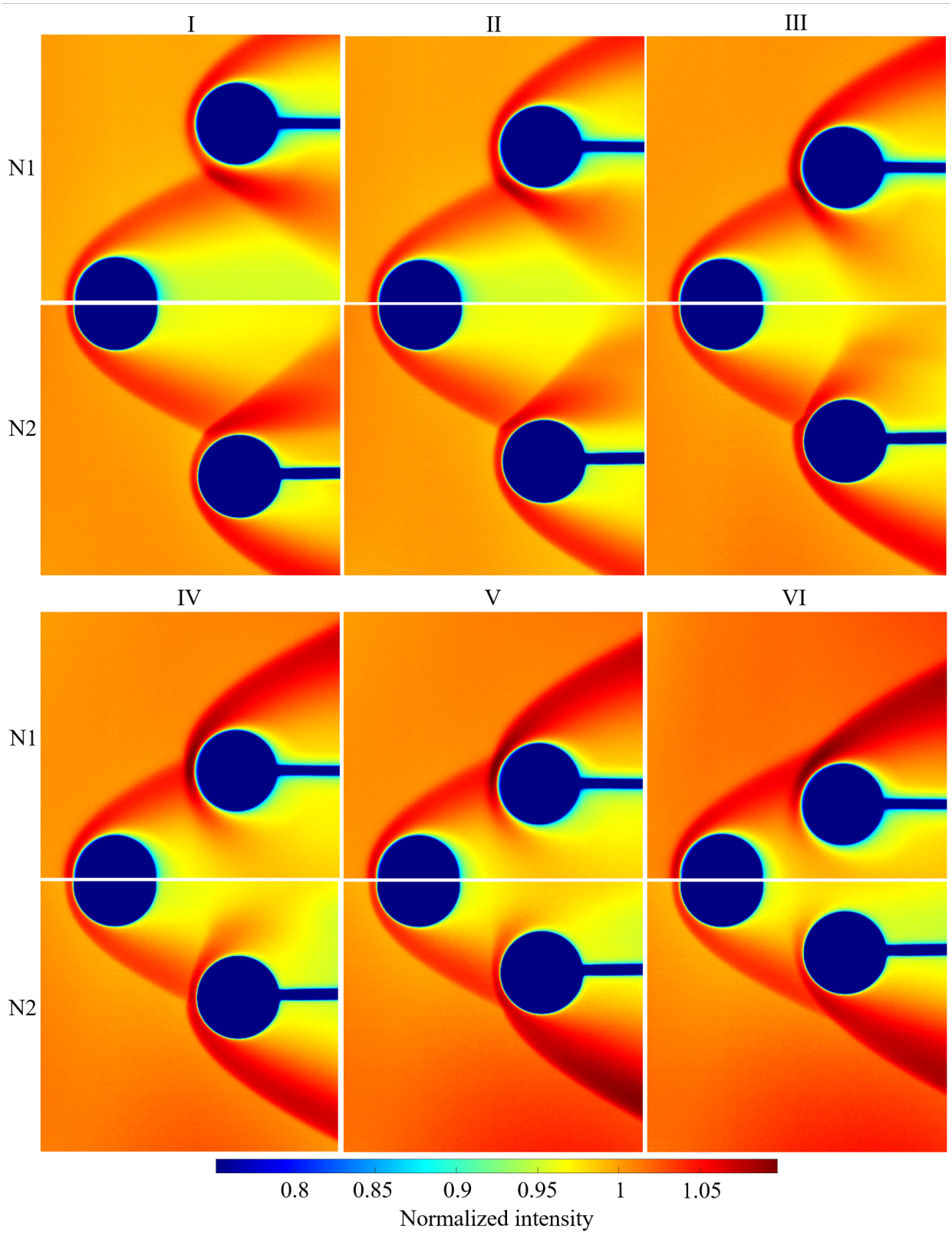

Figure 9.1: Images of the SSI of C_1, in N1 (top) and N2 (bottom) flow-fields.

In addition to the flow-field visualisations, the shock-waves were detected with the FSD method described in section 5.2.4. In Figure 9.2, we superposed the shocks detected around S_2 for N1 and N2. The three regions of shock (FS, MS, and BL) are independently compared for the type III, IV and V interferences.

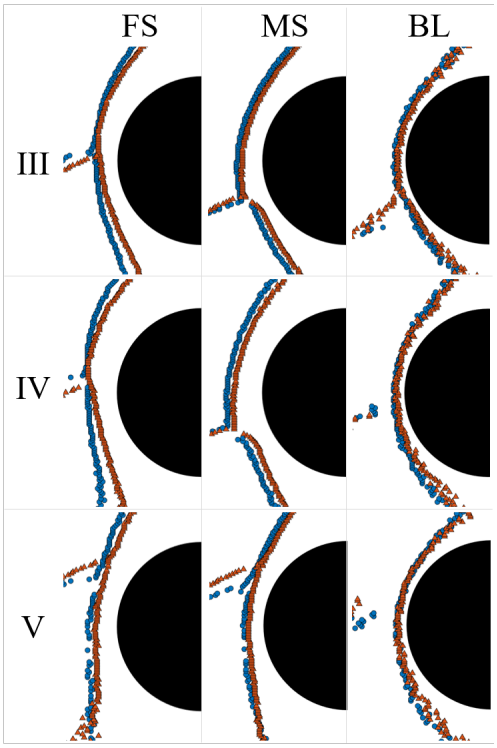

Figure 9.2: Shock-wave superposition of C_1, in N1 (blue) and N2 (orange) flow-fields.

Whatever the type of SSI, the BL of N1 and N2 appears approximately superposed, while, the MS and FS are clearly farther from the surface of S_2 for N1. Thus, the shock-wave of S_2 is thicker for N1 than for N2, as was observed with Figure 9.1. Despite this thickening, at the interaction point the FS in N1 conditions is almost conflated with that of N2. This is not due to a higher compression of the shock for N1 than for N2, but to the higher deformation in N2 flow conditions. Considering the MS, the difference is less obvious but a slightly higher deformation at the interaction point and below is observed for N2. The stagnation pressures in the incident shock-wave for N2, measured with the Pitot pressure probe, are three times higher than for N1. Thus, the incident shock might penetrate deeper the shock-wave of S_2, which might deform extensively S_2 shock-wave and potentially impacting more on its surface.

To quantify these deformations, we noted the values of stand-off distances at the nose of S_2, and the distance of P_i (the intersection point) and P_{ml} (the most luminous point) with the surface of S_2.
The stand-off distances of the shock's three regions are plotted in Figure 9.3. Values are normalised with the reference stand-off distance of S_1, which is equal to that of S_2 when there is no interaction. The stand-off values of the reference cases are given in Figure D.1. At the nose of S_2, the three regions of the shock shows the same repartition of the deformation for N1 and for N2. For type I, the stand-off distances are similar to the reference case, since S_2 is globally exposed to the free-stream flow. As S_2 goes down in the incident shock, the shock moves away from S_2 until the type III SSI. Then, as its altitude keeps decreasing, the stand-off suddenly decreases until the type V SSI. Below a certain altitude, the stand-off increases again, this time due to the decrease in pressure that suffers S_2, since it is mostly located in the wake of S_1. The variation in the stand-off distances is due to several combined effects. For one part, they are due to the interaction effects, but also to the variation of the upstream flow seen by S_2. Indeed, as S_2 crosses the incident shock, the temperature, pressure, and velocity of the flow-field evolve (among others), varying, as a consequence, the local viscosity, Mach and Reynolds number.
The FS and MS show that the maximal stand-off distance is observed for the type III SSI, but it seems that, for N2, this maximum slides towards $\Theta_i = 0°$. In the same manner, the MS shows that the minimum, observed for the type V SSI, also slides towards $\Theta_i = 0°$ for N2. This observation may be the consequence of

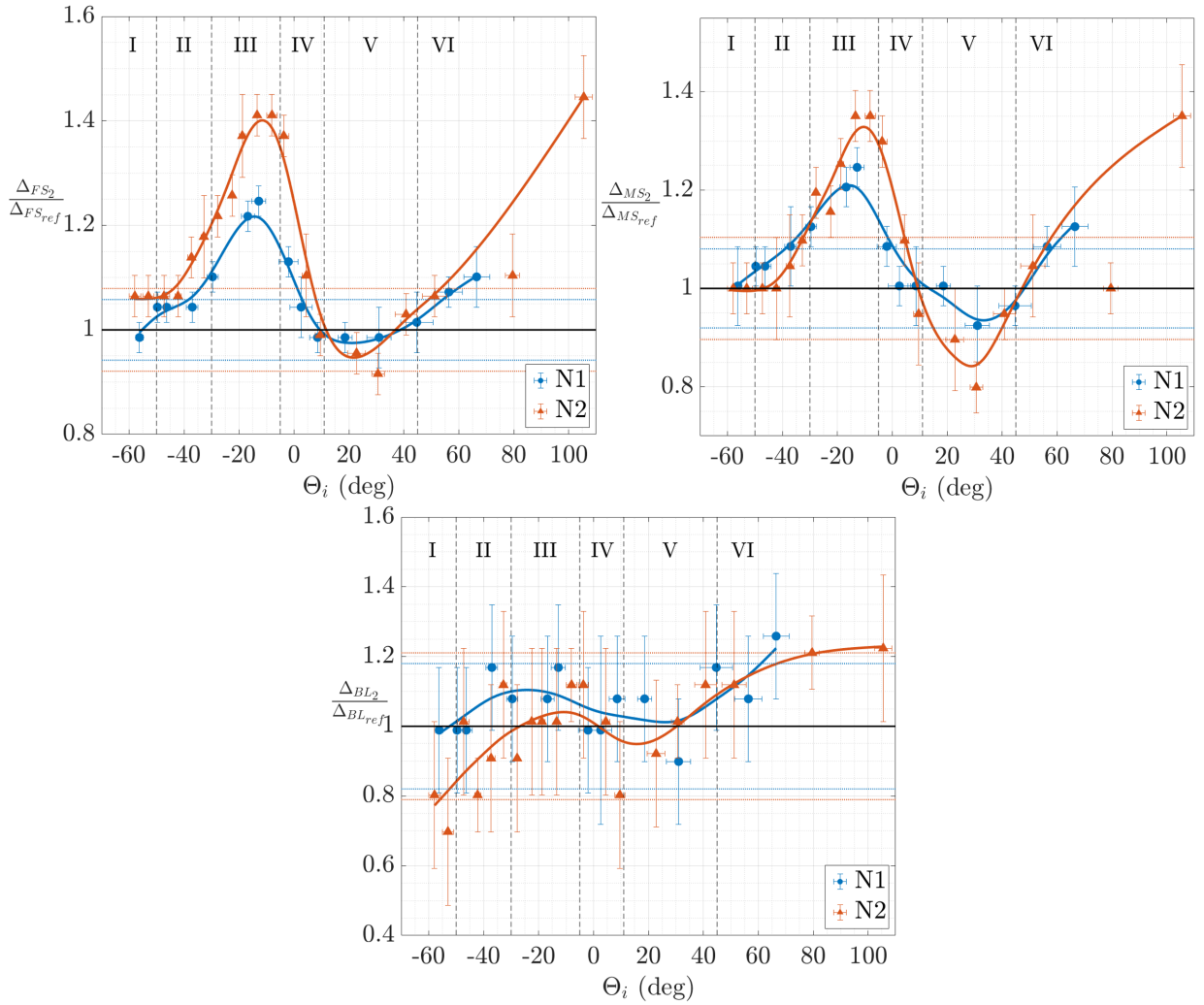

Figure 9.3: Stand-off distances of C_1, in N1 (blue) and N2 (orange) flow-fields.

a lack of points, so the following statement is to take with caution. If the maximal deformations ($\Delta_{2_{max}}$ and $\Delta_{2_{min}}$) are observed in a smaller range of interaction angle, it would mean that the SSI area is also smaller. As the shock-waves, and in particular the incident shock-wave, are thinner for N2, it seems consistent to observe a smaller impacted area, which, as a reminder, was slightly visible with the images of Figure 9.1. The magnitude of the stand-off distances is higher for N2, which implies a greater deformation of the shock at the nose of S_2, how it was already suggested by observing the images of Figure 9.1. Concerning the BL region, the variations observed are very little compared to the inaccuracies. However, since the tendency is coherent with the other two regions, results demonstrate a very weak impact of the SSI on the BL, still higher for N2 flow conditions.

Figure 9.4 presents the distances of P_i (d_i left graph) and P_{ml} (d_{ml} right graph) with the surface of S_2. d_i and d_{ml} are respectively normalised with the stand-off distances of the MS and of the BL. Indeed, we remind that P_i is the intersection point between the middle of shocks of both spheres, while P_{ml} is the most luminous point and thus is located in the BL region.

In the intersection area, the shock-wave is pushed farther from S_2 for the lower rarefaction level. Also, we observe a more pronounced variation of d_i for the type IV SSI, where the "∧"-shape for N2 is clearly visible and not just suggested as for N1. Moreover, for N2, a second "∧"-shape is observed around 20°, where the Δ_{FS_2} reaches the minimum value. In Figure 7.12, the SSI type V observed in Fisher's experiment show, in the interaction area, that the shock is bumped right above P_i. Observing really carefully at the image of SSI type V for N2, we can see, with difficulty, a bumped shape, that could lead to the second

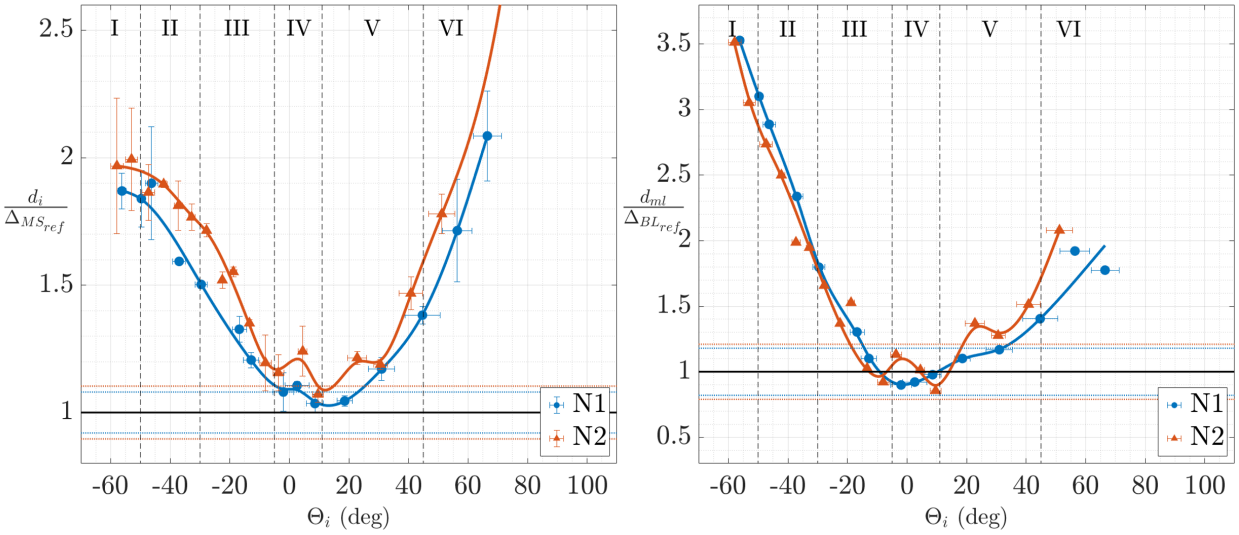

Figure 9.4: Distances of P_i (left) and P_{ml} (right) from the surface of S_2, for C_1 in N1 (blue) and N2 (orange) flow-fields.

"∧"-shape. This specificity is not observed for N1 flow conditions, probably because of the diffusive nature of the shock-waves.
The right graph shows distance of the most luminous point in the interaction (P_ml) which can also be related to the point of maximal local density. For SSI types I to III, the evolution of the distance is linear, and both conditions seem to behave similarly. The distance of N1 is slightly higher than for N2, which could be due to the increase in the rarefaction level, but the difference is not much more significant. However, from SSI type IV, the flow conditions seems to mark a difference. For N1, P_{ml} slowly goes away from S_2, but if looking back to Figure 7.8, the trends follow those of the BL, as if this last was not impacted by the SSI for type IV to VI. For N2, the same observation cannot be made since the BL seems to be deformed as the MS is. This means that the incident shock penetrate more deeply the bow shock of S_2 when the rarefaction level is lower.

With the images, it is also possible to analyse the intensity level, that are representative of the local density. In Figure 9.5 are plotted I_{02}, the intensity at $P_{0_{BL}}$ *i.e.* the maximal intensity at the nose of S_2, and I_{ml}, the intensity at P_{ml} (see Figure 5.11). Both are normalised with I_{01} so that the two flow-field can be compared. At the nose of S_2, the evolution of intensity in the left graph is similar for both conditions. For type I, whether for N1 or N2, I_{02} is equal to the reference value, which was expected since S_2 is mostly located in the free-stream flow. As S_2 gets down, entering the incident shock, I_{02} increases until type IV, where it reaches a peak. For N1, we saw that this peak corresponds to the position of S_2 where its wall pressure is the highest, so we can think the same for N2. Then, one S_2 is mainly below the MS of S_1, I_{02} decreases, and even reaches values that are inferior to the reference, which is due to a less dense environment. What is unexpected are the variations of intensity which are smaller for N2 than for N1, while it was described as a condition with stronger SSI impacts. Here it seems that this phenomenon is due to the rarefaction level. Indeed, considering a same volume of gas with two different densities, the compression rate will be higher for the less dense gas. This is what we observe here, N1 shows a higher compression rate at the nose of S_2 than N2.
In the interaction area, the variation of intensity is quite different for N1 and N2. For N1, the maximal local density corresponds to the type IV SSI, where we observed the higher pressure peak; while for N2, the intensity reaches its maximum for the type VI SSI. For N2, this means that the local density in the interference area is not obtained because of the SSI but to the merging of the incident shock with the bow shock of S_2 that form one single stronger shock-wave. Since the highest density are located on the upper part of S_2, it can be imagined that the lift forces will be mainly negative when S_2 is positioned so as $\Theta_i > 0°$.
All these observations seem to show that when the flow is more rarefied and viscous, the local effects of the

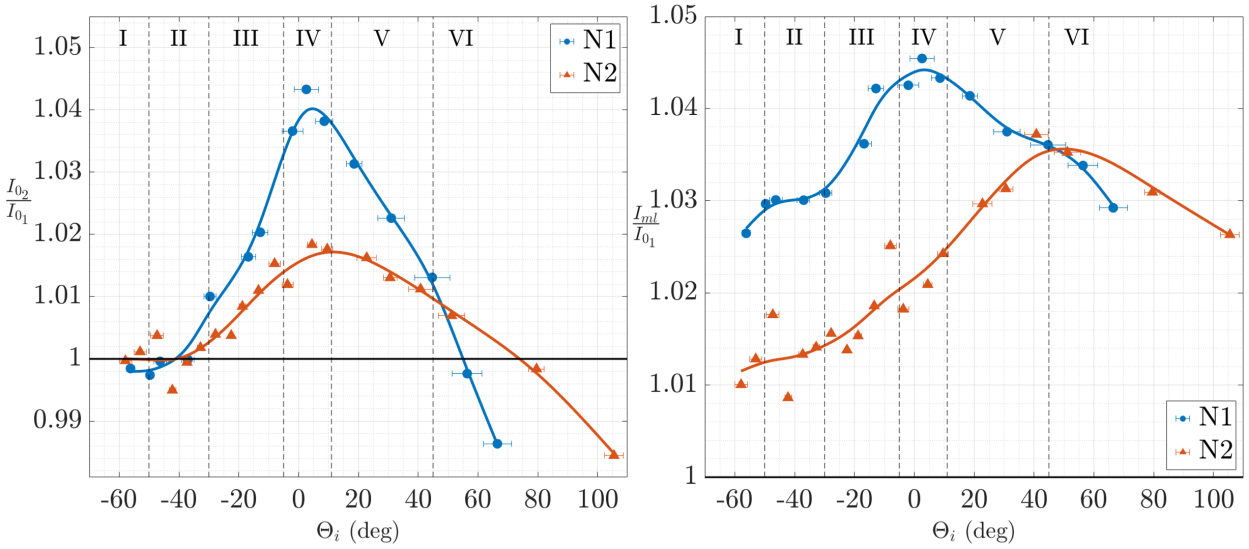

Figure 9.5: Normalized luminous intensities of $P_{0_{BL2}}$ (left) and P_{ml} (right), for C_1 in N1 (blue) and N2 (orange) flow-fields.

interaction are amplified compared to the corresponding reference values.

9.1.2 Aerodynamic forces

The numerous images recorded (see Figure F.3 and Figure F.4) allowed to select six locations: one for each type of SSI. For these locations, the aerodynamic forces endured by S_2 were recorded with the balance described in 5.4.1. Results are shown in Appendix G (Figure G.1 and Figure G.2), and plotted in Figure 9.6 along with the results obtained for C_1 in N1 flow-field. In the left graph, the drag forces are normalised with the reference drag force which values are given in Figure D.1. The lift forces, shown in the right graph, cannot be normalised since the lift of the reference case is 0 mN in both conditions; however some differences will be discussed.

The drag forces obtained for N1 and N2 show a similar evolution. For type I, where S_2 is mainly located in the free-stream flow, the drag is that of the reference. As S_2 goes down, it suffers more and more from

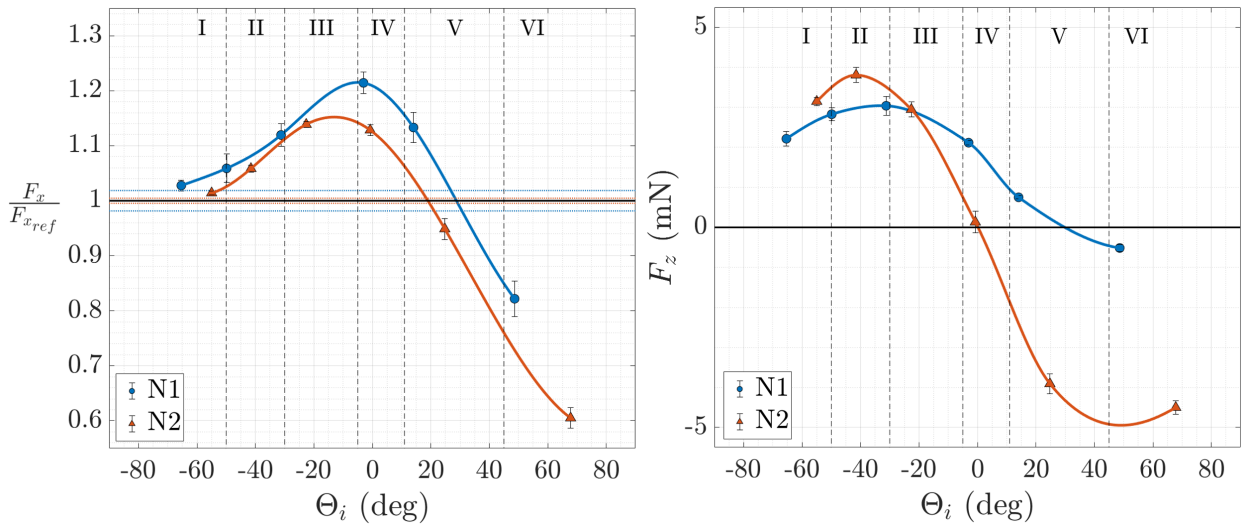

Figure 9.6: Drag and Lift forces, for C_1 in N1 (blue) and N2 (orange) flow-fields.

the influence of the incident shock which increases its drag force. Beyond a certain altitude, the influence of the incident shock on S_2 decreases, resulting in the decrease in drag force. Once the sphere is mainly in the wake of S_1, as the flow density and pressure are lower than that of the free stream, drag force value are inferior to the reference. Two remarks can be made when comparing the two flow conditions. First, as for the luminous intensities, N2 normalised drag forces are lower than that of S_1, which means that the SSI have less impact on the aerodynamic of S_2, proportionality to the free stream. Moreover, the maximal drag force is not located for the same interaction angle: for N1, $F_{x_{max}}$ is reached for $\Theta_i \approx -4°$, while for N2 it is obtained for $\Theta_i \approx -12°$. As a consequence, the maximum is not even reached for the same type of SSI: type IV for N1, and type III for N2. Thus, as the level of rarefaction decreases, the maximal longitudinal repulsion of S_2, which decreases, appears for higher altitudes of S_2. The longitudinal attraction also appears for higher altitude, but this time increases with the decrease in Knudsen number.
The lift forces also show similar evolutions. However, if the lift forces of N1 are mainly positive, it is not the case for N2, for which, once S_2 is below the MS of S_1, sees its values becoming negative. Besides, we observe that for N2, on the negative side, values are higher, which means that, transversally, the attraction is preponderant over the repulsion.

The resulting force, $\vec{D_F}$, calculated with Equation 8.3, represents the displacement of S_2 towards S_1, as shown in Figure 9.7. In both conditions, when S_2 is mainly above the incident shock, for types I, II (and III for N1), it moves away from S_1 almost radially. It is interesting to observe that type IV in N1 and type III in N2 follow the same direction. This specific behaviour corresponds to the interference angle for which the maximal drag force is reached. In Figure 9.8, the trajectories of both experiments have been plotted on a same graph, along with the localisation of the different regions of the shocks. For the two positions previously mentioned, corresponding respectively to $Z_2 = 22.6$ mm and 26.56 mm, we clearly see that the first one is beneath the MS, while the second one is above the FS. This means that the pressure in the shock-wave is not the only factor that generate forces. For the rest of the SSI, we clearly observe a difference in terms of directions, mostly due to the negative lift forces. Based on the results of chapter 8, we know the importance of the viscous effects on the lift forces. Here, N2 presents a lower level of rarefaction, thus, from Figure 6.17, viscous effects are also reduced. Consequently, the fact that the lift forces of S_2 decrease faster for N2 than for N1 as the sphere goes down is consistent with this statement. The wall pressure measurements presented in the next section will help evaluate the contribution of pressure and viscous effects.
Globally, for types I to III, S_2 is expelled by S_1 flow-field. For the other SSI types, S_2 is more easily expelled from the flow-field of S_1 in the N1 flow-field, and inversely more easily attracted in S_1 wake in the N2 flow-field. In the continuum regime, Register et al. [178] simulations showed that when S_2 is initially located in the wake of S_1, it hardly gets out of it. S_2 trajectory shows the sphere bouncing back against S_1 shock-wave before going to the other side of the shock, etc. Eventually,S_2 gets away from S_1 longitudinally,

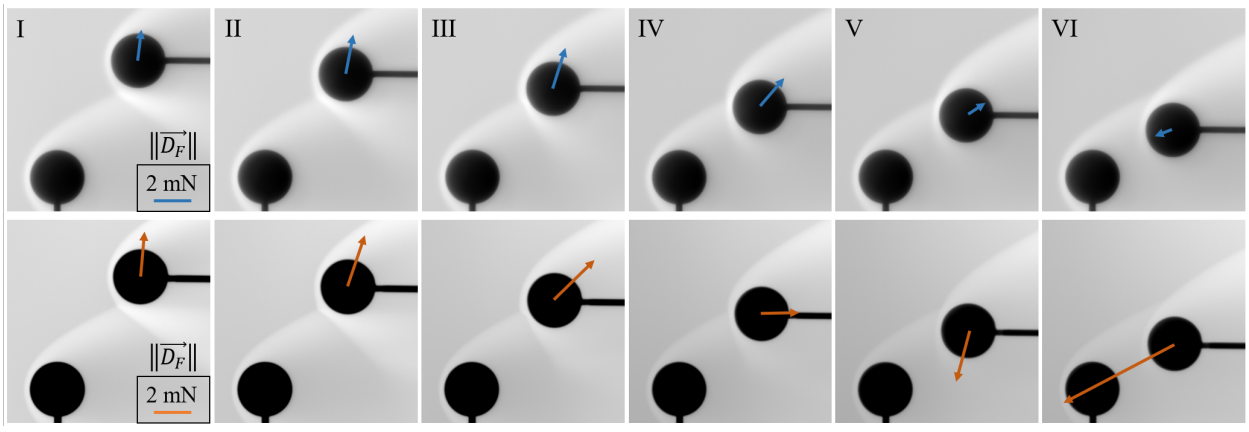

Figure 9.7: Displacement of S_2 towards S_1 on images, C_1 in N1 (top, blue arrows) and N2 (bottom, orange arrows) flow-fields.

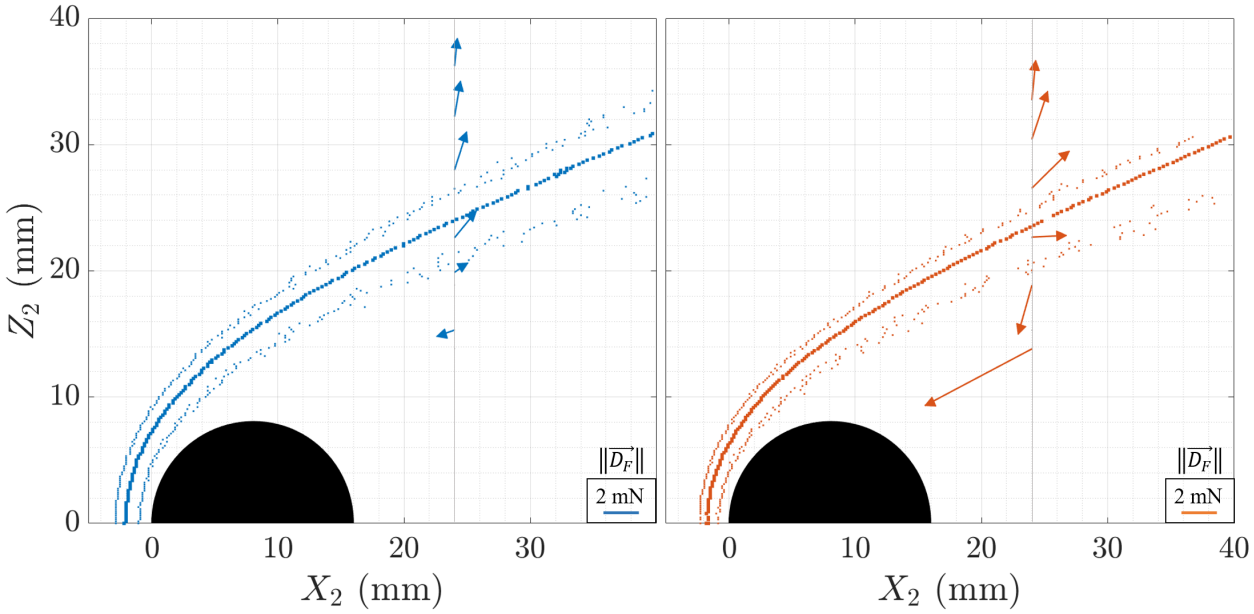

Figure 9.8: Displacement of S_2 towards S_1, C_1 in N1 (top, blue arrows) and N2 (bottom, orange arrows) flow-fields.

while remaining in the far wake of S_1. It seems that the conditions in N2 flow-field led to a behaviour of S_2 that matches more with these results than it is the case of N1.

Out of curiosity, we wished to search for a potential shock-wave surfing condition as discussed by Laurence and Deitering [115]. Unfortunately, as for N1, Figure 9.9 shows only one unstable location for $Z_2 = 24$ mm where S_2 is located just above the MS of S_1, corresponding to $\Theta_i \approx -10°$. For N1, it was located for $\Theta_i \approx 25°$ ($Z_2 \approx 18.5$ mm), thus, well below the incident shock. This equilibrium location corresponds, in fact, to the area where S_2 changes direction, as shown in Figure 9.8.
The drag and lift coefficients are presented in Figure 9.10 calculated with free-stream values (subscript ∞) and with the local flow-field seen by S_2 (subscript loc) obtained with the DS2V simulations.
The Cd_∞ and Cl_∞ both reveal higher values for N1 than for N2. The study of a single sphere in the free stream (section 6.3.1) showed that the drag coefficient increases when decreasing the Reynolds number after

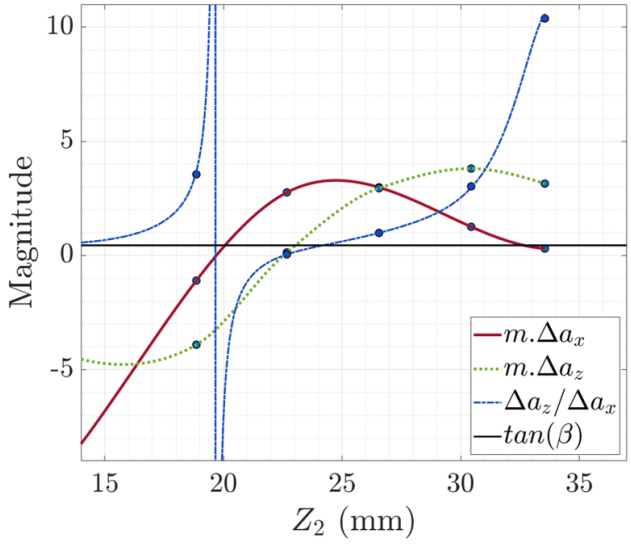

Figure 9.9: Shock-wave surfing detection for C_1 in N2 flow-field.

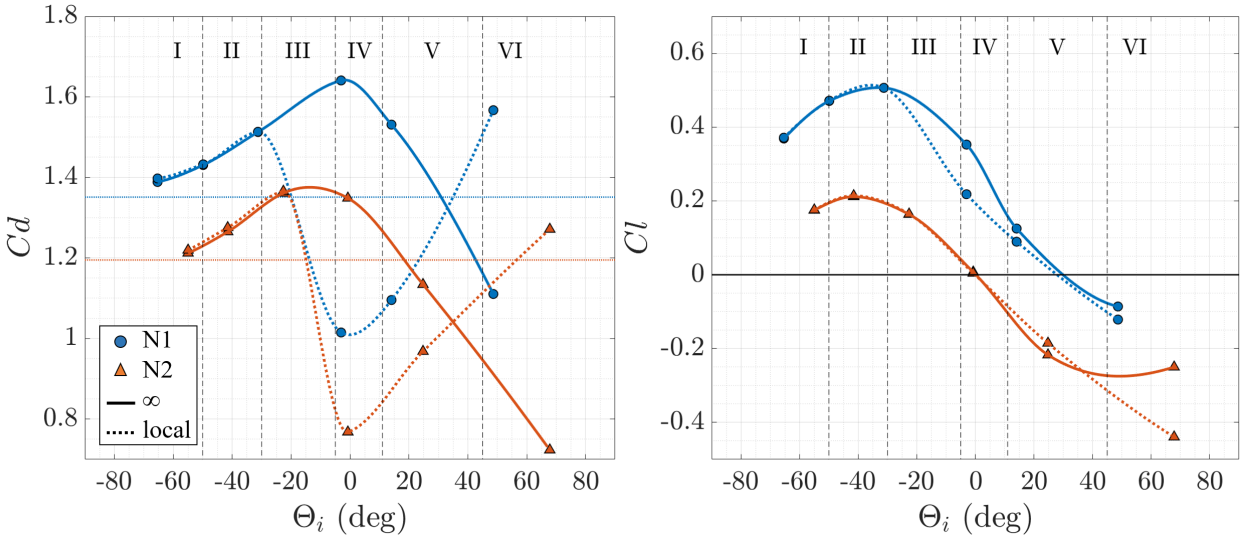

Figure 9.10: Drag and lift coefficients of S_2 for C_1 in N1 (blue) and N2 (orange) flow-fields.

shock. At iso-Mach number conditions, as it is the case between N1 and N2, a decrease in Re_2 implies an increase in Kn, thus to a higher level of rarefaction. As a consequence, a higher level of rarefaction induces an increase in drag coefficient, which is what we observe here. However, in the literature, it was shown by Schlegat [185] that the lift coefficient of a non-axisymmetric model increases with a decrease in the Knudsen number. Thus, our results disagree with those of Schlegat. In our case, the lift is not that of a single object, but is induced by the incident shock-wave. The free-stream pressure and thus the pressure in the incident shock decrease when increasing the rarefaction level. Still the lift coefficient increases, which means that, for a same sphere diameter, the pressure decreases faster than the force produced by the incident shock. As a consequence, we may think that the increase in Cl is due to an increase of the viscous effect in the incident shock, that partly compensate for the decrease in pressure. In the case of a single object in the free stream, as for Schlegat, since the model is not interacting with the incident shock, the viscosity of the flow alone must not be sufficient to compensate the decrease in pressure, which explains the decrease in Cl he observed.
Whether for the infinite drag or lift coefficients, we observe that the maximum value is reached for lower Θ_i, *i.e.* for a slightly higher location of S_2, as the level of rarefaction decreases. This difference in location might be due to the intensity and thickness of the incident shock. As the level of rarefaction increases, the density in the shock-wave decreases but its thickness increases. As a consequence, S_2 suffers a less impacting shock, the distances of shock stand-off (Figure 9.3) and of P_i and P_{ml} (Figure 9.4) showing a lower deformation of S_2 shock-wave for N1 than for N2. Moreover, for N2, the variations of the stand-off distances seemed to get closer to $\Theta_i = 0°$. This might reveal a more local deformation of S_2 shock-wave as the level of rarefaction decreases, which matches with the fact that the incident shock-wave gets thinner. Therefore, we can assume that, for N1, forces are lower but distributed on a greater area of S_2 surface, slightly changing the position of the maximal pressure forces. This point will be more extensively studied thanks to the wall pressure measurements describe in the following section.
The aerodynamic coefficient calculated with free stream conditions only reflects the forces endured by S_2, while, with the local coefficient, the local flow seen by S_2 is also taken into account. The local drag coefficient shows a very different behaviour than previously observed for infinite values. The trends of both conditions are similar but it can be observed that the curves are merging for the type III SSI. In order to better understand the aerodynamic behaviour of S_2, the local drag has been normalised with the reference drag in Figure 9.11. The types I and II SSI shows approximately a same impact on the drag coefficient. For the type III, we observe a drop of the drag for both conditions with a slight difference that might be attributed to the thickness of the incident shock, impacting S_2 for lower Θ_i in the case of N1. However, due to a lack of data for N1 in this area, we will remain cautious about this statement. Unlike Cd_∞, the drag coefficients pass through a minimum value. For both conditions, the minimal value is reached for the type IV SSI at $\Theta_i = 0°$, when

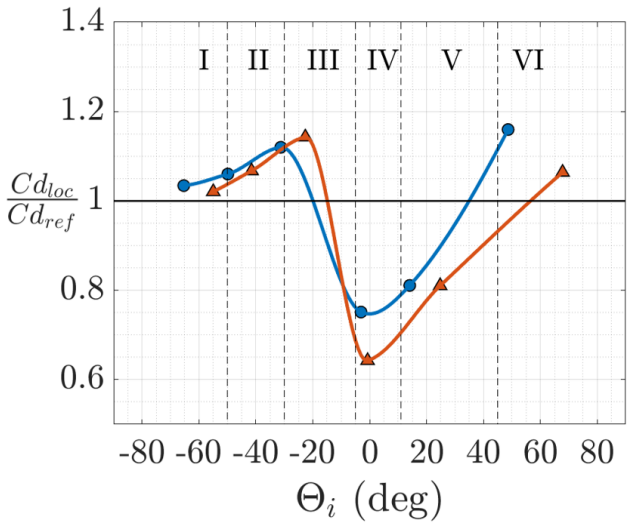

Figure 9.11: Normalized local drag coefficient of S_2 for C_1 in N1 (blue) and N2 (orange) flow-fields.

S_2 nose meets with the middle of the incident shock. From type IV to VI, Cd_{loc} is greater for N1 than for N2, which could be due to an increase of the viscous effects. The wall pressure measurements will help understand this increase.

9.1.3 Wall pressure distribution

Results of the wall pressure measurements are shown in Figure 9.12. Pressure values are normalised with p_{w_0}, the wall pressure at the stagnation point of the reference cases of each flow condition. The values of the reference cases are given in Appendix D (Figure D.2), and p_{w_0} is 54.17 Pa for N1 and 164.04 Pa for N2. This normalisation enables to highlight the differences of pressure distribution due to the rarefaction level.
For each type of SSI, a specific pattern appears, as already discussed in section 8.1.2. Whatever the type of SSI, it seems that the wall pressure distribution is slightly more impacted for N2 than for N1. Indeed, except for the type II, the pressure variations are more pronounced for N2. As a reminder, the analysis of the shock distances (Figure 9.3 and Figure 9.4) have shown a greater shock shape modification for N2 than for N1. Thus results of pressure distribution agree with the image analysis.
Using the pressure distribution, we identified the maximum pressure of each curve. The left graph of Figure 9.13 presents the normalised pressure peak for the different angle of interaction. These curves show a greater variation of the pressure peak for N2, the less rarefied case, in particular for SSI types I to IV. However, if the wall pressure is globally higher for N2, the pressure peak location does not seem to be impacted by the level of rarefaction. An exception may be considered between types II and III SSI, where the breakdown of the curve seems less important for N2 than for N1.
In conclusion, we observed that the impact of the SSI is greater for the lower rarefaction level, giving higher relative pressure values. However, the level of rarefaction did not show an evolution in the pressure peak location. These two remarks do not agree with the aerodynamic forces analysis. As a reminder, the previous section showed that the SSI impacted more the drag forces for the more rarefied flow-field, N1. Moreover, the maximum drag force was not obtained for the same interaction angle. Thus, the role of the pressure on the drag force has to be further investigated.
As already discussed, the pressure forces can be represented by the area under the curve of the wall pressure distribution (AUPC). Figure 9.14 shows the total normalised AUPC (in black). The solid line with symbols contoured in blue are associated to the results of N1, while dotted lines with symbols contoured in orange are associated to the results of N2. The total AUPC is decomposed, as shown in the left graph of Figure 8.14, with forces applied to the inferior part of S_2 (yellow lines for $\Theta_{wp} < 0°$), and those applied to the superior

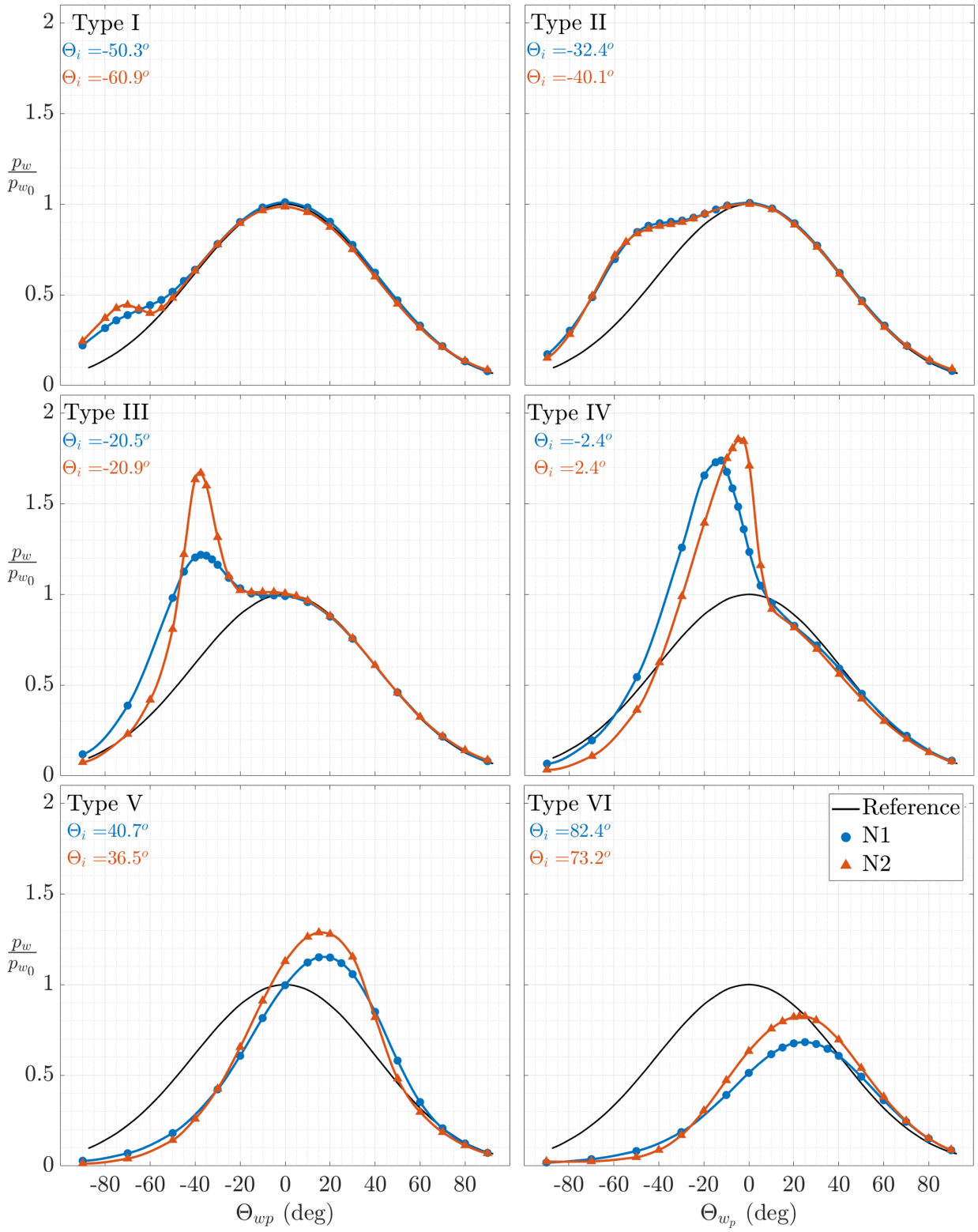

Figure 9.12: Wall pressure distribution on S_2 for C_1 in N1 (blue) and N2 (orange) flow-fields.

part of S_2 (blue lines for $\Theta_{wp} > 0°$). The total AUPC represents the pressure force applied on S_2. The evolution of the two flow conditions are similar. From SSI types I (close to the reference value) to III, the pressure force increases almost the same, with slightly higher importance of N2 for types I and II. However, the maximum of normalised AUPC shows two differences: it is obtained for higher position of S_2 and reaches lower values for N2 flow-field. Then from types III to VI, N1 flow-conditions give a higher relative pressure force than for N2. This evolution is not what expected regarding the pressure distribution analysis, but it is

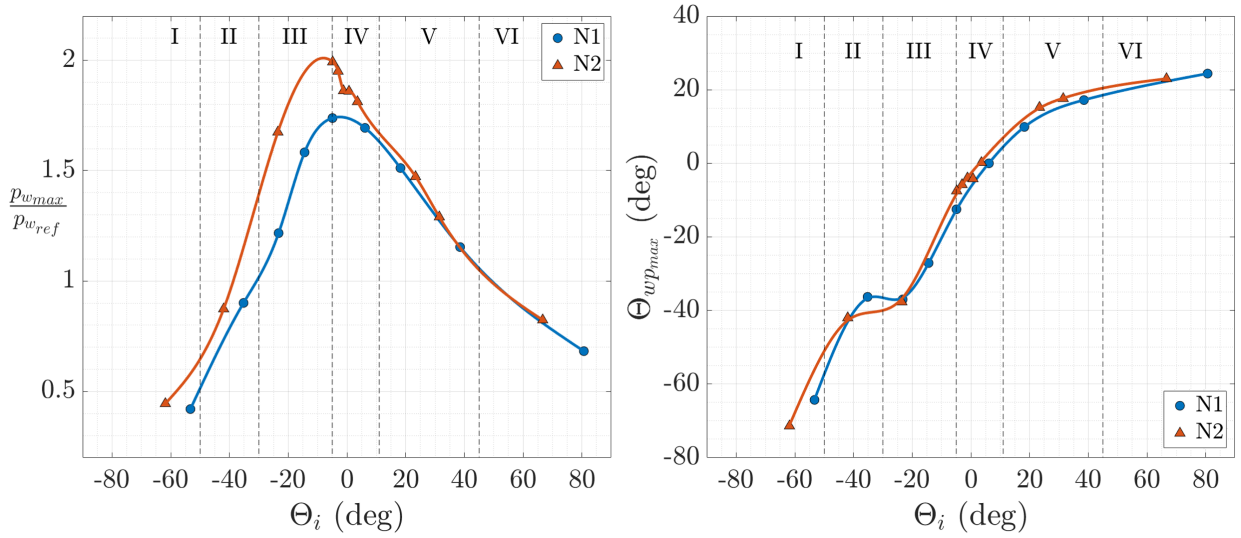

Figure 9.13: Value (left) and angle (right) of the maximal wall pressure peak on S_2 for C_1 in N1 (blue) and N2 (orange) flow-fields.

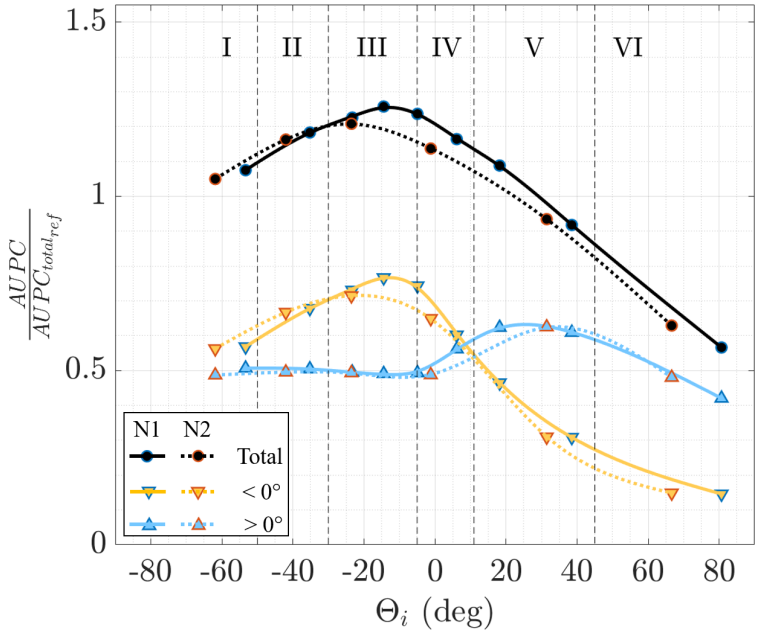

Figure 9.14: Normalized area under wall pressure distribution curves for C_1 in N1 and N2 flow-fields.

in a better agreement with the drag forces.

The pressure forces located on the lower part of S_2 ($< 0°$) shows slightly higher for N2 than for N1. As a reminder, if the main part of the pressure forces are located on the lower part of S_2, it contributes to obtaining positive lift forces. For SSI type I and II, it is the case, which might explain why the lift forces presented in the right graph of Figure 9.6 are greater for N2 than for N1. Then, the lift force values are, as the different AUPC curves, lower for N2 that for N1. For N1, the main pressure force repartition changes sides for $\Theta_i \approx 7°$, while it appears for $\Theta_i \approx 12°$ for N2. The lift force was shown to change sign respectively for 30° and 0°. Since the location for the change in pressure force sign does not match that of the lift, we can think that the viscous effects are involved in these variations.

To complete this statement, we studied the drag coefficient and the contribution of pressure and viscous drag. Results are shown for the local drag and lift coefficients, respectively in the left and right graphs of Figure 9.15. Concerning the drag coefficients, as previously mentioned, the total drag coefficient for N1 is higher than for N2. Regarding the pressure contribution, N1 values are mainly higher than those of N2,

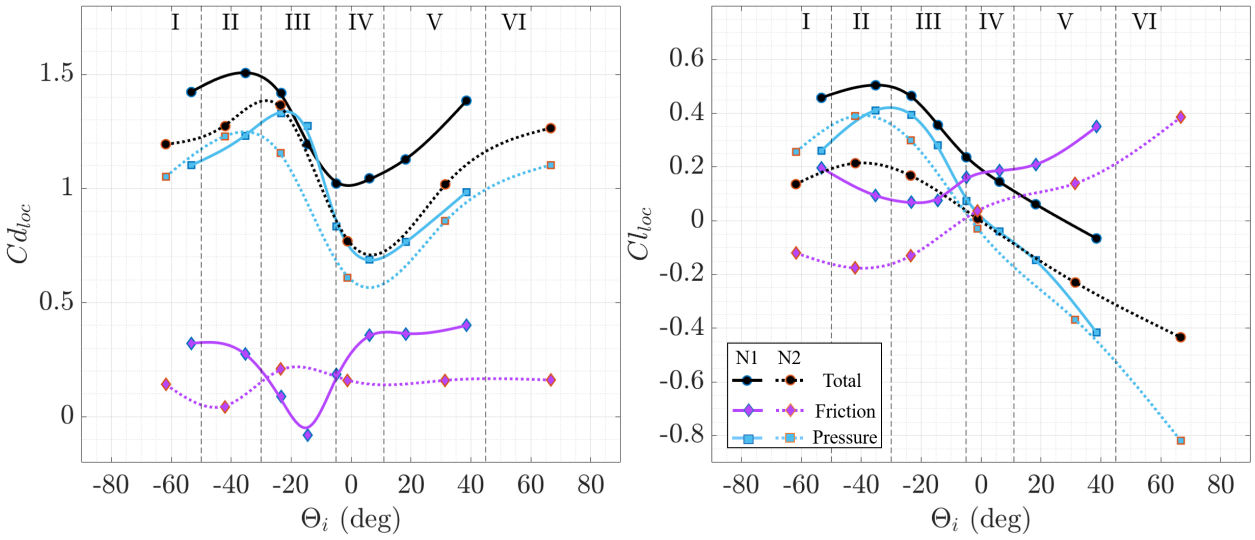

Figure 9.15: Contribution of the pressure and viscous effects in the total local drag (left) and lift (right) coefficients for C_1 in N1 and N2 flow-fields.

except for SSI types I and II. Also, the pressure contribution is maximal for the type III SSI for N1, whereas it is maximal for the SSI type II for N2. Apart from types I and II interference, the contribution of the pressure is more important for condition N1 than N2. This result seems contradictory, especially since the wall pressures show larger peak values for the N2 condition. Nevertheless, due to the rarefaction, the wall pressure peaks are larger for the N1 condition, which results in a larger overall contribution. With respect to the contribution of friction in the drag, for N2, it is almost constant with a slight decrease for the type II, and increase for the type III. In general, the condition N1 shows a higher contribution of the friction, except for SSI type III, where it reaches its minimum value, which is lower than that of condition N2. Observing the lift coefficient, the pressure contribution of both conditions is approximately the same, since the Cl_p are almost superposed. The friction contribution presents similar curves for both conditions, with an increase from the SSI types IV to VI where S_2 is gradually more and more immersed in the wake of S_1. Nevertheless, the contribution of friction is more important for the N1 condition, whatever the type of interaction. This explains why the lift coefficients are higher with the N1 condition while the pressure contribution is the same for both conditions. Finally, we can conclude that the lift is strongly impacted by the viscous effect and so by the rarefaction level.

9.1.4 Comparison with the continuum regime

In order to deepen the analysis of the global rarefaction effect, some results obtained by researchers in the continuum regime will be compared to our results.

9.1.4.1 Drag forces

In the continuum regime, Fisher [71] investigated the aerodynamics of a sphere free-flying in the flow-field of a first sphere, equal in diameter. His study was realised in a Mach 5 flow for Knudsen number ranging between $1.e^{-}5$ and $6.e^{-}5$. Even if the Mach number is slightly higher than our flow conditions, it seemed appropriate to compare these results from the continuum regime with ours. It is to be noted that we do not have the coordinates of S_2 for which force measurements were realised. Thus, the comparison is made with the given information, *i.e.* the type of SSI. It might be a little confusing since we do not exactly know where,

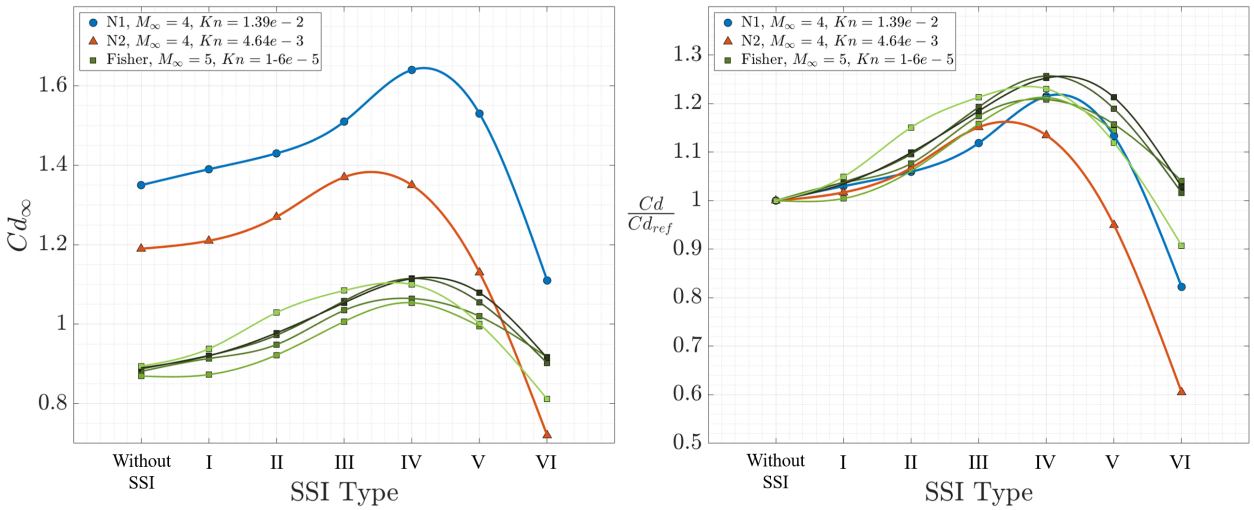

Figure 9.16: Drag coefficient Cd_∞ (left) and normalized coefficient (right) of S_2 for C_1 in N1 and N2 flow-fields, comparison with Fisher's results [71].

in the range of each type of SSI, measurements were made. For example, in our case, some points were measured at the transition between two types of interference and thus, classifying them by their SSI types is not much appropriate.

Also, the drag coefficients are calculated with the free-stream flow-field. Values of Cd_∞ are plotted in the left graph of Figure 9.16. We observe a similar drag coefficient evolution according to the type of SSI. However, depending on the flow conditions, the values of the coefficients are all the greater as the flow gets more rarefied. In our case, the maximal drag coefficient was obtained for a different type of SSI depending on the rarefaction level: type IV for N1 and III for N2. However Fisher obtained the maximal drag for the type IV SSI. At this point it is important to note that, if we consider the local drag coefficient Cd_{loc} (dashed line in the left graph of Figure 9.10), the maximum value differs from those determined with the free stream conditions Cd_∞. Indeed, from Cd_{loc}, the maximum value passes from type II to III respectively for the conditions N1 and N2. This could mean that as the viscous effects diminish, the maximum local drag coefficient tends to slide towards type IV. Nevertheless, it would have been more interesting to compare the drag coefficient according to the angle of interaction. This way, the results would have shown some nuances. However, considering the tendencies of the three test conditions to be equivalent, we do observe a strong decrease of the drag coefficient when S_2 enters deeper in the wake of S_1, *i.e.* for SSI types V and VI.

In the right graph of Figure 9.16, the drag coefficients have been normalised with the reference values. Previously, comparing N1 and N2, we observed lower values of normalised drag coefficients for lower rarefaction level, with a maximum found for a different type of SSI. However, this tendency is not confirmed with Fisher's results which are strongly similar to those obtained for N1. Again, this discussion might have been approached differently with the interaction angle. Nevertheless, it is to be noted that, in Fisher's experiment, S_2, the free-flying sphere, is not located on a vertical axis, but for different longitudinal distances. Thus, the results reflect the SSI occurring for slightly different flow conditions. Even if, in the N1 flow-field, a change in X_2 did not show much of a difference in terms of drag forces (see Figure 8.29), the hypothesis of a pressure variation cannot be excluded for the highly greater pressure of the continuum regime, where viscous effect might be non-existent.

The higher values of Cd for type V and VI in the continuum regime can come from the nature of the flow. Indeed, in the continuum regime, as is described in the left schematic of Figure 9.17, a trailing shock-wave is present in between the wake and the bow shock-wave. Vas *et al.* [202] made Pitot pressure profile measurements in the wake of a sphere in a Mach 16 flow for a Reynolds number of 90.800. Their results, presented in the right graph of Figure 9.17, show an increase in pressure due to the trailing shock, which is not observed in our conditions (see Figure 6.17). Behrens [23] made a similar observation in the flow-field

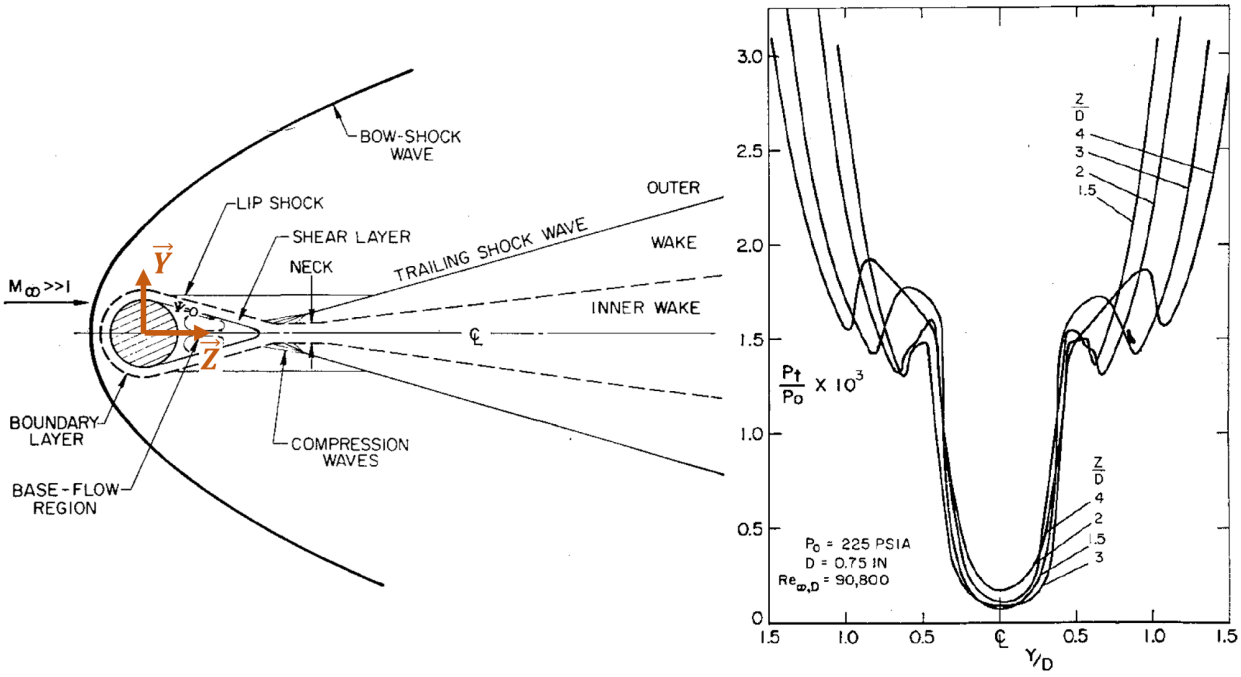

Figure 9.17: Left: schematic view of a sphere flow-field. Right: Pitot pressure profile in the near wake [202].

of a cylinder in a Mach 6 flow. By measuring the Pitot pressure profile for Reynolds number from 320 to 3840, it is shown that this trailing does not exist for the lower Reynolds number, which is in agreement with our measurements. Dewey [59] measured the flow speed for a Mach 6 flow with a Reynolds number of 3250. These flow conditions, close to those of Behrens for the Reynolds 3840, showed that in the trailing shock, an increase in the flow speed is also observed. Thus, below the incident shock-wave, the second sphere of Fisher could experience stronger forces due to the trailing shock. Since the way to measure the drag coefficient does not take into account the local flow conditions, this coefficient is only representative of the normalised drag forces. Thus, we cannot have a proper conclusion on the aerodynamic differences experienced by S_2 for different levels of rarefaction.

9.1.4.2 Wall pressure

In the continuum regime, Edney [65] measured the wall pressure of an interacting hemisphere to characterise the impact of SSI. The free stream is a Mach 4.6 flow with a Knudsen number of about 1.e-6. For this flow condition, the interacting hemisphere, called S_2 to ease the comparison with our case, is displaced around an oblique incident shock-wave, generated by a wedge. Edney measured the wall pressure of S_2 for the six types of interferences and different angles of the incident shock (β). In our case $\beta \approx 25°$, while the wall pressure distributions of Edney are given for $\beta = 15°$ and $20°$. The results' comparisons are presented in Figure 9.18. For each type of SSI, we recalled the image from Edney's experiment for $\beta = 15°$.
As can be observed, globally for the SSI types I, II and III, Edney's results are similar to ours, with the difference that the values of pressure peaks are more important in Edney's case because the pressure conditions of the flow are much higher. However, for the type IV SSI, a clear difference is observed between the continuum and rarefied regimes. In the continuum, the bottom part of the sphere, which is located below the incident shock, sees its wall pressure increases with respect to the free-stream values. From Edney's set-up, it can be seen that the hemisphere is positioned above the shock generator and not behind it. Yet, the flow-field just above a wedge, presents an overpressure. As an example, Khan *et al.* [102] simulated a Mach 2 flow in the continuum regime, which static pressure flow-field is shown in Figure 9.19. This figure clearly

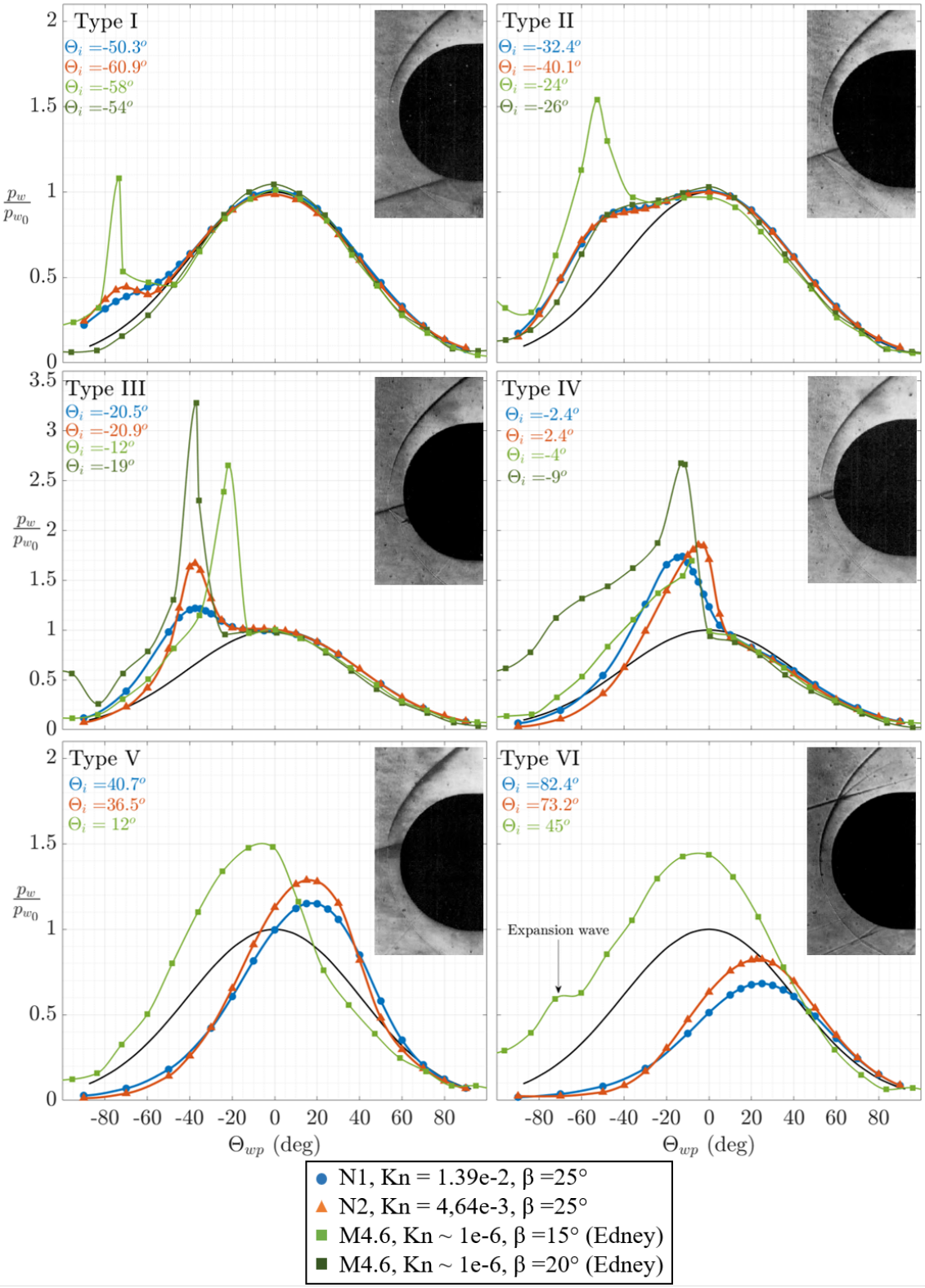

Figure 9.18: Wall pressure distribution C_1 in N1 and N2 flow-fields, comparison with Edney's results [65].

shows a great increase in pressure between the oblique shock and the surface of the wedge. Consequently, the increase in wall pressure on the bottom part of S_2 is most certainly due to an increase in static pressure in the flow between the shock-wave and the surface of the wedge that generates the incident shock. Concerning type V and VI SSI, we observe a maximal pressure around at the nose of S_2, where the pressure is 1.5 times that of the free-stream conditions. The same reasoning as for type IV is considered. As a consequence,

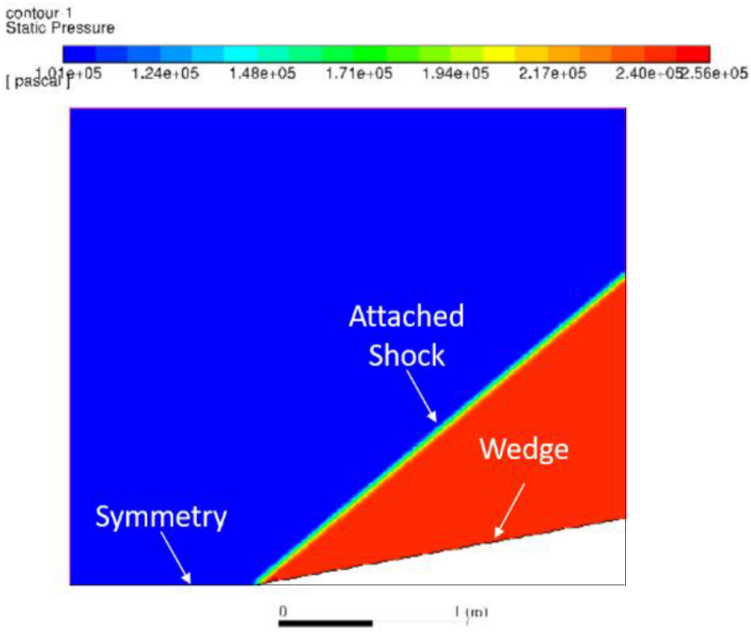

Figure 9.19: Static pressure flow-field around a wedge from Khan's simulation [102].

Edney's pressure distribution for SSI types V and VI is not representative of any disturbance that would be due to the effect of the shock/shock interferences.

For SSI type I to IV, in the intersection area, the main difference between the continuum and the rarefied regimes concerns the amplitude of the pressure peaks. To evaluate this behaviour, the maximal pressure peak values are plotted as a function of the measurement angle. The graph in Figure 9.20 presents the values of Edney for $\beta = 15°$, 20° and 25°, and ours for 25°. Concerning Edney's results, we can evaluate the impact of the angle of the incident shock. As the angle increases, the values of maximal pressure peaks increase too at an equivalent $\Theta_{wp_{max}}$. Another remark can be made concerning the peak of the curves which appears for lower $\Theta_{wp_{max}}$. This means that the angle of the incident shock has an impact on its penetration rate and on the impact location on S_2. Now, if looking at $\beta = 25°$ only, we will be able to estimate the influence of the rarefaction level. But, in the light of the wall pressure distribution discussed for types V and VI interferences, the angles above $\Theta_{wp_{max}} = -5°$ won't be analysed.

From N1 and N2 results, the distribution of maximal pressure begins with a gentle slope, which suddenly increases around -37° or -40°. Two aligned points (or almost) are then observed here, and were already discussed with the left graph of Figure 8.13 or Figure 9.13. This sudden increase is due to a shear layer observed for types II and III SSI, which orientation between the interaction point and the surface of S_2 seems to vary. Indeed, as the level of rarefaction decrease, it seems that the sudden increase vanishes in favour of a constant increase from types I to IV, if looking at Edney's results. For N1, after the sudden increase in $p_{w_{max}}$, the slope becomes way gentler, without leading to a strong peak. For N2, we saw that the sudden increase is gentler, and by fitting the points, a peak seems to appear for $\Theta_{wp_{max}} \approx -25°$. For Edney, there is no sudden increase for types II and III SSI, and the peak is well marked for $\Theta_{wp_{max}} = -25$. In conclusion, an increase in the global rarefaction level seems to decrease the impact of the SSI on the pressure peak. In particular the wall pressure is more widely distributed at the surface of S_2, less focused on a point of the surface as it occurs in a denser flow. Also the shear layer of SSI types II and III deviates which could be the consequence of the increase in viscous effects that reduce the penetration of the incident shock by diffusing it on a larger surface area. Agir *et al.* [1] also studied the effect of increasing rarefaction level on Edney shock patterns with DSMC numerical simulations. The investigated geometry is a wedge-cylinder in a free-stream flow with three different Knudsen numbers 0.0067, 0.0134 and 0.0268. As a reminder, the test cases studied here have a Knudsen number of 0.00465 for N2 and 0.0139 for N1, which is very close to the intermediate condition studied by Agir *et al.* Their results allow leading to the same conclusions even if the

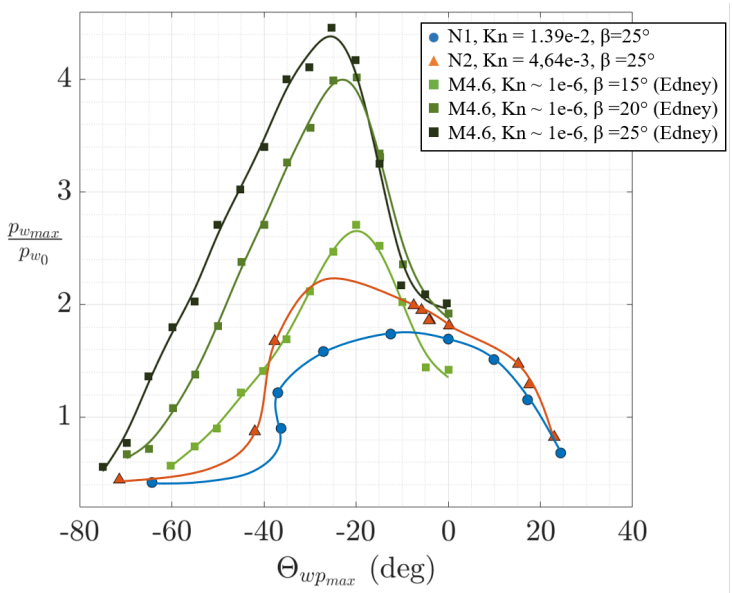

Figure 9.20: Maximal pressure peak along with its angles for C_1 in N1 and N2 flow-fields, comparison with Edney's results [65].

studied geometry is different.

9.2 Local rarefaction effects ($\emptyset_2 = X.\emptyset_1$)

The previous section highlighted the impact of the global rarefaction level of the flow by studying the SSI for the couple of spheres C_1 for two different flow-fields, generated by the Mach 4 nozzles N1 and N2. Here, we propose to study the SSI of one flow-field but for different diameters of S_2. The rarefaction level is characterised by the Knudsen number that takes into account the mean free-path and the size of the model. Thus for a same flow-field, a decrease in $\emptyset_2$ results in an increase in the local rarefaction level. For this study, we will compare, for each nozzle N1 and N2, the four couples of spheres, when possible. The comparison of results will be based on the analysis of images and on the measurements of aerodynamic forces.

9.2.1 Image analysis

Figure 9.21 presents an example of SSI flow-field visualisation. It shows the type III SSI obtained for all couples of spheres, placed in N1 (top images) and in N2 (bottom images) flow-fields. As can be seen, in both flow conditions, a decrease in S_2 diameter seems to reduce the luminous intensity gradient in the interaction area. For the couple C_4, it is even hard to clearly observe the shock-wave of S_2. As a consequence, it gets difficult to properly identify the type of SSI occurring at the vicinity of S_2, letting us think that the SSI effect slowly vanish as the local rarefaction level increase.
In this part of the work, we will base our comparison according to the interaction angle, that determine the type of SSI identified for the couple of spheres C_1. By observing the images and the evolution of the parameters for the couples C_2 and C_3, it seems that the types of SSI are obtained for the same ranges of angles that for C_1. Thus, we will consider the same SSI repartition for the couple C_4, for which the identification gets impossible.
Based on the images, and on the shock-wave detection, the points of interest P_{0_2}, P_i, and P_{ml}, as described in Figure 5.11, were identified. Unfortunately with the decrease in S_2 diameter, the lack of intensity gradient, in particular around S_2 made the detection of shock-waves difficult. Thus, the stand-off and interaction

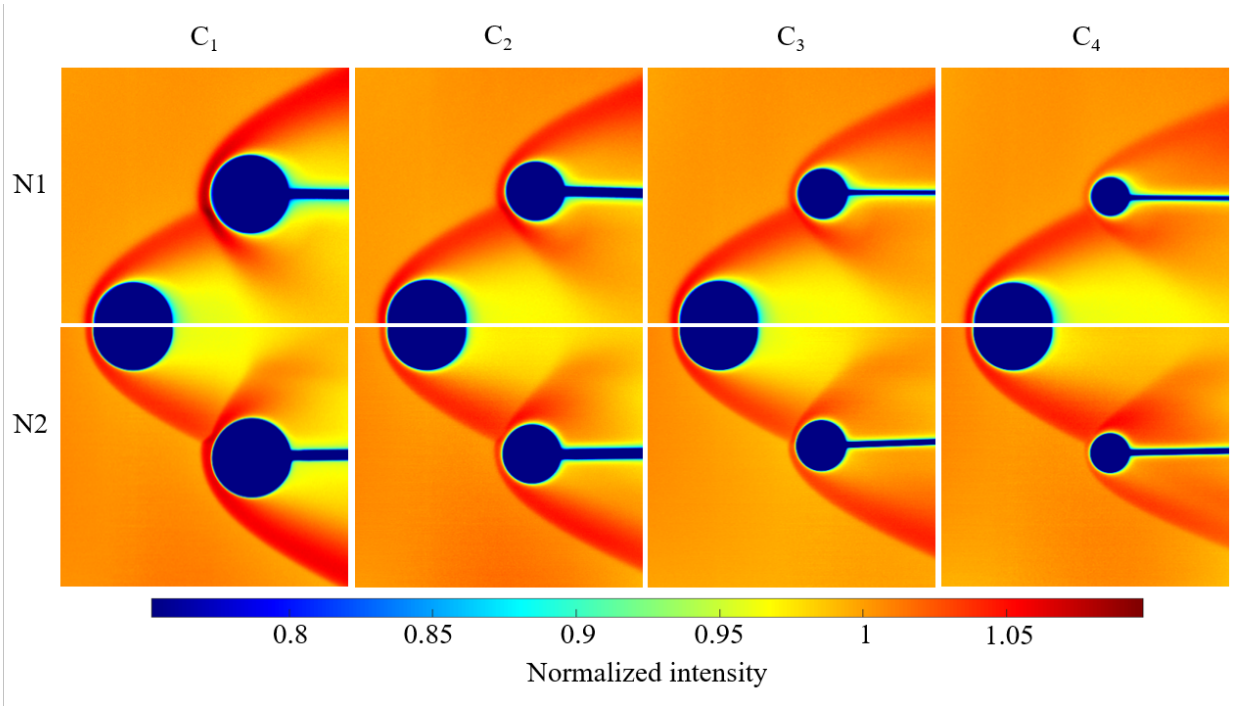

Figure 9.21: Normalized enhanced images of the type III SSI for the different couples of spheres in N1 and N2 flow-fields.

point distances measured around S_2 are less accurate. Moreover, it was not possible to obtain correct P_{ml} tendencies for C_2, C_3 and C_4 whatever the flow-field. Indeed, as the S_2 decreases, the compression of the flow in the interaction area decreases, and most of the time, the maximal intensity was not found near the intersection point. For this reason, we did not wish to present results which are not representative of the SSI impact on S_2.

Figure 9.22 presents the stand-off distances comparison of all the couples for the N1 flow-field on the right graphs, and for N2 flow-field on the left graph. Results of the FS (top), MS (middle), and BL (bottom) are normalised with the corresponding reference values, which are those of the second sphere when there is no SSI. The reference values are given in Appendix D, Figure D.1.

Whether for N1 or for N2 flow-field, we can notice that the trend of the three stand-off distances are very similar, whatever the size of S_2. From the numerical simulations made with DS2V, we calculated the local Knudsen number of S_2 for each couple and free-stream flow-conditions. The evolution of the Knudsen numbers are given in Appendix J. Here, since the couple C_4 did not allow to obtain a sufficient number of results in terms of stand-off distances, the maximum difference in Knudsen number is of 1.55, which is very little. As a reminder, for the comparison of the global rarefaction effect, the Knudsen numbers of N2 was three times that of N1, and even there, the differences in terms of stand-off distances were of maximum 16% from N1 results. Thus, for the study of the local rarefaction effects on the evolution of the stand-off distances, it would have been necessary to have a greater difference of sphere diameters. The poor differences in local Knudsen numbers, along with the decrease in the accuracy of results for the smaller spheres do not allow concluding in any tendencies.

However, another study is possible regarding the maximal stand-off distances obtained for the type III SSI. From the stand-off values determined for single spheres with different sizes in the two experimental operating conditions N1 and N2 (see Figure 6.8), relations were found between the Knudsen number and the stand-off distance for the FS and MS, as described by Equation 6.5 and Equation 6.6. These relations can be applied to determine the local Knudsen numbers from the values plotted in Figure 9.22. The left graph of Figure 9.23 plots the evolution of the calculated local Knudsen number (Kn_{loc}) for the maximum stand-off distances of the couples C_1, C_2 and C_3 in N1 and N2 flow-field, as a function of the free-stream Knudsen numbers

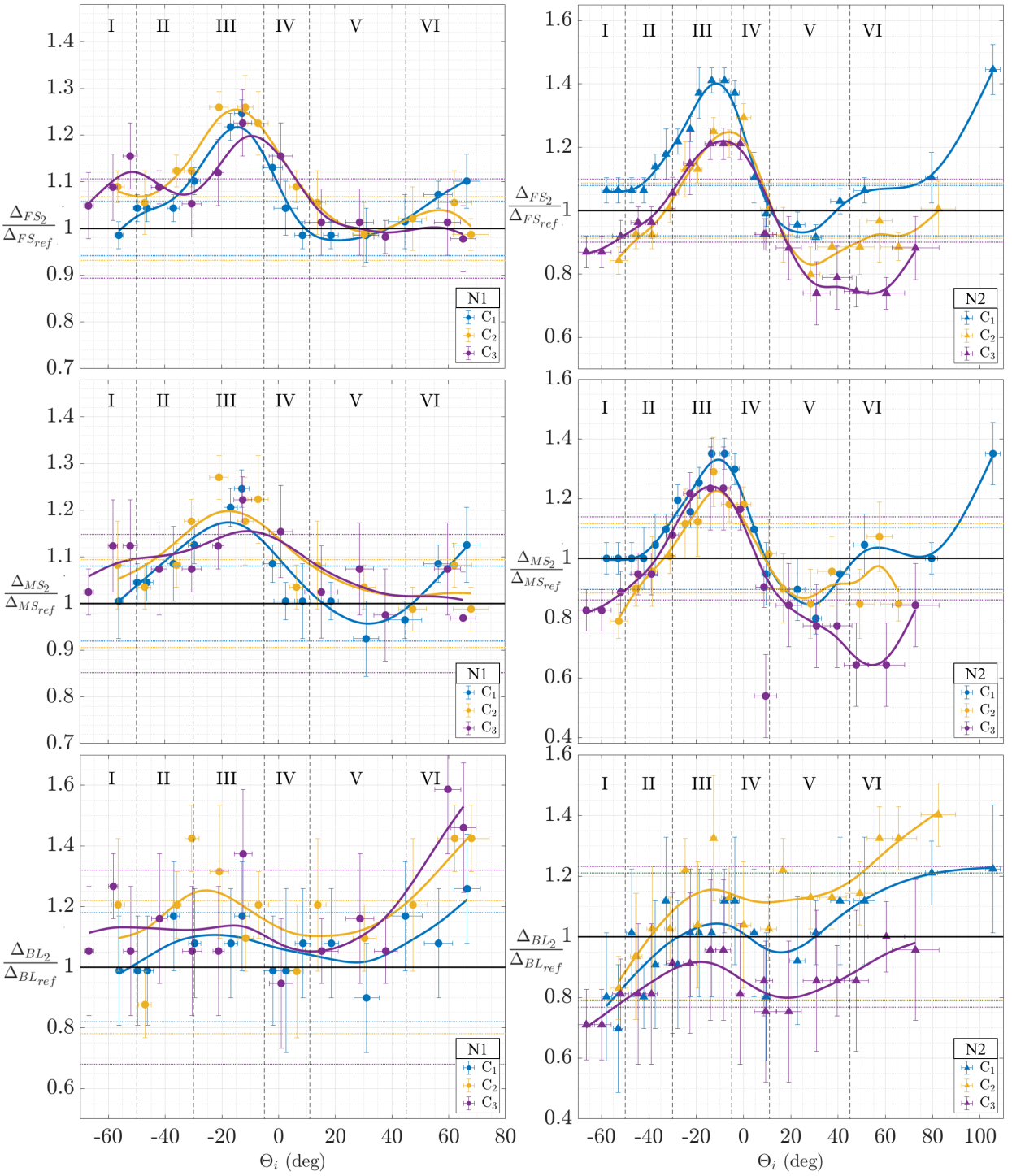

Figure 9.22: S_2 stand-off distances for all the sphere couples in N1 (left) and N2 (right) flow-fields.

(Kn_∞). The maximum stand-off distance is reached for the type III SSI, where the nose of S_2 is still in the free stream, so it is thinkable that the local Knudsen number is equal to Kn_∞. However, the general trend of the results shows an increase in the local Knudsen number with the increase in the global level of rarefaction, *i.e.* when the stagnation pressure and S_2 diameter decrease. One can notice that despite the inaccuracies for the stand-off distances determination, the local Knudsen values determined with the MS and the FS are very close to each other. All the values are greater than the corresponding Kn_∞. To evaluate the impact of the local conditions on the SSI, the difference between the local Knudsen number and the free stream Knudsen number are plotted in the right graph of Figure 9.23. Results clearly present an evolution of the deviation in

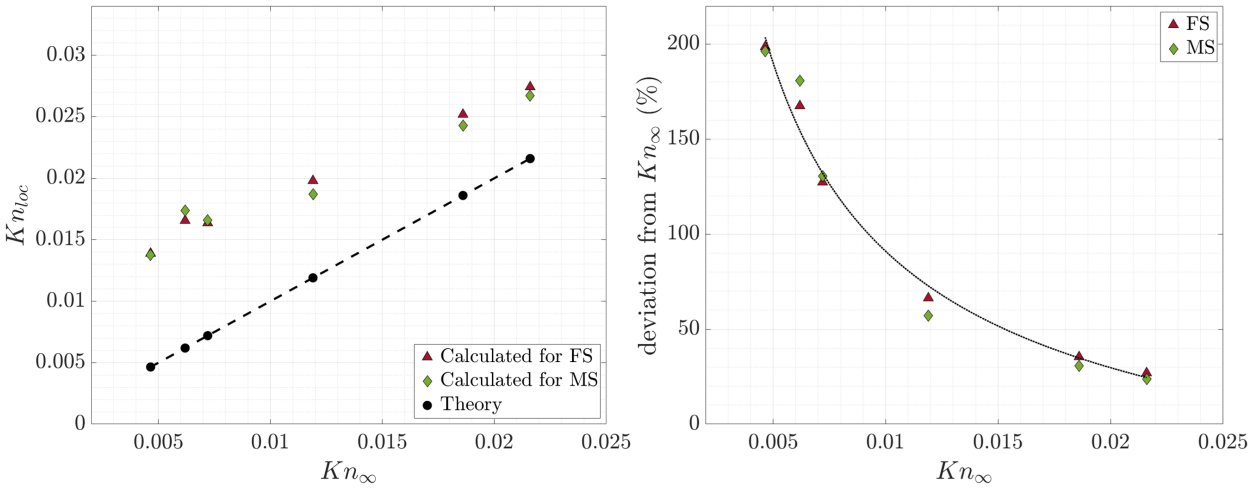

Figure 9.23: Left: calculated local Knudsen from the maximal stand-off distance. Right: Percentage of deviation between Kn_{loc} and Kn_∞.

Knudsen number. For N2, the differences range between 130 and 200 percent with a visible influence on the sphere size; while for the lower pressure conditions (N1), the differences ranged between 25 and 70 percent and the influence of the sphere size seems less significant. These results show that S_2 is more affected by the SSI in the denser flow, showing a greater evolution of the local parameters from the free stream conditions. In other words, the more the experimental conditions are rarefied the less the SSI are strong.

Even-though we could not draw a direct conclusion with the evolution of the stand-off distances, results tend to show an impact in the local rarefaction effect. To deepen this study, we focused on the distance of the intersection point P_i with the surface of S_2, d_i. Figure 9.24 shows the normalised distance d_i obtained for N1 (left graph) and for N2 (right graph) flow-fields. Since P_i is the point of intersection between the middle of shock, the normalisation is made with the MS stand-off distance values. As an example, for the couple C_4, S_2 is 8 mm in diameter, so d_i is normalised with the stand-off distance obtained for the 8 mm-diameter sphere in the flow-field.

For both the flow conditions, the four couples show globally a same trend, with a decrease in d_i as the interaction angle increase towards about 10°, between SSI type I to the transition between SSI types IV and V. Then for lower positions of S_2, while Θ_i, so does d_i. This evolution follows what previously described

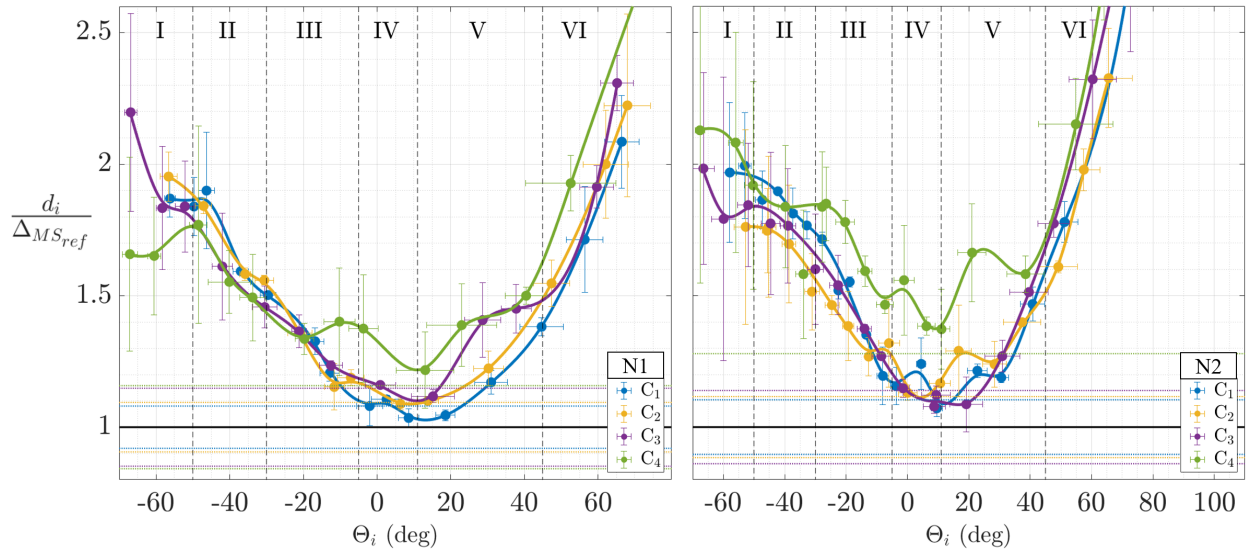

Figure 9.24: d_i for all the couples of spheres in N1 (left) and N2 (right) flow-field.

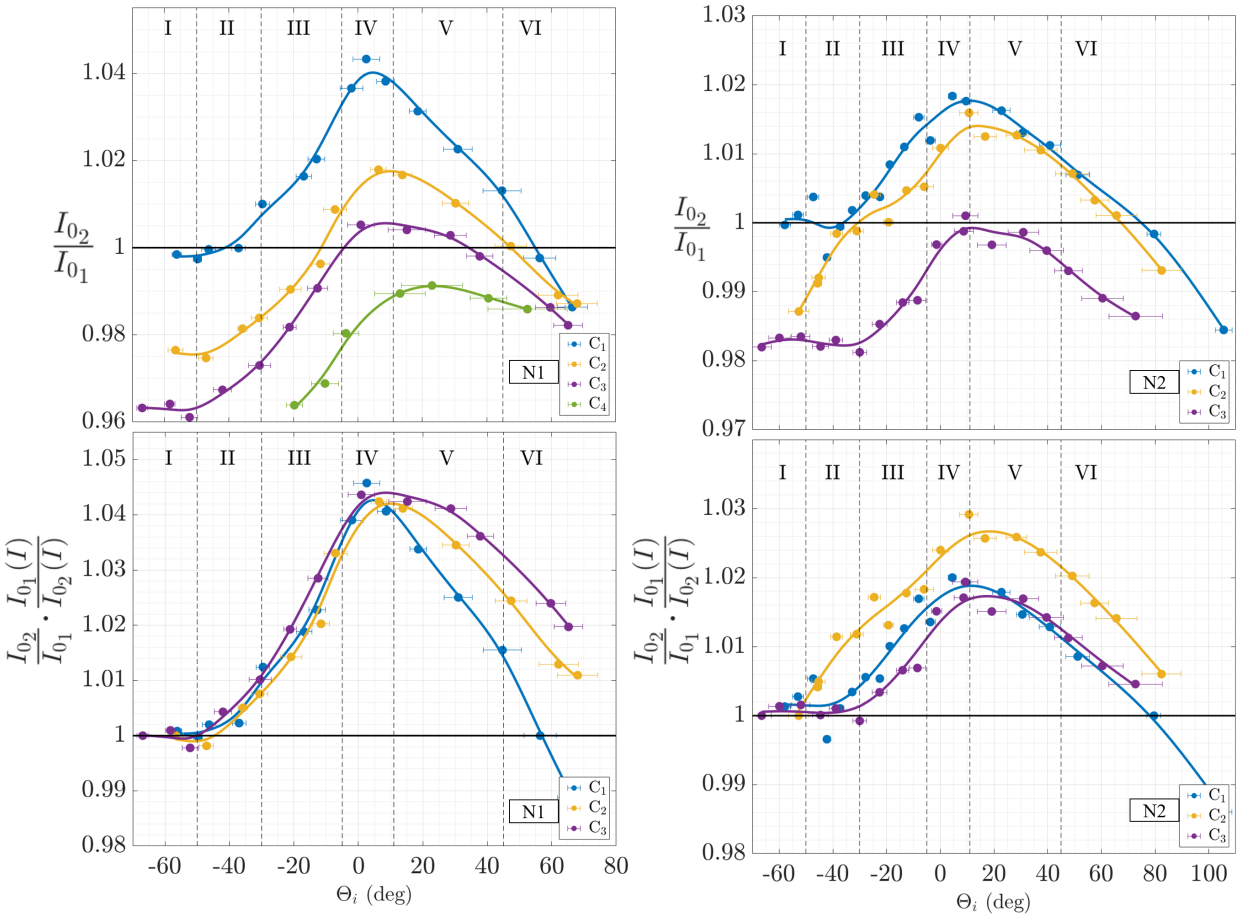

Figure 9.25: Normalized luminous intensities of $P_{0_{BL2}}$ for all the couples of spheres in N1 (left) and N2 (right) flow-fields.

for the couple C_1 in N1 flow-field (see left graph Figure 7.10). The couples C_1, C_2 and C_3 show similar normalised distances, while the couple C_4 seems to stand out with higher values. This would mean that, for a same incident flow-field, as the local level of rarefaction increases, the interaction point gets farther from S_2 surface with respect to the normal distance of S_2 shock-wave. This behaviour agrees with the left graph of Figure 9.23 showing the increase of stand-off distances as the Knudsen number increases. This statement does not agree with the observation made concerning the global rarefaction level (left graph of Figure 9.4), for which we found the opposite result: an increase in the global rarefaction level induced a decrease in d_i. The global rarefaction level is the reflect of the density level of the free stream, while the local rarefaction level is the reflect of the size of the object. It would mean that an increase in the rarefaction level does not have the same impact on the SSI if it is due to a decrease in the free-stream pressure or to a decrease in the size of the sphere as presented in Figure 9.23. Also, comparing results with both conditions, values obtained with N2 conditions are higher from the reference values and the effect of the sphere size is more noticeable, even if for the couple C_4, the inaccuracies are greater.

Contrarily to the measured distances presented in Figure 9.22 and Figure 9.24, the evolution of intensity values shows very significant differences due to the variation in the local rarefaction level. The intensity I_{0_2} corresponds to the most luminous point on the horizontal line passing through the nose of S_2, $P_{0_{BL2}}$. In order to compare the different images, values of I_{0_2} were normalised with I_{0_1} the intensity at $P_{0_{BL1}}$. Top graphs of Figure 9.25 present a comparison of these intensities depending on the size of S_2, for the nozzle N1 on the left, and for N2 on the right. In both conditions, a decrease in the diameter of S_2 leads to a decrease in the intensity level at the nose of S_2. Previously, Figure 9.21 showed that we indeed see a strong decrease

in the luminous gradient, whether at the nose of S_2, but also in the interference area for which we could not even locate the point of maximum luminosity P_{ml}. Thus results are consistent with our previous observation. For one flow-field, whatever the size of S_2, the flow density seen by S_2 is the same. However, the surface on which the molecules are impacted decreases with the diameter of S_2, leading to a less important compression rate, which explains the lower luminous and thus density gradient near S_2.
However, if it is intended to compare the impact of the level of rarefaction on the impact of the SSI, it is necessary to observe the differences on S_2 with and without interferences, and not with S_1, which diameter is 16 mm diameter in any case. For the cases C_1 in N1 or in N2 flow-field, the SSI type I showed intensity values that were approximately those of the reference. Thus, for each couple of spheres, we will consider the values of type I as the intensity value of S_2 alone in the free stream. The normalised results are given in the bottom graphs of Figure 9.25 for N1 (left) and N2 (right) flow-fields. As a reminder, the local intensity is the reflect of the local density variation. For N1, the tendency seems clear: for all the couples of spheres from type I to IV, there is a same increase of the local density at the nose of S_2 with respect to that of SSI type I. The maximum is reached around 5 to 10°, for the type IV SSI. Then, as S_2 goes down behind S_1, the local density decreases slowly. In particular, the slope is gentler for the smaller sphere. Indeed, due to a decrease in S_2 diameter, a same angle Θ_i will not reflect the same vertical location of S_2. As an example for $\Theta_i \approx 45°$, the $Z_2 = 16.5$ mm for $\emptyset_2 = 16$ mm, while $Z_2 = 17.5$ mm for $\emptyset_2 = 12$ mm. Thus, the difference in terms of altitude implies that S_2 will be closer to the incident shock, and thus submitted to higher pressure and density, when reducing its diameter. This difference is not observed for $\Theta_i < 5°$, when S_2 is mostly located above the incident shock, and thus the nose of S_2 sees the free-stream flow. Indeed, with the help of the Pitot pressure profile for $X_2 = 24$ mm (Figure 8.2), one can see that, above the incident shock, the pressure is not much impacted, while it is not the case, below it. Observing the three points aligned horizontally for a normalised value of about 1.025, $\Theta_i \approx 30°$ for C_1, 47° for C_2 and 60° for C_3, S_2 is respectively located at $Z_2 = 17.92$ mm, 17.52 mm and 16.71 mm. If the only parameter that changes the intensity level was the altitude, we would have found the same Z_2 for these three aligned points. This implies that the differences observed in terms of luminous intensity are partly due to the altitude of the S_2 nose, but also to local rarefaction effects. Concerning N2, the results are much less obvious. Indeed, we see that the couples C_1 and C_3 tends to agree with what was previously explained. However, the couple C_2 shows much higher normalised values. It is possible that a local error in the analyse of images did not allow obtaining correctly the reference value for the type I SSI, leading to a vertical shift when normalising the values of intensities. Indeed, the normalised values obtained for C_2 are much higher because the value of the type I used for normalisation is too low. In fact, as can be seen, the couples C_1 and C_3 have constant values for types I and II, while for the couple C_2, a decrease in intensity for the type I is observed, which could be considered a measurement error. If only considering C_1 and C_3, it seems that the tendencies described for N1 are globally followed. However, concerning the SSI types V and VI, the decrease of intensity seems almost not impacted by the decrease in S_2 size.

9.2.2 Aerodynamic forces

For each couple of spheres in N1 and in N2 flow-field, we selected six positions to cover a large range of interaction angles. For these positions, drag and lift force measurements were realised with the aerodynamic balance. The values of drag and lift forces are given in Appendix G.
In Figure 9.26 are presented the values of drag forces, normalised with the drag force of the single sphere of same size, which values are given in Figure D.1. These results are plotted for N1 in the left graph and for N2 in the right one. For both conditions, we observe the same evolution of the curves as presented for C_1 in N1 and N2 flow-fields: from SSI type I to III or IV there is an increase in drag force, and then it decreases, reaching values even lower than the reference case. For N1 and for N2 flow-fields, we observe that a decrease in S_2 diameter leads to an increase in the normalised drag force perceived by S_2. This means that, when the local level of rarefaction increases, the SSI have a greater impact on the drag force of S_2. Moreover, as

the size of S_2 decreases, a slight displacement of the maximal force is observed towards greater interaction angles, *i.e.* for lower altitudes. This maximal displacement was also observed in the left graph of Figure 9.6, in the comparison of the drag forces of the couple C_1 for N1 and N2 flight conditions. This means that the displacement of the maximum is not only due to the size of the sphere but is the result of a joint action with a variation of the global rarefaction level that induces an increase in viscous effects. As a result, for C_1 in N2 flow-field, the less rarefied case, the maximum is reached for the type III SSI, while for C_4 in N1 flow-field, the most rarefied case, it is reached for the type IV SSI. In addition, for N1 flow-field, the force values, compared to their respective reference values, are higher than for N2 flow-field. This shows that, in a more rarefied flow, the SSI are more impacting S_2 aerodynamics.

The local drag coefficients are calculated considering the local flow seen by S_2. The local parameters are obtained at the positions where the drag forces were measured from the DSMC simulations realised for the primary sphere ($\emptyset_1$ = 16 mm) in the N1 or in the N2 flow-field. The values of local drag coefficients are plotted in the top graphs of Figure 9.27 for N1 (left) and N2 (right). In both flow conditions, and for all the interaction angles, we observe an increase in Cd_{loc} when the sphere diameter decreases, which is consistent with the drag coefficients obtained for a single object with a varying Knudsen number. In order to compare the variation in drag coefficient due to a change in S_2 diameter, the coefficient values were normalised with the reference drag of a single sphere. Whatever the conditions of the flow and the size of the sphere, the coefficient of drag goes through a maximum between the types II and III, then through a minimum around the type IV. Nevertheless, these variations are more marked and localised for the less rarefied flow-field (N2). It should be noted that the minimum drag coefficient, reached for the type IV SSI corresponds to the type of interference designed to be the most critical in terms of heat flux load in the continuum regime. For all cases, the drag coefficient passes through the reference value for S_2 between types III and IV, and then, reaches a much smaller value for the type IV SSI, when the incident shock meets with the nose of S_2. In addition, whatever the flow, the minimum value gets lower as the size of S_2 increases.

The lift forces are presented in Figure 9.28. The curves form a sort of 'wave' shape with a maximum around type II and a minimum around type V. The maxima are all the more pronounced as the rarefaction effects decreases, taking into account both the density of the flow and the size of S_2. For the most rarefied cases, *i.e.* C_4 in N1 flow-field, the lift forces have a very small variation remaining always positive and ranging between 2 and 0.5 mN. Then, when the level of rarefaction decreases, the variation in forces becomes more important. As a consequence, the lift force passes through 0, first for the SSI type V and, as the level keep decreasing for the type IV. The results obtained in N1 flow-field (left graph), show two evolutions depending on the sign of the interaction angle. For $\Theta_i < 0°$, when S_2 is mostly located above the incident

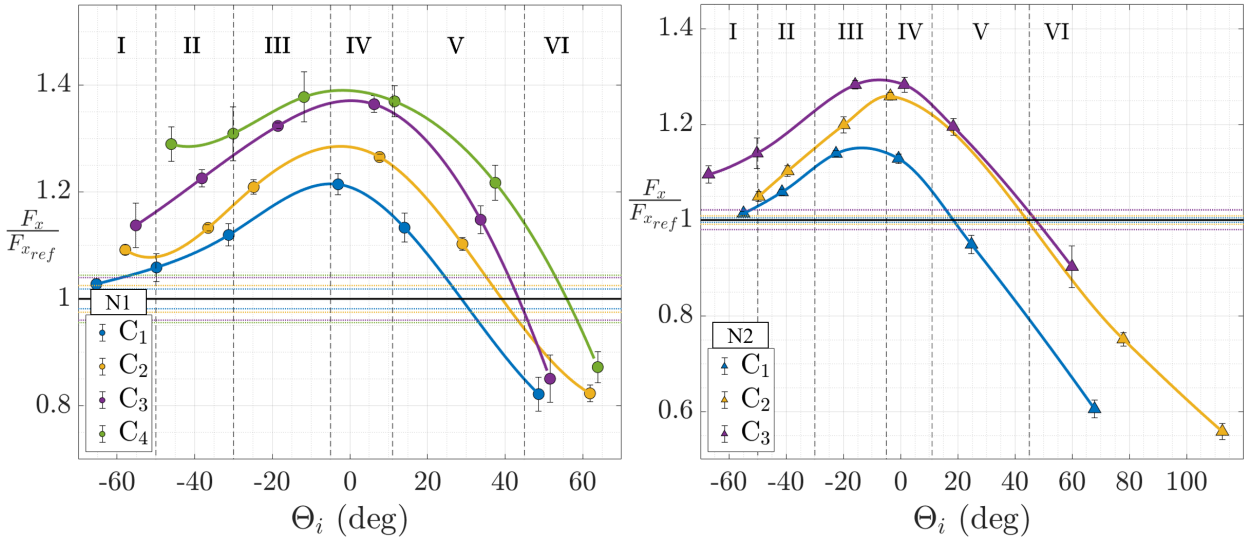

Figure 9.26: Normalized drag forces of S_2 for all couples in N1 (left) and N2 (right) flow-fields.

shock-wave, the lift force decreases with S_2 diameter. On the contrary, for $\Theta_i > 0°$, a decrease in S_2 diameter leads to an increase in the lift force. It is interesting to note that the type I SSI shows similar values of lift force, whatever the size of S_2. Whatever the size of S_2, the tendency of the four curves are globally similar, showing an increase in F_z between type I and II/III, and then a decrease. Two major differences can be noticed concerning the amplitude of the lift force variation and the positioning of the maximum lift force. As S_2 diameter decreases, so does the amplitude of F_z variations according to Θ_i. The increase between type I and II/III slowly vanishes reducing the peak of maximal lift force to a plateau. As for the decrease, as S_2 goes down behind S_1, no negative lift is observed, as if S_2 was attracted by the incident shock-wave. Possibly, if S_2 keeps going down in the wake of S_1, we might observe a negative lift for a brief range of altitude, before it reaches 0 for $Z_2 = 0$ mm. The other observation concerns the distribution of the lift maximum. A decrease in S_2 diameter displaced the maximum value towards $\Theta_i = 0°$. As for the drag force, the displacement of the maximum was also observed when comparing the N1 and N2 flow conditions for C_1. As for the drag coefficients, the local lift coefficients were determined and compared in Figure 9.29. In general, the highest values are observed for type II interactions, and then Cl decreases. The values are greater as the level rarefaction increases. From the SSI type IV, where the drag coefficient is minimum, the evolution of the lift coefficient changes. Indeed, for $\Theta_i > 0°$, S_2 enters the wake of S_1. As a consequence, the slope of Cl gets gentler and values even remains constant for the most rarefied case (C_4 in N1 flow-field). On the contrary, for the less rarefied case (C_1 in N2 flow-field), the lift coefficient keeps decreasing and even gets negative. This behaviour must be even increased in continuum regime.

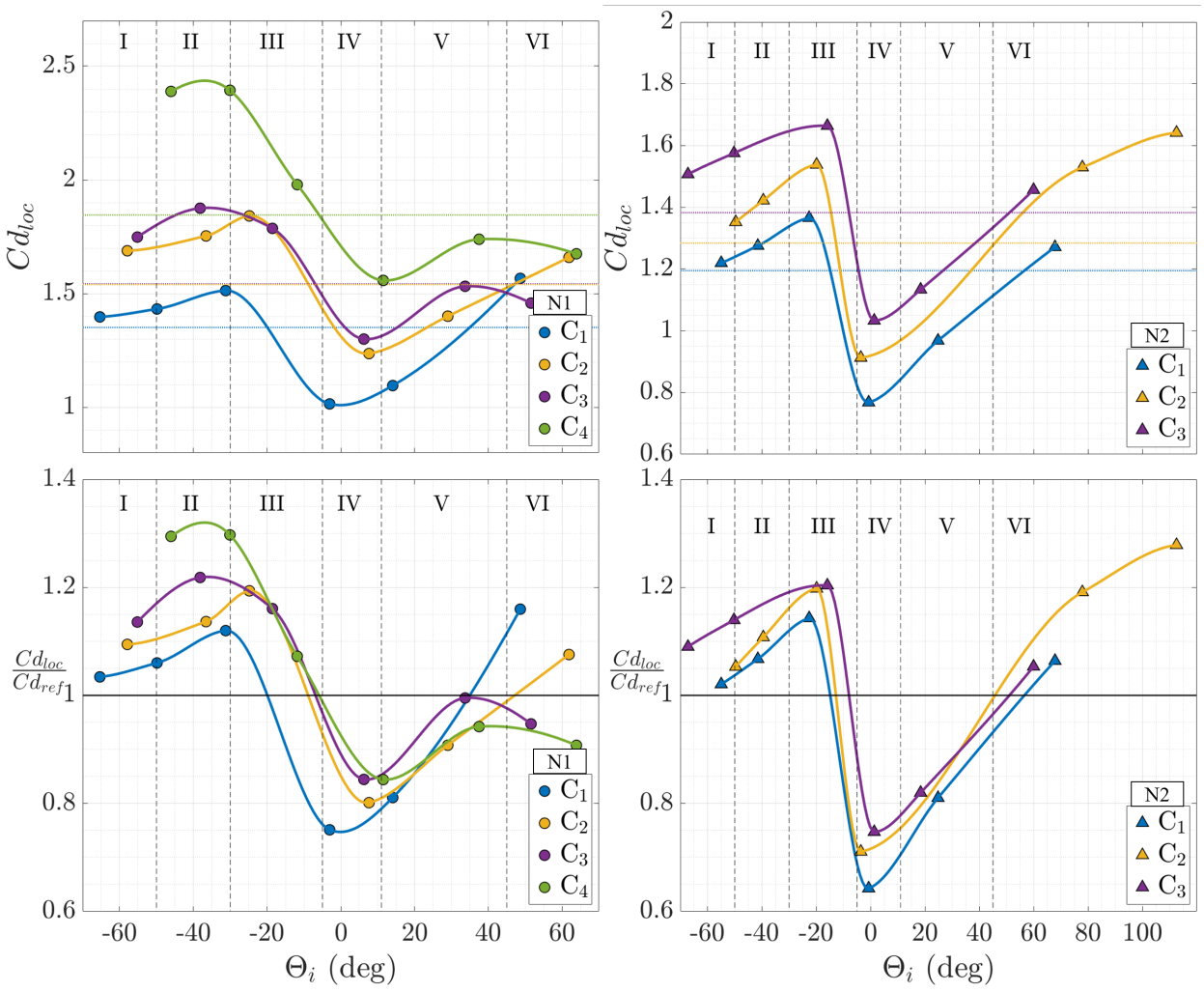

Figure 9.27: Local drag coefficients of S_2 for all couples in N1 (left) and N2 (right) flow-fields.

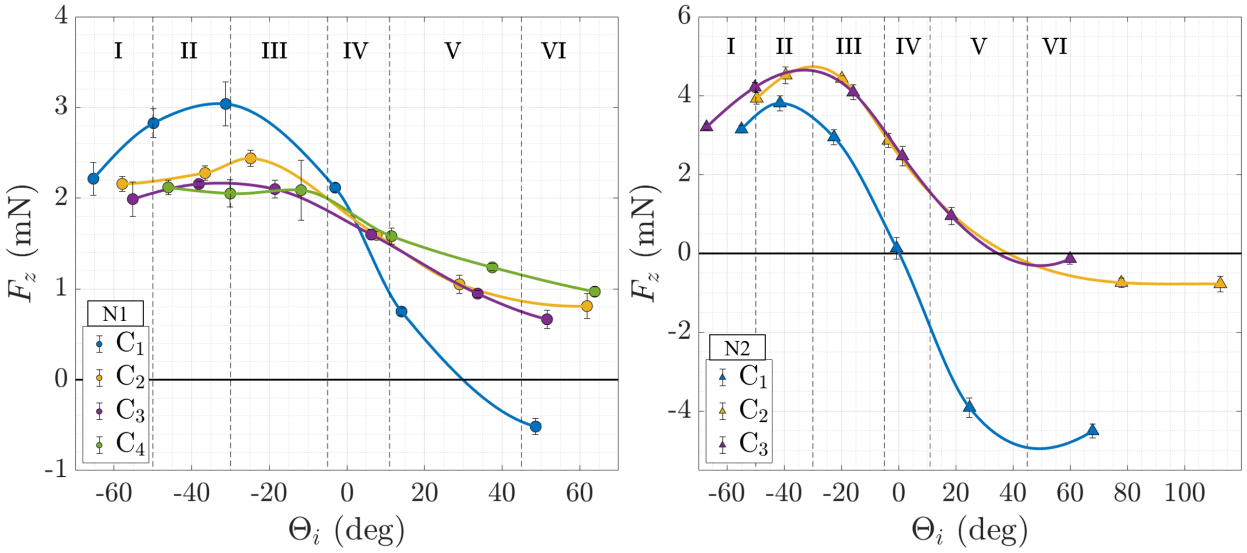

Figure 9.28: Lift forces of S_2 for all couples in N1 (left) and N2 (right) flow-fields.

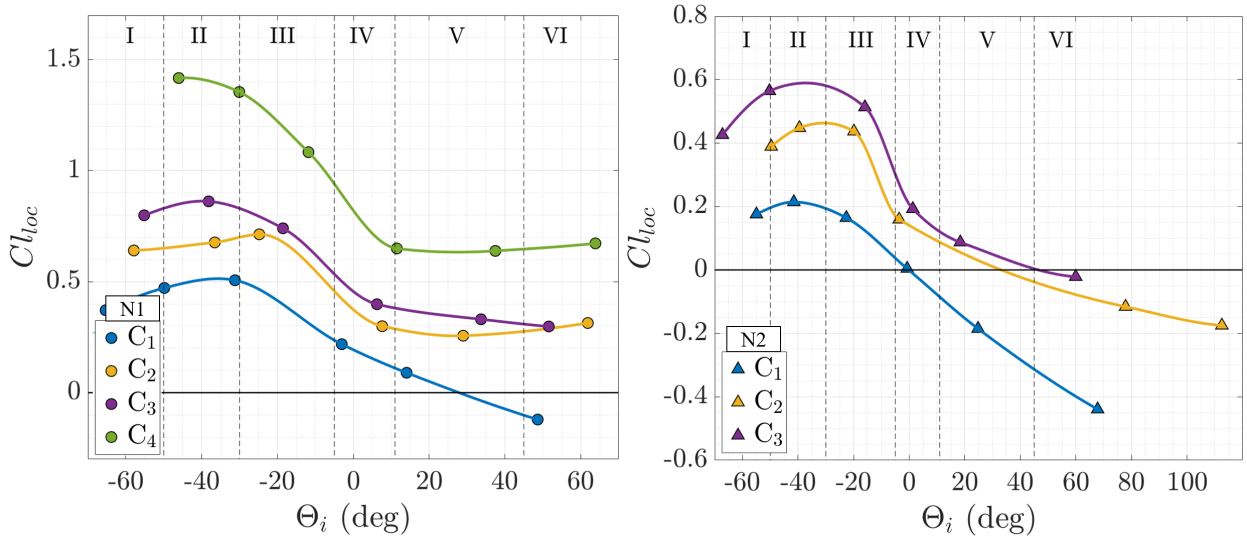

Figure 9.29: Local lift coefficients of S_2 for all couples in N1 (left) and N2 (right) flow-fields.

With the drag and lift force measurements, the displacement $\vec{D_F}$ of S_2 towards S_1 can be calculated with Equation 8.3. Here, it is desired to compare the behaviour of S_2 depending on its diameter for a same flow-field. To obtain the local displacement at a same location of S_2 nose, we interpolated the drag and lift forces according to Z_2. The displacements of S_2 towards S_1 for the two extreme diameters are given in Figure 9.30 for the N1 (left) and N2 (right) flow-fields.

In the N1 flow-field, the left graph of Figure 9.30 compares the local trajectory of S_2 for the couples C_1 ($\emptyset_1 = \emptyset_2$) and C_4 ($\emptyset_1 = 2.\emptyset_2$). In the N2 flow-field, the right graph of Figure 9.30 compares the local trajectory of S_2 for the couples C_1 ($\emptyset_1 = \emptyset_2$) and C_3 ($\emptyset_1 = 1.55.\emptyset_2$). In both cases, the small following spheres present a greater longitudinal displacement, in a completely different direction than for the big ones. It is also interesting to observe that, even if S_2 is located below the incident shock wave, it is not much pushed down by it. However, in these positions, the pressure forces are supposed to act mostly on the upper part of S_2. This could mean that the surface that endured these forces are too small to compensate the viscous effects, which are locally increased by the size of the sphere, and thus are getting predominant on the bottom of S_2 leading it to be pushed up or at least maintained at a same altitude towards S_1. This shows the importance of the size of the sphere. Even though we observed a same distribution of the drag and lift forces with a stronger impact of the SSI on the smallest spheres, it seems that the local rarefaction effects

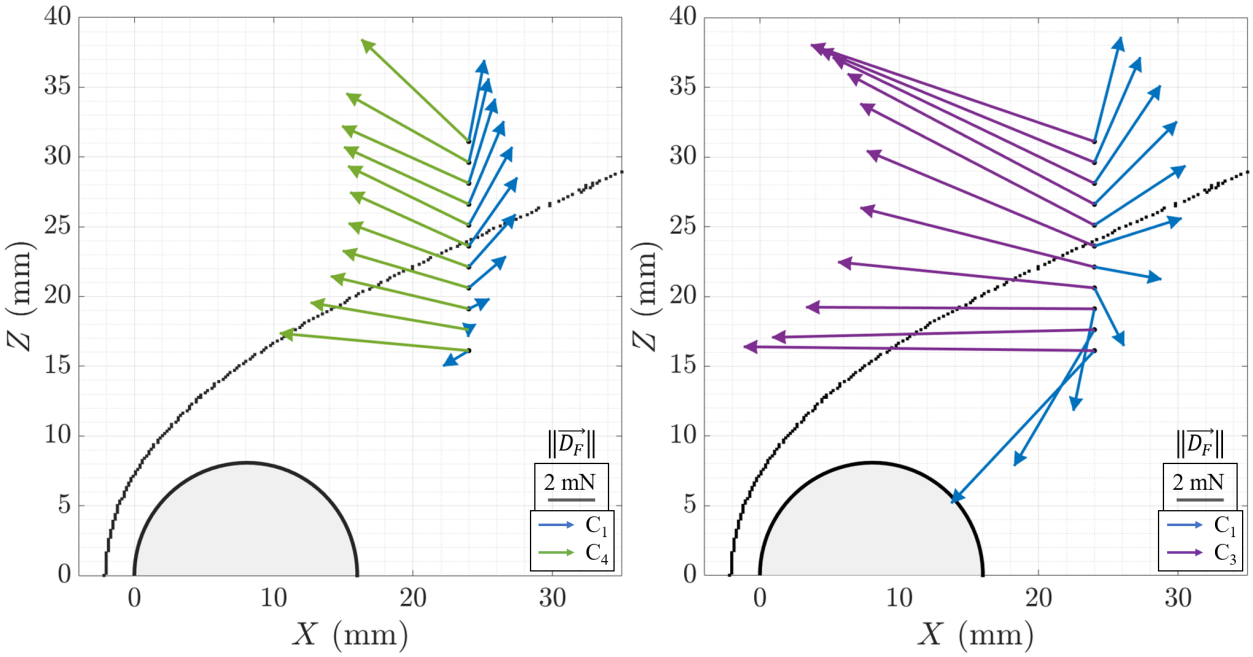

Figure 9.30: Local displacement of S_2 towards S_1 for C_1 and C_4 in N1 flow-field; and for C_1 and C_3 in N2 flow-field.

will have more impact on the local trajectory than the global level of rarefaction.

Chapter 10

Study of the sphere couple C_5 in N3 flow-field

Contents

This chapter focuses on the investigation of SSI in a Mach 20 and rarefied flow-field. The results obtained for the couple of spheres C_5, for which both S_1 and S_2 are 18 mm-diameter spheres were analysed to study the effects of hypersonic velocities and high level of rarefaction. The spheres are placed in the hypersonic rarefied core of the nozzle N3, which generates a Mach 20.2 flow with a free-stream pressure of 0.07 Pa. In order to observe and identify the SSI in this flow, different types of experiments were carried out. A first set of experiments was dedicated to the study of the SSI by moving S_2 on a vertical axis behind S_1 . The second one was dedicated to the mapping of S_2 drag force in the flow-field of S_1.

Due to the high level of rarefaction of the couple C_6, images did not allow obtaining accurately enough results to be enclosed in this work. However, some recorded images are presented in Figure F.7.

10.1 Case X2 = 27 mm : Effect of shock/shock interferences

The measurements presented in supersonic regime were made with a "parent" sphere S_1 of 16 mm in diameter. S_2 was placed on a vertical axis at X_2 = 24 mm, which gives a ratio of 3/2 with respect to the diameter of S_1. In the present case with the N3 nozzle, the diameter of S_1 is of 18 mm. Thus, to respect the inter-sphere distance ratio with supersonic results, the longitudinal coordinate of S_2, X_2, will be fixed at 27 mm. As a reminder, the infinite Knudsen number, calculated for S_1, is of $4.29.10^{-2}$. The global level of rarefaction experienced in N3 flow-field is 10 times higher than for the N2 and 3 times higher than for N1 for the 16 mm-diameter sphere.
In the present chapter, the analysis is based on images and aerodynamic forces, both recorded for a vertical displacement of S_2. This study will start with the analysis of the flow-field visualisation, obtained with the glow discharge technique; and on the aerodynamic forces endured by S_2, obtained with the aerodynamic balance and the swinging sphere technique. The wall pressure measurements were partly acquired, unfortunately, due to technical problems on the wind tunnel, experiments could not be completed.

In order to understand the impact of the SSI on the aerodynamic behaviour of S_2, it is fundamental to first analyse in detail the flow around a single sphere. Indeed, the hypersonic nozzle is conical and consequently the flow is not perfectly homogeneous. It presents a weak gradient in Mach number and in free-stream pressure. As a reminder, the Mach number and stagnation pressure flow-fields, given in Figure C.3, evolve depending on the location of the models. To give an idea of the variations in the core of the flow, we take the example of the Mach number. Along the flow centreline, a distancing of 10 cm in the $\vec{x}$-direction corresponds to 3% of variation. Transversally, the maximal Mach gradient is of 8% in the $\vec{z}$-direction from the centreline. For the purpose of our analysis, the results obtained for S_2 in interaction with S_1 will be compared to a reference value obtained for S_2 positioned at the same location but without S_1, facing the free stream. But as we have just explained, this flow has a radial gradient which means that depending on the height at which S_2 is located, the reference value will be different. Consequently, for each position, described by the interaction angle Θ_i, the reference values will change. Thus, for each position S_2 studied, it is necessary to make two measurements: one with S_1 and S_2 in the flow, and the other with only S_2 in the flow called $S_{2_{ref}}$.

10.1.1 Image analysis

As it was done in the case of supersonic conditions, the image analysis will first allow to identify the types of interferences, and see if the same classification as before can be applied. In a second time, a more detailed analysis will make it possible to analyse the variations of local intensities that reflect the variation of local density.
A large set of images was recorded for X_2 = 27 mm. The enhanced normalised images resulting from the

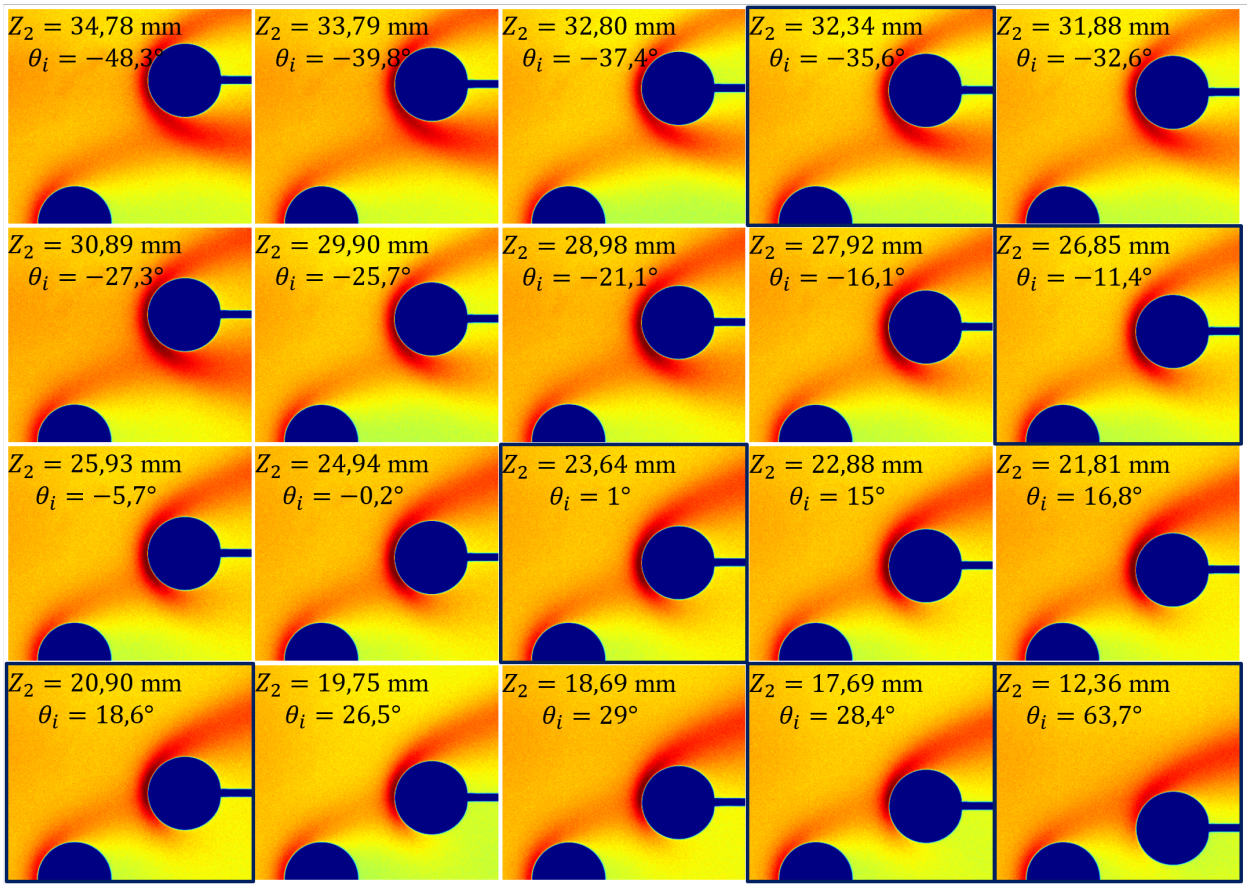

Figure 10.1: Enhanced images resulting from the experiment with C_5, N3 for $X_2 = 27$ mm.

analysis are given in Figure 10.1. These images do not make it possible to clearly identify the particularities of SSI which would have enabled a classification. The shock-wave of S_2 does not seem to be much impacted by the presence of the incident shock-wave in the interaction area. The physics which governs the phenomenon seems to be different from that observed in the experienced supersonic conditions. Indeed, no strong modification of S_2 shock-wave is observed that would be due to a SSI. It is, therefore, clear that the Edney type classification cannot be applied here. One might think that, due to the present Mach 20 conditions, the effects of velocity could produce more significant modifications than those observed. Nevertheless, as S_2 gets down behind S_1, we do observe evolution in the formation of the lower part of S_2 shock-wave. Indeed one can think that the molecules being in the shock-waves of each sphere will mix without being deflected due to the weak local density. Since the global level of rarefaction is already low in the free stream where the mean free-path is of 0.77 mm, it is clear that in the wake of S_1, the mean free-path will be much lower. From the DS3V calculation, we estimate that for $X_2 = 27$ mm, $Z_2 = 0$ mm, the mean free-path is of 72 mm. Comparing this distance to the diameter of the model (18 mm), we can clearly understand why the shock-wave of S_2 cannot be properly formed, even though the flow is supersonic there. Even if we can no longer speak of types of shock/shock interferences, a more detailed analysis will shed light on certain differences between the different interactions. For this purpose, amongst the different images analysed, we decided to select six positions allowing a certain range of interaction angles. The selected cases, contoured in dark in Figure 10.1, are shown in Figure 10.2, with a bit more enhancement to better visualise the intensity variations.

As the flow is not perfectly homogeneous, for each S_2 position presented in Figure 10.2, an image was recorded with only S_2 and analysed to allow a comparison of the corresponding interactions cases. The denser region is described by the dark red area. Whatever the position of S_2 behind S_1, the intensity around S_2 seems to be higher than that around S_2. In particular, the intensity looks higher in the interaction area and around it. This would mean that the shock/shock interferences may affect the wall properties of S_2

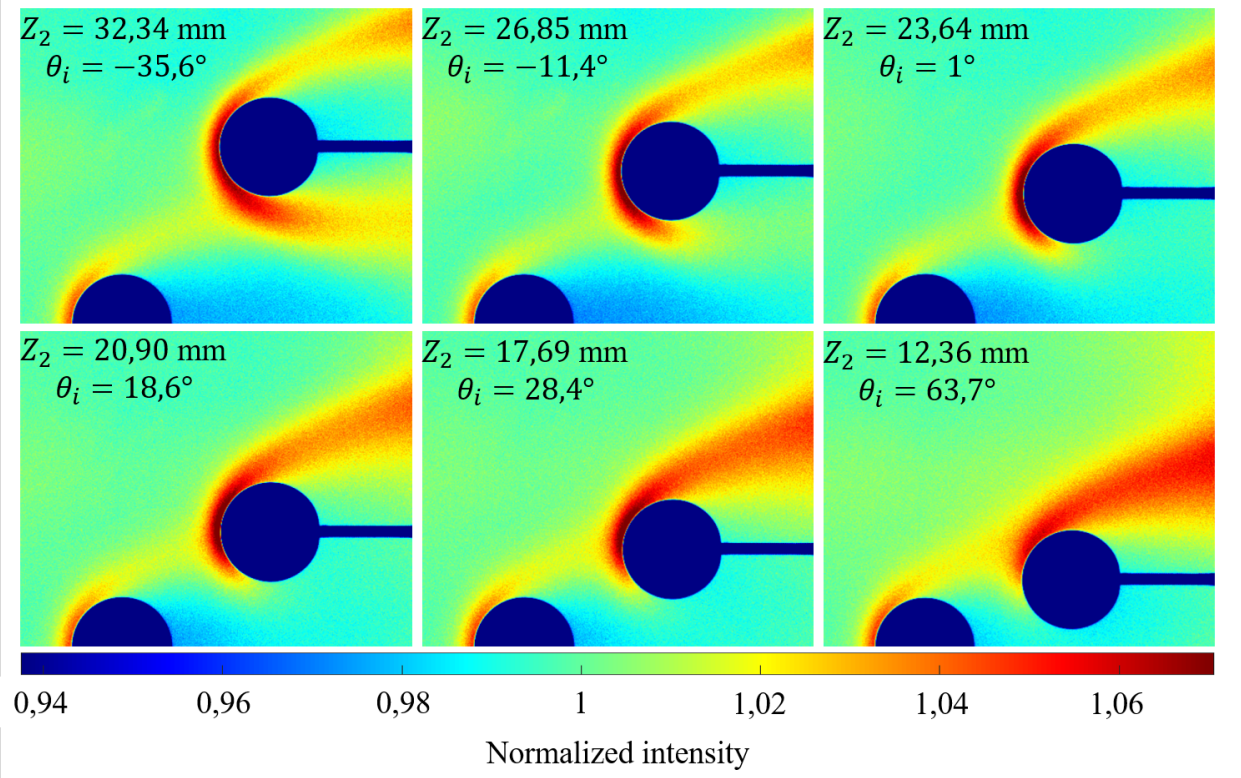

Figure 10.2: Selected enhanced images for C_5 at X_2 = 27 mm, in N3 flow-field.

over an area which is wider than just the intersection area. However, the flow being non-isotropic, a deeper qualitative study will be made later in this work, that tends to confirm those thoughts.
Increasing the angle of interaction Θ_i, *i.e.* decreasing the altitude of S_2, the denser region displaces from the bottom of the sphere to its top, where it is mostly located. Indeed, whatever the position, the redder area is mostly located above S_2. Moreover, it seems that the highest values (dark red) are only observed in front of the sphere or on its top. This suggests that the efforts on S_2 also follow this trend, pushing it into the wake of S_1 in most positions. A measurement of the lift forces will help confirm this statement.
Concerning the thickening of S_2 shock-wave far behind the sphere, it seems that the more S_2 enters the wake of S_1, the more the rear part of its shock diffuses and the local intensity increases. For $\Theta_i \geq 28.4°$, the incident shock-wave seems to merge with the shock-wave created by S_2. Thus, it is possible that they create a denser area than in the shock-wave of a single sphere. Moreover, since S_2 is mostly located in the wake of S_1, the rarefaction level is higher than in the free stream. Which means that, behind S_2, there is even less molecules, so the shock diffuses and spread in the direction of the empty space.

Also, the observations of the images from Figure 10.2 shows that no real deformation is detectable in the interference area. To observe the shock-wave deformation of S_2, we compared the middle of shock (MS) of S_2 obtained with and without SSI, for each position. The superposition of the MS regions is shown in Figure 10.3. The only deformations of shock-waves observed are on the lower part of S_2 shock-wave. This is not due to the SSI, but to the very low molecular density in the wake of S_1 that prevents the formation of a strong shock-wave around S_2. But in the interaction area, no pattern seems to appear, contrarily to continuum [65, 70] or less rarefied flows [41, 182, 211], as we described with the supersonic cases. However, for Θ_i = 18.6° and 28.4°, it seems that, right below the intersection point, a sort of pointed shape is observed, slightly moving the shock-wave away from S_2.
To evaluate these slight variations, we determined the stand-off distances of S_2 with and without SSI. Values are plotted in Figure 10.4.
In black, are shown the reference values of S_2 when S_1 is removed from the flow. The reference values,

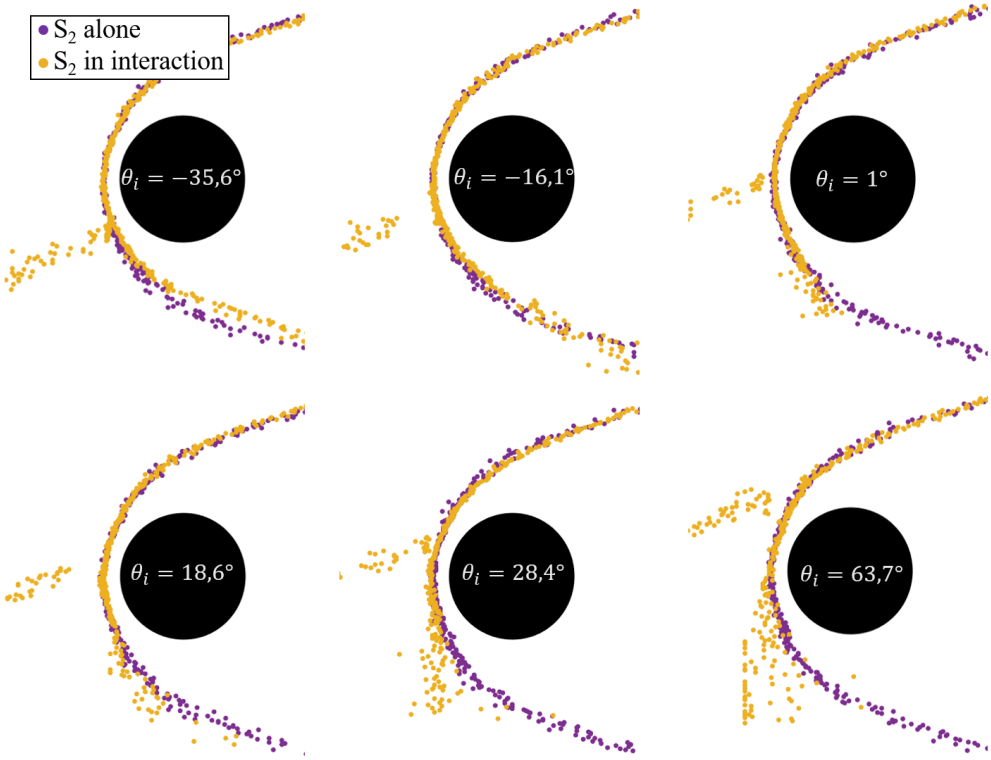

Figure 10.3: Superposition of S_2 MS with and without SSI for C_5 at X_2 = 27 mm, in N3 flow-field.

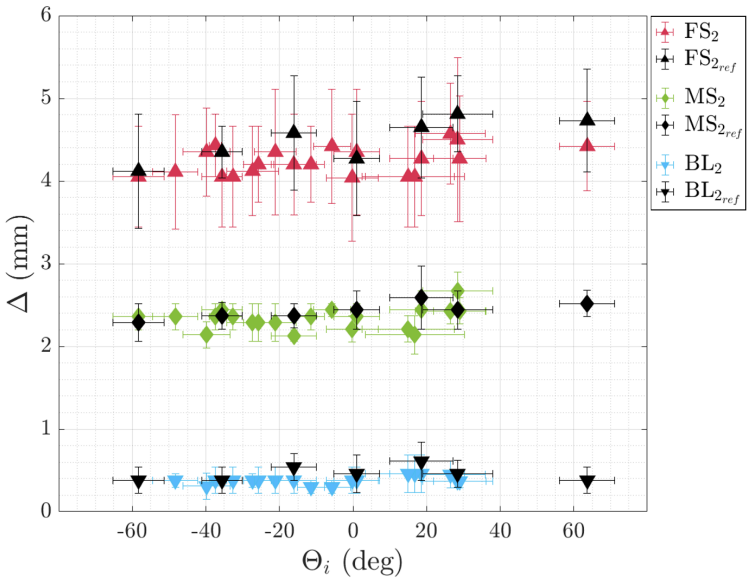

Figure 10.4: Stand-off distances of S_2 for C_5 at X_2 = 27 mm, in N3 flow-field.

in particular for the FS and the MS slightly increases with the angle of interaction, *i.e.* when S_2 altitude decreases. Indeed, from the flow-fields of N3 (Figure C.3), the pressure is minimal at the centre of the nozzle core (for Z_2 = 0 mm). Thus, we may think that the level of rarefaction is higher at this altitude, leading to higher stand-off distances. Moreover, this assumption agrees with the generalised stand-off distance equation proposed in Equation 6.4.

The coloured points correspond to the S_2 stand-off distance in case of SSI, when S_1 is placed in the middle of the nozzle core. As can be observed, a slight increase of the values is observed for the FS and MS. Globally, the values of the SSI case are lower than the reference case. Since the shock-wave coming from

S_1 is very thick, it is probable that the region affected by the SSI is just a little bit more compressed than usual without being much modified. Indeed, the dispersion of the points does not allow to determine any tendency concerning the distancing of S_2 shock-wave for the different types of SSI. This would mean that the SSI pattern vanishes with the increase in the rarefaction level, and only act for a slight decrease in the local rarefaction level seen by S_2, which concludes in the decrease in the stand-off distance. It is to be noted that, even for the low position (high Θ_i), no increase of the shock-wave stand-off is shown, contrarily to what is expected and observed in previous supersonic rarefied studies [42]. From images shown in Figure 10.2, the incident shock is described as thick and diffused. Moreover, for the lowest position, the incident shock seems to merge with S_2 shock-wave, spreading the compression area until the nose of S_2. Thus, it is possible that S_2 has to be even lower in the wake of S_1 to see its stand-off distance increased.

In order to deepen the comparison of shock-waves, a particular interest has been taken on the point of intersection of the middle shocks P_i, and on the point of maximal luminosity P_{ml}. Their distance to the surface of S_2 are plotted according to the angle of interaction in Figure 10.5. By definition (see Figure 5.11), P_i is associated to the middle shock and P_{ml} to the boundary layer of S_2. To detect a deformation of the shock-waves due to the interaction, d_i and d_{ml} have to be compared respectively with $d_{MS_{2_{ref}}}$ (the distance of the non-deformed middle shock towards the surface of $S_{2_{ref}}$), and with $d_{BL_{2_{ref}}}$ (the distance of the non-deformed boundary layer towards the surface of $S_{2_{ref}}$). Since the shock-wave of S_2 depends on its location, the shapes of its three regions vary too according to Z_2. Thus, on the two graphs of Figure 10.5, $d_{MS_{2_{ref}}}$ and $d_{BL_{2_{ref}}}$ are plotted for two altitudes: the highest (purple) and lowest (pink) positions shown in Figure 10.2. For each one, a vertical line is drawn to represent the angle associated to its altitude. This way, if looking at the negative angles, the reference should be taken as the purple curve, while for positive angles, the pink reference is more appropriate.

In the left graph of Figure 10.5, even if most of the green points are in the standard deviation of the references curve, a slight tendency of d_i can be observed. Looking at the negative angles (when S_2 is high behind S_1), it seems that the point of interaction P_i distances itself from the reference middle shock, represented by the purple curve. On the contrary, for positive angles (when S_2 is low behind S_1), P_i seems to get closer from the pink reference. Thus P_i passes on one side and the other of reference shock, the pivot point being around the angle 0. For the distance of the most luminous point (P_{ml}), plotted in the right graph, the two reference values are equivalent so no distinction will be made between them. Around -20°, d_{ml} seems to increase according to the reference, while the rest of the points show a linear behaviour. The variation observed show a deformation of the BL region due to the SSI. This sudden increase could be the sign of a stronger shock

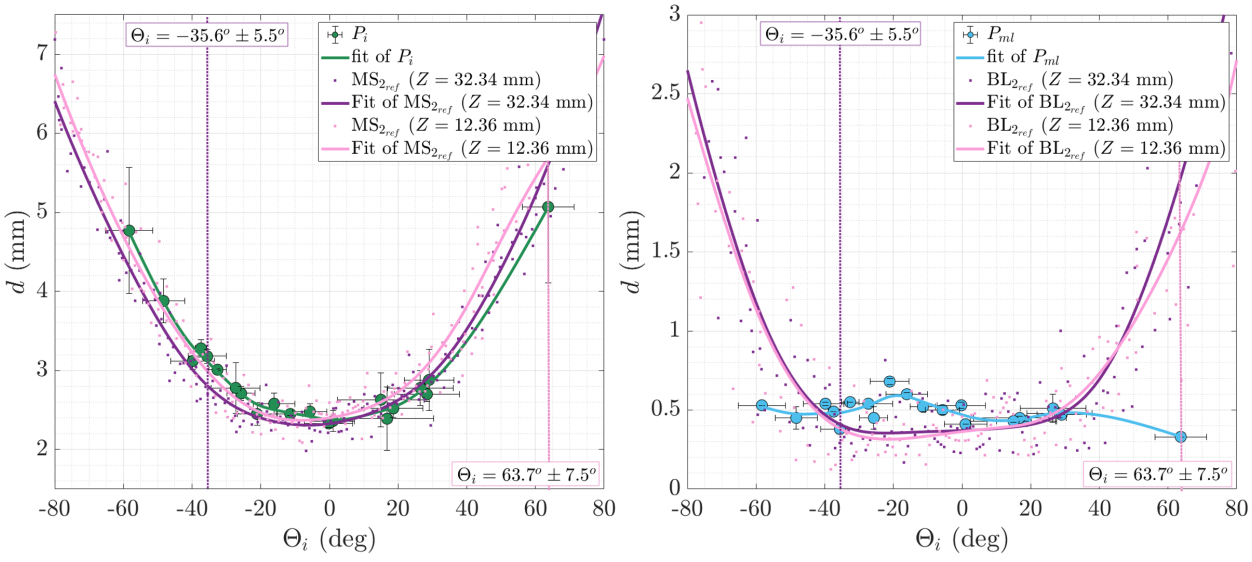

Figure 10.5: Distances of P_i (left) and P_{ml} (right) from the surface of S_2 for C_5 at $X_2 = 27$ mm, in N3 flow-field.

impact for this range of angles. At the extreme angle (63.7°) P_{ml} is way closer to the surface of S_2. Whether this is due to the fact that the shock really deforms itself, or it could be a singularity of measurement. To make a clear statement, more points would be needed in between 30 and 60°.
These two graphs show that there is a setback area on the negative angle which means that a slight deformation of shock-waves is observed for the higher positions. The study of shock/shock interferences in N1 and N2 flow-fields already showed a setback area at the interaction point for SSI type I to IV, in the negative angles. Here, the setback area is not as clear as for the supersonic conditions, but still is slightly noticeable thanks to the distances of P_i and P_{ml}.

The normalised images, in addition to the shock-wave observation, allow to obtain a first look at the local density. Even if the level of intensity is not directly proportional to the local density, it still gives an overview of the density evolution observed for different positions of S_2 behind S_1. In Figure 10.6, the left graph represents the normalised intensities of the brighter pixel at the stagnation point of the spheres and of the point of maximal intensity in the interaction area (P_{ml}). As can be observed, contrarily to the intensity of S_1 (I_{01}), the intensity of $S_{2_{ref}}$ ($I_{02_{ref}}$) changes according to its position in the flow. This is due to the variation of free-stream Mach number and pressure generated by the non-isotropic core. To evaluate only the impact of the SSI, the intensities around S_2 are corrected so that the reference $I_{02_{ref}}$ is constant and equal to the value of S_1 which is located in the perfect conditions. Results of the corrected values are shown on the right graph of Figure 10.6. This graph will be used to analyse the evolution of the local density according to the angle of interaction Θ_i.
Either at the stagnation point (I_{02}) or at P_{ml} (I_{ml}), a clear evolution of the intensities is shown: from -60° to around 10°, the intensity increases, and then it decreases while S_2 penetrates deeper behind S_1. With this information, we may estimate that the local density will be maximum in the BL for the position corresponding to an interaction angle of about 10°. In the supersonic conditions, results showed that the maximum intensity values at P_{ml} shifted towards negative angle with an increase in the rarefaction level. Therefore, in the present hypersonic conditions, the maximum should have been observed for a negative interaction angle, which is not the case. This could mean that the Knudsen number is not a sufficient parameter to describe the different parameters related to the interference behaviour.
At the stagnation point, for $\Theta_i > 40°$, the intensity keeps decreasing, even crosses the reference value, which means that the local density is lower than in the free stream. This phenomenon was expected since, as S_2 enters deeper in the wake of S_1, the rarefaction level increases. Moreover, we have already observed an intensity lower than the reference for N1 and N2 in Figure 9.5. But, since Figure 10.4 did not show

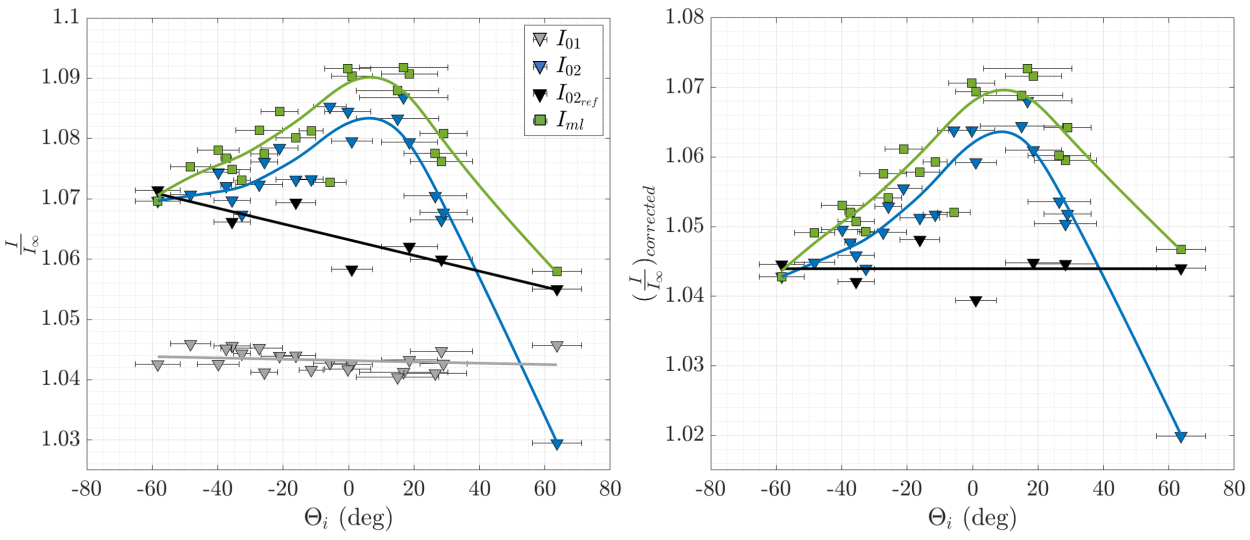

Figure 10.6: Luminous intensity at P_{01}, P_{02}, $P_{02_{ref}}$ and P_{ml} for C_5 at X_2 = 27 mm, in N3 flow-field. Left: normalized values; right: corrected normalized values.

any evolution of the stand-off distances according to different interaction angle, the impact of SSI, at such velocities, and for such a rarefaction level, was reconsidered. The luminosity showing evolution, it allows to confirm that the SSI do act on S_2.
As a result, the images did not allow to clearly identify different types of SSI, as it was possible to do for N1 and N2. Moreover, the analysis of the shock-wave in terms of distances did not show strong variation that would be the sign of a SSI impact. However, the analysis of the luminous intensity brought some information on the evolution of the local density at the nose of S_2, but also at the most luminous point in the interaction area. These last data allowed us to see, a clear variation due to the SSI. It seems that the SSI, as described by Edney [65] do not exist here. Usually, SSI generates strong impact on a small area, each defined by a specificity. These types of interferences were observed previously in this work for N1 and N2 flow-fields. But here, the incident shock and the bow shock of S_2 seem to merge, creating a large shock/shock mixing layer: no real deformation of the shock-waves are observed, and an increase of the density level is present. An electron gun is being developed, and hopefully will help deepen this phenomenon and give a more accurate vision of the physics. For now, it can be stated that, even if the flow has hypersonic velocities, the viscous effects are predominant over the pressure ones, which attenuate the impact of an incident shock interacting with a bow shock.

10.1.2 Aerodynamic forces

This section focuses on the evolution of the aerodynamic forces measured for different interaction angle. Force measurements were realised with the aerodynamic balance, but also with the swinging sphere technique. First, we will described the methodology that allows to correct the effect of non-isotropy of the flow, plus some experimental bias that will be explained. And in a second part, the corrected results will be analysed and discussed.

10.1.2.1 Forces correction

The experiments carried out in the flow of the nozzle N3 add two difficulties compared to experiments carried out in the supersonic flows.
First of all, Figure C.3 shows that the Mach number and static pressure flow-fields are not isotropic in the vertical and transversal directions. Thus, as explained earlier, according to its altitude, the upstream flow seen by S_2 varies. To take into account this bias, aerodynamic measurements with S_2 alone in the flow have been made at different altitudes, which will allow a correction of the values, as it has already been done for the study of light intensities.
The other point to take into account is the force that can be applied to the sphere due to the suction of the pumping group. As a reminder, for the supersonic flows, it was explained in 8.2.1.2 that, depending on the obstruction generated by the models, the free-stream pressure varies and needs to be adjusted by starting an additional pump, or by opening the butterfly valve located between the test chamber and the pumping group (see section 4.2.1). For N3, the functioning is quite different. Indeed, the free-stream pressure is so low that the pumping unit alone is not sufficient. For such a regime, it would require to have a pumping unit with very high performances and thus very expensive. To improve the sucking capabilities of the actual pumping unit, and obtain the working pressure, an extension of the diffuser has been calculated by Raffin [174]. In our specific conditions, the sucking capabilities are improved by a factor 10, when the extension is placed in the test chamber. Thus, the free-stream pressure is supposed to remain as desired, whatever the model position in the nozzle core. However, it seems that the presence of the balance device affects the N3 free-stream flow. Indeed, we measured the drag forces of a single sphere with the aerodynamic balance but also with the swinging sphere technique, and it seems that a difference is observed between the two types of results. Since the swinging sphere technique is a non-intrusive way to measure the drag forces, we suppose that this

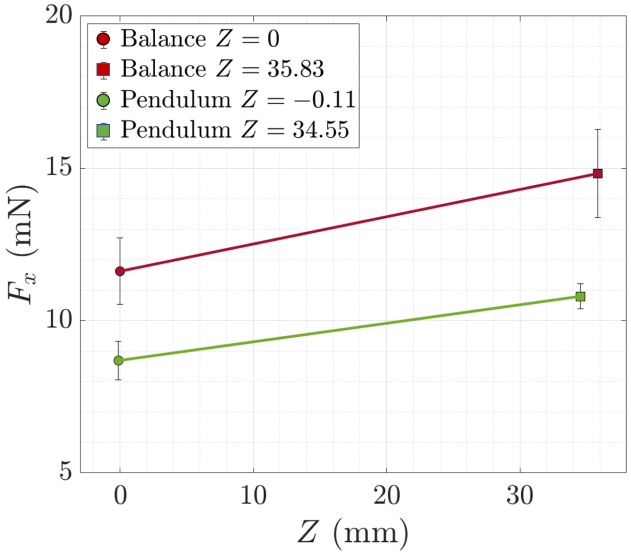

Figure 10.7: Drag force measured for the 18 mm-diameter sphere at different locations in N3 flow-field, and for two types of measurements.

difference comes from a modification of the sucking capabilities, and thus of the free-stream flow parameters.

Aerodynamic force measurements were carried out with the aerodynamic balance and the swinging sphere method as it was already done in the supersonic conditions. To evaluate the influence of the vertical gradient of the flow-field in pressure and Mach number, two measurements have been made at two different altitudes $Z_2 = 0$ mm and $Z_2 \approx 55$ mm. From the flow measurements realised by Christou [48], and given in Figure C.3, between the centre of the nozzle and $Z_2 \approx 35$ mm, the deviation in Mach number is of 5%, and in pressure is of 14%. This nozzle flow characterisation shows that the evolution of these two parameters is almost linear in the $\vec{y}$ or $\vec{z}$-directions, leading to assume that the evolution of the drag force is also linear in these radial directions. Figure 10.7 presents the values of drag forces measured for a single sphere in the N3 flow-field with both methods. The values show that the measured drag forces with the swinging method are smaller of about 24% than those measured with the aerodynamic balance. Moreover, for both methods, the drag force increases with the increase in altitude by almost 21%. However, it seems relevant to consider that the value measured at $Z_2 = 0$ mm is the correct one due to the closer flow conditions from the theory. This value will be used as a reference to correct the values measured along the vertical axis. However, given the difference in values observed between the two techniques, it is natural to wonder which one gives the real drag force value.

Our choice will be made by discussing both measurement methods, and by comparing our drag coefficients with the literature. At first, the measurements of forces were wished to be realised with the aerodynamic balance which allows obtaining both the drag and the lift forces. However, the swinging sphere technique is known to be more precise for the measurement of the drag forces since it is non-intrusive. Moreover, in such a rarefied regime the suspension wire is 8 times thinner than the mean free-path of the flow ($\lambda_\infty = 0.77$ mm). Thus, it is understandable that the probability for particles to collide with the wire is almost null. In consequence, the drag force applied on the wire can largely be neglected, which is why we also realised the measurement with the swinging technique. Regarding the aerodynamic balance, its presence in the flow is more intrusive, which can introduce deviations of the measured forces all the more important as they are very weak. Now considering the drag coefficient at $Z_2 = 0$ mm, where the flow conditions are the isentropic one, for the swinging technique $Cd = 1.74$, and for the balance $Cd = 2.35$. Very few values can be found in the literature for hypersonic and low-density flow conditions. Koppenwallner [111] presented drag coefficient for Mach number between 8 and 13, for $Re_2 < 100$. In our case, $Re_2 = 11.4$, and the equivalent drag coefficient from Koppenwallner is of 1.64. With the numerical simulations of hypersonic

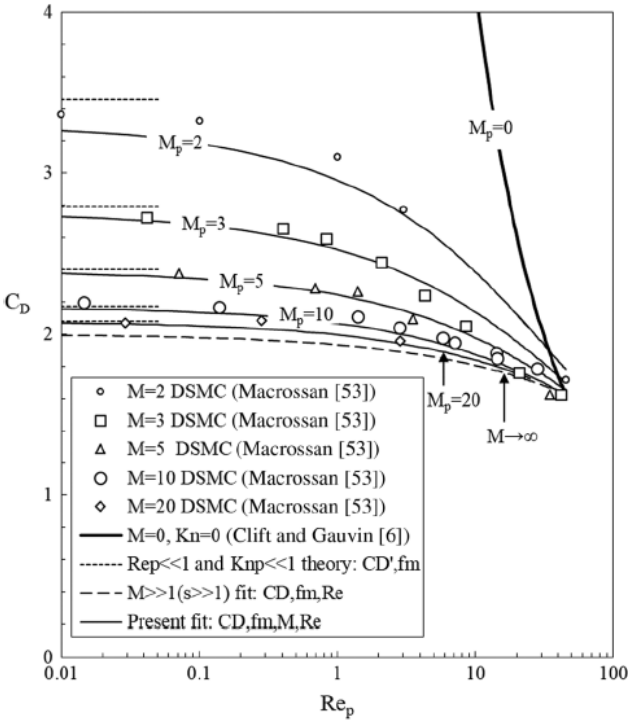

Figure 10.8: Drag coefficient variations in rarefied regime from Loth *et al.* [131].

rarefied flows, Dogra *et al.* [62] obtained the drag coefficient according to a range of Knudsen number. In our case, following the results of Dogra *et al.*, our $Kn = 0.0428$ gives $Cd \approx 1.44$, which is lower than our results, and even lower than those of Koppenwallner. It is important to note that the numerical simulations are approximated because the conditions of accommodation to the wall, imposed in the calculations, remain estimated. In a more recent publication, Loth *et al.* [131] presented a graphic, recalled in Figure 10.8, allowing obtaining the drag coefficient for different Mach numbers and particle Reynolds numbers Re_p, here interpreted as the Reynolds number after shock (Re_2). For $Ma \approx 20$, and $Re_2 = 11.4$, this graphic gives us $Cd = 1.83$. Thus the drag coefficient from the swinging technique is in between those of Koppenwallner and Loth *et al.*. However, the drag coefficient obtained with the balance is well beyond those of the literature. In what follows, we will assume that the measurement obtained with the swinging method at $Z_2 = 0$ mm is the correct one.

In order to study the evolution of the drag force as a function of the position of S_2, a correction has to be made. First, due to the flow-field gradient, a linear correction has to be realised according to the altitude Z_2 of S_2. The correction, realised with Equation 10.1, gives the results presented in the left graph of Figure 10.9.

$$F_x(flow\ correction) = F_x(measured) - 0.0609.Z \tag{10.1}$$

As we consider that the value measured with the swinging technique is the correct one, we apply an additional correction to the values obtained with the first correction (Equation 10.1). This correction, given by Equation 10.2, is certainly due to the greater obstruction implied by the size of the balance.

$$F_x(flow + obstruction\ correction) = F_x(flow\ correction) - 2.92 - 0.0296.Z \tag{10.2}$$

In the end the drag force measured with the balance are corrected with Equation 10.3, the drag force obtained with the swinging method are corrected with Equation 10.1.

$$F_x(flow + obstruction\ correction) = F_x(measured) - 2.92 - 0.0904.Z \tag{10.3}$$

The results of the corrected values of both methods are given in the right graph of Figure 10.9. With these corrections, we will be able to correct all the measurements made for S_2 in interaction with S_1.

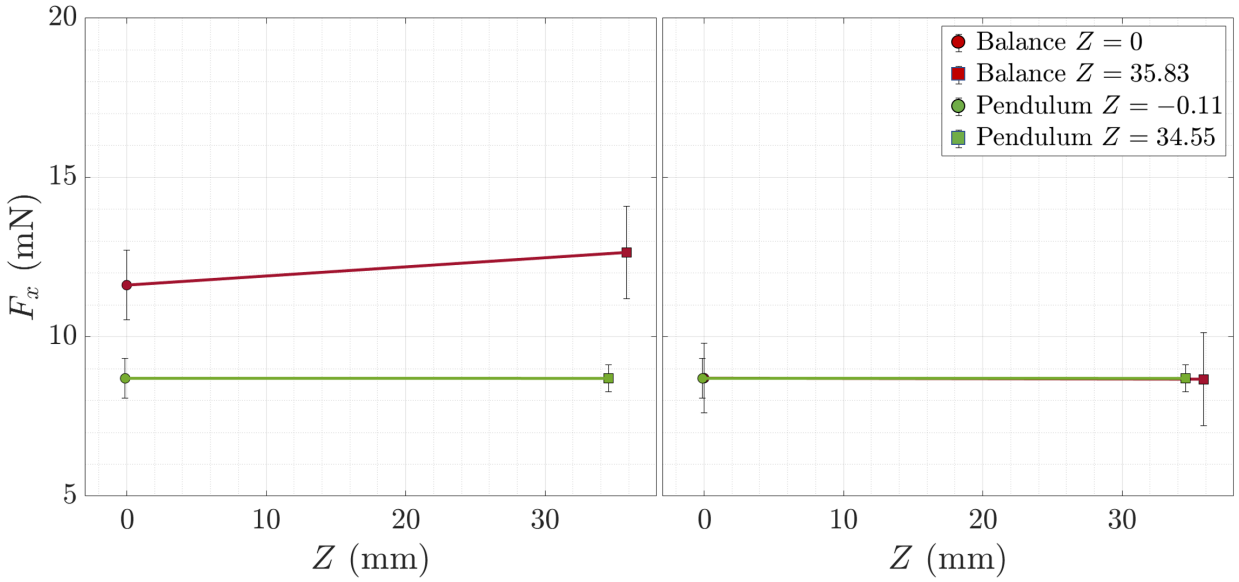

Figure 10.9: Correction of the drag force for the 18 mm-diameter sphere at different locations in N3 flow-field, and for two types of measurements. Left: flow-field correction. Right: flow-field plus obstruction correction.

For the lift forces, another correction has to be made. The values measured with the aerodynamic balance are given in Figure 10.10. As we know, the lift force of a single sphere in a homogeneous free-stream flow is null. Thus, the lift force measured with the balance for $Z_2 = 0$ mm should be 0, since at this altitude the flow in N3 core is axisymmetric. But, as can be seen in Figure 10.10, at the centre of the core, a non-zero force is measured, which is due to a slight angular misalignment of the balance towards the flow direction. Since the balance has not been moved during all the experiments for N3, the misalignment is the same for all the measurements, so the offset value is constant and its value is 0.3625 mN. The shifted values are given in the left graph of Figure 10.11. In this graph, which values are corrected in terms of balance misalignment, we observe a slope of the values as the altitude increases. Indeed, when the sphere is not in the centre of the core, due to the nature of the flow, the pressure below and above the single sphere is different. As a

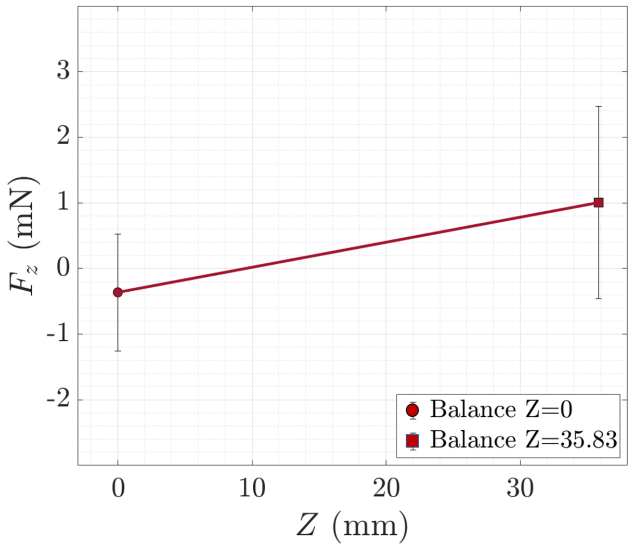

Figure 10.10: Lift force measured for the 18 mm-diameter sphere at different locations in N3 flow-field, and for two types of measurements.

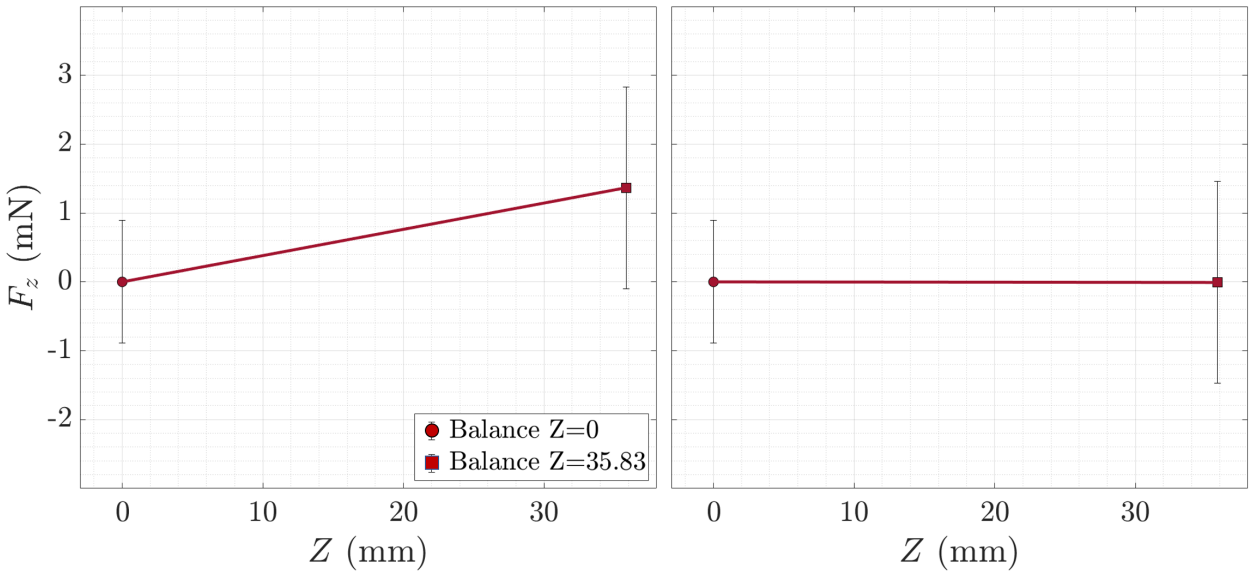

Figure 10.11: Correction of the lift force for the 18 mm-diameter sphere at different locations in N3 flow-field. Left: correction of the balance misalignment. Right: balance misalignment plus flow-field correction.

consequence, a lift force will be measured. A linear correction according to the altitude needs to be applied to counter this effect. The full correction of the lift force is given by Equation 10.4, and the results are shown in the left graph of Figure 10.11.

$$F_z(misalignment + flow\ correction) = F_z(measured) + 0.3625 - 0.0384.Z \tag{10.4}$$

10.1.2.2 Forces analysis

Amongst the positions adopted for the flow-field visualisation, we selected some locations to deepen the study of SSI. Since it was not possible to identify different types of interferences, the locations were chosen in order to cover a wide range of interaction angle Θ_i. For these locations, we measured the drag and lift forces with the aerodynamic balance, but the drag force was also measured with the swinging sphere technique. With the corrections applied to the measured forces, as described in the previous section, we obtain the drag and lift forces presented in Figure 10.12, which values are given in Appendix G, Figure G.5.
The corrected drag forces obtained with both methods seem in good agreement. The drag seems to clearly show a variation du to SSI as S_2 gets down behind S_1. For $\Theta_i \approx -55$, when S_2 is mostly above the incident shock-wave, its drag is slightly higher than the reference value. While S_2 enters deeper into the shock-wave of S_1, the drag increases until around $\Theta_i = -15°$ where the maximal drag force is reached with an increase ratio of 1.1 with respect to the reference value. Note that this ratio is of the same order of magnitude as those determined for supersonic conditions, and very close to the couple C_1 in N1 flow-field. It is to be noted that the difference between the reference value and the maximum drag is of only 1.2 mN, which highlights the low impact that has the SSI on S_2 aerodynamics. However, this maximum is reached for approximately the same interaction angle that showed a deformation of the boundary layer in the interference area (see the right graph of Figure 10.5). This might be an indication showing the most powerful SSI in these specific flight conditions. Yet, the maximal local density was found for $\Theta_i \approx 10°$ (Figure 10.6) and not for the angle corresponding to the maximal drag. For $\Theta_i > -10°$, the drag force is decreasing, which implies that the effects of the SSI on S_2 aerodynamics are also decreasing. Considering that the effects of the SSI are due to pressure and the friction, and knowing that the maximal drag is not observed for the maximal local density, and possibly maximal local pressure, we might think that the maximal impact of the SSI is mostly

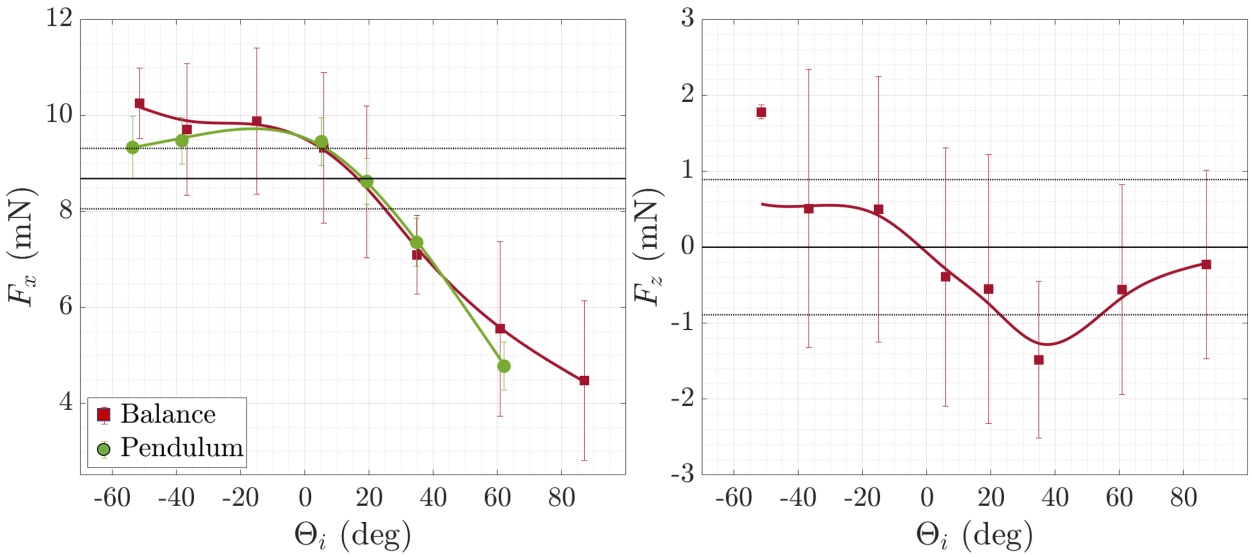

Figure 10.12: Corrected drag (left) and lift (right) forces for C_5 in N3 flow-field.

due to viscous effects. For locations corresponding to $\Theta_i > 20°$, the drag force is lower than the reference case. From this angle of interference, S_2 descends into the wake of S_1, where velocities and pressure are decreasing, preventing S_2, in a much rarefied flow, from being pushed away from S_1.
The little variations observed concerning the lift forces indicate a weak impact of the incident shock on S_2. When S_2 is mostly above S_1 MS ($\Theta_i < 0°$), the lift of S_2 is almost that of the reference value. However, when S_2 crosses this MS going down towards S_1, the lift decreases, reaching negative values. Thus, S_2 is weakly pushed down by the incident shock. Above $\Theta_i \approx 40°$, when S_2 gets out of the incident shock, its lift force slowly increases, retrieving the reference value.
In Figure 10.13, the normalised drag forces are plotted in the left graph, and the lift force obtained experimentally and numerically with DS3V in the right graph. The forces are plotted according to the altitude of S_2 because the angle of interaction was difficult to obtain numerically. As can be seen, the normalised drag forces are in good agreement, particularly between the results of the swinging experiment and those of DS3V, for which the two curves are superposed. However, the drag force obtained with DS3V is of 5.98 mN, while experimentally we obtained 8.68 mN. Thus all the DS3V values are of 2.7 mN lower than the

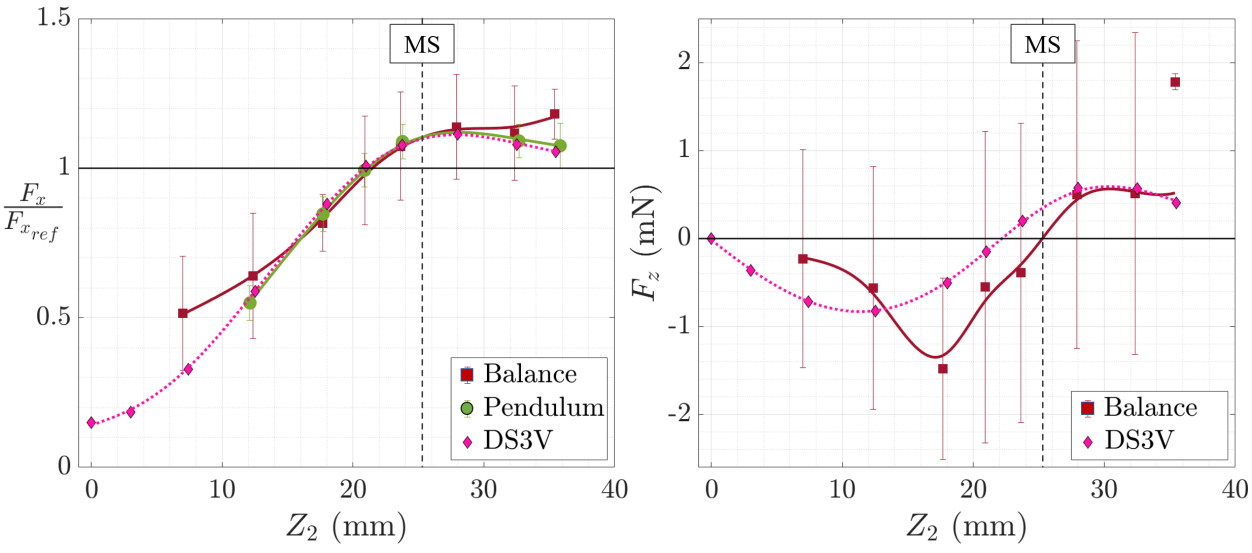

Figure 10.13: Normalized drag forces (left) and lift forces (right) for C_5 in N3 flow-field, comparison with DS3V results.

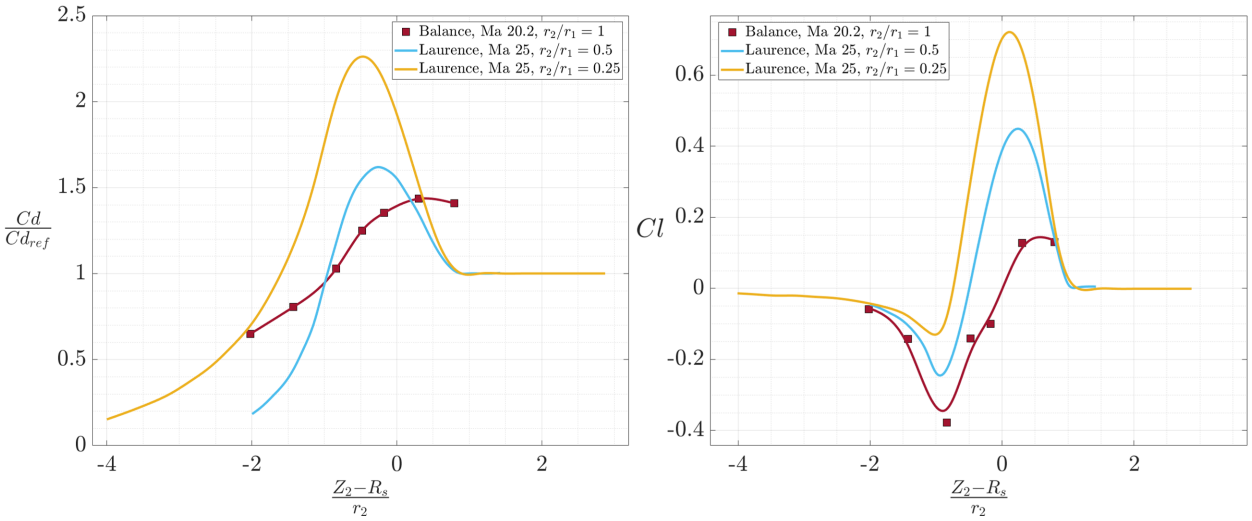

Figure 10.14: Normalized drag coefficient (left) and lift coefficient (right) for C_5 in N3 flow-field, compared with the continuum regime [115].

experimental ones, whatever the simulated case (with or without interferences). Concerning the lift forces, we observe a same tendency between the experiment and numerical results. However, the minimum value and the change in sign are not obtained for the same altitude. It is to be noted that, according to Figure E.14 and Figure E.15, the flow-field behind S_1 alone in the free-stream shows differences with the experimental results, in particular, the location of the MS is lower in the numerical simulation, which can explain the shift in the right graph of Figure 10.13. A second point to be noted is the greater negative value obtained at the minimum for the experiments. This implies a greater repulsion of S_2 due to the incident shock in the $\vec{z}$-direction.

Globally, we observed that the forces obtained numerically are lower than those measured experimentally, which let us think that, even with the good upstream conditions, the slip conditions at the wall of the spheres are not well defined. Unfortunately, since the simulated flow-field of S_1 is very different from the experiment, it would be better to just use the local parameters to calculate the local drag coefficients.

However, the drag coefficient still can be calculated with the free-stream parameters. Results are presented in comparison with numerical results obtained in the hypersonic continuum regime by Laurence and Deitering [115] in Figure 10.14, who simulated the SSI between a primary sphere and a second one with two different diameters in a Mach 25 flow, for the vertical axis $X_2 = 3/2.\emptyset_1$. In our case, the second sphere has the same diameter as the first one but we displace S_2 on the same vertical axis. Both drag and lift coefficients are plotted according to $\frac{Z_2-R_s}{r_2}$, which is representative of the normalised distance between S_2 surface and the middle of the incident shock-wave MS. Concerning the drag coefficients, results were normalised with the drag coefficient of the reference case. From the results of Laurence and Deitering, we observe that, at iso-Mach and free-stream pressure, the decrease in S_2 diameters leads to an increase in the normalised drag coefficient. This means that a small sphere will be more impacted by the SSI than a bigger one. It seems that the size of S_2 changes a bit the location where is observed the maximal drag coefficient: as S_2 diameter decreases, the altitude where the maximal drag is observed slightly decreases. In our case, the Mach number is a bit lower than 25, but the principal difference concerns the pressure, which is very low in the experimented conditions. If looking at the experimental results we obtained, for which the sphere radius is higher than those of Laurence and Deitering, the normalised drag coefficient is lower and the maximum Cd is observed for higher locations, which is consistent with what previously said. However, our results show a gentler slope, with a less marked maximum. We may think that this wider distribution is due to the thickening of the incident shock, impacting S_2 in a wider range of altitude. Moreover, S_2 drag coefficient may retrieve the reference value for higher altitude than those experienced. This suggests that S_2 has to be well above S_1 not to be in interaction with it, and this does not seem to be due to the size of S_2, since Laurence's case retriever

the reference at a same normalised altitude. The lift coefficient calculated by Laurence and Deitering show that, as S_2 diameter decreases, the lift is negative for a smaller range of altitude, and its absolute values are lower. On the contrary, the positive lift shows higher values. The minimal and maximal values of lift are obtained for approximately the same normalised altitude. Thus, the size of S_2 plays an important role in the sign of the lift coefficient, which is a key factor in whether S_2 will be mainly attracted or repelled by the flow of S_1. From our experimental results, we can only confirm what is suggested by the curve from Laurence. There is a slight increase in the altitude where is located the maximal lift, which might be due to the thickening of the incident shock. It seems that the differences observed for the lift coefficient between our results and those of Laurence and Deitering are mostly due to the sphere diameter. As a consequence, one can say that the rarefaction level plays a more important role regarding the drag coefficient than the lift, which is mainly impacted by the size of S_2.

10.2 Full mapping of S_2 drag forces

In order to obtain a full mapping of the drag forces of S_2 when placed in the flow-field of S_1, we used the swinging sphere technique that was previously used for N1, and described in section 8.2. As a reminder, S_2 is suspended by thin non-elastic wires attached to a movable support. S_2 is placed in S_1 flow-field, and then

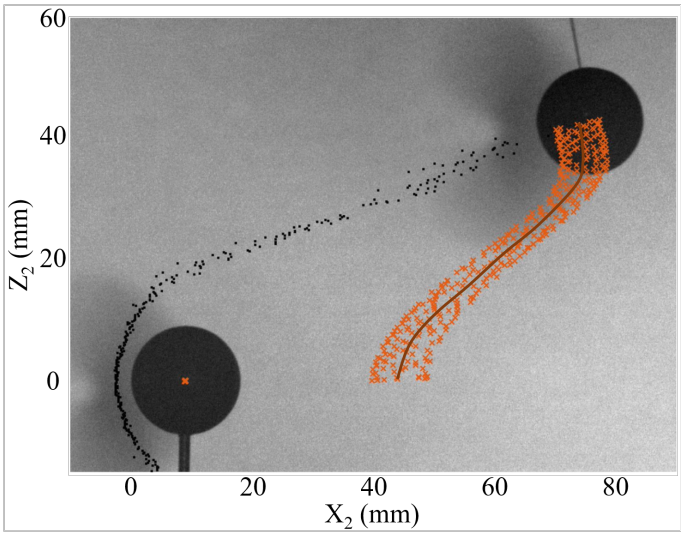

Figure 10.15: Example of trajectory described by S_2 for C_5 in N3 flow-field.

its support is moved up in the $\vec{z}$-direction, or longitudinally in the $\vec{x}$-direction. In Figure 10.15, an example of the trajectory described by S_2 is given. Contrarily to the trajectory described in Figure 8.21, for N1, here we observe a greater oscillatory movement. As the density of the flow is very low, very few particles can support the weight of S_2, and thus, the time for stabilisation between two locations is higher than for N1 flow conditions. However, from the points plotted in Figure 10.15, we were able to calculate the mean trajectory, as shown with the dark curve. Throughout this movement, we also measured the angle of the wire, corrected through camera measurement, as explained in 5.4.2.3. From these angles, we calculated the local drag forces of each point, and finally the mean drag forces associated with the mean trajectory. Then, the forces were corrected according to the altitude Z_2 with Equation 10.1.

With this methodology applied to different trajectories, we obtained the mapping presented in the left of Figure 10.16, which presents the mean trajectories described by S_2 in the flow-field of S_1, associated with its corrected drag forces. On the right of Figure 10.16, the drag forces obtained for the different coordinates have been interpolated. Due to the oscillatory movement, results are given with the accuracy of ±1.1 mN. However, some locations on the map lack of measures to be sufficiently well interpolated, this is why the

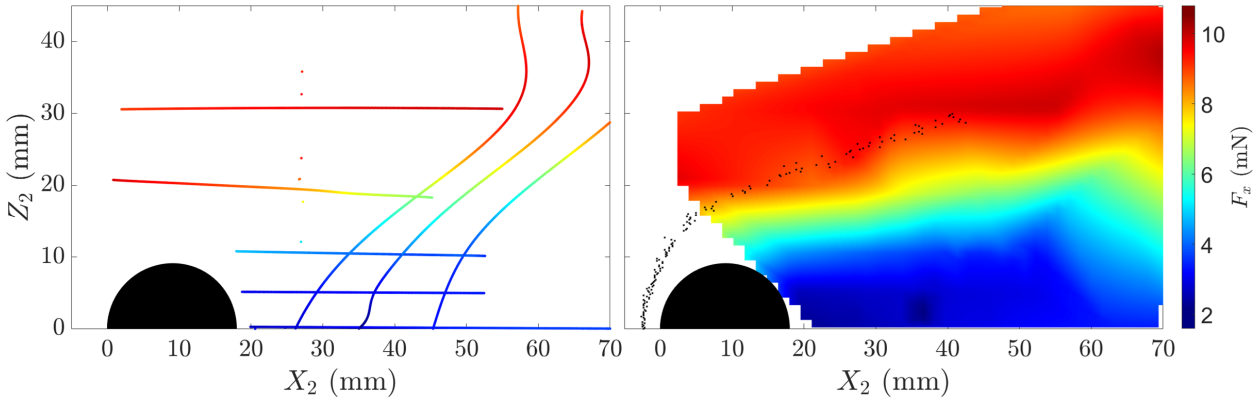

Figure 10.16: Corrected drag forces of S_2 suspended in N3 flow-field. Left: mean trajectory of S_2 associate with its values of drag force. Right: 2D mapping of the interpolated drag forces.

mapping has to be considered with caution. This 2D mapping allows to better visualise the distribution of S_2 drag forces according to its coordinates in the flow-field of S_1. In addition, we plotted the MS of S_1, which helps understand the variations of S_2 drag forces. As can be observed, the highest values of drag force are located around the shock. There is almost no difference between the forces measured in the free stream and those measured in the shock-wave. This means that the impact of S_1 shock-wave on the drag of the following sphere is slight. If comparing this mapping to the one obtained in N1 (see right graph of Figure 8.31), we can see that the distribution of S_2 drag force is similar. However, in N3 flow-field, the highest value seems to be obtained just above the MS, while for N1, they were obtained on the MS.

another comparison of this mapping can be made by calculating the drag coefficient with the free-stream parameters. Indeed, Vashchenkov *et al.* [203] numerically investigated the drag and lift coefficient of a cylinder placed in the flow-field of a primary one. Their Mach 27.5 flow has a free-stream pressure of 0.081 Pa. Thus, their free-stream flow conditions are close to ours. Vashchenkov *et al.* placed a secondary cylinder in the flow-field of a first one. Two sizes of cylinders S_2 were tested: $\emptyset_2 = 0.1.\emptyset_2$ and $\emptyset_2 = 0.001.\emptyset_2$. Results of our drag coefficient are given on the left of Figure 10.17, and those of Vashchenkov *et al.* on the right for the two sizes of cylinders. At first sight, the evolution of the drag force (calculated with the free-stream parameters) is the same in the three graphs. However, as the size of S_2 decreases, the drag coefficient globally increases, with a more pronounced difference in the incident shock-wave region. As a reminder, when studying the impact of local rarefaction level by decreasing the size of S_2, we also noticed that the drag coefficient was increasing (Figure 9.29), which agrees with the results of Vashchenkov *et al.*, even if the flow conditions are different. This means that, the more S_2 size is big, the less we observe a

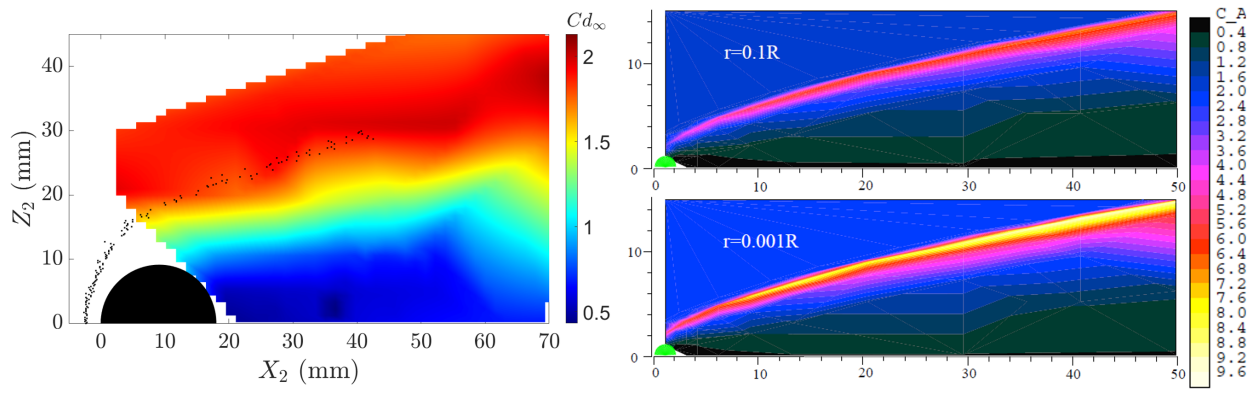

Figure 10.17: 2D mapping of the infinite drag coefficient. Left: C_5 in N3 flow-field. Right: Vashchenkov *et al.* [203]

drag coefficient's variation. From the numerical data of Vashchenkov *et al.*, for $\emptyset_2 = 0.1.\emptyset_2$ ($Re_2 = 10$) a reference drag coefficient of 1.43 was found for the following cylinder. In our case, $Re_2 = 11.4$ and the reference drag coefficient of S_2 is of 1.75. In general, for a same level of rarefaction, the drag of a cylinder is greater than that of a sphere, which is not the case here. This observation could come from the difference in Mach numbers which would point to the non-independence in Mach number in the rarefied regime; or from a bad determination of the slipping conditions at the surface of the models. However, even if the models' shapes are different, we did observe a similar drag force repartition of the following object.

Part IV

Conclusion

Conclusion and Perspectives

Technical conclusion

This experimental work investigated the interactions between two spheres in different flow regimes, where a following sphere, S_2, moves in the wake of a first sphere, S_1. The main objective was to study the influence of viscous effects, due to low density and/or hypersonic flows, on the properties of the interactions between the incident shock from S_1, and the bow shock of S_2.
In a first part, the influence of rarefaction effects has been studied with iso-Mach experimental flows: Mach 4 - 2.67 Pa and Mach 4 - 8 Pa. Different diameters of S_2 were adopted while placed behind a fixed diameter first sphere S_1. This allowed to study the influence of local rarefaction properties which modifies the aerodynamic behaviour of S_2. The viscous effects due to hypersonic flows have been studied in a flow at Mach 20.2 and with a very low pressure of 0.067 Pa.
Various diagnostics have been applied to study the different physical properties of the interaction and their modification according to the position of S_2 towards S_1:

- visualisation of the flows by means of the glow discharge method;
- stagnation pressure measurements with Pitot probes for the characterisation of the flow-field around single spheres;
- measurements of wall pressures distribution;
- measurements of aerodynamic forces by means of an aerodynamic balance (drag and lift forces), and with the pendulum technique (only for drag forces).

In a first approach, the global characterisation of the flow around **a single sphere** has been performed for each of the studied flow conditions. An image post-processing method has been developed specifically to study the detail of the shock structure in viscous flows. Results allowed to detect and determine the shock stand-off distances and their evolution as a function of rarefaction effects. A new law is proposed to calculate the shock stand-off distance of a single sphere whatever the Mach and Reynolds numbers of the flow.
Measurements of drag forces, for spheres of different sizes, made it possible to determine their drag coefficient. By comparison with the literature, the two methods used for the measurement (the two-axis thrust balance and the pendulum method) were validated. Pressure coefficients were evaluated from the distribution of the wall pressure for each flow condition and size of the sphere, making it possible to evaluate the contribution of the pressure forces, and then to deduce the contribution of friction on the coefficient of total drag.
Numerical simulations were carried out with direct Monte Carlo simulation method (DSMC), which is well suited to rarefied flow conditions. The two numerical codes used, DS2V and DS3V developed by G. Bird [30], are free access codes. They allowed to perform respectively two-dimensional and three-dimensional calculations, essential for the simulation of interaction cases. The difficulty of the rarefied regime lies in particular

in the determination of the accommodation coefficients which characterise the slip conditions at the wall. To this day, this is still the weak point of these calculation codes. The experimental results, obtained for the different test cases with a single sphere, were used to find the wall accommodation coefficients giving the best solution, that is to say, for which the numerical results are closest to the experimental results. Thus, the numerical results of a single sphere were applied to complete the experimental description of the flow-field of S_1, in which S_2 is place.

Based on the **shock/shock interactions** (SSI) described by Edney in the continuum regime, the six types of interactions have been identified **in rarefied flow for supersonic flow conditions**. This result was obtained from an in-depth analysis of the images obtained with the two interacting spheres. However, the results showed the attenuation of the specificities of each type of interaction as the rarefaction level increases.
Depending on the position of S_2 relatively to S_1, the evolution of aerodynamic forces and wall pressures revealed differences in behaviour according to the different types of interactions. The type IV SSI is obtained when the incident shock created by S_1 interacts with the shock of S_2 at the stagnation point. In the continuum regime, this interaction is known to be the most impactful, especially in terms of wall pressure and heat flux. Results also revealed a strong impact in the rarefied regime. Indeed, for this type of interaction S_2 undergoes the strongest drag force. The position of S_2 that corresponds to this type IV SSI, also corresponds to the maximal pressure measured in the incident shock with the Pitot probe. The same reason should explain why the highest wall pressure peak was observed for the type IV SSI. However, in comparison with the continuum regime, the wall pressure peaks were broadened and presented lower values.
The lift force reached maximum values when S_2 was just above the incident shock, as if it were "carried" by the shock. This behaviour was observed for the transition between types II and III SSI. For this same location the distribution of wall pressures, mostly distributed over the lower part of the sphere, agrees with the previous statement. Further analysis of the results seemed to show that the value of the resultant force depends on the drag force, while the direction of the resultant force depends on the lift force. Thus, despite the small variations observed in lift, the trajectory of S_2 changed greatly.
For the type V SSI, we observed a specific location of S_2 for which the aerodynamic forces, as well as the pressure forces, are equal to the reference values. An in-depth analysis of the drag and lift forces showed that this position should correspond to a surfing point. Unfortunately, all the conditions are not met for the stability of the phenomenon as was established in the continuum regime.
To determine the aerodynamic coefficients from the measured forces, two methods were used. The first considers the free-stream conditions and allowed a comparison with results from the literature. The resulting values showed that the observed variations therefore depend only on the force values, and not on the flow parameters as seen directly by S_2. The second method consisted in determining the aerodynamic coefficients of S_2 with the local conditions, obtained with the numerical simulations of DS2V, more finely meshed than DS3V. These local coefficients are more realistic in terms of aerodynamics since it considers the force but also the local flow directly interacting with S_2. Considering this local method, the drag and lift coefficients showed a maximum value for the transition interaction between types II and III, where the pressure contribution is also maximum. The local drag coefficient, whose pressure contribution is predominant regardless of the type of SSI, also showed a minimum for the type IV SSI, while the drag force is maximum. This indicates that the local flow, which corresponds to the maximum pressure in the incident shock, predominates over the force experienced by S_2. The lift coefficient, on the other hand, showed the highest contribution of pressure effects when S_2 is above the shock-wave.
Conversely, viscous effects predominate when S_2 is below the incident shock-wave, leading to sustain positive lift forces despite the fact that the wall pressure forces are mainly located over the upper part of S_2. These results were compared with those obtained with numerical simulations. The latter are quite similar, but the numerical results obtained by DSMC exhibited a weaker contribution of friction effects, representative of rarefied flows.
The pendulum technique was applied to measure the drag force of S_2 placed in the wake flow of S_1. First, the technique was validated by comparing the results obtained with balance measurements on a vertical trajec-

tory. Then, the technique was employed on several trajectories, which enabled to obtain a two-dimensional mapping of the drag forces in the wake flow of S_1. From the 2D-axisymmetric simulation of S_1, a mapping in terms of local drag coefficient was deduced. These results demonstrated that the longitudinal distance has little influence on the value of the drag forces obtained, which leads to the conclusion that the wake of S_1 extends well past 3.5 diameters of S_1.
A last axis of study highlighted the wake effects on the aerodynamics of S_1. The pendulum technique was applied to S_1, while moving S_2 behind it, first vertically and then longitudinally. When S_2 is moved vertically behind S_1, the results revealed that the SSI do not seem to affect the aerodynamics of S_1. On the other hand, when S_2 approaches S_1 longitudinally the drag force of S_1 decreases. In both cases, the results exhibited a modest variation (3%) in the drag force of S_1, when S_2 comes to place itself just behind it.

In the last part of supersonic results, it was intended to evaluate the **effect of the rarefaction level on the SSI**. Different couples of spheres, with a variation of S_2 diameters, have allowed to examine the effects of global rarefaction for the two supersonic flow conditions: for the same couple of spheres C_1 ($\emptyset_1 = \emptyset_2 = 16$ mm), a second flow condition was investigated at iso-Mach but with a free-stream pressure three times higher. In the second case, the experimental work focused on the effects of local rarefaction: for the same flow condition, the influence of the diameters ratio between S_1 and S_2 was analysed. The results showed that, more generally, the level of global rarefaction reflects the density of the upstream flow, while the level of local rarefaction also reflects the effects of the sphere size. In both cases, the studies were built around the analysis of images, aerodynamic forces, as well as the distribution of wall pressures (1st case only). Regarding the global rarefaction effects, the analysis of the images laid out that the boundary layers of the shocks are overlapping, which was not the case for the other regions of the shock. The middle of shock and the foot of shock detach from the sphere as the rarefaction level increases. However, whatever the shock regions, the magnitude of stand-off distance deviations are much larger for the least rarefied flow conditions (higher pressure force), while the compression ratio of shock S_2 is not larger.
Likewise, the variations of aerodynamic forces are smaller as the rarefaction level decreases. Furthermore, the lift force becomes negative when S_2 passes under the incident shock, and thus under the pressure peak in the incident shock. Therefore, once S_2 is the wave of S_1, it is very likely that the viscous effects, which are less present, no longer help sufficiently S_2 to be pushed up towards the incident shock. Calculations of the displacement of S_2 relatively to S_1 showed that the changes in direction are more abrupt for the least rarefied flow, reflecting greater local pressure effects. However, the drag coefficient is minimum for the same position in any flow, where the pitot stagnation pressure is maximum in the S_1 flow.
Wall pressure measurements provided fairly comparable distributions with the two flow conditions. The specificities of types III and IV interactions seem to be enhanced with the decrease of the global rarefaction level. Furthermore, the wall pressure peaks measured for each type of interaction are globally higher for the lower rarefaction level. Despite this, the pressure forces are slightly lower, which could be explained by a wider distribution of wall pressures in the more rarefied case, which is counterbalanced by the lower values of the pressure peaks. The calculation of the pressure drag coefficient yields equivalent results in both conditions, leading to the conclusion that viscous effects are responsible for the increase in the total drag coefficient. A comparison with the continuum regime was proposed based on the drag coefficient and the wall pressure distribution. The results seem to agree with the discussion presented earlier.
The study of the influence of the local rarefaction was achieved with different sizes of S_2. The visualisations showed that the decrease in diameter gives rise to weaker light intensity gradients, leading to some difficulties to detect shock-waves with accuracy. The evolution of the stand-off distances is consistent whatever the diameter of the sphere. However, from the maximum stand-off distance values obtained for the type III SSI, the calculation of the local Knudsen number allowed to conclude that the shock of S_2 is more affected when the flow is locally less rarefied.
The study of the light intensities at the S_2 stagnation point demonstrated that the change in the local density of types I to IV SSI does not depend on the size of the sphere, in contrast to types V and VI where S_2 is mainly in the wake of S_1. This suggests that the density variations do not only depend on the size of S_2, but

are also impacted by the level of local rarefaction. For the same flow, the aerodynamic drag or lift forces of S_2 increase with the local rarefaction level, regardless of the type of interaction considered. The variation in lift forces decreases with the size of S_2. For the most locally rarefied cases, negative lift is no longer observed when S_2 undergoes a type V or VI SSI, while the pressure induced by the incident shock is confined on its upper part. This results in a drastic change in the displacement of S_2 relatively to S_1, especially when S_2 is located in the wake of S_1. Global and local rarefaction effects have distinct effects. For the same local Knudsen number, it is important to distinguish the upstream free-stream Knudsen number, since according to our results, and in the case of shock interactions, the two complement each other.

The viscous effects in hypersonic flow at very low density were also investigated with a Mach 20.2 flow and a pressure of 0.067 Pa. In this case, the viscous effects of the hypersonic regime merge with the viscous effects of the rarefied regime. The analysis of the images did not allow the detection of shock/shock interactions in the sense that Edney defined them in the continuum regime, and which could be observed with the supersonic flows studied earlier in this work. In the hypersonic case, the different interference cases showed a diffuse evolution of the S_2 shock-wave which thickens strongly. Unfortunately, the diffusivity made it impossible to associate the interactions with the type I to VI SSI defined by Edney. In addition, the detection of shock-waves is very difficult due to the wide dispersion of the shocks. Moreover, even the determination of the shock stand-off distances is made difficult, increasing the inaccuracies. Only a slight increase of the stand-off distance of the boundary layer has been detected in the interaction area for an interaction angle of around -20°. Also, whether at the S_2 stagnation point or in the interaction area, the luminous intensity of images, which reflects the local density gradient, follows the same trend as in supersonic flow conditions. Thus, despite the difficulties recognised in identifying the different types of interference with confidence, the overall analysis of all the investigated aerodynamic parameters enabled to observe modifications in the aerodynamic behaviour of S_2 depending on its position in the wake flow of S_1.
The measurements carried out with the aerodynamic balance showed similar drag and lift force evolution than those of the Mach 4 experimental conditions. However, for the different position of S_2, the magnitude of deviation of the measured forces is much smaller than those observed in supersonic flow, with even very small lift force values that are of the same order of magnitude as the standard deviation of the reference values. It should be noted that the hypersonic flow studied at Mach 20.2 has a much lower reference pressure than the supersonic flows. This suggests that the aerodynamic forces are more sensitive to pressure effects than to Mach effects, even though, in the calculation of the aerodynamic coefficients, the Mach term is squared.
The aerodynamic forces and coefficients were compared with the numerical results obtained with the DS3V numerical simulation, and with literature results determined in the steady state also by numerical simulations. The comparison with the results of the Monte Carlo numerical simulations showed good agreement with the experimental results. Comparison with the steady-state results showed that the area of change in the drag coefficient of S_2 is larger in the rarefied regime, suggesting that the thickening of the shock-waves due to the overall rarefaction of the medium has a significant influence. In contrast, the behaviour of the lift coefficient shows a similar trend in terms of evolution to that predicted in the literature in the continuum regime. This result suggests that the behaviour of the lift coefficient does not depend on the global rarefaction of the free stream but rather on the size of S_2, and thus on the local rarefaction parameter. A bidimensional mapping of the drag forces, as well as the drag coefficient calculated with the free-stream flow conditions, were determined from the measurements achieved with the pendulum method. The results showed that the distribution of S_2 drag force in the flow of S_1 is similar to that obtained in supersonic flow. However, the gradient of drag force values in the shock interaction area seems to be less important with increasing global Knudsen number, probably due to a decrease of the local pressure effects. Indeed the wall pressure distribution is more widely distributed around S_2. This mapping was compared with results from the literature, obtained numerically for a flow similar to that undergone by our couple of spheres, showing strong similarities.

Global analysis of aerodynamic forces acting on S_2

A general behaviour of the rarefaction effects can be realised from a global analysis of the studied parameters taking into account all the couples of spheres in the three flow conditions studied in this work. We will first consider the maximal value drag and lift forces, measured for each pair of spheres and each experimental condition. Figure 11.1 presents the evolution of the maximal drag force as a function of the Knudsen number calculated with the free stream condition for each sphere size S_2. Figure 11.1 shows that the maximal drag force follows an exponential trend which depends on the Knudsen number: it decreases as the corresponding Kn_∞ increases.

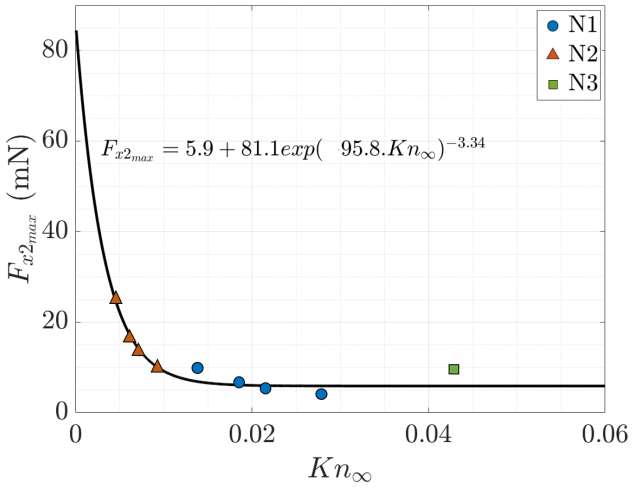

Figure 11.1: Maximal drag force of each experimented case according its free-stream Knudsen number.

Figure 11.2 shows the same maximum drag values, but normalised with their corresponding reference value. This time, the normalised maximal force is plotted according to the local Knudsen numbers. Only Mach 4 flow conditions are considered. For each condition N1 and N2, their behaviour is linear and the force

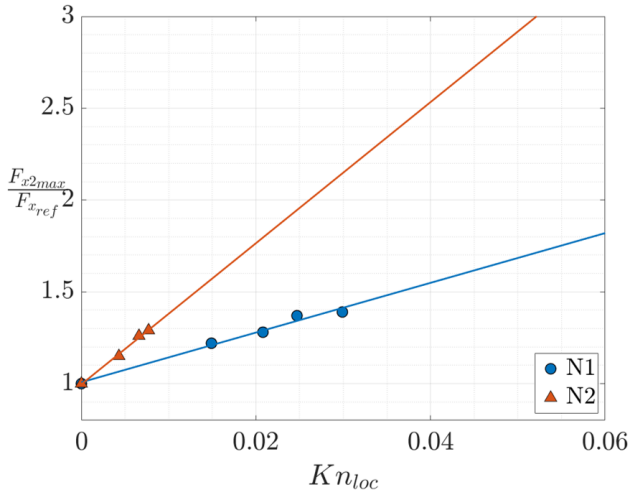

Figure 11.2: Normalized maximal drag force of each experimented case according its local Knudsen number.

ratio increases with the local Knudsen number. This force ratio is equivalent to the ratio of the local drag coefficients with respect to the reference coefficient determined for the free-stream conditions. This evolution suggests a linear increase of the local drag coefficients with the local Knudsen number. To a flow condition (Mach - pressure), corresponds to a unique line passing by 1. This behaviour suggests that it would be sufficient to have only one $F_{x2_{max}}/F_{x_{ref}}$ value for a local Knudsen number to determine the $F_{x2_{max}}/F_{x_{ref}}$ values of the different possible interference cases.

Another interesting behaviour is that of the maximal lift force plotted according to the similarity parameterFigure 11.3. The trend also follows an exponential progression. As a reminder, this curve represents

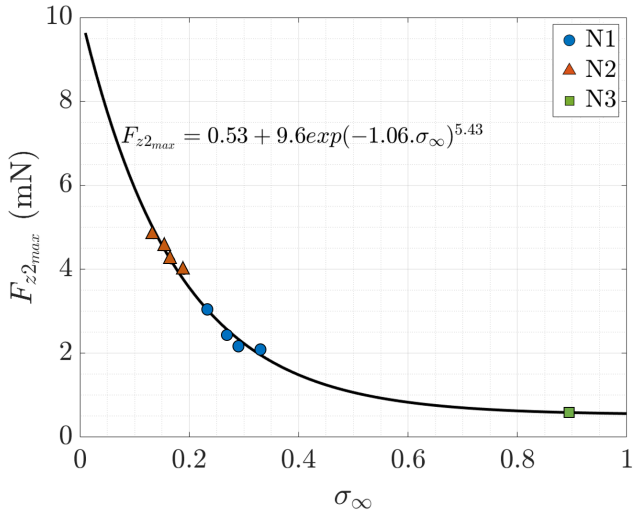

Figure 11.3: Maximal lift force of each experimented case according its free-stream similarity parameter.

the maximal lift force experienced by S_2 when interacting with S_1, whatever the size of sphere S_2 and the flow condition. This behaviour seems quite universal and would allow us to predict the maximal lift force of S_2, as long as the similarity parameter can be calculated. It should be noted that, as the evolution of the maximal lift force depends on the similarity parameter, it integrates the number of Mach and the free-stream condition of the free flow.

Finally, Figure 11.4 presents the ratio of maximal lift to drag as a function of the similarity parameter. For each Mach 4 flow condition, we notice a linear behaviour which seems to indicate that, when the size of S_2 is smaller than S_1, its ability to move forward, without losing altitude, will be easier. This ability is increased with the decrease of the rarefaction effects, as shown very clearly with the Mach 20 condition, for which we extrapolated the linear behaviour.

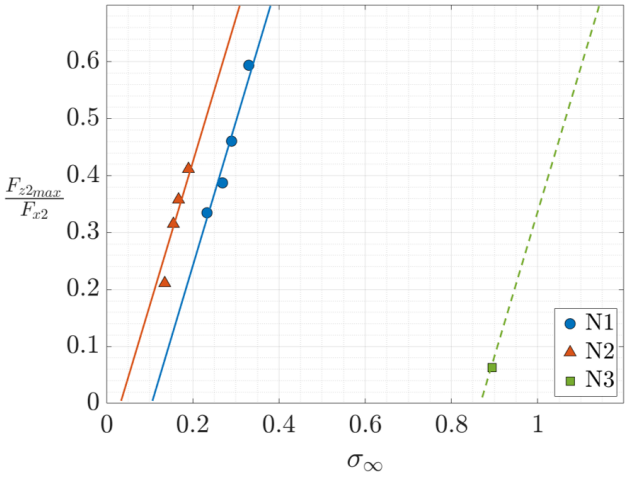

Figure 11.4: Maximal lift-to-drag ratio of each experimented case according its free-stream similarity parameter.

Overall conclusion

In the low space environment (60 to 90 km), aerodynamic interactions in rarefied flows are of great interest. This phenomenon can occur during the atmospheric re-entry of space debris, but also of meteoroids, or space shuttles. They as well can be encountered during the launch of TSTO, due to the geometry of the spacecraft, or at the separation of the different stages. In any case, aerodynamic interactions can either lead to a variation in the predicted trajectory, or to structural damages on spacecraft.

A lot of work has been devoted to shock/shock interferences and aerodynamic behaviour of proximal bodies, but few take into account the viscous effects induced by the rarefaction level of high altitude flow. This work experimentally explored this aspect in the MARHy wind tunnel.
Three free-stream flow conditions were experimented (N1 (Ma 4 - 2.67 Pa), N2 (Ma 4 - 8 Pa), and N3 (Ma 20.2 - 0.07 Pa)), with a set of 6 couples of spheres. These supersonic and hypersonic rarefied flows allowed to obtain an important database thanks to the experimental diagnosis exposed in Figure 11.5. In addition to this experimental database, some numerical simulations were realised with the open-access codes DS2V and DS3V.

	N1				N2				N3	
	C_1	C_2	C_3	C_4	C_1	C_2	C_3	C_4	C_5	C_6
Flow-field visualisation	✓	✓	✓	✓	✓	✓	✓	✓	✓	✓
Drag and lift forces of S2 (Balance)	✓	✓	✓	✓	✓	✓	✓	✓	✓	
Wall pressure of S2	✓				✓				✓	
Drag forces of S2 (Swinging technique)	✓				✓					
Drag forces of S1 (Swinging technique)	✓									

Figure 11.5: Summary table of the experimental diagnostics.

The overall results allowed to evaluate the shock/shock interferences and aerodynamic behaviours of a sphere flying in the vicinity of a primary one, coupled with the viscous effect characteristic of the rarefied regime. Results showed that the main differences observed between the continuum and the rarefied regimes come from the increase in viscous effect. In the hypersonic case, if one could have expected much stronger shock/shock interferences, we observed the contrary. Indeed, due to the high level of rarefaction, the viscous effects of hypersonic flows are coupled with those of the slip regime. As a consequence, the shock-waves are much thicker and more diffused than in supersonic, which dissipate the SSI near the surface of the following sphere. However, while images were not allowing identifying different types of SSI in the sense of Edney, we did observe a variation of the aerodynamic behaviour of the following sphere, as was the case in the supersonic rarefied flows. This let us think that, the surface of the flying debris will be less impacted in terms of heat transfer and pressure load, but its trajectory will still depend on the SSI.

Perspectives

This work has shown the importance of the rarefaction effect for two supersonic iso-Mach flow-fields, and for a Mach 20.2 flow at very low density conditions with 0.07 Pa. In order to complete our investigation, an additional flow condition can be investigated. Indeed, the MARHy wind tunnel possesses another Mach 20 nozzle, but with a free-stream pressure of 0.21 Pa. This nozzle will be interested since the mean free-path

of the flow is about that of the Mach 4 flow with a free-stream pressure of 2.67 Pa. As a consequence, such flow conditions would allow investigating:

- the effect of Mach number at iso-Knudsen (Ma 4, 2.67 Pa vs. Ma 20, 0.21 Pa)
- the effect of global rarefaction level at iso-Mach in hypersonic conditions (Ma 20, 0.07 Pa vs. Ma 20, 0.21 Pa)

Moreover, supplementary material could be investigated, and particularly for the hypersonic condition. Indeed, due to the very low density, the visualisation method (glow discharge) did not allow clearly observing the SSI as defined by Edney. A visualisation by electron beam delivered thanks to the electron gun currently is under development in our team. It would give much better results in terms of local visualisation of the flow. Furthermore, it is a non-intrusive method to measure the local density in the flow, which would improve the knowledge of the different flow-field.
Moreover, in the near future, we intend to complete the wall pressure measurements for the hypersonic conditions, which, unfortunately, were not achieved due to technical issues. Another information that would be interesting to have is that of the heat flux. Indeed, wall pressure and temperature measurements would help better describe the aerodynamic phenomena occurring for SSI in hypersonic flow conditions. Above all, it would bring information on whether the high critical conditions encounter for the type IV SSI in the continuum regime are still as damaging when strong viscous effects appear. The heat flux measurement will be measured with the thin-walls temperature technique. The model for this measurement is a hollow sphere made of stainless steel, which wall is of less than 1 mm, to conduct as little as possible the thermic effects. For this purpose, a micro-thermocouple have to be welded on the inner surface of the sphere as shown in Figure 11.6. The welding technique is very specific and requires the knowledge and welding equipment of an expert. The fitting up of the sphere with thermocouples is currently in progress. Unfortunately, due to the size of the sphere, and the very small number of people who know this technique, the model is not yet finished.

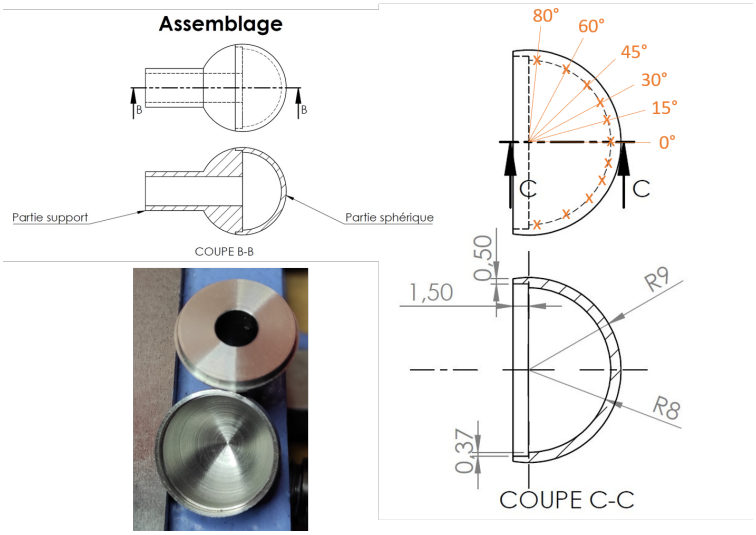

Figure 11.6: Model for heat flux measurement.

The study of spheres brought new knowledge on a typical canonical geometry. However, during the re-entry, different shape of objects are found, in particular cubes or cylinders. Unfortunately, the cylinder shapes develop large shock-waves which implies to use very little model. As a consequence, the measurement technique will have to be adapted.
The problems related to the interaction of shocks can also be found with more complex geometries like satellites. To this aim, preliminary studies with a common satellite shape that could re-enter the atmosphere,

different CubeSat models were experimented for three iso-Mach flow conditions with the following free-stream pressures: 2.67 Pa, 5.33 Pa and 8 Pa. In a first approach, we investigated the shock-waves of 1U, 2U, 3U CubeSat model, but also the body of the 3U alone, and the solar panel of the 3U alone. The shock-wave visualisations are presented in Figure 11.7.

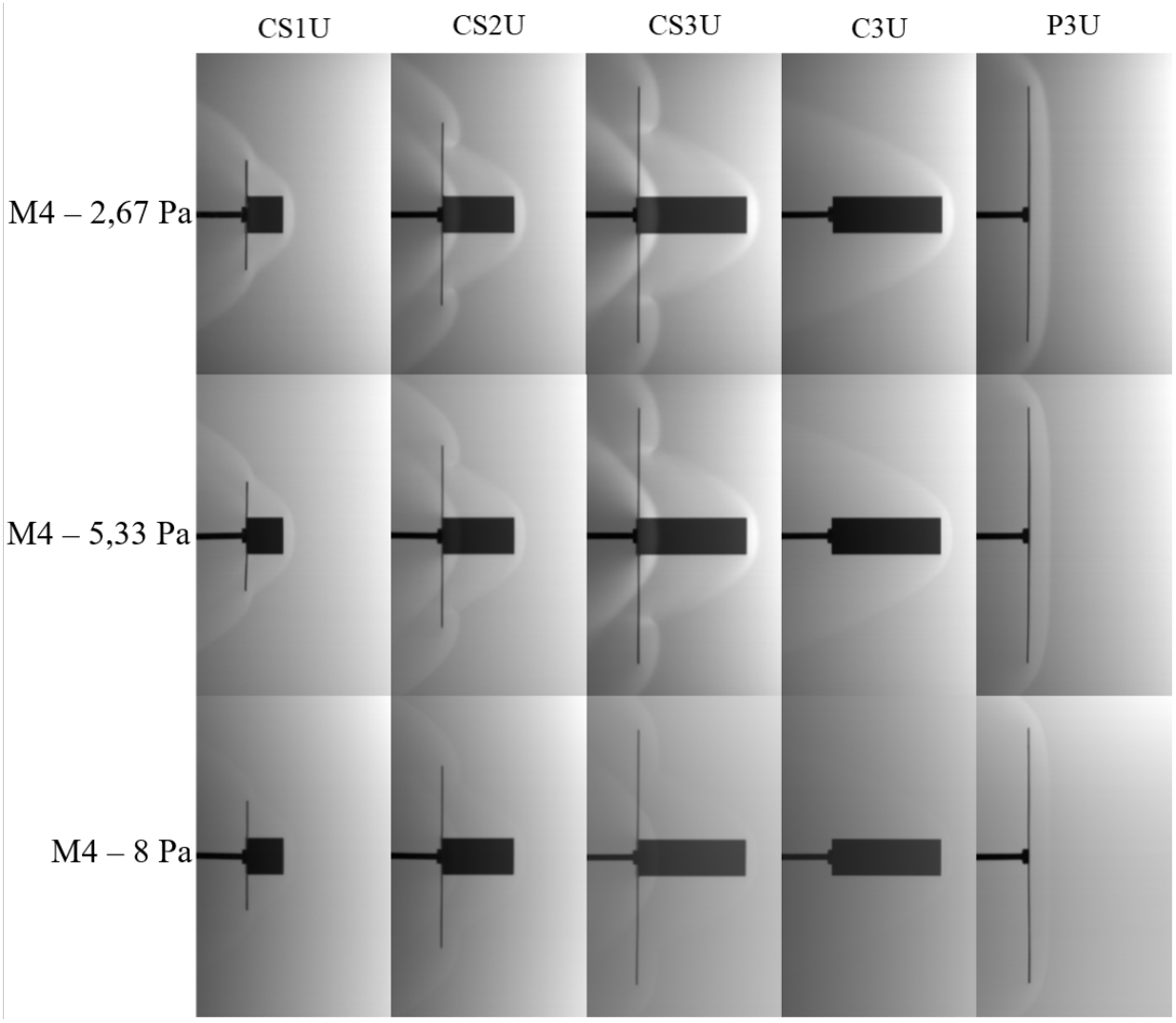

Figure 11.7: Flow-field visualisation of different CubeSat configurations, and decompositions.

If looking more in detail at the 3U CubeSat for the Ma 4 - 2.67 Pa shown in Figure 11.8, we do observe shock/shock interferences, which is interesting in the context of this thesis. Thanks to the three nozzles of the MARHy wind tunnel, we have been able to experiment with three different levels of rarefaction without changing the free-stream velocity, which allows investigating one parameter at a time. The database has given an important number of physic interests. First of all, the size of the CubeSat model is an important parameter considering the changes in the angle, and diffusivity of the incident shock, when arriving close to the shock/shock interference region on the panels. The angle may change the interference type, whereas the diffusivity can change the aero-thermodynamic parameters. Considering the rarefaction level, a change in Knudsen number seems to have consequences on the intersection and maximum intensity points. These coordinates and values show variations on the location and also on the density of the interaction region. This preliminary study has given a good insight into the interest in further studying the interactions between objects during their re-entry into the atmosphere, and particularly on more complex object shapes. Both numerical and experimental studies are needed to better understand the physics of shock/shock interferences. In a middle-term it would be interesting to characterise the aerothermal loads occurring during atmospheric re-entry to provide interesting information about the fragmentation breakpoints

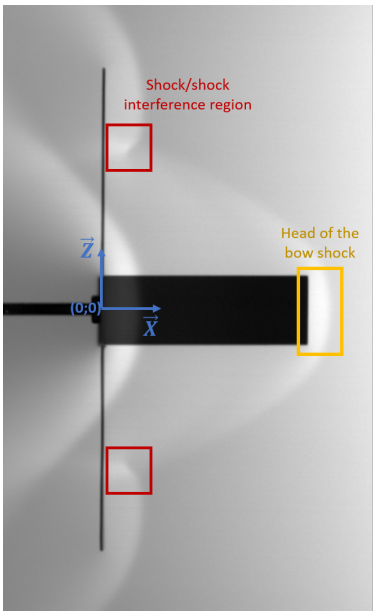

Figure 11.8: Flow-field visualisation of a 3U CubeSat in a Ma 4 - 2.67 Pa.

and the aerodynamic characteristics of the new fragments.

Appendix

Appendix A

Main studies on the aerodynamic interactions

Author	year	Num / XP	Flow conditions							Flow regime	Interaction configuration	out put
			Mach	Pressure Density	Temperature	Reynolds	Altitude	Knudsen	Similarity Number			
Agir, White, Kontis	2022	XP	10	[3,92e-4 ; 1,96e-3 ; 9,79e-5] kg/m^3	52,5 K	[1820 ; 910 ; 455]		[0,0067 ; 0,0134 ; 0,0268]		continuum & slip	wedge_cylinder	Cp, Ch, Cf for all SSI evolution of density, rotationnal temp, translational temp along Z=0
Albertson	2005	XP	6	4,8e-2 kg/m^3	61 K	1,312e7 /m					wedge_angled cylinder	flow field visualization for SSI types III and IV
Artem'eva, Shuvalov	1996 2001	Num					20-50 km			continuum	cylinder-spheres-cubes, meteorites	behaviour meteorites
Barri	2009 2010	Num	6							continuum	spheres	Cd, Cl with different sphere sizes
Berry	1997	XP	6	[9,3e-3 - 1,1e-1] kg/m^3		[1,5e5 - 2,44e6] /m				continuum	wedge _ sweep	flow-field visualisation Q/Qo
Bertrand	1997	XP	4,96			12,74e6 /m				continuum	wedge_cylinder	flow-field visualisation Q/Qo, p/po for SSI type III and IV
Boiko, Klikov, Poplavskii	2003	XP	[1,15 - 1,75]							continuum	spheres	flow-field visualisation front shock interaction of 2 spheres (Mach reflection)
Boldyrev, Borovoy	1997 2001	XP TsAGI short duration wind tunnel UT-1	6			[2,2e4 ; 1,6e6]		[4,04e-4 ; 5,56e-6]	[0,0405 ; 0,0047]	continuum & limit slip	wedge_cylinder	flow-field visualisation Q/Qo for SSI type III and IV
Botin	1993	XP + Num	6,5	1,54 Pa 5e-5 kg/m^3	106 K	32		0,065		slip	wedge _ cylinder	flow-field visualisation Stanton number
Bramlette	1974	Theoretical	6							continuum		prediction of the transition between SSI types III and IV
Butler, Whalen, Sousa,	2021	XP + Num	6,3	600 Pa 0,02 kg/m^3	100 K					continuum	wedge_ free flying sphere	Cd, Cl, center line pressure, trajectory

Figure A.1: Bibliography list 1 [1, 6, 20, 22, 21, 25, 27, 32, 33, 35, 36, 37, 38, 191].

Author	year	Num / XP	Flow conditions							Flow regime	Interaction configuration	out put
			Mach	Pressure Density	Temperature	Reynolds	Altitude	Knudsen	Similarity Number			
Carlson	1992	Num DSMC	15	9,2e-3 kg/m^3	241 K		35				wedge_cowl lip	
D'Ambrosio	2006	Num	10	5,9 Pa	52,5 K	1,66e5 /m ==> 2656			0,195	transitional	wedge _ cylinder	flow-field visualisation of all SSI, wall pressure, heat flux
Edney	1968	XP FFA small hypers wind tunnel Hyp 200	4,6			[4,05e6 ; 4,75e7]/m ==> [1,2e5 ; 1,4e6]		[5,61e-5 ; 4,79e-6]	[0,0133 ; 0,0039]	continuum & limit slip	wedge_cylinder wedge_sphere wedge_square	flow field visualization pressure distribution
Fisher	2018	XP HSST facility free fligth	5			[711000 220400 125700]		[1,04 3,34 5,8]e-5	[0,0059 0,0107 0,0141]	continuum	spheres	images Edney types interferences , schlieren, CD
Glass, Moss	1989 1999	Num, CFD (comparision with expe POT, and DSMC Moss)	10	5,9 Pa	52,5 K	1,66e5/m ==> 2658			0.194	slip	wedge_cylinder	interferences type III and IV
Goluveb	2012	Num	[2-6]			5.2e+05	20 km	1,70E-05	0.0083	continuum	concave shapes	Cd, Cl for aligned spheres
Grasso, Purpura, Chanetz, Délery	2003	XP R3CH wind tunnel	[9.56 ; 9.95]					[7e-4- 8,65e-5]	[0.062 -0,022]	continuum	wedge-cylinder	SSI types III and V p/po, Q/Qo
Gusev	2004	XP + Num	6,5			[5-128]					wedge_cylinder	Ch, Cp
Holden	1992	XP	[11,9 - 16,3]	[3,1 - 145] Pa	[40 - 54] K	[1,31e5 - 5,25e6]/m ==> [2100 - 84000]		[2,22e-4 - 1,03e-2]	[0,32 - 0,0431]	continuum & limit slip	wedge-hemispherical	SSI types III and IV Cp, Q/Qo
Keyes	1973	Analytic + XP	[6 ; 20]					[5.8e-05 ; 6.8e-06] [1.9e-04 ; 2.3e-05]	[0.0053-0.0153] [0.0175-0.0511]	continuum	wedge_hemispherical	all types of SSI p/po, Q/Qo
Khatta, Gopalan	2017	XP , shock tube HST_2	5,62	2 kPa	145 K	6,7e6/m ==> 335000		2,50E-05	0,0097	continuum	wedge_hemispherical	SSI types III and IV, flow-field visualisation, shock distance

Figure A.2: Bibliography list 2 [43, 57, 65, 70, 71, 77, 78, 79, 81, 82, 87, 101, 103].

Author	year	Num / XP	Flow conditions							Flow regime	Interaction configuration	out put
			Mach	Pressure Density	Temperature	Reynolds	Altitude	Knudsen	Similarity Number			
Kianvashrad	2019 2020	Num	14,6	0,95 kPa	47,37 K	0,14e6 /m ==> 4500		4,80E-02		continuum	wedge_hemispherical	SSI types III and IV
Klopfer	1988	Num	[8 ; 15]							continuum	wedge _ cowl lip	all SSI, stream line, surface pressure
Laurence, Deitering	2011	Num	10, 25							continuum	2 spheres, wedge _ sphere	images, trajectories wedge 20° schock angle 6°
Laurence, Deitering, Hornung	2007	Num + XP	10							continuum	2 spheres	Cd, Cl, different sphere sizes and distance
Leiser	2022	XP	7			6.1e+04	76 km	1,50E-04	0.0284	continuum	cylinders	flow-field visualisation, trajectory, aerodynamic forces
Li	2004	Num	1,96			45			0,292	transitional	2 spheres	Cd, Cl, Cp for aligned spheres
Li	2005	Num + XP	4							continuum	sphere _ cube	
Li	2016	Num	4							continuum	2 spheres	
Lind	1995 1996 1997	Num	8							continuum	wedge _ cowl lip	SSI type IV, p/po, flow-field visualisation
Lu	2013	Num	[6 ; 7 ; 8]								coalesced and non coalesced compression wave cylinder	SSI types III and IV, streamline, wall pressure, heat flux
Marwege A	2018	Num + XP	7	136,44 Pa	46 K	3,32e-6/m		6,25E-05	0,0172	continuum	2 spheres	Cd, Cl, shock wave surfing
Mason	2020	XP + Num	6	[0,4 ; 0,85 ; 1,72] kPa	61 K	[0,3 ; 0,6 ; 1,22]e6 /m					wedge _ vertical cylinder	oil flow
Moss, Pot, Chanetz, Lefrevre	1999	XP R5CH Num DSMC	10	5,9 Pa	52,5 K	1,66e5/m ==> 2658			0.194	slip	wedge _ cylinder	SSI type IV, Q/Qo, p/po, temperature profiles

Figure A.3: Bibliography list 3 [104, 105, 108, 116, 115, 117, 119, 120, 122, 121, 125, 124, 123, 133, 137, 138, 144].

Author	year	Num / XP	Flow conditions							Flow regime	Interaction configuration	out put
			Mach	Pressure Density	Temperature	Reynolds	Altitude	Knudsen	Similarity Number			
Paoli	2018	Num	[9.56-9.95]					[7e-4 ; 8,65e-5]	[0.062 -0,022]	continuum	blique shock _ cylind	SSI types III and IV, thermochemical relaxation effets
Park C	2012	XP shock tube	12	0,1577kg/m^3						continuum	spheres fragments	fragment trajectory
Park SH	2020 2021		6	1,2 kPa 0,017 kg/m^3						continuum		separation velocity and trajectory
Passey and Melosh	1980	Num + observation craters					<70 km			continuum	meteorites fragmentation	break up meteorites
Peng	2020 2022	Num	8,03	985 Pa	111,56 K	6,7e6/m				continuum	wedge_cylinder	
Pot, Chanetz, Lefevre, Bouchardy	1998	XP R5CH	10	5,9 Pa	52,5 K	1,66e5/m ==> 2658			0.194	slip	wedge_cylinder	SSI DLCARS
Riabov	2002	Num, DSMC	10			148		0,1	0,82	transitional	side to side cylinders	interaction side to side cylinders, effetc H/R
Riabov	2002	Num, DSMC	10					0,02-0,32		transitional	side to sideplates	interaction side to side cylinders, effetc H/R
Riabov, Botin	1999	XP + Num Navier stockes et DSMC	6,5			[15.5-124]		[0.012-0.1]	[1,65-0.58]	slip	wedge_cylinder	all SSI types, flow-field visualisation, Stanton number

Figure A.4: Bibliography list 4 [158, 159, 161, 162, 164, 166, 167, 170, 182].

Author	year	Num / XP	Flow conditions						Similarity Number	Flow regime	Interaction configuration	out put
			Mach	Pressure Density	Temperature	Reynolds	Altitude	Knudsen				
Sanderson	1995	XP T5 shock tube		Velocity (m/s) 2540 4450 5350 Density (kg/m³) 0.0218 0.0155 0.0157 Pressure (kPa) 1.03 5.48 11.4 N concentration (kg/mole) 9.9×10^{-5} 6.9×10^{-1} 3.65×10^{0}					continuum with real gas effets	blique shock-cylinde	SSI types III and IV, thermochemical relaxation effets, real gas effetcs
Singh	1991	Num	[5,94 ; 8,03]			[18600 ; 387500]		[4,74e-4 ; 3,07e-5]		continuum	wedge_cylinder	SSI type IV, p/po, Q/Qo
Vashchenkov Kashkovsky, Ivanov	2003	Num DSMC	27,5	8,1e-2 Pa	178 K	2220	95 km	0,018	0,57	slip	cylinders	Cd, Cl 2D mapping
Whalen, Laurence	2020 2021	Num + XP	6							continuum	spheres	spheres cluster, trajectory, lateral velocity, Cd, Cl
White, Kontis	2018	Num	10					[0.0067, 0.0133, 0.0267]		continuum and slip	wedge-cylinder	SSI types IV, flow-field visualisation, Cp, Ch, rotationnal temp along Z=0
Wieting	1967	XP HTT high temperature tunnel Langley	6,47							continuum	oblique shcock_cylinder	SSI types III, IV and V, flow-field visualisation, p/po, Q/Qo
Zhdan	2004	Num	[1,75 - 6]							continuum		Cx, Cy
Windisch, Reinrtz, Muller	2016	Num CFD	[5,5 ; 6,28]							continuum	oblique shock-cylinder	insteady SSI types IV and VII AIR and CO2 atmospheres with chemical reactions

Figure A.5: Bibliography list 5 [184, 190, 203, 209, 211, 212, 219, 215].

Appendix B

Hypersonic wind tunnels

Name Year of operation	Company and location	Mach number	Nozzle exit diameter [m]	Useful core [m]	Test gas	Flow regime	T0 [K]	P0 [atm]	Re 10-7 [1/m]	Running time [s]	Channels of data
U-6 1953	TsNIIMASh Korolev Moscow reg	6, 7, 8, 9.5 6, 8	f 0.276 f 0.35	f 0.166 f 0.21	Air	Blow-down (possible use of turbo-exhaust system)	493 -923	< 80	0.7 - 7	< 60	100
T-131B	TsAGI Zhukovsky	5 to 8	f 0.4	f 0.24	Air Supply of : GH2: 220g/s GO2: 1500 g/s	Blow-down	800-2350	< 110	0.01 - 1	< 180	
T117	TsAGI Zhukovsky	8 to 20	f 1	f 0.6	Air	Blow-down	700- 3000	8-200	0.015 - 0.4	60 to 180	
T-326 1975	ITAM Novosibirk	6 to 10, 14	f 0,2 M 6-10 contoured nozzle M 14 conical nozzle	f 0,12m	Air	Blow-down	< 3000	< 100	0.06 - 7	300	
T-313 1965	ITAM Novosibirsk	2 - 6	f 0,15 Test section : 0.6x0.6x2	f 0,09	Air	Blow-down	< 850	< 16	0.5 - 7	300	100
T121	TsAGI Zhukovsky	4,5,6 6,7,8,9	0,2x0,2 f 0,2	0.12x0.12 f 0,12	Air	Blow-down	1100	100	0.5 - 5	480	100
T116	TsAGI Zhukovsky	5,6,7,9,10 (+ 1.8 - 4)	f 1 (1x1)	f 0,6	Air	Blow-down	300 - 1075	<80	0.2 - 3.5	300	
U-306-3 1991	TsNIIMASh Korolev Moscow Reg	3,4,6,8	f 1.2 Test section : f 2.5 L 6 m	f 0.72	Air	Blow-down (possible use of turbo-exhaust system)	250 - 1000	< 100	0.05 - 20	0.5 - 600	60 15 (dyn.)
U4M 1975	TsNIIMASh Korolev Moscow Reg	1;8, 2 - 6	Test section : 0.6x0.6x2.	0.36x0.36	Air	Blow-down (possible use of turbo-exhaust system)	250 - 500	< 100	0.08 - 20	< 60 continuous	
LONG SHOT	VKI Brussels	14 15 to 20	f 0,43 f 0,6	f 0,258 f 0,36	N2 CO2	Shock tube	<2400	4000	<1.5	5 to 10 ms	64

Figure B.1: wind tunnels 1.

Name Year of operation	Company and location	Mach number	Nozzle exit diameter [m]	Useful core [m]	Test gas	Flow regime	T0 [K]	P0 [atm]	Re 10-7 [1/m]	Running time [s]	Channels of data
RWG	DLR Göttingen	5, 6, 6.8	f 0,5	f 0,3	Air	Blow-down	<670	<40	<6	<0.4	32 anal 32 digi
R3	ONERA Chalais-Meudon	10	f 0,35	f 0,21	Air	Blow-down	<1100	12 to 120	0,18 to 1,2	10	144
H2K	DLR Köln	5.3 6 7 8.7	f 0,60	f 0,36	Air	Blow-down	<1400	45	<2	<30	30
R2	ONERA Chalais-Meudon	5,6,7	f 0,326	f 0,196	Air	Blow-down	<700	<80	0,16 to 22	10 to 60	144
M7T	ARA Bedford	6, 7, 8	f 0,3	f 0.18	Air	Blow-down	<850	100-200	0.3-0.7	<60	
S4 1992	ONERA Modane	6.4 10 12	f 0,685 f 0,994 f 0,994	f 0,411 f 0,596 f 0,596	Air	Blow-down	500 to 1800 1000 to 1600 1300 to 1550	10 to 42 15 to 120 30 to 120	<2.8 <0.78 <0.32	40 to 90 25 to 85 25 to 85	48 to 120
R5	ONERA Chalais-Meudon	10	f 0,35	f 0,21	Air	Blow-down	<1100	2,5	0.167	90	
HYP500	FFA Bromma Stockholm	7	f 0,5	f 0,3	Air	Blow-down	<720	10 to 105	0,07 at 0,4 0,12 at 0,18	<120	64 analog 13 digi
V2G	DLR Göttingen	12-25	f 0,4	f 0,24	Air	Rarefied	<2000	100	<0.001	continuous	
V3G	DLR Göttingen	7-28	f 1,3	f 0,78	Air	Rarefied	800	50	<0.001	continuous	
SR3	CNRS Orléans	0.8-20			Air Nitrogen	Rarefied	300-1300	0.0002-120	0.00025-0.007	continous	

Figure B.2: wind tunnels 2.

Name Year of operation	Company and location	Mach number	Nozzle exit diameter [m]	Useful core [m]	Test gas	Flow regime	T0 [K]	P0 [atm]	Re 10-7 [1/m]	Running time [s]	Channels of data
UT-1M	TsAGI Zhukovsky	5, 6 16 6, 8, 10	f 0,3 f 0,4 f 0,5 Test section : f 0.5 L 1 m	f 0.18 f 0.24 f 0.30	Air, N2 He CF4 CO2	Ludwig (M 5 - 10) & shock (M 10 - 16) tunnel	500 - 2200	< 30	0.033 - 8	5, 20, 40 ms	96
U-12 1959	Ts NIIMASh Korolev, Moscow Reg	6-10	f 1,4 conical Channel section : f 0.5 L 200 m	f 0,84	Air N2 Co2 Gas mixtures	Shock tube	500 - 3000	<50	0,1 - 50	0.025 - 0.1	40
AT-303 1999	ITAM Novosibirsk	8 to 20	f 0,3, 0.6 M 8-12 contoured or conical nozzle M 12-20 conical nozzle	f 0.18, 0.36	Air N2 CO2	Adiabatic compression with pressure multiplier	500 - 2500	< 3000	0.5 - 20	0.04 - 0.2	60
IT 302 M 1980	ITAM Novosibirsk	5 and 6 7 to 15	0.2 at M=5 contoured 0.3 at M=6 contoued 0.33 at M=7 conical 0.5 at M=15 conical	f 0.12 f 0.18 f 0,198 f 0.3	Air N2 CO2	Hot-shot	< 3000	< 1000	0.06 -6	0.08 - 0.25	128 digi.
PGU U-7 1959/1993	Ts NIIMASh Korolev, Moscow Reg	10 to 15	f 0.4 f 0.8 Test section : f 1.4 L 6 m	f 0.24 f 0.48	Air, N2 CO2 He	Free piston non isentropic multi-cascade compression	< 3000	< 2500	0,01 - 3	0.1 - 1	32 digi.
VAT-3	TsAGI Zhukovsky	10, 12, 18, 20	f 0.15, 0.3	f 0.09, 0.18	N2 CO2	Blow-down	1000 - 2000	20 - 60	0.05-0.15 for M = 12 0.001-0.01 for M = 20	< 5	
T-327 1972	ITAM Novosibirk	16 to 25	f 0.2 conical	f 0.12	N2 pure from impurity	Blow-down	<1500	< 200	0.007-0.2	60	

Figure B.3: wind tunnels 3.

Appendix C

Free-stream flow-fields

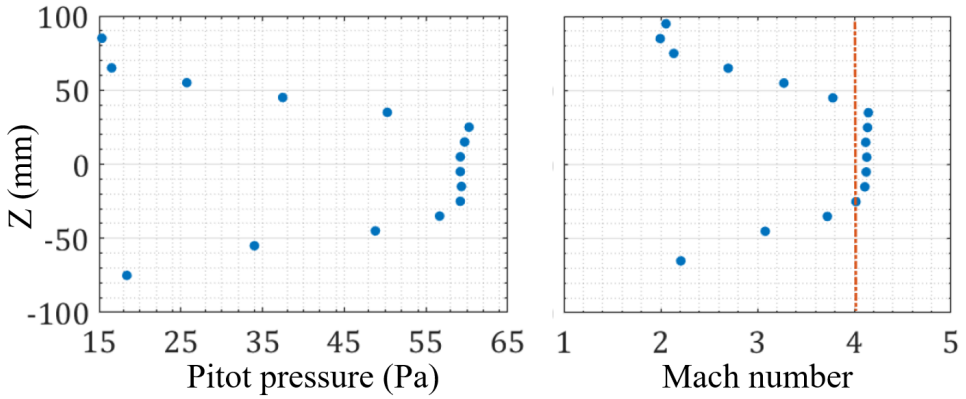

Figure C.1: Stagnation pressure and Mach number profile in N1 flow-field [179].

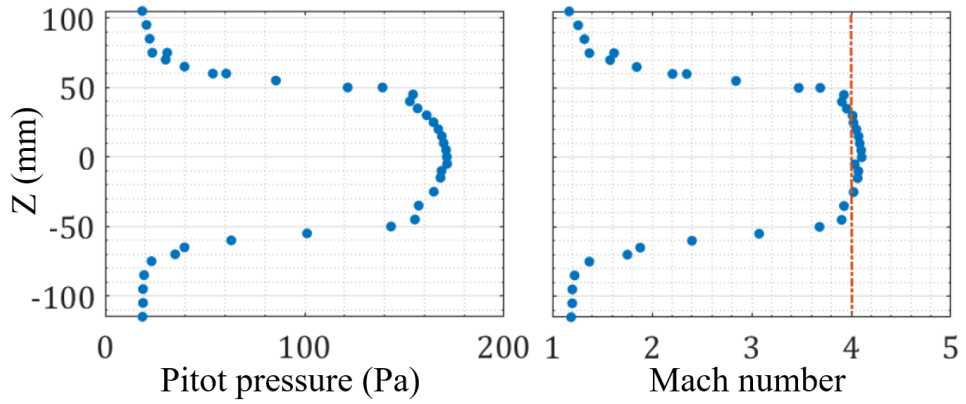

Figure C.2: Stagnation pressure and Mach number profile in N2 flow-field [179].

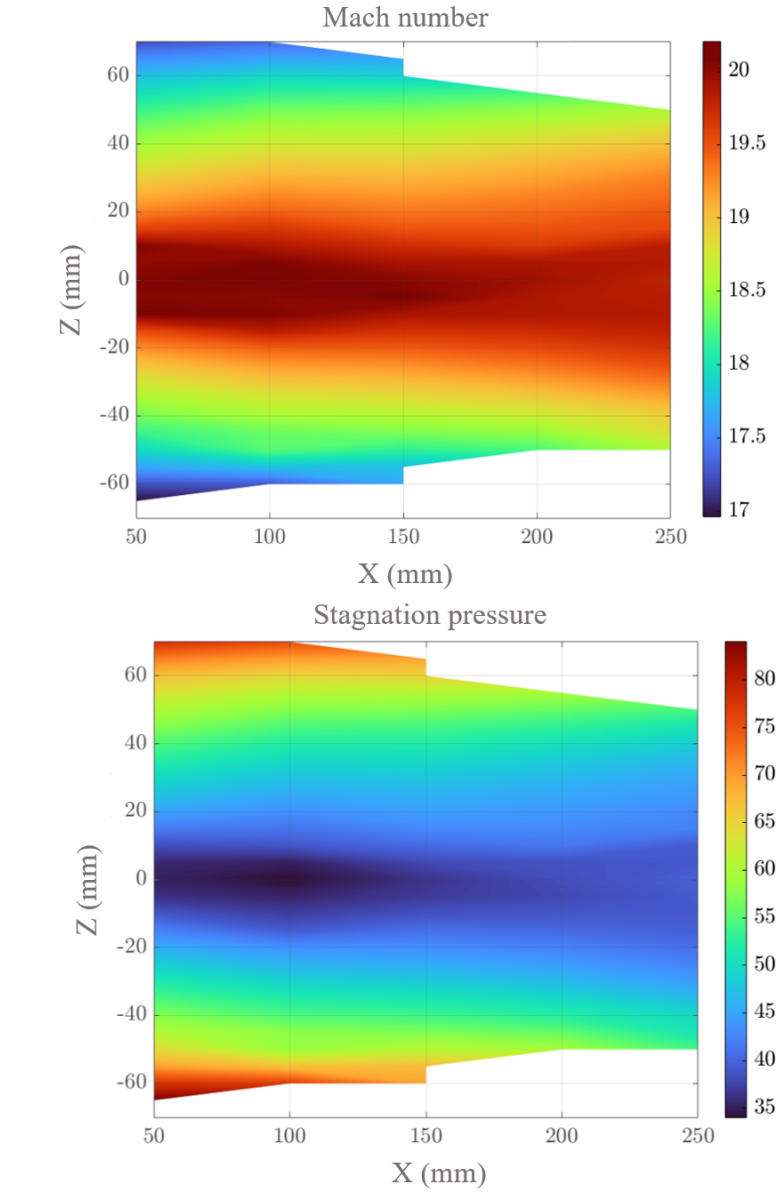

Figure C.3: Mach and stagnation pressure flow-field of N3.

Appendix D

Experimental data for a single sphere

		Standoff (mm)						Force de trainée	std
	$Ø_1$ (mm)	**PC**	std	**MC**	std	**BL**	std	**Fx (mN)**	(mN)
N1	16	2,76	0,16	1,99	0,16	0,89	0,16	8,11	0,15
	12	2,35	0,16	1,7	0,16	0,73	0,16	5,21	0,13
	10,3	2,26	0,24	1,62	0,24	0,75	0,24	3,83	0,17
	8	2,16	0,24	1,52	0,24	0,72	0,24	2,77	0,11
N2	16	2,02	0,16	1,54	0,16	0,76	0,16	21,52	0,10
	12	1,84	0,16	1,38	0,16	0,77	0,16	13,01	0,26
	10,3	1,61	0,16	1,15	0,16	0,69	0,16	10,32	0,10
	8	1,18	0,24	0,86	0,24	0,71	0,16	6,58	0,22
N3	18	4,5	1,02	2,48	0,23	0,46	0,23	8,68	0,68
	12			2,3	0,38	0,46	0,23		

Figure D.1: Stand-off distances and drag forces of the single spheres cases.

N1		N2		N3	
$Ø_1$ = 16 mm		$Ø_1$ = 16 mm		$Ø_1$ = 18 mm	
θ_{wp} (deg)	p_w (Pa)	θ_{wp} (deg)	p_w (Pa)	θ_{wp} (deg)	p_w (Pa)
92,50	3,76	90	14,57	90	4,32
82,50	6,29	80	23,99	80	5,39
72,50	10,49	70	37,66	70	7,61
62,50	16,23	60	56,46	60	10,84
52,50	23,58	50	79,92	50	15,43
42,50	32,10	40	106,28	40	20,6
32,50	40,68	30	132,01	30	26,15
22,50	48,23	20	152,43	20	30,68
12,50	53,59	10	165,29	10	33,58
7,50	55,20	5	167,91	5	34,43
2,50	56,04	0	168,50	2,5	34,71
0,00	56,17	-5	167,07	0	34,71
-2,50	56,04	-10	163,40	-2,5	34,71
-7,50	55,28	-20	149,31	-5	34,48
-17,50	51,33	-30	128,09	-10	33,58
-27,50	44,94	-40	102,58	-30	25,64
-37,50	36,88	-50	76,82	-50	15,03
-47,50	28,36	-60	54,36	-70	6,7
-57,50	20,49	-70	36,20	-90	2,9
-67,50	13,97	-80	23,55		
-77,50	9,00	-90	14,74		
-87,50	5,45				

Figure D.2: Wall pressure values of a single sphere.

X (mm)	Z (mm)	P_{pitot} (Pa)
8	9,51	32,90
	10,11	41,61
	12,23	71,33
	12,68	78,46
	13,13	85,79
	13,28	88,42
	13,58	90,86
	13,66	92,55
	13,74	93,22
	13,89	93,54
	14,04	93,66
	14,11	93,36
	14,64	86,11
	15,09	73,49
	15,55	63,91
	16,15	59,09
	16,60	57,45
	17,06	56,72
	18,11	56,23
	19,02	56,17

X (mm)	Z (mm)	P_{pitot} (Pa)
24,081	-0,16	6,33
	0,97	6,96
	3,07	8,21
	5,01	10,07
	7,11	13,19
	9,05	17,55
	10,99	23,15
	13,09	30,00
	14,06	34,36
	15,03	39,03
	15,52	41,83
	16,00	44,32
	16,48	47,44
	17,13	50,55
	17,62	54,29
	18,10	57,71
	18,26	59,89
	18,59	61,76
	18,75	63,63
	19,07	65,49
	19,23	67,99
	19,56	69,85
	19,88	71,72
	20,20	73,59
	20,36	76,09
	20,53	78,57
	20,85	81,07
	21,01	82,93
	21,33	84,81
	21,66	87,29
	21,82	89,16
	21,98	90,42
	22,14	91,04
	22,22	91,65
	22,30	92,28
	22,38	92,89
	22,46	93,52
	22,55	94,15
	22,63	94,77
	22,71	95,40
	22,79	96,02
	22,87	96,02
	23,11	96,01
	23,43	94,77
	23,60	92,89
	23,92	88,55
	24,08	82,94
	24,40	77,34
	24,57	71,73
	25,05	64,26
	25,21	61,15
	25,70	58,66
	26,10	56,79
	26,51	56,17
	26,99	56,17

X (mm)	Z (mm)	P_{pitot} (Pa)
32	0,15	10,92
	3,92	12,49
	8,00	17,60
	12,08	25,76
	16,15	37,59
	18,11	45,88
	20,08	55,92
	22,04	68,12
	24,15	80,65
	24,75	85,08
	25,21	88,19
	25,74	90,56
	25,89	91,32
	26,11	92,00
	26,19	92,13
	26,34	92,19
	26,57	91,75
	27,17	86,52
	28,23	68,54
	29,13	58,69
	29,58	57,20
	30,19	56,64
	31,09	56,28
	32,08	56,17

Figure D.3: Values of Pitot pressure in the wake of a 16-mm diameter sphere in N1 flow-field.

X (mm)	Z (mm)	P_{pitot} (Pa)
8	9,35	90,42
	10,30	146,58
	11,25	191,79
	11,72	212,34
	12,20	234,26
	12,67	257,55
	13,15	283,58
	13,31	294,54
	13,62	304,13
	13,78	313,72
	13,94	321,94
	14,10	326,05
	14,26	306,87
	14,89	213,71
	15,37	171,24
	15,84	169,87
	16,32	168,50
	16,79	168,50
	17,74	168,50

X (mm)	Z (mm)	P_{pitot} (Pa)
32	0,16	24,07
	9,92	62,30
	14,88	97,70
	19,68	169,92
	20,80	188,33
	21,76	208,15
	22,72	227,98
	23,68	247,80
	24,32	257,71
	24,48	261,96
	24,64	266,21
	24,80	270,46
	24,96	274,70
	25,12	278,95
	25,44	281,78
	25,60	286,03
	25,76	290,28
	26,08	293,11
	26,24	297,36
	26,40	298,78
	26,56	300,19
	26,72	291,70
	27,04	227,98
	27,52	179,83
	28,00	169,92
	28,48	168,50
	28,80	168,50
	31,68	169,92

Figure D.4: Values of Pitot pressure in the wake of a 16-mm diameter sphere in N2 flow-field.

Appendix E

DSMC of single spheres

In this appendix are presented the results of the simulations realized for single spheres. This calculations allowed to validate the input accommodation coefficients of the DSMC code of Bird (DS2V and DS3V), as presented in Table 6.3, thanks to a comparison with the experimental data. The same methodology as the one presented in 6.5 has been employed.

D16, N1, DS3V

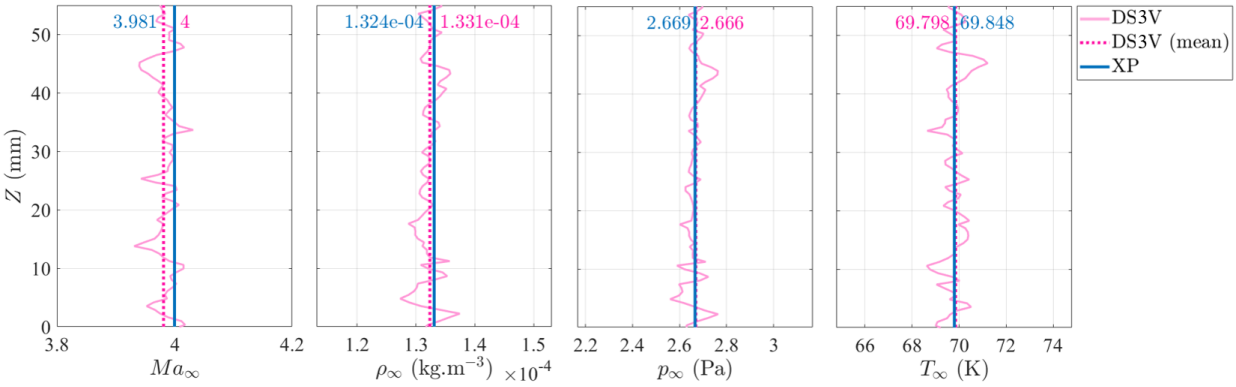

Figure E.1: Upstream conditions of the DS3V simulation for D16, N1.

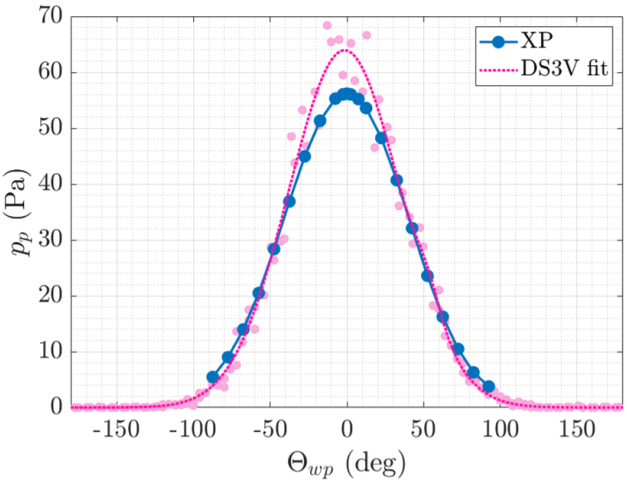

Figure E.2: Wall pressure distribution of the DS3V simulation for D16, N1.

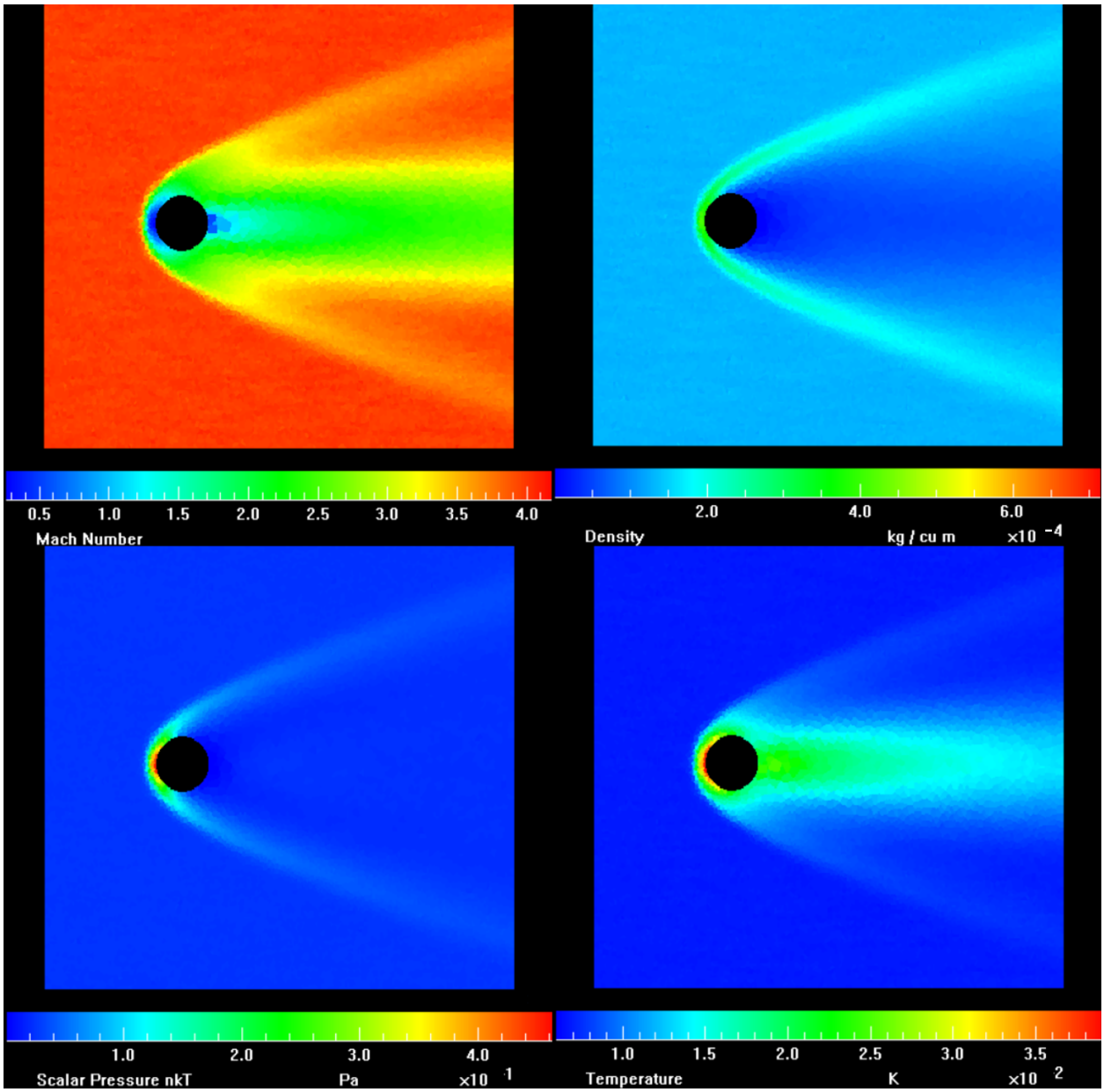

Figure E.3: Flow-fields of the DS3V simulation for D16, N1.

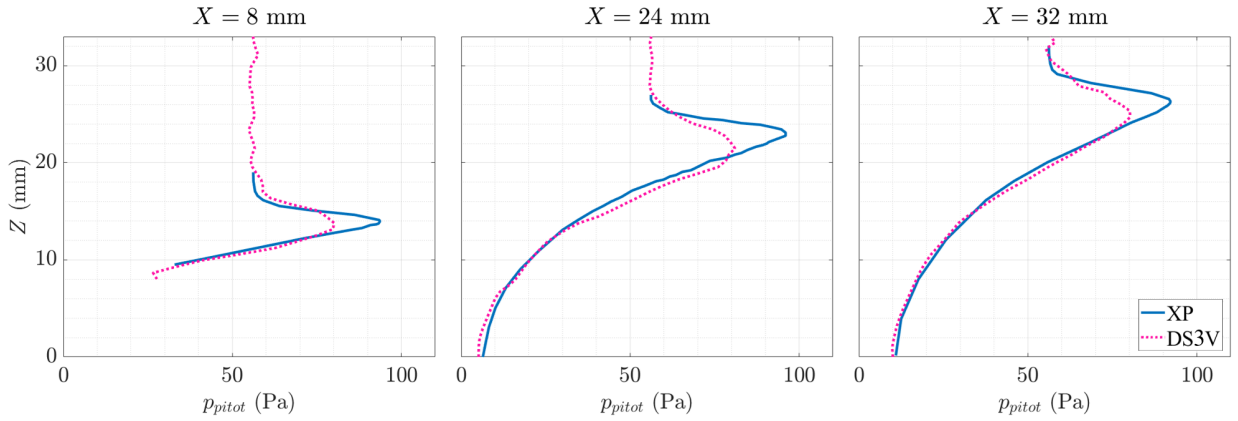

Figure E.4: Pitot pressure profiles of the DS3V simulation for D16, N1.

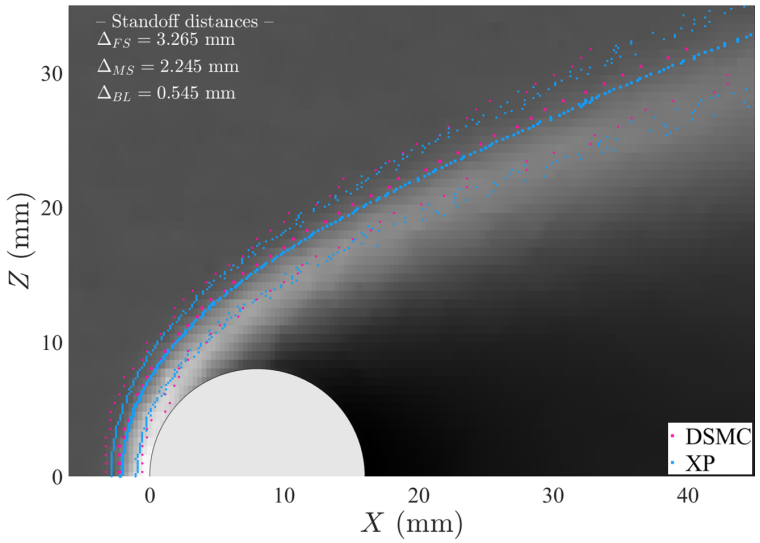

Figure E.5: Density flow-field with shock detection of the DS3V simulation for D16, N1.

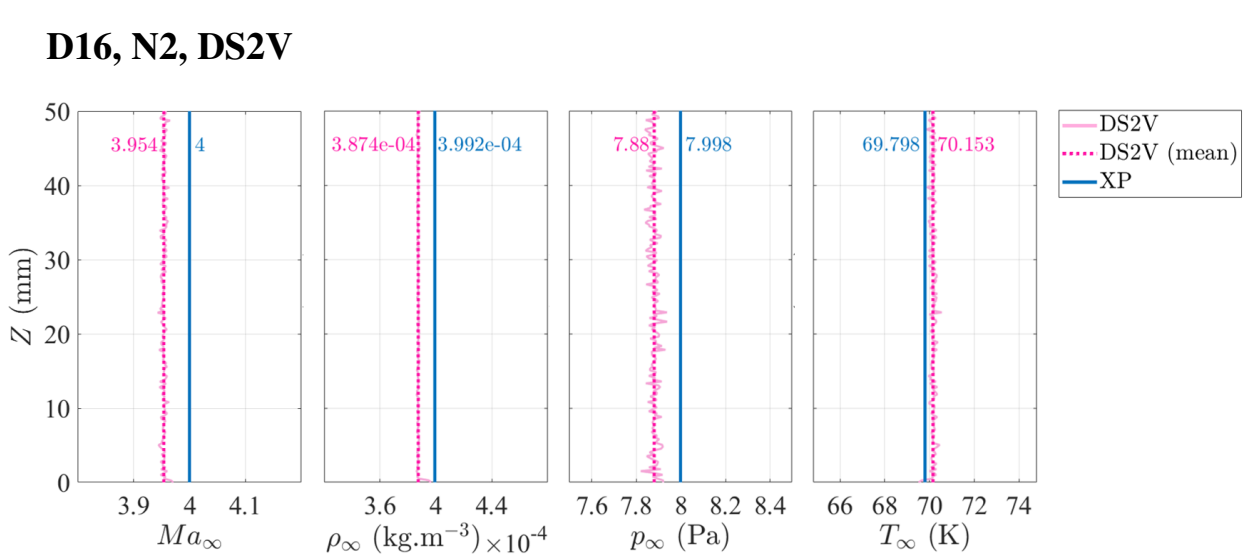

Figure E.6: Upstream conditions of the DS2V simulation for D16, N2.

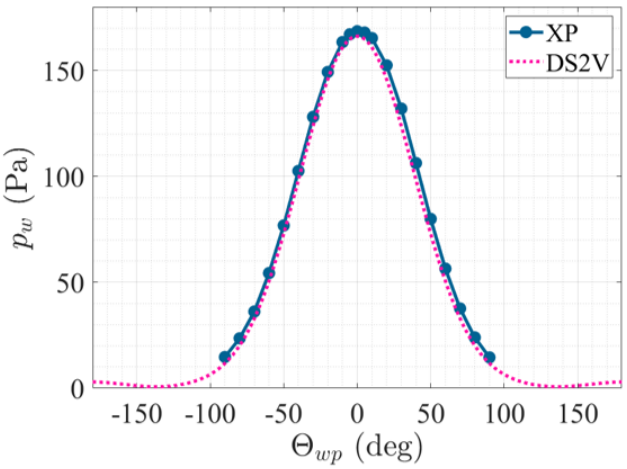

Figure E.7: Wall pressure distribution of the DS2V simulation for D16, N2.

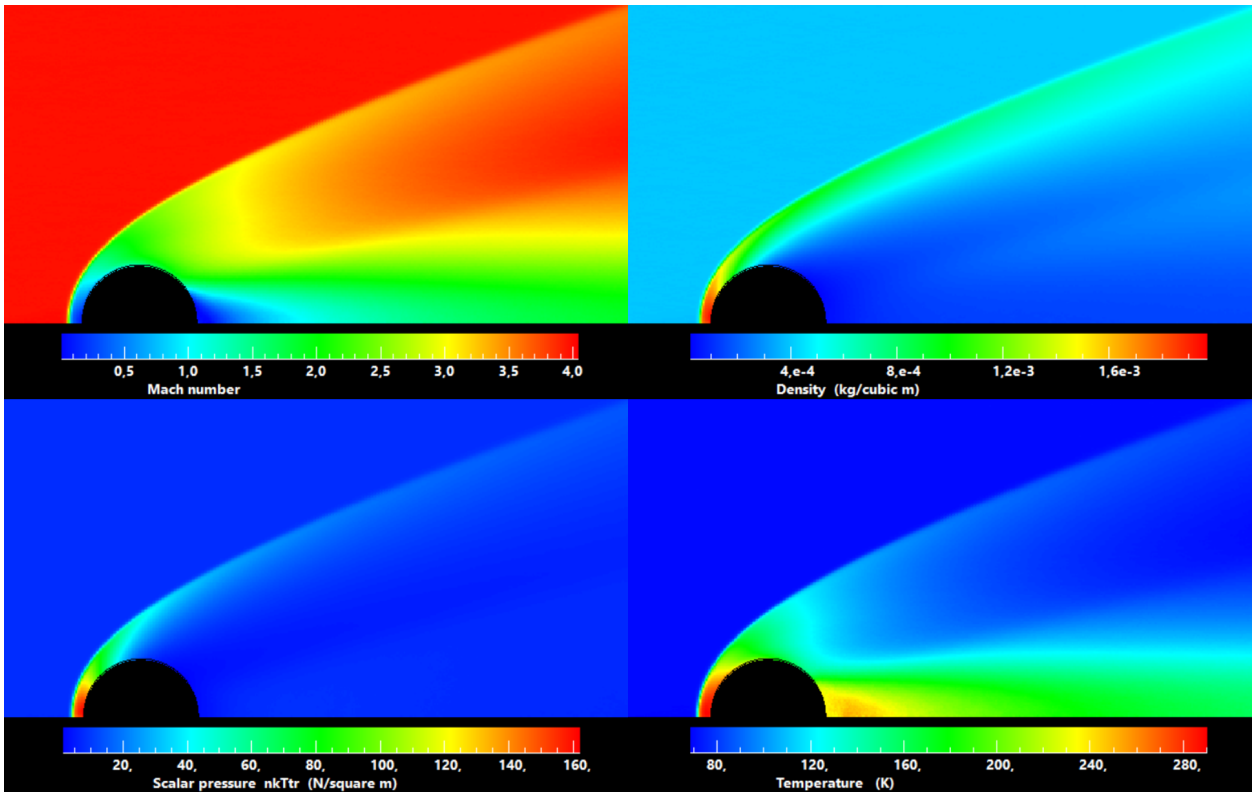

Figure E.8: Flow-fields of the DS2V simulation for D16, N2.

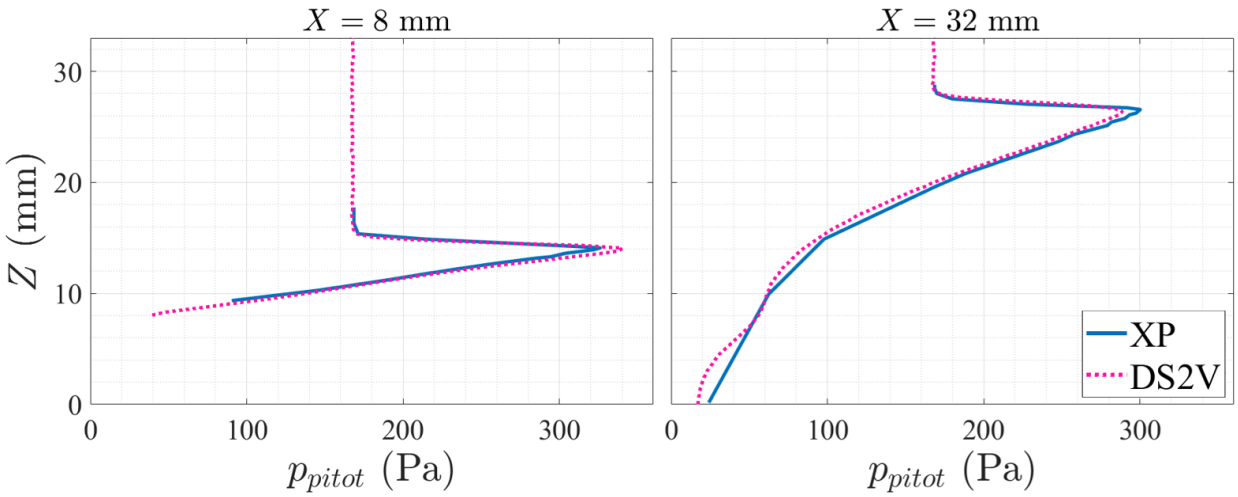

Figure E.9: Pitot pressure profiles of the DS2V simulation for D16, N2.

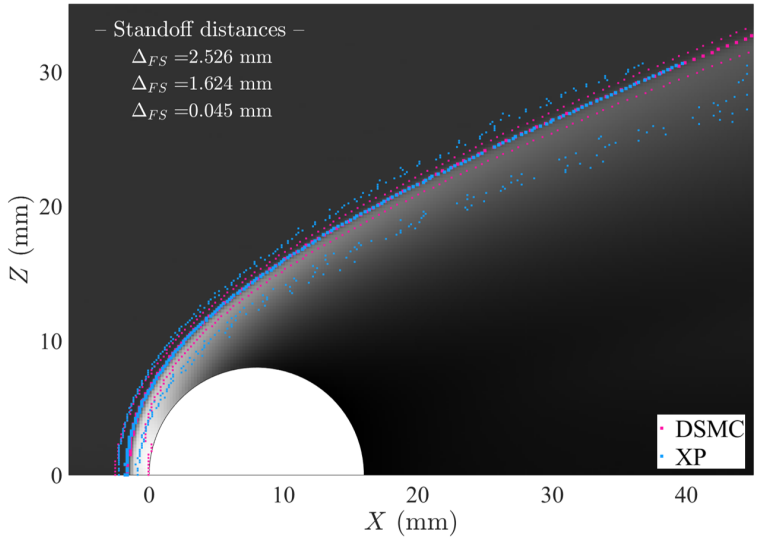

Figure E.10: Density flow-field with shock detection of the DS2V simulation for D16, N2.

D18, N3, DS3V

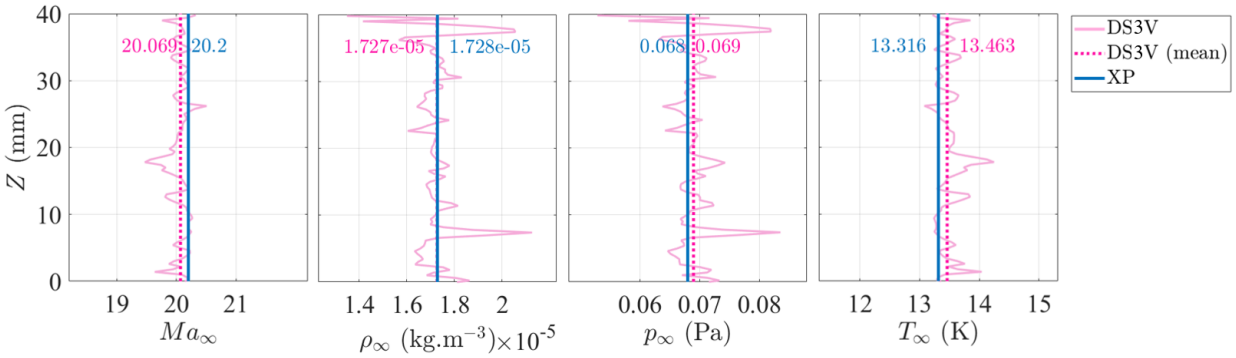

Figure E.11: Upstream conditions of the DS3V simulation for D18, N3.

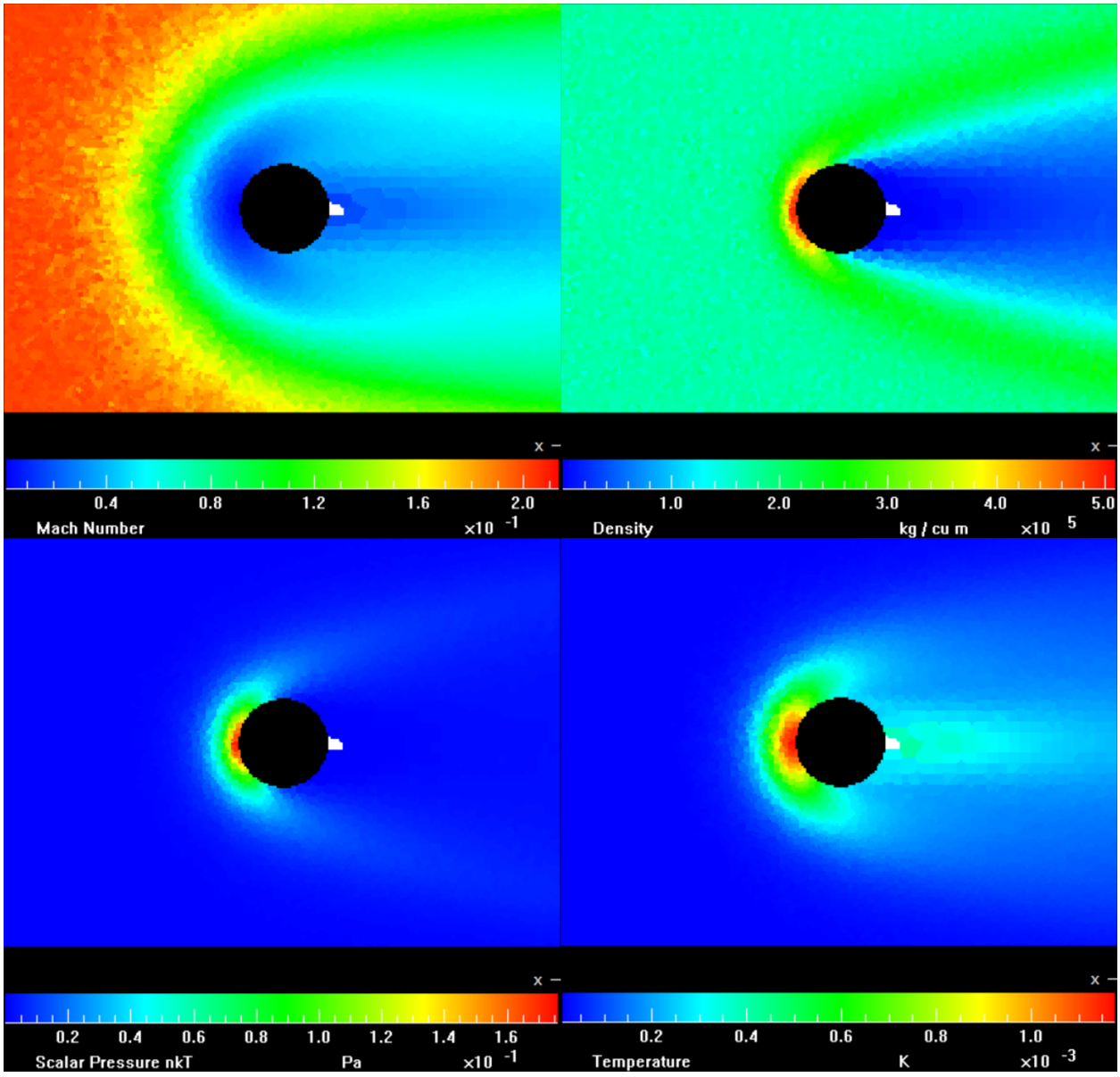

Figure E.12: Flow-fields of the DS3V simulation for D18, N3.

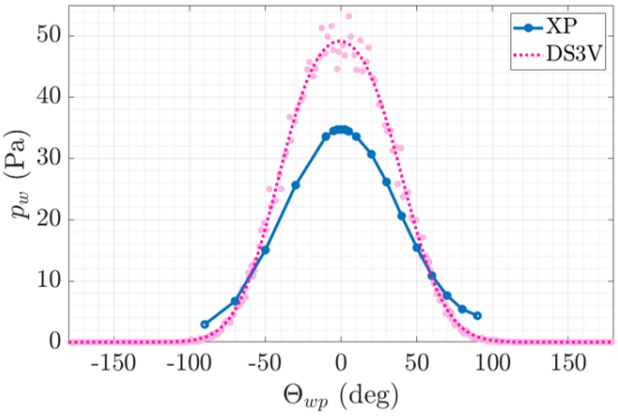

Figure E.13: Wall pressure distribution of the DS3V simulation for D18, N3.

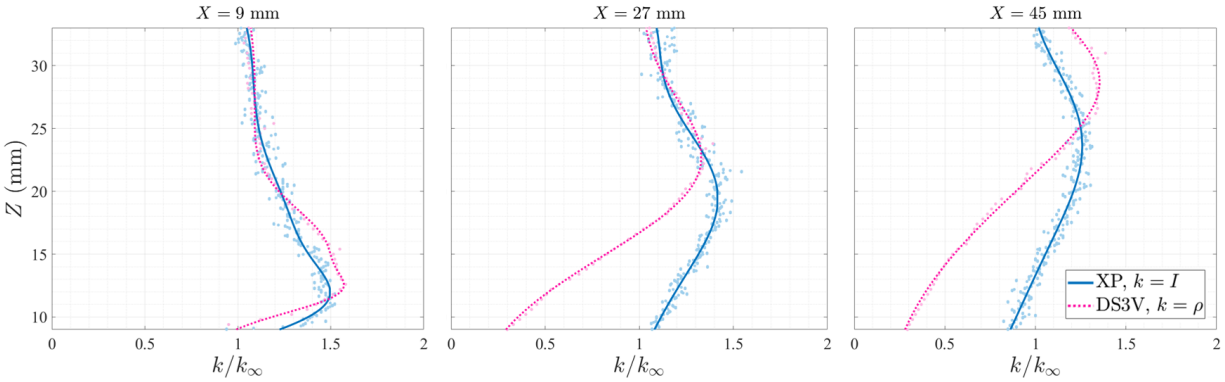

Figure E.14: Pitot pressure profiles of the DS3V simulation for D18, N3.

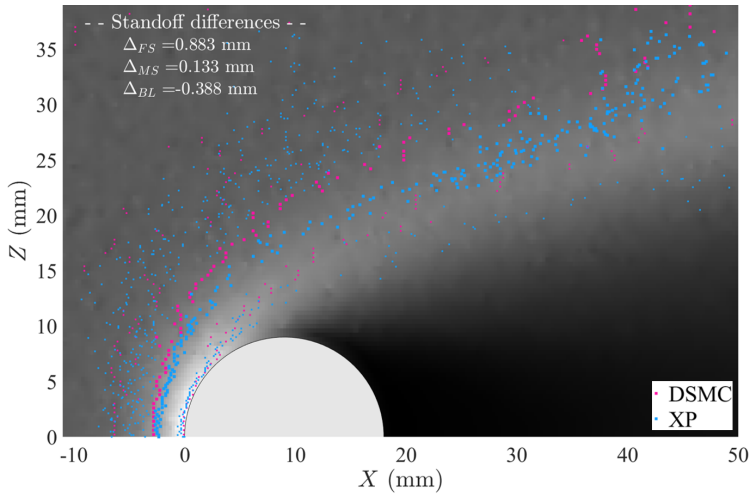

Figure E.15: Density flow-field with shock detection of the DS3V simulation for D18, N3.

Appendix F

Experimental images (normalized and enhanced)

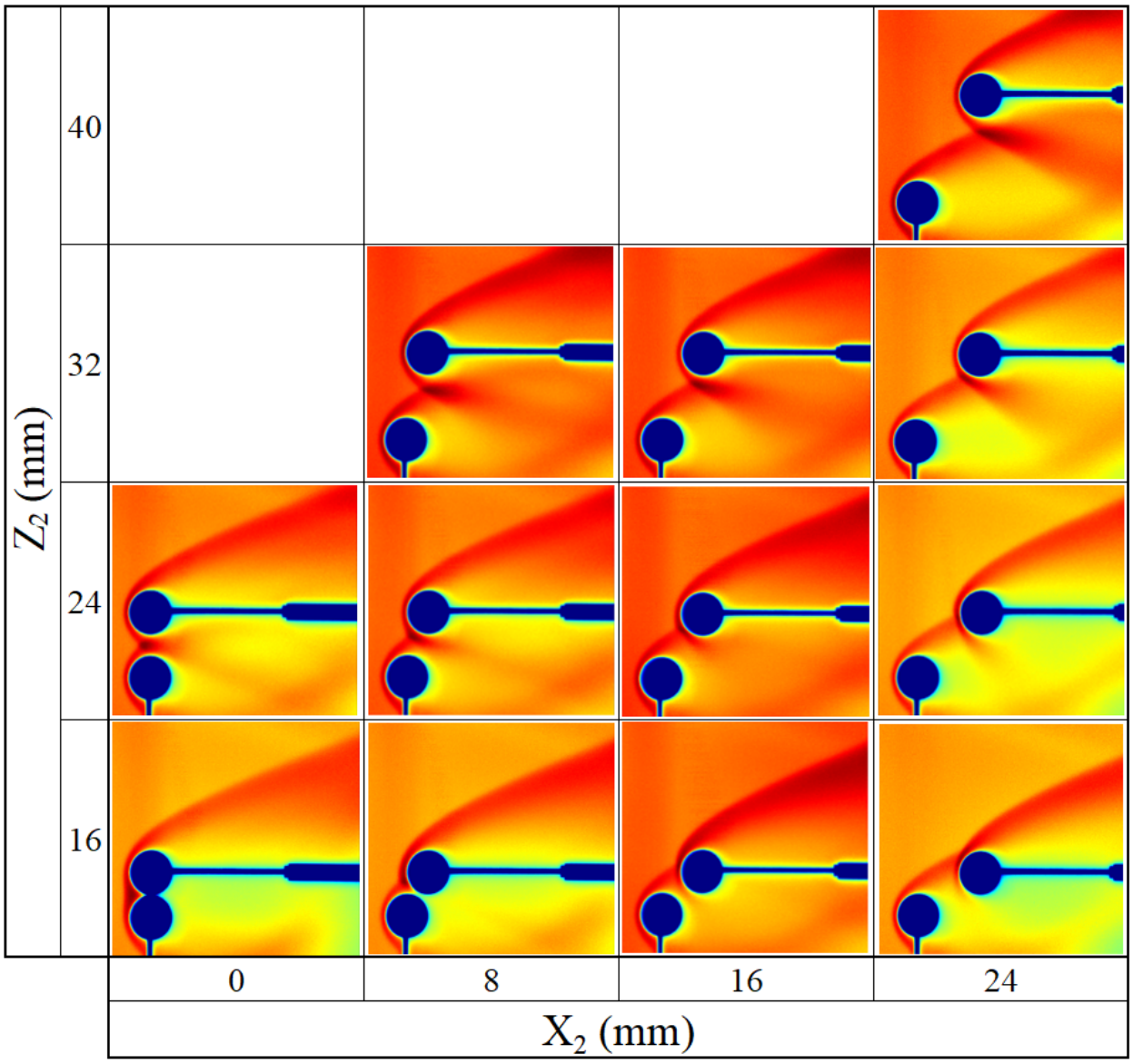

Figure F.1: C_1 in N1 flow-field, full mapping, part 1.

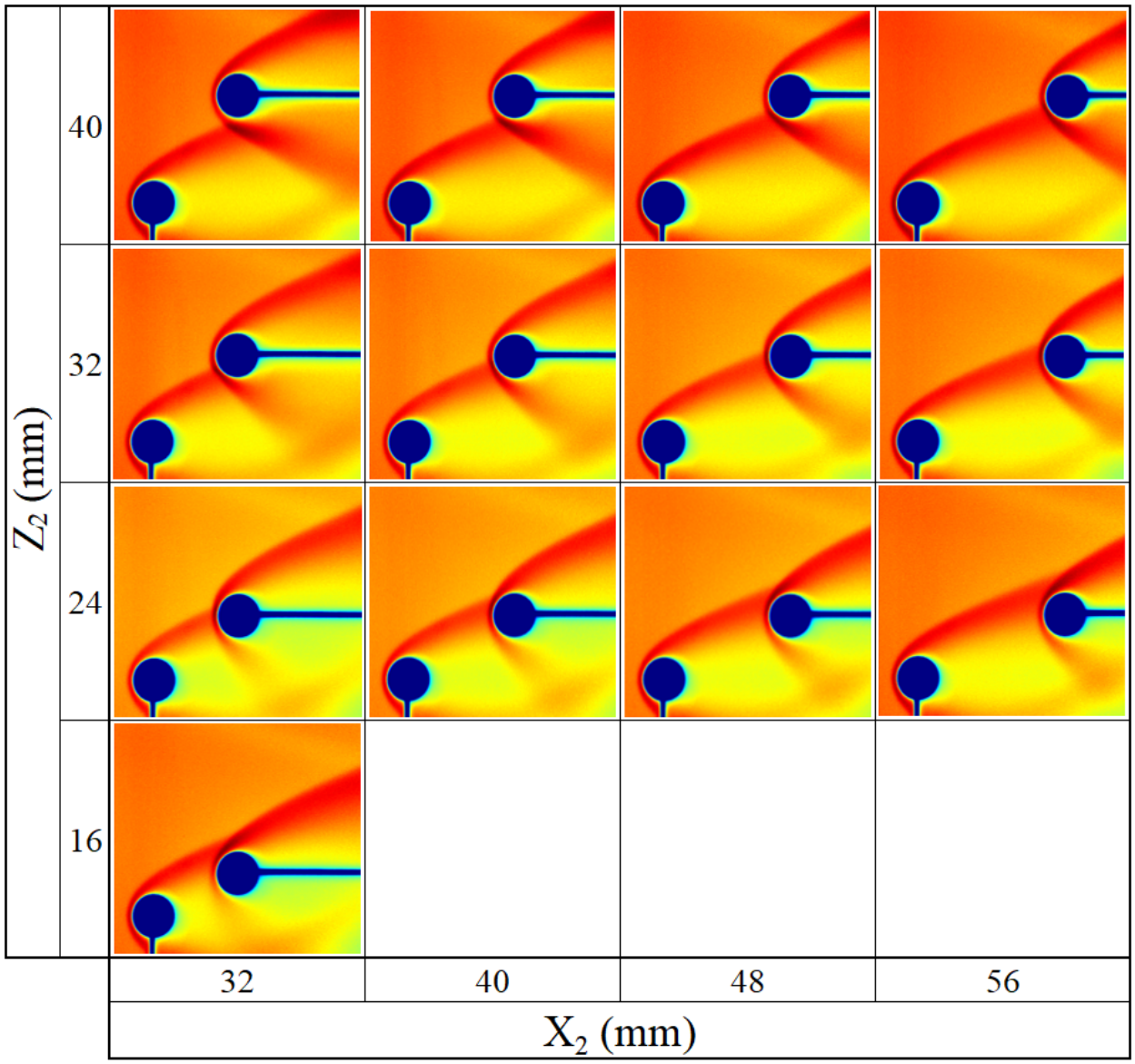

Figure F.2: C_1 in N1 flow-field, full mapping, part 2.

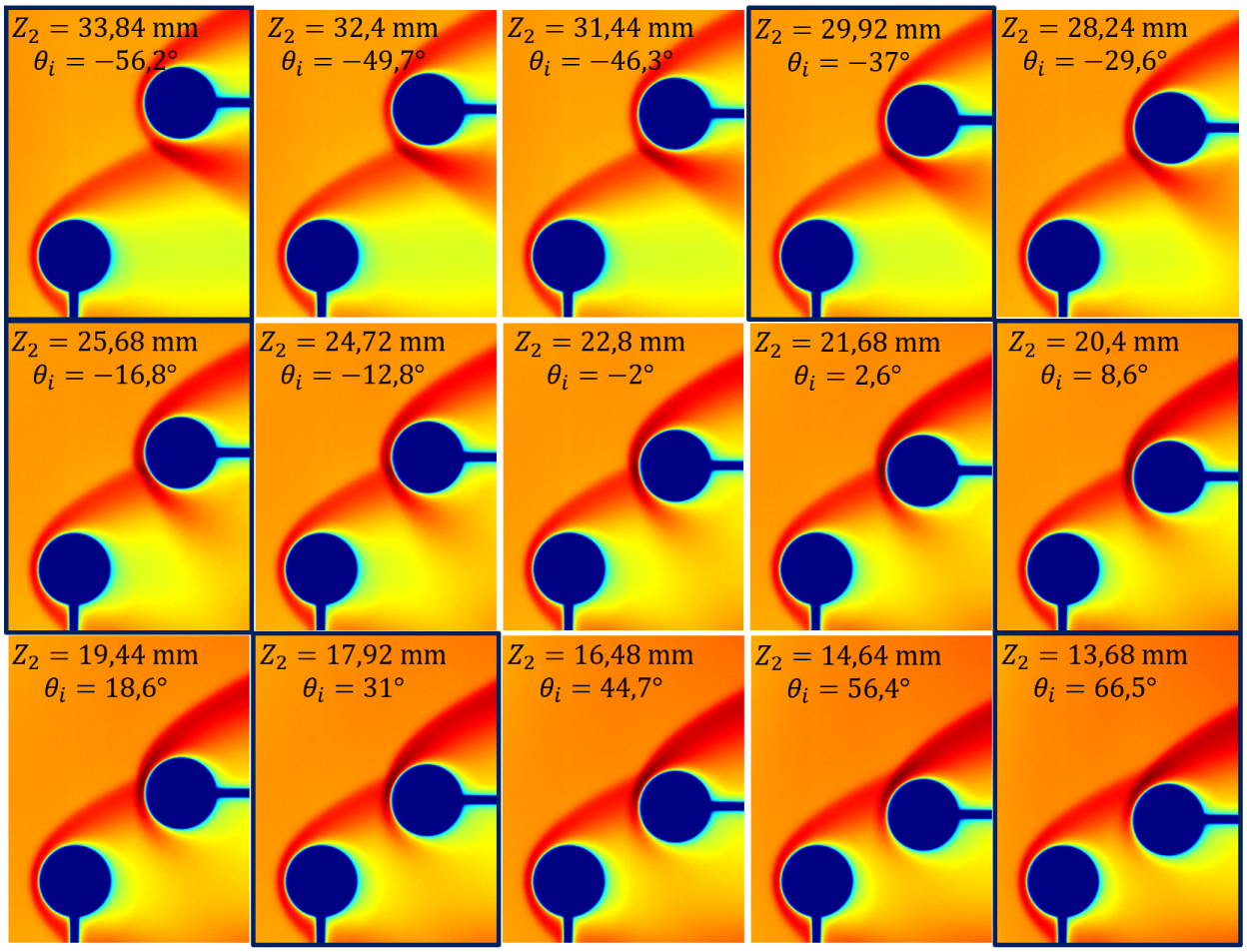

Figure F.3: C_1 in N1 flow-field, $X_2 = 24$ mm.

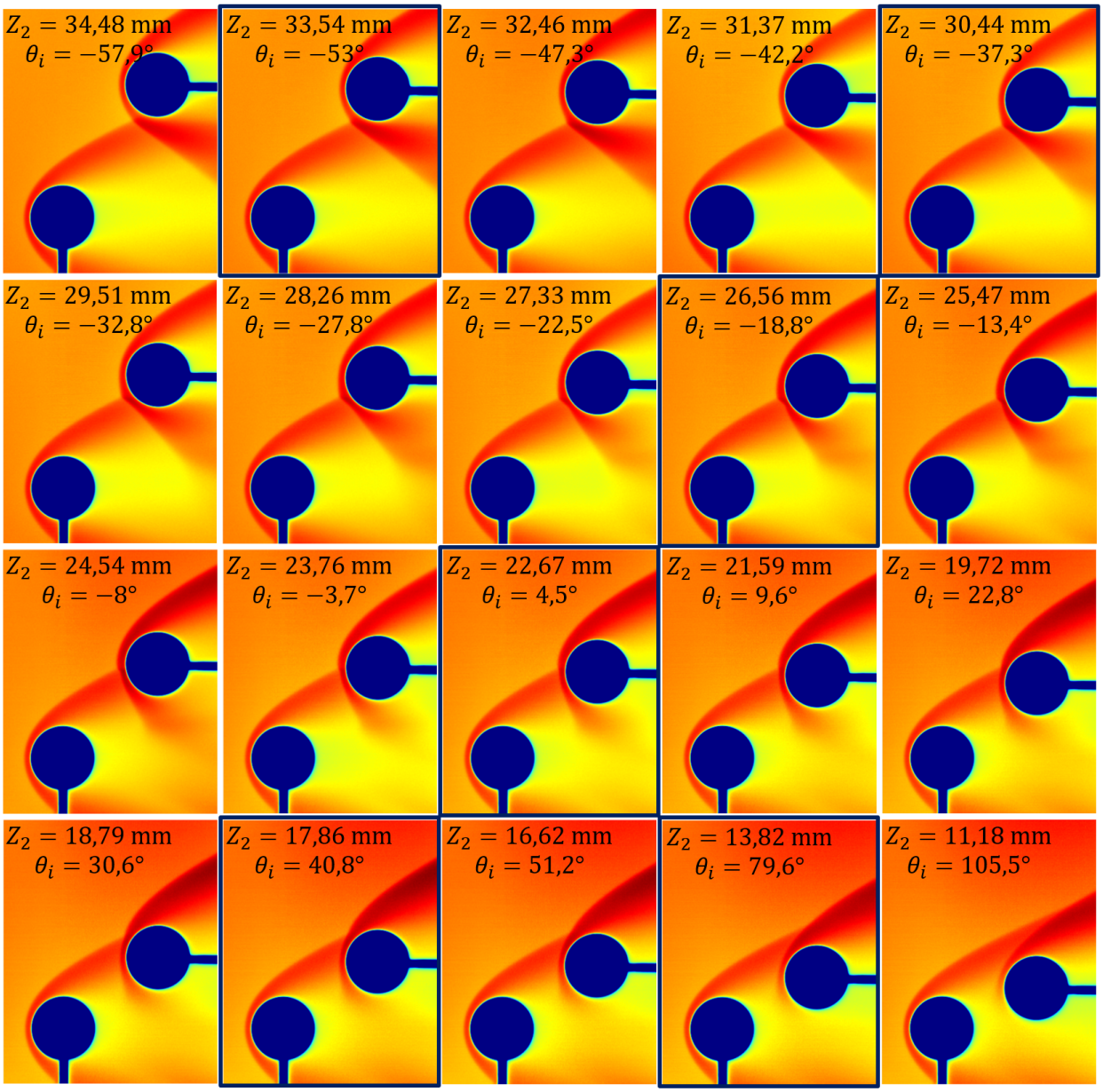

Figure F.4: C_1 in N2 flow-field, $X_2 = 24$ mm.

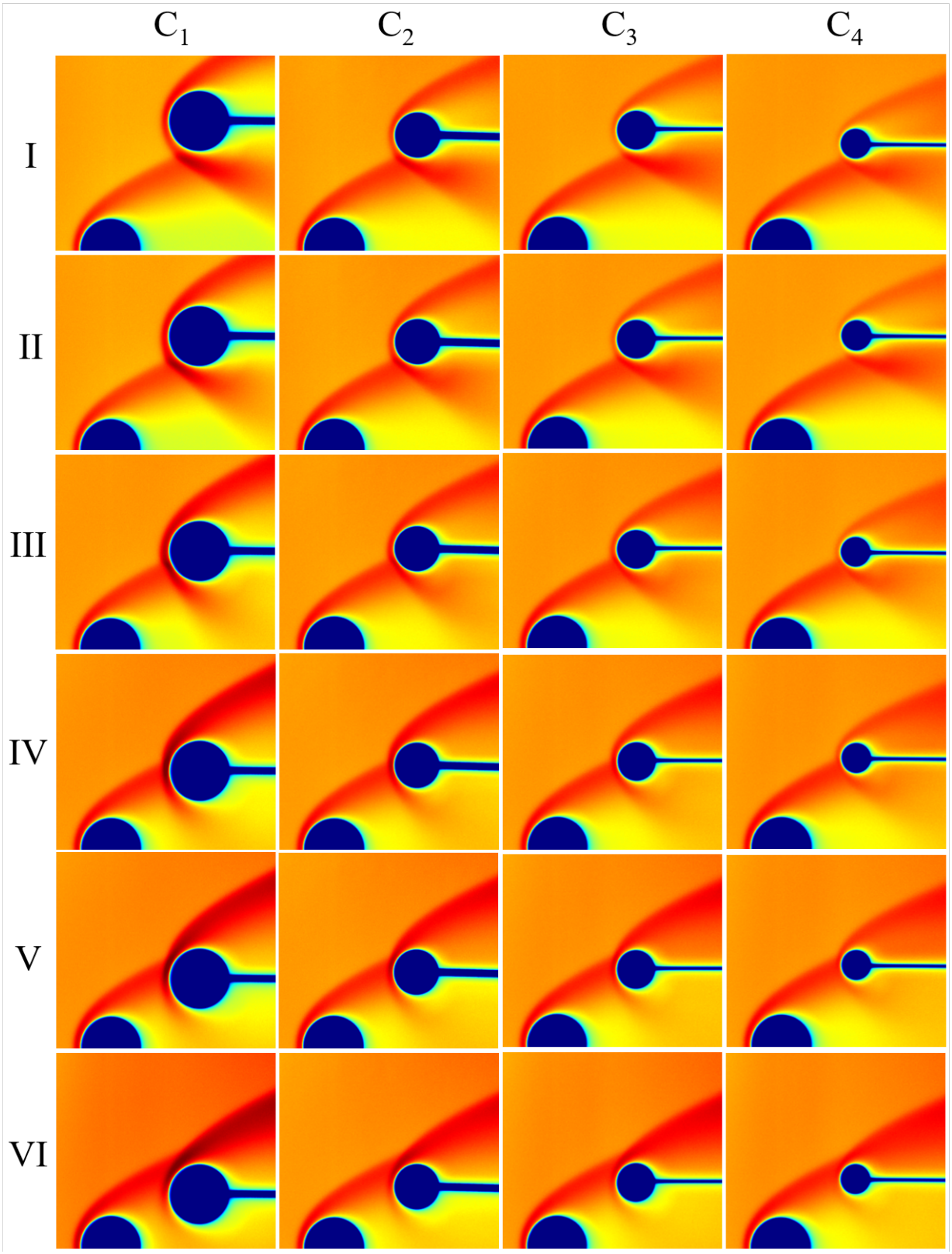

Figure F.5: C_1, C_2, C_3, C_4 in N1 flow-field, X_2 = 24 mm.

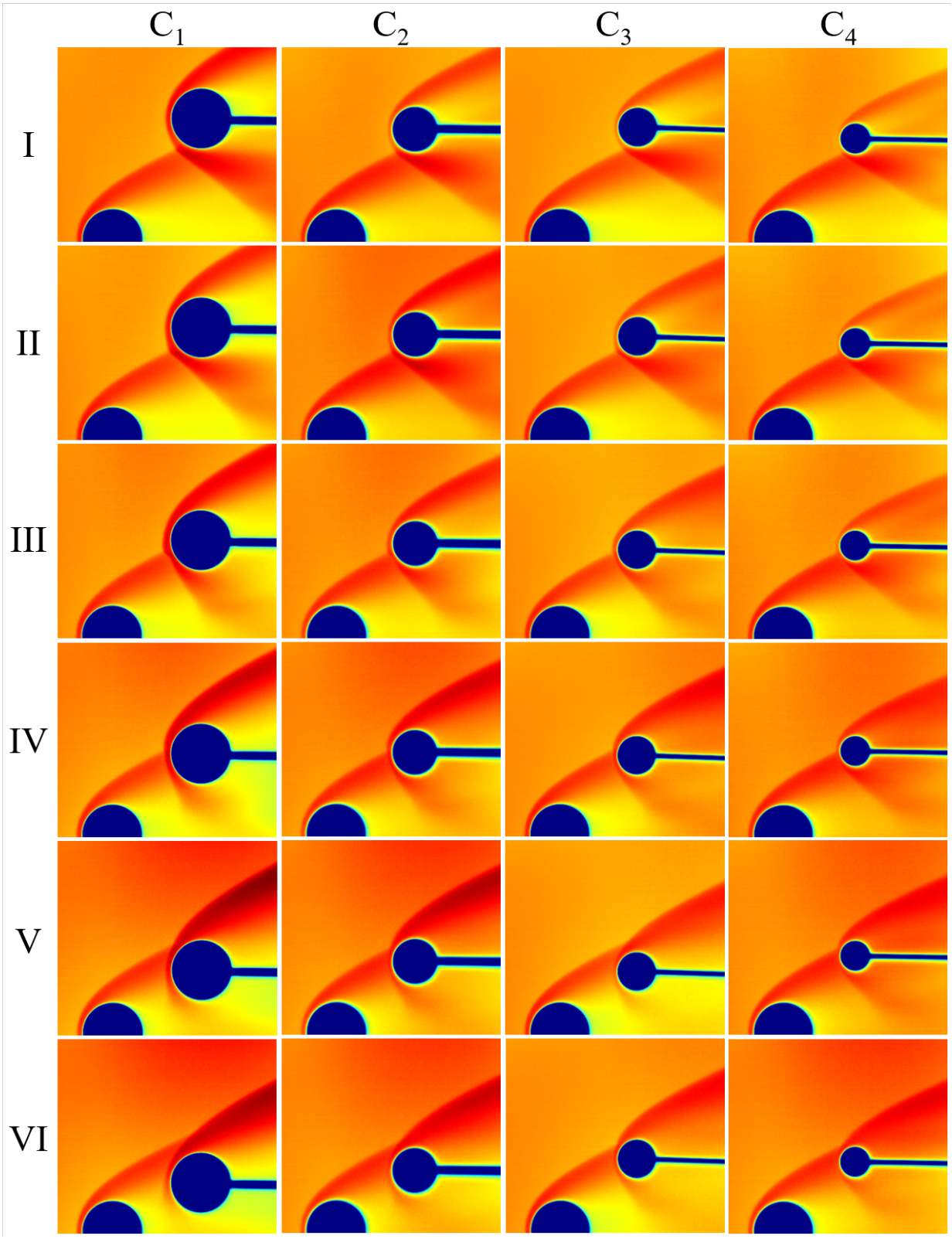

Figure F.6: C_1, C_2, C_3, C_4 in N2 flow-field, X_2 = 24 mm.

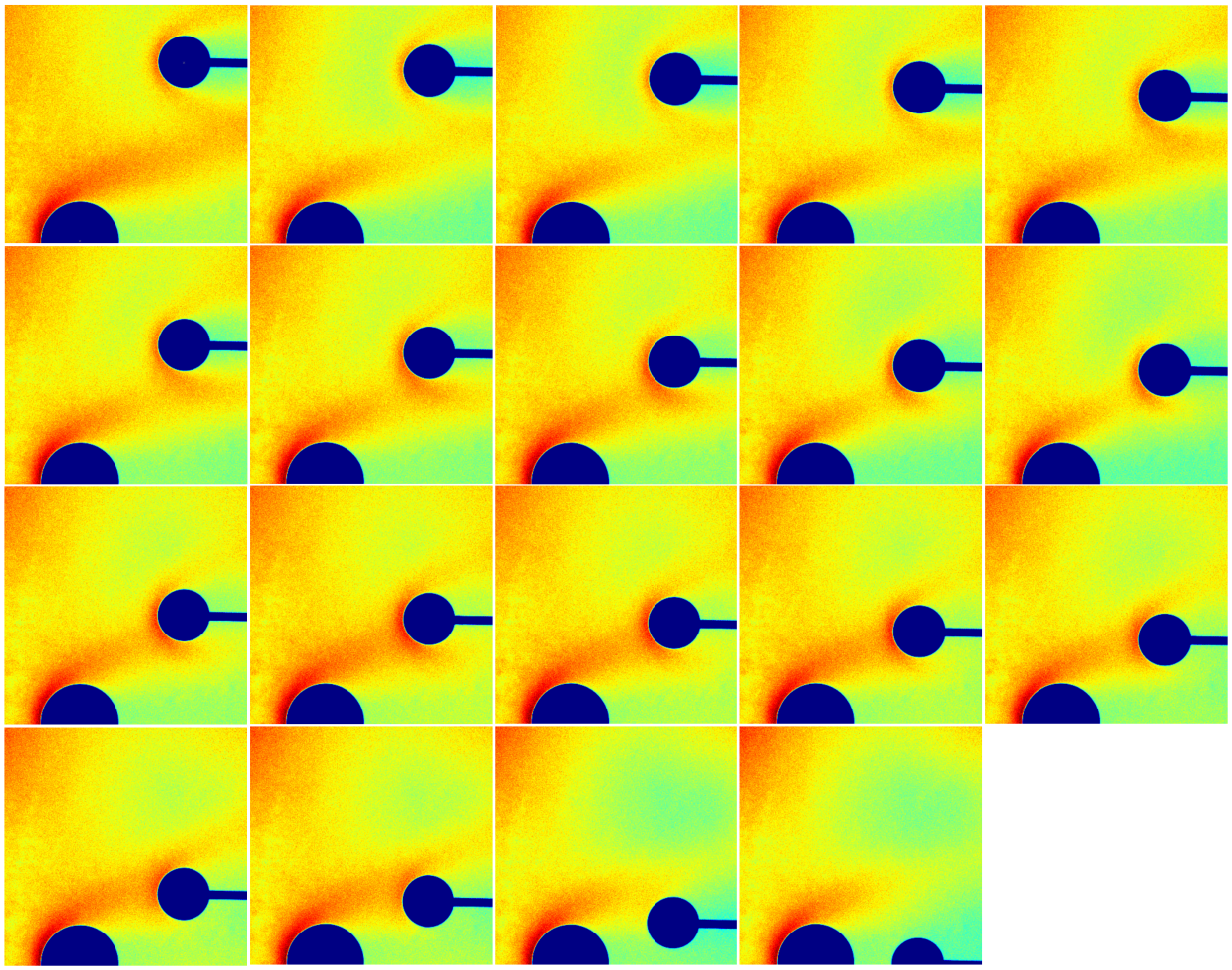

Figure F.7: C_6 in N3 flow-field, X_2 = 27 mm.

Appendix G

Experimental data of the following sphere S_2

Nozzle	Spheres	X_2 (mm)	Z_2 (mm)	θ_i (°)	F_x (mN)	std F_x (mN)	F_z (mN)	std F_z (mN)
N1	C1	22,97	15,31	48,7	6,67	0,26	-0,52	0,09
		22,51	19,89	14,1	9,19	0,22	0,75	0,04
		22,63	22,63	-3,0	9,85	0,16	2,12	0,05
		22,74	28,00	-31,2	9,08	0,17	3,04	0,24
		22,86	32,23	-49,9	8,59	0,21	2,83	0,16
		22,97	36,23	-65,3	8,34	0,08	2,21	0,18
	C2	24,06	16,12	61,9	4,29	0,08	0,81	0,14
		24,06	19,45	29,0	5,74	0,06	1,05	0,10
		24,06	21,99	7,6	6,59	0,03	1,60	0,04
		24,06	26,47	-24,8	6,30	0,07	2,44	0,09
		24,06	28,32	-36,5	5,90	0,03	2,28	0,08
		24,06	32,00	-57,9	5,69	0,05	2,16	0,08
	C3	23,77	17,14	51,6	3,26	0,17	0,67	0,10
		23,77	18,86	33,7	4,40	0,10	0,95	0,04
		23,54	21,83	6,2	5,22	0,06	1,60	0,06
		23,66	24,91	-18,6	5,07	0,02	2,10	0,10
		23,54	27,66	-38,2	4,69	0,06	2,16	0,03
		23,54	30,29	-55,2	4,36	0,16	1,99	0,19
	C4	23,89	17,60	63,9	2,42	0,08	0,97	0,05
		23,43	19,77	37,5	3,37	0,09	1,24	0,04
		23,77	22,17	11,5	3,79	0,08	1,58	0,09
		23,89	24,57	-11,8	3,82	0,13	2,09	0,33
		23,89	26,63	-30,1	3,63	0,14	2,05	0,15
		23,89	28,57	-46,1	3,57	0,09	2,12	0,08

Figure G.1: Aerodynamic forces of S_2 for N1 flow-field.

Nozzle	Spheres	X_2 (mm)	Z_2 (mm)	θ_i (°)	F_x (mN)	std F_x (mN)	F_z (mN)	std F_z (mN)
N2	C1	24,07	13,82	67,8	13,02	0,40	-4,50	0,17
		24,23	18,86	24,8	20,42	0,41	-3,91	0,25
		24,23	22,67	-0,7	24,28	0,21	0,13	0,27
		24,23	26,56	-22,6	24,51	0,12	2,95	0,19
		24,23	30,44	-41,5	22,78	0,14	3,81	0,19
		24,23	33,54	-55,0	21,82	0,08	3,15	0,10
	C2	24,55	12,09	112,5	7,26	0,22	-0,77	0,20
		24,37	14,69	77,9	9,77	0,18	-0,74	0,12
		24,55	23,25	-3,6	16,38	0,11	2,86	0,18
		24,55	25,48	-19,9	15,60	0,22	4,43	0,07
		24,37	28,46	-39,5	14,34	0,15	4,52	0,21
		24,55	30,13	-49,7	13,65	0,13	3,93	0,15
	C3	24,37	16,74	59,9	9,31	0,45	-0,14	0,14
		24,37	20,65	18,4	12,33	0,18	0,95	0,22
		24,55	22,51	1,3	13,24	0,16	2,47	0,24
		24,55	24,55	-15,9	13,24	0,09	4,08	0,19
		24,18	29,20	-50,3	11,76	0,33	4,21	0,12
		24,74	31,81	-67,2	11,30	0,19	3,20	0,07
	C4	23,81	22,32	7,6	9,62	0,10	3,32	0,12
		23,99	22,69	3,2	9,96	0,11	3,61	0,45
		23,99	24,37	-15,9	9,62	0,17	3,96	0,13
		23,99	24,92	-22,2	9,42	0,10	3,78	0,18
		23,62	27,53	-50,3	9,56	0,01	3,61	0,11
		24,18	27,90	-54,2	8,58	0,10	3,47	0,20

Figure G.2: Aerodynamic forces of S_2 for N2 flow-field.

	Nozzle	Spheres	X_2 (mm)	Z_2 (mm)	θ_i (°)	F_x (mN)	std F_x (mN)	F_z (mN)	std F_z (mN)
Balance	N3	C5	27	35,39	-51,5	10,25	0,73	1,78	0,09
			27	32,34	-36,6	9,7	1,37	0,51	1,83
			27	27,92	-15,1	9,88	1,52	0,5	1,75
			27	23,64	5,827	9,32	1,57	-0,39	1,7
			27	20,9	19,2	8,61	1,58	-0,55	1,77
			27	17,69	34,86	7,09	0,82	-1,48	1,03
			27	12,36	60,87	5,55	1,82	-0,56	1,38
			27	7	87,03	4,47	1,66	-0,23	1,24
Swinging	N3	C5	27	35,83	-53,7	9,33	0,65		
			27	32,68	-38,3	9,47	0,49		
			27	23,78	5,144	9,45	0,5		
			27	20,88	19,3	8,62	0,48		
			27	17,7	34,81	7,35	0,5		
			27	12,12	62,04	4,77	0,5		

Figure G.3: Aerodynamic forces of S_2 for N3 flow-field.

Type I		Type II		Type III (1)		Type III (2)		Type IV(1)		Type IV (2)		Type IV (3)		Type V		Type VI	
X_2 (mm)	Z_2 (mm)	X_2	Z_2	X_2	Z_2	X_2	Z_2	X_2	Z_2	X_2	Z_2	X_2	Z_2	X_2	Z_2	X_2	Z_2
25,23	34,15	25,38	30	25,54	27,54	25,38	25,85	25,38	24,15	25,38	22,31	25,38	20,46	25,38	17,69	25,38	13,08

θ_i (deg)

-53,3		-35,2		-23,3		-14,4		-4,9		6,1		18,2		38,5		80,7	
θ_{wp} (deg)	p_w (Pa)	θ_{wp}	p_w	θ_{wp}	p_w	θ_{wp}	p_w	θ_{wp}	p_w	θ_{wp}	p_w	θ_{wp}	p_w	θ_{wp}	p_w	θ_{wp}	p_w
90	4,42	90	4,49	90,00	4,49	90	4,60	90,00	4,67	90	4,55	90	4,42	90,00	4,03	90	4,86
80	7,45	80	7,58	70,00	12,10	80	7,70	70,00	12,34	70	11,58	80	7,26	80,00	6,94	80	8,47
70	12,16	70	12,23	50,00	25,78	70	12,28	50,00	25,38	50	23,91	70	11,18	70,00	11,65	70	13,70
60	18,55	60	18,55	30,00	42,42	60	18,34	40,00	33,18	40	31,28	60	16,49	60,00	19,78	60	20,34
50	26,36	50	26,29	20,00	49,26	50	25,78	30,00	40,35	30	39,52	50	23,33	50,00	32,62	50	27,63
40	34,94	40	34,88	10,00	53,78	40	34,10	20,00	46,42	20	52,62	40	32,94	40,00	47,71	40	34,09
30	43,54	30	43,34	0,00	55,65	30	42,04	10,00	53,44	10	78,81	30	50,62	30,00	59,39	35	36,28
20	50,70	20	50,25	-5,00	55,84	20	48,42	5,00	58,86	5	90,30	20	75,14	25,00	62,81	30	37,76
10	55,15	10	54,83	-10,00	55,91	10	52,54	0,00	69,32	2,5	93,65	15	82,30	20,00	64,55	25	38,35
0	56,76	0	56,57	-15,00	56,43	5	53,97	-2,50	76,35	0	95,14	10	84,68	15,00	64,62	20	37,96
-10	55,15	-10	55,73	-20,00	58,04	0	55,52	-5,00	83,32	-2,5	94,23	5	83,32	10,00	63,01	15	36,67
-20	50,63	-15	54,50	-25,00	61,26	-5	57,84	-7,50	89,01	-5	92,23	0	79,59	0,00	55,97	10	34,60
-30	43,79	-20	53,15	-30,00	65,33	-10	63,20	-10,00	94,10	-10	86,10	-10	67,57	-10,00	45,78	0	28,80
-40	35,84	-25	51,99	-32,50	67,01	-15	72,43	-12,50	97,64	-30	50,50	-20	52,42	-20,00	34,10	-10	21,96
-45	32,36	-30	51,08	-35,00	68,17	-20	81,91	-15,00	97,07	-50	21,39	-30	37,46	-30,00	23,71	-30	10,47
-50	29,00	-35	50,70	-37,50	68,43	-22,5	85,59	-20,00	93,01	-70	7,52	-50	15,97	-50,00	10,16	-50	4,60
-55	26,50	-40	50,25	-40,00	67,59	-25	87,98	-30,00	70,67	-90	2,23	-70	5,71	-70,00	3,91	-70	2,08
-60	24,87	-45	49,47	-45,00	63,20	-27,5	88,81	-50,00	30,55	90	4,63	-90	1,97	-90,00	1,58	-90	1,05
-65	23,39	-50	47,54	-50,00	55,07	-30	87,72	-70,00	10,94			90	4,55	90,00	4,16	90	4,86
-70	21,79	-60	39,15	-70,00	21,71	-35	79,78	-90,00	3,71								
-75	20,16	-70	27,33	-90,00	6,62	-40	67,52	90,00	4,92								
-80	17,78	-80	16,95	90,00	4,63	-50	43,21										
-90	12,42	-90	9,66			-60	25,86										
90	4,62	90	4,63			-70	15,00										
						-90	4,89										
						90	4,89										

Figure G.4: Wall pressure of S_2 for N1 flow-field.

Type I		Type II		Type III		Type IV (1)		Type IV (2)		Type IV (3)		Type IV (4)		Type IV (5)		Type V		Type V (2)		Type VI	
X_2 (mm)	Z_2 (mm)	X_2	Z_2	X_2	Z_2	X_2	Z_2	X_2	Z_2	X_2	Z_2	X_2	Z_2	X_2	Z_2	X_2	Z_2	X_2	Z_2	X_2	Z_2
22,79	34,80	22,79	30,03	22,64	26,18	22,18	22,18	22,33	21,87	22,33	21,41	22,48	22,48	22,33	22,79	22,18	18,48	22,33	17,40	22,18	13,40
θ_i (deg)																					
-61,8		-42,0		-23,5		-1,2		0,7		3,6		-3,0		-4,9		23,4		31,5		66,7	
θ_{wp} (deg)	p_w (Pa)	θ_{wp}	p_w	θ_{wp}	p_w	θ_{wp}	p_w	θ_{wp}	p_w	θ_{wp}	p_w	θ_{wp}	p_w	θ_{wp}	p_w	θ_{wp}	p_w	θ_{wp}	p_w	θ_{wp}	p_w
90	14,53	90	15,19	90	14,55	90	13,32	10	162,36	10	187,32	10	154,84	60	53,76	60	49,05	90	11,68	90	14,98
80	22,90	80	23,55	80	23,57	80	21,70	7,5	182,61	7,5	227,14	5	169,93	40	99,08	40	105,41	80	19,03	80	25,58
70	35,76	70	36,63	70	36,62	70	34,14	5	221,62	5	266,97	2,5	198,94	20	141,37	30	177,69	70	31,30	70	41,92
60	53,54	60	54,20	60	54,59	60	50,70	2,5	271,04	2,5	295,15	0	252,65	10	155,46	20	241,42	60	50,07	60	64,16
50	75,79	50	77,27	50	77,07	50	71,52	0	304,53	0	305,36	-2,5	309,63	5	160,57	15	248,15	50	81,11	50	90,91
40	101,11	40	103,60	40	102,59	40	94,41	-2,5	314,74	-2,5	299,84	-5	328,42	0	200,17	10	245,50	40	138,08	40	117,26
30	126,44	30	128,71	30	127,69	30	117,69	-5	310,65	-5	291,84	-7,5	326,59	-2,5	256,73	5	236,92	30	194,23	30	135,22
20	147,27	20	149,34	20	148,33	20	137,70	-7,5	303,71	-7,5	281,21	-10	316,38	-5	323,50	-5	206,29	20	215,47	25	138,91
10	160,96	10	163,64	10	162,62	10	154,85	-10	294,32	-10	268,17	-15	284,12	-7,5	335,78	-15	160,35	15	216,90	22,5	139,10
0	166,07	0	168,53	5	166,91	5	195,49	-30	165,47	-30	155,22	-30	179,15	-10	332,30	-30	89,92	10	212,81	20	138,28
-10	162,60	-10	166,49	0	169,35	0	288,00							-15	299,62	-60	18,84	0	190,15	15	134,20
-20	150,78	-20	159,36	-5	170,57	-2,5	310,86							-30	187,70	-90	4,94	-10	153,39	10	127,47
-30	130,97	-25	155,07	-10	170,59	-5	312,49											-20	110,31	0	106,65
-40	106,46	-30	151,80	-15	170,38	-7,5	304,12											-30	71,72	-10	79,50
-50	81,35	-35	149,76	-20	172,22	-10	294,91											-40	43,74	-20	51,32
-55	71,76	-40	148,13	-25	185,29	-20	234,89											-50	23,92	-30	28,47
-60	67,26	-45	145,47	-30	221,64	-30	166,69											-70	6,78	-40	14,79
-65	71,14	-50	141,17	-35	269,61	-40	105,22											-90	2,29	-50	8,05
-70	74,81	-55	133,22	-37,5	281,26	-50	61,10											90	11,46	-70	4,18
-75	71,76	-60	120,76	-40	275,33	-70	18,18													-90	4,18
-80	62,57	-70	83,19	-45	205,71	-90	5,53													90	14,98
-90	41,13	-80	47,65	-50	136,27	90	13,14														
90	14,35	-90	25,61	-60	70,53																
		90	14,77	-70	38,68																
				-90	12,51																
				90	15,18																

Figure G.5: Wall pressure of S_2 for N2 flow-field.

Appendix H

Evolution of S_1 and S_2 aerodynamic forces in the continuum regime

In the continuum regime, Golubev [79] numerically studied the drag and lift forces of two spheres interacting with each other. For a fixed inter-distance between the spheres ($l = D_1 = D_2$), he varied the angle between them, and obtained the results shown in Figure H.1 for a Mach 3 flow. Results cannot be directly compared

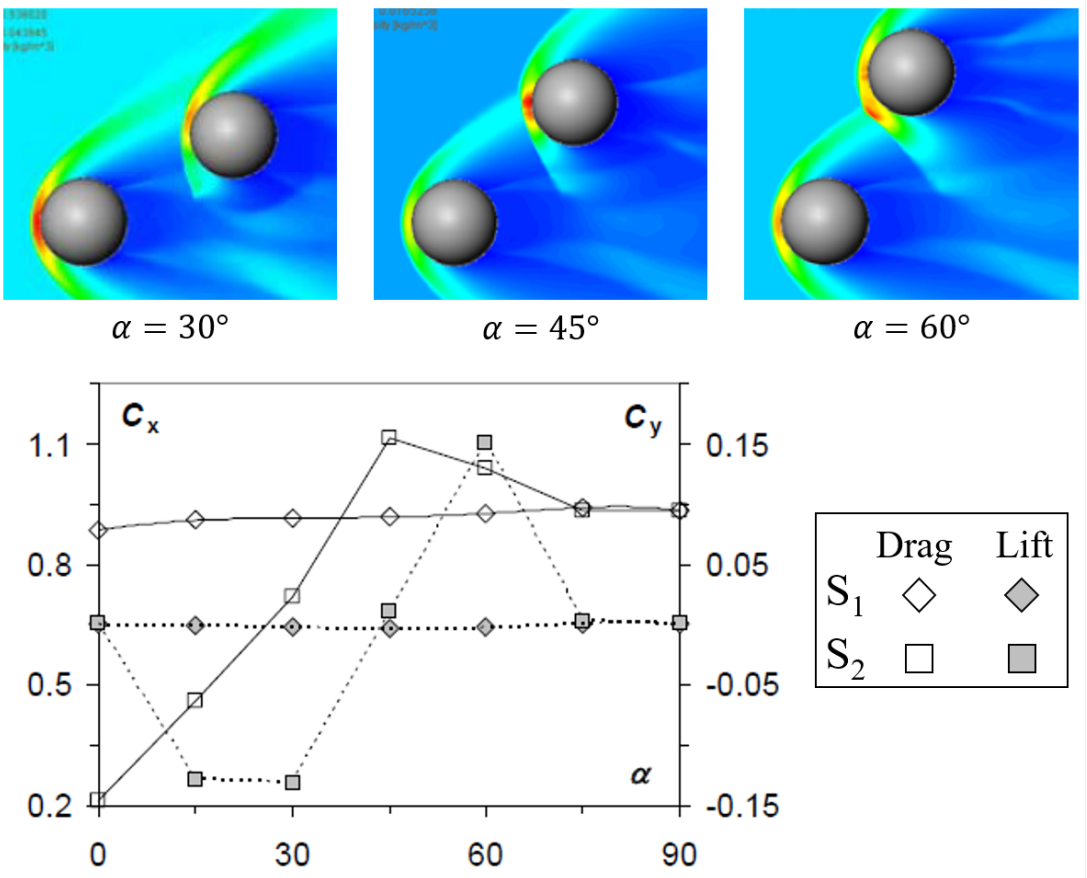

Figure H.1: Enhanced images resulting from the experiment with C_1, N2 for X_2 = 24 mm.

to our experimental results, since the Mach number is not the same, and that the location of S_2 are different from ours. However the behaviours of forces evolution are equivalent to ours.

Appendix I

Global rarefaction level impact on SSI

Image analysis

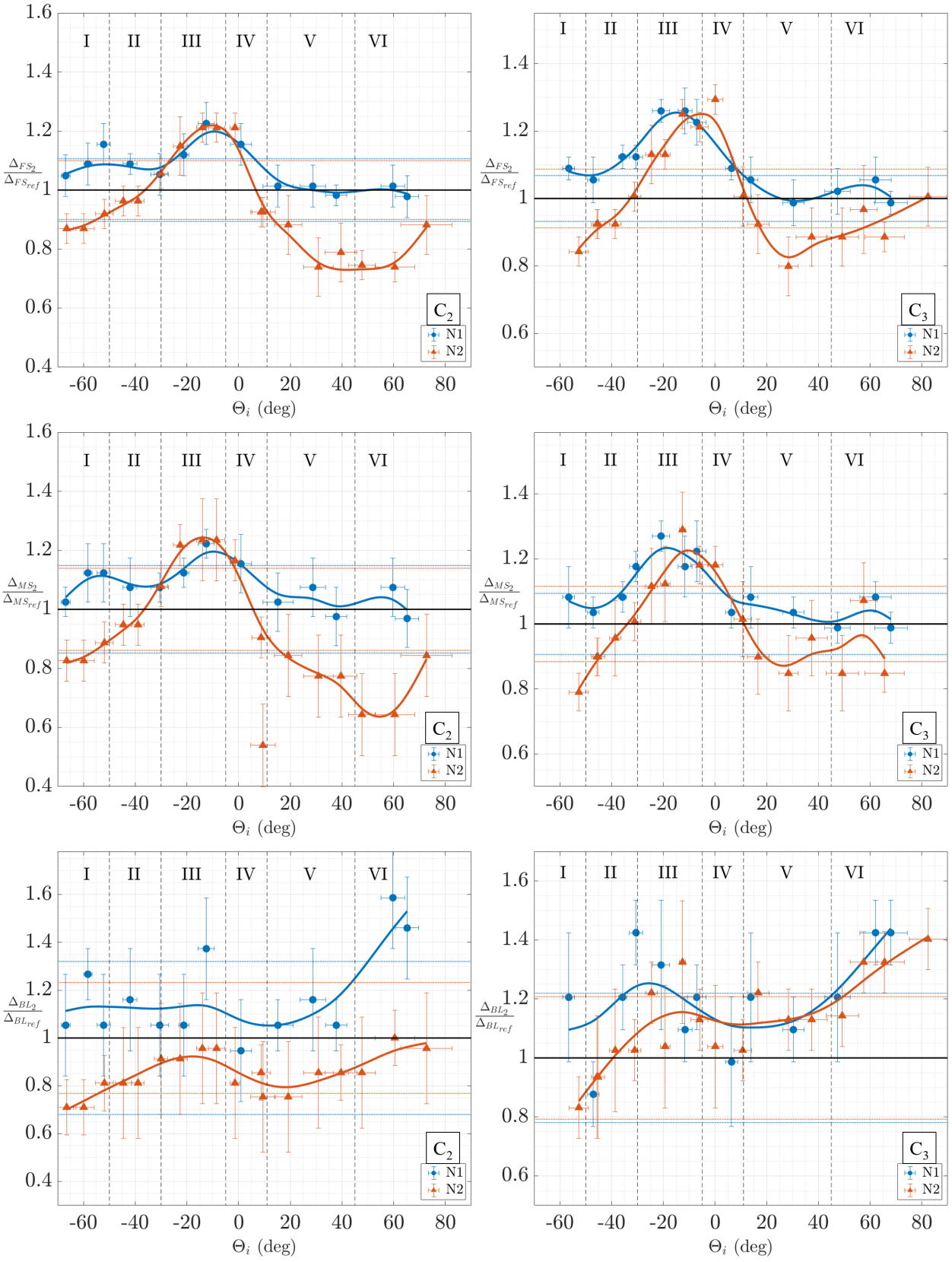

Figure I.1: Stand-off distances of C_2 (left) and C_3 (right), in N1 (blue) and N2 (orange) flow-fields.

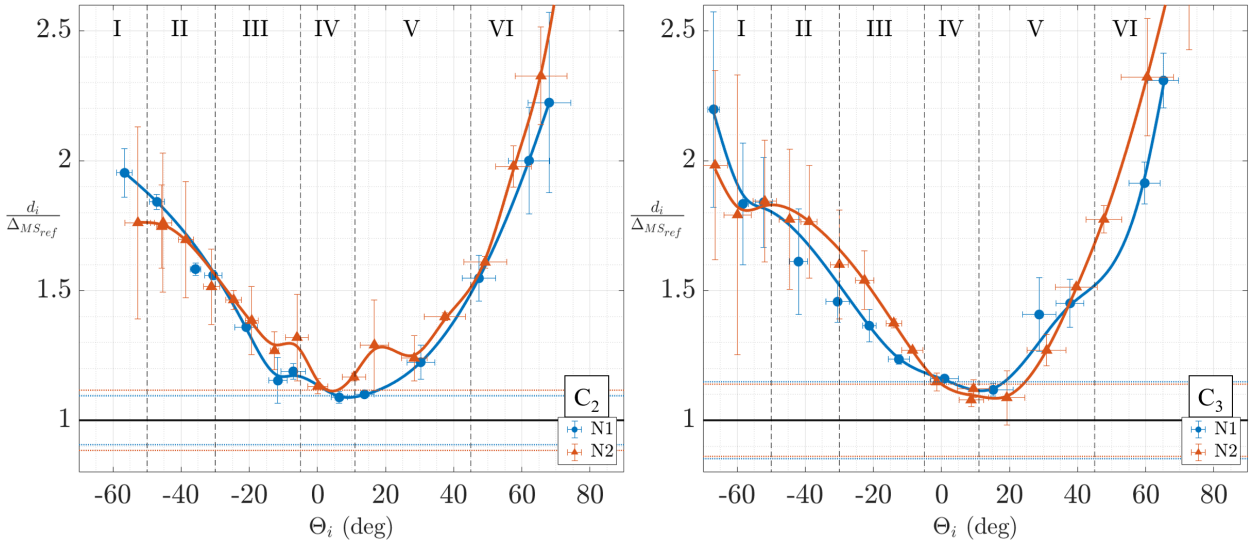

Figure I.2: Distance of P_i from the surface of S_2 for C_2 (left) and C_3 (right), in N1 (blue) and N2 (orange) flow-fields.

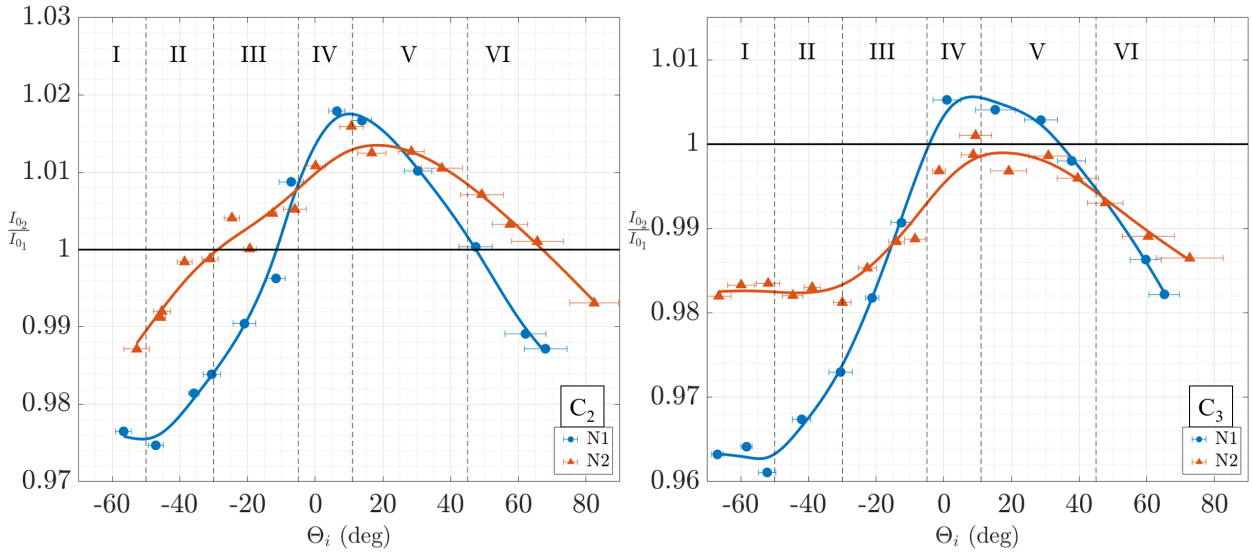

Figure I.3: Normalized intensity at P_{02} for C_2 (left) and C_3 (right), in N1 (blue) and N2 (orange) flow-fields.

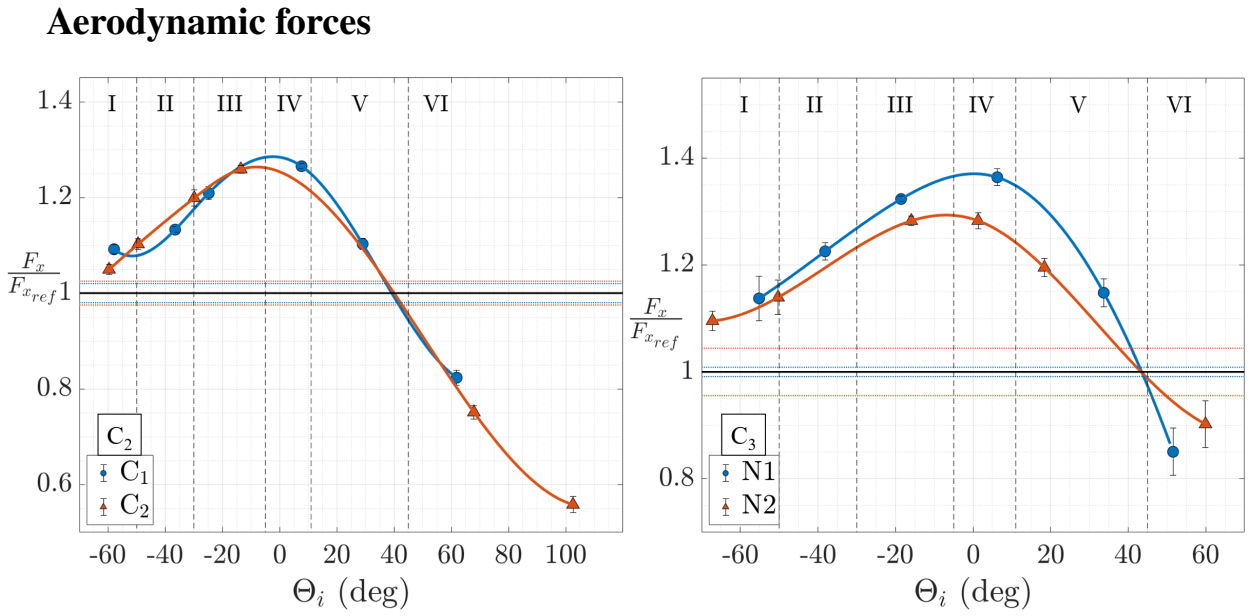

Figure I.4: Drag forces of S_2 for C_2 (left) and C_3 (right), in N1 (blue) and N2 (orange) flow-fields.

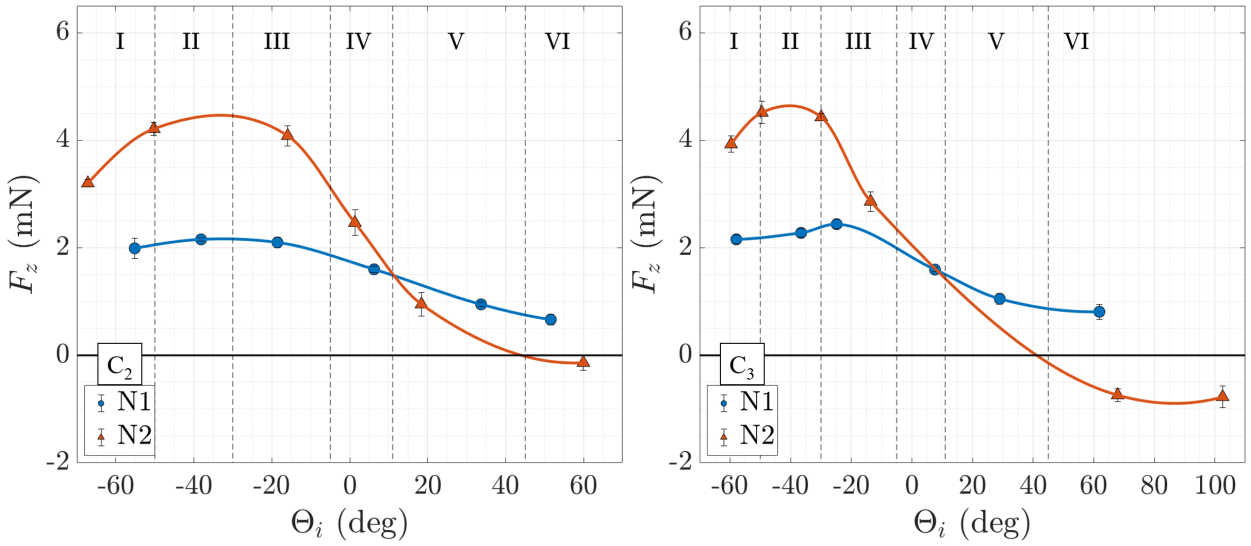

Figure I.5: Lift forces of S_2 for C_2 (left) and C_3 (right), in N1 (blue) and N2 (orange) flow-fields.

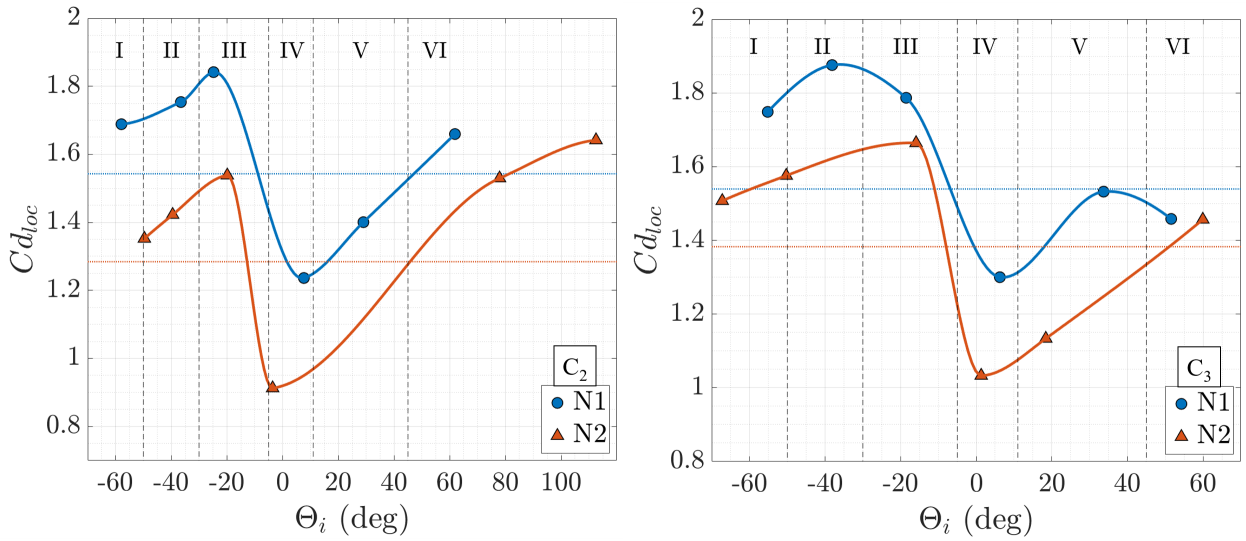

Figure I.6: Drag coefficients of S_2 for C_2 (left) and C_3 (right), in N1 (blue) and N2 (orange) flow-fields.

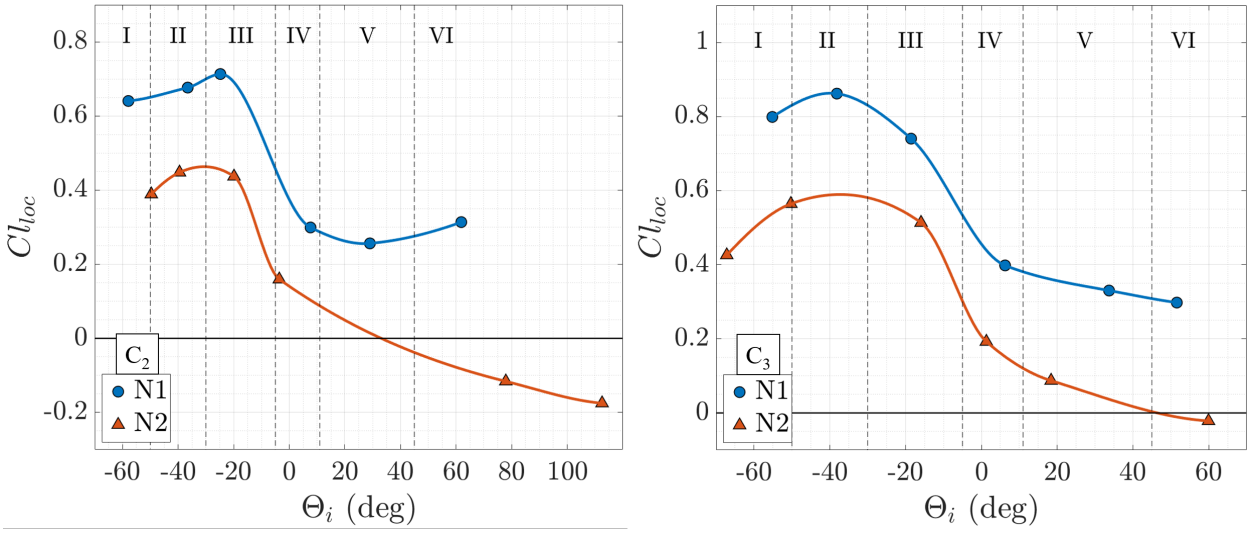

Figure I.7: Lift coefficient of S_2 for C_2 (left) and C_3 (right), in N1 (blue) and N2 (orange) flow-fields.

Appendix J

Local Knudsen number

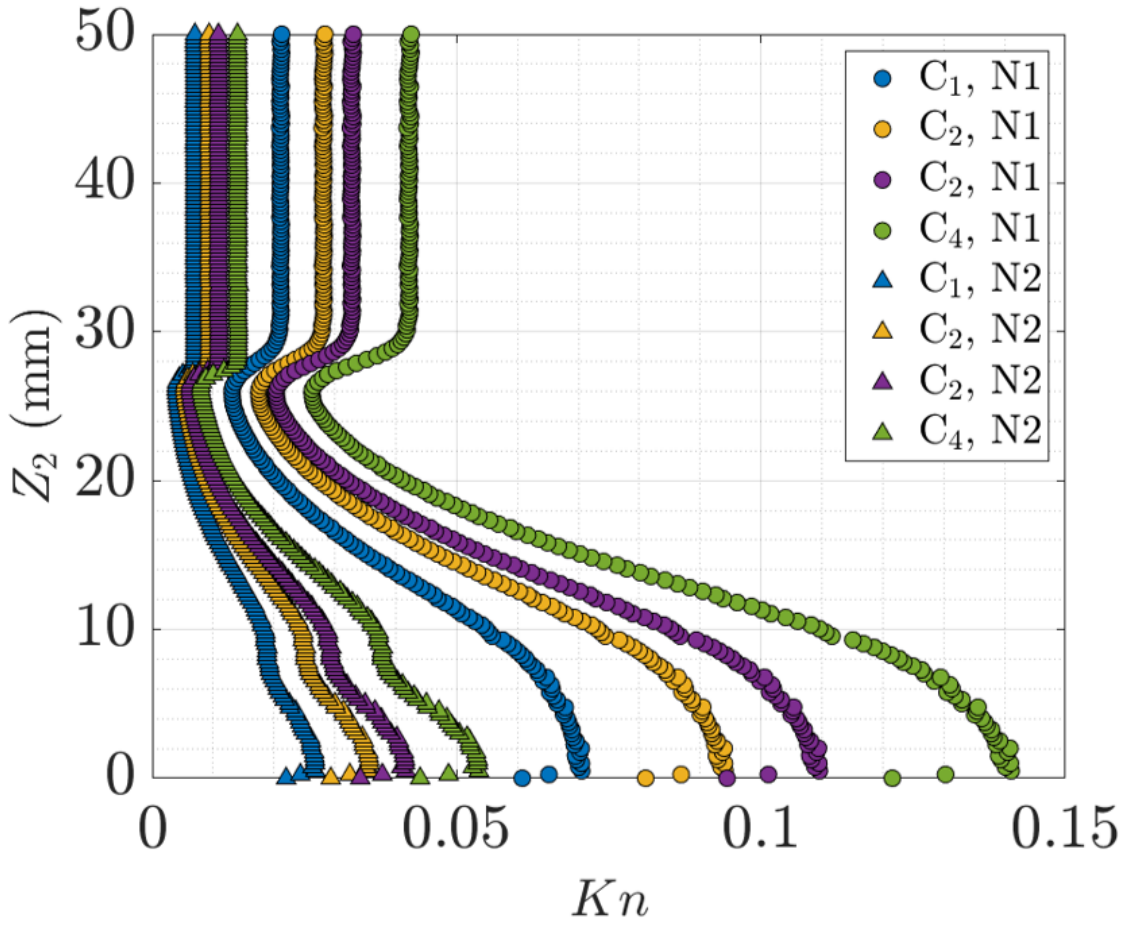

Figure J.1: Local Knudsen number of S_2 in N1 and N2 flow-field on the axis X_2 = 24 mm.

Bibliography

Bibliography

[1] M B Agir, C White, and K Kontis. "The effect of increasing rarefaction on the formation of Edney shock interaction patterns: type-I to type-VI". In: *Shock Waves* 32.8 (2022), pp. 733–751. DOI: https://doi.org/10.1007/s00193-022-01109-y.

[2] N Ahmad and E Fitri. "Preliminary Determination of Footprint Area of Uncontrolled Space Debris: Case Study of Tiangong-1 Space Station". In: *Indonesian Journal of Geography* 53.2 (2021). DOI: https://doi.org/10.22146/ijg.54247.

[3] W Ailor et al. "Analysis of reentered debris and implications for survivability modeling". In: *4th European Conference on Space Debris*. 2005, p. 539.

[4] H Akhlaghi, A Daliri, and M R Soltani. "Shock-Wave-Detection Technique for High-Speed Rarefied-Gas Flows". In: *AIAA Journal* 55.11 (2017), pp. 3747–3756. DOI: https://doi.org/10.2514/1.J055819.

[5] H Akhlaghi and E Roohi. "Generalized description of the Knudsen layer thickness in rarefied gas flows". In: *Physics of Fluids* 33.6 (2021), p. 061701. DOI: https://doi.org/10.1063/5.0052263.

[6] C Albertson and V Venkat. "Shock interaction control for scramjet cowl leading edges". In: *AIAA/CIRA 13th International Space Planes and Hypersonics Systems and Technologies Conference*. 2005. DOI: https://doi.org/10.2514/6.2005-3289.

[7] J Allegre, D Bisch, and JC Lengrand. "Experimental rarefied heat transfer at hypersonic conditions over 70-degree blunted cone". In: *Journal of Spacecraft and Rockets* 34.6 (1997), pp. 724–728. DOI: https://doi.org/10.2514/2.3302.

[8] J Allegre, M Cabaret, and M Raffin. *Méthode de mesure des basses pressions pas thermitances et détermination des effets d'orifice dans des écoulements de gaz raréfié*. Rapport 71-6. CNRS, Laboratoire d'Aérothermique, France, 1971.

[9] J Allegre and M Raffin. "Obtention de nombres de Mach compris entre 15 et 30 dans une soufflerie à fonctionnement continu". In: *L'aéronautique et l'Astronautique* 37 (1972), pp. 67–79.

[10] J Allegre et al. "Rarefied hypersonic flow over a flat plate with truncated leading edge". In: *Progress in Astronautics and Aeronautics* 160 (1994), pp. 285–285. DOI: https://doi.org/10.2514/5.9781600866326.0285.0295.

[11] A Ambrosio and A Wortman. "Stagnation-point shock-detachment distance for flow around spheres and cylinders in air". In: *ARS Journal* 32.2 (1962), pp. 281–281. DOI: https://doi.org/10.2514/8.5988.

[12] J Annaloro et al. "Aerothermodynamics modelling of complex shapes in the DEBRISK atmospheric reentry tool: Methodology and validation". In: *Acta Astronautica* (2020). DOI: https://doi.org/10.1016/j.actaastro.2020.03.006.

[13] J Annaloro et al. "Comparison between two spacecraft-oriented tools: PAMPERO & SCARAB". In: *Journal of Space Safety Engineering* 4.1 (2017), pp. 15–21. DOI: https://doi.org/10.1016/j.jsse.2017.02.004.

[14] P Anz-Meador, J Opiela, and J-C Liou. *History of on-orbit satellite fragmentations*. TP-20220019160. NASA, 2023. URL: https://ntrs.nasa.gov/api/citations/20220019160/downloads/HOOSF_16e_all_for_STRIVES.pdf.

[15] A Aprovitola et al. "Phase-A design of a reusable re-entry vehicle". In: *Acta Astronautica* 187 (2021), pp. 141–155. DOI: https://doi.org/10.1016/j.actaastro.2021.06.034.

[16] J Aroesty. *Sphere drag in low density supersonic flow*. No. HE-150-192. California Univ Berkley Inst of Engineering Research, 1962.

[17] A B Bailey. *Sphere drag measurement in aeroballistics range at high velocities and low Reynolds numbers*. Tech. rep. ARO INC ARNOLD AFS TN, 1966.

[18] A B Bailey and J Hiatt. "Sphere drag coefficients for a broad range of Mach and Reynolds numbers". In: *Aiaa Journal* 10.11 (1972), pp. 1436–1440. DOI: https://doi.org/10.2514/3.50387.

[19] R Bansal. "The Sky Is Falling!" In: *IEEE Antennas and Propagation Magazine* 63.5 (2021), pp. 140–140. DOI: 10.1109/MAP.2021.3101443.

[20] N G Barri. "Aerodynamic interaction of meteor-body fragments: The collimation effect". In: *Doklady Physics*. SP MAIK Nauka/Interperiodica, 2009, September, pp. 423–425. DOI: https://doi.org/10.1063/1.3506048.

[21] N G Barri. "Basic aerodynamical properties of meteoroid fragments in the terrestrial atmosphere". In: *AIP Conference Proceedings*. American Institute of Physics. 2010, pp. 137–144. DOI: https://doi.org/10.1063/1.3506048.

[22] N G Barri. "Meteoroid fragments dynamics: Collimation effect". In: *Solar System Research* 44.1 (2010, October), pp. 55–59. DOI: https://doi.org/10.1134/S0038094610010077.

[23] W Behrens. "The far wake behind cylinders at hypersonic speeds. II." In: *AIAA Journal* 5.12 (1967), pp. 2135–2141. DOI: https://doi.org/10.2514/6.1967-32.

[24] G Ben-Dor et al. "Hysteresis processes in the regular reflection - Mach reflection transition in steady flows". In: *Progress in Aerospace Sciences* 38.4-5 (2002), pp. 347–387. DOI: https://doi.org/10.1016/S0376-0421(02)00009-X.

[25] S A Berry and R J Nowak. "Fin leading-edge sweep effect on shock-shock interaction at Mach 6". In: *Journal of Spacecraft and Rockets* 34.4 (1997), pp. 416–425. DOI: https://doi.org/10.2514/2.3247.

[26] J J Bertin. *Hypersonic Aerothermodynamics*. Educations series. American Institute of Aeronautics and Astronautics, 1994.

[27] F Bertrand. "Etude du flux thermique généré par interaction d'ondes de chocs sur les mâts d'injection d'un statoréacteur à combustion supersonique". PhD. Université d'Orléans, 1997.

[28] F S Billig. "Shock-wave shapes around spherical-and cylindrical-nosed bodies". In: *Journal of Spacecraft and Rockets* 4.6 (1967), pp. 822–823. DOI: https://doi.org/10.2514/3.28969.

[29] G A Bird. *Molecular gas dynamics and the direct simulation of gas flows*. Vol. 42. Oxford: Clarendon press, 1994.

[30] G A Bird. "Monte-Carlo simulation in an engineering context". In: *PrAA* 74.239-255 (1981).

[31] G A Bird. *The DSMC method*. CreateSpace Independent Publishing Platform, 2013.

[32] V M Boiko, K V Klinkov, and S V Poplavskii. "Collective bow shock ahead of a transverse system of spheres in a supersonic flow behind a moving shock wave". In: *Fluid Dynamics* 39.2 (2004), pp. 330–338. DOI: https://doi.org/10.1023/B:FLUI.0000030316.35579.73.

[33] S M Boldyrev et al. "A thorough experimental investigation of shock/shock interferences in high Mach number flows". In: *Aerospace science and technology* 5.3 (2001), pp. 167–178. DOI: https://doi.org/10.1016/S1270-9638(01)01094-X.

[34] W Bordelon, A Frost, and D Reed. "Stage separation wind tunnel tests of a generic TSTO launch vehicle". In: *21st AIAA Applied Aerodynamics Conference*. 2013, p. 4227. DOI: https://doi.org/10.2514/6.2003-4227.

[35] V Y Borovoy et al. "Interference between a cylindrical bow shock and a plane oblique shock". In: *AIAA journal* 35.11 (1997), pp. 1721–1728. DOI: https://doi.org/10.2514/2.41.

[36] A Botin. "Interference between a blunt edge shock layer and an impinging inclined shock at low Reynolds numbers". In: *Fluid Dynamics* 28.1 (1993), pp. 126–130. DOI: https://doi.org/10.1007/BF01055675.

[37] T T Bramlette. "Simple Technique for Predicting Type III and IV Shock Interference". In: *AIAA journal* 12.8 (1974), pp. 1151–1152. DOI: https://doi.org/10.2514/3.49435.

[38] C S Butler et al. "Dynamics of a spherical body shedding from a hypersonic ramp. Part 2. Viscous flow". In: *Journal of Fluid Mechanics* 906 (2020). DOI: https://doi.org/10.1017/jfm.2020.757.

[39] G Cammi et al. "Automatic detection of oblique shocks and simple waves in Schlieren images of two-dimensional supersonic steady flows". In: *Measurement* 168 (2021), p. 108260. DOI: https://doi.org/10.1016/j.measurement.2020.108260.

[40] A Carbognani. "The great Chinese fireball of December 22, 2020". In: *The European Physical Journal Plus* 136.6 (2021), pp. 1–9. DOI: https://doi.org/10.1140/epjp/s13360-021-01504-x.

[41] V Cardona, R Joussot, and V Lago. "Shock/shock interferences in a supersonic rarefied flow: experimental investigation". In: *Experiments in Fluids* 62.6 (2021), pp. 1–14. DOI: https://doi.org/10.1007/s00348-021-03225-4.

[42] V Cardona and V Lago. "The effect of rarefaction level on shock/shock interferences applied to atmospheric re-entry: experimental study in a supersonic rarefied flow". In: *2nd International Conference on Flight Vehicles, Aerothermodynamics and Re-entry Missions and Engineering*. 2022.

[43] A B Carlson and R G Wilmoth. "Shock interference prediction using direct simulation Monte Carlo". In: *Journal of Spacecraft and Rockets* 29.6 (1992), pp. 780–785. DOI: https://doi.org/10.2514/3.25531.

[44] P A Chambre and S A Schaaf. "Flow of rarefied gases". In: *Flow of Rarefied Gases*. Princeton University Press, 1961. DOI: https://doi.org/10.1515/9781400885800.

[45] A C Charters and R N Thomas. "The aerodynamic performance of small spheres from subsonic to high supersonic velocities". In: *Journal of the Aeronautical sciences* 12.4 (1945), pp. 468–476. DOI: http://dx.doi.org/10.2514/8.11287.

[46] J Cheng et al. "Aerothermodynamic study of Two-Stage-To-Orbit system composed of wide-speed-range vehicle and rocket". In: *Acta Astronautica* 183 (2021), pp. 330–345. DOI: https://doi.org/10.1016/j.actaastro.2020.11.034.

[47] A Chpoun and J C Lengrand. "Confirmation expérimentale d'un phénomène d'hystérésis lors de l'interaction de deux chocs obliques de familles différentes". In: *Comptes Rendus de l'Académie des Sciences-Series IIB-Mechanics-Physics-Chemistry-Astronomy* 324.1 (1997), pp. 1–8. DOI: https://doi.org/10.1016/S1251-8069(99)80001-3.

[48] P Christou. "Développement de moyens de diagnostic utilisables dans des écoulements raréfiés". Paris 6, 1997.

[49] F Colas et al. "FRIPON: a worldwide network to track incoming meteoroids". In: *Astronomy & Astrophysics* 644 (2020), A53. DOI: https://doi.org/10.1051/0004-6361/202038649.

[50] Inter-Agency Space Debris Coordination Comittee. *IADC Space Debris Mitigation Guidelines*. 2020. URL: https://orbitaldebris.jsc.nasa.gov/library/iadc-space-debris-guidelines-revision-2.pdf.

[51] Inter-Agency Space Debris Coordination Comittee. *IADC Space Debris Mitigation Guidelines*. 2021. URL: https://www.iadc-home.org/documents_public/file_down/id/5249.

[52] S Coumar. "Study of physical mechanisms induced by a plasma actuator for super/hypersonic rarefied flows applied to atmospheric entries". Université d'Orléans, 2017. URL: https://tel.archives-ouvertes.fr/tel-01868262.

[53] S Coumar and V Lago. "Influence of Mach number and static pressure on plasma flow control of supersonic and rarefied flows around a sharp flat plate". In: *Experiments in Fluids* 58.6 (2017), p. 74. DOI: https://doi.org/10.1007/s00348-017-2346-6.

[54] H Covington. "Quanta". In: *Physics World* (2009). DOI: 10.1088/2058-7058/22/01/1.

[55] R N Cox. "Experimental facilities for hypersonic research". In: *Progress in Aeronautical Sciences* 3 (1962), pp. 137–178. DOI: https://doi.org/10.1016/B978-1-4831-9984-9.50006-X.

[56] S Cui et al. "Image processing techniques in shockwave detection and modeling". In: *Journal of Signal and Information Processing* 4.3B (2013), p. 109. DOI: doi:10.4236/jsip.2013.43B019.

[57] D D'Ambrosio. "Numerical prediction of laminar shock/shock interactions in hypersonic flow". In: *Journal of spacecraft and rockets* 40.2 (2003), pp. 153–161. DOI: https://doi.org/10.2514/2.3947.

[58] G Dechriste. "Méthodes numériques pour la simulation d'écoulements de gaz raréfiés autour d'obstacles mobiles". Université de Bordeaux, 2014.

[59] C F Dewey. "Near wake of a blunt body at hypersonic speeds". In: *AIAA journal* 3.6 (1965), pp. 1001–1010. DOI: https://doi.org/10.2514/3.3045.

[60] S Dietrich and I Boyd. "A scalar optimized parallel implementation of the DSMC method". In: *32nd Aerospace Sciences Meeting and Exhibit*. 1994, p. 355. DOI: https://doi.org/10.2514/6.1994-355.

[61] B Diop. "Développement d'un instrument de mesure basée sur la FFE (Fluorescence par Faisceau d'Electrons) pour la caractérisation d'écoulements hypersoniques de basses densités en aérodynamique de rentrée". PhD. Ecole Polytechnique, 2011.

[62] V K Dogra, R G Wilmoth, and J N Moss. "Aerothermodynamics of a 1.6-meter-diameter sphere in hypersonic rarefied flow". In: *AIAA Journal* 30.7 (1992), pp. 1789–1794. DOI: https://doi.org/10.2514/3.11137.

[63] V K Dogra et al. "Hypersonic rarefied flow past spheres including wake structure". In: *Journal of Spacecraft and Rockets* 31.5 (1994), pp. 713–718. DOI: https://doi.org/10.2514/3.26503.

[64] V G Dulov, V Y Levchenko, and A M Kharitonov. "Progress of aerodynamic research at the Institute of Theoretical and Applied Mechanics, Siberian Branch, Academy of Sciences of the USSR". In: *Journal of Applied Mechanics and Technical Physics* 28.4 (1987), pp. 550–567.

[65] B Edney. *Anomalous heat transfer and pressure distributions on blunt bodies at hypersonic speeds in the presence of an impinging shock*. Tech. rep. Flygtekniska Forsoksanstalten, Stockholm (Sweden), 1968.

[66] J T Emmert et al. "NRLMSIS 2.0: A whole-atmosphere empirical model of temperature and neutral species densities". In: *Earth and Space Science* 8.3 (2021), e2020EA001321. DOI: https://doi.org/10.1029/2020EA001321.

[67] ESOC. *ESA's annual space environment report GEN-DB-LOG-00288-OPS-SD*. Tech. rep. ESA, 22 April 2022. URL: https://www.sdo.esoc.esa.int/environment_report/Space_Environment_Report_latest.pdf.

[68] S. Fauqueux. *Marine pollution caused by space debris*. Ed. by Space Legal Issues. 2020. URL: https://www.spacelegalissues.com/marine-pollution-caused-by-space-debris/.

[69] C Finzi et al. "Simulation of the ariane 5 epc reentry with the fragmentation tool suite". In: *7th European Conference on Space Debris, ESA*. 2017.

[70] T Fisher, M K Quinn, and K Smith. "Free-Flight Testing of Hypersonic Edney Shock Interactions". In: *2018 Aerodynamic Measurement Technology and Ground Testing Conference*. 2018, p. 4283. DOI: https://doi.org/10.2514/6.2018-4283.

[71] T B Fisher. *Development of advanced techniques for aerodynamic assessment of blunt bodies in hypersonic flows*. The University of Manchester (United Kingdom), 2019.

[72] A Flores-Abad et al. "A review of space robotics technologies for on-orbit servicing". In: *Progress in aerospace sciences* 68 (2014), pp. 1–26. DOI: https://doi.org/10.1016/j.paerosci.2014.03.002.

[73] T R Fujimoto, T Kawasaki, and K Kitamura. "Canny-Edge-Detection/Rankine-Hugoniot-conditions unified shock sensor for inviscid and viscous flows". In: *Journal of Computational Physics* 396 (2019), pp. 264–279. DOI: https://doi.org/10.1016/j.jcp.2019.06.071.

[74] Michael A Gallis. *Graeme A. Bird*. 2019. DOI: https://doi.org/10.1063/1.5134652.

[75] B Gao and JD Mathews. "High-altitude meteors and meteoroid fragmentation observed at the Jicamarca Radio Observatory". In: *Monthly Notices of the Royal Astronomical Society* 446.4 (2015), pp. 3404–3415. DOI: https://doi.org/10.1093/mnras/stu2176.

[76] A Gares. *Une météorite illumine le ciel dans le Nord-Ouest de la France*. 2020. URL: https://actu.fr/insolite/l-image-une-meteorite-illumine-le-ciel-dans-le-nord-ouest-de-la-france_36717435.html.

[77] C Glass, A Wieting, and M Holden. "Effect of leading edge sweep on shock-shock interference at Mach 8". In: *27th Aerospace Sciences Meeting*. 1989, p. 271. DOI: https://doi.org/10.2514/6.1989-271.

[78] C E Glass. *Numerical simulation of low-density shock-wave interactions*. Tech. rep. NASA Langley Research Center, 1999.

[79] V K Golubev. "Computational visualization of aerodynamic interaction of simple objects in supersonic flows". In: *15th International Symposium on Flow Visualization*. 2012.

[80] A Grantz. "X-37B orbital test vehicle and derivatives". In: *AIAA Space 2011 Conference & Exposition*. 2011, p. 7315. DOI: https://doi.org/10.2514/6.2011-7315.

[81] F Grasso et al. "Type III and type IV shock/shock interferences: theoretical and experimental aspects". In: *Aerospace Science and technology* 7.2 (2003), pp. 93–106. DOI: https://doi.org/10.1016/S1270-9638(02)00005-6.

[82] V N Gusev and A I Erofeev. "Oblique shock/bow shock interference in rarefied flow past a cylinder". In: *Fluid dynamics* 39.5 (2004), pp. 827–835. DOI: https://doi.org/10.1007/s10697-005-0017-4.

[83] K Hanai, H Ozawa, and Y Nakamura. "Two-stage-to-orbit booster configuration for reducing aerodynamic heating at hypersonic speed". In: *37th AIAA Fluid Dynamics Conference and Exhibit*. 2007, p. 4220. DOI: https://doi.org/10.2514/6.2007-4220.

[84] J K Harvey, R W Jeffery, and D C Uppington. *The Imperial College graphite heated hypersonic wind tunnel*. Tech. rep. Imperial College, Department of Aeronautics, 1971.

[85] P E Hemke. *Influence of the orifice on measured pressures*. N.A.C.A. Technical Note No.250. Langley Memorial Aeronautical Laboratory, 1926.

[86] A J Hodges. "The drag coefficient of very high velocity spheres". In: *Journal of Aeronautical Sciences* 24.10 (1957), pp. 755–758. DOI: http://dx.doi.org/10.2514/8.3958.

[87] M Holden, K Rodriguez, and R Nowak. "Studies of shock/shock interaction on smooth and transpiration-cooled hemispherical nosetips in hypersonic flow". In: *22nd Fluid Dynamics, Plasma Dynamics and Lasers Conference*. 1992, p. 1765. DOI: https://doi.org/10.2514/6.1991-1765.

[88] M S Holden, J R Moselle, and J Lee. *Studies of aerothermal loads generated in regions of shock/shock interaction in hypersonic flow*. Tech. rep. Calpsan-ub Research Center Buffalo, New York, 1991.

[89] S H Hossein et al. "Sapienza Space debris Observatory Network (SSON): A high coverage infrastructure for space debris monitoring". In: *Journal of Space Safety Engineering* 7.1 (2020), pp. 30–37. DOI: https://doi.org/10.1016/j.jsse.2019.11.001.

[90] E Howell. "Trash bag jettisoned from space station in waste-management first". In: *Space.com* (2022). URL: https://www.space.com/trash-bag-jettisoned-space-station-nanoracks.

[91] C G Miller III. *An experimental investigation of support interference on a blunt body of revolution at a mach number of approximately 20*. Tech. rep. 1965.

[92] P Jenniskens et al. "Bolide fragmentation: What parts of asteroid 2008 TC3 survived to the ground?" In: *Meteoritics & Planetary Science* 57.9 (2022), pp. 1641–1664. DOI: https://doi.org/10.1111/maps.13892.

[93] J Jia et al. "Hypersonic aerodynamic interference investigation for a two-stage-to-orbit model". In: *Acta Astronautica* 168 (2020), pp. 138–145. DOI: https://doi.org/10.1016/j.actaastro.2019.11.038.

[94] E Josyula and J Burt. *Review of rarefied gas effects in hypersonic applications*. Tech. rep. U.S. Air Force Research Laboratory Wright-Patterson Air Force Base, Ohio, USA, 2011.

[95] S Kaineg. "The Growing Problem of Space Debris". In: *Hastings Envt'l LJ* 26 (2020), p. 277.

[96] V M Kalugin. "Glow discharge measurement of gas density in supersonic rarefied flow". In: *Journal of Applied Mechanics and Technical Physics* 10.2 (1969), pp. 277–281. DOI: https://doi.org/10.1007/BF00913117.

[97] S Kan. "China's anti-satellite weapon test". In: Library of Congress Washington DC Congressional Research Service. 2007. URL: https://apps.dtic.mil/sti/pdfs/ADA468025.pdf.

[98] P Kärräng, T Lips, and T Soares. "Demisability of critical spacecraft components during atmospheric re-entry". In: *Journal of Space Safety Engineering* 6.3 (2019), pp. 181–187. DOI: https://doi.org/10.1016/j.jsse.2019.08.003.

[99] L L Kavanau. "Base pressure studies in rarefied supersonic flows". In: *Journal of the Aeronautical Sciences* 23.3 (1956), pp. 193–207. DOI: https://doi.org/10.2514/8.3536.

[100] D J Kessler. *Orbital debris environment for spacecraft designed to operate in low Earth orbit*. Vol. 100471. National Aeronautics and Space Administration, 1989.

[101] J W Keyes and F D Hains. *Analytical and experimental studies of shock interference heating in hypersonic flows*. NASA-TN-D-7139, L-8423. NASA, 1973.

[102] S A Khan, A Aabid, and C A Saleel. "CFD simulation with analytical and theoretical validation of different flow parameters for the wedge at supersonic Mach number". In: *International Journal of Mechanical and Mechatronics Engineering* 1 (2019).

[103] A Khatta and J Gopalan. "Hypersonic shock tunnel studies of Edney Type III and IV shock interactions". In: *Aerospace Science and Technology* 72 (2018), pp. 335–352. DOI: https://doi.org/10.1016/j.ast.2017.11.001.

[104] N Kianvashrad and D D Knight. "Shock-Shock Interaction over a Hemisphere in Hypersonic Flow". In: *AIAA Scitech 2019 Forum*. 2019, p. 0890. DOI: https://doi.org/10.2514/6.2019-0890.

[105] N Kianvashrad and D D Knight. "Shock-Shock Interaction over a Hemisphere in Hypersonic Flow-Part II". In: *AIAA Scitech 2020 Forum*. 2020, p. 2056. DOI: https://doi.org/10.2514/6.2020-2056.

[106] S Kim et al. "Procedure and methodologies for managing the risk of space object reentry". In: *Advances in Space Research* 67.6 (2021), pp. 1844–1858. DOI: https://doi.org/10.1016/j.asr.2021.01.003.

[107] K Kitamura et al. "CFD Analysis of Aerodynamic Interference between a Delta Wing and a Hemisphere-cylinder". In: *42nd AIAA Aerospace Sciences Meeting and Exhibit*. 2004, p. 1378. DOI: https://doi.org/10.2514/6.2004-1378.

[108] G Klopfer and H Yee. "Viscous hypersonic shock-on-shock interaction on blunt cowl lips". In: *26th Aerospace Sciences Meeting*. 1988, p. 233. DOI: https://doi.org/10.2514/6.1988-233.

[109] M Knudsen. *Kinetic theory of gases*. Ed. by London Methuen & co. Ltd. 1934.

[110] G Koppenwallner. "The drag of simple shaped bodies in the rarefied hypersonic flow regime". In: *20th Thermophysics Conference*. 1985, p. 998. DOI: https://doi.org/10.2514/6.1985-998.

[111] G Koppenwallner and H Legge. "Drag of bodies in rarefied hypersonic flow". In: *Progress in Aeronautics and Astronautics* 103.44 (1986). DOI: 10.2514/4.865770.

[112] G Koppenwallner et al. "SCARAB - A multi-disciplinary code for destruction analysis of space-craft during re-entry". In: *Fifth European symposium on Aerothermodynamics for Space Vehicles*. 2005, p. 281.

[113] L Kovacs et al. "Detection method for shock-waves in viscous flows". In: *Experiments in Fluids* 63.1 (2022), pp. 1–16. DOI: https://doi.org/10.1007/s00348-021-03360-y.

[114] P H Krisko. "The predicted growth of the low-Earth orbit space debris environment—an assessment of future risk for spacecraft". In: *Proceedings of the Institution of Mechanical Engineers, Part G: Journal of Aerospace Engineering* 221.6 (2007), pp. 975–985. DOI: https://doi.org/10.1243/09544100JAERO192.

[115] S J Laurence and R Deiterding. "Shock-wave surfing". In: *Journal of fluid mechanics* 676 (2011), pp. 396–431. DOI: https://doi.org/10.1017/jfm.2011.57.

[116] S J Laurence, R Deiterding, and G Hornung. "Proximal bodies in hypersonic flow". In: *Journal of Fluid Mechanics* 590 (2007), pp. 209–237. DOI: https://doi.org/10.1017/S0022112007007987.

[117] S J Laurence, N J Parziale, and R Deiterding. "Dynamical separation of spherical bodies in supersonic flow". In: *Journal of fluid mechanics* 713 (2012), pp. 159–182. DOI: https://doi.org/10.1017/jfm.2012.453.

[118] A Ledkov and V Aslanov. "Review of contact and contactless active space debris removal approaches". In: *Progress in Aerospace Sciences* 134 (2022), p. 100858. DOI: https://doi.org/10.1016/j.paerosci.2022.100858.

[119] D Leiser et al. "Analysis of Reentry and Break-Up Forces from Impulse Facility Experiments and Numerical Rebuilding". In: *Journal of Spacecraft and Rockets* (2022), pp. 1–13. DOI: https://doi.org/10.2514/1.A35204.

[120] G Li et al. "Particle-to-particle long range interaction and drag in supersonic flows". In: *42nd AIAA Aerospace Sciences Meeting and Exhibit*. 2004, p. 1064. DOI: https://doi.org/10.2514/6.2004-1064.

[121] T Li, J Sui, and C Wu. "Numerical investigation of dynamical behavior of tethered rigid spheres in supersonic flow". In: *Applied Mathematics and Mechanics* 37.6 (2016), pp. 749–760. DOI: http://dx.doi.org/10.1007/s10483-016-2090-6.

[122] T Li et al. "Dynamical separation of rigid bodies in supersonic flow". In: *Science China Technological Sciences* 58.12 (2015), pp. 2110–2121. DOI: https://doi.org/10.1007/s11431-015-5966-1.

[123] C A Lind. "Effect of geometry on the unsteady type-IV shock interaction". In: *Journal of aircraft* 34.1 (1997), pp. 64–71. DOI: https://doi.org/10.2514/2.2136.

[124] C A Lind and M J Lewis. "Computational analysis of the unsteady type IV shock interaction of blunt body flows". In: *Journal of propulsion and power* 12.1 (1996), pp. 127–133. DOI: https://doi.org/10.2514/3.24000.

[125] C A Lind and M J Lewis. "Unsteady characteristics of a hypersonic type IV shock interaction". In: *Journal of aircraft* 32.6 (1995), pp. 1286–1293. DOI: https://doi.org/10.2514/3.46876.

[126] J-C Liou. "Risks from orbital debris and space situational awareness". In: (2020).

[127] T Lips. "Equivalent re-entry breakup altitude and fragment list". In: *6th European Conference on Space Debris*. 2013, p. 54.

[128] T Lips and B Fritsche. "A comparison of commonly used re-entry analysis tools". In: *Acta Astronautica* 57.2-8 (2005), pp. 312–323. DOI: https://doi.org/10.1016/j.actaastro.2005.03.010.

[129] T Lips et al. "Spacecraft destruction during re-entry–latest results and development of the SCARAB software system". In: *Advances in Space Research* 34.5 (2004), pp. 1055–1060. DOI: https://doi.org/10.1016/j.asr.2003.01.012.

[130] Y Liu et al. "A CNN-based shock detection method in flow visualization". In: *Computers & Fluids* 184 (2019), pp. 1–9. DOI: https://doi.org/10.1016/j.compfluid.2019.03.022.

[131] E Loth et al. "Supersonic and hypersonic drag coefficients for a sphere". In: *AIAA journal* 59.8 (2021), pp. 3261–3274. DOI: https://doi.org/10.2514/1.J060153.

[132] E S Love. *A summary of information on support interference at transonic and supersonic speeds*. Tech. rep. 1954.

[133] H Lu et al. "Interaction of isentropic compression waves with a bow shock". In: *AIAA journal* 51.10 (2013), pp. 2474–2484. DOI: https://doi.org/10.2514/1.J052373.

[134] F K Lutgens and E J Tarbuck. *Transparency Pack: The Atmosphere*. Prentice Hall, 2001. URL: https://cpb-us-e1.wpmucdn.com/journeys.dartmouth.edu/dist/f/8272/files/2021/12/Meteorology-Textbook-compressed.pdf.

[135] MN Macrossan. "Scaling parameters for hypersonic flow: correlation of sphere drag data". In: *25th International Symposium on Rarefied Gas Dynamics*. St Petersburg, Russia, 2007, pp. 759–764.

[136] D Marren and F Lu. *Advanced hypersonic test facilities*. 2002. DOI: https://doi.org/10.2514/4.866678.

[137] A Marwege et al. "Superposition Method for Force Estimations on Bodies in Supersonic and Hypersonic Flows". In: *Journal of Spacecraft and Rockets* 55.5 (2018), pp. 1166–1180. DOI: https://doi.org/10.2514/1.A34128.

[138] M L Mason. *Experimental Investigation of Shock-Shock Interactions Over a 2D Wedge at M= 6*. TP-20205011524. NASA, Langley Research Center, Hampton, Virginia, 2020.

[139] J C McDowell. "The edge of space: Revisiting the Karman Line". In: *Acta Astronautica* 151 (2018), pp. 668–677. DOI: https://doi.org/10.1016/j.actaastro.2018.07.003.

[140] P M Mehta et al. "Surrogate model for probabilistic modeling of atmospheric entry for small NEO's". In: *Spaceflight Mechanics 2016. Advances in the Astronautical Sciences*. 2016, pp. 1807–1822.

[141] E Meisse and J E Martinez-Morales. "Preliminary Design of a Space Vehicle for Active Debris Removal (ADR): PERSEPHONE". In: *9th European Conference for Aeronautics and Space Sciences (EUCASS)*. 2022. DOI: DOI:10.13009/EUCASS2022-7219.

[142] A More and S Murugan. "Dynamics of morphing robotic arm with space debris capture". In: *8th European Conference on Space Debris*. ESA Space Debris Office, 2021.

[143] M Moreno-Ibanez et al. "Verification of the flow regimes based on high-fidelity observations of bright meteors". In: *The Astrophysical Journal* 863.2 (2018), p. 174. DOI: https://doi.org/10.3847/1538-4357/aad334.

[144] J N Moss et al. "DSMC simulation of shock/shock interactions : emphasis on type IV interactions". In: *22nd International Symposium on Shock Waves*. 1999.

[145] J Murcia, U Guedes, and A Prado. "Propagation of the trajectories for reentry spherical debris including rotation, melting fragmentation and voxel method". In: *Journal of Physics: Conference Series*. IOP Publishing. 2019, p. 012011. DOI: https://doi.org/10.1088/1742-6596/1365/1/012011.

[146] S K Muthoo and C L Brundin. "Near wake flow field measurements behind spheres in low Reynolds number hypersonic flow". In: *Rarefied gas dynamics* (1974).

[147] W Nachtigall and U Hanauer-Thieser. "Flight of the honeybee". In: *Journal of Comparative Physiology B* 162.3 (1992), pp. 267–277. DOI: 10.1007/BF00357534.

[148] T Nagata et al. "Investigation on subsonic to supersonic flow around a sphere at low Reynolds number of between 50 and 300 by direct numerical simulation". In: *Physics of Fluids* 28.5 (2016), p. 056101. DOI: https://doi.org/10.1063/1.4947244.

[149] I Nakamura. "Steady wake behind a sphere". In: *The Physics of Fluids* 19.1 (1976), pp. 5–8. DOI: https://doi.org/10.1063/1.861328.

[150] NASA. "Orbital debris". In: *Quarterly News* 25.1 (2021), pp. 1–12. URL: https://orbitaldebris.jsc.nasa.gov/quarterly-news/pdfs/odqnv25i1.pdf.

[151] H Noubel and V Lago. "Experimental Analysis of Waverider Lift-to-Drag Ratio Measurements in Rarefied and Supersonic Regime". In: *Hypersonic Vehicles-Applications, Recent Advances, and Perspectives*. IntechOpen, 2021. DOI: http://dx.doi.org/10.5772/intechopen.100328.

[152] *NRLMSIS Atmosphere Model*. https://kauai.ccmc.gsfc.nasa.gov/instantrun/msis.

[153] C Ostrom and C Sanchez. "ORSAT Modelling and Assessment". In: *International Workshop on Space Debris Re-Entry*. JSC-E-DAA-TN52795. 2018.

[154] N Pachler, I Del Portillo, and E F Crawleyand B G Cameron. "An updated comparison of four low earth orbit satellite constellation systems to provide global broadband". In: *2021 IEEE international conference on communications workshops (ICC workshops)*. IEEE. 2021, pp. 1–7. DOI: 10.1109/ICCWorkshops50388.2021.947.

[155] R Paciorri and A Bonfiglioli. "Accurate detection of shock waves and shock interactions in two-dimensional shock-capturing solutions". In: *Journal of Computational Physics* 406 (2020), p. 109196. DOI: https://doi.org/10.1016/j.jcp.2019.109196.

[156] I Pădurariu. "Space debris, another environmental issue". In: *Challenges of the Knowledge Society* (2022), pp. 323–331.

[157] B N Pamadi et al. "Simulation and analyses of stage separation of two-stage reusable launch vehicles". In: *Journal of Spacecraft and Rockets* 44.1 (2007), pp. 66–80. DOI: https://doi.org/10.2514/1.17896.

[158] R Paoli. "Numerical Simulations of Shock-Shock Interactions". In: *Open Journal of Fluid Dynamics* 8.4 (2018), pp. 392–403. DOI: https://doi.org/10.4236/ojfd.2018.84025.

[159] C Park and J D Brown. "Fragmentation and spreading of a meteor-like object". In: *The Astronomical Journal* 144.6 (2012), p. 184. DOI: https://doi.org/10.1088/0004-6256/144/6/184.

[160] S H Park, H D Kim, and G Park. "Orbit, orbital lifetime, and reentry survivability estimation for orbiting objects". In: *Advances in Space Research* 62.11 (2018), pp. 3012–3032. DOI: https://doi.org/10.1016/j.asr.2018.08.016.

[161] S H Park and G Park. "Separation process of multi-spheres in hypersonic flow". In: *Advances in Space Research* 65.1 (2020), pp. 392–406. DOI: https://doi.org/10.1016/j.asr.2019.10.009.

[162] S H Park et al. "Experimental study of separation behavior of two bodies in hypersonic flow". In: *Acta Astronautica* 181 (2021), pp. 414–426. DOI: https://doi.org/10.1016/j.actaastro.2021.01.037.

[163] S H Park et al. "Re-entry survival analysis and ground risk assessment of space debris considering by-products generation". In: *Acta Astronautica* (2020). DOI: https://doi.org/10.1016/j.actaastro.2020.09.034.

[164] Q R Passey and H J Melosh. "Effects of atmospheric breakup on crater field formation". In: *Icarus* 42.2 (1980), pp. 211–233. DOI: https://doi.org/10.1016/0019-1035(80)90072-X.

[165] R P Patera. *Spacecraft Reentry*. ATR-2004(9368)-6. 2004.

[166] J Peng et al. "Parameter-correlation study on shock–shock interaction using a machine learning method". In: *Aerospace Science and Technology* 107 (2020), p. 106247. DOI: https://doi.org/10.1016/j.ast.2020.106247.

[167] J Peng et al. "Transitional wave configurations between Type III and IV oblique-shock/bow-shock interactions". In: *Chinese Journal of Aeronautics* (2022). DOI: https://doi.org/10.1016/j.cja.2022.08.006.

[168] A Pikus et al. "DSMC-SPARTA implementation of majorant collision frequency scheme". In: *AIP Conference Proceedings*. Vol. 2132. 1. AIP Publishing LLC. 2019, p. 070026. DOI: https://doi.org/10.1063/1.5119580.

[169] O P Popova et al. "Formation of disturbed area around fast meteor body". In: *The Institute of Space and Astronautical Science* Report SP No. 15 (2003), p. 199.

[170] T Pot et al. "Fundamental study of shock/shock interference in low density flow: flowfield measurements by DLCARS". In: *RGD : rarefied gas dynamics (Marseille, 26-31 July 1998)*. 1999, pp. 545–552.

[171] J Potter and A Bailey. "Pressures in the stagnation regions of blunt bodies in rarefied flow". In: *AIAA Journal* 2.4 (1964), pp. 743–744. DOI: https://doi.org/10.2514/3.2387.

[172] J Potter and A Bailey. "Pressures in the stagnation regions of blunt bodies in the viscous-layer to merged-layer regimes of rarefied flow". In: *Conference on Physics of Entry into Planetary Atmospheres*. 1963, p. 436. DOI: https://doi.org/10.2514/6.1963-436.

[173] Y Prevereaud et al. "Debris aerodynamic interactions during uncontrolled atmospheric reentry". In: *AIAA Atmospheric Flight Mechanics Conference*. 2012, p. 4582. DOI: https://doi.org/10.2514/6.2012-4582.

[174] M Raffin. "Etude expérimentale d'un diffuseur en écoulement hypersonique de gaz raréfié". PhD thesis. 1971.

[175] G P D Rajasooria and C L Brundin. *An experimental investigation of the laminar near wake behind a circular cylinder in a Mach 6, rarefield air stream*. University of Oxford, 1970.

[176] *Recovered Debris*. 2022. URL: https://reentry.esoc.esa.int/home/recovereddebris.

[177] B L Reeves and L Lees. "Theory of laminar near wake of blunt bodies in hypersonic flow." In: *AIAA journal* 3.11 (1965), pp. 2061–2074.

[178] P J Register et al. "Interactions between asteroid fragments during atmospheric entry". In: *Icarus* 337 (2020), p. 113468. DOI: https://doi.org/10.1016/j.icarus.2019.113468.

[179] N Rembaut. "Rentrée atmosphérique de débris spatiaux: simulations expérimentales en souffleries hypersonique raréfiée et supersonique haute enthalpie". PhD. Université d'Orléans, 2021.

[180] N Rembaut, R Joussot, and V Lago. "Aerodynamical behavior of spherical debris in the supersonic and rarefied wind tunnel MARHy". In: *Journal of Space Safety Engineering* 7.3 (2020), pp. 411–419. DOI: https://doi.org/10.1016/j.jsse.2020.07.031.

[181] E Renard et al. "Maneuvers to reduce Ariane 5 upper stage lifetime duration in orbit". In: *Acta Astronautica* 173 (2020), pp. 442–448. DOI: https://doi.org/10.1016/j.actaastro.2020.04.020.

[182] V V Riabov and A V Botin. "Shock interference in hypersonic rarefied-gas flows near a cylinder". In: *17th Applied Aerodynamics Conference*. 1999, p. 3207. DOI: https://doi.org/10.2514/6.1999-3207.

[183] F Robben and L Talbot. "Measurement of shock wave thickness by the electron beam fluorescence method". In: *The Physics of Fluids* 9.4 (1966), pp. 633–643. DOI: https://doi.org/10.1063/1.1761728.

[184] S Sanderson. "Shock wave interaction in hypervelocity flow". PhD. California Institute of Technology, 1995.

[185] T Schlegat. "Experimental investigation of rarefaction effects on aerodynamic coefficients of slender and blunt re-entry vehicles". DLR, 2018.

[186] M Schouler, Y Prévereaud, and L Mieussens. "Survey of flight and numerical data of hypersonic rarefied flows encountered in earth orbit and atmospheric reentry". In: *Progress in Aerospace Sciences* 118 (2020), p. 100638. DOI: https://doi.org/10.1016/j.paerosci.2020.100638.

[187] P M Sforza. "Chapter 2 - Earth's Atmosphere". In: *Manned Spacecraft Design Principles*. Ed. by Pasquale M. Sforza. Boston: Butterworth-Heinemann, 2016, pp. 13–46. DOI: https://doi.org/10.1016/B978-0-12-804425-4.00002-7.

[188] M A Shoemaker, J C Van Der Ha, and K Fujita. "Trajectory reconstruction of Hayabusa's atmospheric reentry". In: *Acta Astronautica* 71 (2012), pp. 151–162. DOI: https://doi.org/10.1063/1.323828.

[189] W R Sieling. "The Effect of Sting Diameter and Length on Base Pressure at M= 3.88". In: *Aeronautical Quarterly* 19.4 (1968), pp. 368–374.

[190] D J Singh, A Kumar, and S N Tiwari. "Numerical simulation of shock impingement on blunt cowl lip in viscous hypersonic flows". In: *Numerical Heat Transfer, Part A Applications* 20.3 (1991), pp. 329–344. DOI: https://doi.org/10.1080/10407789108944825.

[191] C E Sousa, R Deiterding, and S J Laurence. "Dynamics of a spherical body shedding from a hypersonic ramp. Part 1. Inviscid flow". In: *Journal of Fluid Mechanics* 906 (2020). DOI: https://doi.org/10.1017/jfm.2020.756.

[192] S M Steele. *Can international law provide a basis for actively removing space debris ?* 2020. URL: https://amostech.com/TechnicalPapers/2020/Orbital-Debris/Steele.pdf.

[193] W B Stephenson. *Use of the Pitot tube in very low density flows*. Tech. rep. CALSPAN FIELD SERVICES INC ARNOLD AFS TN AEDC DIV, 1981.

[194] V P Stulov. "Meteoroid destruction and fragmentation in the atmosphere". In: *Doklady Physics*. SP MAIK Nauka/Interperiodica, 2009, pp. 458–461. DOI: https://doi.org/10.1134/S1028335808080132.

[195] VV Svotina and MV Cherkasova. "Space debris removal–Review of technologies and techniques. Flexible or virtual connection between space debris and service spacecraft". In: *Acta Astronautica* (2022). DOI: https://doi.org/10.1016/j.actaastro.2022.09.027.

[196] I Szucs-Csillik. "Analysis and prediction of Tiangong-1 reentry". In: *Romanian Astronomical Journal* (2017).

[197] S Taneda. "Experimental investigation of the wake behind a sphere at low Reynolds numbers". In: *Journal of the physical society of Japan* 11.10 (1956), pp. 1104–1108. DOI: https://doi.org/10.1143/JPSJ.11.1104.

[198] G Tedeschi, H Gouin, and M Elena. "Motion of tracer particles in supersonic flows". In: *Experiments in Fluids* 26.4 (1999), pp. 288–296. DOI: https://doi.org/10.1007/s003480050291.

[199] P Thomas. *Où est tombée la météorite du 25 janvier 2008 ?* URL: http://culturesciencesphysique.ens-lyon.fr/ressource/QS_meteorite_janvier_2008.xml.

[200] D Toussaint et al. "Influence of the rarefaction degree on the aerodynamic performances of hypersonic waveriders: experimental and numerical analysis". In: *2nd International Conference on Flight Vehicles, Aerothermodynamics and Re-entry Missions & Engineering (FAR)*. 2022.

[201] I E Vas and G Koppenwallner. *The Princeton University high pressure hypersonic nitrogen tunnel N-3*. Report 690. Princeton University Department of Aerospace and Mechanical Sciences, 1964.

[202] I E Vas, A M Murman, and S M Bogdonoff. "Studies of wakes of support-free spheres at m equal 16 in helium". In: *AIAA Journal* 3.7 (1965), pp. 1237–1244. DOI: https://doi.org/10.2514/3.3115.

[203] P Vashchenkov, A Kashkovsky, and M Ivanov. "Aerodynamics of fragment in spacecraft wake". In: *Rarefied Gas Dynamics: 23rd International Symposium*. 2003, pp. 226–233. DOI: https://doi.org/10.1063/1.1581554.

[204] J Virgili, P CE Roberts, and N C Hara. "Atmospheric interface reentry point targeting using aerodynamic drag control". In: *Journal of Guidance, Control, and Dynamics* 38.3 (2015), pp. 403–413. DOI: https://doi.org/10.2514/1.G000884.

[205] T Wang. "Analysis of Debris from the Collision of the Cosmos 2251 and the Iridium 33 Satellites". In: *Science & Global Security* 18.2 (2010), pp. 87–118. DOI: https://doi.org/10.1080/08929882.2010.493078.

[206] Y Wang et al. "Experimental study of longitudinal stage separation of two-body configuration in shock tunnel". In: *AIAA Journal* 60.12 (2022), pp. 6940–6946. DOI: https://doi.org/10.2514/1.J062135.

[207] P P Wegener and H Ashkenas. "Wind tunnel measurements of sphere drag at supersonic speeds and low Reynolds numbers". In: *Journal of Fluid Mechanics* 10.4 (1961), pp. 550–560. DOI: https://doi.org/10.1017/S0022112061000354.

[208] T J Whalen and S J Laurence. "Experiments on the separation of sphere clusters in hypersonic flow". In: *Experiments in Fluids* 62.4 (2021), pp. 1–19. DOI: https://doi.org/10.1007/s00348-021-03157-z.

[209] T J Whalen, S J Laurence, and R Deitering. "A numerical investigation of clustered spheres separating in Mach 20 flow". In: *AIAA AVIATION 2020 FORUM*. 2020, p. 2970. DOI: https://doi.org/10.2514/6.2020-2970.

[210] L F Wheeler, P J Register, and D L Mathias. "A fragment-cloud model for asteroid breakup and atmospheric energy deposition". In: *Icarus* 295 (2017), pp. 149–169. DOI: https://doi.org/10.1016/j.icarus.2017.02.011.

[211] C White and K Kontis. "The effect of increasing rarefaction on the Edney type IV shock interaction problem". In: *International Conference on RailNewcastel Talks*. Springer, Cham, 2018, pp. 299–311. DOI: https://doi.org/10.1007/978-3-319-73180-3_23.

[212] A R Wieting. "Experimental Study of Shock Wave Interference Heating on a Cylindrical Leading Edge". PhD. Mechanical & Aerospace Engineering, Old Dominion University, 1987. DOI: https://doi.org/10.25777/d4hn-kp95.

[213] T W Williams and J M Benson. *Preliminary investigation of the use of afterglow for visualizing low-density compressible flows*. NACA - Technical Note 1900. National Advisory Committee for Aeronautics, 1949.

[214] R G Wilmoth, R A Mitcheltree, and J N Moss. "Low-density aerodynamics of the stardust sample return capsule". In: *Journal of spacecraft and rockets* 36.3 (1999), pp. 436–441. DOI: https://doi.org/10.2514/2.3464.

[215] C Windisch, B U Reinartz, and S Müller. "Investigation of unsteady Edney type IV and VII shock–shock interactions". In: *AIAA Journal* (2016), pp. 1846–1861. DOI: https://doi.org/10.2514/1.J054298.

[216] Z Wu et al. "Review of shock wave detection method in CFD post-processing". In: *Chinese Journal of Aeronautics* 26.3 (2013), pp. 501–513. DOI: https://doi.org/10.1016/j.cja.2013.05.001.

[217] W Wuest and G Koppenwallner. "The hypersonic low density wind-tunnel of the Aerodynamische Versuchsanstalt Goettingen-Operational behaviour and results on vibrational relaxation". In: *6th Aerospace Sciences Meeting*. 1968, p. 49. DOI: https://doi.org/10.2514/6.1968-49.

[218] Y Yamamoto. "Study of Complex Three-dimensional Hypersonic Shock Interactions for Future Reusable Space Transport Systems". In: *36th AIAA Thermophysics Conference*. 2003, p. 3900. DOI: https://doi.org/10.2514/6.2003-3900.

[219] I A Zhdan, V P Stulov, and P V Stulov. "Aerodynamic interaction of two bodies in a supersonic flow". In: *Doklady Physics*. Nauka/Interperiodica, 2004, pp. 315–317. DOI: https://doi.org/10.1134/1.1763624.

[220] C Zhu, SC Liang, and L Sh Fan. "Particle wake effects on the drag force of an interactive particle". In: *International journal of multiphase flow* 20.1 (1994), pp. 117–129. DOI: https://doi.org/10.1016/0301-9322(94)90009-4.

[221] W Ziniu et al. "Space debris reentry analysis methods and tools". In: *Chinese Journal of Aeronautics* 24.4 (2011), pp. 387–395. DOI: https://doi.org/10.1016/S1000-9361(11)60046-0.

[222] I Znamenskaya, I Doroshchenko, and N Sysoev. "Edge detection and machine learning application for shadowraph and Schlieren images analysis". In: *19th International Symposium on Flow Visualization*. 2021.

[223] G Zuppardi and D Paterna. "Influence of partial accommodation coefficients on the aerodynamic parameters of an airfoil in hypersonic, rarefied flow". In: *Advances in aircraft and spacecraft science* 2.4 (2015), p. 427. DOI: https://doi.org/10.1243/095441002321029026.

Vincente CARDONA

Interactions aérodynamiques de débris spatiaux lors de la rentrée atmosphérique : étude expérimentale en régime raréfié

Cette thèse porte sur l'étude expérimentale des débris spatiaux pénétrant l'atmosphère à des altitudes de l'ordre de 90 km, où l'air, peu dense, est dit raréfié. A ces altitudes, l'air se densifie peu à peu, menant à d'intenses charges thermiques et de pression. Contraints à ses efforts, les débris vont, dans la majorité des cas, se fragmenter. Si les petits fragments se vaporisent dans l'air, les plus gros vont pénétrer plus amplement l'atmosphère, et possiblement atteindre la surface terrestre. L'inquiétude se pose quant aux risques humains et environnementaux. Il est donc primordial de connaître avec précision la zone et le date d'impact. Deux éléments rendent cette détermination difficile : les interactions entre fragments de débris, et la faible connaissance des écoulements raréfiés. En effet, au sein d'un nuage de débris, les fragments peuvent évoluer à proximité les uns des autres, provoquant des interactions aérodynamiques. Dans le cas d'un débris secondaire évoluant au sein du sillage d'un débris primaire, les interactions aérodynamiques peuvent induire des conditions aérothermodynamiques sévères (pression dynamique, flux thermique), un phénomène de « surf » sur l'onde de choc primaire, ou une modification des coefficients aérodynamiques des débris secondaires. Ces différents impacts sur les débris auront comme conséquence la modification de leur trajectoire et donc de leur impact. Dans le cas d'une fragmentation se produisant à haute altitude, les interactions aérodynamiques vont concerner les régimes d'écoulements raréfiés (de glissement, de transition), caractériser par le nombre de Knudsen. Ces régimes, encore peu connus, nécessitent toujours un gros effort scientifique pour les caractériser. Les codes de calculs actuels peinent encore à identifier, notamment, les conditions de glissement à la paroi des objets, ce qui rend difficile la prise en compte des effets visqueux provenant directement du niveau de raréfaction. En conséquence, les prédictions d'impacts sont encore peu précises et connues bien trop tardivement. A l'heure actuelle, très peu de travaux ont été menés dans ces conditions d'écoulement et pour des configurations d'intérêt : forme et position des débris, nombres de Mach et de Knudsen. L'objectif de cette thèse est de répondre à ce besoin, en étudiant expérimentalement les interactions aérodynamiques entre deux objets sphériques, et plus particulièrement, les interactions choc/choc en découlant. Cette étude expérimentale est réalisée dans la soufflerie MARHy qui permet de générer des écoulements supersoniques et hypersoniques de faible densité. Grâce à différents dispositifs expérimentaux, les interactions choc/choc ont pu être évaluées visuellement, mais également en termes de forces aérodynamiques et pressions pariétales. Pour mieux comprendre les effets de raréfaction locale d'un écoulement, différents ratios de diamètres de sphères ont été étudiés. De même, les effets de raréfaction globale ont pu être évalués avec à une étude iso-Mach (Mach 4) mais différents nombres de Knudsen, rendue possible grâce des tuyères interchangeables. Enfin, une étude hypersonique (Mach 20) raréfiée a mis en évidence une forte augmentation des effets visqueux. Ces expériences ont permis une meilleure compréhension du rôle des effets de raréfaction sur les interactions aérodynamiques entre deux sphères. L'acquisition de cette importante base de données expérimentales pourra enrichir les codes de calculs considérant les écoulements supersoniques et hypersoniques de hautes altitudes, et à long termes, améliorer la prédiction des impacts terrestres.

Mots clés : interaction choc/choc, aérodynamique expérimentale, supersonique / hypersonique, Régime raréfié, soufflerie MARHy, rentrée atmosphérique.

Aerodynamic interaction of space debris during atmospheric re-entry: experimental study in rarefied flow regime

This thesis deals with the experimental study of space debris entering the atmosphere at altitudes of the order of 90 km, where the air, low in density, is said rarefied. At these altitudes, the air gradually becomes denser, leading to intense thermal and pressure loads. In most of the cases, the debris will fragment. While the smaller fragments will vaporize in the air, the larger ones will penetrate further into the atmosphere and possibly reach the Earth's surface. This raises concerns about the human and environmental risks. It is therefore essential to know the precise area and date of impact. Two elements make this determination difficult: the interactions between fragments of debris, and the poor knowledge of rarefied flows. Indeed, within a debris cloud, fragments can evolve in close proximity to each other, causing aerodynamic interactions. In the case of secondary debris evolving in the wake of primary debris, aerodynamic interactions can induce severe aerothermodynamic conditions (dynamic pressure, heat flux), a "surfing" phenomenon on the primary shock wave, or a modification of the aerodynamic coefficients of secondary debris. These different impacts on the debris will result in the modification of its trajectory and therefore its impact. In the case of fragmentation occurring at high altitude, the aerodynamic interactions will concern the rarefied flow regimes (slip, transitional), characterized by the Knudsen number. These regimes, which are still not well known, require a major scientific effort to characterize them. Current calculation codes still struggle to identify, in particular, the slipping conditions at the wall of objects, which makes it difficult to take into account the viscous effects coming directly from the rarefaction level. As a result, the prediction of impact is still not very accurate and known far too late. Currently, very little work has been carried out under these flow conditions and for configurations of interest: shape and position of debris, Mach and Knudsen numbers. The objective of this thesis is to address this need, by experimentally studying the aerodynamic interactions between two spherical objects, and more particularly, the resulting shock/shock interactions. This experimental study is carried out in the MARHy wind tunnel, which allows the generation of low density supersonic and hypersonic flows. Thanks to different experimental devices, the shock/shock interactions can be evaluated visually, but also in terms of aerodynamic forces and parietal pressures. To better understand the local rarefaction effects of a flow, different ratios of sphere diameters were studied. Similarly, the effects of global rarefaction could be evaluated with an iso-Mach study (Mach 4) but different Knudsen numbers, made possible by interchangeable nozzles. Finally, a rarefied hypersonic study (Mach 20) showed a strong increase in viscous effects. These experiments allowed a better understanding of the role of rarefaction effects on the aerodynamic interactions between two spheres. The acquisition of this important experimental database will enrich the calculation codes considering supersonic and hypersonic flows at high altitudes, and in the long term, improve the prediction of terrestrial impacts.

Keywords: shock/shock interferences, experimental aerodynamics, supersonic / hypersonic, rarefied regime, MARHy wind tunnel, atmospheric re-entry.

ICARE – CNRS
1c Avenue de la Recherche Scientifique
45071 Orléans Cedex 2, France